The Role of Impact Driven Chemistry on the Lithosphere of Mars

By

Nisha Khama Ramkissoon

Thesis submitted to the University of Kent

for the degree of

Doctor of Philosophy

School of Physical Sciences

University of Kent

Canterbury, U.K.

October 2016

Declaration

The content of this thesis has been composed by the author, and has not been submitted for a further degree at any other higher educational institute.

The content comprising of Chapter 8, Section 8.1, was adapted and extended from work which has been published by Price & Ramkissoon, *et al.*, (2013).

All data used in this thesis is the author's own, unless stated otherwise.

Abstract

Impacts affect solid bodies in a number of ways, such as causing an immediate chemical change in the shocked minerals. These chemical changes can affect the formation and evolution of terrestrial bodies in the Solar System, particularly atmospheric composition and surface mineralogy. This thesis examines two specific and (potentially) impact induced processes, serpentinisation and devolatilisation, which were investigated using the light gas gun at the University of Kent, and Raman spectroscopy.

The first series of experiments explores impact induced serpentinisation, to determine if it is possible for serpentine to form as a result of water ice and olivine experiencing an impact, and thus produce methane. Autodyn simulations showed the pressures for serpentinisation to occur were achieved within the crater, although, analysis of the target material from laboratory experiments did not corroborate this. However, there were two instances (from one shot) that indicated serpentinisation may have occurred. Overall, results from these experiments did not conclusively prove or disprove impact induced serpentinisation can occur, but it did indicate that it might be possible.

The second process, devolatilisation, was explored using the minerals goethite and gypsum. Two types of experiments were conducted: 1) a quasi-static heating experiment and, 2) impact experiments. Heating experiments showed that both minerals show particular Raman peak characteristics as a result of increasing temperature, which would mean they could be used a geo-thermometers. However, results from the impacts showed that pressure can change the devolatilisation temperature, especially in the case of gypsum. These results also showed that impacts produce changes in the peak characteristics of Raman spectra that were not observed during the heating experiments. They also presented a general trend between the impact velocity and Raman peak characteristics, particularly for goethite. These devolatilisation experiments have shown that it is possible to show the loss of volatiles from minerals and that these types of minerals could, potentially, be used as a shock barometer.

Raman spectroscopy has been used extensively as the main analysis technique for both sets of experiments. Results from these experiments could be used to assist in the interpretation of Raman spectra obtained from the *ExoMars* and *Mars 2020* rovers, which will both have Raman spectrometers on-board.

Acknowledgements

Firstly, I would like to thank my supervisor Dr. Mark Price, for his guidance, support and patience over the course my PhD. I would also like to thank Prof. Mark Burchell for his advice and input during weekly lab meetings, which have been invaluable.

I would like to take the opportunity to thank the University of Kent for allowing me to do my PhD, and UKSA/STFC *Aurora* science for my funding. I would also like to show my gratitude to Anton Kearsley (previously at the NHM) for providing me with some of the samples used in my experiments.

My sincerest thanks go to Dr. Penny Wozniakiewicz and Dr. Kathryn Harriss who have also been there to help with my geology questions and allowing me to bend their ears when I needed to. Mike Cole, thank you for teaching me how to use the light gas gun, discussing problems that came up in my experiments, the general chats we had and most importantly allowing me to take my "brain breaks" in the impact lab. Thank you to all my friends in 104, who made the hard days a lot easier and all the days fun.

I would also like to thank my wonderful family and friends in London who have always been immensely supportive and understanding, but particularly even more so during the final stages of my PhD.

Contents

List of Figures

List of Tables

Chapter I

Introduction

Impacts have played a major role in the formation and evolution of terrestrial planets, satellites and other planetary bodies since the beginning of the Solar System's history. Terrestrial bodies throughout the Solar System show the scars created by impacts that have occurred since their formation. Computer modelling suggests impacts between small particles of dust formed planetismals, under the influence of gravity. These planetismals eventually collided to form larger bodies and planets; this theory on planet formation has become known at the accretion model (described in Chambers, 2004). It is thought that planetary atmospheres may have arisen during this early period in their history through the release of volatile compounds, such as H_2O and CO_2, which were trapped within minerals (Benlow & Meadows, 1976). Impacts may also have an effect on the evolution of terrestrial atmospheres through this process, or possibly acting as a trigger to produce trace compounds found in atmospheres.

Mars has been of increasing interest over the past four decades to both planetary scientists and astrobiologists. It is the most probable place other than Earth to find life, which either exists today or may have existed in the distant past. It may also have had the right conditions for liquid H_2O to have existed on the planet's surface. As a result of this, numerous spacecraft (both orbiter and lander missions) equipped with diagnostic equipment have been sent to the red planet to unlock the many secrets it holds, and piece together its 4.6 billion year history. Over the past 15 years three different scientific groups (Mumma *et al.*, 2009; Forminsano *et al.*, 2004; Krasnopolsky *et al.*, 2004) have detected methane within the planet's atmosphere through remote observations. In December 2014 the science team from the National Aeronautics and Space Administration's (NASA) Mars Science Laboratory (MSL) rover announced the detection of methane in the vicinity of Mt. Sharp (Webster *et al.*, 2014). Data obtained from the Tunable Laser Spectrometer (TLS),

a part of the Sample Analysis at Mars (SAM) instrument on board MSL (over a 20 month period), showed mean background levels of methane at 0.69 ± 0.25 parts per billion by volume (ppbv) and an elevated level of 7.2 ± 2.1 ppbv over 60 sols (Webster *et al.,* 2014). The detection of methane on Mars (Webster *et al.,* 2014; Mumma *et al.,* 2009; Forminsano *et al.*, 2004; Krasnopolsky *et al.,* 2004) is of great interest as the vast majority of methane on Earth is formed by biological process. It is believed that the detection of this gas on Mars may point towards the existence of some form of life on the planet, but non-biological processes can also generate methane.

The release of volatile compunds resulting from impacts is of particular interest when examining the surface of Mars. The release of water from hydrated minerals could help provide an answer to questions such as whether or not there has ever been liquid water on Mars and, if it was present for a sufficient duration of time to result in the formation of secondary minerals (such as serpentine, gypsum, goethite). If hydrated minerals were, in fact secondary minerals, then subsequent impacts may have erased them from the planet's surface mineralogy resulting in an incomplete surface history.

1.1 Thesis Objective

The objective of this investigation was to examine the effects of impacts on minerals and, to see if it is possible to indirectly detect these effects by achieving the following goals:

1) Determine if impacts can be used to trigger chemical changes in a mineral that would result in serpentinisation and thus the production of methane.
2) Determine if we can identify the loss of volatiles found within mineral structures as a result of impact and, if the degree of loss could be used as a shock barometer.
3) Determine if either of these changes (goals 1 and 2) can be detected using Raman spectroscopy to support future missions to Mars equipped with such instrumentation.

The two stage light gas gun at the University of Kent was used to simulate impacts, which assisted in achieving the goals outlined above. An investigation into methane production via impact induced serpentinisation assisted in determining if chemical changes in minerals can be induced by impacts. A second investigation into the devolatilisation of minerals, specifically goethite and gypsum, studied how the loss of volatile components through impacts can affect these minerals. Both sets of experiments used a Raman spectrometer to determine whether or not these processes can be indirectly identified. This was achieved

by observing changes in the spectra as a result of the impact and, determining if there are any distinguishing features within the spectra that indicate impact induced changes occurred within the mineral.

1.2 Outline of Thesis

Chapter II provides a general introduction to Mars. It then goes into more detail regarding impacts, mineral devolatilisation, Martian methane and the process of serpentinisation. The aim of this chapter is to provide a solid background for the topics this investigation will contribute to.

Chapter III explains what happens as a shock wave passes through a material upon impact, which also forms the fundamentals of numerical modelling. It also describes the types of numerical solvers and the limitations of the solvers used to model impacts. In addition, this chapter provides information on the modelling software package, Autodyn, which was used to model laboratory impacts in order to determine the impact pressures and temperatures.

Chapter IV goes into detail about the main pieces of equipment utilised for this investigation, which were the two stage light gas gun, Raman spectrometer and scanning electron microscope. Each section provides a general history to the development of the equipment, the theory behind their operating procedures, their construction, and details of limitations for each piece of equipment.

Chapter V outlines the methodology for the first experiment, which examined the possible process of impact induced serpentinisation (which is the focus of goal 1, outlined above). A description of how targets were made and how impacted materials were collected and prepared for analysis is given. It also explains the tests carried out in order to ensure the analysis technique used did not cause any changes that would influence the results and/or damage the impacted materials.

Chapter VI provides the experimental setup for investigating the devolatilisation of minerals (which explores goal 2, outlined above). In addition to this, this chapter explains the experiments undertaken to determine if volatile loss could occur as a result of the analysis technique. A description of the preparation of the mineral projectiles and targets is also provided. It also outlines the procedure used in acquiring Raman spectra whilst

minerals were subjected to heating, which was undertaken to assist with the analysis of results from impacts (goal 3 of this investigation).

Chapter VII details the results obtained from the heating experiments conducted on the materials used in the devolatilisation experiment. It discusses the changes that occurred as a result of increased temperatures and thus, the loss of volatiles. The results from this chapter assisted with the analysis of impacted materials in the devolatilisation experiment.

Chapter VIII presents the results from both sets of impact experiments. Results from the serpentinisation experiment examined shocked olivine grains to determine if serpentinisation had occurred. The results from the devolatilisation experiments were analysed using the results obtained from the heating experiments, to determine if it is possible to quantify the loss of volatiles from impacted materials using Raman spectroscopy.

Chapter IX summarises this investigation's main findings and explains the conclusions drawn from the results. It also suggests future research that can be conducted to further our understanding of this research area.

The final appendices section contains the quantification data obtained from Scanning Electron Microscope (SEM)/Energy Dispersive X-ray analysis (EDX), Raman spectra taken throughout the course of this investigation and images of the impacted target plates.

Chapter II

Background

2.1 Mars

Mars has always been of great interest to humans, this is apparent by the numerous exploration missions that have been sent to the planet. These missions have enabled us to piece together its history from remotely sensed data, obtained by terrestrial telescopes, orbiting spacecraft, rovers and meteorites.

Early observations of Mars made before, and after, the development of the telescope provided much information about the planet's orbit and rotation. But it was not until 1877 that it was discovered that Mars had two orbiting satellites (Phobos and Demios) and high altitude clouds were observed in the planet's atmosphere (in a review by Barlow, 2008). At about the same time humans became fascinated with the idea that Mars may be home to an alien species, which began when Giovanni Schiaparelli reported seeing canals on the surface. However, this was actually the result of a mistranslation from Italian, where he had reported seeing "canali", which mean channels in Italian. But potentially due to the word resembling the English word for canals, these features were believed to be canals and a possible indication for life. It was later discovered that these canals were in fact optical illusions generated by dust storms on the surface. However, that has not dampened humanity's interest in the planet, or the question of whether or not life has or does exist somewhere on the planet, which is seen with the ample amount of fiction books written about Mars and life on Mars.

2.1.1The Exploration of Mars

Over the past 46 years there have been 43 missions sent to observe Mars and its moons, but only 20 of these missions were successful, or partially successful. Seven of the missions to reach Mars were able to successfully deploy landers to the surface of the planet. These

spacecraft and landers have provided a wealth of data about the surface topography, atmosphere composition, surface processes and surface mineralogy and composition.

The first set of images of the surface of Mars taken by spacecraft flybys were obtained from Mariner 4, Mariner 6 and Mariner 7 between 1964 and 1969. The images taken by these spacecraft showed a world void of intelligent life and heavily cratered, much like the Moon. Mariner 4 also discovered the Martian atmosphere was predominantly made up of CO_2 and, the atmospheric pressure was ~ 3 mbar (see review of Mars exploration by Stooke, 2012). Images taken by Mariners 6 and 7 revealed craters, areas of chaotic terrain, and features in the southern polar ice cap (presented in Collins, 1971; Figure 2.1.1).

Figure 2.1.1 (source: Collins, 1971) Images of the Martian surface taken from Mariners 6 and 7. a) The chaotic terrain found on the surface next to relatively smoother terrain. b) Impact craters found in Meridiani Sinus. c) The edge of the southern poles ice cap, which show the shape of craters in the "snow" covered regions. Seeing these features helped to determine that the polar ice caps were not made of water.

Mariner 9 became the first spacecraft to be placed in orbit around Mars, and the Soviet Union's Mars 2 became the first lander to reach the surface, although it did crash. Mars 3 however, did reach the surface relatively intact and was able to send ~20 seconds of data back to Earth; a dust storm occurring at the time is believed to have resulted in the failure of the lander (described in Perminov, 1999). Mariner 9 provided images of tectonic, erosional and depositional activity, which indicates Mars's geological evolution is somewhere in between that of Earth and the Moon (McCauley *et al.*, 1972). The Mars 2 and 3 spacecraft were are able to provide additional information on atmospheric composition, pressure, the variation in surface temperature between day and night, and it showed that Mars had a magnetic field (in a review by Perminov, 1999). These spacecraft marked the beginning of a series of spacecraft and rovers designed to explore the diversity of the planet; with each mission came better analysis equipment and increased instrument sensitivity, providing scientists with an increasingly detailed view of the surface and

atmosphere. The Viking landers, 1 and 2, sent by NASA in 1976 were able to send back images and data on the chemical and physical properties of the surface, temperature and wind direction, gravity, atmospheric water, and thermal mapping (in a review by Greeley, 2013). After the success of these Viking landers and orbiters there was a long gap before spacecraft were sent to observe Mars (with the exception of Fobos missions that were sent to explore Phobos) until finally in 1997 Mars Pathfinder successfully arrived and landed on Mars (Greeley, 2013; Zubrin *et al.,* 2009).

2.1.2 Martian Geology

The Martian surface was first characterised by Scott & Carr (1978) into three stratigraphic units based on features associated with the terrain, which were later subdivided into eight units by Tanaka (1986). The oldest of the three terrains is the Noachian (4.1 to 3.7 Gyr) and is characterised by a high crater density, high erosion and a high rate of valley network formation; the Hesperian (3.7 to 3.0 Gyr) terrains have ridged plains from volcanism, a relatively lower cratering rate than the Noachain, large outflow channels and lower erosion rates; the youngest unit called the Amazonian (3.0 Gyr to present) is dominated by smooth plains from volcanism.

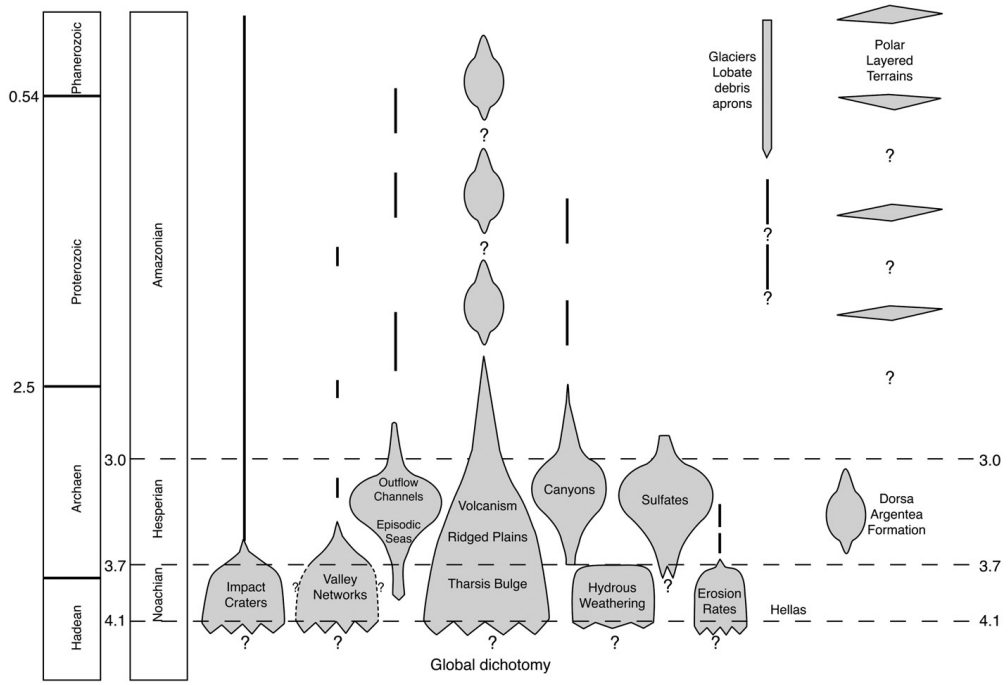

Figure 2.1.2 (Source: Carr & Head, 2010) A schematic of the geological history of Mars, with the formation and lifetimes of specific processes and events. It illustrates that the vast majority of the surface features found on Mars are believed to have formed/occurred within the first 1.5 Gyr of the planet's lifetime.

Mars is home to the largest volcano in the solar system, Olympus Mons, which along with other volcanoes found on the planet shows Mars was once magmatically active. Carr & Head (2010) proposes that volcanism on Mars occurred early in its history when the heat flow was also high, with the majority of activity occurring during the Noachian and until the end of the Hesperian when it began to peter out (Figure 2.1.2). One of the most prominent features on Mars is the Tharsis bulge, which is 4000 km across and 10 km high. It is home to some of Mars's most dominant features, Olympus Mons, the Tharsis Montes volcanoes, and Valles Marineris is located just east of the uplift. Cerberus Fossae, in Elysium Planitia, is believed to be one of the youngest volcanic lava flows on Mars, and has been dated at 200-500 Myrs (Plescia, 1992). The most recent thermal activity is believed to have occurred within the same region around 20 Myr ago, which was the result of a dyke emplacement (Head *et al.*, 2003). Evidence suggests that Mars was once a geologically active planet, but this activity has since died out. Past volcanic activity has resulted in a predominantly basaltic composition of surface rocks; there is also evidence of some alternation producing clays and oxides (Soderblom & Bell, 2008). This has meant that a range of minerals are therefore present on Mars, including pyroxenes, olivine feldspars, sulphates and iron oxides. Data from instruments, such as the Compact Reconnaissance Imaging Spectrometer for Mars (CRISM) and Observatoire pour la Minèralogie l'Eau, les Glaces et l'Activitè (OMEGA), have permitted the mineralogy of the surface to be mapped, and enabled the examination of the distribution of minerals on the surface. The surface can be divided into high and low albedo regions, with each region having a particular mineralogy. Banfield (2002) characterises high albedo regions by poorly crystalline iron oxides, and low albedo areas are distinguished by Ca-rich pyroxenes. In addition Banfield (2002) shows two separated compositions found within the low albedo areas; 1) a more basaltic surface, with higher concentrations of Ca-pyroxenes and plagioclase, and 2) an andesitic surface, which shows lower concentrations of Ca-pyroxene, but with high plagioclase. Hydrous minerals, such as goethite, gypsum and serpentine (Klingelhöfer *et al.*, 2005; Langevin *et al.*, 2005; Showstack, 2011; Wray *et al.*, 2010) have also been detected on Mars. Carter *et al.*, (2013) used both CRISM and OMEGA data to map the distribution of a variety of hydrous minerals, such as Al-rich smectites, phyllosilicates and serpentine to name a few, on older terrains (aged at ~ 4 Gyr). The detection of hydrous minerals has a huge implication for the search for contemporary water on Mars. In addition, the presence of hydrous minerals indicates there was once

water on the Martian surface, which indicates that Mars may have once been able to sustain life.

Martian meteorites have also provided details on the geology of Mars and have allowed scientists to directly analyse them on Earth. Perhaps the most famous Martian meteorite is AH 84001, which was once believed to show evidence of life on Mars (McKay *et al.,* 1996).

There are three main groups of Martian meteorites: 1) Shergottites, which are basaltic in origin, dominated by clinopyroxenes, with some plagioclase; 2) Nakhlites are rich in clinopyroxenes and have experienced aqueous alteration producing secondary minerals, such as carbonates and sulphates, and 3) Chassignites which are composed of approximately 90 % olivine (Grady *et al.,* 2014; Papike *et al.,* 2009). Martian meteorites, particularly from the Nakhlite group, shows evidence of aqueous alteration forming secondary minerals (Gillet *et al.,* 2002; Bridges *et al.,* 2001; Ling and Wang, 2014), which provides additional evidence that water was once present on Mars.

2.1.3 Valley Networks

Valley networks are also prevalent on the Martian surface. On Earth, valley networks are predominantly formed as a result of surface runoff. Therefore, these features would indicate that liquid water was once present on the Martian surface, which itself would indicate that the Martian climate was once much warmer than it is today (Harrison & Grimm, 2005). If these features were produced by surface runoff then it is more than likely that Mars had a hydrological cycle. However, these valley networks may have been formed by alternative processes, such as ground water sapping (Goldspiel & Squyres, 2000). Ground water sapping may have resulted from subsurface aquifers, or from the melting of water ice from thermal activity. It is also possible that these valley networks formed from non-fluvial processes, such as volcanism, lava erosion, fracturing or subsidence (Sharp & Malin, 1975). The formation mechanism for these valley networks would have biological impactions for Mars. The presence of liquid water on the surface would show a warmer, and wetter, climate once existed, and would mean there was a much greater potential for life to have existed on the planet. However, it is possible that water generated from thermal activity may have produced these valley networks (Head *et al.,* 2003). Geomorphological studies of valley networks have shown that surface runoff, from precipitation, have contributed to their formation (e.g. Mangold *et al.,* 2004; Craddock &

Howard, 2002; Hynek *et al.,* 2010). The formation of valley networks formed through precipitation would mean that large bodies of water would have formed on the surface for a period of time.

2.1.4 The Martian Atmosphere

The atmosphere of Mars today is primarily composed of CO_2 (95%), with some N_2, H_2O, O_2, NO and Ar (Mahaffy *et al.,* 2015; Jakosky, 1999, Freedman & Kaufmann III, 2005). Relatively recently detections of methane have been made within the Martian atmosphere, which has gathered the attention of the science community, as it may indicate extant life (Section 2.4 discusses the detection of methane on Mars in more detail). Blamey *et al*., (2015) analysed trapped gases with the Martian meteorites showing a mixture of gases, particularly CO_2, CH_4, H_2 N_2 and some O_2 and Ar. The gases found trapped within Martian meteorites would most likely represent the species of gases found in the atmosphere and the presence of CH_4 corresponds to the detection of this gas made over the past decade.

The indications that have pointed towards the presence of liquid water on the surface would suggest that Mars once had a different atmosphere, which produced warmer surface temperatures, than what are seen today. It has been suggested that Mars had a much denser CO_2 atmosphere (Sagan *et al.*, 1973) or had a CO_2 atmosphere with some CH_4, NH_3 or SO_2 (Squyres & Kasting, 1994), which would have enabled liquid water to flow on the surface. Impact erosion (Melosh & Vickery, 1989) is one possible process that may have resulted in the thinning of the atmosphere, and a second is solar wind erosion. A study by de Niem *et al.,* (2012) suggests that impacts during heavy bombardment may have actually increased the atmospheric pressure by the addition of volatiles, instead of an overall loss of material from the atmosphere. It has also been proposed that either large or multiple, moderately sized, impacts may have resulted in the vaporisation of H_2O ice (Segura *et al.,* 2002; 2008). Segura and colleagues proposed that water vapour could be realised into the atmosphere as a result of impacts melting subsurface ice on Mars. The water vapour in the atmosphere would produce a greenhouse climate that could increase the surface temperatures to above freezing and enable a hydrological cycle to form; these warmer temperatures could potentially last from ~100 days to 10s of years.

2.1.5 Impacts on Mars

Over the course of Mars's history it has been subjected to numerous impacts, which have greatly contributed to what we see on the planet's surface today. Impact craters are wide spread on the surface, and one of the largest of these craters is the Hellas impact crater, found in the southern hemisphere. A variation in the number of impact craters between the northern and southern hemispheres highlights the global topographic dichotomy found on Mars. The dichotomy itself may have been created by a single large impact (Wilhelms & Squyres, 1984) or by smaller multiple impacts (Frey & Schultz, 1989), which would have occurred approximately 300 Myr after the formation of the planet's core (Keller & Tackely, 2008). Impacts have played a role in the evolution of Mars's surface, but craters have also provided an insight into the surface processes occurring on the planet and, they have also exposed subsurface geology. The ejecta and the interior morphology of craters can provide information about the volatile content of the target material (Barlow & Bradley, 1990).

Impacts still occur on the surface of Mars today, and the high resolution cameras on-board orbiters have made it possible to detect new craters down to two metres in diameter (Malin *et al.*, 2006; Ivanov *et al.*, 2010). McEwen *et al.*, (2015) reports that close to 500 new impact craters have been discovered using before and after images taken of the surface (Figure 2.1.3). Twenty of these impact craters were identified by Malin *et al.*, (2006) within an area of 21.5×10^6 km^2, with diameters ranging between 2 and 150 metres, over the course of approximately seven years. New impact craters are detected by examining images of the surface for "dark spots", which are a result of dust on the surface being disturbed by the impact event (Malin *et al.*, 2006). These new craters, and the ability to determine a time frame of when they formed, have enabled better cratering rates to be predicted, such as Daubar *et al.*, (2013) who presents a current impact rate of 1.65×10^{-6} craters/km^2/yr with diameters equal to, or greater than, 3.9 m. However, the technique used for detecting new impact craters is dependent on being able to see these dark spots, and as a result the majority of new craters are found in higher albedo regions and so this number of new impacts craters may be lower than the true number.

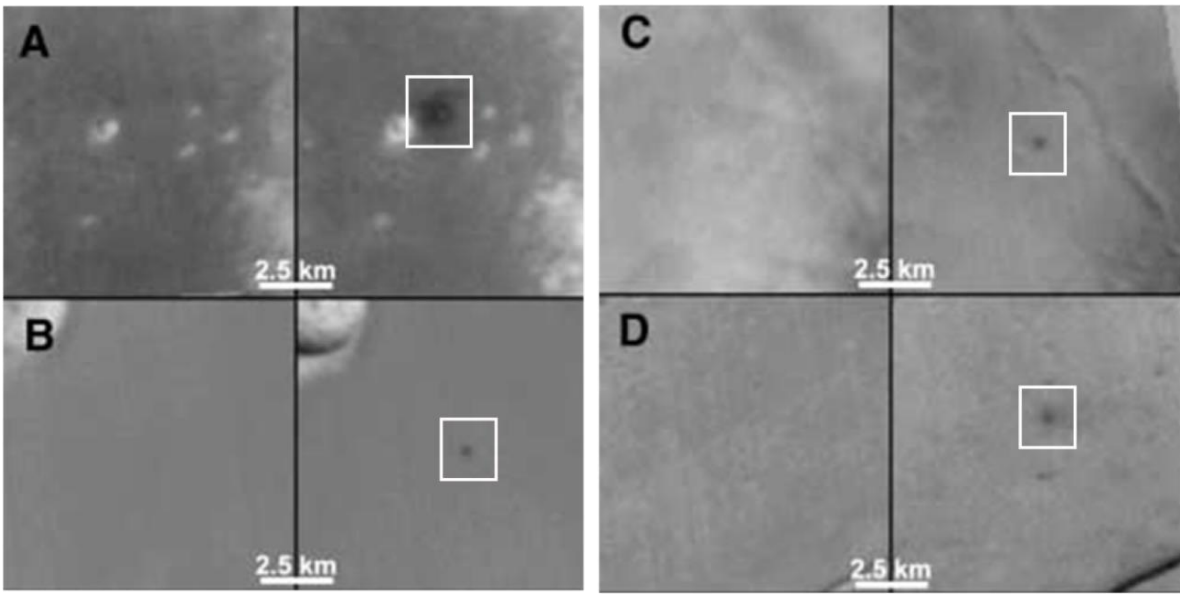

Figure 2.1.3 (Source: Malin *et al.*, 2006) Examples of before and after images, taken using the Mars Orbiter Camera (MOC), showing dark spots that are used to identify new craters. The white boxes highlight the new craters found in after images.

2.1.6 Section Summary

The exploration of Mars has spanned almost 50 years, and has generated a plethora of information that has enabled us to gain an insight into the geological evolution of the planet. However, there is still much knowledge to be gained from future missions regarding the atmosphere and surface evolution. Impacts have played a major role in the evolution of the planet's surface and may have had an effect on, and contributed to, the atmosphere. It is therefore important to understand the different processes that can occur as a result of impacts on Mars (or other terrestrial bodies), and if it is possible to indirectly detect these processes. As explained in Chapter I, two impact induced processes are examined in this thesis, the remaining sections will provide a background on impacts, impact induced devolatilisation, methane on Mars and serpentinisation.

2.2 Impacts

The formation and evolution of the Solar System has been greatly influenced by impact events. It is widely accepted that the planets in our Solar System formed as a result of impacts of dust particles found in the proto-planetary disk (Montmerle *et al.*, 2006; Chambers, 2004). Initially impacts, driven by the motion of gas in the proto-planetary

disk, resulted in dust particles coalescing to form aggregates and then 'pebbles'; eventually they gained enough mass for gravity to play a larger role in the impact events finally forming the planets (Chambers, 2001; Chamber, 2004).

Since that turbulent time in the Solar System's formation, impacts have continued to play a major role on the evolution of the surfaces of planets and their satellites (Kenkmann *et al.*, 2014). They may have also had an effect on the formation and evolution of atmospheres. Benlow & Meaadows (1977) proposed that impact induced devolatilisation may have contributed to the formation of the terrestrial planet's early atmospheres (see Chapter II, Section 2.3). Incoming impactors can also result in the loss of atmospheric mass. Melosh and Vickery (1989) explain a sizable amount of atmospheric mass can be ejected as a result from an impact. This concept suggests all the material in either a vapour plume or a region (*H*) above a tangent will be ejected from the atmosphere as a result of an impact. However, which of the two quantities is dependent on the size of the impactor (Figure 2.2.1; Pierrehumbert, 2010; Newman *et al.*, 1999). As the impactor travels through the atmosphere it compresses, accelerates and heats the material in its path as a result of an expanding shock wave. Once the material reaches a critical energy the material is ejected.

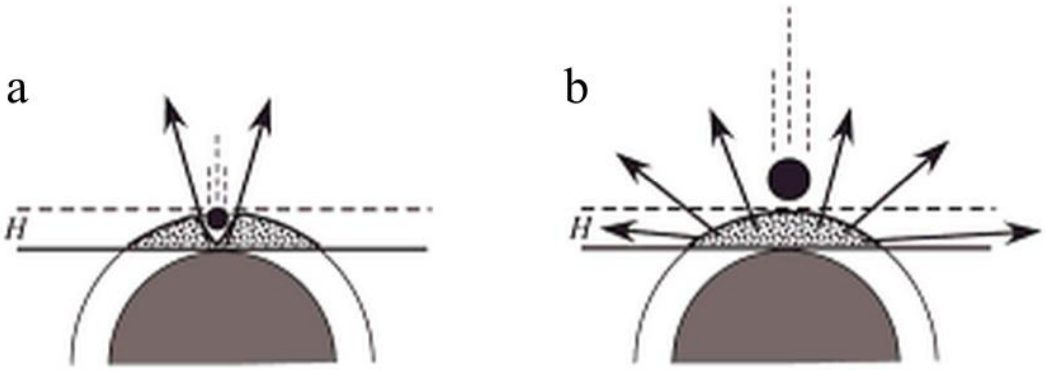

Figure 2.2.1 (source: Pierrehumbert, 2010) Schematic showing the area of atmosphere ejected by an incoming impactor (described in the text) resulting from a smaller impactor (a) and a large impactor (b).

In addition to the loss of atmosphere, impacts can also temporarily alter the climate of planets through devolatilisation, which can be either local or planet-wide, depending on the size of the impactor. Currently, Earth provides the only location where in-depth analysis of impacts craters can be carried out; investigations have shown the Earth has been struck by meteorites numerous times throughout its history, with 180 craters detected with diameters between ~1.8 km and ~250 km (Osinski *et al.*, 2013). However, Earth has a

number of processes, such as plate tectonics and weathering, that erase impact craters from the planet's surface. Planets and satellites such as the Moon, Mercury and Mars, experience less modification processes, and so show more impact craters that can be examined.

Impact craters are one of the most widely spread geological landforms on rocky or icy bodies (Osinski & Pierazzo, 2013). They can provide great insight into planetary crusts from surface rovers/landers or orbiting spacecraft. This can be seen by the recent deployment of NASA's *MSL* rover to Gale crater, which has a central mound 6 km high and is composed of sediments (Schwenzer *et al.*, 2012a). Sending exploration missions to impact craters provide access to rocks and minerals that have an origin deeper within planetary crusts, which would otherwise be unattainable without drilling equipment. In turn, this enables us to gain a better understanding of the localised geology.

2.2.1 Crater Formation

Physics governs the impact cratering mechanism, and so the underlying process will be the same on all bodies (Osinski & Pierazzo, 2013). Factors such as gravity, the presence (and density) of an atmosphere, surface temperature, surface geology, etc., can an effect on crater morphology. However, the stages of impact crater formation remain constant on all rocky bodies (Figure 2.2.2). There are generally considered three stages to crater formation: 1) Contact and compression, 2) excavation, and 3) modification (Melosh, 1989).

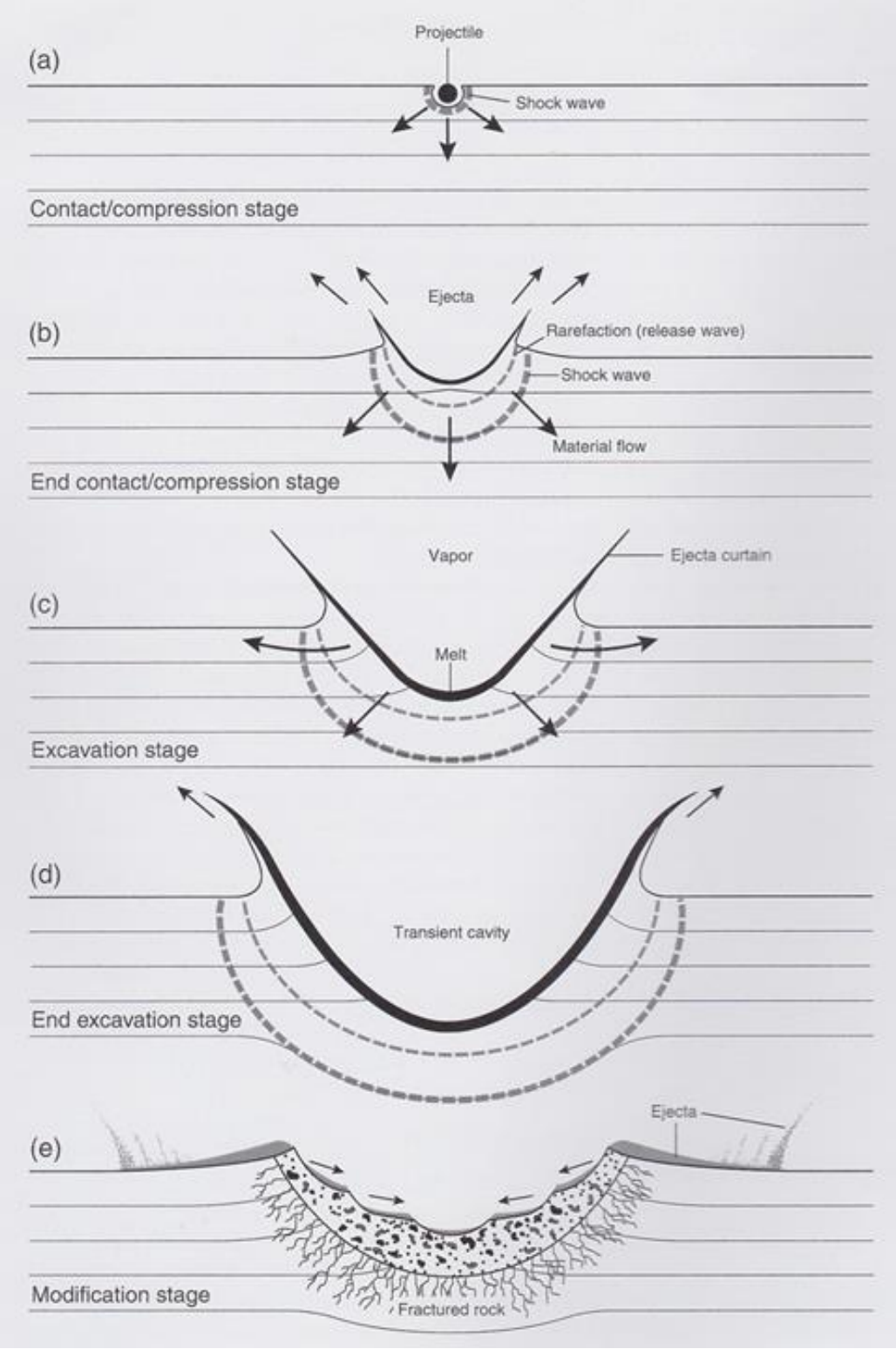

Figure 2.2.2 (Source French, 1998) stages of impact crater formation. a) The initial contact stage, where the impactor impacts the target, compresses and accelerates material downwards. b) – d) The excavation stage represents the widening of the crater until the formation of the transient crater. e) Modification is the final stage of the crater forming process, where gravity and rock mechanics affect the final crater morphology.

Contact and Compression

The contact and compression phase is a brief phase (Kenkmann *et al.*, 2014), lasting a few times longer than is required for the impactor to travel the distance of its diameter (Melosh, 2011) and can be expressed as:

$$t_{cc} \approx \frac{L}{v_i} \qquad \text{Equation 2.2.1}$$

(Source: Melosh, 2011)

Where, t_{cc} (in seconds) is the duration of the contact and compression phase, L (in metres) is the diameter of the impactor and v_i (in m s^{-1}) is the velocity of the impactor. This initial phase describes the moment when the impactor, makes contact with the surface or target, where the force of the impactor causes compression and, downward and outward, acceleration of the target material (Grieve, 1987). The impactor itself can travel up to three times its diameter into the target, where it redistributes its kinetic energy (Melosh & Ivanov, 1999) and momentum to the target material (Melosh, 2011) in the form of shockwaves, which travel through both objects from the contact interface. As the shock wave propagates through the material there is an abrupt change in pressure, density and temperature between the shocked and un-shocked material, which is described by the Rankine-Hugoniot relations (Chapter III describes these relations in more detail). The peak pressure experienced during this initial phase can be calculated using the planar impact approximation (PIA), or from Hugoniot plots (described in more detail in Chapter III). The pressures experienced during this initial stage are greater than the strength of the target material (Melosh & Ivanov, 1999), making the material strength negligible and thus unnecessary for determining the shock effects at this point. The shock waves generated spread through the target in a hemispherical shape from the site of impact, with pressure decreasing exponentially with distance (Barlow, 2008; Thoma *et al.*, 2005). In addition, the energy of the shock front also decreases with distance from the crater through heating, acceleration and deformation of material, and the increasing area the shock front covers as it expands (French, 1998). The pressure experienced at the point of contact, for large impact craters, can be greater than 100 GPa and will decrease exponentially with distance (Norton, 2002). As the shock waves travel away from the impact site, the waves turn into plastic waves, where deformation of the target material occurs (Barlow, 2008). The

deformation occurs as the compression of both target and impactor material produces an increase in pressure and temperature, which can cause chemical changes in the material. Eventually the plastic wave turns into an elastic wave, where the material is able to return to its original state once the wave passes through it (French, 1998). When the initial shock wave reaches a free surface a rarefaction, or relief wave, is generated, which travels back through the material (Osinski & Pierazzo, 2013). When the pressure is first released the pressure of the shocked material is above its critical point, causing it to behave as a single phase hot fluid, as the material is neither a vapour or melt (Melsoh, 2013). The critical point represents a pressure that determines how the material behaves, i.e. as a single phase or two phases; when the pressure falls below the critical point, the material forms one or two phases: a melt and/or a vapour (Melsoh, 2013). Vaporised material can expand out, and travel away, from the crater in a vapour plume (Melosh, 2013). Once the relief wave generated from the back, or top, of the impactor reaches the interface between the target and impactor, the 'contact and compression' phase of crater formation ends.

Crater Excavation

The excavation stage describes the formation of the bowl shaped cavity, also known as the transient cavity, and the ejecta deposits (Osinski *et al.*, 2013). An approximate duration time (t_{ex} in seconds) can be calculated using Equation 2.2.2:

$$t_{ex} \approx \sqrt{\frac{D}{g}}$$ Equation 2.2.2

(Source: Melosh, 2011)

Where, g (in m s^{-2}) is acceleration due to gravity and D (in metres) represents the diameter of the crater when crater formation is dominated by gravity (Melsoh, 2011).

During this stage the impactor does not have a major role, the widening of the crater occurs as a result of the expanding shock wave through the target (Osinski *et al.*, 2013). Some of the energy from the shock waves is converted into kinetic energy, which is used to accelerate ejected material out and away from the crater (Barlow, 2008). The strength of the target material plays a more important role in the excavation stage, as

stresses exceeding the strength of the rock causes the fragmentation of the near surface target material (French, 1998). A pressure gradient is generated behind the shock due to the target's free surface, resulting in some material being deflected towards the surface (Melosh & Ivanov, 1999). It is this process that expands the transient crater by ejecting material out of the developing crater. As mentioned earlier, the strength of the shock wave decreases with increasing distance from the point of impact, and so does the amount of material ejected. The ejection process arises when the kinetic energy is larger than that required to overcome gravity and moves a mass of the already fragmented material (Wünnemann *et al.*, 2011). Almost a similar quantity of material is displaced downward by plastic flow as is ejected out of the crater (Melosh & Ivanov, 1999). The end of the excavation stage occurs when displacement of material ceases, and the transient crater reaches it maximum size (Barlow, 2008), which will have a depth approximately one third of the crater's diameter (Grieve, 1987).

Modification

The modification stage lasts the longest of all of the three stages in crater formation, as it begins when the transient crater has formed to the time when the crater is destroyed (Barlow, 2008). However, the end of the modification stage can also be defined as when "things stop falling" (French, 1998). During this stage, shock waves passing through the material become elastic waves and no longer have an effect on the crater (Norton, 2002). Immediately after transient crater formation, the morphology of the crater can be altered as a result of gravity and rock mechanics to form a final crater (Melosh, 2011). Crater walls generally begin to slump back into the crater under gravity, leaving breccia on the crater floor (Grieve, 1987). Immediate crater modification processes also include: crater floor uplift, central peak formation and the formation of stepped terraces (Melosh & Ivanov, 1999). These modification processes can produce complex craters such as craters with a central peak, peak rings or ringed depressions (Melosh & Ivanov, 1999). The modification stage also encompasses the effects of other processes that can alter the crater, such as depositional geological processes. The morphology of impact craters can provide a catchment for infilling materials (Barlow, 2015) resulting in the infilling of the crater cavity to the point where it may not be recognised as a bowl shaped crater from the surface.

2.2.2 Effects on Solid Bodies

As a mineral is compressed it can behave either plastically or elastically. Plastic behaviour results in irreversible changes, whereas elastic behaviour is defined as when the mineral can return to its original state once the pressure is released. The boundary between these behaviours is known as the Hugoniot Elastic Limit (HEL; described in Deutsch *et al.*, 2015; Thoma *et al.*, 2005; Kenkmann *et al.*, 2014). Fractures in rocks normally occur at pressures below the HEL from the tensile waves acting on the material, with plastic deformation occurring at pressures above the HEL (Thoma *et al.*, 2005). The plastic deformation of minerals arise as they are unable to equilibrate to the high pressures experienced in a short time as a shock passes through it (Langenhorst, 2002; Thoma *et al.*, 2005), and so becomes permanently altered. There are three dominant effects from impacts onto solid bodies: 1) structural modification, 2) immediate chemical changes and, 3) chemical activation (Boslough, 1991). As the pressure experienced from the impact decreases with increasing distance from the site of impact, the degree of alteration and deformation experienced also decreases (Thoma *et al.*, 2005). Examination of structural modifications focuses on the effects of shock metamorphism in rocks and minerals, such as the formation of planar deformation features (PDF), twining, impact glasses, and polymorphs (Langenhorst, 2002; Boslough, 1991), which occur at relatively low pressures $\leq$ 35 GPa (French, 1998). PDFs (Figure 2.2.3) are amorphous, parallel lamellae, ~1 µm wide features found along lattice planes 2-4 µm apart, with the same composition of the host mineral (Duetch *et al.*, 2015; Vernooij & Langenhorst, 2005). These features have been used as a key indicator for the identification of impact structures on Earth (French & Koeberl, 2010). However, features similar to PDFs can also be generated by tectonic activity and can be mistaken for them (Langenhorst, 2002). Vernooij & Langenhorst (2005) outline the key differences between PDFs and tectonic deformation lamellae to avoid the misidentification of PDFs, which includes the orientation of the lamellae and the effects hydrous alteration can have on PDFs. The width of the amorphous lamellae increases with increased shock pressure. At shock pressures greater than 30 GPa complete grains can become amorphous and form diaplectic glass (Stöffler & Hornemann, 1972). These glasses form without the need for the melting of the mineral, but as a result of the breakdown of the crystal lattice as the shock wave passes through it (Deutsch *et al.*, 2015).

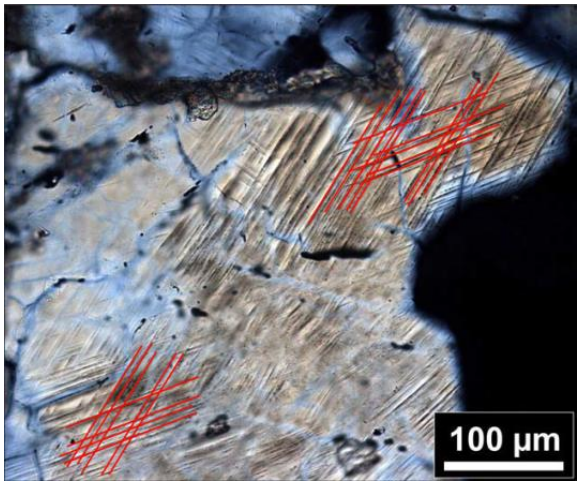

Figure 2.2.3 (Source: French & Koeberl, 2010) Quartz sample showing two sets of PDFs intersecting, which is highlighted with red lines. The sample was taken from the Bosumtwi impact structure in Ghana.

Polymorphs occur when changes in the crystal structure of minerals arise resulting from pressures and temperatures experienced as a shock wave passes through it (Glushak & Machalov, 2006). Xie *et al.,* (2012) provides an example of an olivine fragment with a high pressure phase of ringwoodite towards the outer edge of the fragment (Figure 2.2.4). The ringwoodite surrounding the olivine core indicates the high pressure phase was formed from a polymorphic transformation and not the melting and recrystallisation of the olivine.

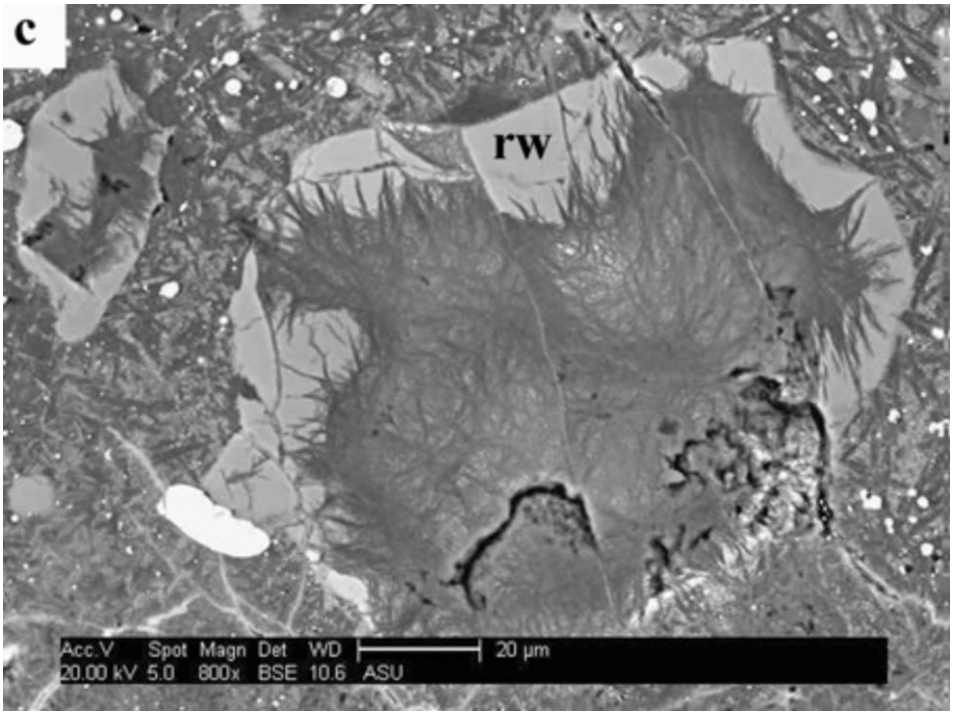

Figure 2.2.4 (Source:Xie *et al.,* 2012) BSE image of an olivine fragment from Antarctic chondrite GRV022321. The bright rim indicates ringwoodite, a high pressure phase of olivine, with the darker core indicating olivine.

In some instances the shock event can result in increased rates of chemical alteration, specifically through increasing the number of reaction locations, i.e. increasing the surface area through fracturing (Boslough & Cygan, 1988; Furukawa *et al.*, 2011). For example, increasing reaction locations on minerals can have an effect on the production rate of serpentines formed from impacts. Large impacts onto mixtures of water ice and rock can generate hydrothermal systems; Osinski *et al.*, (2013) provide a list of 70 terrestrial impact structures that have signs of an impact generated hydrothermal system. The rate of aqueous alteration of minerals within these impact induced hydrothermal systems could be increased as a result of shock increasing the temperature and surface area of the minerals. Increasing the rate of alteration of minerals can therefore affect the production of serpentines. In the case of Mars, this could have an effect on the rate of methane production via the serpentinisation of minerals in impact generated hydrothermal systems.

Finally, immediate chemical changes can result in the synthesis of new materials, which may be through decomposition (Wittmann *et al.*, 2006), shock synthesis (Furukawa *et al.*, 2011) or the melting and recrystallisation of minerals (Miyahara *et al.*, 2008). The pressure and heat generated by impacts can cause minerals to lose volatile components and leave behind oxides that did not vaporise, such as zircon ($ZrSiO_4$), which can decompose to ZrO_2 and SiO_2 (Wittmann *et al.*, 2006). The process of devolatilisation can result in the partial, or complete, decomposition of minerals when subjected to impacts. The volatiles released would most likely end up in the atmosphere resulting in changes to its composition, but this is dependent on the volume and type of volatiles released. The quantity of volatiles released would depend on the size of the impactor and target material. Large impacts (Chicxulub size) would release enough volatiles to alter the atmosphere, whereas smaller impacts would add trace amounts of volatiles to localised areas of an atmosphere.

2.2.3 Simulating Impacts

Impact craters can be studied through examining impact structures, computational simulations or in the laboratory. All three of these methods provide a viable insight into the effects of impacts on solid surfaces.

The examination of impact structures on Earth have helped scientist to determine the effects impacts have on rocks and minerals (discussed in subsection 2.2.2). The information gathered from impact structures have helped to determine pressure regimes,

which assists with our interpretation of impact events and their effects on Earth. However, impact craters on Earth are relatively old and have experienced modification due to weathering, tectonic and aqueous activity, which makes it difficult for scientist to truly understand the immediate effects of impacts. Therefore laboratory experiments are used to help better examine specific impact induced processes and crater formation.

Laboratory impact experiments provide an excellent way to examine the effects of impacts on materials immediately after an impact and in a controlled environment. Laboratory impact experiments can be conducted using a number of instruments, such as propellant guns, dust accelerators, electric rail guns and the more commonly used light gas guns. Dust accelerators are capable of reaching velocities of 60 km s^{-1} for projectiles with masses in the range of 10^{-15} to 10^{-9}g (Thoma *et al.*, 2005). Light gas guns are able to fire projectiles from sub-millimetre to cm is diameter at velocities up to 9 km s^{-1}, Table 2.2.1 summaries key parameters for some two stage light gas guns at hypervelocity impact facilities worldwide.

Table 2.2.1 Summary of light gas guns found worldwide.

Gun parameter	**Institute**								
	CAPS Kent[1]	TiTech[2]	EMI SLGG[3]	NASA AMES[4]	NASA AMES[4]	LLNL[5]	EMI[6]	AEDC[7] 3.3″	AEDC[7] 8″
Pump tube length (m)	0.7	4.2	1.8	15.18	15.18	10.0	14	30.5	30.5
Pump tube diameter (mm)	12.7	50	40	45.0	64.4	90	150	355.6	355.6
Launch tube length (m)	0.7	3.58	1.5	–	3.9	9.0	12	30.5	58.5
Launch tube diameter (mm)	4.3	11.8	8.5	5.6	12.7	28	50	83.8	203.2
Maximum projectile mass (g)	78	0.6	0.0048*	0.0453*	0.94	15.9	100	500	12000
Maximum projectile velocity (km s^{-1})	7.5	8.9	9.1	11.3	9.54	7.54	7.8	7	4

N.B. Table modified from Lexow *et al.,* (2013) and references therein.

[1]CAPS Kent: Centre for Astrophysics and Planetary Science, UK.

[2]TiTech: Tokyo Institute of Technology, Japan.

[3]EMI SLGG: EMI's Space Light-Gas Gun, Germany.

[4]NASA AMES: Ames Research Center, USA.

[5]LLNL: Lawrence Livermore National Laboratories, USA.

[6]EMI: Ernst-Mach-Institute's Very Large Light-Gas Gun, Germany.

[7]AEDC: Arnold Engineering Development Center, USA.

*Projectile mass excluding sabot.

The larger light gas guns have launch tube diameters of 83.8 and 203.2 mm, which means projectiles will have diameters slightly smaller to fit inside a sabot (see Chapter IV, Section 4.1 the light gas gun). Therefore, the craters produced are much smaller (mm to cm) than those examined on planetary surface like Mars and on Earth, which range from metres to kilometres (when excluding micrometeorite impacts). This would make it difficult to detect subtle changes that can occur within the crater from the centre to the crater rim. The spatial resolution or interaction area for some instruments (such as a Raman spectrometer or SEM) would be similar to diameter or the crater, resulting in any variation in the impact residue being lost. Although peak impact pressure and peak impact temperatures would be the same, the duration of these effects would be different.

The effects from an impact in laboratory experiments can last for microseconds, whereas on large impacts on planetary bodies they can last for hours (Holsapple *et al.*, 2002). In large impacts on planetary bodies, such as Mars, post impact temperatures can result in the production of hydrothermal systems in the crater structure (Osinski *et al.*, 2013). The formation of these hydrothermal systems can result in alteration to the mineralogy (Schwenzer & Kring, 2013) or any alteration that may occur as a result of temperature post-impact cannot truly be simulated in a laboratory impacts. It is possible to examine the effects of high temperatures post-impact with the aid of a furnace, but this would not take into account pressures and therefore would not truly represent the post-impact effects. Although laboratory impacts cannot justly represent large planetary scale impacts they do show the immediate changes that occur in minerals as a result of the high pressures and temperature. These changes in turn provide an insight into the instantaneous effects of impact onto solid surfaces.

In order to examine pressure and temperature regimes, and their duration, in larger planetary scale impacts computational modelling can be used (Chapter III describes computational modelling in more detail). Laboratory impacts can be used to calibrate computer simulations before the simulation are scaled-up to represent larger impacts. However, rocks and minerals are very difficult to model as their crystal structures can change, as a result of the high pressure and temperature, to form different minerals with different material properties.

Individually each of these three methods for studying impact events provides valuable information that aids our understanding of this process. However, each method has its limitations and needs to be used in conjunction with the other methods to truly understand and represent what happens in an impact event.

2.2.4 Section Summary

The effects of impact on solid bodies results in formation of craters, which can displace large quantities of material. In addition to this, impacts result in the alteration of rocks and minerals through either structural modification, immediate chemical changes or chemical activation (Boslough, 1991). The two experimental programmes conducted during this investigation focused on the immediate chemical changes that occur as a result of impact. The remaining sections of this chapter will discuss the two processes (devolatilisation and serpentinisation) that have been investigated.

2.3 Impact Induced Devolatilisation

The devolatilisation of minerals is a process that results in the release of volatiles at high temperatures and pressures. The high pressure and temperature conditions experienced upon impact can result in this process occurring. Impact induced devolatilisation (which can also be referred to as impact degassing) would have an effect on both the atmospheres and surfaces of terrestrial bodies.

2.3.1 Atmosphere Formation

There are three dominant theories that have been proposed to explain the formation of the early atmospheres of the terrestrial planets (in a review by Pepin, 2006). The first theory suggests atmospheres may have been formed from the gravitational capture of gases from the solar nebula after planetary accretion. A second theory is the delivery of volatiles and noble gases to the terrestrial planets by comets and asteroidal meteorites (Owen *et al.*, 1992). Finally, impact induced devolatilisation may have also resulted in the formation of terrestrial atmospheres. Benlow & Meadows (1977) suggests the formation of atmospheres near the end of planetary accretion; when planetismals reach a critical size, impacts cause material to vaporise and thus, release volatiles. Computational modelling conducted by Schaefer & Fegely (2010) showed that the dominant species of volatiles from chondrites were H_2, H_2O, CO_2 and CO (Table 2.3.1). They also showed that at higher temperatures (1500 – 2500 K) S, P, Cl. F, Na and K are also released, which indicates a range of volatiles can be released as a result of various impact temperatures.

However, as Schaefer & Fegely (2010) point out, for H_2O dominant atmospheres a large proportion of accreting material would need to be carbonaceous chondritic material. Therefore, it is presumed that early atmospheres would have been H_2 rich.

Table 2.3.1 Volatiles released from different types of chondrites.

Type of chondrites	Main minerals	Volatiles
CI carbonaceous	Hydrated phyllosilicates (serpentine), talc	H_2O
CM carbonaceous	Hydrated silicates, pyroxene, olivine, talc	H_2O
Ordinary H	Bronzite, olivine, iron-nickel	H_2, CO and H_2O
Ordinary L	Hyperstene, olivine , iron-nickel	H_2, CO and H_2O
Ordinary LL	Hyperstene, olivine , iron-nickel	H_2, CO and H_2O
EH (high iron)	Enstatite, iron-nickel, sulphides	H_2, CO and H_2O
EL (low iron)	Enstatite, iron-nickel, sulphides	CO, H_2, CO_2 and H_2O
CV	Olivine, sulphide	CO_2 and H_2O

N.B. Table modified form Schaefer & Fegley, (2010) and Lodders & Fegley, (1998).

It is quite possible that all three of these mechanisms played a role as the atmospheres of the terrestrials planets formed and evolved over time. But it is difficult to determine exactly how the atmospheres formed, as atmospheric erosion can also occur over time. Atmospheric erosion can be a result of thermal and non-thermal processes, such as atmospheric escape (described in Johnson *et al.*, 2008), sputtering (described in Johnson, 1994; Tarduno *et al.*, 2014) and impact erosion (Melsoh & Vickery 1989). In addition to this, volcanism has also added to terrestrial atmospheres and contributed to them over time.

2.3.2 Atmosphere Evolution

Impact induced devolatilisation can also result in temporary changes in the composition of atmospheres. Large impactors striking the surfaces of solid bodies could liberate large quantities of volatiles into atmospheres, which may be capable of changing the climate. The type of volatiles released into the atmosphere is dependent on the makeup of both the target and impactor. One of the most greatly studied impact events on Earth is the bolide impact that may have triggered (or contributed to) a mass extinction event, at the end of the cretaceous period. This event is believed to have resulted from the impact that formed the Chicxulub crater (165 km in diameter) in the Yucatan Peninsula, Mexico (Hildebrand *et al.*, 1991). A geological study of the area has shown that the target material was

dominantly made up of anhydrite, gypsum, dolomite and limestone (Koeberl, 1993; Pope *et al.,* 1994), which would have released sulphur and carbon oxides upon impact. Chen *et al.,* (1994) calculated that between 4×10^{17} and 8×10^{18} g of sulphur oxides and between 5×10^{18} and 2×10^{19} g of carbon dioxide were released into the atmosphere. It was suggested that this amount of sulphur oxides released would have reduced temperatures by 10-20 K for several years, and a subsequent increase in temperature of 2-10 K for 10000 to 100000 years as a result of the carbon dioxide released (Chen *et al.,* 1994). Pope *et al.,* (1997) suggests this impact would have generated 5×10^{17}g of carbon dioxide and 2×10^{17} g of both sulphur dioxide and water vapour, which would have meant a temperature decline between 9-31 K for less than 10 years and carbon dioxide would result in an increase of ~1 K. The variations in the quantity of volatiles released represent differences in the way in which the calculations were made; Pope *et al.,* (1997) calculated the amount of volatiles released from the expected energy from the impact event, whereas Chen *et al.,* (1994) used impact experiments to help determine the amount of volatiles released on impact. Although there is some variation on the times scales of the effects these volatiles had on the Earth's atmosphere when they were released, they show large amount of volatiles released on impact are capable of effecting the composition enough to produce changes in global temperatures.

Segura and colleagues (Segura *et al.,* 2002; 2008) have suggested that large, or moderately sized, impacts on Mars may have generated enough heat to vaporise ice, which would have generated a greenhouse effect. Depending on the mineralogy of the surface prior to impact, it might be possible that volatiles (such as CO_2 and H_2O) may have also been released and contributed to a greenhouse effect on Mars. It may also be possible that substantial amounts of CO_2 could be released into the Martian atmosphere from large impacts, similar to what occurred when CO_2 was released from the Chicxulub impact event. However, this would again be dependent on if there has ever been any carbonate minerals in the Martian crust. This idea was one of the motives of Gupta *et al.,* (2002), who conducted impact experiments investigating the devolatilisation of calcite ($CaCO_3$), using a two stage light gas gun, to determine the pressure required to liberate CO_2. These impact experiments showed that pressures of ~110 GPa were required for CO_2 release, whereas under static high pressure and high temperature conditions (not shocked) devolatilisation (via decomposition) occurs between 3.5 to 4.0 MPa (Gupta *et al.,* 2002). Kawaragi *et al.,* (2009) suggests that actually CO would be the dominate gas released from the devolatilisation of calcite (with a CO/CO_2 ratio of 2.02 ±0.41), which, on Earth, would

result in an increase in CH_4 and O_3 levels (produced from photochemical reactions in atmosphere). Kawaragi *et al.,* (2009) determined that a Chicxulub sized impact would result in 2-5 ˚C increase in temperature that would last for several years. Sizeable impacts on the Martian surface may have resulted in similar effects and may have increased surface temperatures, but again this is dependent on the early geology of Mars.

2.3.3 Surface Modification

The devolatilisation of minerals from impacts is an immediate chemical change and would result in the partial, or complete, decomposition of minerals. Therefore, in addition to the effect on atmospheric composition, modification of surface minerals will also occur as a result of impact induced devolatilisation. The release of volatiles from some minerals would result in the generation of different minerals, which could be used as indicators to determine if devolatilisation has occurred. A good example of this is the dehydration of minerals, e.g. gypsum ($CaSO_4.2H_2O$), talc ($Mg_3Si_4O_{10}(OH)_2$) and serpentine ($(Mg,Fe)_3Si_2O_5(OH)_4$), whereby the loss of water would generate new anhydrous minerals (Table 2.3.2). Therefore, impacts could erase the presence of specific volatiles from surface minerals, which would affect our understanding of palaeosurfaces. It might also be possible that devolatilisation of minerals from thermal processes may be mistaken for impact induced devolatilisation if they are in the proximity of craters, which could influence the interpretation of geological histories of heavily cratered bodies, like Mars, which makes it important for us to understand the effects of impact induced devolatilistion.

Table 2.3.2 Dehydration reactions for gypsum, talc and serpentine.

Reaction	Equation
1	$CaSO_4 \cdot 2H_2O = CaSO_4 + 2H_2O$
2	$CaSO_4 \cdot 2H_2O = CaSO_4 \cdot 0.5H_2O + 1.5\ H_2O$
3	$Mg_3Si_4O_{10}(OH)_2 = 3MgSiO_3 + SiO_2 + H_2O$
4	$2(Mg,Fe)_3Si_2O_5(OH)_4 = 3(Mg,Fe)_2SiO_4 + SiO_2 + 4H_2O$

Although Benlow & Meadows (1977) first proposed impacts may have produced the atmospheres of terrestrial planets, it was Boslough *et al.,* (1980) who experimentally showed the devolatilisation of minerals would occur upon impact. Boslough *et al.,* (1980) demonstrated that water loss from serpentine occurred at a pressure less than 23.5 GPa when impacted using a flyer plate accelerated by a propellant gun. Additional experiments

conducted by Lambert & Lange (1982), again showed that devolatilisation of minerals (in this instance the loss of water) can occur when impacted. However, they also showed that incipient dehydration of antigorite (a polymorph of serpentine) occurred at pressures >20 GPa and complete dehydration occurred at pressures >60 GPa. These results are mirrored in additional shock experiments conducted by Lange *et al.*, (1985). This suggests that varying amounts of volatiles are lost at various impact pressures. Lange & Ahrens (1982) also demonstrated this, by determining the water content of the recovered shocked samples. Lange & Ahrens (1982) were also able to show there was a change in the infrared absorption spectra, which could be used to quantify the loss of water. If it is possible to quantify the loss of volatiles from the altered surface materials then we would be able to better estimate the amount of volatiles released into planetary atmospheres, and determine the effects these volatiles would have on the planet's climate.

The temperature range at which minerals lose volatiles is not dependent on the specific volatiles (Table 2.3.3), i.e. not all minerals containing H_2O will dehydrate at the same temperature. Instead different minerals will release their volatiles at various temperatures. Therefore, it might be possible to use volatile minerals as geo-thermometers in impact environments, which would assist in our understanding of the effects of impacts on rocky surfaces. However, it will be vital to determine if pressure changes the devolatilisation temperature, to ensure the correct interpretation of the conditions resulting from an impact.

Table 2.3.3 Temperatures determined for volatile loss from various minerals.

Mineral	**Volatile**	**Temperature (˚C)**
Serpentine - $(Mg,Fe)_3Si_2O_5(OH)_4$	OH	600 – 700
Topaz – $Al_2SiO_4(F,OH)_2$	OH, F	140 -330, 850 -900
Talc - $(Mg, Fe)_3Si_4O_{10}(OH)_2$	H_2O	800
Gypsum – $CaSO_4.2H_2O$	H_2O, S	100 - 150, 1400
Siderite – $FeCO_3$	C	580
Calcite – $CaCO_3$	CO_2	675
Chlorite	H_2O	600
Smectite clays	H_2O, OH	100-250, 700

N.B. Table modified from Deer *et al.,* 1992 and Bell, 2014.

2.3.4 Section summary

Impact induced devolatilisation of minerals may have played a considerable role in the formation of terrestrial atmospheres. In addition, it can have a substantial effect on pre-existing atmospheres, altering the climate of planets and affecting the surface mineralogy. To understand the palaeosurface conditions it is important that we understand the role impact induced devolatilisation has played throughout a planet's history. These minerals may also provide clues to the conditions generated as a result of impacts. The devolatilisation experiments conducted here (Chapter VI) aimed to examine the effects of impacts on volatile bearing minerals.

2.4 Methane on Mars

Over the past 46 years of Mars exploration, one discovery (albeit controversial) that has received much attention has been the detection of methane in its atmosphere. In December 2014 there was confirmation that NASA's Mars Science Laboratory (MSL; Webster *et al.*, 2014) had confirmed the presence of methane at Gale crater through the direct sampling of the Martian atmosphere. Until then, methane had only been detected through infrared spectra from orbiting spacecraft (Formisano *et al.,* 2004) and from observations made using terrestrial ground based telescopes (Mumma *et al.*, 2009; Krasnopolsky *et al.*, 2004; Krasnopolsky, 2012).

2.4.1 Methane Detection

Using data from the Cryogenic Echelle Spectrograph (CSHELL) at NASA's Infrared Telescope Facility (IRTF) and Near Infrared Spectrometer (NIRSPEC) at the Keck-2 telescope, both located in Hawaii, Mumma *et al.,* (2009) reported the detection of a plume of methane during the late summer of 2003. In addition Krasnopolsky *et al.,* (2004) detected methane in the Martian atmosphere at 10 ± 3 ppb, using the Canada-France-Hawaii Telescope's Fourier Transform spectrometer. A second detection of methane by Krasnopolsky (2012) was made using IRFT/CSHELL; observations during February 2006 over the Valles Mariners region, which showed methane abundances of ~10 ppb and ~3 ppb in the area just outside the Valles. It has been argued by Zahnle *et al.,* (2011) that the methane detected by terrestrial based telescopes was actually picking up $^{12}CH_4$ found in

Earth's atmosphere, where the signal is 2000 times stronger than its Martian equivalent and the $^{13}CH_4$ signal is 20 times stronger than $^{12}CH_4$, which makes it difficult to discriminate Martian methane. While this argument may have some weight when discussing Earth based observations, it does not stand up against the findings of Formisano *et al.,* (2004), Geminale *et al.,* (2008) and Fonti & Marzo (2010), which used spectral data obtained from an orbiting spacecraft. Formisano *et al.,* (2004) determined a global average mixing ratio of 10 ± 5 ppbv using the Planetary Fourier Spectrometer (PFS) on board the Mars Express spacecraft in orbit around the planet. However, only one methane identification band, at 3000 cm^{-1}, could be used as a methane marker as Faunhofer lines were present in the 6000 cm^{-1} band, and the signal-to-noise ratio was very low in the 4400 and 1300 cm^{-1} bands, making it difficult to confidently confirm a methane signature from these bands (Formisano *et al.,* 2004). A second study using PFS data and using the 3018 cm^{-1} band provided an average mixing abundance of 14 ± 5 ppbv from the northern spring-summer to southern summer (Geminale *et al.,* 2008). Fonti & Marzo (2010) used spectral data of the second strongest spectral band at 1306 cm^{-1}, which was collected by the Thermal Emission Spectrometer (TES) aboard the Mars Global Surveyor (MGS). Data taken over the course of three Martian years, from 31/7/1999 to 20/9/2004, around the equinox of each year and between 60° S and 60° N in latitude showed a range of methane abundances, from a minimum of 5 ± 2 ppbv to a maximum of 33 ± 9 ppbv (Fonti & Marzo, 2010), for various temporal periods. One weakness of the data obtained from orbiting spacecraft is the focus on the identification of only one specific methane band, which Zahnle *et al.,* (2011) points out "*a single line of a spectrum is not a fingerprint*". It is, however, difficult to refute the direct measurements made by MSL (Webster *et al.,* 2014), where a background value of 0.69 ± 0.25 ppbv was made by SAM's Tunable Laser Spectrometer (TLS). The TLS uses infrared laser absorption and a multipass sample cell that enables a spectral resolution of 0.0005 cm^{-1} and has a detection limit for methane of 0.3 ppbv (Mahaffy *et al.,* 2012). The spectrometer is capable of detecting three isotopes of methane, $^{12}CH_4$, $^{13}CH_4$ and $^{12}CH_3D$, where three, four and one strong line(s), respectively, can be detected (Mahaffy *et al.,* 2012). Methane detected by Webster *et al.,* (2014) was determined using the three lines found in the 3030 cm^{-1} band for $^{12}CH_4$. It is worth pointing out the identification of methane does again appear to be centred around a single band at 3000 cm^{-1}, but unlike other detection methods MSL has been able to directly sample the Martian atmosphere.

2.4.2 Lifetime of Martian Methane

The observations made by Mumma *et al.,* (2009) and Fonti & Marzo, (2010) showed a shorter than expected lifetime of methane within the atmosphere of approximately four Earth years and less than one Earth year, respectively. If the methane from the 2003 plume was globally circulated, then an average mixing ratio of 6 ppb (Mumma *et al.,* 2009) would be present in the Martian atmosphere. Data taken in the spring of 2006 showed a global mean mixing ratio of 3 ppb. Fonti & Marzo, (2010) saw a decrease from 33 ± 9 ppbv in June 1999 to 14 ± 4 ppbv in December 2000. The expected photo-chemical lifetime of the gas within the Martian atmosphere is believed to be between 300 - 600 years (Mumma *et al.*, 2009; Zahnle *et al.,* 2011; Lefèvre & Forget, 2009; Geminale *et al.*, 2008). The reduction of methane concentrations over time detected by Mumma *et al.,* (2009) and Fonti & Marzo (2010) suggests there are additional mechanisms to remove methane from the atmosphere other than those resulting from atmospheric chemistry. It also suggests the process for either the formation, or release, of methane into the atmosphere has occurred in the near past and is possibly still occurring. These findings are supported by Formisano *et al.,* (2004) who found variations in methane abundances across three sets of longitude ranges, where abundances of 25 ± 5, 15 ± 5 and 10 ± 5 ppbv were detected. MSL's TLS has also shown some variability in methane concentrations. An increase in concentration with a mean value of 7.19 ± 2.06 ppbv was detected on sols 466, 474, 504 and 526, whereas measurements taken on sols 79, 81, 106, 292, 573 and 684 showed values less than 1 pppv, except sol 81 with a value of 1.43 ± 4.94 ppbv (Webster *et al.*, 2014). However, sols 306 and 313 gave values of 5.78 ± 4.54 and 2.13 ± 4.04 ppbv, which does not correspond with the increase seen across the 20 month period, but all values do fall into the same range when including error values. The lower methane measurements were taken ~ 1 km before, and ~ 1 km after, the highest concentration was detected, which would indicate a localised source. Although, this particular detection is on a much smaller scale, high abundances were measured 200 – 300 m away from each other, than the plume observed by Mumma *et al.,* (2009). According to Webster *et al.,* (2014) this indicates either a weak source in the area or a stronger source from further afield. It may also have been the result of a very short lived local source.

2.4.3 Occurrences of Methane on Mars

The occurrences of methane within the planet's atmosphere has not been restricted to a few regions, but to a number of different regions; Krasnopolsky (2012) reported methane over Valles Marineris, Mumma *et al.,* (2004) found methane present southeast of Syrtis Major, east of Ariabia Terrae and Nili Foassae; Fonti and Marzo (2010) confirmed sources at Arabia Terrae, Elysium and Tharsis; and MSL is currently located in Gale crater, which sits on the edge of Elysium Plantia. Although Formisano *et al.,* (2004) identified methane over the planet with variations in abundances from various ranges of longitude; 1) - 55° to - 170°, 2) + 52° to - 55° and 3) + 52° to + 190°, ranges which cover almost the entire planet. Currently it appears that local sources of methane appear to be found in regions that were once geologically active.

2.4.4 Methane Sources

The detection of methane is of great astrobiological importance as 90-95% of Earth's methane is generated from biological sources (Atreya *et al.,* 2011). Terrestrial sources include oceans, natural gas, rice paddies, termites, cattle and marshes (Formisano *et al.,* 2004). Due to methane's biological origins on Earth, it has been thought the presence of methane on Mars could be a signature for the presence of life (Atreya *et al.,* 2007). If the methane detected was indeed created by biological life, then it was probably produced within the past 300 - 600 years (or less), which indicates life was present on Mars very recently. However, currently the surface of Mars has an environment that is inhospitable to life as we know it, with strong UV radiation, a low pressure of ~ 6 mbar and a low temperature of ~200 K, which makes it more probable to find subsurface life (Geminale *et al.,* 2008; Max & Clifford, 2000).

There are also a number of non-biological process that can release methane which are: the photolysis of H_2O and CO (Bar-Nun & Dimitrov, 2006), meteorite/cometary impacts (Formisano *et al.,* 2004) or geological processes (Oze & Sharma, 2005). It is also possible that the detected methane may have been the result of a slow release from subsurface reservoirs (Chastain & Chevrier, 2007; Max & Clifford, 2000; McMahon *et al.,* 2012a), but these reservoirs do not conclusively point towards any single formation process. Any single proposed mechanism would be required to produce an annual quantity

of methane per year to account for the observed global average of 10 ppb. However, the exact quantity required varies from a lower estimation of 1.26×10^5 kg (Formisano *et al.*, 2004) to a maximum estimation of 3×10^5 kg (Ryan *et al.*, 2006).

Methane Reservoirs

The methane that has been detected today could potentially have come from the slow release of methane reservoirs on Mars, but it does not provide an actual formation mechanism. Clathrate hydrates could potentially provide a suitable reservoir for methane, which could be found in the polar caps at Mars's north and south poles and, perhaps, in the subsurface, before being released at a later date (Chastain & Chevrier, 2007; Max & Clifford, 2000). These clathrates are formed when water crystallises in the presence of gases, such as methane, where the gas is pushed into crystal lattice spaces. Essentially, methane becomes trapped within the crystal structure of the frozen water, allowing the gas to be stored in compact and stable, cage-like structures (Chastain & Chevreir, 2007). Naturally occurring hydrates found on Earth normally develop in permafrost areas at depths of 150-200 m and in low temperature and pressure regions in intergranular pore spaces of rocks (Max & Clifford, 2000 and references therein). The formation of methane clathrates requires H_2O, methane and the appropriate pressure - temperature regime (Chastain & Chevreir, 2007). Max & Clifford (2004) suggest the formation of methane clathrates would occur at a depth of ~15 m beneath the surface and could be ~ 1 km form the cryosphere's base. A variation in the thickness in the region where methane clathrates are stable has been predicted at depths 8-13 km near the poles and 3-5 km near the equator (Max and Clifford, 2004). A variation in the stability region beneath the surface is predicted by Gloesener *et al.*, (2013), where the stability depth of the region decreases towards the poles, which could result in methane being resealed in these regions.

Another reservoir for methane is within intergranular pore spaces of rocks, particularly basalts. Laboratory rock crushing experiments have shown that methane can be liberated from a wide range of terrestrial basalts, i.e. altered, unaltered, subaerial, pillow basalts, in formation location and in age, with CH_4/CO_2 ratios > 0.5 (McMahon *et al.*, 2012a). It was found that lower CH_4/CO_2 ratios were determined for red basalts, but not in the case for a hematite vein halo from one of the samples (McMahon *et al.*, 2012a), which may have some interesting implications for Mars. It is uncertain if the amounts of methane released from terrestrial basalts will be the same for those found on the Martian surface.

Unlike, the methane clathrates, the release of methane from basalt reservoirs may provide some indication as to the formation mechanism of the gas. As on Earth, minerals found in basalt, such as olivine and pyroxene, are prone to alteration from interactions with water (McMahan *et al.*, 2012a; Raymond, 2002).

Mantle Outgassing

The mantle of Mars could also be a potential reservoir for methane, as it has the potential to trap volatiles released from various processes, which can later be delivered to the atmosphere (Etiope & Klusman, 2002). This would mean volcanoes could release a large amount of methane from them. A study using thirteen years of data from monitoring the gas emissions from the Mauna Loa volcano in Hawaii (the largest volcano on Earth), was conducted by Ryan *et al.*, (2006). It was discovered that 9000 kg of methane was emitted from the volcano, which would only amount to 3% of that required to sustain a 10 ppb level, indicating that ~ 33 volcanoes of comparable size would be required to achieve the observed abundances. This would also require continued volcanic activity on Mars, activity which is not seen on the surface today.

Photolysis

Observed methane may have been produced from the photolysis of H_2O and CO (Bar-Nun & Dimitrov, 2006). An experimental investigation into the photolysis of H_2O in the presence of CO, where both are in gas phases, showed methane is a product of this reaction (Bar-Nun & Chang, 1983). Bar-Nun & Dimitrov (2006) explain water photolysis occurs during the break down of the H_2O molecule into OH and H, where the OH goes on to react with CO forming a CO_2 molecule, leaving molecular hydrogen through the following reactions:

$$H_2O \xrightarrow{h\nu} OH + H$$

$$OH + CO \longrightarrow CO_2 + H$$

$$H + H + M \longrightarrow H_2 + M$$

(Bar-Nun & Dimitrov, 2006)

Where, M is an additional gas, such as N_2. Some of the H can react with CO to form compounds such as methane, ethane, ethylene, acetylene, propane, formaldehyde, acetaldehyde, methanol, ethanol, acetone and acetic acid (Bar-Nun & Chang, 1983). These experiments did show methane as the third most abundant product, next to H_2 and CO_2. Bar-Nun & Dimitrov (2006) also suggest the quantity of methane should increase with increased irradiance times. The presence of CO and H_2O within the Martian atmosphere (Encrenaz *et al.,* 2004), would suggest there is the possibility of this process occurring, however there should also be traces of the additional compounds found, either in the atmosphere or trapped within the rocks.

Impacts

Meteorite and cometary impacts could also be a source for the methane, as Lange & Ahrens (1982) have shown that impacts have contributed to the evolution of planetary atmospheres. On Earth, large scale impacts are believed to have had such an effect; they altered the atmospheric chemistry enough to have resulted/contributed to the Cretaceous-Tertiary mass extinction event (Chen *et al.,* 1994). Formisano *et al.,* (2004) also proposed comets could potentially deliver methane to the Martian atmosphere, where it is stated Oort cloud comets can have a mixing ratio of CH_4/H_2O in the range of 0.1 to 1.5 % with a maximum was found of 2.3%. Calculations using a methane abundance of 1% in a comet with a 1 km radius, and an average impact rate of 1.6×10^{-8} per year showed a total of 1000 kg of methane would be delivered to Mars per year (Formisano *et al.,* 2004). Krasnopolsky *et al.,* (2004) also point out there is an approximately 2% probability of a comet, with a size exceeding 1 km, having recently impacted Mars and delivered methane to the atmosphere. However, their calculations estimated the delivery of ~ 5000 kg of methane. Both estimated quantities alone would not achieve an average mixing ratio of ~10 ppb, and would require an addition source of methane to achieve the observed abundance. Using micrometeorites as an exogenic source of carbon, Formisano *et al.,* (2004) calculated an average of 70000 kg of carbon will be delivered to Mars per year, and if all of this carbon was converted into methane it would produce a comparable, ~93500 kg, amount of methane. But this is assuming all the carbon from meteorites goes on to form methane, and all the meteorites are carbonaceous. It is possible that the carbon from these meteorites may have been converted into methane as a result of UV irradiation (Schuerger *et al.,* 2012). Laboratory experiments using Murchison samples, with 0.2 to

1.69 wt% of carbon, showed abundances between 2.2 and 11 ppbv could be obtained if 20 to 100 % of carbon from interplanetary dust, 2.4×10^5 kg per year, were converted into methane (Schuerger *et al.*, 2012). Flynn (1996) calculated an infall of the order of 10^6 kg per year of organic material, which would account for a steady abundance of ~10 ppb if all the material formed methane. Any contribution of methane to the Martian atmosphere from meteorites is dependent on the meteorites being carbonaceous, or rich in organics (Schuerger *et al.*, 2012; Formisano *et al.*, 2004; McMahon *et al.*, 2012b). However, only 3.9% of meteorite falls on Earth are classified as carbonaceous (Norton, 2002). Studies also show all the carbon from the meteorites is required to transform into methane to produce the observed abundances, which may not be the case.

Meteorites may not directly contribute to the current atmospheric methane budget, but may add to methane reservoirs to be released at a later date. Impact experiments conducted by McMahon *et al.*, (2012b) found that the methane content of sandstones increases as a result of being impacted by an organic rich projectile. The enrichment of methane is centred about the crater; the central crater is found to have slightly more methane than the crater walls, but the actual ejected material, which presumably includes projectile material, has the greatest concentration (McMahon *et al.*, 2012b). This result indicates potential reservoirs of methane in, and around, impact basins that have been trapped within the bedrock, in intergranular pore spaces, sealed fractures and vesicles formed upon impact. Price *et al.*, (2013) conducted additional impact experiments in order to determine if impacts themselves could release methane trapped with basaltic rocks. The experiment showed no substantial change in the abundance of methane after impact, signifying, at least at laboratory scales, impacts would be unable to access bedrock methane reservoirs.

Geological Processes

Geological processes are the most likely cause of methane generated on Mars. On Earth, geological sources for methane include buried organic material (Etiope & Klusman, 2002) or water-rock interactions. On Earth, methane can also be produced from the decomposition of biological material buried under sedimentary deposits, or through chemical decomposition resulting from the high temperatures found deep within the crust (Etiope & Klusman, 2002). It has been shown that organic molecules are present in comets, meteorites, interplanetary dust particles and the interstellar medium (ten Kate,

2010), if these organic molecules could be transferred to Mars, the burial of this material may be transformed into methane as a result of its thermal breakdown deep within the Martian crust, before being released through micro-seepages (Etiope & Klusman, 2002). Although, the quantity of organic material that would be transferred from in falling material to the surface, how much of this material would go on to form methane, and via which process is uncertain.

Hydrothermal fluid-rock interactions have also been proposed as a potential methane producing process, whereby carbon-rich waters alter basalt (Lyon *et al.*, 2005). It is postulated that a magmatic intrusion emplaced within the Martian crust will melt subsurface ice, forming liquid water. The water moves downwards, and then begins to rise again (as it heats up), which results in alteration of the basalt occurring along regions of decompression (Lyon *et al.*, 2005). However, Lyon *et al.*, point out this model is dependent on the permeability of the crust, quantity of reactants available, and heat source. The carbon content of the Martian mantle will determine the amount of methane generated from fluid-rock interactions. Lyons *et al.*, (2005) calculates a dike intrusion 10 km in width and 1000 km long would generate an atmospheric methane abundance of ~ 0.1 ppm over 1 million years, which would equate to 0.001 ppb per year. One problem with this particular model is the heat source. It requires magmatic intrusions to initiate the alteration of the basalt. The most recent thermal activity detected on Mars appears to have been found at Cerberus Fossae, which has had much attention as it is thought to represent an area with the most recent fluvial and volcanic activity ~ 20 Ma (Head *et al.*, 2003 and references therein). In this same region thermal images detected elevated temperatures, although evidence did not point towards a strong internal heat source (Milazzo & McEwen, 2005). If hydrothermal fluid-rock interactions have made a contribution to the atmospheric methane budget, then there should be strong evidence for internal heat sources that could generate the hydrothermal fluid in the past few million years.

Serpentinisation is another geological process that could produce methane as a result of mafic minerals, such as olivine and pyroxenes, converting into serpentine in the presence of water. A by-product of this alteration is H_2, which can later form methane in the presence of CO_2, or produce methane in a single stage alteration process if CO_2 is present when the mafic minerals are being altered. This process is discussed in more detail Section 2.4.6.

2.4.5 Methane Sinks

It has been suggested that two different mechanisms act to remove methane form the Martian atmosphere as a result of atmospheric chemistry, which are dependent on altitude, photolysis above 60 km and oxidation at lower altitudes (Lefèvre & Forget, 2009). However, there have been other mechanisms suggested, such as dust storm generating electric fields resulting in electrochemical processes or oxidation from within the Martian regolith (Farrell *et al.*, 2006; Lefèvre & Forget, 2009). Recently, Jensen *et al.*, (2014) have suggested an additional method where methane could be sequestered from the Martian atmosphere by reacting with reactive sites on minerals, which are generated by wind driven erosion.

In order to better isolate the mechanisms for Martian methane, long term observations need to be conducted into the Martian atmosphere, specifically to constrain the distribution and temporal occurrences. If there is a steady quantity of methane present in the Martian atmosphere, then any formation process would need to be long term, or would need to be combined with processes that would produce methane reservoirs.

2.4.6 Serpentinisation

An abiotic process that has gathered much attention as a possible source of Martian methane is serpentinisation (Oze & Sharma, 2005; Guzmán-Marmolgo *et al.*, 2013; Neubeck *et al.*, 2011; Chassefière & Leblanc, 2011; Quesnel *et al.*, 2009 and references therein). Serpentinisation is a process that results in the transformation of mafic or ultramafic rocks into serpentinites. In some cases olivine and pyroxenes, rich in Mg, transform into serpentines by the simple addition of water (Raymond, 2002). This process not only forms serpentine but also brucite, iron oxides, hydrogen and quartz depending on the initial constituents (Andreani *et al.*, 2013; Quesnel *et al.*, 2009). Oze & Sharma (2005) suggests the entire inventory of methane on Mars could be produced via the serpentinisation of olivine within the Martian crust, as methane can be produced as a by-product during serpentinisation in the presence of CO_2 or CO. Table 2.4.1 shows some serpentinisation reactions.

Table 2.4.1 Serpentinisation reactions

Reaction Number	Reaction
1	$Fo_{80-95} + H_2O + CO_2 = Sp + Mt + Br + CH_4$
2	$Fo_{75} + H_2O + CO_2 = Sp + Mt + CH_4$
3	$Fo_{70} + H_2O + CO_2 = Sp + Mt + En_{100} + CH_4$
4	$En_{95} + H_2O + CO_2 = Sp + Mt + Q + CH_4$
5	$En_{67-90} + H_2O + CO_2 = Sp + Mt + Q + CH_4$
6	$Fo_{95} + En_{40-85} + H_2O + CO_2 = Sp + Mt + Br + CH_4$
7	$Fo_{70-95} + En_{40-94} + H_2O + CO_2 = Sp + Mt + Q + CH_4$
8	$Fo_{75} + Fs + H_2O + CO_2 = Sp + Mt + Q + CH_4$
9	$Fo_0 + H_2O = Q + Mt + H_2$
10	$Fo_0 + H_2O = Sp + Mt + H_2$
11	$Fo_{100} + H_2O = Sp + Mt + H_2$
12	$Fo_0 + H_2O + CO_2 = Sp + Mt + CH_2$
13	$H_2 + CO_2 = CH_4 + H_2O$

(Source: Quesnel *et al.*, 2009; Oze & Sharma, 2005) Fo, Forsterite ($(Mg,Fe)_2SiO_4$); Sp, Serpentine ($(Mg,Fe)_3Si_2O_5(OH)_4$); Mt, Magnetite (Fe_3O_4); Br, Brucite ($Mg(OH)_2$); En, Enstatite ($(Mg,Fe)_2Si_2O_6$); Q, Quartz(SiO_2); Fs,Ferrosillite ($Fe_2Si_2O_6$). Subscripts for Fo and En represents the Mg content for each mineral.

On Earth, serpentinisation occurs dominantly in areas of tectonic uplift or exposure of mantle material (Schrenk *et al.*, 2013), particularly at mid-ocean ridges and subduction zones (Chassefière & Leblanc, 2011; Hyndman & Peacock, 2003). In addition to hydrothermal systems (Chassefière & Leblanc, 2011; Schrenk *et al.*, 2013) it is also possible for serpentine to be produced from the weathering of olivine (Neubeck *et al.*, 2011). Serpentinisation is the most commonly observed hydration reaction for ultramafic rocks (Godard *et al.*, 2013), which would indicate this process would occur on other planetary bodies where both ultramafic minerals and water are present. Experimental studies have shown the serpentinisation of olivine specifically can occur at temperatures between ~ 20 and 430 ˚C and at pressures between 10 and 200 MPa (Vance *et al.*, 2007; Seyfried *et al.*, 2007; Alt & Shanks, 1998). Lafay *et al.*, (2012) shows the replacement of olivine by serpentine can begin to occur within three hours in a solution. After three hours, 10% of the grain was converted to serpentine when in an alkaline solution with a pH of 13.5. Lafay *et al.*, also explain how the conversion of grains occurs. Firstly serpentine forms in notches and pits created by the dissolution at the surface, and then serpentine

forms within fractures that formed as the grain increases in volume, finally the complete transformation occurs (Figure 2.4.1).

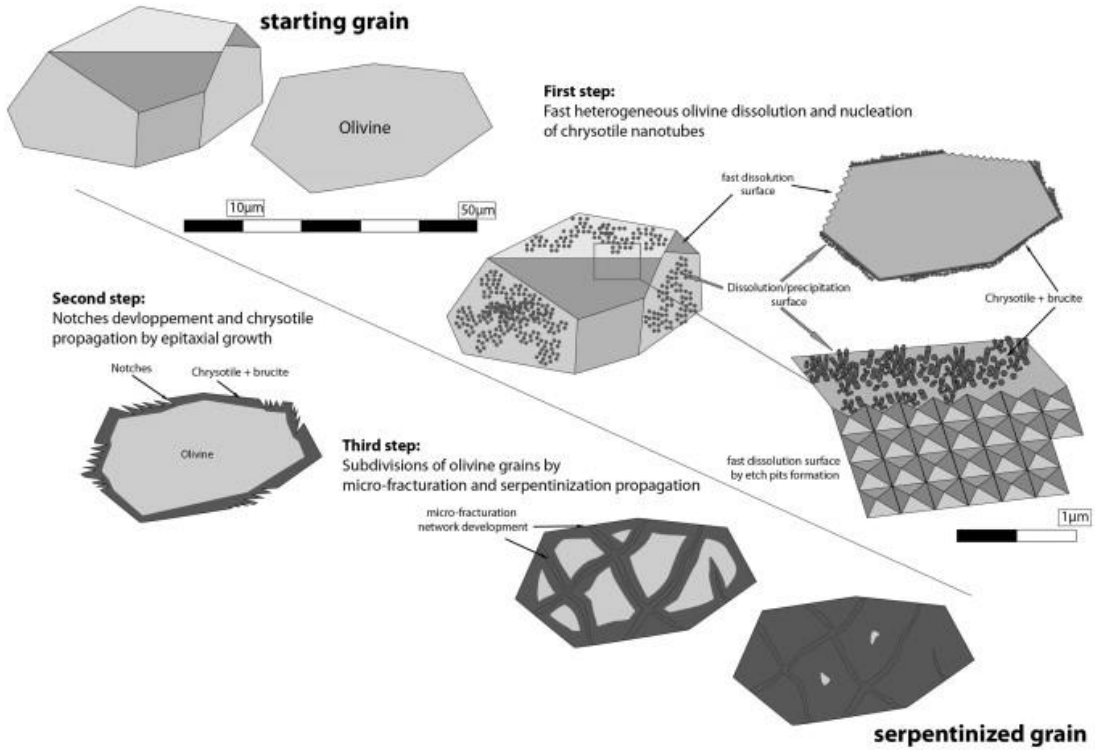

Figure 2.4.1 (Source: Lafay *et al.*,2012) The stages of the serpentinisation of olivine. The initial development of serpentine occurs in notches and pits, and then begins to form in factures before the entire grain becomes serpentine.

Serpentines on Mars

Data obtained from the Mars Reconnaissance Orbiter and Mars Express showed the presence of serpentine on the Martian surface (Carter *et al.,* 2013; Ehlmann *et al.,* 2010). Serpentine has been identified in three locations: 1) near Isidis basin in olivine rich regions; 2) within impact craters in the southern highlands, and 3) Nili Fossae and Claritas Rise (Ehlmann *et al.,* 2010). According to Carter *et al.,* (2013) the serpentine spectral class is not the most common hydrous mineral detected on the surface of Mars, which is the Fe/Mg phyllosilicates spectral class, it does show serpentine is present on Mars's surface. There does appear to be a strong connection with the occurrences of serpentine and exposed olivine. Although Ehlmann *et al.,* (2010) points out there has not been a detection of serpentine in some olivine rich regions, such as Argyre and Terra Tyrrhena, but it has been discovered within craters in the olivine-poor Arabia Terra. If the production mechanism for serpentine was purely through the serpentinisation of olivine, serpentine should be found in olivine-rich areas, which is not what seems to be observed. However,

this could be due to all the olivine in the past olivine-rich regions having undergone alteration, resulting in low olivine concentrations on the surface, or the olivine in these regions is not exposed. The occurrence of these outcrops of serpentine corresponds with the locations of methane detected, particularly at Nili Fossae, Arabia Terrae and Valles Mariners (Fonti & Marzo, 2010; Krasnopolsky, 2012), which may indicate a connection between the two.

Possible Serpentinisation on Mars

The presence of serpentines on the surface of Mars suggests that water was/is present on the Martian surface, as serpentines form from the hydrous alteration of mafic and ultramafic minerals. Olivine and pyroxenes appear to be wide spread on the Martian surface and over a range of ages (Flahaut *et al.,* 2012; Mustard *et al.,* 2005). Hoefen *et al.,* (2003) detected an olivine rich (of Fo_{30} to Fo_{70}) region covering 30000 km^2 in the Nili Fossae area, with smaller outcrops distributed between 60˚N and 60˚S. Spectral data obtained from the Observatoire pour la Minèralogie l'Eau, les Glaces et l'Activitè (OMEGA) infrared and visible mineralogical mapping spectrometer showed the presence of olivine, and both low-Ca and high-Ca pyroxenes on the surface of Mars (Mustard *et al.,* 2005). The High Resolution Imaging Science Experiment (HiRes) and Compact Reconnaissance Imaging Spectrometer for Mars (CRISM) data have additionally revealed olivine and low-Ca pyroxene deposits in the walls of the Valles Mariners (Flahaut *et al.*¸2012).

The current conditions on Mars do not allow water to be present on the surface. However, the presence of valley networks, alluvial fans, lake beds, deltas and hydrous alteration minerals (Masson *et al.,* 2001; Carr, 2012; Mustard *et al.,* 2005) suggest that water was once present in the past. Recent studies (Ojha *et al.,* 2015; Martín-Torres *et al.,* 2015) have suggested water, in the form of brines, could potentially be found on Mars today. Although these findings are interesting, and point towards the possibility of finding water on Mars, they have not actually detected water on Martian surface or subsurface.

The presence of water in Mars's history would suggest that serpentinisation occurred in the past, which may have resulted in the generation of methane; but it would not explain current concentrations. Large impacts, and the craters that formed, could produce hydrothermal systems that enable water-rock interactions and thus serpentinisation to occur. Schwenzer & Kring (2013) used an impact-hydrothermal model to examine the

mineral assemblages that would form from a hydrothermal system created by an impact on Mars. The results showed the water-to-rock (W/R) ratio affected the mineral assemblages generated, at high W/R hematite formed; intermediate W/R ratios generated hematite - clay with some pyrite, ± quartz and ± chlorite, and finally low W/R ratios produced serpentine – chlorite and some amphibole – talc – magnetite ± garnet ± quartz. Schwenzer & Kring (2013) conclude that hydrous minerals will be formed in fractures, central peak, peak rings and modification zones, but this will change with repeated impact events on the terrain, and hydrous minerals in Noachian terrains most likely formed from impact induced hydrothermal systems. These results indicate serpentines found in impact craters, may have formed as a result of impact induced hydrothermal systems.

The surface conditions on Mars would affect the rate at which the alteration of olivine would occur. Computer simulations conducted by Stopar *et al.,* (2003) examine the dissolution rate of olivine on Mars, and discovered the dissolution time of grains between 0.001mm and 10 mm in diameter at 5 ˚C was ~ 100 times longer than the time at 100 ˚C and at various pHs, with a neutral pH having the longest dissolution time. It was found that grains 10 mm in diameter could completely dissolve in solution in less than 10,000 years (Stopar *et al.,* 2003), whereas Mg-rich olivine required a longer time for complete dissolution to occur. The complete dissolution of a 1 mm Fo_{50} olivine grain can occur within five years at a pH of 2, just over 10 years when at a pH of 13 and approximately 500 years with a neutral pH and at a temperature of 25 ˚C (Stopar *et al.*, 2003). These results, and the work of Oze & Sharma (2005), show the dissolution of olivine is dependent on grain size, Mg content, temperature and pH, and the fast dissolution times of less than 12 hours can occur for Fe – rich olivine (fayalite). The olivine currently detected on the surface is intermediate in composition at Fo_{30} to Fo_{70} (Hoefen *et al.*, 2003; Oze & Sharma, 2005), which would suggest longer dissolution times. However, Lafay *et al.*, (2012) has shown the incipient alteration of olivine can occur in less than three hours for grains 30 µm in size and at 200 ˚C in an alkaline solution. Martian soil is neutral, with a pH of 7.7 ± 0.3 (Kounaves *et al.,* 2010), which would indicate higher dissolution times, according to the dissolutions rates determined by Stopar *et al.,* (2003). The longer times for dissolution would mean there is a longer interaction times between the olivine and the liquid solution, which would result in more chance of the serpentinisation of olivine to occur.

Shock Induced Serpentinisation

Shock experiments using olivine, iron and water conducted by Furukawa *et al.,* (2007) found the formation of ultrafine particles of, what was presumed to be serpentine, resulting from the impact. A second experimental programme conducted by the same team (Furukawa *et al.,* 2011) showed the formation of serpentine on the surface of shocked olivine. Both sets of experiments used an olivine and water mixture sealed within a steel sample container and impacted with a flyer plate. Furukawa *et al*., (2007; 2011) believe the alteration occurs as a result of the water being heated to the point where it becomes sub- or supercritical. Above this point there is no distinction between the liquid and gas phases, which would enable alteration and dissolution of substances (Furukawa *et al.,* 2011). The critical pressure and temperature for water to turn into a supercritical fluid occurs at 22.064 MPa and 373.95 ˚C (Pioro & Mokry, 2011). Although these results show serpentinisation can occur as a result of an impact, they do not replicate the effects of an impact on a terrestrial surface like Mars. The shock waves are reflected back once they reach the interface with the container, resulting in the sample experiencing multiple shocks, which would not occur in a naturally occurring impact. There is also the possibility for the serpentine crystals to have formed as a result of being held in water for enough time for serpentinisation to occur and, even though H_2O is found on Mars, the surface conditions means it is found as water ice. In addition, these results do not necessarily show serpentinisation occur as a result of the shock wave passing through starting materials. It appears to be as a result of the increased pressure within the sealed container. This particular impact induced serpentinisation process could occur within a body of water, as in the case of Earth, or at depth on a rocky body most likely beneath the point of impact.

2.4.7 Section Summary

In this section the evidence indicating the presence of methane on Mars is presented, along with potential sources that may have resulted in its formation. A recent study showed the formation of serpentine as a result of shocking olivine and water. The serpentinisation experiment carried out here (Chapter V) examined if this process could occur (and also create methane) when a mixture of olivine, water ice and CO_2 ice is impacted.

Chapter III

Understanding Impacts

A branch of physics (shock physics) is used to help understand the conditions materials experience when undergoing a shock, whether that be from an impact or some form of explosive. Impacts generate extremely high pressures and temperatures as a result of a shock wave passing through material, which can affect rocks and minerals in a number of ways, such as: melting, vaporisation or fracturing (see Chapter II, Section 2.2 for more information).

In the modern era (post Second World War) the main driving force for the examination of high pressure effects on materials has been as a result of nuclear weapons development and nuclear deterrents (Trunin, 1998; Marsh, 1980). A long series of experiments were conducted by the USA and USSR to determine the response for a range of materials, including rocks and minerals, to intense shock compression.

Laboratory impact experiments use accelerators such as light gas guns, electrostatic dust accelerators and plasma drag accelerators (Thoma *et al.*, 2005) to simulate impacts and to assist in determining their effects on materials. In addition to laboratory experiments, computational modelling has also played a key role in our understanding of the conditions experienced by impacts.

3.1 The Shock Effects of Impacts

Upon impact the shock wave propagates through the target material. These waves are created when the stress (from a pressure disturbance) exerted on a material is greater than the elastic limit of the material (Zukas, 2004). The waves travel through the material in pulses, the first pulse is generated on initial contact between the projectile and target, with additional pulses generated as a result of the continuous forward motion of the projectile at its initial impact velocity. The initial wave is travelling at a lower velocity than the later

waves, as wave velocity increases with the increased pressure in the shocked material (Zukas, 2004). The increase in velocity of later waves means, eventually, they will catch up to the initial wave and a single wave-front moves through the material. This creates a mathematical discontinuity between unshocked and shocked materials in front of, and behind, the shock front (Figure 3.1.1).

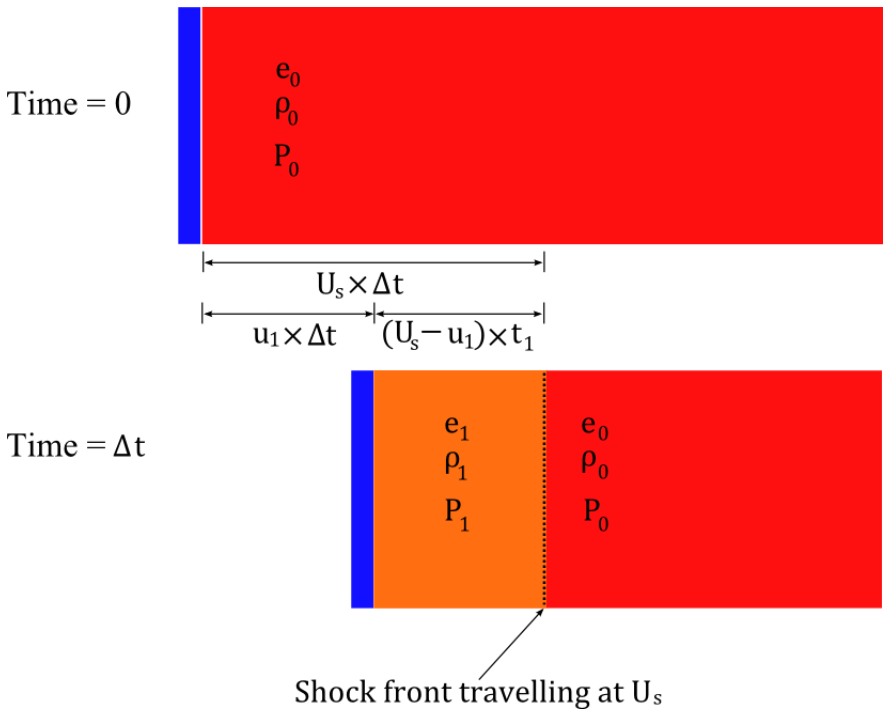

Figure 3.1.1 (Diagram modified from "Key concepts of Shock Hydrodynamics" course handbook) The diagram shows a flyer plate (blue) impacting, with a velocity u_1, a thicker target (red), which represents a 1-D impact and does not take into account any reflection or release waves. The dashed line denotes the shock front, travelling at a velocity U_s, as it travels thorough the target material. It also shows the abrupt change between shocked material (orange) and unshocked material (red).

The conditions on either side of the shock wave are related to each other through the Rankine-Hugoniot relations (named after William Rankine and Pierre-Henri Hugoniot in recognition of their contribution to shock wave theory), which are based on the principles concerning the conservation of mass, momentum and energy (Collins *et al.*, 2013; Thoma *et al.*, 2005). These laws can be explained using a simple 1-D example of a flyer plate, impacting a target plate (Figure 3.1.1). A 1-D example only explains the effects of a single shock wave produced from the impact and not the effects of additional release and reflected waves, which can be generated when the shock wave reaches an interface between different materials. The force produced when the flyer plate impacts the target causes the target material to move a distance, $u_1 \times \Delta t$, at a velocity of u_1(in m s^{-1}) within a

certain amount of time, t_1 (in seconds). A shock front, moving at a distance, $(U_s - u_1) \times t_1$, ahead of the initial compression has a velocity, U_s and travels over a time of Δt. The compression of the material results in a difference in density before (ρ_0), and after (ρ_1), the passing of the shock front, as a result of the change in volume, but as mass is conserved in the region we obtain the following equation:

$$\rho_0 U_s = \rho_1 (U_s - u_1) \qquad \text{Equation 3.1.1}$$

The rate of change in momentum of the material, $(\rho_0 (U_s - u_0)(u_1 - u_0))$, as a shock wave passes through it is used to express the conservation of momentum. The force exerted by the flyer plate results in an increase in momentum of the material as it moves a given distance, $u_1 \times \Delta t$, with a velocity of u_1. Therefore the net force $(P_1 - P_0)$ is equal to the change in momentum of the system (Equation 3.1.2).

$$P_1 - P_0 = \rho_0 (U_s - u_0)(u_1 - u_0) \qquad \text{Equation 3.1.2}$$

The conservation of energy equates the compressional work done by the impactor, $(P_1 u_1)$, to the total energy in the system, both kinetic energy $(\frac{1}{2}\rho_0 U_s u_1^2)$ and total internal energy $(\rho_0 U_s (e_1 - e_0))$, which gives us Equation 3.1.3.

$$P_1 u_1 = \frac{1}{2}\rho_0 U_s u_1^2 + \rho_0 U_s (e_1 - e_0) \qquad \text{Equation 3.1.3}$$

The conservation of energy equation can also be written in its popular form of the Rankine-Hugoniot equation (Equation 3.1.4).

$$e_1 - e_0 = \frac{1}{2}(P_1 + P_0)\left(\frac{1}{\rho_0} - \frac{1}{\rho_1}\right) \qquad \text{Equation 3.1.4}$$

Where subscript 0 and 1 in Equations 3.1.1 – 3.1.4 represent the state of the material before and after the shock wave passed through it respectively. These relationships describe the conditions of a material as a shock wave passes through it, in a 1-D situation, before interference waves (i.e. reflected waves from interfaces etc.) affect the shocked material. They also assume the material is a continuous medium, with no voids or spaces.

Hugoniot plots describe a material's response as a result of shock, and can be represented in a number of ways, but are most commonly plotted in the U_s-u_1 plane, u_1-P plane and/or the P – v plane (where v is the specific volume). Shock experiments are normally conducted to determine U_s and u_1 values, where a plot of U_s versus u_1 are linearly related for many materials. The relationship can be expressed as:

$$U_s = c + Su_1 \qquad \text{Equation 3.1.5}$$

Where u_1 is particle velocity, U_s (in mm μs^{-1}) is the velocity of the shock wave, and material constants are represented by S (slope gradient) and c (slope intercept, which is the bulk sound velocity). This equation can also act as an equation-of-state (described in more detail below), but it does not incorporate temperature and entropy (Melosh, 2013). Therefore, is not a full equation-of-state, which normally describes the state of the material under a range of pressures, temperatures and densities. These material constants 'c' and 'S' can be used to approximate the peak shock pressures experienced on impact, by either plotting the P - u_1 plane Hugoniots, or by using the planar impact approximation equation determined by Jay Melosh in his 1989 book on impact cratering (Melosh, 1989). Both approximations aim to calculate the peak pressures experienced on contact between the projectile and target. The projectile does not interpenetrate the target and so the target material is compressed and is given a velocity equal to the deceleration the projectile experiences (Melsoh, 2013). This also means the pressure experienced by both projectile and target are equal at this contact stage for a given impact velocity. Therefore, by calculating the pressure (Equation 3.1.6) and plotting P - u_1 plane Hugoniots for both materials (where the Hugoniot for the projectile is reversed, Equation 3.1.7), the peak pressure can be determined from the intersection – an example is given below.

$$P = \rho_0(c + Su_1)u_1 \qquad \text{Equation 3.1.6}$$

$$P = \rho_0(c + S(v_i - u_1))\,(v_i - u_1) \qquad \text{Equation 3.1.7}$$

Where v_i is the impact velocity of the projectile (ms^{-1}).

Figure 3.1.2 shows the principal Hugoniot for an aluminium-6061 target being impacted by a hematite projectile at a velocity of 3 km s^{-1}. The Hugoniot for the hematite projectile is calculated using Equation 3.1.7.

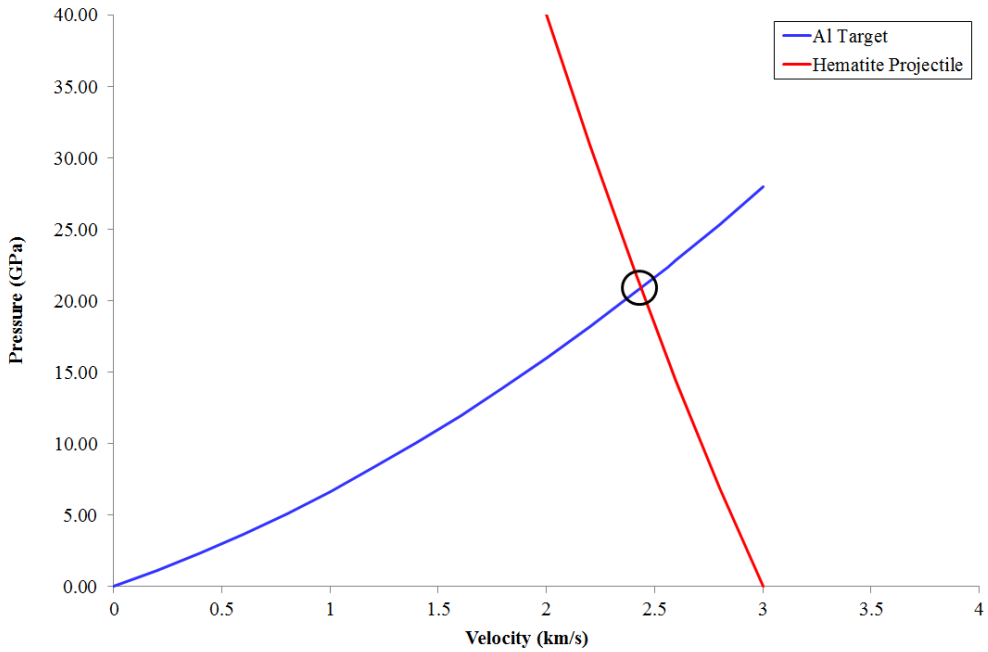

Figure 3.1.2 Hugoniot curves in the p – u_1 plane showing the peak pressure where the Al target Hugoniot (blue line) and hematite projectile Hugoniot (red line) intersect during a 3 km s^{-1} impact. The peak shock pressure in this example is 22.36 GPa, and is circled.

The planar impact approximation (Equation 3.1.8) assumes the projectile impacts the target face-on, with both projectile and target represented as plates that are infinitely wide. Using infinitely wide plates means the impact can be modelled in 1-D, and the effects of edges and material interfaces can be ignored (Melosh, 2013). However, the angle of the impact can be added to the equation to calculate the peak pressures for oblique impacts.

$$P = -\rho_{0p} u_t (c_t + S_t u_t) \qquad \text{Equation 3.1.8}$$

The subscripts t and p denote parameters for the target and projectiles respectively, c and S are the material constants (from Equation 3.1.5), ρ_0 represents the density of material before impact and u_t is the velocity of the target on impact and is calculated using Equation 3.1.9.

$$u_t = \frac{-B \pm \sqrt{B^2 - 4AC}}{2A}$$ Equation 3.1.9

Where,

$$A = \rho_{0t} S_t - \rho_{0p} S_p$$ Equation 3.1.10

$$B = \rho_{0t} c_t + \rho_{0p} c_p + 2\rho_{0p} S_p + v_i$$ Equation 3.1.11

$$C = -\rho_{0p} v_i \left(c_t + S_p v_i\right)$$ Equation 3.1.12

(Source: Melosh, 2013.)

Again subscript 0 represents the parameter before the shock wave passed through the material, subscripts t and p relates the parameter for the target and projectile, respectively, ρ is the density, S and c are the material constants taken from Equation 3.1.5, and v_i is the impact velocity (in m s^{-1}).

Although peak pressures upon impact can be estimated by assuming a 1-D system with only one shock wave passing through the material, in reality more than one shock wave will occur. Waves will be generated when the initial shock wave reaches a free surface or at an interface between two materials. A second Hugoniot for the second wave can be calculated using the variables of the material after the first shock wave has passed through it as the initial variables.

The techniques for calculation pressure described above are predominantly used to determine the peak pressure of an impact. In order to calculate the changes in pressures and temperatures over time computational modelling is required.

3.2 Computational Modelling

The behaviour of materials experiencing an impact can be very complicated, so computer codes have been employed to study them. They are a reliable way to study impact events, providing information on the pressures, density, temperatures, crater morphology, ejecta and timescales of impacts. Particular types of data, such as temperature, are very difficult/impossible to determine on the timescales that are conducted in laboratory experiments (using a light gas gun for example). Computer modelling assists with understanding small scale laboratory experiments, which can then be connected to the

much larger craters observed on rocky bodies (Pierazzo, 2006). It also offers a way of scaling-up impacts and provides insight into planetary scale events, such as the Chicxulub crater forming impact (Pierazzo & Melosh, 1999; Collins *et al.*, 2002).

To create realistic models of impacts an equation of state (EoS) is required, which helps to determine the state of a material that has already undergone a shock event. An EoS relates pressure, density (or volume) and temperature (or internal energy), and describes a number of thermodynamic properties, such as compressibility and shock heating of a material (Collins *et al.*, 2013; Pierazzo & Collins, 2004). There are a number of EoSs that can be used such as: Mie-Grünieisen (Mie, 1903: Grüneisen, 1912) and Tillotson (Tillotson, 1962). The EoS is vital during the early stages of the impact process, as the strength of the material (megapascals) is almost insignificant in comparison to the high pressures (gigapascals) experienced (Pierazzo, 2006). The negligible strength of the material during the contact and compression stage of crater formation is why the target and projectile materials can be treated as a fluid. However, the strength of the material becomes more important in the latter stages of crater formation, and helps determine crater morphology and traits (Pierazzo, 2006; Pierazzo & Collins, 2004). In computational modelling, relations of stress to strain and rate-of-strain are required, as they provide information on a material's response to uniaxial and multi-axial stress (Isobell, 2005). Constitutive models (also known as strength, or deviatoric stress, models) are used to determine how target materials respond from stresses induced during impact. The models use relations that describe the amount of distortion that occurs as a result of the stress the material experiences. Hooke's law is a classic example of a simple constitutive relation; where the amount of deformation is proportional to force applied to a spring. Solid materials, such as metals and rocks, possess a yield strength; when the stress exerted on the material is greater the yield strength the material distorts irreversibly, thus acting plastically. If the material yield strength is greater than the applied stress the material acts elastically, so when the stress is removed, the material is able to revert back to its initial state (Collins *et al.*, 2013). Constitutive models essentially use the relations between stress, strain and strain rate to calculate the total stress applied and then compare it to the yield strength of the material. They calculate the strain, and rate-of-strain, of the material that should occur as a result of a given stress. Stress has six stress tensors in 3-D space, so these models also combine the stresses to provide one total value that is generally used. The yield strength of materials can change as a result of temperature, pressure, strain, rate-of-strain, porosity and size - particularly for geological materials (Collins *et al.*, 2013).

Therefore, constitutive models need to account for these additional physical and environmental parameters. Another important factor to take into account is the materials granular structure, as with increasing confining pressure the yield strength also increases (Collins *et al.*, 2013). There are a number of constitutive models that can be used which incorporate some, or all, of the variables that can affect yield strength. A wide range of models exist, such as Johnson-Cook (Johnson & Cook, 1983), Johnson-Holmquist (Holmquist *et al*, 1993), von Mises (Mises, 1913), and Steinberg (Steinberg *et al*, 1980) to name a few.

Computational modelling separates the stress tensor into two components: 1) isotropic scalar (or hydrostatic pressure) and, 2) deviatoric stress. The isotropic scalar component describes the pressure being exerted and the resulting changes in volume and energy (Glushak, 2006), which is related by the EoS and, as mentioned earlier, is important in the early stages of the impact (Pierazzo & Collins, 2004). Deviatoric stresses express the change in shape that occurs from compression or expansion (Glushak, 2006); these stresses are important in the later stage of impacts and are related by constitutive models (Pierazzo & Collins, 2004).

3.2.1 Numerical Solvers

Impact modelling is used to realistically (or as realistically as possible) recreate the impact event and provide information on specific variables of interest throughout the event. Numerical solvers are used to assist with this process by utilising the conservation equations, EoS and constitutive models. There are three widely used solvers that are currently used, 1) Lagrangian, 2) Eulerian and 3) Smoothed Particle Hydrodynamics (SPH). These numerical solvers use discrete computational cells which allow the computer (which has a finite memory) to divide the objects, and their materials, into a smaller number of cells. The behaviour of the individual cells is governed by the conservation equations (Equations 3.1.1 - 3.1.4), the material's EoS and constitutive models, to replicate the material's response.

Target and projectile geometries can be defined with all three solvers, but the nature of the computational cells are different. Both Lagrangian and Euler solvers use a mesh, but in different ways, whereas the SPH solver is a meshless grid. In Lagrangian approaches the mesh generated fills in the defined geometries of the projectile and target,

where the size of the cells is defined by the user. The cell has a fixed mass of material, but the dimensions of the cell itself are able to change in reaction to external and internal forces (i.e. the mesh deforms). Eulerian techniques place a mesh around the projectile, target and the surrounding space, where the dimensions of the mesh are fixed and materials move in and out of the cells. SPH solvers populate the defined geometries with individual pseudo-particles (nodes) in the corners of each cell that defines the geometry. The SPH cells represent the immediate area, and are treated, and can be thought of, as physical fluid particles (Pierazzo, 2006). Changes in the meshes, or particles, positions resulting from the external and internal forces are tracked and cells are updated with each timestep. Both SPH and Lagrangian solvers allow the mesh and particles to move with the materials, so it is seen from the frame of reference of the material. Eulerian solvers on the other hand have an external frame of reference from the material, meaning the projectile and target travel through a mesh, with their geometries occupying cells in the mesh. Figure 3.2.1 visualises the difference between the three solvers. The diagram shows extreme distortion of Lagrangian cells can occur, but the same distortion does not occur in Eulerian solvers. SPH solvers show the interaction between objects, as the behaviour of the particles is modelled as a fluid.

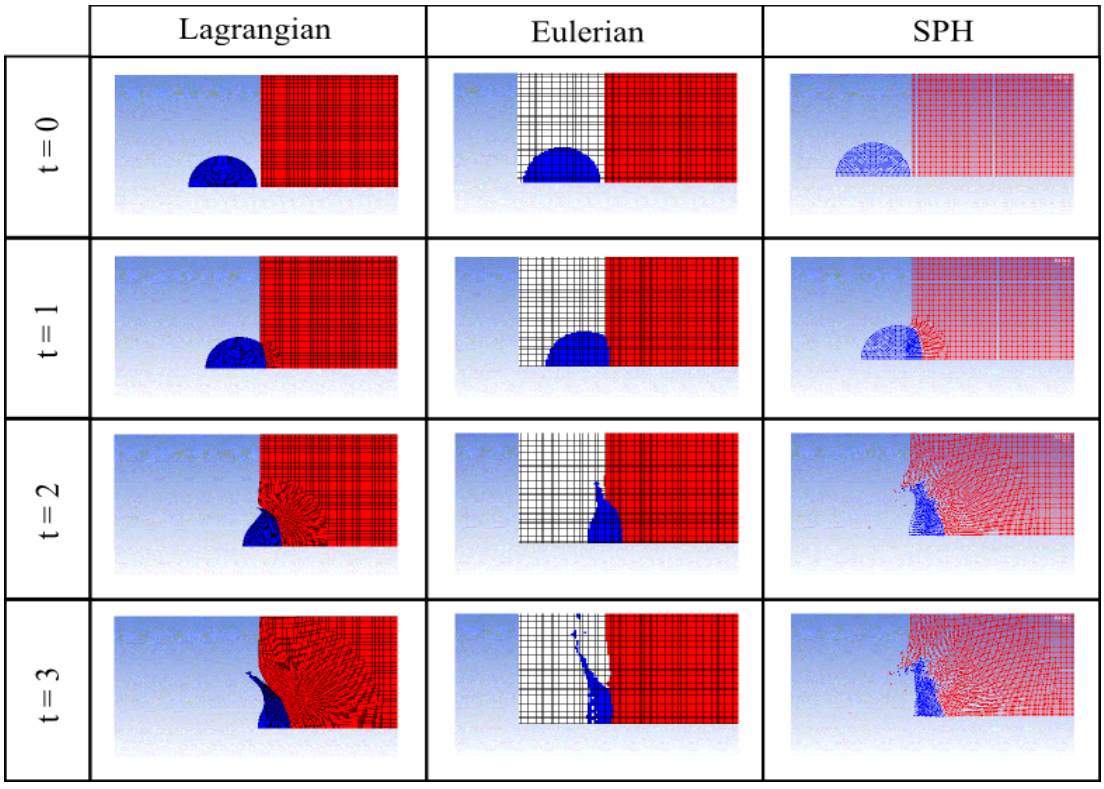

Figure 3.2.1 (Images courtesy of Mark Price) Impact models using the three different numerical solvers at t = 0, 1, 2 and 3 (t values refer to arbitrary units of time and are not relative to one another).

The cell size determines the resolution of the simulation, and (for impact work) is commonly referred to as Computational cells Per Projectile Radius (CPPR). A smaller CPPR means more detail can be simulated about features such as melt production (Pierazzo, 2006), although crater traits, such as crater depth and diameter, are insensitive to resolution (above a certain limit, Collins *et al.*, 2013). Resolution can also be dependent on the computing power of the machine, storage and the model dimensions. The dimensions of the modelled objects will mean the need for more cells (for larger objects), which necessitates more computing power, storage and time. Thus, the resolution selected needs to fit the required outputs and the available resources (Pierazzo, 2006).

One of the major limitations of Lagrangian solvers occurs when cells become very distorted. This Lagrangian method uses cells centred on finite mass elements (Vignjevic *et al.*, 2001), so when computational cells become heavily distorted they can begin to fold over on themselves generating negative volumes, or the distortion leads to greatly increased run times due to the reduction in the computational timestep (Vignjevic *et al.*, 2001; Pierazzo, 2006; Zukas, 2004). To manage the problem of cell distortion the simulation can be stopped and the model re-meshed. This re-meshing can be time consuming and produce inaccuracies in the output data. It is also possible to delete the distorted cells once the distortion reaches a critical value. Increased run-times resulting from cell distortion is caused by one of the cell's dimensions being reduced, which shortens the length of timesteps. Timesteps are determined by the size of cells, as a timestep has to be smaller than the amount of time it takes information to transverse the smallest dimension of a cell (Pierazzo & Collins 2004). Lagrangian solvers are generally a simpler code to use, have fewer computations per update and provide good modelling of the strength of materials (Autodyn handbook, 1997). Eulerian solvers are not plagued with the same cell distortion problems that affect Lagrangian solvers, as the fixed mesh does not deform and modern Eulerian solvers can also track multiple materials in a single cell. However, interfaces between different materials in Eulerian solvers are difficult to distinguish and track throughout a simulation run (Pierzzo & Collins, 2004). The fixed mesh means mixtures of materials can be made within single computational cells, and it can be difficult to determine material boundaries, unlike the Lagrangian where the mesh attached to the material provides discrete boundaries. In addition, a problem develops when material occupying cells are less than approximately 0.1% of the total cell volume (Zukas, 2004). These small material volumes will produce very small values for physical parameters (such as density and pressure within the cell) and can become difficult to

manage, leading to rounding errors which, in some modelling software, will cause the simulation to end. Modelling software will normally have a minimum value for the relative volume of material occupying the cell and, below the set value, the software will round down to zero occupancy. SPH solvers do not have the same limitations as Lagrangian or Eulerian solvers as the cells are not fixed to a mesh. These solvers allow tracking of nodes separated by large distances (Zukas, 2004) without the same problems seen in Lagrangian solvers when the cells become greatly distorted. However, the large distance between nodes does produce issues with resolution. As the region in-between nodes develops a low resolution and the data region is smoothed between the adjoining nodes. The constitutive models are also difficult to implement in SPH solvers and waves are reflected when they reach the edge of objects (Pierazzo & Collins, 2004). SPH solvers can also be coupled with Lagrangian solvers resulting in simulations benefitting from the advantages of both types of solvers. Areas that would produce high deformation, and result in a great degree of Lagrangian cell distortion can be modelled using SPH particles, and the remaining areas modelled with Lagrangian cells.

3.2.2 Autodyn

Modelling of the laboratory impact experiments carried out in this investigation were conducted using ANSYS' Autodyn software (Hayhurst & Clegg, 1997), where pressures and temperatures experienced during the impact can be determined. The software was initially released in 1986 by Century Dynamics and, in 1991, Autodyn-3D was released. It is well equipped to examine non-linear dynamics, with the ability to be used on personal computers as well as supercomputers.

All three types of numerical solvers can be used in Autodyn, and it allows for the joining of SPH components to Lagrangian structures. To overcome large cell distortions, cut offs can be determined to allow for these types of cell to be deleted (or in Autodyn speak 'erode') from the run and thus prevent increased run times or the run stopping prematurely. Gauges (or tracers) can be attached to cells, or nodes, to collect information at specific locations across the projectile and target materials, which can then be plotted as a function of time.

Autodyn comes with an inbuilt material library with a wide range of materials, including a range of metals and plastics. Each material has an associated EoS and

constitutive model that can be used for modelling objects. The software also enables the input of new materials, where the EoS and constitutive model can be determined by the user. The minerals used in this investigation were not available in the material database, and were added using the Shock EoS and Von Mises constitutive model. Data regarding the temperature of impacts as a function of time can also be determined by including the initial temperature, the thermal conductivity and specific heat of the material. Information regarding the thermal properties is not provided for materials in the material library and can be added if required. However, currently, the SPH solver is unable to model the transmission of heat across an object.

Autodyn is also able to model oblique impacts and the impacts of rotating projectiles. The rotation of the projectile would accurately model the motion of the projectile in laboratory experiments, as the projectile rotates inflight due to the rifling within the launch tube (explained in Chapter IV, Section 4.1.1). The ability to show the rotation of the projectile does provide a more realistic model for the laboratory experiments, but it is not necessary for the needs of this investigation, where only impact pressures and temperatures are required.

3.3 Chapter Summary

Chapter II, Section 2.2 described the effects impacts can have on solid and rocky bodies. Here, what occurs in the material as shock waves pass through it has been described. This chapter also describes some of the fundamentals of computation modelling, which uses shock physics to create models of impact events for study. The three methods described here to determine peak pressures (Hugoniot plots, PIA calculation and computational modelling) have been used to determine the peak pressures from serpentinisation and devolatilistion experiments described in Chapters V and VI, respectively.

Chapter IV

Equipment

A light gas gun, a Raman spectrometer and a scanning electron microscope (SEM) were the primary pieces of equipment used in this investigation. The light gas gun has been used to simulate impacts by accelerating projectiles towards a target at a range of velocities. The Raman spectrometer is the primary analysis technique used to examine targets/target material that were subjected to impacts. In addition to this, it is also used to examine material from additional experiments conducted to assist with analysing of the results from impact experiments. Complementary scanning electron microscopy and energy dispersive X-ray analysis was conducted on residues from impact and heating experiments, and to characterise the minerals used in this investigation.

4.1 The Light Gas Gun

Gas guns were originally developed to study terminal and external ballistics (Crozier & Hume, 1957). Today they are still used for such studies, in addition to investigations into: shock compression, crater morphology, effects of debris in low earth orbit and planetary atmosphere evolution. They are used to simulate hypervelocity impacts under laboratory conditions, enabling the retrieval of impacts samples for investigation (Isobell, 2005).

In the early years of ballistic experiments, projectiles were required to be accelerated to velocities of 6-8 km s^{-1}, which was unachievable by powder guns, where carefully configured guns could only reach up to 3 km s^{-1} (Charters, 1995). During the mid-1940's it was proposed that a gas with a low molecular weight could be used to attain high velocities (in review by Crozier & Hume, 1957). This is due to the fact that the maximum possible speed of a projectile (Equation 4.1.1) is related to the speed of sound in an ideal driver gas (Moritoh *et al.*, 2001; Doolan, 2001), via:

$$U_{p\,max} = \frac{2}{\gamma - 1}\, c \qquad \text{Equation 4.1.1}$$

$$c = \sqrt{\frac{\gamma RT}{m}} \qquad \text{Equation 4.1.2}$$

Where, c = speed of sound (ms^{-1}), γ = specific heat ratio, R = gas constant ($J\ kg^{-1}\ K^{-1}$), T = gas temperature (K), and m = molecular weight of driver gas (g).

Equation 4.1.2 shows the relationship between the speed of sound in the driver gas and the molecular weight of the gas. The lower the molecular weight of the driver gas the faster the speed of sound is within the gas. As a result of this relationship, hydrogen and helium are commonly used as the driver gas in a light gas gun. The maximum speed of the projectile is increased further by increasing the temperature of the driver gas (Equation 4.1.2), which is achieved through adiabatic compression (Doolan, 2001; Yokoo *et al.*, 2001).

Modern two stage light gas guns work via the ignition of a propellant that pushes a piston, which compresses a column of light gas. The compressed gas is then rapidly released by the rupture of a burst disc, which acts like a diaphragm controlling when the gas is released. The rapid release of the gas accelerates the projectile to impact the target (Burchell *et al.*, 1999). Such light gas guns have the capability to accelerate projectiles up to speeds of 9-10 km s^{-1} (Angrilli *et al.*, 2003).

The light gas gun enables the firing of a variety of projectiles, in size and material, at a range of velocities. The light gas gun at the University of Kent can fire projectiles up to 4.50 mm in diameter (which, at this size, is normally a solid nylon projectile). However, in theory anything that can fit inside a sabot can be fired in the gun. This makes it ideal for the experiments in this investigation (Chapters V and VI), whereby the minerals under investigation can be used as projectiles.

4.1.1 Components of the Light Gas Gun

The schematic below (Figure 4.1.1) shows the sections and assembly of the light gas gun, which are explained in detail in the following sections.

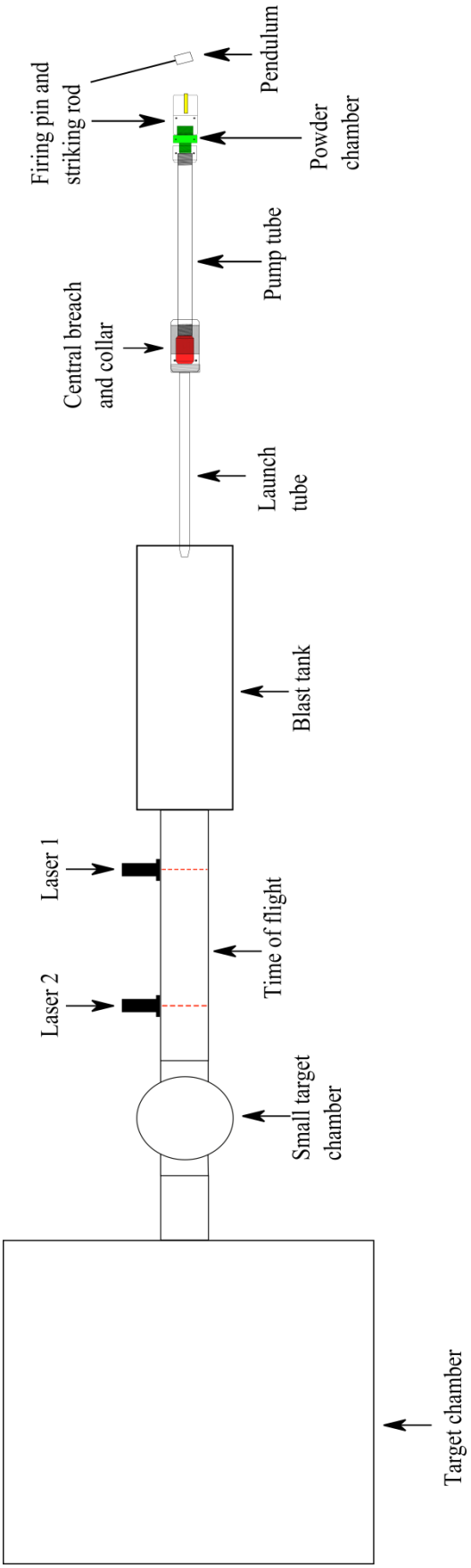

Figure 4.1.1 A schematic (not to scale) of the light gas gun at the University of Kent.

Pendulum, Firing Pin and Control Panel

A brass pendulum is used to hit the striking rod, pushing the firing pin into contact with the primer cap, which results in the ignition of the powder. The release of the pendulum is carried out remotely by use of a control panel located in an adjacent room. The gun room is evacuated and all the doors leading into the room need to be locked before releasing the pendulum to minimise the risk of injury to staff, students and visitors in the event of a misfire or gun malfunction.

Powder Chamber

A shotgun cartridge is used for the ignition propellant cartridge, which is held into position by the powder chamber. The cartridges are made on-site using standard shotgun cartridge hulls. The primers fitted into the cartridges are not suitable for the needs of the gun and so, are replaced with a new primer ("Magnum 209"). Cartridges are filled with 8-12 g (depending on the speed required) of rifle powder and stuffed with wadding before being sealed by crimping the cartridge.

Three types of rifle powder are currently used for firing the gun, "Alliant Reloader" 7, 19 and 22; which one used is dependent on the velocity of the shot required. The variation in the type of rifle powder used results in a variation in the velocity at which the projectile travels (Table 4.1.1). The different powders have individual burn rates, resulting in different pressure profiles being produced to push the piston down the pump tube: the faster the ignition powder burns, the greater the velocity the piston is accelerated to.

Table 4.1.1 The type of rifle powder used for various velocities.

Type of powder	Relative quickness (%)*	Velocities used for (kms^{-1})
Reloader 7	19.4	5 and above
Reloader 19	11.3	3 – 5
Reloader 22	11.1	Less than 3

*Taken from the Guide provided by the manufacturing company.

Pump Tube

The pump tube is used to store the light gas (driver gas) before firing and is joined to the powder chamber by a connecting nut. The type and pressure of the driver gas is dependent on the required velocity (Figure 4.1.2).

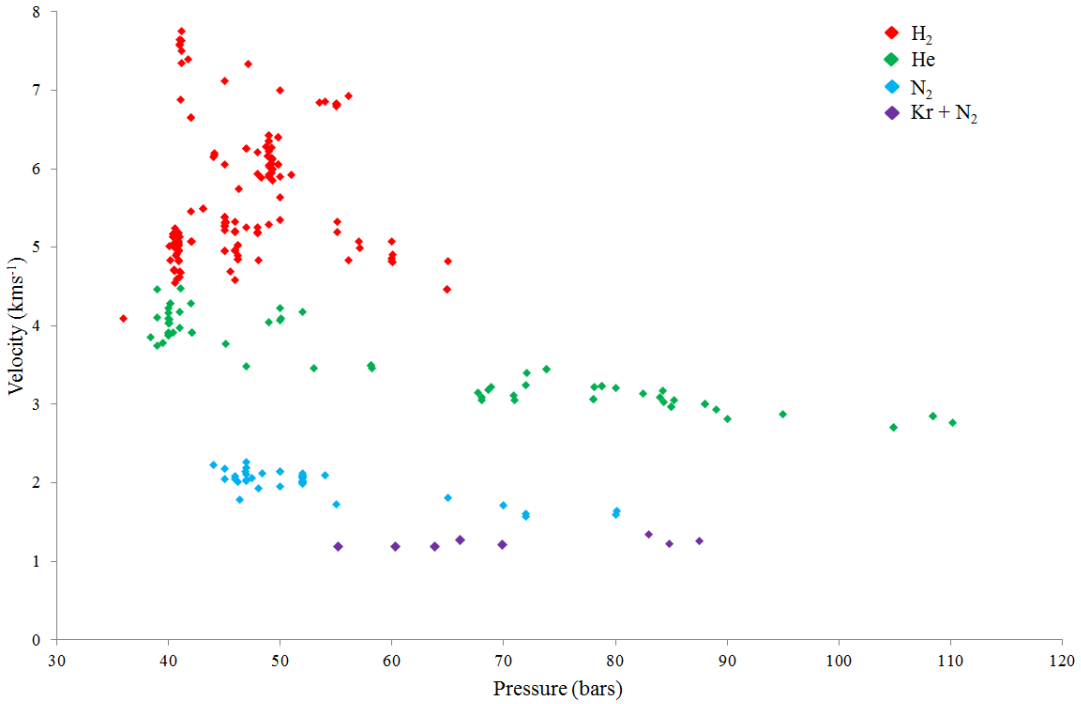

Figure 4.1.2 (Data courtesy of Mike Cole) Graph shows the range of velocities that can be achieved using various gases at the University of Kent's LGG facility. Information regarding the type of rifle powder used, projectile and pump tube used has been omitted for clarity.

A nylon piston is inserted into the pump tube before the powder chamber is connected by a connecting nut. The pistons have two rubber "O" rings, ensuring there is a tight seal between the piston and the inner wall of the pump tube, so that none of the driver gas can escape when compression of the gas begins. Once the powder has been ignited, the piston is pushed down the pump tube at a speed of ~ 1 km s^{-1}, which, in turn, compresses the driver gas. The compression of the gas increases the temperature, resulting in a greater projectile velocity. The piston also helps to sustain the increased pressure generated behind the sabot (Doolan, 2001) after the burst disc has ruptured, which helps to maintain the acceleration of sabot and projectile. Figure 4.1.3 shows the acceleration stage of the LGG.

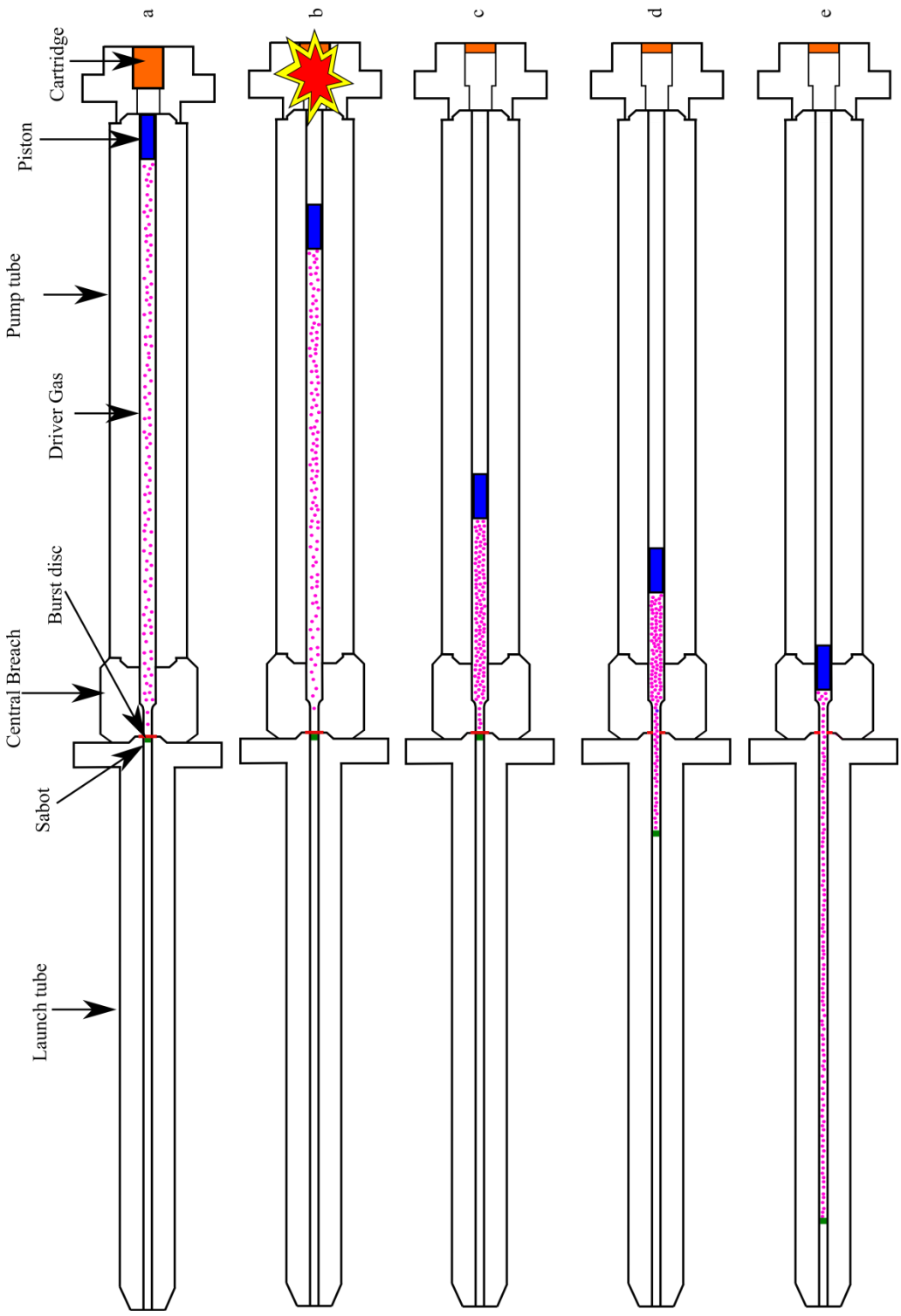

Figure 4.1.3 Schematic (not to scale) showing the movement of gas through the initial stages (or projectile acceleration stage) of the LGG. a) The set up (not including the firing pin and pendulum) before triggering the release of the pendulum. b) Detonation of cartridge accelerates the piston, which begins to compress the driver gas. c) The driver gas is compressed further between the piston and burst disc. d) The burst disc ruptures allowing the driver gas to begin accelerating the sabot; the piston is still pushing the driver gas down the gun. e) The piston cannot travel any further down the gun, due to the change in bore width, as the driver gas expands the sabot continues to accelerate into the next section of the gun.

Central Breach and Collar

The central breach acts as a funnel (Figure 4.1.4), channelling the driver gas from the pump tube to the launch tube.

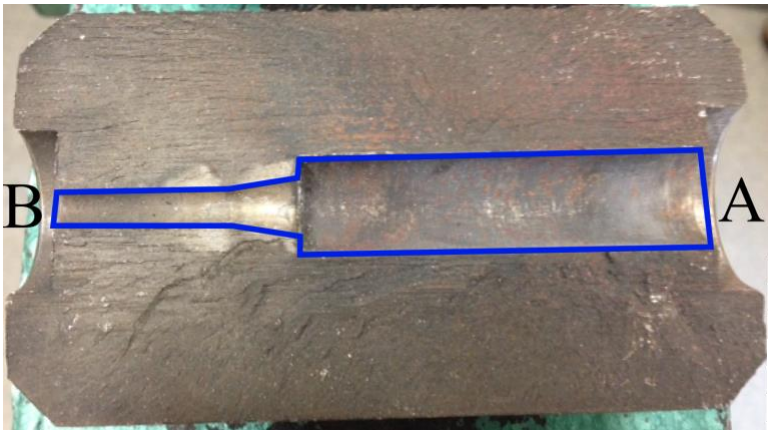

Figure 4.1.4 A cross section of the central breach showing the reduction in bore diameter across the length of the central breach (highlighted in blue). The driver gas is pushed by the piston from the pump tube, which is attached at position A towards the launch tube attached at position B.

It can also capture the piston, preventing it from impacting the launch tube. The collar covers the central breach, joining the pump tube and the launch tube. It also acts as a safety mechanism in the unlikely event that the central breach fails, as the high pressure gas may result in the forceful segmentation of the central breach.

Burst disc and Sabot

An aluminium alloy disc (the "burst disc") with a diameter of 12.7 mm, is placed in-between the launch tube and the central breach. This disc serves as a diaphragm preventing the driver gas from moving down the launch tube (and setting the sabot on its way) until the correct pressure is achieved. Once the correct pressure has been reached the burst disc ruptures (Figure 4.1.5) allowing the driver gas to pass through the launch tube and accelerates the sabot. Again, depending on the speed required, the burst disc can be scored with a central cross. The scores are made at either a pressure of 7 kN or 9 kN, depending on the size of the launch tube bore. An un-scored burst disc is used for speeds greater than 5 km s^{-1}. Scoring the disc guarantees it ruptures at the required pressure and into four petal segments each time. Un-scored discs use variegated edge sharpness to "cut" the disc in a peeling fashion, which ensures this circular piece of metal remains intact as a single fragment and does not travel down the gun and impact the target.

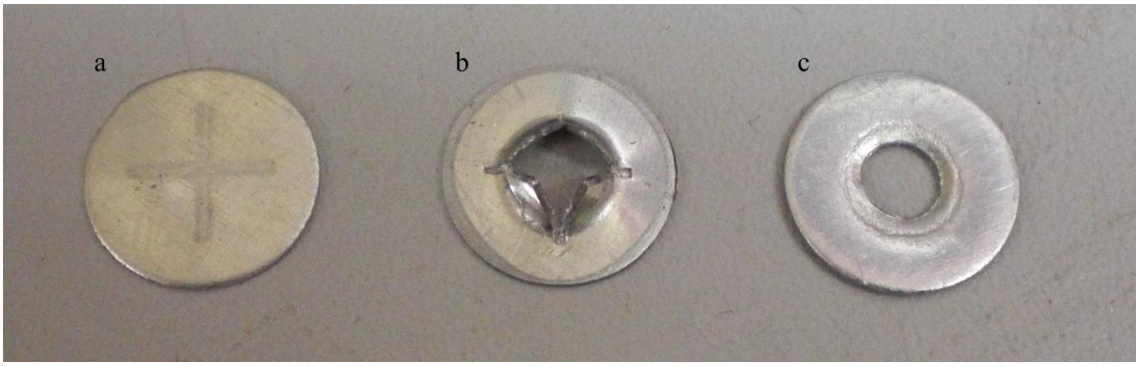

Figure 4.1.5 a) A scored burst disc to the left. b) A burst disc after rupturing showing the four intact petals, which are formed from the scoring of the disc. c) An un-scored burst disc produces no petals. Instead the edge of the launch tube cuts the burst disc, rupturing it as a result of the great pressure being exerted on it from the compressed driver gas; ensuring a single piece of burst disc is produced.

A sabot is used to hold the projectile whilst inside the launch tube. The sabot has approximately the same diameter as the bore of the launch tube; which enables the driving gas to push the sabot down the launch tube without loss of pressure. There are two types of sabots that are used: 1) A sabot which is made of four sections of isoplast (Figure 4.1.6). Each section of the sabot has serrated edges, which locks the pieces together, ensuring they move as one object when being propelling down the launch tube.

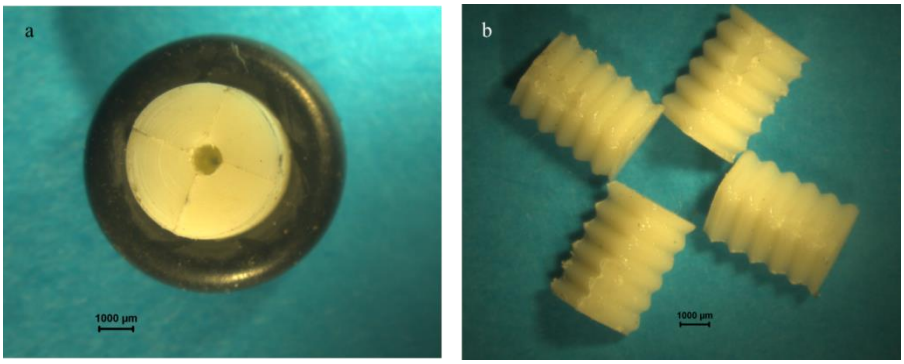

Figure 4.1.6 a) 4 way split sabot being held together with a small rubber O-ring. The O-ring is removed when the sabot is loaded into the launch tube. b) The four separate pieces of the sabot. The serrated edges can clearly be seen along the sabot sections. These serrated edges lock the sabot together whilst in the launch tube and separate once in the blast tank.

2) A solid "sabot" is made of nylon. These projectiles are single pieces of material that can have either a cavity created to hold projectile material or can be a solid single piece (Figure 4.1.7).

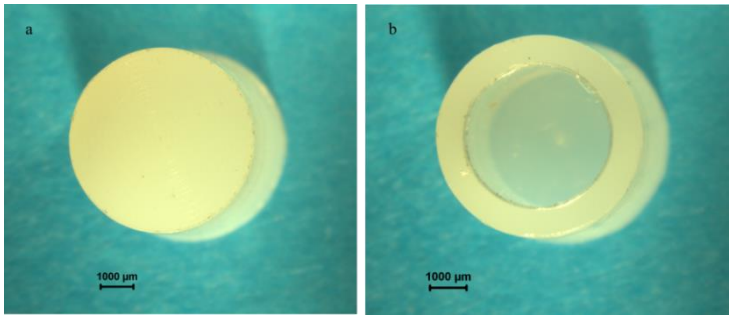

Figure 4.1.7 a) A solid nylon projectile and b) a solid nylon projectile with a central cavity drilled out.

It is possible to shoot two types of projectile, a single object or buckshot. Currently, an object between 0.8 and 3 mm in diameter (Burchell *et al.*, 1999) can be shot as a single shot. There is only one object loaded into the sabot, which produces a single crater on a target. Buckshots use a number of smaller particles loaded into a 4-way split sabot, resulting in a spray of particles hitting the target.

Launch Tube

The sabot is located at the start of the launch tube (Figure 4.1.3). This section of the gun is used to accelerate the sabot once the column of driver gas has been released. It also serves to direct the flight of the sabot once it has left the muzzle.

The bore of the launch tube is rifled (the rifling constant is one turn in 0.76 m), which causes the sabot to spin as it moves down the tube. The rotation of the sabot eventually results in the separation of the four sections, assuring none of the sabot makes it to the target chamber where it can impact the target.

The light gas gun uses various launch tubes depending on the requirements of the shot, such as, velocity and projectile material, size and shape. The variations in launch tubes are the result of the bore size and the shape of the rifling. The larger launch tube bore has a bore diameter of 0.22" (5.558 mm). There are two types of launch tube for this size, one with shallow rifling (Figure 4.1.8a) and the other has no rifling (Figure 4.1.8 b).

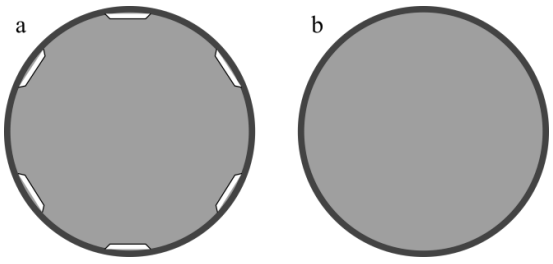

Figure 4.1.8 Schematic (not to scale) of the bores of the 0.22" launch tubes. a) Shows six bit and shallow rifling (white areas) b) No rifling.

The 0.22” launch tube with shallow rifling (Figure 4.1.8a) is infrequently used, but it is used for large and awkwardly shaped projectiles. The second 0.22” launch tube (Figure 4.1.8b) is used to shoot ice projectiles (without a casing). The smooth surface means the brittle projectile will not break apart in transit, which happens when using a rifled launch tube.

Another set of launch tubes are also used, which have a slightly smaller bore at 0.177” (4.50 mm) and 0.170” (4.32 mm). These launch tubes also have a different rifling (Figure 4.1.9), primarily due to changes by the manufacturers.

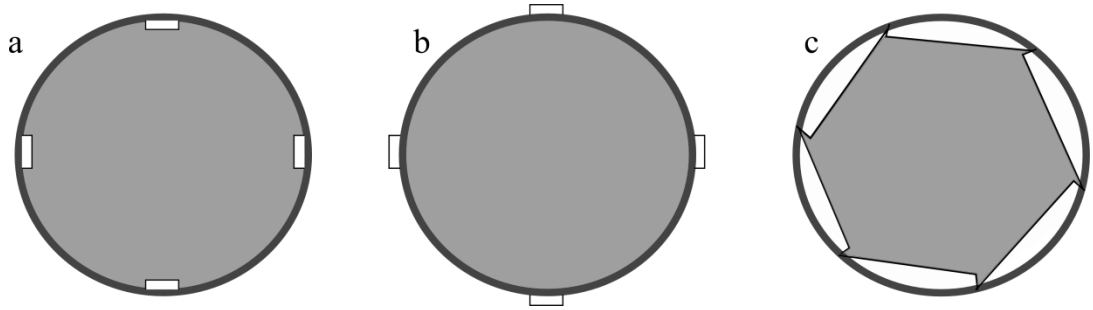

Figure 4.1.9 Schematic (not to scale) of the various types of rifling within the smaller bored launch tubes. a) The 0.177” bore, b) and c) are for the 0.170” launch tubes.

As with the 0.22” launch tubes, these are also used for different types of shots. The 0.177”, 4 bit and internal squared rifling launch tubes (Figure 4.1.9a) are used for the slow speed shots, launch tube 0.170” with the 4 bit, external rifling (Figure 4.1.9b) is commonly used for high velocity shots (greater than 7 km s^{-1}), and the second 0.170” launch tube with the 6 bit, wedged rifling (Figure 4.1.9c) is used the most often for medium reliability shots. The various tubes provide a varying degree of friction which will affect the velocity of the sabot, the 0.177” launch tube provides a greater degree of friction, and will thus slow the sabot as it travels through. The externally rifled 0.170” (Figure 4.1.9b) launch tube is comparatively smoother internally, resulting in less friction being produced allowing a greater sabot velocity. However, this is at the expense of less positive rifling engagement, which could result in the sabot not separating properly in flight.

Blast Tank

Within the blast tank the sabot is no longer confined to the narrow diameter of the launch tube and is able to split into its component sections, which is a result of the spin caused by

the rifling of the launch tube. The rifling constant for the launch tube is one turn every 0.76 m. As the sabot spins the four pieces acquire a tangential component to their velocity and move outward from the centre when released into the blast tank and off-axis. The greater diameter of the blast tank provides the space for the separation of the sabot to occur (Figure 4.1.10).

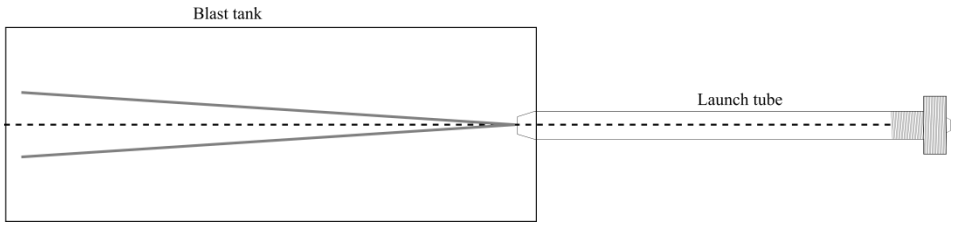

Figure 4.1.10 Schematic (not to scale) showing axis of flight for the projectile (black dotted line) and the path of the sabot pieces (solid grey lines) as a result of the spin created by the rifling in the launch tube.

An aperture is located at the exit of the blast tank, which allows the projectile to pass through to the next section of the gun. The small diameter of the aperture means material other than the projectile is unable to pass through, although occasionally addition material can make it through to the target chamber. A stop plate is located just before the aperture; it prevents the off-axis sabot sections (and the petals from burst disc that may have broken off) from impacting and damaging the inside of the blast tank. The stop plate is also equipped with a sensor, which is used to determine the velocity of the sabot to an accuracy of ± 4% (Burchell *et al.*, 1999).

The information collected by the sensor is recorded by an oscilloscope. The impact of the segments onto the stop plate generates a shock wave through the stop plate, which the sensor picks up. The travel time of the shock wave can be determined by measuring the distance from the impact (on the stop plate) to the sensor, providing the time of impact onto the stop plate. Once this has been determined it can be used with the muzzle detector (located at the start of the blast tank) to determine the velocity of the sabot.

Time of Flight

The speed of the projectile is calculated using two lasers curtains (separated by a distance of 0.499 m) in the time-of-flight section (Figure 4.1.1). The lasers are class 3R and emit visible radiation at a wavelength of 633 nm. A light curtain is generated when the laser

beams pass through a barrel lens, which broadens the beam before passing through a slit creating a curtain. The laser curtains pass through another barrel lens before hitting photo-diodes on the opposite end of the unit, which are connected to an oscilloscope. As the projectile passes through each curtain the connection with the photo-diode is interrupted, which is recorded by an oscilloscope. The velocity of the projectile is calculated using the distance between the lasers, divided by the time in-between the interruption of each laser curtain, which is obtained from the information recorded on the oscilloscope and has an accuracy of approx. ±1% (Burchell *et al.*, 1999).

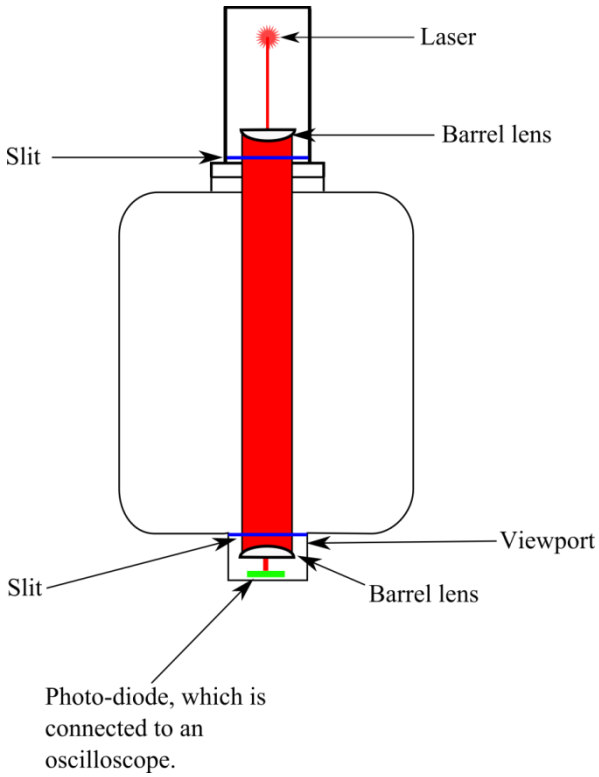

Figure 4.1.11 Schematic (not to scale) of the generation of the laser curtain used to determine the velocity of the projectile. The red areas show the path of the laser throughout the system. The photo diode is connected to an oscilloscope which shows changes in the illumination as the projectile passes through the curtain.

Target Chambers

There are two target chambers attached to the light gas gun, a small chamber and the larger main chamber. The small chamber, that can be used for small targets, and the main chamber (1.14 × 1.14 × 1.15 m) which was lent to the University in March 2012 by NASA. Targets can be mounted to the door, or placed free-standing in the centre of the main chamber, depending on the requirement of the investigation. The main chamber has a number of ports that make observation of the target possible during impact. There is also the ability to rotate targets in the chamber and impact targets of varying temperatures.

As mentioned above, there are many variables in the projectile acceleration stage that need to be determined for different velocities. Type and pressure of gas, amount and type of rifle powder, length of pump tube, burst disc type and rifling type on the launch tube, are all dependent on the velocity required and the projectile being used. Tables 4.1.2 and 4.1.3 provide a general guide for the configuration of the light gas gun for different types of shots, and the gas required for different velocities.

Table 4.1.2 The range of gases and pressures used for a variety of velocities.

Velocity (kms^{-1})	Gas	Pressure (bar)
> 4	Hydrogen	36.6 - 64.9
3.2 - 4.5	Helium	38.4 - 110.2
< 3	Nitrogen	44.0 - 80.0
~ 1	Krypton and Nitrogen	55.2 – 87.5

Table 4.1.3 The launch tube required for various types of projectile at a different velocities.

Projectile type	Velocity (kms^{-1})	Launch tube / type of rifling*
Frozen	1 -7	0.22" smooth or 0.170" four-bits and external
Large or awkwardly shaped	1-7	0.22" / six-bits and shallow
Solid single / Buckshot	7 and above	0.170" / four-bits and external
Solid single / Buckshot	up to 7	0.177" / four-bits and internal

*Selection of launch tube and rifling will change depending on availability.

4.1.2 The Cold Gun

The light gas gun can also be configured to fire frozen projectiles at a range of velocities. Frozen projectiles can either be encased within a hollow solid "sabot" or without the casing. In order to keep the projectiles frozen, the launch tube is placed in a freezer at -140˚C overnight, and the central breach and collar are placed in the fridge at 5˚C before they are needed. The clamps that hold the launch tube in place are also cooled using a pump and an insulating box. A second insulating box is used to keep the sabot end of the launch tube, the central breach and the collar cold. The temperature of the launch tube is measured before and after the shot, which can confirm the projectile was frozen when it was accelerated down the LGG. When firing frozen projectiles contained within the hollow "sabot" the casing keeps the frozen material intact and contained, meaning the

material will impact a target placed in the target chamber. A frozen projectile without the casing is not as robust and will break-up before reaching the target chamber. In these instances targets can be placed in the blast tank in the position of the stop plate, just before the blast tank exit aperture.

4.1.3 Section Summary

The LGG at the University of Kent with its numerous configurations has enabled various projectiles to be fired at a range of velocities as part of this investigation. A unique "cold gun" configuration has meant ice projectiles can be fired as part of the serpentinisation experimental programme (Chapter V). The next section (Section 4.2) describes the main analysis technique used for both impact experiments.

4.2 Raman Spectrometer

The minimally-invasive nature and the (relatively) straight-forward operation of Raman spectrometers have made them a useful tool in various scientific fields: such as forensic science, biology, materials science (Das & Agrawal, 2011) and geology (McMillan, 1989; Kuebler *et al.*, 2006; Liu *et al.*, 2009). In addition to science, Raman spectroscopy has also been used extensively in art and archaeology (Vandenabeele *et al.*, 2007; Brosseau *et al.*, 2009). The widespread use of this analytical tool in various fields is most likely due to its ability to examine samples of either trace amounts, or in bulk; portable spectrometers are also available allowing the examination of samples that are too big to be placed in the spectrometer, or to obtain readings of samples in situ. In addition, Raman spectroscopy provides a quick identification of samples, no sample preparation is required, it is generally a non-destructive technique and, spectra can be obtained from solid, liquid or gas samples (although specialised samples containers are required for gases).

Raman spectrometry is also becoming more widely used in planetary science, via the analyses of extra-terrestrial material and planetary analogue materials (Wang *et al.*, 2015; Price *et al.*, 2014; Price *et al.*, 2012; Burchell *et al.*, 2006; Popp *et al.*, 2002; Ostrooumov & Hernández-Bernal, 2011; Cortés *et al.*, 2012). Raman spectrometers are also being incorporated on both the European Space Agency's (ESA) *Exomars* rover, and NASA's *Mars 2020* rover (Bost *et al.*, 2015; Berlanga *et al.*, 2015; Beegle *et al.*, 2014;

Rull *et al.*, 2013), to be used on the Martian surface. The use of spectrometers to examine extra-terrestrial minerals means it is important to understand the effects impacts can have on minerals. Section 4.2.4 goes describes the use of Raman spectroscopy in planetary science and provides detail on the spectrometers that will be incorporated onto the Martian exploration rovers.

Raman spectroscopy is a vibrational spectroscopy that examines molecular vibrations, which causes the scattering of light. It uses a monochromatic light source to irradiate a sample; the incident light causes the molecules' electron cloud to distort and thus vibrate, resulting in the inelastic scattering of light to different wavelengths. 0.0001% of light is inelastically scattered by the interaction between the incident light and the molecule, which is called Raman scattering. The remaining 99.9999% of light is elastically scattered, and is known as Rayleigh scattering. The difference in wavelength between the incident light and the scattered light is plotted against the intensity to provide a spectrum, with each peak representing a vibrational mode of a specific bond. Unlike elemental analysis techniques, such as Energy Dispersive X-ray analysis, which provides information on the elemental composition of a material, Raman spectroscopy provides information on the bonds between the various atoms within the molecules of a sample, enabling the identification of minerals phases and polymorphs.

Raman spectroscopy was deemed ideal for use in both experiments being described in this thesis. The size of the light gas gun restricts the size of the projectile, which is particularly important where minerals are used as projectiles. It means only small quantities of impact residues can be obtained from craters. The main advantage Raman spectroscopy has over other analysis techniques, such as GC-MS, infrared spectroscopy, X-ray diffraction and X-ray fluorescence, is its ability to examine trace amounts of samples with no need for sample preparation. Due to the scale of the impact events, the amount of material produced is very small and would most likely not provide enough material for analysis by other techniques. In addition, collecting impact residues and sample preparation could result in alteration of the shocked material, which would provide spurious results. It also shows simple phase changes of minerals, making it easy to determine if any alteration has occurred. It is also possible to detect a combination of minerals, which will be important when analysing samples from serpentinisation experiments (discussed in Chapter V).

The Raman effect was named after the physicist who discovered it in 1928, Sir Chandrasekhara V. Raman, the discovery of which led him to being awarded the physics

Nobel prize in 1930. Raman's work in optics revolved around determining the nature of light and how it is scattered by liquids (Raman, 1928). His interest in the scattering of light led to a series of experiments developed by himself, and his colleague Sir Kariamanickam S. Krishnan, initially using sunlight and filters. When examining the scattered light they noticed some of the light had been shifted, or scattered, to a different wavelength (Figure 4.2.1; Raman, 1928), the phenomenon was named the Raman effect. Almost simultaneously two Russian scientists, Landsberg & Mandelstam (1928), also discovered the same phenomenon whilst observing the scattering of light in quartz (good historical reviews of these experiments can be found in Brand, 1989 and Long, 2008).

Early Raman spectrometers used a prism spectrograph with a photographic plate (in review by Adar *et al.*, 2007). Today modern Raman spectrometers are coupled with a microscope, lasers providing the incident light and sensitive, cooled, CCDs to detect the shifted light. These developments have also meant that trace samples can be observed and the acquisition time for Raman spectra is much lower allowing Raman mapping to be undertaken of samples.

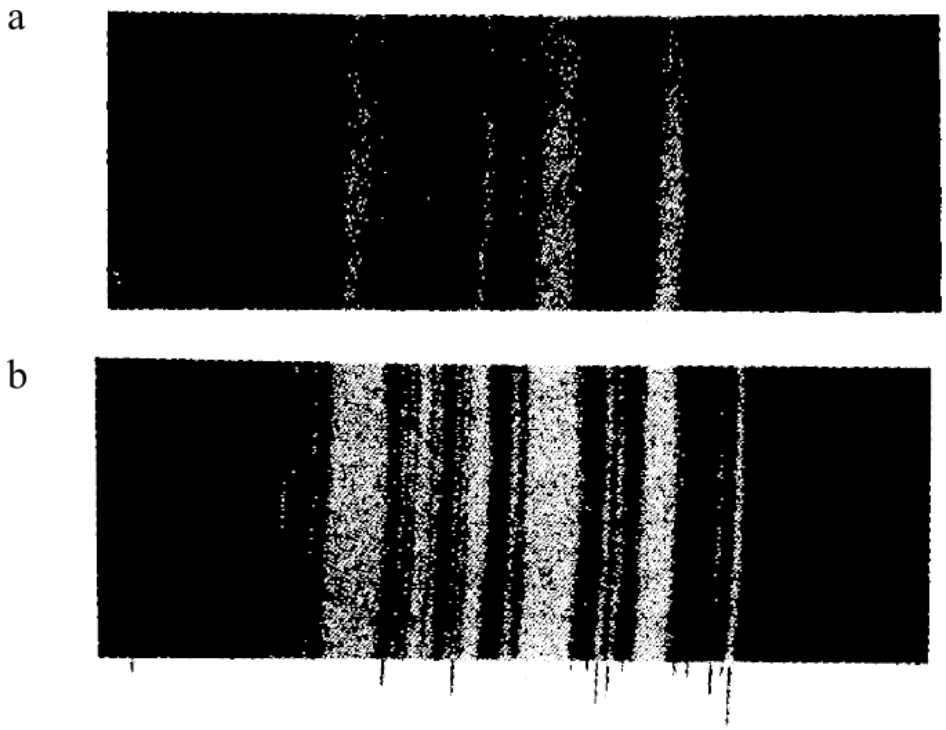

Figure 4.2.1 (Source: Raman, 1928) Early spectrograms showing light scattered by the Raman effect. a) Show a spectrograph of the incident light, provided by a quartz mercury arc lamp and then filtered using a blue filter. b) A spectrograph showing the Raman effect when the incident light (a) interacts with benzene liquid. Additional lines are generated by the scattered light from the interaction with the benzene.

4.2.1 The Physics of Raman Spectroscopy

The Raman effect can be explained both classically, and via quantum theory. Both explanations show that scattered light arises from the energy of incoming radiation being absorbed by the molecule within a sample, this changes the energy (or vibrational frequency) the molecule has; when the molecule relaxes, energy is released in the form of a photon. Using the relationship between energy and wavelength (Equation 4.2.1), the wavelength of the scattered light can be determined, which determines if the light has been elastically (Rayleigh) or inelastically (Raman) scattered,

$$E_p = \frac{h\,c}{\lambda} \qquad \text{Equation 4.2.1}$$

Where, E_p is the energy of the photon (Joules), h is Planck's constant (6.62607×10^{-34} J s), c is the speed of light in vacuum (2.998×10^{8} m s^{-1}) and λ is wavelength (in m).

Electromagnetic radiation is made up of magnetic and electric fields that are perpendicular to one another. Both fields can result in scattering, but the electric field scatters relatively more photons (Long, 2002) and so is only considered here. As the light source irradiates the sample the electric field distorts the electron cloud, which induces a dipole moment in the molecule. The electrons within molecules are able to move about the structure, and the molecule becomes polarised within the electric field of the incident light wave (Figure 4.2.2). As the incident light interacts with the molecule, the electron cloud moves to align itself with the "positively charged" part of the wave. This movement initiated by the electron cloud causes the molecule to oscillate.

If we imagine the bond, within a simple two atom molecule, as a spring (Figure 4.2.3) the resulting oscillation produces harmonic motion over time, with both atoms vibrating at the same frequency (Larkin, 2011). The vibrational frequency, or natural frequency, (v_0 in Hz) of the bond is determined by the mass of the individual atoms and the bond strength (k), which can be calculated using Equation 4.2.2. The vibration results in the molecule gaining energy that is proportional to the frequency (Equation 4.2.4). The natural frequency the molecule vibrates at is the fixed frequency of shift that occurs when light is re-emitted. This means that for Raman shifted light the change in frequency is the same as the natural vibration of the bonded atoms. For example if the natural frequency

for two atoms bonded together in a molecule is v_0 and the frequency of the incident light is v_i, then Raman shifted light will have a frequency of $v_i - v_0$.

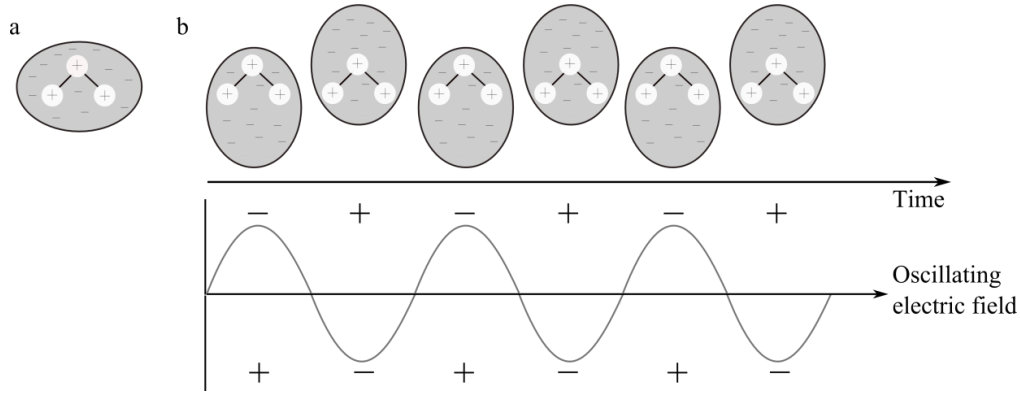

Figure 4.2.2 These simplified diagrams show the distortion of a molecules electron cloud in an oscillating electric field. a) Shows the electron cloud of a molecule (grey area) not affected by an electric field. b) Illustrates how the electric field distorts and can become polarised in the presence of an oscillating electric field over time. The negatively charged electron cloud moves to align itself with the positive section of the wave.

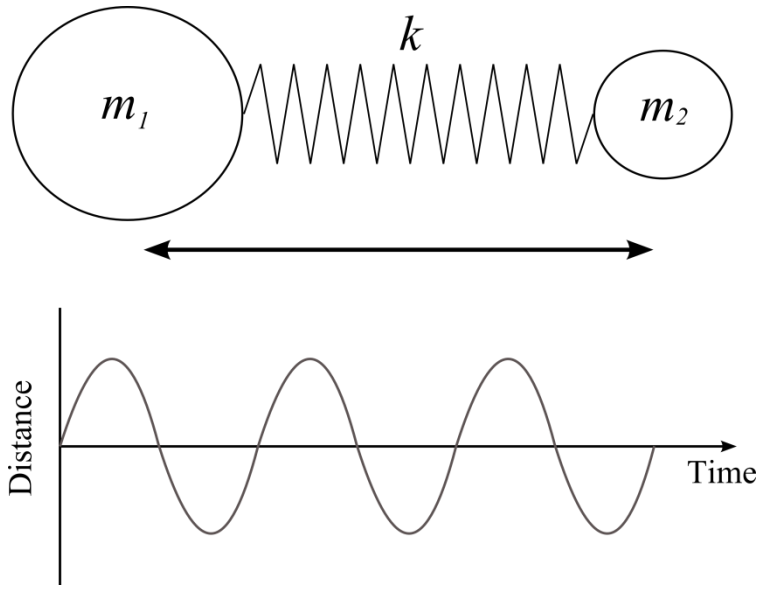

Figure 4.2.3 Schematic of two 'atoms', of mass m_1 and m_2, connected together with a spring, with a bond strength of k. The lower schematic shows the separation distance between the two atoms over time as the atoms oscillate.

$$v_0 = \frac{1}{2\pi}\sqrt{\frac{k}{m}}$$ Equation 4.2.2

Where,

$$m = \frac{m_1 m_2}{m_1 + m_2} \qquad \text{Equation 4.2.3}$$

$$E_p = hv \qquad \text{Equation 4.2.4}$$

Here m represents the reduced mass of the two atoms, k is the bond force (in millidynes /Ångström) between the atoms (Table 4.2.1), h is Planck's constant (in J s) and v is the frequency (in Hz). When k is stronger it produces a greater vibrational frequency and when the mass of the atoms are higher it produces a lower vibrational frequency (Wartewig, 2003).

Table 4.2.1 Approximate ranges of bond force values.

Bond type	k (millidynes /Ångström)
Single	3 – 6
Double	10 – 12
Triple	15 – 18

(Source: Larkin 2011)

The quantum theory explanation of Raman scattering is similar to the classical explanation, except it accounts for the quantised nature of the vibrations (Smith & Dent, 2005). In quantum theory the change from one wavelength to another requires either the addition, or removal, of energy. Incoming photons from the incident light are absorbed by the molecule, providing the energy required for the oscillations (or change in electronic energy level) within the molecule to occur. The additional energy, provided by the incident photon, can promote an electron to a higher virtual electronic energy state. This state is known as a virtual state as the electron is only in this excited state for a very short time (less than a nanosecond) and when the electron relaxes to a lower electronic energy level it emits a photon. Again, if the wavelength of the emitted light is different to the incident light, Raman scattering has occurred. The vibrational energy (E_{vib}) experienced here is determined using Equation 4.2.5.

$$E_{vib} = hv_0\left(n + \frac{1}{2}\right) = \frac{h}{2\pi}\sqrt{\frac{k}{m}}\left(n + \frac{1}{2}\right) \qquad \text{Equation 4.2.5}$$

Where v_0 is the vibrational frequency (Hz, Equation 4.2.2), n is the vibrational number of the oscillations, or electronic energy level in terms of 0, 1, 2 etc, where level zero is the ground-state energy level and known as the zero point energy, determined by Equation 4.2.6.

$$E_{vib,0} = \frac{1}{2} h v_0 \qquad \text{Equation 4.2.6}$$

The electronic energy levels are discrete energy levels that are related to the atoms making up the molecule. It is these energies that provide the various stable electronic energy levels for the excited electrons to relax to in Raman scattering.

As stated before Raman scattering occurs when the photons released, after the relaxation of the electrons, have a different energy to the incident light. If the scattered light has an energy less than the incident light, Stokes scattering occurs, and if it is greater, anti-Stokes scattering occurs (Figure 4.2.4). Stokes scattering is considered the "normal" type of Raman scattering; the electron gains energy, exciting it from the ground electronic energy level to a virtual electronic energy level, it relaxes and falls to a higher energy level. Anti-Stokes scattering occurs when the electron is already at a higher energy level before being excited to a virtual electronic energy level and relaxing; the electron relaxes to an energy level lower than its starting energy level. Anti-Stokes requires the electron to be at a higher electronic energy level than the ground state, which can occur when some energy has already been absorbed by molecules from the environment (i.e. at increased temperature). By comparison, the number of photons experiencing Stokes shift are greater than those undergoing anti-Stokes shift. As, when the sample is in thermal equilibrium at room temperature, there are fewer electrons in higher electronic energy levels than the number in the ground state (Pask, 2003).

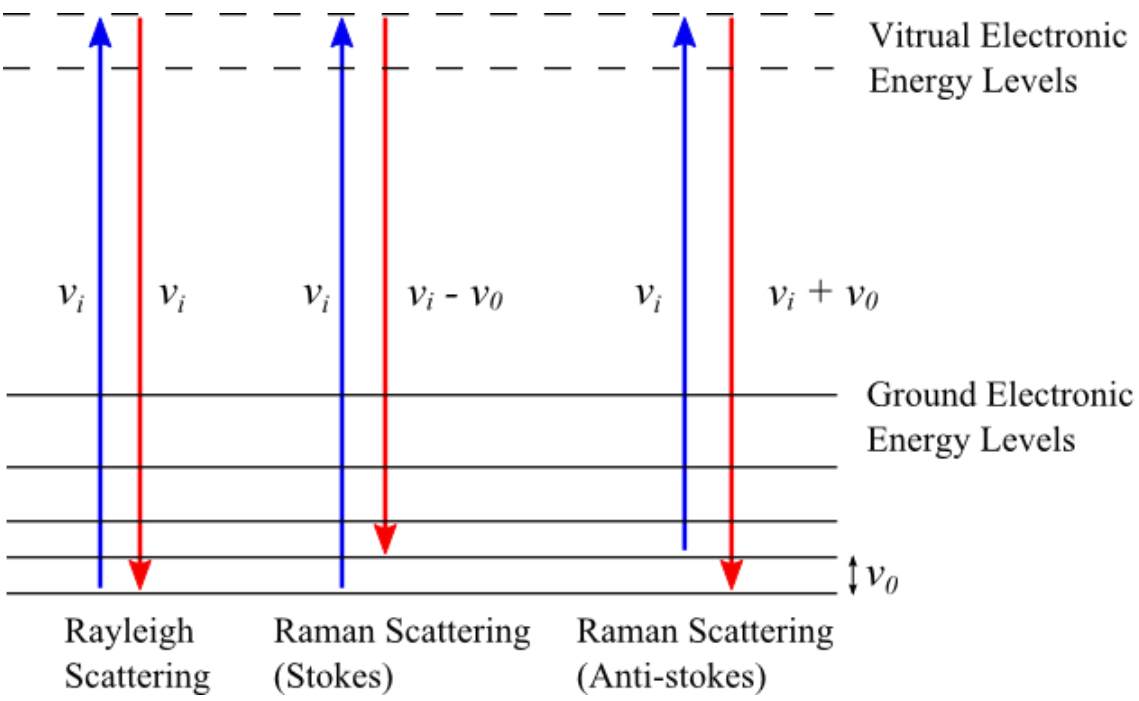

Figure 4.2.4 Energy level diagram demonstrating the difference the two types of Raman scattering and Rayleigh scattering.

A simple diatomic molecule provides a simple way to understand how the molecule can vibrate upon interacting with light, as is vibrates in only one way. However, molecules can be made up of numerous atoms that are bonded together, which means the vibration along these bonds can be different to the way the diatomic bond vibrates. The number of vibrational modes of a molecule is related to the number of degrees-of-freedom: given by $3N - 5$ for linear, and $3N - 6$ for non-linear molecules (where N is the number of atoms making up the molecule). All molecules are able to move in 3-dimensional space and the number of degrees of freedom is related to the number of atoms in the molecule (N), which is therefore $3N$ (Hollas, 2004). Depending on if the molecule is linear, or non-linear, the molecule will have an additional two or three degrees of freedom respectively, related to rotation (Larkin, 2011). As a result five, or six, is subtracted from the $3N$ to determine the maximum possible number of vibrational modes of a molecule. However, not all of these modes are Raman active and so will not be detected. Raman active modes are determined by it polarizability. A distortion of the electron cloud has to occur around a bond when interacting with incident light to be classes as a Raman active mode.

4.2.2 Spectrometer Construction

Modern Raman spectrometers (Figure 4.2.5) have four major components: 1) an excitation source (typically a high power laser), 2) a light collection system, 3) a monochromator and 4) a detector (Zhu *et al.*, 2014).

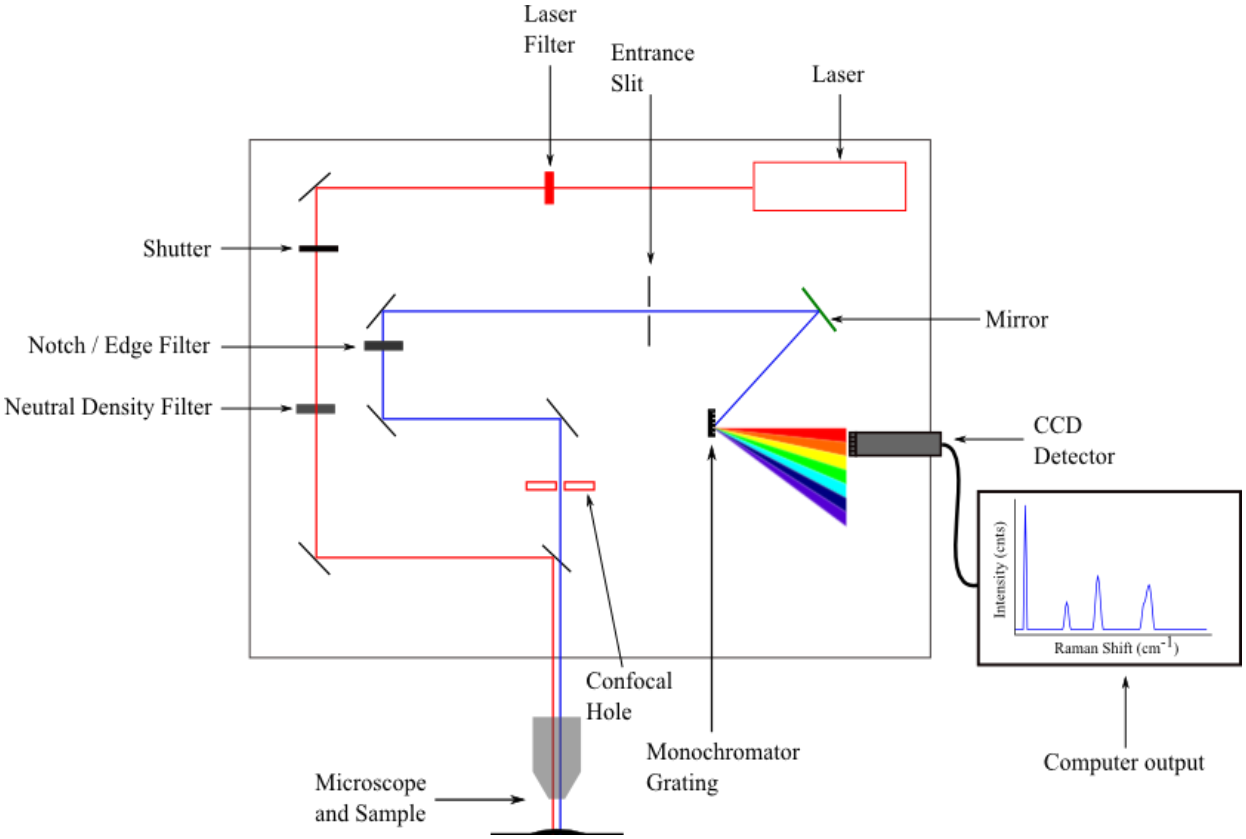

Figure 4.2.5 Schematic (not to scale) of the Raman spectrometer used at the University of Kent. Red lines represent the path of the incident beam from the laser, and blue lines show the path of the light after interacting with the sample. Additional lenses are used to focus the light before, and after, interaction with the sample, but they are not depicted in the schematic to maintain clarity.

Excitation Source

Lasers have been used as the excitation source since their development in the 1960s (which Adar *et al.*, 2007 notes in a comprehensive review of the evolution of Raman spectrometers). They provide a monochromatic source of light, which makes it easier to distinguish between the excitation source and the Raman scattered light. The wavelength of lasers used in spectrometers range from ultra-violet wavelengths to mid-infrared wavelengths (Ferraro *et al.*, 2003). An initial notch filter (commonly referred to as a 'clean-up' filter) is used to ensure only light of the laser wavelength interacts with the

sample. The length of exposure of the laser onto the sample is typically defined by the user through two parameters: the acquisition time and the number of accumulations. These parameters control the shutter, which opens and closes depending on the length of the acquisition time. Spectrometers are usually light tight, minimising the probability of contamination from environmental light, and to prevent damage to parts. Even though Raman spectroscopy is generally a non-destructive analysis tool, intense laser power can result in the damage of delicate samples, such as biological samples and some minerals, through laser heating. To reduce such damage, neutral density filters are employed to reduce the intensity of the laser light interacting with the sample. Neutral density filters (N.D.) reduce the amount of light transmitted through the filter, and therefore reduce the amount of laser power reaching the sample, so it is a compromise between obtaining a good signal-to-noise ratio in a reasonable amount of time, versus possibly damaging the sample.

Light Collection

The light source passes through some initial filters before being exposed to the sample. Today Raman spectrometers are coupled with microscopes that can reduce the laser spot size from 1 – 2 mm to 0.1 mm with basic lens systems (Ferraro *et al.*, 2003). The use of a microscope objective also increases the efficiency of collecting the scattered light, as it has a higher numerical aperture value than a simple lens (Hollricher, 2010). The numerical aperture value indicates the range of angles the emitted (Raman scattered) light can be collected from, which is related to the focal depth and physical size of the objective lens. The Raman shifted light emitted from the sample will be emitted in all directions from the point of interaction, so a large collection angle will mean more Raman shifted light is collected. A long focal length would result in a smaller numerical aperture value, and so a smaller range of emitted light will be collected than with an objective with a shorter focal length (Figure 4.2.6). A higher numerical aperture value also produces a greater spatial resolution, allowing greater detail to be resolved, but this is also dependent on the wavelength of the laser (Adar, 2001).

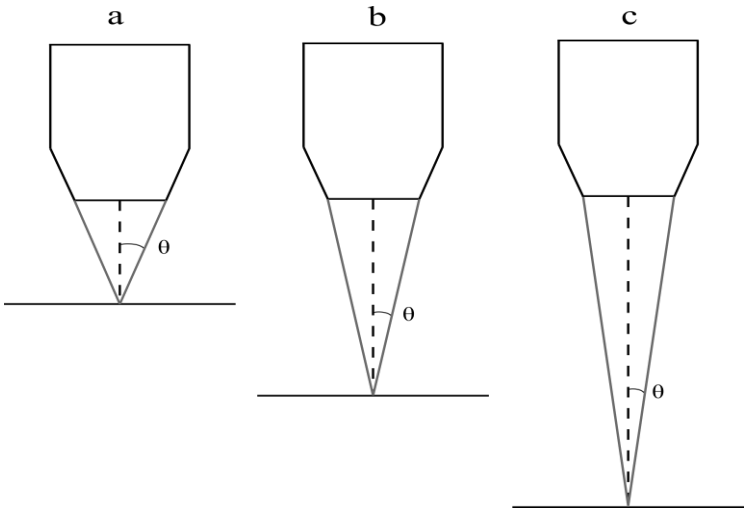

Figure 4.2.6 Schematic of light cones the formed form various numerical apertures at different focal lengths. Larger numerical aperture values (a) will collect light from a larger range of angles than a smaller numerical aperture (c).

There are two angles, 180˚ and 90˚, which spectrometers can use to deliver the incident beam to the sample. At 180˚ the incident beam comes through the same objective lens that is used to collect the emitted light, and at 90˚ the incident beam comes in at a 90˚ angle from the collection lens (Larkin, 2011). Both geometries are effective for the collection of emitted light, with the 180˚ configuration commonly used with microscopes (Smith & Dent, 2005).

Confocal imaging can also be carried out by Raman spectrometers, where spectra can be taken along the *z*-axis as well as along the *x*- and *y*-axes (described in Zhang *et al.*, 2009a) and the greatest spatial resolution, determined by the setup, can also be achieved. Both of these are attained through the adjustment of a confocal hole (also referred to simply as "the hole"). The hole alters the amount of light that is passed through the spectrometer to the detector and therefore the interaction volume. To obtain the highest possible spatial resolution, determined by the Raman setup, the confocal hole is used to prevent unfocused light from reaching the detector. However, the adjustment of the hole will affect the amount of light reaching the detector, which results in lower intensity spectra.

Monochromator and Filters

The collected light passes through a second filter, which blocks light that has been subjected to Rayleigh scattering and any laser light that has been reflected by the sample.

The filters are designed to block out a specific wavelength – the excitation laser wavelength - allowing the remaining (Raman scattered) wavelengths to pass through, therefore filters are specifically designed to be used with individual laser wavelengths. There are two types of filters: edge and notch. Edge filters allow the transmission of wavelengths above, or below, a certain wavelength, whilst notch filters block a range of wavelengths centred at the laser wavelength, but light at higher and lower frequencies can be observed (Slater *et al.*, 2001). Edge filters are used to transmit only light that has experienced Stokes (or very rarely anti-Stokes) Raman shift, whereas notch filters are able to transmit both Stokes and anti-Stokes Raman shifted light (Figure 4.2.7), blocking the laser wavelength. However, a very small percentage of light at the incident wavelength is transmitted through the filters for calibration. In general, edge filters for Stokes shift are normally used when conducting Raman analysis as a greater amount of photons are scattered through Stokes scattering.

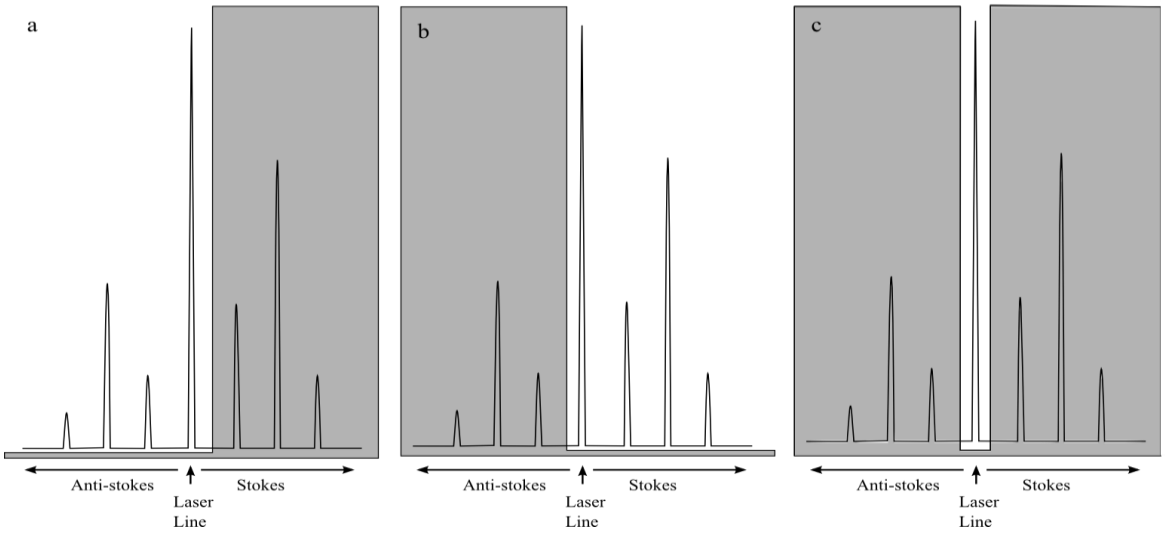

Figure 4.2.7 Schematic showing the Raman scattered light filters transmission, highlighted by the shaded regions. Images (a) and (b) represent edge filters for Stokes and anti-Stokes respectively. c) shows a notch filter that is able to transmit both Stokes and anti-Stokes scattered light.

Once the light has passed through this filter it passes through an adjustable aperture, known as the entrance slit, and onto a mirror. The light is collimated by a mirror to reduce any dispersion of the light as it passes through the spectrometer (Adar, 2013). The mirror reflects the collimated light onto a monochromator grating, which splits the light up into its constituent wavelengths and onto the CCD detector. The gratings provide the resolution for the wavelengths detected. The Raman spectrometer at The University of Kent has two gratings: 600 groves per mm (g/mm; low resolution) and 1800 g/mm (high resolution). The

number of groves determines the degree of dispersion: the higher the number of groves the greater the dispersion of the diffracted light and thus a higher resolution. The detector array has a finite number of pixels and can therefore only collect a finite number of wavelengths per acquisition. In order to collect data across an entire spectral range (typically 100 – 4000 cm^{-1}), numerous sections, of a given number of wavelengths, need to be collected, which means the grating needs to be moved during acquisition sequences. The number of sections required per acquisition is determined by the spectral range required, the grating being used, and the wavelength of the incident light. The acquisition software automatically stitches together the acquired sections to produce a continuous spectrum. However, if there is fluorescence (discussed in Section 4.2.3) the individual sections will be noticeable (as there is a discontinuity between the sections) which can affect peak identification.

Detector and Display

Adar *et al.*, (2007) and Adar (2001) explains that the first detectors used in early Raman spectrometers to collect light were photographic plates, with photomultiplier tubes (PMTs) becoming standard on instruments during the 1960s and 1970s. Today, charged coupled devices (CCDs) are used as detectors. These are made up of an array of light sensitive diodes connected to capacitors (as described by Hollricher, 2010), which temporarily stores the electric charge created by the diode when a photon is detected. CCD detectors work by storing the charge generated by the photon striking a pixel, and transferring it to a register line, where the output is individually read out (Figure 4.2.8; LaPlant, 2010).

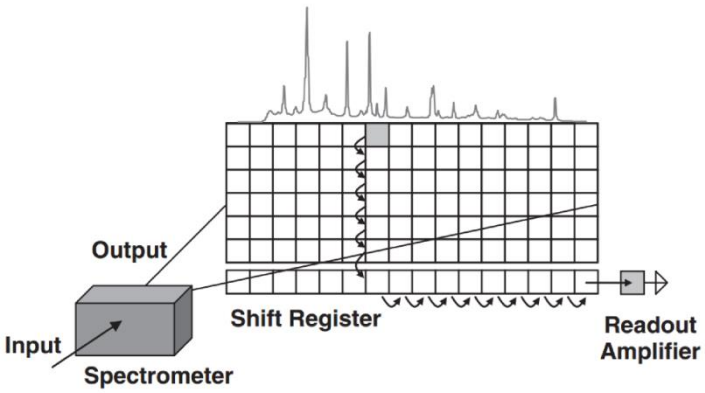

Figure 4.2.8 (Source: LaPlant, 2010) Schematic of the movement of the charges collected by the CCD from collection, to the read-out of the charge.

The information from the detector is transferred to a computer where the data are normally displayed as a graph with the intensity (counts) plotted along the *y*-axis, and the *x*-axis shows the Raman shift in (cm^{-1}), wavelength (nm), energy (eV) or (rarely) frequency (THz). Spectra are made up of a series of points joined together; the spectral resolution can be seen as the distance (usually quoted in wavenumbers) between the points. The closer the points are, the higher the resolution of the spectrum. High spectral resolutions means peaks are sharper and it may be possible to discern individual peaks which may make up a broad feature.

Occasionally spurious, sharp and intense spikes are seen in spectra. These spikes are generated by high energy particles that originate from space and are known as cosmic rays. The spikes are problematic as they can resemble Raman peaks and interfere with an actual Raman peak, which can affect peak analysis. Today, modern acquisition software is able to remove spikes as the data are being acquired. This is achieved by using an algorithm to compare Raman spectra from separate accumulations to determine which peaks are "real" Raman peaks and which peaks are artefacts generated by cosmic rays. It is also possible to remove these spikes post acquisition using a separate piece of software, such as "Crystal Sleuth" (which is software designed by the developers of the RUFF database; http://rruff.info/), where spikes can be identified manually, or automatically. However care has to be exercised as, in some cases, the removal of these artefacts can result in modification to the shapes of the Raman peaks.

Calibration

Calibration of the Raman spectrometer is conducted using a clean silicon wafer sample, which has a single peak at 520.6 cm^{-1}. This single peak, and the laser line at 0 cm^{-1}, are used to automatically realign the spectrometer, as the peak positions may drift as lasers and gratings are changed. The calibration method, in essence, moves the laser line to 0 cm^{-1} and the silicon peak to 520.6 cm^{-1}. Some software, such as Horiba's Labspec 6, have automated the calibration process, in these cases the software will make the required adjustments to get the nearest peak to one of the two positions, but manual calibration may be required occasionally to ensure the correct peaks are being observed at the correct peak position.

4.2.3 Problems

Fluorescence

One of the major issues that arise in Raman spectroscopy is fluorescence. It is seen in spectra where the baseline is raised to higher intensities and not at a baseline of (approximately) zero (Figure 4.2.9). The intensity of this phenomenon can be $10^6 - 10^8$ times greater than that of Raman shifted light (Mosier-Boss *et al.*, 1995) and so can "drown" the signal from the Raman scattered photons. Where intense fluorescence occurs it can mask weaker Raman peaks and the fluorescence will need to be removed/reduced before satisfactory Raman spectra can be taken (techniques to remove/reduce fluorescence are discussed later in this Section). Lower intensity fluorescence can cause slight problems for analysis, especially where the areas of the peaks are used in analysis (Martins Ferreira *et al.*, 2010; Zhu *et al.*, 2007). Raman peaks can have a Lorentzian profile (Meier, 2005), which have tails on either side of the peak; when peaks overlap, or are next to each other, it can appear as fluorescence of the sample (natural/background fluorescence).

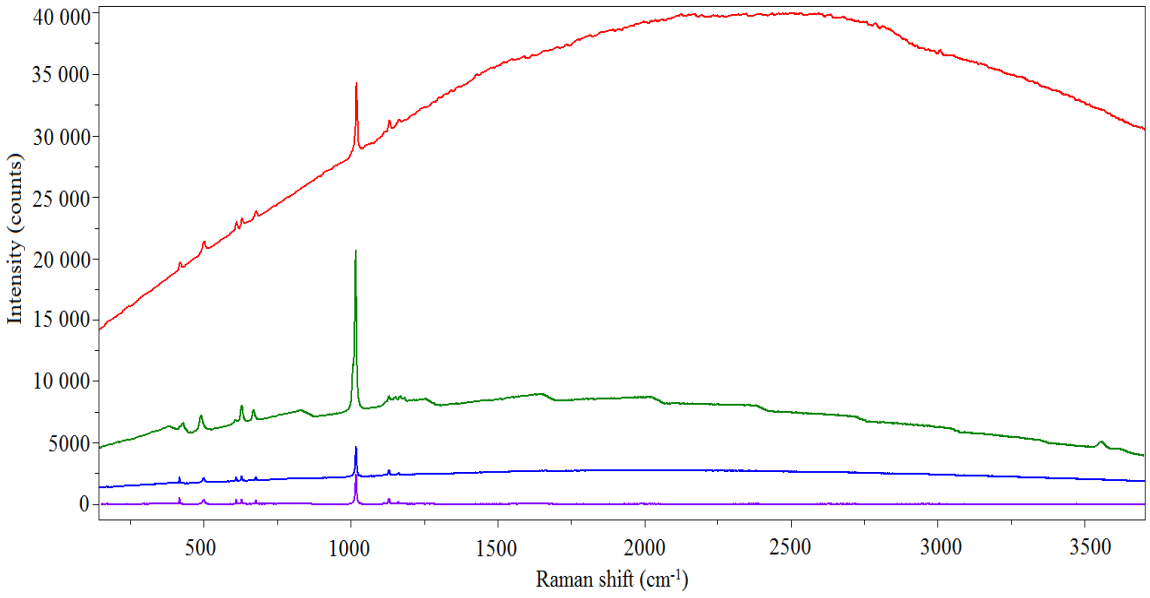

Figure 4.2.9 Raman spectra of gypsum showing, a highly fluorescent spectrum (red), a fluorescent spectrum with photo-bleaching causing it to appear "stepped" (green), a spectrum with low fluorescence (blue), and a low fluorescence spectrum that has undergone base-line correction (purple).

In the "normal" scattering process the excited electron is raised to a higher virtual electronic energy level, before relaxing and falling to either its original electronic energy

level, or a level higher or lower the original level, releasing a photon. Fluorescence occurs when the promoted electron cascades down from higher to lower excited electronic energy levels, until reaching the lowest excited energy level, where it then falls to non-excited levels and emits a photon (Figure 4.2.10). The lifetime of the electron in these excited electronic levels is in the range of nanoseconds (Sauer *et al.*, 2011), differing from Raman scattering, as the electrons do not actually enter the excited energy levels, but a virtual excited level and exists there for a very short time (less than a nanosecond).

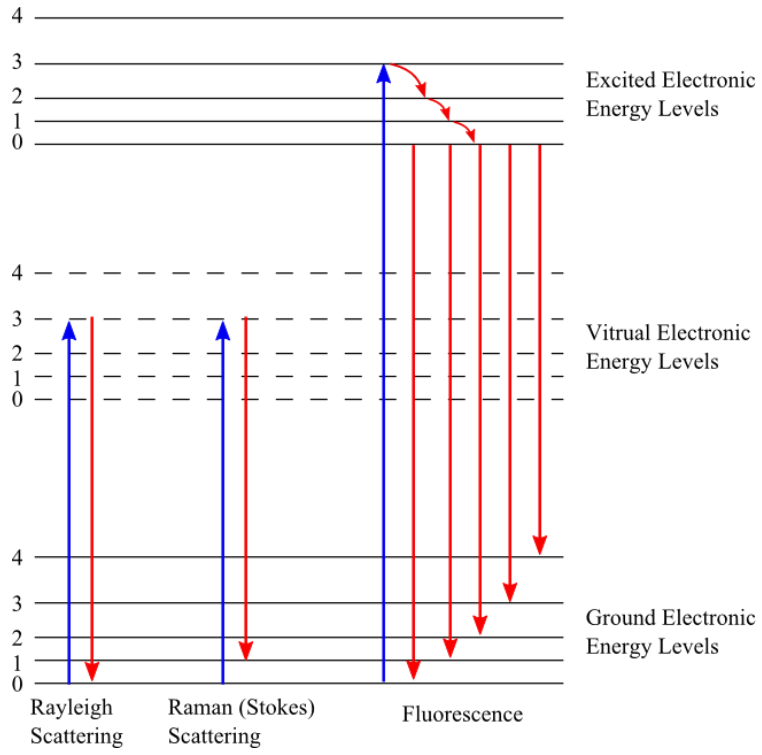

Figure 4.2.10 A schematic of the electronic energy levels electrons pass through as they experience scattering, or fluorescence. The blue lines indicate the path of the electrons as they absorb an incident photon, and the red lines represent the path of the electron as it relaxes to the ground electronic energy levels. In fluorescence the electron relaxes from the lowest excited energy level regards of what ground energy level it reaches.

Fluorescence occurs as a result of impurities within a sample. These impurities can be in the form of chromophore or fluorophore compounds. Fluorophore compounds found within samples cause them to fluorescence (Sauer *et al.*, 2011), whereas chromophores are responsible for the colour within samples, and so results in some coloured samples fluorescing. A simple way to reduce the fluorescence is to remove the impurities from within the sample. This can be achieved by either creating a pure sample, or using a solvent to remove the impurities but leave the sample of interest unmodified. A pure

sample would mean that only the molecules of the sample being observed are present and so would be the only molecules scattering light. In practise it can be very difficult to make samples pure, as they may have been samples collected from the field, or are too valuable to risk potential damage. Therefore, additional techniques are required to minimise fluorescence, such as changing the wavelength of the excitation source. Wavelengths in the ultra-violet and near-infrared regions have been found to produce less fluorescence than those in the visible region, with near-infrared producing lower fluorescence to a greater degree than ultra-violet (Smith & Dent, 2005).

A process known as "photo-bleaching" can also reduce the effects of fluorescence in a Raman spectrum. In this technique, the sample is irradiated with the excitation laser for a period of time, normally minutes to hours, to degrade the effect of fluorophores in the sample. The continuous exposure to light results in the fluorescent particles becoming unable to fluoresce (Diaspro *et al.*, 2006). Photo-bleaching can be effective in reducing fluorescence, but the constant exposure to the light could cause localised heating, which could damage samples.

Increasing the Raman signal can also counteract the effects of fluorescence, as more intense peaks might become visible above the background fluorescence. This can be achieved by increasing the intensity of laser light transmitted through neutral density filters. In most cases, where there is no fluorescence, full laser power is not required to produce a satisfactory Raman spectrum. It is also possible to increase the Raman signal by using Resonance Raman Spectroscopy (RRS), or Surface Enhanced Raman Spectroscopy (SERS). These types of spectroscopy can increase the number of photons that experience Raman scattering. In RRS the wavelength of the excitation source is chosen to induce electronic transitions to the excited state (Clark & Dines, 1986). The wavelengths needed for these transitions to occur, for the majority of samples, falls in to the UV range, which could explain why changing to UV wavelengths can help to effectively supress some fluorescence. Saying that, resonance Raman spectroscopy can also generate fluorescence, as well as increasing the Raman signal by as much as five orders of magnitude (Ru *et al.*, 2012). Surface enhanced Raman scattering utilises a rough metal surface to amplify the intensity of the incident light in the area of interest, which in turns increases the intensity of scattered light (Fleischmann *et al.*, 1974). Haynes *et al.*, (2005) explains that a metal substrate, normally gold, silver or copper, is used with the sample; the rough metal surface intensifies the electromagnetic field and so it also increases the intensity of the Raman scattered radiation.

Altering the acquisition parameters can also increase the Raman signal. Increasing the acquisition time can increase the intensity of the Raman signal as the light is collected on the CCD for longer. Adjustment of the confocal hole size can also result in increasing the Raman signal, as the hole affects the number of scattered photons reaching the detector.

Fluorescence (which has not swamped an underlying Raman signal) can be removed post-acquisition through the use of baseline correction algorithms. The algorithm fits a line to the baseline of the fluorescent spectrum, before subtracting it from the entire spectrum resulting in a baseline at zero. Polynomial and linear algorithms are commonly used, and more advanced adaptive techniques have been developed (e.g. Zhang *et al.*, 2009b; He *et al.*, 2014). *LabSpec* uses either a linear or polynomial fitting algorithm to subtract fluorescence, whereby nodes (the number of which can be defined by the user) are added to the fluorescent spectrum to best match the shape of the baseline fluorescence. The more nodes fitted to a spectrum will produce a better fit, and thus be more effective at producing a flat zero baseline (Figure 4.2.9). However, it can be difficult to fit a polynomial or a linear curve to the baseline if the baseline is not smooth. The effect of photo-bleaching can produce a stepped spectrum (Figure 4.2.9) over a long spectral range, as a long spectral range (e.g. 100 to 4000 cm^{-1}), can consist of numerous sections being stitched together. Photo-bleaching would result in varying the overall intensities for each of the sections, the resulting steps are then seen when the sections are stitched together. A spectrum with these steps would produce features that could be mistaken for peaks after baseline correction has occurred.

Heating Samples

Raman spectroscopy is generally considered a non-destructive analysis technique. However, lasers can heat samples resulting in permanent alteration, as some energy is absorbed by the samples as heat via the laser. Johansson *et al.*, (2002) has reported temperature increases of 38 – 60 ˚C and 20 – 30 ˚C, with laser powers of 1.5 W and 0.7 W respectively, of solid pharmaceutical samples. In addition, Hanesch (2009) reported a noticeable change in the Raman spectra of heated goethite for more than 10 minutes of exposure to a laser power of 0.1 mW. Localised heating of samples can occur in a number of ways: through continuous exposure and/or high magnification and/or high laser power. The Raman spectrometer at the University of Kent is equipped with four lasers with wavelengths at 473 nm, 532 nm, 633 nm and 784 nm, with maximum power outputs (as

measured at the laser aperture) of 500 mW, 542 mW, 30 mW and 150 mW, respectively. The neutral density filters reduce the power of the laser according the percentage of light that is allowed to be transmitted through the filter. However, some of the laser light reaching the objective is lost as it passes through the spectrometer to the sample, so the power is further reduced. Table 4.2.2 shows the power measured at the microscope objective for each of the neutral densities filters fitted in the University of Kent's Raman spectrometer.

Table 4.2.2 Laser power output at the microscope objective using various neutral density filters.

Neutral Density filter (%)	**Power (mW)**			
	473 nm	532 nm	633 nm	784 nm
100	4.87	6.29	1.65	20.10
50	2.49	4.81	0.86	10.30
25	1.33	2.86	0.38	6.50
10	0.44	1.04	0.18	2.63
1	3.90×10^{-2}	0.12	2.52×10^{-2}	0.33
0.1	3.01×10^{-3}	2.10×10^{-2}	3.86×10^{-3}	8.20×10^{-2}
0.01	4.90×10^{-4}	1.05×10^{-2}	4.20×10^{-4}	1.61×10^{-2}

Continuous exposure to the laser, such as during photo-bleaching, or long acquisition exposure times will cause some heating in the acquisition area. Long acquisition times can also cause heating of the sample, especially if a large spectral range is being collected. As mentioned earlier, data for a range of wavelengths is taken in sections, depending on the laser being used and the grating resolution. For example, if the exposure time is set to 5 seconds, and the accumulation number is set to 15 then four sections are required to cover the spectral range of -90 to 4000 cm^{-1} using the 532 nm laser and a 1800 g/mm grating, then sample is exposed to laser for a total of 12.5 minutes. So, if long exposure times are needed to obtained satisfactory Raman spectra the total exposure time can increase to a point that may cause alteration to the sample.

The magnification of the microscope objective used to examine the sample could also result in localised heating of the sample. The magnification of each of the microscope objectives results in a different spot size the laser interacts with on the sample (Table 4.2.3).

Table 4.2.3 Spot sizes for the various laser wavelengths and microscope objectives available for the Raman spectrometer used in this study.

Objective magnification	Numerical aperture	Spot size diameter (nm)			
		473 nm	532 nm	633 nm	784 nm
× 10	0.25	2308	2596	3089	3826
× 50	0.55	1049	998	1404	1739
× 100	0.80	721	686	965	1196

The spot size is calculated using Equation 4.2.7, which is dependent on the wavelength of the laser (λ) and the objective being used.

$$\text{Spot size} = \frac{1.22\,\lambda}{NA} \qquad \text{Equation 4.2.7}$$

Where *NA* is the numerical aperture values of the microscope objective and 1.22 is a factor used to calculate the Airy disk. The Airy disk is an area of high intensity when light is passed through a lens and diffraction occurs, for circular lenses. A low magnification will produce a larger spot size and so the laser power is distributed over a larger area, whereas a high magnification reduces the spot size and decreases the area to which the laser power is delivered. Therefore, there is a greater chance of localised heating of a sample when using a higher magnification.

4.2.4 Planetary Exploration

As mentioned previously Raman spectrometers are being widely used in planetary science. It provides a quick and easy method for the identification of minerals, as there is very little overlap of characteristic bands, particularly for silicates (Wang *et al.*, 1995). It is also well suited for the identification of polymorphs, and can distinguish between mineral transition phases (Sarma *et al.*, 1998), which is not always achievable with techniques such as Energy Dispersive X-ray (EDX) analysis. Spatial information can also be gathered, when used in combination with a microscope, and could potentially show changes in composition of a mineral with zoning. Compositional information can also be obtained from Raman spectra; for example Keubler *et al.*, (2006) was able to use Raman spectra to determine the Mg-to-Fe content of olivine grains. They showed slight changes in the peak positions for olivine's characteristic doublet peak, which resulted from the variation in the

Mg to Fe content. However, Hibbert & Price (2014) have also that shock events (i.e. impacts) can produce similar changes in the peak positions of high purity olivine. This finding suggests the composition of olivine could be misinterpreted if the sample has undergone shock. It also shows changes from shock events can also be detected by Raman spectroscopy.

Mars Rovers

The development of portable Raman spectrometers has made is possible for this instrument to be incorporated into exploration rovers and sent to the surface of Mars. Both ESA's *ExoMars* and NASA's *Mars 2020* rovers will both be equipped with Raman spectrometers. The spectrometers are set to assist with rock and mineral identification, the search for organics and identify key water related processes (NASA, 2014; Rull *et al*., 2011). The *ExoMars* Raman spectrometer, known as the Raman Laser Spectrometer (RLS), will use a 532 nm green laser as the excitation source and have a spectral resolution of ~7 cm^{-1} (Rull *et al.,* 2013). The Raman spectrometer, Scanning Habitable Environments with Raman and Luminescence for Organics and Chemicals (SHERLOC), proposed for the *Mars 2020* rover will use a 248.6 nm ultra violet laser and will use resonance Raman spectroscopy (NASA, 2014). At this wavelength (248.6 nm) electronic transitions to the excited electronic energy levels are induced which increases the amount of Raman scattered light.

The Raman spectrometer at the University of Kent is equipped with a 532 nm green laser, like the laser that will be used by *ExoMars's* RLS, but it does not have a ultra-violet laser such as the one proposed for the *Mars 2020* SHERLOC instrument. The spectral resolution for RLS (*ExoMars*) is also much larger than the largest spectral resolution, of ~2 cm^{-1}, that can be obtained using the 532nm laser on the University's Raman spectrometer.

4.2.5 Section Summary

Raman spectroscopy can distinguish between mineral polymorphs and can show a mixture of minerals, which is ideal for determining if alteration of minerals has occurred. It is due to these traits that Raman spectroscopy has been used as the primary analysis technique for the experiments conducted in this thesis (Chapters V and VI). In this section the phenomenon of Raman scattering and how Raman spectrometers work have been described. The main problems with Raman spectroscopy have also been explained and

some methods that can be used to counteract them. In addition, information on the use of Raman spectroscopy in planetary sciences has also been provided.

4.3 Scanning Electron Microscopy

The history of the Scanning Electron Microscope (SEM) dates back to the early 1900s, when scientists were trying to develop a microscope with a resolution greater than those of the day (Bogner *et al.,* 2007). SEMs today can reach resolutions of ~1 nm using high performance immersion lenses and field emission guns (Joy, 2011). Otherwise, spatial resolutions of 100 nm and 10 nm for compositional and topographic data, respectively, can be achieved (Reed, 2005).

In 1933 Ernst Ruska used an incident beam of electrons directed onto a sample at a grazing angle to illuminate it, obtaining a magnification of ×10, and in doing so invented the first Transmission Electron Microscope (McMullan, 1995). The work was the result of two important discoveries in electron optics; 1) the realisation that an electron beam could be "focused" using a magnetic coil, in a similar manner to when light passes through a lens, and 2) a wavelength can be associated with charged particles (Bogner *et al*., 2007; Hawkes, 2004).

Scanning electron microscopes use an electron beam to examine specimens. The interactions between the electron beam and the specimen can provide various types of information, concerning topography and relative composition. If the SEM is also equipped with an Energy Dispersive X-ray spectrometer (EDX) elemental characterisation of specimens can also be acquired. One of the main advantages of SEMs used in physical sciences is the non-destructive manner in which it can obtain a range of information.

SEM and EDX analysis provides and indepth look at geological samples, enabling different phases and . Maps produce use SEM analysis allows the

4.3.1 Types of Information

Scanning electron microscopes have the ability to provide information on a sample's surface topography, composition and elemental data when coupled with energy dispersive X-ray or wavelength dispersive X-ray spectrometers. The various types of information

obtained are dependent on how incident electrons interact with the sample and if they experience elastic of inelastic scattering (Reed, 2005).

Images are acquired by accelerating electrons towards a specimen, where they then interact with a specimen in two specific ways: 1) incident beam electrons are deflected off the specimen in a process known as back scattering. 2) Electrons from the incident beam remove electrons from the specimen; ejected electrons are detected and form secondary electron images. Elemental data are produced when electrons in a sample are knocked out and then replenished by electrons in the outer shells of the atom in the sample, generating X-rays of an energy characteristic of the element.

Backscatter

Images produced from the detection of backscattered electrons show the relative composition of the sample. These images show relatively heavier elements with bright shades (white and light greys) and lighter elements with darker shades of grey to black. Figure 4.3.1 is an example of a backscattered image taken of the Zagami meteorite (a Martian meteorite discovered in 1962), showing the different mineral phases present within the meteorite. Each phase is represented by a grey scale, which in turn is dependent on the atomic mass of the mineral. Phase “b” is a pyroxene with high abundances of Si, Ca, Mg and Fe, and phase “c” is a calcium aluminium silicate phase (feldspar) with Al, Si, and Ca. The bright white phase, phase “a”, has a high Fe content with some Ti, making it relatively more dense than the surrounding mineral phases.

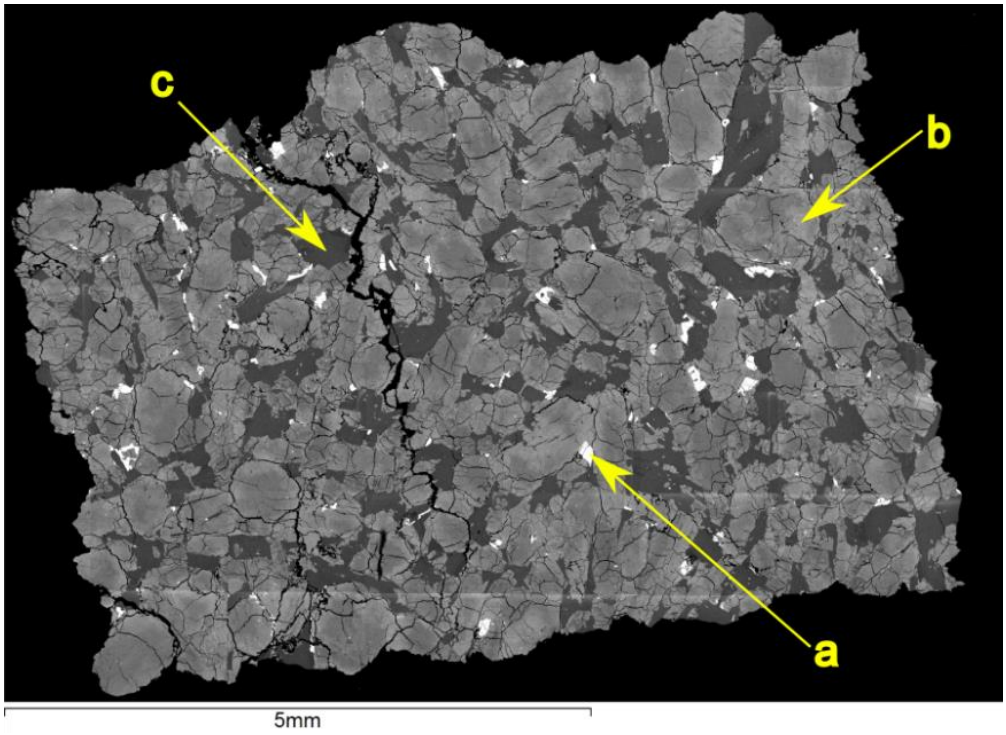

Figure 4.3.1 Example of a BSE map at ×100 magnification (20 kV) taken of the Zagami meteorite. The sample has been polished flat and mounted onto a glass slide. a. Areas with high Fe content and the presence of some Ti. b. A pyroxene and c. is feldspar.

Images obtained using backscattered electrons are produced as a result of the elastic scattering of incident electrons. The nuclei of atoms within the sample deflect incident electrons as they pass through the sample, the angle of deflection (γ) is determined using the following equation:

$$\tan(\gamma/2) = Z\,(1.4\rho E) \qquad \text{Equation 4.3.1}$$

Source: Reed, 2005

Where, Z responds to atomic weight, ρ (in nm) is the minimum distance from the electrons unaltered path to the nucleus and E (in keV) represents the energy of the deflected electron.

It is possible for the electron to be deflected at an angle > 90°, which is also known as Rutherford scattering, occurring as a single event (Krinsley et al, 1998). There is also the potential for electrons to be deflected at lower angles on multiple occasions as it passes through the sample. This process will eventually lead to the electron being diverted back out of the sample just as an incident electron being deflected at an angle > 90°, and is known as backscattering (Krinsley *et al.,* 1998; Reed, 2005).

The interaction volume for backscattered electrons is predominantly dependent on the *Z* values of elements found with the sample. Elements with a higher *Z* value (thus a heavier nuclei) are more likely to deflect incident electrons at angles > 90° those with lower *Z* value; elements with low *Z* values will backscatter electrons through multiple deflections (Reed, 2005). This dependence is seen when examining the backscatter coefficient (η), which represents the portion of incident electrons that are expelled from the surface of the sample as a result of being backscattered (Reed, 2005). Elements with a higher *Z* value will backscatter more electrons than elements with lower values. It is this percentage of backscattered electrons that provide a yield contrast and is dependent on the *Z* value (Zhou *et al.*, 2007), which is seen in BSE images: were elements with a high *Z* values are brighter as more BSEs have been collected. The Z values of elements also effects the depth incident electrons penetrate a sample before being deflected. At shallow depths, elements with high *Z* values will deflect incident electrons and a greater penetration depth is required for low *Z* value elements (Figure 4.3.2).

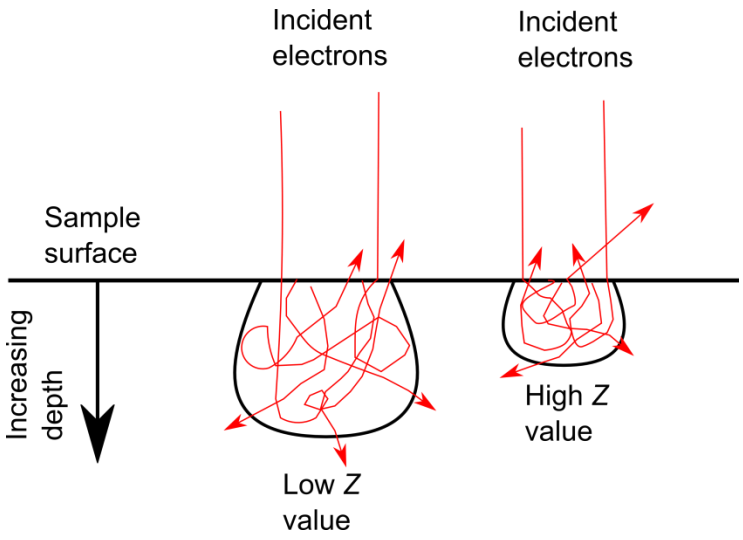

Figure 4.3.2 (redrawn from Krinsley *et al.*, 1998) schematic of the interaction depth of electrons for a sample with high and low *z* values. There is a shallower and smaller, interaction volume for materials with a higher *z* values compared to ones with a lower *z* value.

Using Monte Carlo simulations, Khursheed (2010) shows elements with a greater *Z* value eject a greater portion of electrons with BSE energies very similar to the incident energy. Whereas there is a much broader range of BSE energies for elements with lower *Z* values and the spectra are much lower (Figure 4.3.3).

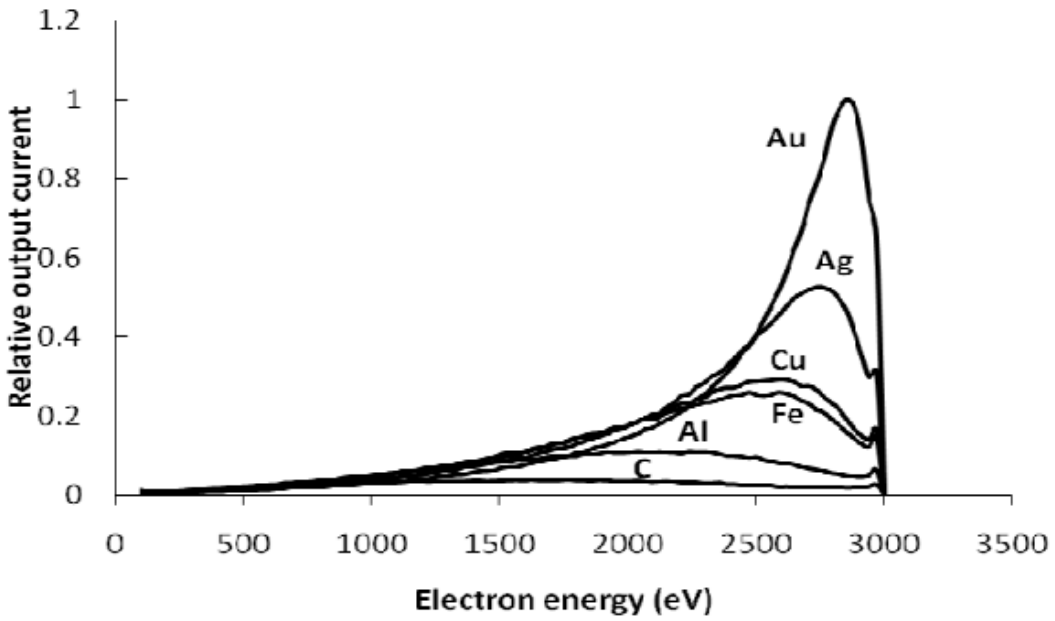

Figure 4.3.3 (source: Khursheed, 2010) BSE energies taken for different materials using Monte Carlo simulations. The incident electron energy is 3 keV and sample thickness is 1 μm thick. The relatively heavier elements with a greater Z value eject more electrons, seen by the greater relative output current.

Secondary electrons

Secondary electrons (SE) are electrons that have been ejected from the atom by the incident electron and generally come from a region close to the surface, resulting in a higher resolution (Vernon-Parry, 2000). They can be produced as a result of the incident electron beams interaction on/near the surface of the sample, or due to a BSE ejecting an electron from an atom on its way out of the sample. In comparison to backscattered electron SEs have a lower energy of approximately a few eV (Reed, 2005; Hall and Lloyd, 1981), and are generally distinguished as having an energy less than 50 eV (Zhou, 2007; Goldstein *et al.*, 1981). However, some BSEs may also have energies less than 50 eV, the secondary electron coefficient, δ, determines the amount of SE resulting from an incident electron (Reed, 2005). δ can be determined by using the following equation:

$$\delta = \frac{n_{SE}}{n_B} = \frac{i_{SE}}{i_B}$$ Equation 4.3.2

Source: Goldstein *et al.*, 1981

where, n_{SE} represents the number of SEs, n_B is the number of incident electrons and i is the current of the secondary electron (SE) and incident electron (B).

SE images show the surface topography or roughness, of a sample's surface, which is predominantly due to the low energy of the emitted electrons. Any SE generated within the sample will not have enough energy to leave the sample and reach the detector, so only SEs generated near the surface (nanometres) are detected (Reed, 2005).

X – Rays

The interaction between incident electrons and a specimen can result in the production of X-rays in two distinct ways; 1) continuous and 2) characteristic (Reed, 2005). Continuous X-rays are produced when an incident electron emits an X-ray photon as it drops to a lower energy state, due its close proximity to the nucleus of an atom in the sample (Reed, 2005). The continuous X-rays produce a continuum background of X-rays when detected using the EDX detector, this background is also knows as bremsstrahlung (Reed, 2005; Zhou *et al.*, 2007).

Characteristic X-rays are produced when an incident electron knocks out an electron in one of the orbiting shells within an atom and is replaced by an electron from an outer shell, this change on electron orbit results in emission of an X-ray photon (Vernon-Parry, 2000). The energy of the emitted X-ray photon varies depending on the element and the electron shell the replacement electron came from. The energy of the photon emitted is determined by the energy difference between the energy levels of the electron shells in question (Reed, 2005). The amount of energy required for an electron to be knocked out of each shell decreases the further away from the nucleus of the atom, e.g. K shells have a higher energy than L shells, Figure 4.3.4 shows the energy released from the various transitions of silver.

The elemental data from X-rays are normally presented in a graph with energy as the *x*-axis and counts along the *y*-axis (Figure 4.3.5). The continuous X-rays produce background ground values which are detected, and characteristic X-rays appear as peaks at the specific energies for the element. Peak lines from the transition of electrons from one shell to the other are dominantly classified as K_α, K_β, L_α, L_β, M_α or M_β lines, this classification is dependent on what shell the initial electron was knocked out from by the incident electron beam (also shown in Figure 4.3.4).

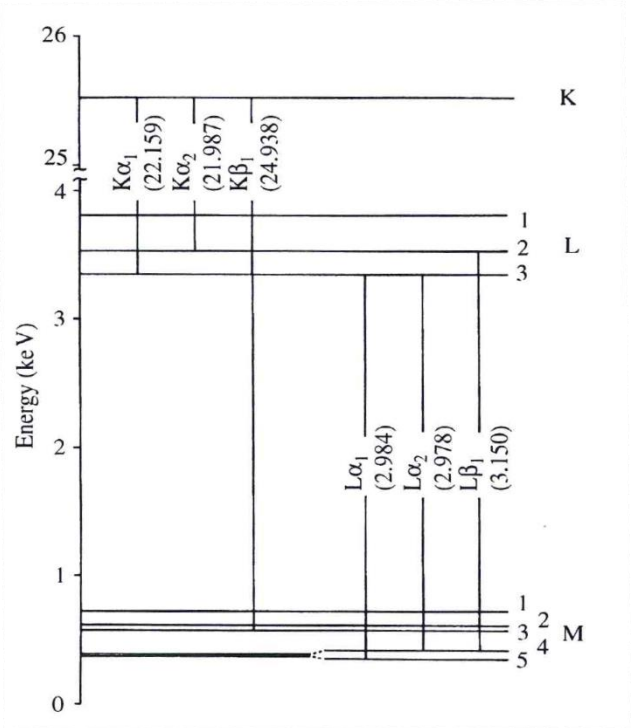

Figure 4.3.4 (source: Reed, 2005) Diagram showing the energy released as x-rays as a result of the transition of electrons from one electron shell to another for silver, with the classification and energy of each transition highlighted.

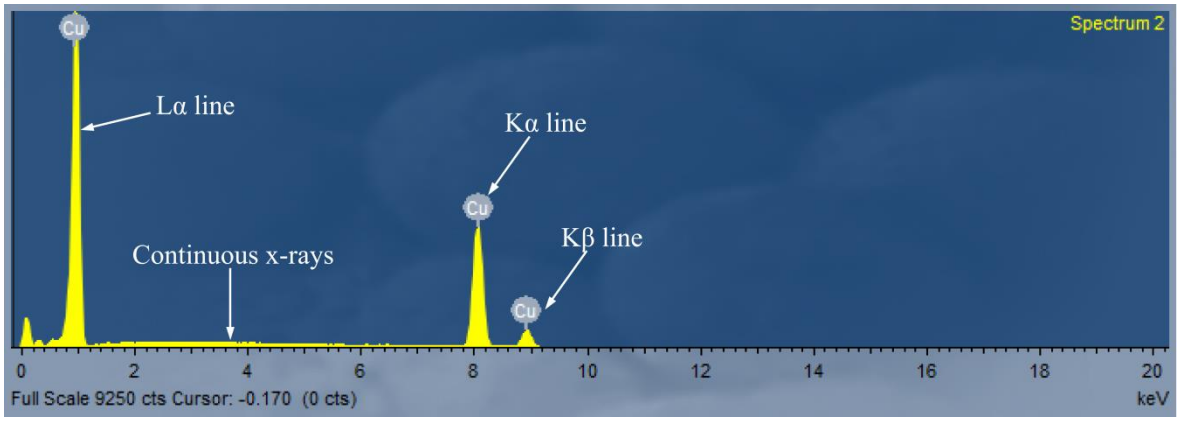

Figure 4.3.5 An example of the spectrum generated for the X-ray emission of a copper plate. The continuous X-rays have been labelled showing the background spectrum they generate as well as the peak produced from characteristic X-rays.

4.3.2 SEM Construction

There are four main sections to an SEM: 1) electron gun, 2) electron column, 3) specimen chamber, and 4) visual interface / output.

Electron gun

The electron gun emits electrons, which are accelerated towards the sample at voltages between 2 and 40 keV (Vernon-Parry, 2001). Typically, tungsten thermionic guns are used, where a tungsten filament is bent into a point. The filament is then heated to temperatures between 2500 - 2700°C by passing a current through it. At high temperatures the electrons on the filament have enough energy to be emitted from the source in a process called thermionic emission (Goldstein *et al.*, 1981). The filament itself is bent into a "V" shape and mounted upside down onto a ceramic, non-conducting, holder. The whole assembly is covered with a Wehnelt cap, which has a small aperture that is found just below the filament, this assembly is known as the Wehnelt assembly (Figure 4.3.6). The "V" shape of the filament assists with the orientation of the electron beam, directing it through the aperture. The Wehnelt cap has a negative charge which repels the electrons through the aperture, again assisting to direct the electron beam. A positively charged anode, with an aperture, is placed just below the Wehnelt assembly, this positive anode attracts the electrons towards it. The electrons are accelerated through the aperture by a voltage gradient from the Wehnelt cap, with up to -2500 V, and the positively charged anode, at + 1000 to 50 000 V (Goldstein *et al.*, 1981).

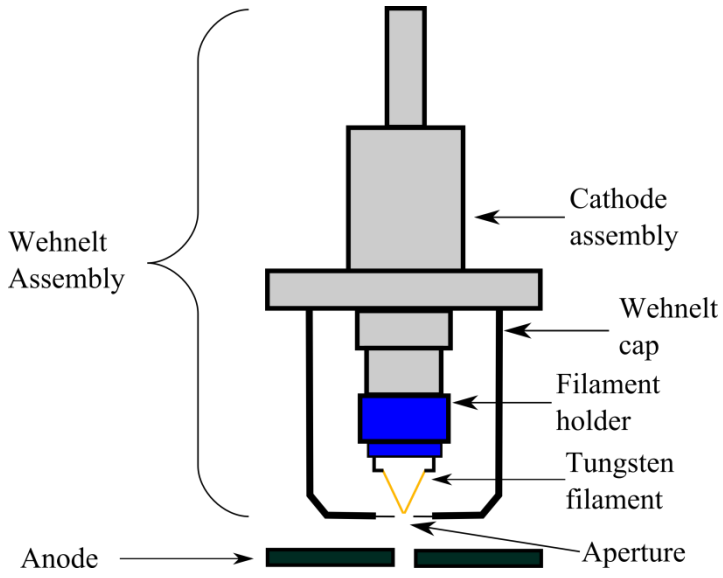

Figure 4.3.6 (Source: EMPA course notes.) Schematic of the Wehnelt assembly.

Electron column

The electron beam passes through condenser lenses, deflection coils and an objective lens, which, along with the electron gun, make up the electron column (Figure 4.3.7).

The condenser lenses are used to help focus and demagnify the electron beam as it travels down the electron column (Goldstein *et al.,* 1981). These lenses are made up of coiled copper wire that is enclosed in an iron casing, which form a doughnut shape within the column. The iron casing has a small gap in the centre of the casing an equal distance between the two poles (Goldstein *et al.,* 1981). A current is passed through the copper wire, which results in the formation of a magnetic field. The gap in the casing enables the magnetic field generated to interact with the electron beam. The magnetic field deflects the electron beam along the centre of the column (Reed, 2005; Goldstein *et al.,* 1981).

An aperture after the condenser coils works to focus the incident beam and prevent stray off-axis electrons from progressing further down the column (Reed, 2005). These off axis electrons can produce spherical aberrations, which result in blurring of the electron image being produced. Another method to correct this aberration is to adjust the working distance, although this method is limited when generating EDX data (Reed, 2005). Imperfections in the coils, and a build-up of contamination, can result in astigmatism, where the beam loses symmetry, which results in the distortion of the image and can reduce the resolution (Reed, 2005; Zhou *et al.,* 2007; Goldstien *et al.,* 1981). This astigmatism can be corrected using an additional set of coils, which are designed to create a weak field to counteract the astigmatism and produce a symmetrical beam (Goldstien *et al.,* 1981).

Deflection coils (also known as scanning coils) are used to manipulate the electron beam in order to scan in a raster fashion over the sample. Coils, in multiples of four, are placed within the column, a variation in potential across these coils are created to change the angle of the electron beam along the *x* and *y* axis (Zhou *et al.,* 2007; Reed, 2005; Khursheed, 2010). These coils are also used to position the beam when collecting localised information (Khursheed, 2010), such as point data for elemental information.

The final lens in the electron column is the objective lens, which is similar to the condenser lenses. The objective lens, which is a pinhole lens, also uses an electromagnet to generate a magnetic field, which is used to focus the incident electron beam. However, without the gap used to expose the magnetic field close to sample, a polepiece is used

instead to minimise the magnetic field near the sample (Reed, 2005; Zhou *et al.*, 2007) so it does not interact with ejected electrons from the sample.

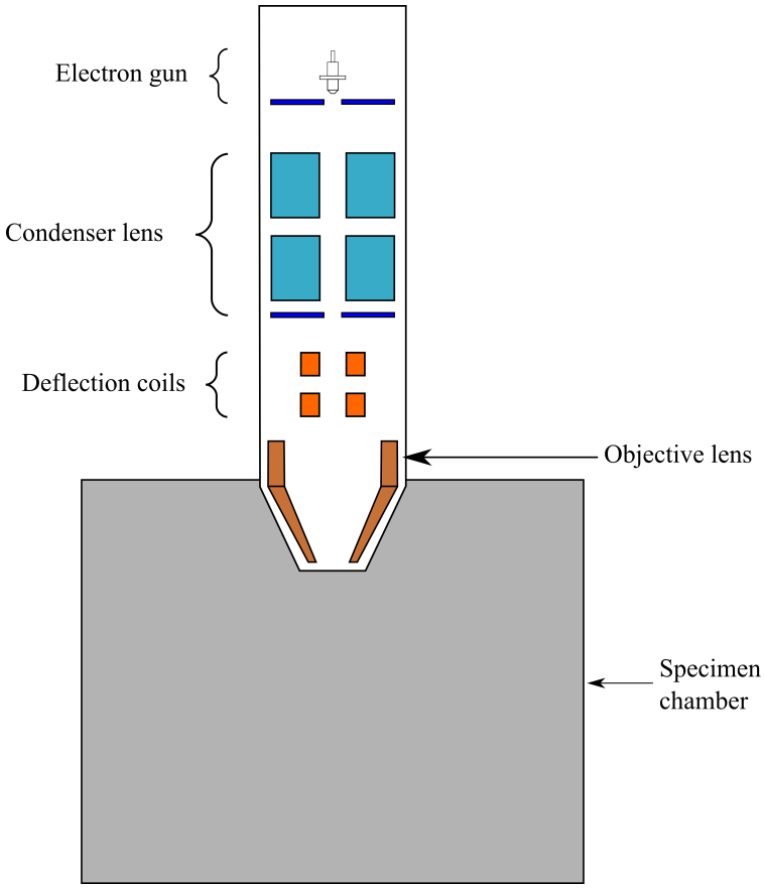

Figure 4.3.7 (Source: modified from Hitachi SEM handbook) Schematic of the electron column.

Specimen chamber

The specimen chamber is home to the three main detectors used in generating data from the SEM, a secondary electron detector, a backscatter detector and an energy dispersive X-ray detector (Figure 4.3.8). The sample chamber is normally used under vacuum, unless the samples are being examined in variable pressure mode (see below), and is brought back up to atmospheric pressure when changing samples. The sample stage has the ability to move in *x*, *y*, and *z* directions, but the amount of movement is dependent on the size of the sample, and the size of the chamber.

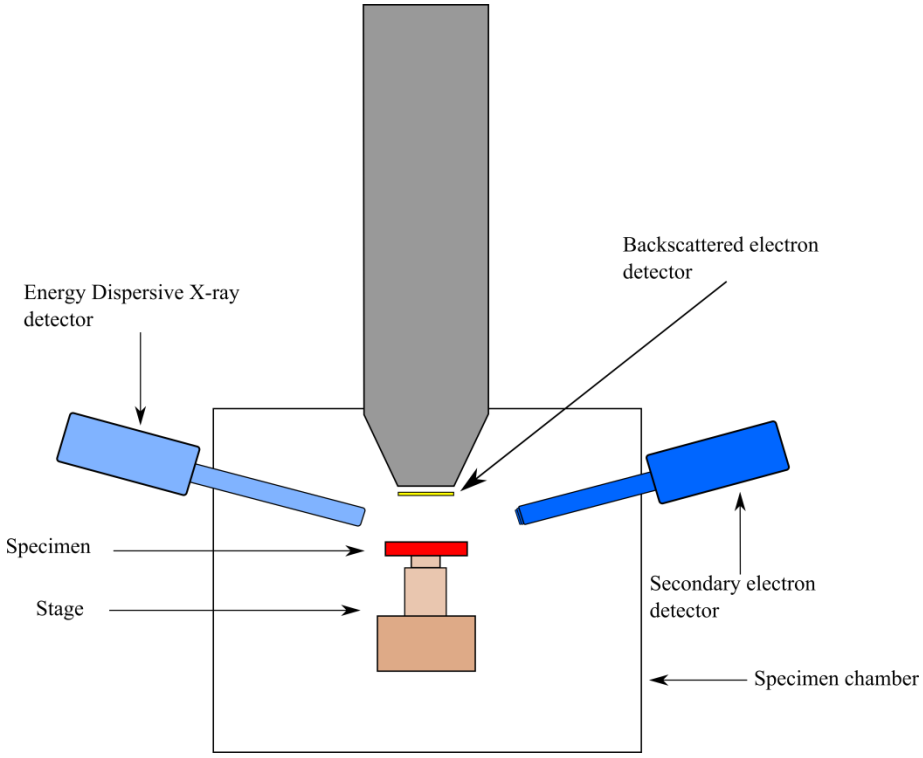

Figure 4.3.8 (Source: modified from Hitachi SEM handbook) Schematic of the specimen chamber showing the locations of the three detectors.

A scintillator is used to detect SEs ejected from a sample and is located to the side of the stage and sample. Scintillators work by converting electron strikes into flashes of light, before a photomultiplier changes these into an electrical signal (Reed, 2005; Zhou *et al.*, 2007). To ensure the SEs striking the scintillator have enough energy to produce a light flash, a positive potential, of 10 kV is applied to it, increasing the energy and ensuring a light flash is generated (Reed, 2005; Zhou *et al.*, 2007). There is a possibility for non SEs to be collected by the scintillator, or there to be a deviation to the incident beam. In order to prevent these occurrences from happening, a grid with a potential of + 200 V is placed in front if the scintillator, which (along with the scintillator, light pipe and a photomultiplier) are collectively known as a Everhart-Thornley detector (Reed, 2005; Zhou *et al.*, 2007). The position of the grid results in the attraction of the low energy SEs without interfering with the incident beam (Reed, 2005; Zhou *et al.*, 2007). The high energy, > 50 eV, BSEs are not readily attracted by the grid, but it is possible for some to be collected by the SE detector (Reed, 2005).

BSEs are detected using a solid state detector located directly above the sample (Reed, 2005), which uses the high angle of the BSEs from the incident beam (Zhou *et al.*, 2007) to produce BSE data. Unlike the SE detector, a grid with a positive potential is not employed to attract electrons, but a negative potential is used to avoid collecting SE,

ensuring only BSEs are detected (Zhou *et al.,* 2007). The detector is composed of four segments, with a hole for the incident electron beam to pass through at centre of the detector. Individual segments of the detector can be switched off, which enables topographic information to be generated from BSE electrons (Reed, 2005). One of the main disadvantage to these detectors is they are inefficient when dealing with electrons with an energy lower than 10 keV (Reed, 2005).

EDX spectrometers work by converting X-ray photons into an electrical pulse. This is achieved by promoting valance electrons (those electrons orbiting atomic nuclei) to conduction bands (where electrons are not orbiting atomic nuclei), within an element such as silicon or germanium, to produce electron hole pairs (Reed, 2005). The energy of the X-ray determines the number of pairs produced and so the number of pulses, which are eventually converted into a spectrum showing the intensity and energy in keV (Reed, 2005) from which the elemental composition of a sample can be determined.

Visual interface / output

A computer display is used to control the magnification, stage movement, detectors being used and displays the images from the detectors. Scanning coils are used to move the incident electron beam in a raster type fashion; the detected electrons can be displayed in real time on screen (Reed, 2005). An additional piece of software is used to collect and store images generated in addition to the EDX data obtained, the University of Kent uses Inca software to do this.

4.3.3 Variable Pressure Mode

The specimen chamber is preferably used under vacuum at a pressure lower than 0.1 Pa, this low vacuum allows the electron to travel to the sample without being scattered by gas (Reed, 2005). There are some occasions however when a pressure greater than 0.1 Pa may be required, such as when looking at biological, wet samples or non-conducting samples, which would require a variable pressure SEM. The SEM used at the University can be used in a variable pressure mode (VP). In this instance the pressure inside the specimen chamber is set, by the user, to a value between 0.1 and 1000 Pa. The main advantage of using the SEM in VP mode is to reduce the effect of charging on the sample. Charging occurs when there is a build-up of electrons on the surface of a sample, which is the result

of the electron being unable to be "drained" away from the specimen to the specimen holder, which is earthed (Reed, 2005). This charging will affect the quality of the image (Goldstein *et al.,* 1981) as the number of incident electrons interacting with the sample is reduced. The presence of gas in the chamber reduces the number of low energy SEs being detected as they interact with the gas present, resulting in the SE detector being unable to be used in this mode.

The SEM was used in VP mode when examining samples non-conducting samples in this investigation, particularly those embedded in epoxy resin.

4.3.4 Section Summary

SEM and EDX analysis has been used to characterise the minerals the used in this investigation and to examine residues produced from heating and impact experiments, particularly to confirm the loss of sulphur from gypsum. In this section the types of information obtained from a SEM and how it is generated has been discussed. In addition to this the construction of the SEM has also been discussed and how the instrument works in variable pressure mode.

Chapter V

Experiment 1: Serpentinisation

Serpentinisation is a process whereby Fe – Mg bearing minerals, such as olivine and pyroxene, are processed into serpentine (Mg/Fe_2SiO_4) as a result of interacting with H_2O (Figure 5.1). In addition to the formation of serpentine (see Chapter II, Section 2.4.1), methane can also be generated. This experimental programme focused on the transformation of olivine to serpentine, with a particular emphasis on whether impacts can cause, or induce, the reactions listed in Table 5.1. Table 5.1 lists the serpentinisation reactions and products of olivines with various forsterite compositions (Mg content of the mineral). In reactions 1 – 3, olivine, CO_2 and H_2O are the starting materials; these single reactions produce methane as a product of the serpentinisation process. Reactions 4 – 6 involve olivine (again with various forsterite compositions) and H_2O alone. In these reactions, free H_2 is produced and a further reaction (reaction 7) is required to produce methane. It is unclear, without direct analysis of the gases produced, as to whether a single or two stage reaction is likely to occur in order to produce methane. Unfortunately, gas analysis was not available and so the detection of serpentine after impact would indirectly show methane could have been produced.

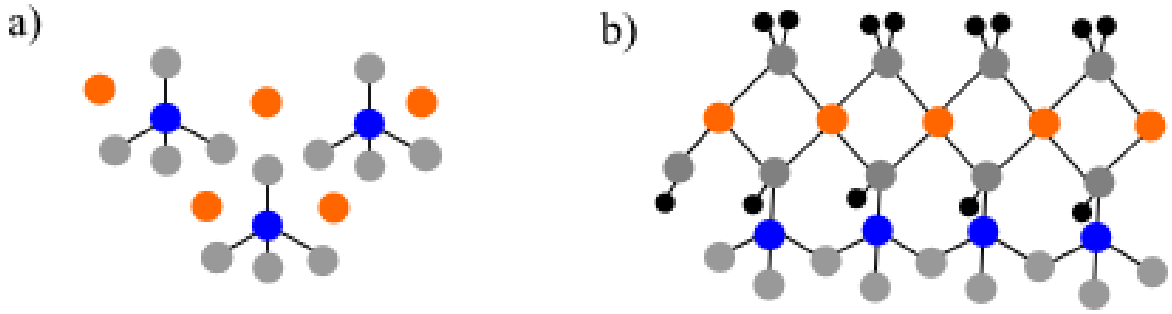

Figure 5.1 (redrawn from Downs & Wallace, 2003) Crystal structure of olivine (a) and serpentine (b). Orange atoms are magnesium, grey atoms are oxygen, blue atoms are silicon and black atoms are hydrogen.

Table 5.1 Serpentinisation reactions for olivine. Table has been modified from Quesnel *et al.,* (2009) and Oze & Sharma (2007).

Reaction	Equation	Olivine composition
1	Olivine + Water + Carbon Dioxide = Serpentine + Magnetite + Brucite + Methane	Fo_{90-85}
2	Olivine + Water + Carbon Dioxide = Serpentine + Brucite + Methane	Fo_{75}
3	Olivine + Water + Carbon Dioxide = Serpentine + Brucite + Pyroxene + Methane	Fo_{70}
4	Olivine + Water = Serpentine + Quartz + Brucite + Hydrogen	Fo_{50}
5	Olivine + Water = Serpentine + Brucite + Hydrogen	Fo_{75}
6	Olivine + Water = Serpentine + Brucite	Fo_{100}
7	Hydrogen + Carbon Dioxide = Methane + Water	N/A

Methane has been detected within the Martian atmosphere in localised regions (Webster *et al.*, 2014; Mumma *et al.*, 2009). A number of processes have been suggested as possible sources for methane (see Chapter II Section 2.4 for a full discussion), with serpentinisation being one of them. However, this process requires the presence of liquid H_2O to occur, yet to date, liquid H_2O has not been directly detected on the Martian surface. Although, hydrated salts have been detected on Mars (Ojha *et al.*, 2015), which suggests water may have been on the surface there is still no direct evidence for water on Mars today. Impacts could play a role in inducing serpentinisation on Mars, as they would provide sufficient energy to transform water ice on the surface (or subsurface) into a liquid, and thus induce serpentinisation. Experiments performed by Furukawa *et al.*, (2011) found serpentine crystals formed on the surfaces of olivine grains when shocked. In their shock experiments they used a combination of liquid water and olivine within a sealed container, which was then impacted by a flyer plate. The experimental program described here instead used H_2O ice mixed with olivine, which more closely resembles the materials found on the Martian surface.

Images taken by orbiting spacecraft, such as HiRISE, show impacts are still occurring on Mars, with some recent impacts having produced craters up to 150 m in diameter (Malin *et al.*, 2006; Ivanov *et al.*, 2010). As mentioned previously (Chapter II, Section 2.4.1), serpentines have been detected within some craters on Mars (Ehlmann *et al.*, 2010), which indicates a potential link between the two processes. If impacts were to induce serpentinisation, and thus produce methane, it would result in localised occurrences, providing a potential explanation for some of the methane detected on Mars. It is therefore important to understand if impact induced serpentinisation can occur, and if so, how much methane could potentially be generated as a result.

5.1 Target Mineral

Initial experimental designs used olivine in the JSC Mars-1 simulant, which displays a spectral resemblance (reflected spectra) to the Martian surface (Singer, 1982). The simulant was taken from Pu'u Nene, which is located on the Mauna Kea volcano, Hawai'i (Allen *et al.,* 2000, 1998, 1997; Seiferlin, 2008) and, Allen *et al.,* (2000) describes the collection and post-processing of the JSC Mars-1 simulant before distribution. However, examination of individual grains (undertaken by the author, see Figure 5.1.1) using SEM analysis showed small fragmented crystals of olivine within a glassy matrix, which makes it difficult to detect any changes in the olivine using Raman spectroscopy. As a consequence of the size, and distribution, of olivine crystals within the JSC Mars-1 simulant, it was decided to use individual grains of olivine, as changes would be more easily detectable using Raman spectroscopy.

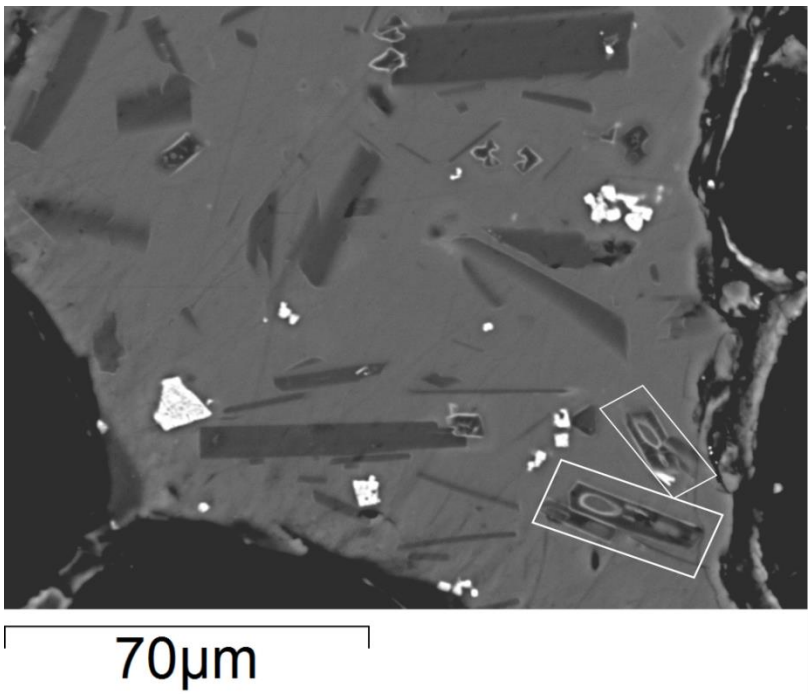

Figure 5.1.1 SEM BSE image of JSC Mars-1 embedded in epoxy resin. The bright crystals are Fe- and Ti-rich, with small crystals of olivine appearing as darker, lathe shaped crystals (examples highlighted with white boxes). Black regions towards the edges of the image represent the epoxy resin.

The batch of grains selected for this experimental programme had a diameter of <355 µm, and varied in colour, suggesting minerals other than olivine were also present. It was therefore important to characterise the grains found in the batch and identify grains that

were not olivine. Nine different grain types were identified and characterised using optical microscopy, SEM EDX analysis and Raman spectroscopy (see Appendix A for details of grain characterisation). The various grain types were identified as pyroxene (grain types I), quartz (grain type VI), high Mg olivine (grain types II-V and VIII) and grain type VII and IX could be either an amphibole or pyroxene. In addition to this Raman analysis indicated the presence of small hydrous inclusions that were not detected by SEM and EDX analysis. These inclusions are believed to be actinolite and talc, which are hydrated minerals with OH features found between 3665- 3715 cm^{-1} Raman shift.

It is important to take these inclusions of hydrated minerals into consideration during analysis, to prevent the misidentification of serpentine. All of these grains were used in the targets, so it was important to identify the various minerals present that may affect the results. Even though some pyroxene was found within the grains used to make the target, we only examined the serpentinisation of the olivine grains.

5.2 Raman Damage

Tests were carried out to determine if olivine and serpentine (provided by Anton Kearsley) could be damaged by the Raman spectrometer's 473 nm laser, due to localised heating caused by the laser. Olivine grains (<355 µm in diameter) that were characterised in section 5.1 (Figure 5.1 grain types II- V and VIII) and fine grained serpentine were used for this test. Samples of each mineral were exposed to the laser for varying lengths of time before a spectrum was taken. This was done to establish if heating the minerals would cause any damage or modification to the samples. A Raman spectrum, at low power (10% of the maximum power, corresponding to a power of 0.44 mW at the sample), was taken before and immediately after the grain was exposed to the laser. Table 5.2.1 shows filter conditions, objective used and the length of time for which each olivine grain was exposed to the laser for. No damage (i.e. scorch marks and change to the overall Raman spectrum) was observed in any specimen indicating that it would take a laser exposure time greater than 30 minutes (far beyond our needs), with the laser on full power (equivalent to 4.87 mW) to cause any damage or modification of the grains being used in this set of impact experiments.

Table 5.2.1 Olivine grains exposure to the 473 nm Raman laser**.**

Grain ID	Objective	N.D. filter	Total exposure time (mins)	Power (mW)	Damage
4a	×50	10%	2	0.44	None
5a	×50	10%	2	0.44	None
5b	×50	10%	10	0.44	None
8a	×100	100%	30	4.87	None
8a	×100	100%	30	4.87	None

N.B. The 473 nm laser has an output power of 500 mW measured at the laser aperture.

The fine grained serpentine powder was exposed to the 473 nm laser for a total of 30 minutes using the ×10 objective lens and a 10% N.D. filter. Again this test revealed a longer exposure time would be required to cause any damage (burning, alteration to the Raman spectrum or dehydration) that would result in a change to the sample. In addition, separate heating experiments of the serpentine showed a temperature of 500 ˚C was required to cause any change in the Raman spectra, through the loss of OH (discussed in Section 5.3).

5.3 Experimental Setup

Two experimental setups were used in this investigation: the first impacted stainless steel sphere (2 mm in diameter) projectiles into a target composed of the mineral grains in a mixture of CO_2 and H_2O ice. The second impacted projectiles composed of a mixture of olivine grains in H_2O ice into targets of either aluminium or stainless steel. Both sets of experiments used the mineral grains characterised in Section 5.1 in an attempt to determine if impacts could trigger the chemical changes needed for the production of methane via the process of serpentinisation.

Although pyroxene is present within the mineral grains being used in the experiment, only the conversion from olivine into serpentine will be examined. As it can be ensured that any previous hydration to the olivine grains is removed and so will not affect the results.

Characterisation of olivine grains showed hydration (particularly grain type II), this hydration needed to be removed to ensure any hydration detected post-impact occurred from impact induced serpentinisation. When heated at 600 ºC in air, serpentine changes into anhydrous olivine via the reaction below (Deer *et al.*, 1992):

$$2Mg_3Si_2O_5(OH)_4 = 3Mg_2SiO_4 + SiO_2 + 4H_2O$$

To test this reaction, small amounts (~1mg) of serpentine powder were heated using the Raman spectrometer's environmental stage. Grains were heated to a temperature of 600 ºC and held at that temperature for 20 minutes, when a change in the Raman spectra was observed. A second sample of serpentine was heated in a *Lenton* furnace at 600 ºC for 12 hours, which showed the total conversion of serpentine to olivine upon examination. As a result of these tests, all the grains used in the impact experiments were heated in a furnace to 600 ºC for 12 hours to remove any previous hydration caused by serpentinisation, which, again, was confirmed using Raman spectroscopy. This temperature is below the melting temperature of olivine (which is ~1900 ˚C) and would not cause any phase changes.

Olivine has a characteristic SiO_4 doublet peak around 820 and 850 cm^{-1} (Keubler *et al.*, 2006), which is used for olivine identification. This feature is absent in the serpentine Raman spectrum, but there is an OH feature at 3600 – 3740 cm^{-1} Raman shift and peaks at 377, 680 and 1045 cm^{-1} Raman shift, which are not present in olivine (Figure 5.3.1).

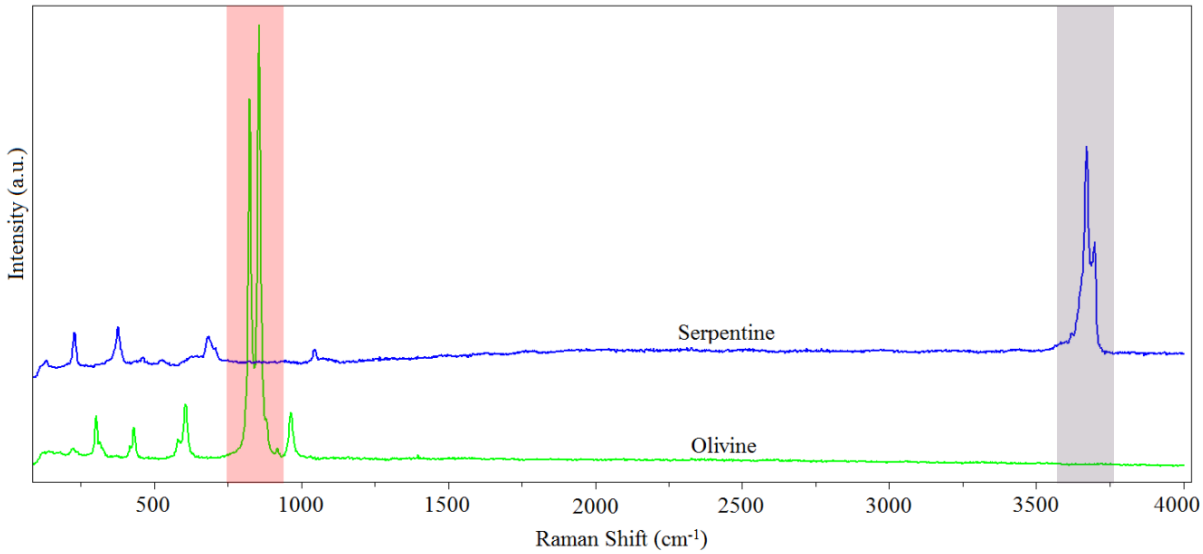

Figure 5.3.1 The Raman spectra of olivine (green) and serpentine (blue). Both spectra were taken using a 473 nm laser, ×10 objective, 600 lines per mm grating, 10% laser power, 2 sec exposure time and 15 accumulations. Olivine's characteristic doublet peak (region highlighted in red) is not present in the serpentine spectrum. The OH peak found in serpentine (region highlighted in grey) is not present in unaltered olivine. The spectra have been vertically offset for clarity.

5.3.1 Target and Projectile Making

Olivine Targets

The targets were made using a 2:2:1 weight ratio of crushed H_2O ice, CO_2 ice, and olivine (respectively) with a total weight of 100 g. This mixture was spread over a layer of H_2O ice and CO_2 ice which was used to prevent damage to the target holder and target chamber during impact. It's surface was then sprayed with high purity water before being placed into a chest freezer at -140 ˚C until required. This final fine top layer of high purity water, once frozen, prevented the surface of the target crumbling when inserted into the horizontal target holder. A small sample from this initial mixture was removed and acted as a control for each impact experiment, being subjected to the same preparation process as the target, but not the shock event.

Olivine Projectiles

Two types of olivine projectiles (Figure 5.3.2) were made. Type 1 used a hollow nylon projectile casing that was half filled with olivine grains and then topped up with high purity water. The projectile was then placed into an upright freezer at -21 ˚C overnight before being used in the experiment. Type 2 projectiles were made of olivine grains and H_2O ice without a nylon casing. For these, a mould was used to create the projectile (following the same procedure as type 1 projectiles) and one day before the scheduled experiment the projectile was released from the mould and placed back into the freezer. Just prior to shooting it was placed into a brass holder (which was also kept in the upright freezer). The brass holder kept the projectile frozen whilst it was being transported to the LGG for loading when it was required.

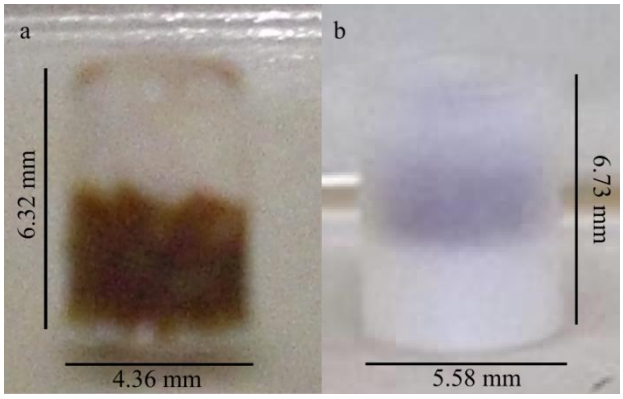

Figure 5.3.2 a) Olivine and ice project without the sabot. b) Olivine and ice projectile within the nylon container. Image resolution is poor due to the camera used to take the images.

5.3.2 Target and Projectile Setup

Olivine targets

The targets were placed into a horizontal target holder mounted onto the chamber door. An ejecta capture system (ECS – described below) was used to collect the grains ejected from the target on impact (Figure 5.3.3). The top of the target cylinder was lined up to the top of the ECS in order to collect the maximum quantity of ejected material.

The ECS is made up of four shallow cylindrical segments with an aluminium disc in-between each segment. These discs have circles cut through the centre allowing material to pass through in each direction with the exception of the bottom segment (labelled 4 in Figure 5.3.4), which has a smaller circle cut into the disc, which only allows passage for the projectile. Each segment is designed to collect ejected material at various angles, with low angle (i.e. material ejected closest to the incoming path of the projectile) captured in segment 4.

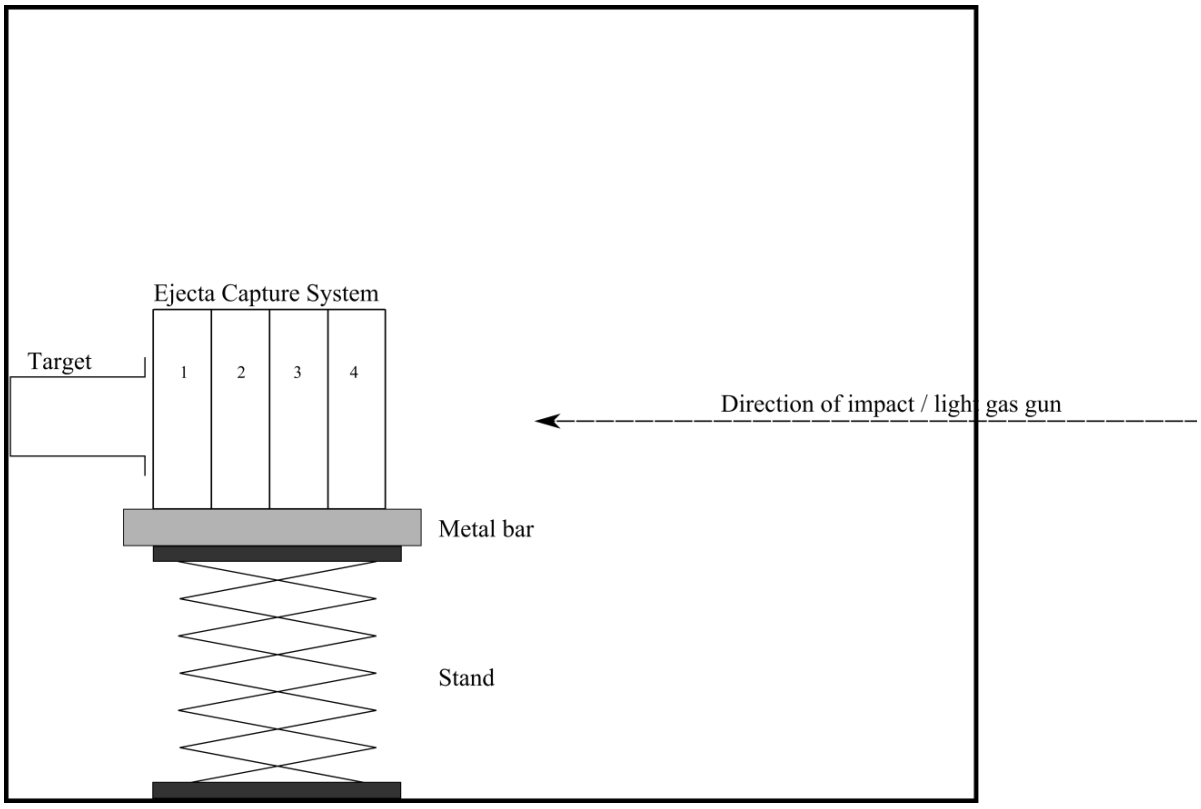

Figure 5.3.3 A schematic (not to scale) showing the experimental setup of the target and ejecta capture system (ECS) within the target chamber in relation to the LGG and the direction of impact.

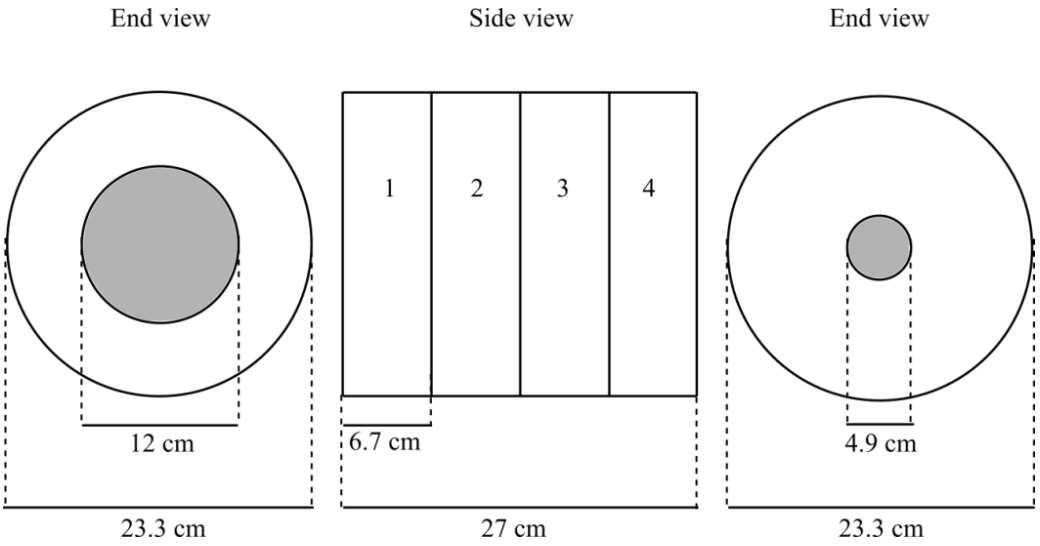

Figure 5.3.4 A schematic (not to scale) of ECS used to collect ejected material from the target. The segments of the ECS are labelled 1 to 4, with segment 1 the first segment in front of the target and segment 4 furthest away from the target.

The ice/olivine targets were impacted using a 2 mm diameter stainless steel sphere at velocities between 3.90 and 5.82 km s^{-1}.

Olivine projectiles

Two different targets were used for the olivine projectiles, as their construction meant they would travel down the LGG differently according to their strengths. Type 1 projectiles, where the projectile material was contained within a nylon casing, were stronger and able to travel the length of the LGG. Three aluminium plates measuring 100 mm × 100 mm in size, were mounted on the target chamber door. The first (closest to the incoming projectile) of these plates was 3 mm thick and second and third plates were each 1.5 mm thick.

The frozen olivine and H_2O ice projectile, which was not contained in a nylon casing (type 2), was fragile and would breakup on flight to the target chamber (as observed in previous experiments conducted by the impact group). The target, a stainless steel plate 50 mm × 85.5 mm and 20 mm thick, was therefore mounted in the blast tank in place of the usual stop plate. Positioning the target in this location meant all of the projectile would hit the target at/near the intended velocity (Figure 5.3.5).

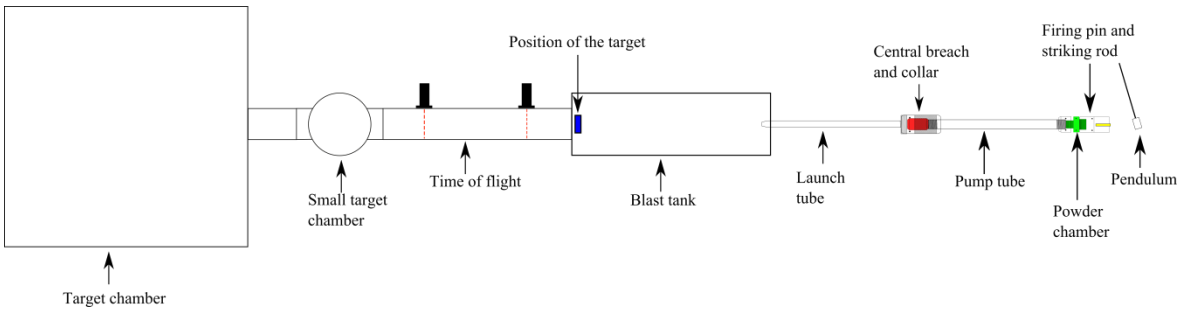

Figure 5.3.5 Schematic of the LGG (not to scale) with the position of the target plate in the blast tank highlighted.

Both types of projectiles required the LGG to be setup in a "cold gun" configuration for the firing of frozen projectiles (see Chapter IV, Section 4.1.2 for details on the setup for the cold gun). The temperature of the launch tube was taken immediately post-impact to ensure the temperature had not risen above 0 °C, and hence the projectile was frozen on impact.

5.4 Analysis Technique

After impact, the ECS and target container were removed as soon as the target chamber had been brought back up to atmospheric pressure. The grains at this point were still mixed with the ices and required separating. The mixture of ices and grains from each of the ECS segments, and any remaining material in the target container and the control, were placed onto a funnel and filter paper and then into a fume cupboard for separation. This allowed any remaining CO_2 to sublimate from the mixture, and water ice to be filtered away into a beaker, leaving only sample material left on the filter paper. The grains were left overnight in the fume cupboard to dry before analysis.

Analysis of impacted material from both experimental setups was conducted using Raman spectroscopy (described in Chapter IV, Section 4.2). Tests prior to the impact experiments outlined above (Section 5.2, Raman damage) showed the laser being used would cause no damage to either the olivine grains, or any serpentine that may have been produced. To determine if serpentinisation had occurred, analysis of the olivine grains, or residue, focused on the detection of a hydroxyl peak found between 3600 and 3740 cm^{-1} Raman shift. As mentioned earlier, olivine grains demonstrated some evidence of hydration, which was removed by heating samples to 600 ˚C. However, inclusions of minerals such as talc and actinolite, which also show a hydration peak in the spectral

region of interest, were found in the grains. It was therefore important to be able to distinguish between those minerals and serpentine. Figure 5.4.1 shows the Raman spectra of olivine, serpentine, actinolite and talc. Although, the Raman spectra of actinolite and talc appear to be somewhat similar (the peak widths for talc are much narrower), the Raman spectra for these minerals and serpentine are very different to each other. The hydroxyl peak for serpentine is a much broader feature than what is observed for either actinolite or talc, and they also have a strong, sharp peak at ~195.1 cm^{-1} that is not present in serpentine. These differences in Raman spectra made it possible to distinguish between these three hydrated minerals, which meant the misidentification of talc or actinolite as serpentine did not occur.

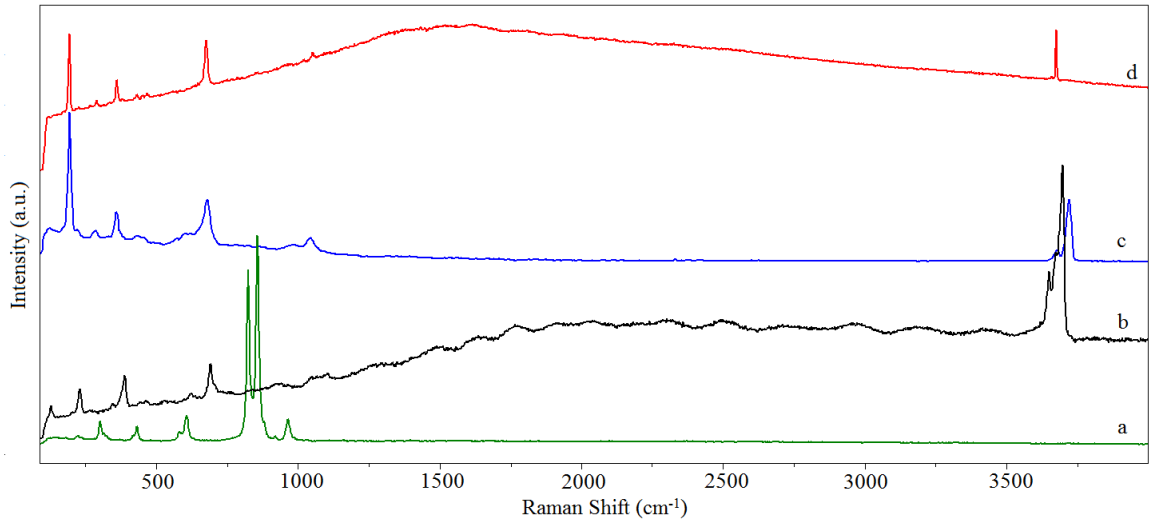

Figure 5.4.1 The Raman spectra of olivine (a), serpentine (b), actinolite (c) and talc (d). The spectra was taken using 473 nm laser, ×10 objective, 600 lines per mm grating and 10% N.D. filter.

5.5 Chapter Summary

In this chapter the method used for making olivine/ice targets and the projectiles for the impact programme have been described. In addition to the preliminary tests and actions that were taken to ensure any serpentinisation found from analysis occurred as a result of impacts. The results from this experimental programme are presented and discussed in Chapter VIII.

Chapter VI

Experiment 2: Devolatilisation

Mineral devolatilisation occurs when a mineral loses its volatile components as a result of experiencing high temperatures and/or pressures. This process can result in the formation of different minerals, or the complete decomposition of the mineral into (mainly oxides of) its individual elements. For example, $ZrSiO_4$ (zircon) decomposes to SiO_2 (quartz) and ZrO_2 (baddeleyite or zirconia).

Terrestrial bodies in the Solar System have experienced frequent and highly energetic impact events since their formation. Such impacts would generate the high pressures and temperatures required to liberate volatiles from minerals, from both the impactor and target material. Mineral devolatilisation, occurring during planetary accretion, has been proposed as a possible source for the formation of early planetary atmospheres. Benlow & Meadows (1977) proposed that high velocity impacts onto planetary embryos would cause material to vaporise, and thus liberate volatiles, which would form a primary atmosphere around the body. Schaefer & Fegley (2010) showed the main volatiles released from different types of chondrites are H_2, CO, H_2O, and CO_2, along with S, P, Cl, F, Na, and K at higher temperatures (1500 – 2500 K). These results indicate that additional processes – such as volcanic outgassing - are required to produce the atmospheres we see today. However, impact induced mineral devolatilisation occurring later in a planet's history can also result in temporary changes of atmospheric chemistry, leading to alterations in a planet's climate. For example, the impact event that produced the Chicxulub impact crater, would have released large quantities of sulphur and carbon oxides into the atmosphere, as the country rock in this location on Earth was composed of carbonates and evaporates (Koeberl, 1993). Kring (2007) summarised the consequences this impact event would have on Earth, which included global warming resulting from the release of greenhouse gases. The magnitude of these climate changing effects is dependent on the amount of material released, therefore, it is important to understand how volatiles

are lost from both the impactor and target material if we are to provide more accurate estimations of the quantities of volatiles released upon impact. Understanding the impact induced devolatilisation of minerals will also help in our understanding of palaeosurface conditions, and could provide an indication of impact velocities. In addition, if devolatilisation does occur in minerals when impacted, they may act as a shock pressure/temperature barometer/thermometer (or shock barometer) for impact craters.

6.1 Minerals

A series of impact and heating experiments were conducted to determine if impacts would release volatiles from within the mineral structure, and if they could be used as a shock barometer/thermometer. These experiments used two Martian relevant minerals: 1) goethite and 2) gypsum (Figure 6.1.1).

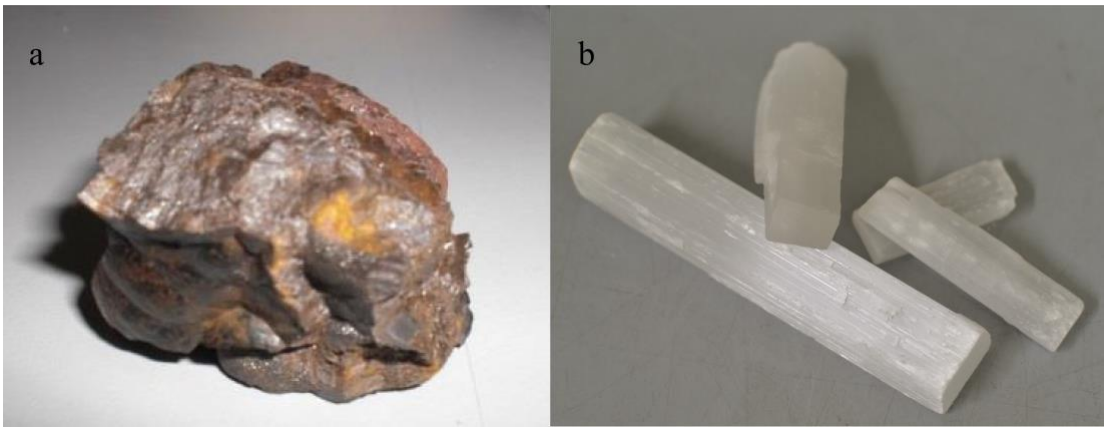

Figure 6.1.1 a) Sample of goethite (29.12 × 36.06 × 19.75 mm) that was used to make both mineral projectiles and target. b) Gypsum crystals (between 149.51 × 19.57 × 27.20 mm and 9.17 × 16.76 × 54.57 mm in size) used for projectiles.

1) Goethite (Figure 6.1.2), FeO(OH), is an iron oxyhydroxide, which is predominantly formed as a result of the weathering of the Fe-bearing minerals siderite, magnetite and pyrite in oxidising environments (Bishop *et al.*, 2003 and Deer *et al.*, 2013). The goethite nodule used in this investigation was obtained from the Natural History Museum, London.

   Goethite was detected on the Martian surface at Gusev crater by NASA's *Spirit* rover (Klingelhöfer *et al.*, 2005) and is a possible candidate for a 0.9 μm near-infrared spectral feature found in the bright soils covering the Arabia region

(Murchie *et al.*, 1993). As this mineral is usually formed in aqueous environments, its presence on Mars indicates water was present on the planet's surface at some point throughout its history.

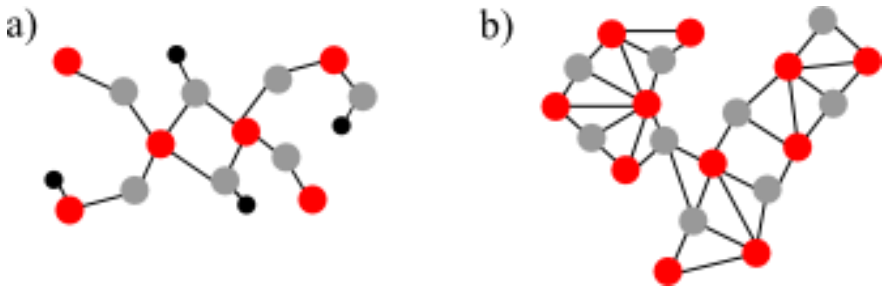

Figure 6.1.2 (redrawn from Downs & Wallace, 2003) Crystal structure of goethite (a) and hematite (b). Red atoms are in red, oxygen atoms are grey and hydrogen atoms are black.

2) Gypsum ($CaSO_4 \cdot 2H_2O$) is a sulphate mineral, forming mainly as an evaporate deposit in sedimentary layers (Deer *et al.*, 2013). It can also be formed where sulphuric gases have reacted with limestone; in volcanic areas (Bishop *et al.*, 2003) and as a result of the circulation of meteoric waters (precipitation) in sandstones (Wenk & Bulakh, 2012). $CaSO_4 \cdot 2H_2O$ has a semi-hydrous (basanite; $CaSO_4 \cdot {}^1/_2H_2O$) and anhydrous (anhydrite; $CaSO_4$) state (Figure 6.1.3), each of which can be generated through hydration and dehydration reactions:

$$CaSO_4.2H_2O \underset{\text{Dehydration}}{\overset{\text{Hydration}}{\rightleftharpoons}} CaSO_4.{}^1/_2H_2O \underset{\text{Dehydration}}{\overset{\text{Hydration}}{\rightleftharpoons}} CaSO_4$$

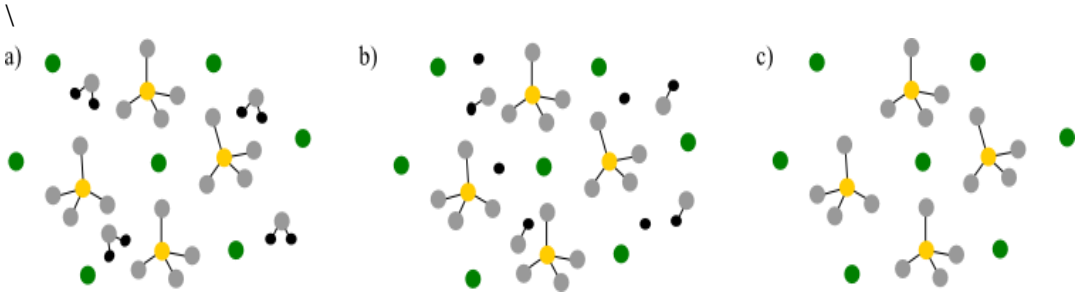

Figure 6.1.3 (redrawn from Downs & Wallace, 2003) Crystal structure of gypsum (a), bassanite (b) and anhydrite (c). Green atoms are in calcium, yellow atoms are sulphur, oxygen atoms are grey and hydrogen atoms are black.

Two forms of gypsum were used as projectiles during the impact experiments: 1) natural gypsum (Figure 6.1.1b), purchased from a mineral supplier, 2) and Plaster

of Paris (PoP) purchased from a craft shop, in a semi-hydrous powder form and mixed with water to produce hydrated PoP/gypsum.

Spectral data from the Observatoire pour la Minéralogie, l'Eau, les Glaces et l'Activité (OMEGA) has shown the presence of gypsum in northern circumpolar dunes on Mars (Langevin *et al.*, 2005) and in 2011 what is believed to be a gypsum vein was found in Endurance crater by NASA's *Opportunity* rover (Showstack, 2011). In addition to the detections of gypsum, bassanite and anhydrite have also been found on the Martian surface. Initial findings from the Miniature Thermal Emission Spectrometer (Mini-TES), on-board the *Opportunity* rover, showed evidence of Ca-sulfates, at various outcrops in Meridiani Planum (Christensen *et al.*, 2004), which was later shown to be bassnaite and anhydrite (Clark *et al.*, 2005; Glotch *et al.*, 2006). In addition, bassanite has also been detected in the Mawrth Vallis within thick layered deposits by Wray *et al.*, (2010). As with goethite, the presence of gypsum and bassanite on the Martian surface indicates liquid water was once present on the planet.

Samples from both mineral specimens were embedded in epoxy resin and polished flat (using sand paper, then diamond and alumina polish), before being analysed by SEM using an accelerating voltage of 20kV and in variable pressure mode under a pressure of 25 Pa. SEM EDX analysis of goethite confirmed the presence of water within the sample, due to a low total weight % of between 69 – 64 % (Table 6.1), which is lower than an accepted weight % of between 98 and 102 when conducting EDX analysis. A low amount of Si at 2.13 % (of the total weight) was also detected, which is found in natural goethite samples (Gialanella *et al.*, 2010). SEM BSE images (Figure 6.1.4) show the sample appears to be homogenous in composition; however, there are a number of indentations on the surface, which have been made apparent through polishing. These indentations appear to be a result of crystals coming lose from the grain as it was being polished. The BSE images also show the sample is homogenous in composition, which is confirmed in the quantitative data (Appendix B, Table B1).

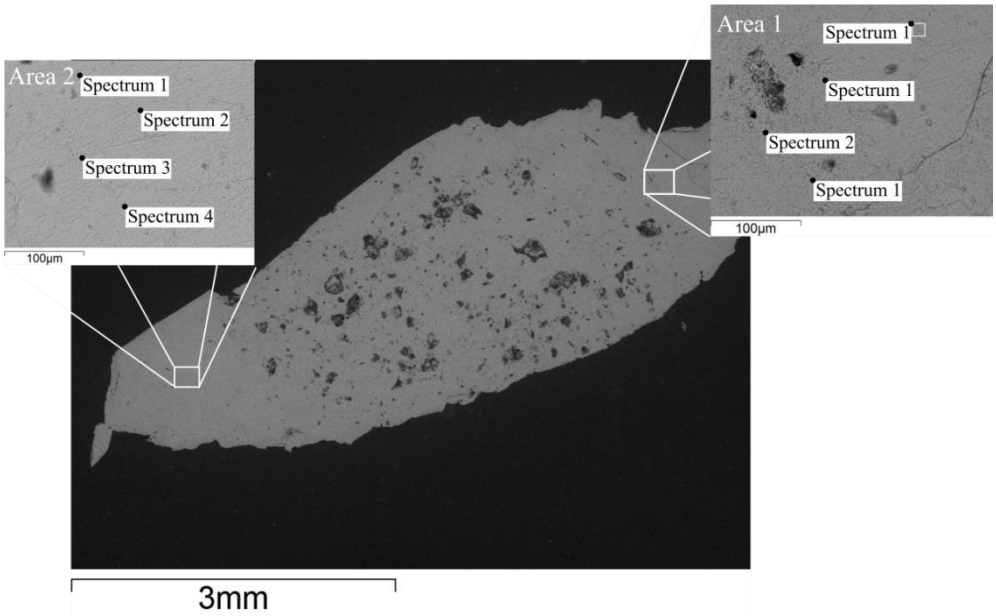

Figure 6.1.4 SEM BSE image of goethite embedded into epoxy resin. The inset images highlight the approximate location the EDX data came from. BSE images and EDX spectra were taken at a pressure of 25Pa with an accelerating voltage of 20kV.

Table 6.1.1 EDX weight % data for goethite, taken at the locations shown in Figure 6.1.4.

Element	**Weight (%)**							
	Area 1				Area 2			
	Spectrum 1	Spectrum 2	Spectrum 3	Spectrum 4	Spectrum 1	Spectrum 2	Spectrum 3	Spectrum 4
Si K	1.07	2.13	1.55	0.78	0.79	0.64	0.59	0.76
Fe K	46.04	45.28	45.92	45.01	44.60	44.32	43.91	45.05
O	21.01	21.88	21.5	20.23	20.07	19.78	19.54	20.23
Total	**68.12**	**69.29**	**68.97**	**66.02**	**65.47**	**64.74**	**64.03**	**66.04**

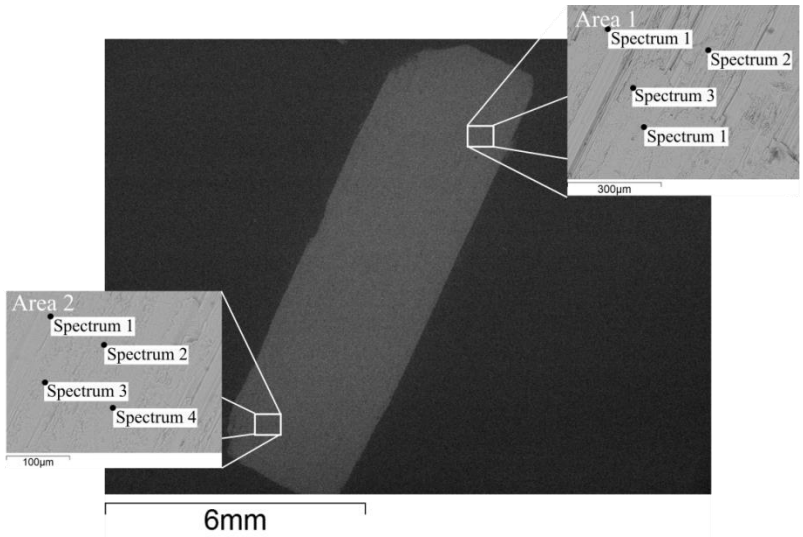

Figure 6.1.5 SEM BSE image of gypsum used for projectiles embedded in epoxy resin. The inserted images highlight the approximate area the EDX data came from. BSE images and EDX spectra were taken at a pressure of 25Pa with an accelerating voltage of 20kV.

Table 6.1.2 EDX weight % data for natural gypsum, taken at the locations shown in Figure 6.1.5.

Element	Weight (%)							
	Area 1				Area 2			
	Spectrum 1	Spectrum 2	Spectrum 3	Spectrum 4	Spectrum 1	Spectrum 2	Spectrum 3	Spectrum 4
S K	12.82	13.09	12.69	12.85	13.07	12.78	12.51	12.7
Ca K	16.71	16.27	15.9	16.36	16.7	16.12	15.94	16.76
O	25.85	26.09	25.34	25.77	26.24	25.57	25.09	25.7
Totals	**55.38**	**55.45**	**53.93**	**54.98**	**56.01**	**54.48**	**53.53**	**55.16**

The natural gypsum sample (Figure 6.1.5) has a homogenous composition, but there is some variation in textures due to crystal formation and fracturing where crystals are needle-like. As with goethite, SEM EDX data of the natural gypsum sample (Appendix B, Table B2) has a low total weight %, of 56.0 to 53.5% (Table 6.1.2), confirming the presence of water within the sample. Unlike the goethite sample, the sample of gypsum did not have any detectable impurities.

Possible volatile loss mechanisms for each of these minerals are summarised in Table 6.1.3 Goethite loses its hydroxyl to form the mineral hematite, which is an iron oxide. Gypsum will lose either some, or all, of its water to form bassanite or anhydrite respectively. Bassanite can also lose its water to form anhydrite, or all three phases can break down completely into their component parts. It is possible for the products of gypsum and bassanite dehydration reactions to rehydrate over time.

Table 6.1.3 Reactions for the loss of volatile component for goethite, gypsum, bassanite and anhydrite.

Reaction	Equation	Reaction type
1	$2FeO(OH) = Fe_2O_3 + H_2O$	Dehydration
2	$CaSO_4 \cdot 2H_2O = CaSO_4 + 2H_2O$	Dehydration
3	$CaSO_4 \cdot 2H_2O = CaSO_4 \cdot 0.5\ H_2O + 1.5\ H_2O$	Dehydration
4	$CaSO_4 \cdot 0.5\ H_2O = CaSO_4 + 0.5\ H_2O$	Dehydration
5	$CaSO_4 \cdot 0.5\ H_2O = CaO + SO_2 + 0.5\ O_2 + 0.5\ H_2O$	Decomposition
6	$CaSO_4 = CaO + SO_2 + 0.5\ O_2$	Decomposition

6.2 Exploratory Tests

A series of tests were carried out to determine if using Raman spectroscopy would affect the results obtained from the impact and heating experiments. An additional test would

conducted using the plaster of Paris to determine how long it would take to completely dry, and if this would have an effect on its Raman spectra.

6.2.1 Raman Spectra of Minerals

The minerals investigated will produce different minerals as a result of the loss of volatiles. Samples of goethite and gypsum were heated, and Raman spectra were taken, before and after heating, to determine the end minerals produced.

de Faria and Lopes (2007) note the onset of goethite dehydration occurs at 250 ˚C with dominant spectral changes taking place, and when goethite is heated to 300 ˚C magnetite bands can form. Therefore, a sample of goethite was heated, under air, at 400 ˚C and 1000 ˚C for two hours to ensure the sample had completely lost its volatile components. The spectra obtained after heating at 400 ˚C shows the loss of Fe-OH peaks and broad Fe-O peaks, which are most likely the result of disorder in the mineral crystal structure. The Raman spectrum obtained from heating goethite to 1000 ˚C displays much narrower peaks than those found when heating to 400 ˚C. The narrowing of the peaks occurs as a result of increasing the temperature, most likely as a result of the increasing crystallinity of the sample. The dominant changes that are visible (Figure 6.2.1) as a result of heating are: 1) the loss of peaks generated from Fe-OH bonds; 2) the apparent shift of the peak found in goethite between 350 and 450 cm^{-1} (named Feature A for the rest of this thesis): the peak changes from a position of 386.7 cm^{-1} to 408.8 cm^{-1}; 3) the formation of a doublet peak at 611.2 and 657.7 cm^{-1} (known as Feature B from here on) and; 4) the formation of a broad peak at 1315.6 cm^{-1}.

Table 6.2.1 shows the peak positions for the goethite used in this experiment, and the peak positions obtained after heating the sample to 400 ˚C and 1000 ˚C, which formed a non-crystalline and a completely crystalline form of hematite, respectively. The peak positions obtained during this experiment and those obtained by Legodi & de Waal (2007) vary considerably by ±14 cm^{-1} for goethite Feature A, ±5 cm^{-1} for hematite (1000 ˚C) Feature A, ±12 cm^{-1} for hematite (1000 ˚C) Feature B (peak 1) and ±42 cm^{-1} for hematite (1000 ˚C) Feature B (peak 2), which could be a result of the manner in which the various samples were prepared for their experiments. However, peak positions produced by de Faria & Lopes (2007) are closer, with differences of only ±1 cm^{-1} for goethite Feature A and ± 2 cm^{-1} for hematite (1000 ˚C) Feature B (peak 1) when compared to those obtained during this experiment.

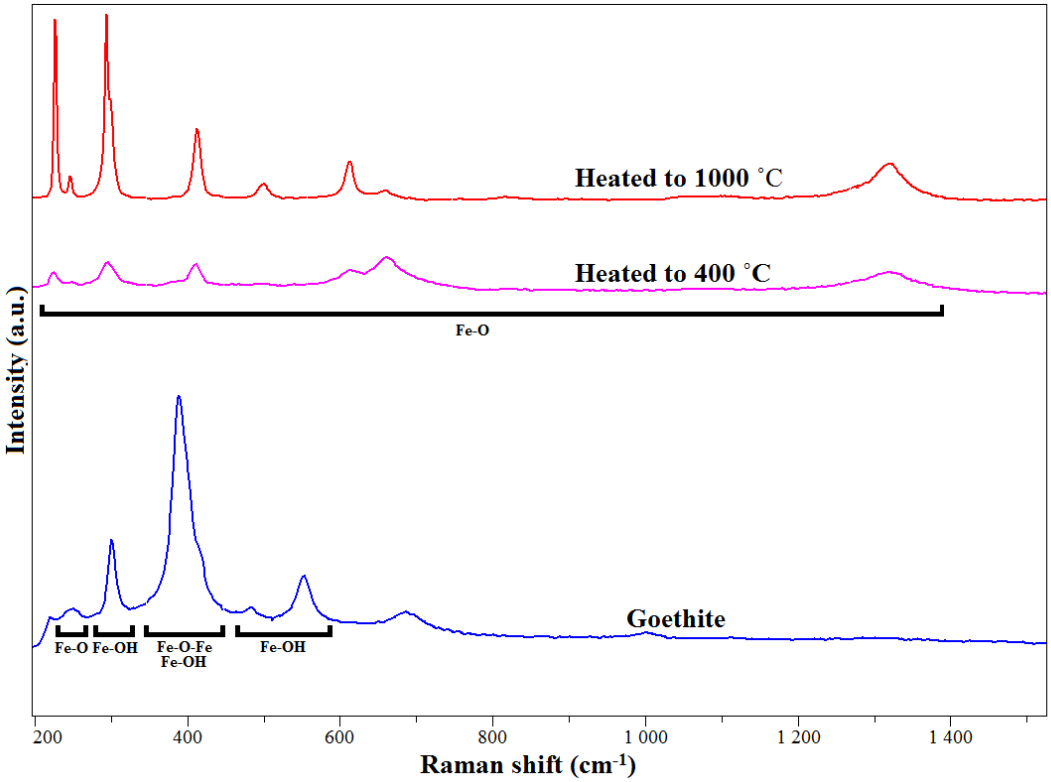

Figure 6.2.1 Raman spectra for the sample of goethite (blue) at room temperature, the sample after heating to 400 ˚C (pink) and 1000 ˚C (red). Raman spectra were taken using the 633 nm laser, 10 % N.D. filter, ×50 microscope objective and 600 g/mm grating.

Table 6.2.1 Peak positions for goethite and hematite.

Mineral	Peak position (cm^{-1})							
Goethite	227.1	298.0	386.7	470.5	549.5	686.6	912.3	-
	223.0	297.0	392.0	484.0	564.0	674.0	-	-
	-	299.0	400.0	-	550.0	-	-	-
	243.0	299.0	385.0	479.0	550.0	-	-	-
Hematite	223.8	294.5	-	409.9	500.4	614.8	661.8	1320.0
	225.9	245.3	294.4	411.3	497.5	612.2	658.5	1320.0
	226.0	-	292.0	406.0	495.0	600.0	700.0	-
	225.0	247.0	293.0	412.0	498.0	613.0	-	-
	227.0	246.0	293.0	412.0	498.0	610.0	-	1322.0

N.B. Averaged peak positions from the goethite used in the devolatilisaton experiments are in black and blue. Goethite heated to 400 ˚C (poorly crystalline) is in blue, with black representing goethite heated to 1000 ˚C (highly crystalline). Values in red and orange have been taken from Legodi & de Waal (2007) and show the experimental and pure oxide peak positions, respectively. Values in purple were obtained from de Faria & Lopes (2007). Raman spectra for material conducted by the author were acquired using the 633 nm laser, 10 % N.D. filter, ×50 microscope objective and 600 g/mm grating.

Pieces of the natural gypsum and PoP used for making projectiles and targets were heated, under air, in a Vacutherm VT6060P oven at 120˚C and 400˚C for two hours, to examine the semi-hydrous and anhydrous states and Raman spectra were taken after each

heating cycle. Figure 6.2.2 displays the spectra obtained and Table 6.2.2 lists the peak positions of the SO_4 bonds. Gypsum and both semi-hydrous and anhydrous phases all exhibit four vibrational bonds for SO_4, referred to as $\upsilon 1$, $\upsilon 2$, $\upsilon 3$ and $\upsilon 4$, which will be used herein to identify specific features in the Raman spectra of gypsum and its dehydrated products. The numbers in brackets indicate the peak the values was taken from, with "1" indicating the first peak of the vibrational mode from low to high Raman shift, this method for identifying individual peaks will be used from here on. Liu *et al.,* (2009) characterise the peak positions for gypsum, bassanite and anhydrite, showing all three of these minerals have a variation in the peak positions of the SO_4 bonds. The $\upsilon 3$ and $\upsilon 4$ bonds exhibit features composed of three peaks for anhydrite, whereas these bonds only have one and two peak structures, respectively, for both bassanite and gypsum (Table 6.2.2). Raman spectra taken before heating the samples show there are distinct changes in spectra from the loss of water as a result of heating. Semi-hydrous $CaSO_4$ presents a broad and low intensity feature between 1105.2 and 1193.1 cm^{-1} (where the $\upsilon 3$ peaks would be located), instead of a single peak found by Liu *et al.,* (2009). Peak $\upsilon 4$ (1) also presents a shoulder feature, which could indicate the emergence of the additional peak formed in the anhydrous phase. A shoulder is also present on the $\upsilon 1$ SO_4 peak, which is not visible in the mineral's hydrous and anhydrous phases. In addition to this, the $\upsilon 1$ mode shows an increase in peak position as the water is lost, which is also noted by Liu *et al.,* (2009). There is also a change in the H_2O feature from the hydrous mineral to semi- hydrous, and completely disappears (as expected) for the anhydrous mineral.

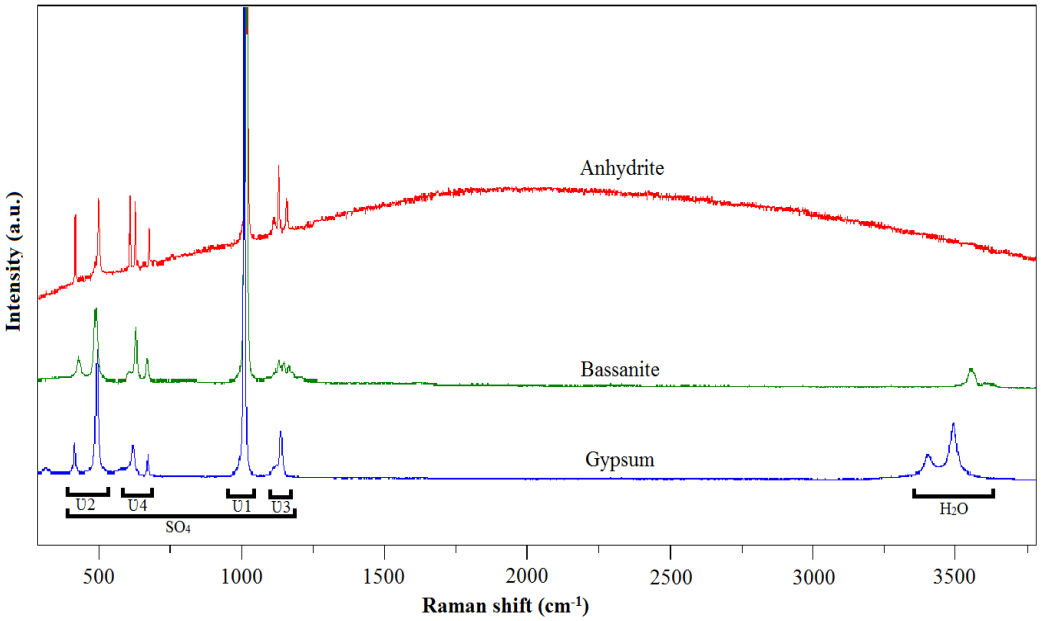

Figure 6.2.2 Raman spectra for gypsum (blue), bassanite (green) and anhydrite (red). Spectra shown here represent the peak formation of hydrous (gypsum), semi-hydrous (bassanite) and anhydrous (anhydrite) states formed when heated from the samples used in the devolatilistion experiments. Raman spectra were taken using 532 nm laser, 10 % N.D. filter, ×50 objective and 1800 g/mm grating.

Table 6.2.2 Raman peak positions for gypsum, bassanite and anhydrite.

Mineral	Peak position (cm^{-1})								
	U1 (1)	U2 (1)	U2 (2)	U3 (1)	U3 (2)	U3 (3)	U4 (1)	U4 (2)	U4 (3)
Gypsum	1008.0	415.0	439.0	1135.0	-	-	620.0	670.0	-
	1008.0	420.0	494.0	1141.0	-	-	623.0	-	-
	1008.1	414.4	493.6	1137.3	-	-	619.6	670.7	-
	1008.7	414.9	494.2	1135.9	-	-	620.2	671.0	-
Bassanite	1015.0	427.0	489.0	1128.0	-	-	628.0	668.0	-
	1014.0	421.0	490.0	1152.0	1174.0	-	630.0	680.0	-
	1015.5	428.9	488.9	-	-	-	628.7	668.1	-
	1016.5	429.3	490.4	-	-	-	629.9	669.2	-
Anhydrite	1017.0	416.0	499.0	1110.0	1128.0	1159.0	612.0	629.0	676.0
	1026.0	424.0	490.0	1105.0	1152.0	1174.0	608.0	628.0	668.0
	1017.4	417.2	499.4	1111.3	1129.5	1160.3	609.4	627.9	676.0
	1017.5	417.5	499.4	1113.1	1129.6	1160.5	609.8	628.5	676.4

N.B. Values in green have been taken from Prasad *et al* (2001), where an additional fourth peak at 685 cm^{-1} was found for SO_4, U4 bond. Prasad *et al* anhydrite values were taken at 152 ˚C. Values in black have been taken from Liu *et al* (2009). Red and purple values are the average of five Raman spectra taken after each heating cycle for natural gypsum, and PoP, respectively, used in the devolatilisation investigation. Peak positions from this experiment for the U3 were not included in the table, as this feature was made up of three to five low intensity peaks in the region of 1105.2 and 1193.1 cm^{-1}.

Peak positions obtained from these experiments differ slightly, ± 3 cm^{-1} for all peak and mineral phases, to those taken by Liu *et al.*, (2009), which is mostly likely a result of

impurities and variations in the samples used for each investigation. However, peak positions obtained by Prasad *et al.,* (2001) vary greater, by ± 23 cm^{-1} for anhydrite U3 and ± 8 cm^{-1} for anhydrite U1, which is due to their anhydrite measurements being taken at 152 ˚C.

6.2.2 Plaster of Paris

The Plaster of Paris (PoP) used in these devolatilistion experiments was made using a 2:1 ratio, as suggested by the manufacturer, of PoP to reverse osmosis water (R.O. water). As the material was being made on-site by mixing fine grained bassanite with H_2O it was important to determine how long it would take the mixture to completely dry and how it could change after being exposed to a vacuum; effects that could potentially influence results from the impact experiments.

To examine the effect of time on the PoP, several blocks approximately 38 × 39 × 15 mm were made and weighed over the course of five days, and a test was also conducted to establish if drying the sample on different materials would affect the length of time required for the blocks to dry. The stability in weight after three days demonstrated that any excess water left in the sample had been completely removed by this time. Bigger blocks (approximately 38 × 39 × 30 mm in size) were made and left to dry on various materials (paper, foil, plastic, glass and on the table surface). Weight measurements were taken at various times over the course of five days and the results are shown in Table 6.2.3. Raman spectra of these PoP blocks were taken to determine if any changes occurred during the drying process. Results from this test showed that a reasonably consistent weight was achieved by samples drying on the table top and on paper within 48 hours after making; foil and plastic had a stable weight after 50 hrs 30 mins and 69 hrs 55 mins, with glass taking the longest at 120 hrs 55 mins.

Table 6.2.3 Mass measurements from PoP drying tests

Total time after making (hrs:mins)	Mass (g)				
	Paper	Foil	Plastic	Glass	Table top
24:45	38.62	37.86	37.99	47.61	35.54
25:35	38.34	37.66	37.81	47.33	35.33
26:53	37.88	37.33	37.64	46.92	34.95
28:52	37.17	36.69	37.06	46.19	34.21
45:09	33.4	32.86	33.57	42.12	30.42
46:50	33.08	32.58	33.29	41.75	30.11
47:55	32.85	32.36	33.07	41.48	29.88
49:20	32.64	32.11	32.78	41.08	29.65
50:39	32.50	31.97	32.58	40.73	29.52
69:55	32.20	31.70	31.7	39.20	29.50
71:45	32.40	31.60	31.5	39.00	29.30
93:25	32.30	31.60	31.5	39.00	29.10
118:40	32.30	31.50	31.5	39.00	29.20
120:55	32.16	31.48	31.38	38.80	29.15
123:11	32.15	31.48	31.37	38.80	29.15
142:25	32.15	31.48	31.38	38.80	29.15
Total mass lost (g)	**6.47**	**6.38**	**6.61**	**8.81**	**6.39**

Raman spectra of the samples taken one day after they had been made and spectra taken one week later shows there are some changes in peak positions (Appendix C, Table C1), particularly of the SO_4 vibrational bonds as excess water was lost. Figure 6.2.3 shows the peak positions of the SO_4 bond peaks taken 24 hrs after making the samples, and one week after being made. A clear shift in the peak positions of the SO_4 U1 (1), U2 (1) and U4 (2) bond peaks occurs, with U3 (1), U2 (2) and U4 (1) peaks not having as clear a shift between the two time periods. The shift in the peak position can be attributed to the loss of water in the sample as it is drying. Therefore it was essential to ensure the PoP had completely dried before use in the impact experiments as such a shift as seen in these tests, could potentially produce false positive results.

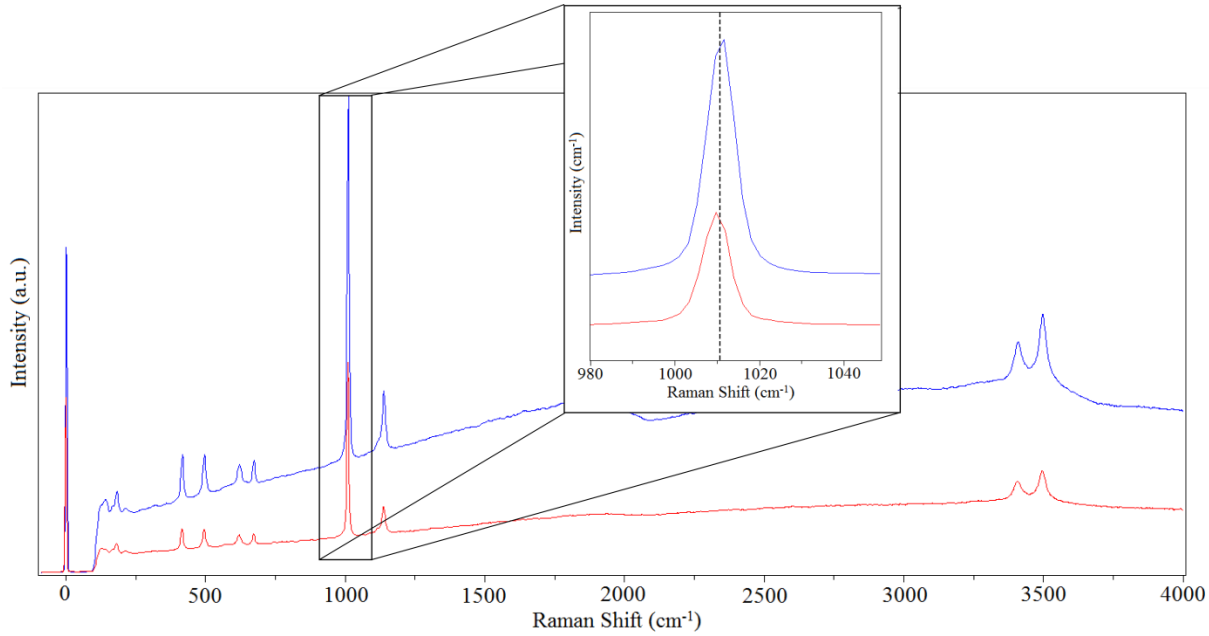

Figure 6.2.3 An example of Raman spectra taken from the drying test (using various drying surfaces); spectra were taken 24 hrs (red) and one week (blue) after making. Both spectra are indicative of gypsum, however the highlighted U1 peak (inserted spectra) clearly shows a difference in peak position between the two spectra. Raman spectra were taken using 473 nm laser, 10% N.D. filter, × 10 objective and 600 g/mm grating.

A final drying test was conducted on a block of PoP with the dimensions of the final target (11.2 × 11.3 × 2.2 cm) to determine how long a block of this size would take to completely dry. This test showed a total of six days from manufacturing was needed to ensure the material was completely dry and thus peak shifts due to the loss of excess water would not affect the results from impact experiments.

Finally, a block of PoP, approximately 38 × 39 × 15 mm in size, was placed inside the LGG's target chamber in an experiment to determine if the lower pressures within the target chamber would have an effect on the water content of the PoP block. The block was left inside the target chamber for 45 minutes, which is the time it would take to pump down the target chamber, complete the shot and then re-pressurise the target chamber. The total mass lost as a result of this was 0.07g (the initial mass before going into the chamber was 13.58g), which is 0.5% of the initial, demonstrating the depressurising of the target chamber would not cause any drastic changes in mass due to loss of water, and thus affect the Raman spectra.

6.2.3 Raman Laser Damage

The main volatile lost for the minerals selected is water, which can occur at relatively low temperatures, between 100 and 250 ˚C (gypsum also loses sulphur at 1400 ˚C). Although the Raman spectra were not obtained using the full power of the illuminating laser, it was important to determine if Raman lasers could result in the dehydration of the sampled area. Tests using grains (< 1 × 1 mm) were performed to determine if the devolatilisation of the minerals could occur from the laser alone.

Exposure tests were carried out on both minerals to examine how a maximum exposure time of 15 minutes would affect minerals. Appendix C Tables C2, C3 and C4, details the parameters used in these tests for both goethite and gypsum, and the peak positions for selected peaks, Feature A for goethite and SO_4 U1 (1), U2 (1) and U2 (2) peaks for gypsum. Results show there is no change in peak positions for goethite after a total of 15 minutes when using a combination of a × 10 or ×50 microscope objective, and 10% or 25%, of the full laser power (532 nm for gypsum and PoP samples and 633 nm for goethite sample) when sampling a spectral range of -90 to 1000 cm^{-1}. Goethite shows a slight change, of +0.3 cm^{-1}, after 3 minutes with a 25% N.D. filter and a grating of 1800 groves per mm, and a change of -0.3 cm^{-1} between and 12 minutes with the 50% N.D. filter an 1800 groves per mm grating, both of which can be attributed to calibration drift during analysis. Tests on the natural gypsum show no changes in peak positions for 10%, 25% and 50% N.D. filter when using objective lens of ×10 and ×50, and a diffraction grating of 1800 groves per mm over a spectral range of -90 to 4000 cm^{-1}. PoP does show a slight change, of 0.5 cm^{-1}, in U1 peak positions between 3 and 6 minutes total exposure, when using the 25% N.D, and a 0.5 cm^{-1} change in the U2 peak position between 6 and 9 minutes total exposure when using the 50% N.D. filter and a microscope objective of ×50, over a spectral range of -90 to 4000 cm^{-1}. This could be due to a calibration drift during analysis, like the goethite sample, as the change in position is similar to the 0.5 cm^{-1} resolution of the spectrometer.

6.2.4 Thermogravimetric Analysis

An initial experiment to determine the temperature(s) where loss of volatiles would occur within the selected minerals was conducted using thermogravimetric analysis (TGA) and a differential scanning colorimeter (DSC). TGA is a technique that is used to examine

chemical changes induced in a sample when exposed to temperatures (such as dehydration or oxidation). This is achieved by measuring the change in mass of a sample as a function of temperature, making it ideal for examining the dehydration and decomposition of minerals. A DSC measures the amount of energy required to heat a sample to a specific temperature. This analysis provides information on the physical changes, such as melting, the sample experiences as a function of temperature. The machine used at the University of Kent is a Netzsch STA 409 PG/PC, which couples TGA with a DSC, and consequently provides a detailed picture of what happens, both chemically and physically, to a material when it is heated.

Samples were heated to a maximum temperature of 1000 ˚C for goethite and 1500 ˚C (the maximum operating temperature for the TGA/DSC) for both types of gypsum, at a rate of 10 ˚C/min and then cooled back down to room temperature; compressed air was passed through the heating chamber with a flow rate of 60 mL/min at 0.5 bar.

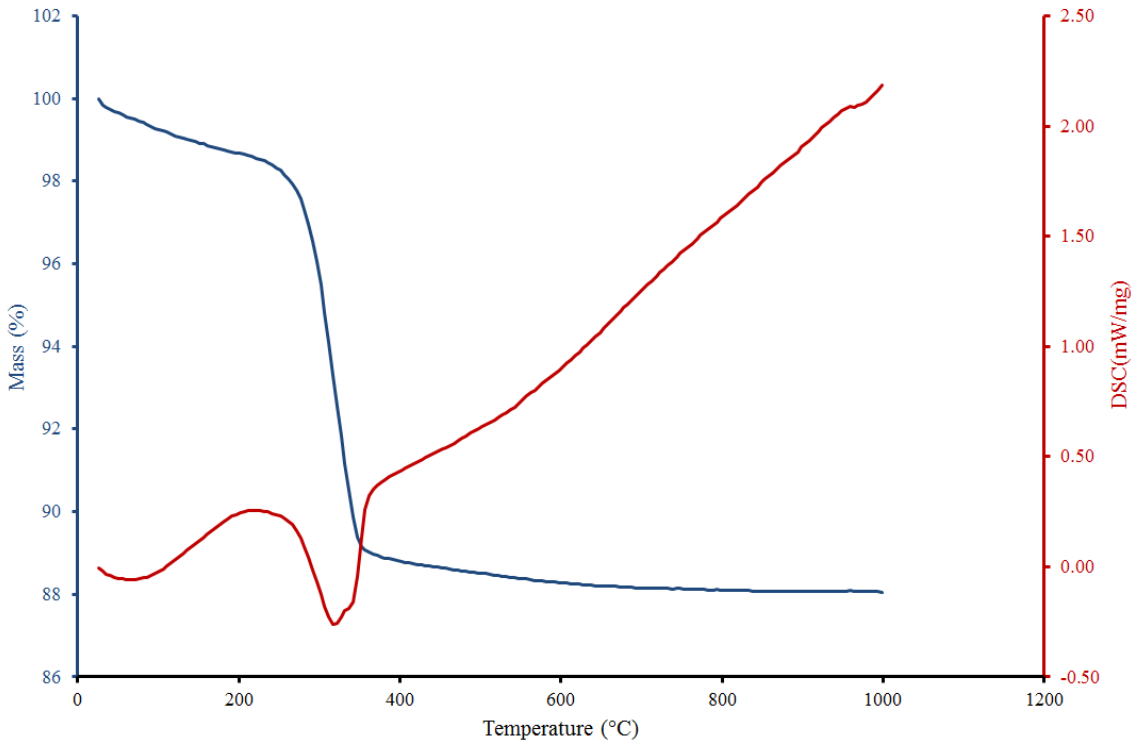

Figure 6.2.4 TGA curve showing the changes in mass (blue) and the DSC (red) as a result of increasing temperature for goethite.

Figure 6.2.4 shows the TGA/DSC curves produced as a result of heating goethite to 1000 ˚C from 25 ˚C. The TGA curve shows a steady loss of mass between 26.0 and 271.8 ˚C, with a mass loss between 0.02 and 0.16 % for each 5 ˚C temperature step. A large decrease of 8.5% in mass occurs between 271.8 and 357.0 ˚C, and then there is a slow mass loss in

the range of 0.00 to 0.05%, between 357.0 and 1000 ˚C. The large change in mass occurs as a result of dehydration. The DSC curve shows a change in the material's physical property begins at 216.6 ˚C, with dehydration starting at a temperature of 271.8 ˚C, which is 21.8 ˚C greater than the temperature of incipient dehydration given by de Faria & Lopes (2007). The DSC curve shows two peaks at 317.0 and 322.0˚C, indicating two physical changes occur as the sample loses OH. Similar tests, using differential thermal analysis, conducted by Gialanella *et al.*, (2010) on a natural and commercial sample of goethite showed DSC peaks at 344 and 324 ˚C, respectively. The temperatures for these peaks are greater that the temperature found in this experiment. Gialanella *et al.*, (2010) also reports a two-step dehydration process for their commercial sample, which has been attributed to the actual composition and microstructure of the sample. SEM EDX analysis of the sample of goethite used here (Appendix B, Table B1) did not show any evidence of any mineral inclusions that may have resulted in this DSC feature. Therefore, it is believed that the sample of goethite being used in these experiments will dehydrate in two stages.

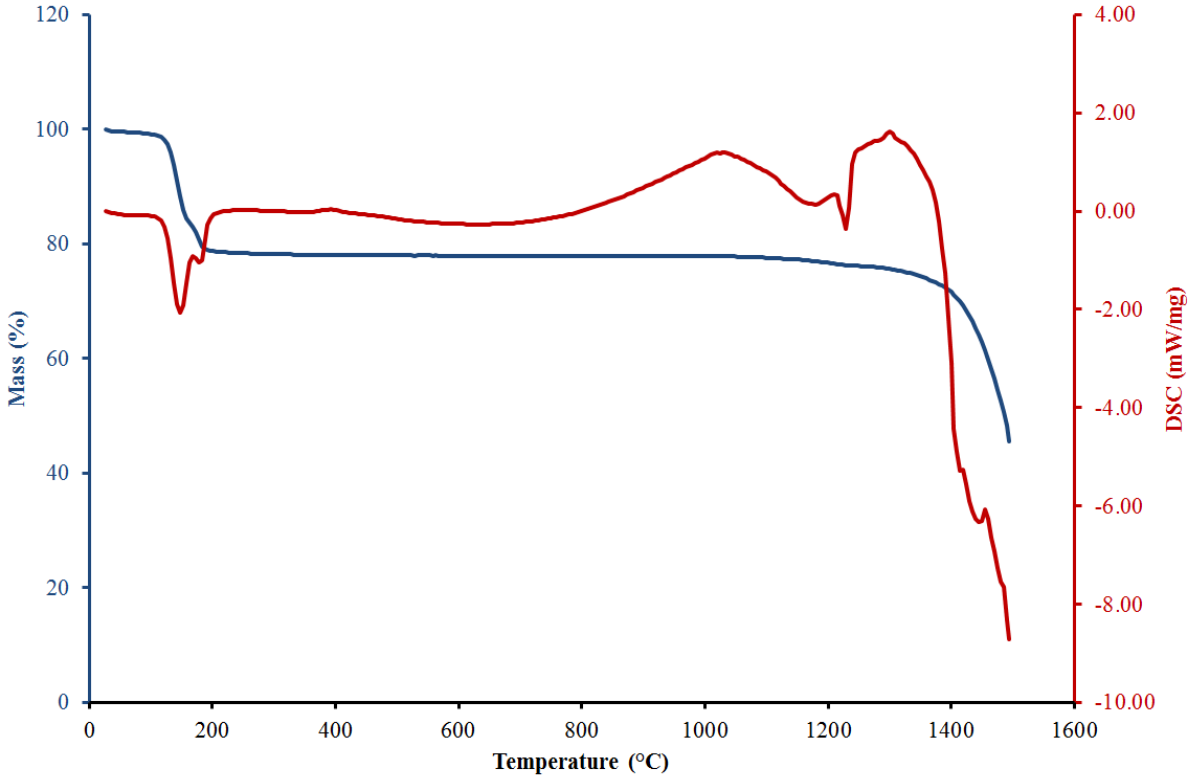

Figure 6.2.5 TGA curve showing the changes in mass (blue) and the DSC (red) as a result of increasing temperature for PoP.

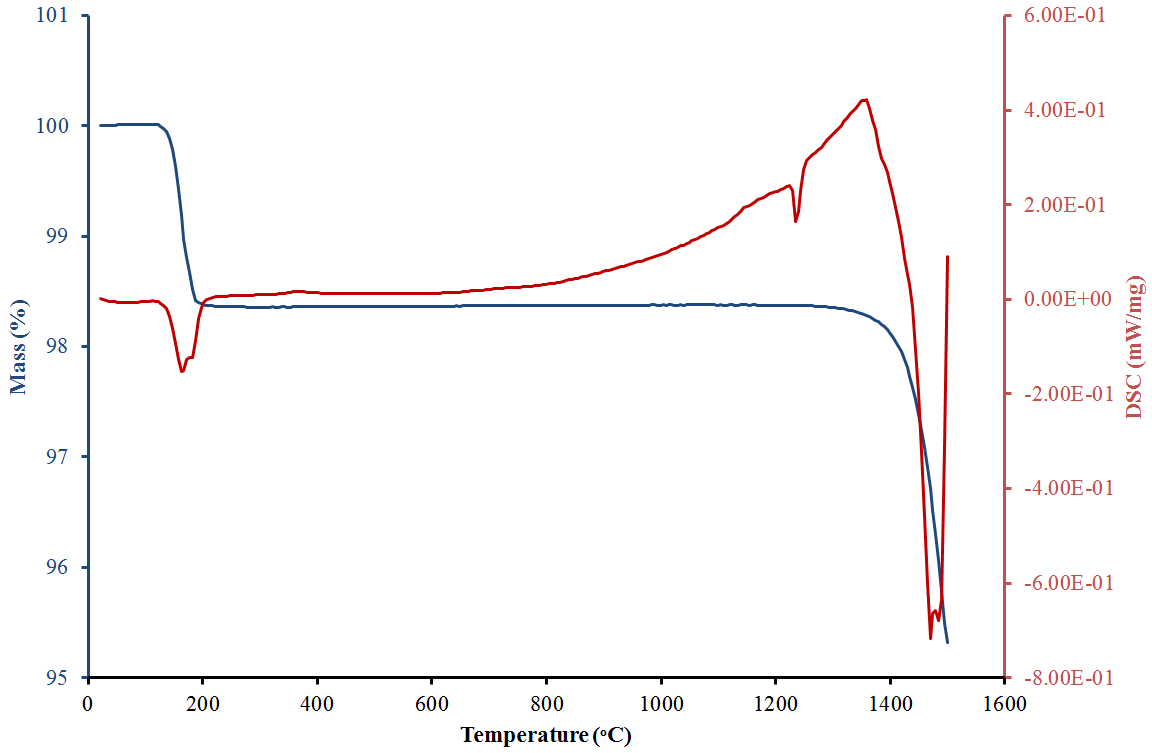

Figure 6.2.6 TGA curve showing the changes in mass (blue) and the DSC (red) as a result of increasing temperature for natural gypsum.

The TGA/DSC curves for PoP and natural gypsum are shown in Figures 6.2.5 and 6.2.6, respectively. The PoP is fine grained, composed of particles sizes < 70 µm, whereas the natural gypsum grains are approximately 100 × 300 µm in size and have a needle like structure (Figure 6.2.7).

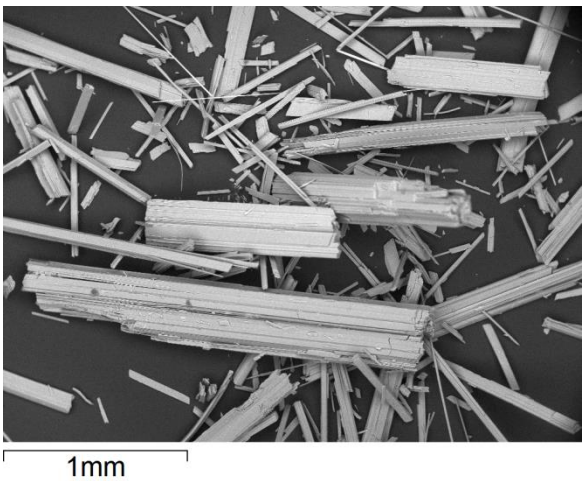

Figure 6.2.7 SEM/BSE image (taken in VP mode at 20 Pa, ×40 magnification and with a 20kV electron beam) of natural gypsum samples used in the devolatilistion experiments.

These differences in size and structure may have caused these samples to behave differently, particularly in terms of changes in physical properties. TGA data for both forms of gypsum shows two instances of mass loss, which occur at temperatures of

112.4 and 1304.3 ˚C for PoP and 127.2 and 1299.2 ˚C for natural gypsum. PoP displays a more gradual loss in mass, of 0.10% or less for each temperature step, between each of the larger mass loss features. Natural gypsum shows almost no variation, with the maximum value of 0.01 %, in mass between these larger mass loss features. The variations seen in PoP could be due to either trace impurities that may be present in the mixture, or due to the fine grain size of the sample. The first mass loss feature is assigned to dehydration, with a total mass loss of 17.81% for PoP and only 1.62% for natural gypsum. This result is interesting as the calculated water mass loss, from the chemical formula, is 20.9% for gypsum and 5.2% for bassanite. PoP losses approximately the expected mass for gypsum. Natural gypsum on the other hand losses considerably less, with a value that resembles the water mass loss expected for bassanite. The DSC curves show two peaks at 167.2 and 182.3 ˚C for natural gypsum and 147.2 and 182.5 ˚C for PoP. The peaks seen in the DSC curve are the result of the dehydration, with the first peak temperature indicating the transformation from gypsum to bassanite, and the second peak indicating the sample changing from bassanite to anhydrite. There is a difference in temperature (of 20 ˚C) for the first mineral transformation, which may be a result of a variation in grain size between the two samples. Although, the temperature required for the second transformation (bassanite to anhydrite) occurs at the same temperature for both samples, seen by the position of second dehydration peak in the DSC curves. The temperatures seen here are 20 to 40 ˚C greater than the temperatures found for the transformation gypsum to bassanite found by Hudson-Lamb *et al.,* (1996). Sirokman (2014) explains that the transformation of gypsum to bassanite occurs at 120 ˚C, which is lower than the temperatures seen in the DSC curve for this analysis, but does correspond to the incipient temperature shown by the TGA curve. However, the transformation of bassanite to anhydrite seen in this analysis corresponds to that presented in Sirokman (2014). The DSC curves also show a melting feature, where there is no change in mass, with a starting temperature of 1033.8 ˚C for PoP and 1219.1 ˚C for natural gypsum. Here the variation in temperature is due to the nature in which the samples melt. The DSC curve for PoP indicates the sample completely melts, from solid to liquid, whereas the curve for the natural gypsum suggests the sample forms liquid-crystals. The final physical change occurs at 1354.3 and 1329.3 ˚C for natural gypsum and PoP, respectively. This final change in the physical property of the samples coincides in with a drop in mass, which indicates devolatilisation, mostly likely the loss of sulphur

(Figure 6.2.8). These temperatures correspond to the decomposition temperature seen by van der Merwe *et al.*, (1999), but are 30 to 55 ˚C greater. However, Miao *et al.*, (2012) explains that the decomposition of gypsum occurs at temperatures over 1350 ˚C in an inert atmosphere and this temperature is reduced to 950-1000 ˚C when in a reducing atmosphere. The decomposition temperature in an inert atmosphere, giving by Miao *et al.*, (2012), is close to the decomposition temperatures seen here when heated in air. Unlike PoP, the natural gypsum sample shows two distinct peaks in the DSC curve, the first at 1469.5 ˚C and the second at 1484.5 ˚C, where the first peak most likely indicates loss of sulphur and the second peak is the loss of Ca (which has a boiling temperature if 1484 ˚C).

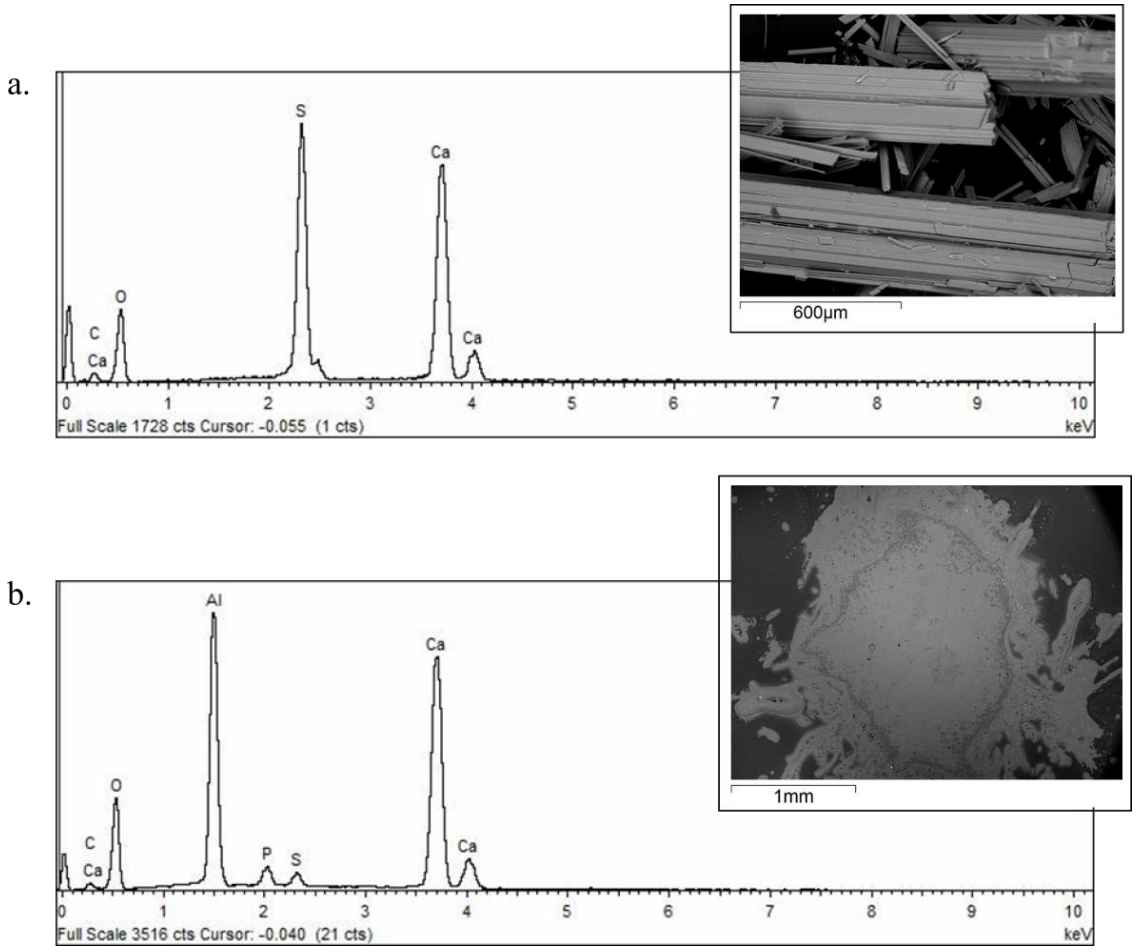

Figure 6.2.8 SEM EDX analysis of natural gypsum heated to 1450 ˚C in the Raman environmental stage. a. EDX spectrum of gypsum before, the insert is a SEM BSE image (taken in VP mode at 20 Pa, ×90 magnification and with a 20kV electron beam) of gypsum crystal not heated. b. EDX spectrum of gypsum residue after heating to 1450 ˚C in the Raman environmental stage. The inserted image is a SEM BSE image of the residues formed after heating (taken in VP mode at 30 Pa, × 40 magnifications and with a 20kV electron beam).

6.3 Heating Experiments

In order to determine how the Raman spectra of these two minerals changes as a result of heating, and potentially quantify the loss of volatiles from their spectra, two heating experiments were conducted. The first heating experiment was in situ, using one of the two environmental stages for the Raman spectrometer (referred to as in-situ), which is able to reach a temperature of 1500 ˚C. In the second experiment samples were heated in an *Elite* furnace with Raman spectra and measurements of mass taken after each heating cycle, to quantify the loss of volatiles from the mineral (and is referred to as ex-situ from here on).

A sample of the mineral was ground into coarse grains (~ 100 × 300 μm) using a pestle and mortar and washed with water for use in in-situ heating experiments. In-situ heating experiments heated the mineral samples in the spectrometer to a maximum temperature of 1200 ˚C and 1450 ˚C for the goethite and gypsum respectively. The samples were heated to the desired temperature and held at that temperature for 10 minutes, and then cooled back down to a temperature below 30 ˚C before a spectrum was taken. A Raman spectrum for each temperature was taken from the same position (or close as to as possible) on the mineral grain to ensure any heterogeneity in the sample did not affect the data. Ex-situ heating experiment samples were heated to the required temperature in an *Elite* furnace, held for 10 minutes and then allowed to cool to room temperature before measuring their weight and taking Raman spectra. However, unlike the Raman heating experiment, ten Raman spectra from different spots on the sample were taken, as the samples were larger (measuring 2.44 × 2.20 × 6.06 mm and 5.00 × 1.81 × 3.16 mm for the gypsum and goethite samples, respectively).

6.4 Impact Experiments

In a similar fashion to the serpentinisation experiment (described in Chapter V) this set of experiments had two experimental setups. Setup 1 used the minerals as the projectile material and the setup 2 used mineral samples as the target.

6.4.1 Target and Projectile Making

Mineral Projectiles

Mineral projectiles were shaped into a cuboid approximately 1.5 × 1.5 × 2.0 mm (Figure 6.4.1 shows an example of a mineral projectile). Goethite projectiles were made from pieces of the original nodule, which were cut using a Dremel diamond wheel cutter. Natural gypsum and anhydrite projectiles were made from the same gypsum crystal. Goethite projectiles were shaped using a diamond file and both forms of gypsum (which are softer than goethite) were shaped using a file, sand paper and a scalpel. The anhydrite projectile was made from the dehydration of gypsum where the sample was heated at 400 ˚C for two hours, and was confirmed as anhydrite using Raman spectroscopy. Shaping of the projectiles needed to be done carefully as fracturing along crystal boundaries would result in the projectile breaking before the required size was achieved. Once the projectiles had been shaped into the desired dimensions, they were gently washed with water to remove any fine grained mineral particles. This last step was conducted as the shaping process may have generated fine grained particles with a lower volatile content (particularly water), which could potentially affect the Raman spectra taken of the projectile before impact.

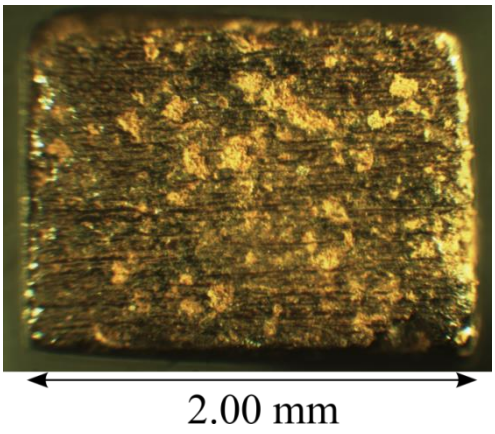

Figure 6.4.1 An example of a cuboidal projectile (2.00 × 1.54 × 1.54 mm) used for shot I.D. G061113#2.

Mineral Targets

The goethite target was made by embedding the remainder of the goethite nodule in epoxy resin using a mould 50 mm in diameter. The sample was then polished flat using sand paper (400, 1200 and 1500 grit) and alumina polish. A Raman map was taken of small areas of the sample to provide an average spectrum before the impact experiment.

Solid blocks of PoP were used for gypsum targets. These were made using a 2:1 ratio of PoP powder to R.O. water and set into a mould, before being left to dry in air for six days. Leaving the sample to dry in air meant any excess water in the sample was removed, which was determined in exploratory tests (described previously), before being impacted.

6.4.2 Experimental Setup

Mineral Projectiles

Mineral projectiles were fired onto aluminium plates at velocities between 1 and 6 km s^{-1}. Goethite projectiles used multiple target plates in an attempt to maximise the amount of residue obtained from each impact. Both PoP and natural gypsum projectiles only required a single aluminium alloy plate target plate, as they are softer minerals than the goethite. Target plates were mounted horizontally onto the target chamber door, 90˚ to the axis of the projectile's path.

Mineral Targets

Goethite and PoP targets were mounted horizontally on the target chamber door, again, at a 90˚ angle to the axis of the projectile's path. Aluminium foil was placed on the floor of the chamber to collect any ejected material from the targets.

6.5 Analysis Techniques

Analysis of Raman spectra obtained from both heating and impact experiments focused on the changes of peak positions and peak widths of both types of minerals and the intensity of selected peaks. These data were obtained using baseline correction and peak fitting functions available in *LabSpec* 5 (Horiba LabRam-HR) software.

Results from goethite specifically examined changes in positions of Feature A, found between 380 and 415 cm^{-1} Raman shift, and the formation of Feature B as the mineral changes from goethite to hematite (Figure 6.5.1). In addition, analysis examined the evolution of these features as a result of increased temperature alone as well as any changes due to impact.

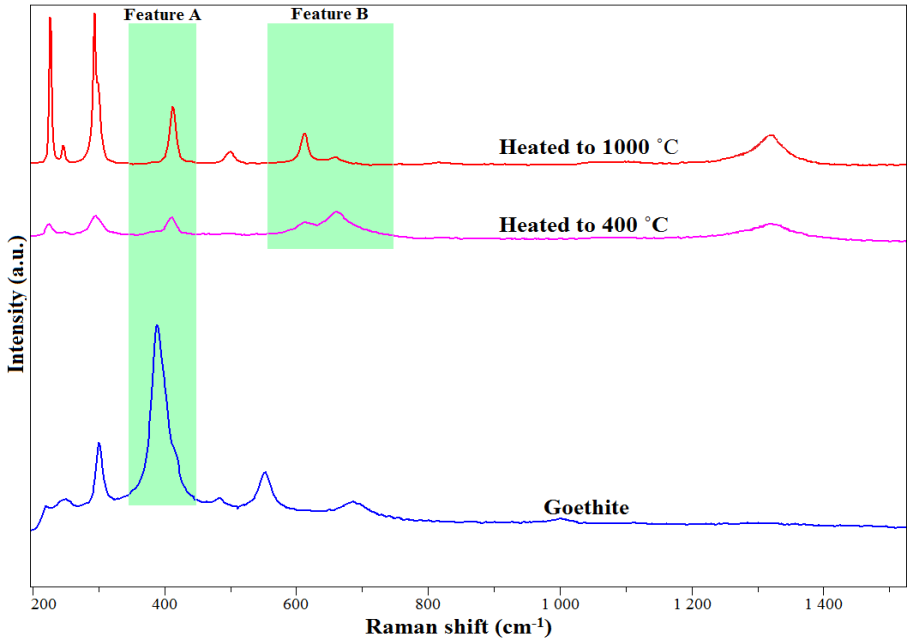

Figure 6.5.1 Raman spectra for the sample of goethite (blue) at room temperature, heated to 400 °C (pink) and 1000 °C (red), with Feature A and Feature B highlighted in green regions. Spectra have been offset for clarity.

Analysis of gypsum examined the changes from gypsum to bassanite to anhydrite. The peaks that were examined in detail were those that belonged to SO_4 ʊ3 and ʊ4 bonds (Figure 6.5.2), which appear to be stronger in Raman spectra and will also be affected when sulphur is lost at 1400 ˚C. The main product that could be indirectly detected as a result of gypsum, bassanite and anhydrite decomposition is CaO (Bell, 2010). However, CaO may not remain in the oxide form for long and will most likely combine with CO_2 to form $CaCO_3$.

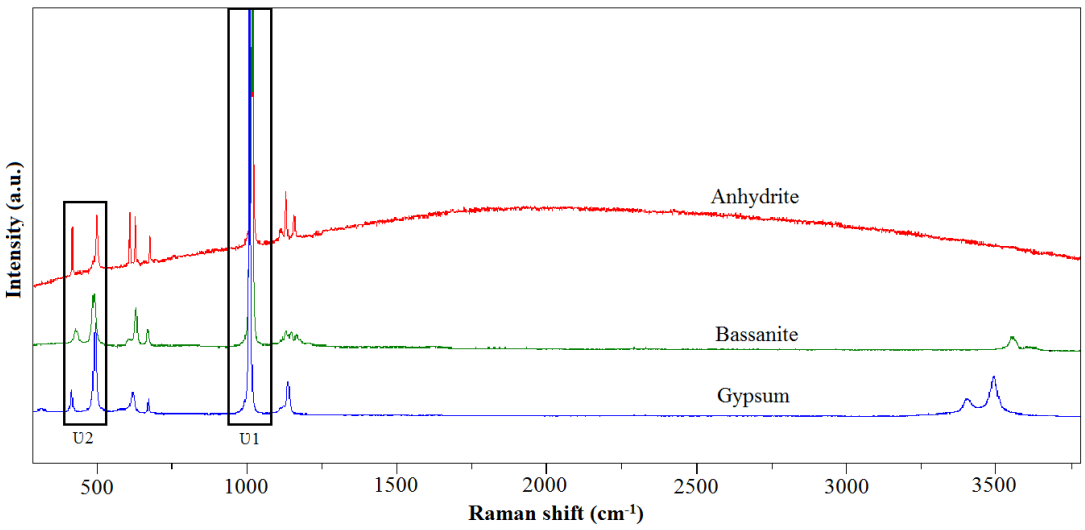

Figure 6.5.2 Raman spectra of gypsum (blue), bassanite (green) and anhydrite (red), with the specific features highlight by black boxes. Spectra have been offset for clarity.

6.6 Chapter Summary

The exploratory tests conducted here ensure the methods used in preparing the samples, for both heating and impact experiments, will not affect the overall results. It also shows Raman spectroscopy (which is the primary tool for analysis) will not result in dehydration of the samples, and thus will not have an effect on the results. This chapter also explains how both heating and impact experiments and the subsequent analyses were conducted. The results from the heating experiments and impacts experiments are presented and discussed in Chapters VII and VIII, respectively.

Chapter VII

Results and Analysis: Heating Experiments

A database of Raman spectra at a range of temperatures was gathered to assist in determining the maximum temperatures reached during an impact for both goethite and gypsum. In doing this it was possible to determine the temperatures at which volatiles were lost and changes in mineral crystallinity occurred. In addition, it would also assist in potentially quantifying the degree of devolatilisation.

Heating experiments (described in Chapter VI, Section 6.2) were conducted to determine how the Raman spectra of goethite and gypsum changed as a result of increasing temperature. Mineral samples were heated to a target temperature, held at that temperature and then allowed to cool before taking Raman spectra, for both in-situ and ex-situ experiments.

Analysis of the Raman spectra was carried out by observing changes in peak positions, peak widths and, in the instance of Feature B in the goethite experiments, the peak intensity. These parameters were determined using a curve fitting function available in the *Labspec* 5 software (used on the Horiba LabRam-HR spectrometer), which provides a more consistent and unbiased determination of peak positions. An automated fitting function is also able to deconvolute features made up of multiple peaks, such as Feature B from the goethite experiments.

Analysis of Raman spectra first required baseline corrections to be conducted, which ensured the baseline was flat and approximately at zero. This step assured the peak heights and peak widths were correct, and did not incorporate background noise or florescence, which could affect the peak intensity values, and enabled more accurate fitting profiles for peaks with an intensity of 50 counts or less. A test was carried out fitting curves to spectra using a baseline correction of 2^{nd}, 4^{th}, 6^{th} and 8^{th} degree polynomials (Appendix D). This showed that broad curves are incorrectly fitted to lower intensity peaks

where no baseline correction or low degree polynomials are used. Therefore, an 8^{th} degree polynomial was fitted to the raw baseline to achieve a baseline of zero, or as close as possible to zero.

Labspec 5 includes three curve fitting functions: Gaussian, Lorentzian and Gaussian-Lorentzian. Meier (2005) states Lorentzian profiles are the profiles generated by Raman vibration bands, but the peak position, width and amplitude are consistent between the three fitting functions. However, visual examination of how each of the three fitting functions fit reveals the model profile generated by the Gaussian-Lorentzian function provides a closer match to the spectra, and therefore the Gaussian-Lorentzian function was used throughout.

7.1 Goethite

Raman analysis of the transition from goethite to hematite was focused on two features called Feature A (found between 380 and 415 cm^{-1}) and Feature B (a two peaks feature found at ~ 615 and 660 cm^{-1} when the sample turns into hematite), as described in Chapter VI. Each spectrum was also qualitatively classified as "goethite-like", "hematite-like" or "intermediate", depending on the peaks present in the spectrum. The third classification, intermediate, described instances where spectra exhibited peaks from both goethite and hematite.

Raman spectra were taken using a 633 nm laser (as it provided a good spectrum with low fluorescence) and the 10 % N.D. filter, resulting in a power of 0.18 mW reaching the sample. A single Raman spectrum was taken for in-situ measurements and ten spectra were taken for ex-situ measurements.

7.1.1 In-situ Raman Heating Experiment

Raman spectra of goethite were taken after heating to the required temperature at a rate of 50 ˚C per minute, holding for 10 minutes and cooling back down to below 30 °C. All spectra were taken using a 633 nm laser, with 10% of the total available laser power, a grating with 1800 g/mm and a ×10 microscope objective. This experiment was conducted over three days, so a new spectrum was taken at the start of each new day (after calibration), which resulted in two sets of measurements at 350 and 800 ˚C.

Results taken from this heating experiment shows the spectrum begins to resemble a more hematite pattern after being heated to 275 ˚C, with the appearance of Feature B and the complete loss of all but one of the Fe-OH peaks. At this temperature (275 ˚C) Feature B appears as a very low intensity feature that could be mistaken for background noise. Up to 250 ˚C there is some fluctuation in peak positions of approximately two wavenumbers. This fluctuation could be a result of the way in which peaks are fitted. Table 7.1.1 shows the peak positions, amplitude and widths (taken at full width half maxima; FWHM) for Feature A, and the two peaks that make up Feature B.

Table 7.1.1 Goethite Raman data for the in-situ heating experiment peak.

		Feature A		**Feature B**					
Temperature (˚C)					Peak 1			Peak 2	
		Position (cm^{-1})	Width (cm^{-1})	Position (cm^{-1})	Width (cm^{-1})	Intensity (counts)	Position (cm^{-1})	Width (cm^{-1})	Intensity (counts)
	22	389.8	21.2	-	-	-	-	-	-
	100	387.8	18.0	-	-	-	-	-	-
	200	389.1	21.2	-	-	-	-	-	-
	225	387.8	18.6	-	-	-	-	-	-
	250	389.1	21.1	-	-	-	-	-	-
	275	395.2	26.9	613.2	31.0	9.7	657.2	49.8	15.8
	300	408.6	18.5	616.0	62.2	18.2	663.0	65.1	27.2
	325	410.9	14.7	617.5	43.4	16.8	662.7	47.9	27.8
Day 1	350	409.3	17.9	616.0	31.0	18.8	662.4	49.7	28.5
Day 2	350	410.5	15.3	616.9	41.5	19.1	665.5	51.8	30.4
	375	409.3	28.7	615.7	30.4	14.6	662.4	37.4	28.0
	400	408.6	18.5	612.6	29.1	22.3	663.3	50.3	38.7
	500	411.5	14.7	616.0	33.5	24.3	662.4	42.3	43.2
	600	412.8	11.5	613.2	29.1	27.9	660.3	44.2	38.8
	700	412.1	12.8	615.4	29.7	29.8	660.3	48.2	29.6
Day 2	800	410.2	14.7	613.2	26.0	33.2	661.5	41.5	28.1
Day 3	800	409.7	12.1	611.9	24.2	32.6	656.9	52.5	25.7
	900	410.9	12.8	611.3	15.5	36.6	626.9	43.4	22.8
	1000	412.2	10.8	612.2	15.5	50.9	660.6	31.2	23.4
	1100	412.2	10.8	613.5	13.0	60.6	661.8	23.8	18.9

N.B. The days indicate the day of the experiment. For each new day a measurement was taken before the new heating cycle began.
All Raman spectra were obtained using a 633 nm laser, 10% N.D. filter, × 10 microscope objective and 1800 g/mm grating.

The Raman spectra show a complete transformation from goethite to hematite occurs between 275 and 300 ˚C. It is believed incipient transformation occurs between 250 and 275 ˚C, as spectra taken after heating to 275 ˚C shows peaks of both goethite and hematite.

Feature A Analysis

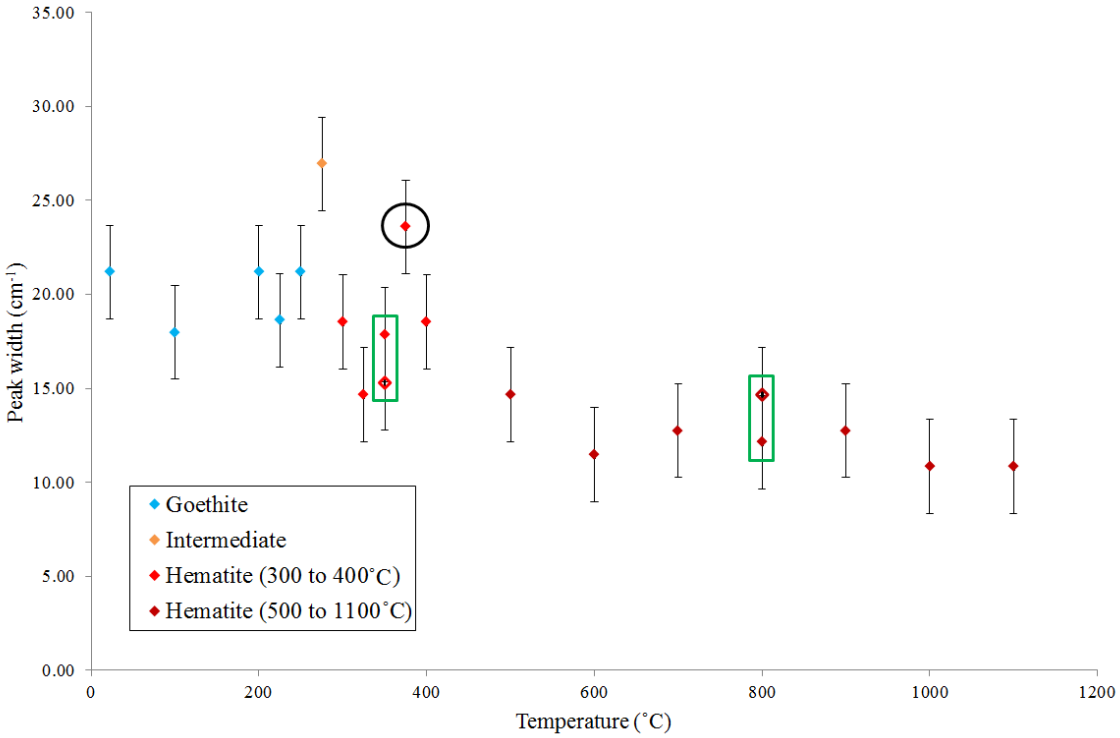

Figure 7.1.1 Peak widths (taken at FWHM) of Feature A against temperature. The point indicated by the black circle indicates an unexpected value recorded at 375 ˚C and values in the green boxes highlight the temperatures where two spectra were taken. Error bars represent the maximum difference in peak width for spectra taken at the same temperature.

The peak widths of Feature A show there is a general trend of peak widths decreasing with temperature (Figure 7.1.1). The reduction in width after 300 ˚C is believed to be related to the sample becoming more crystalline; between 22 and 250 ˚C there is a fluctuation in the width, with values between 18.0 and 21.2 cm^{-1}. The maximum peak width occurs at 275 ˚C, which is also the peak that has been classified as intermediate. Feature A is composed of two individual peaks, a Fe-OH peak at ~ 388 cm^{-1} and a Fe-O peak at ~ 410 cm^{-1}. However, the two peaks appear as a single peak with a shoulder (which in some spectra can resemble a single peak). This appearance of a single peak is most likely caused by a combination of the two peaks being relatively close to each other (22 wavenumbers) and background fluorescence. The apparent changes in peak position for this feature is a result of changes in the dominant peak as water is lost; for a goethite spectrum the Fe-OH peak is dominant and in a hematite spectrum the Fe-O peak is dominant, producing an overall increase in peak position (Appendix E explains this in more detail). An intermediate spectrum with a broad Feature A, such as the spectrum for 275 ˚C, occurs at a point where

both peaks are of similar intensities. Figure 7.1.2 confirms this, as there are two regions of dominant peak positions for Feature A: 388 ±1 cm^{-1} and 410 ±2 cm^{-1}, with an intermediate peak position of 395 cm^{-1} at 275 ˚C. An unexpectedly broad peak occurs a 375 ˚C, it is unclear why this peak is so broad. The peak widths for spectra taken on different days show a peak width 2.5 cm^{-1} lower than those taken the day before, which could indicate the sample was still warm when the spectra was taken after heating. However, the peak positions of spectra taken for temperatures that crossover two days show varied results. Increasing temperatures produce a decrease in peak position (Hibbert *et al.*, 2015a), which would explain the increase in peak position 350 ˚C (from day one to day two). However, spectra taken at 800 ˚C, shows a decrease in peak position of 0.5 cm^{-1} (between the day 2 and day 3), which is the opposite of what would be expected if the sample was warmer on the day 2. This indicates that the variation in peak widths is not due to the sample not having cooled down. It might be a result of the sample shifting slightly over the two days when the spectrometer was being calibrated, regardless of the best efforts made to keep the sample in the same position.

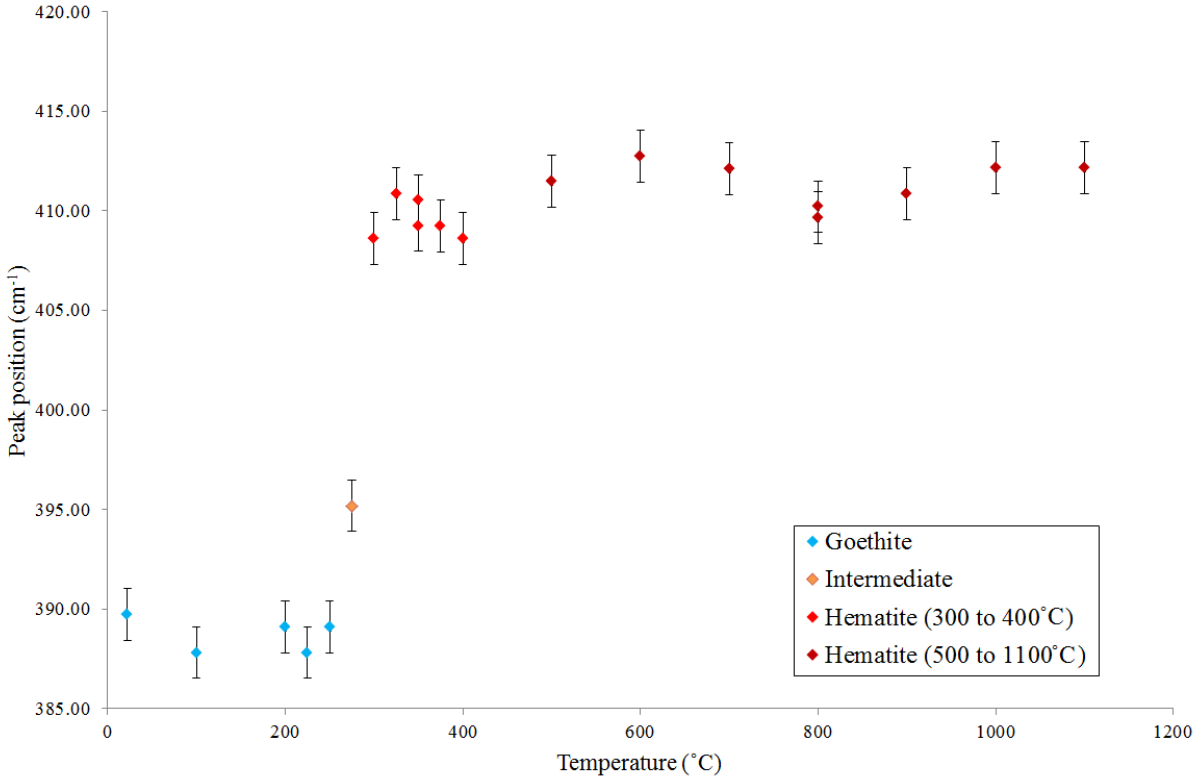

Figure 7.1.2 Feature A peak positions taken after the sample was heated to the indicated temperature. Error bars show the maximum difference in peak position for spectra taken at the same temperature.

Feature B Analysis

Feature B appears in spectra at 275 ˚C, but has a very low intensity and could be mistaken as noise. It is not until 300 ˚C that this feature appears as two peaks, and at 600 ˚C they appear as almost individual peaks (Figure 7.1.3).

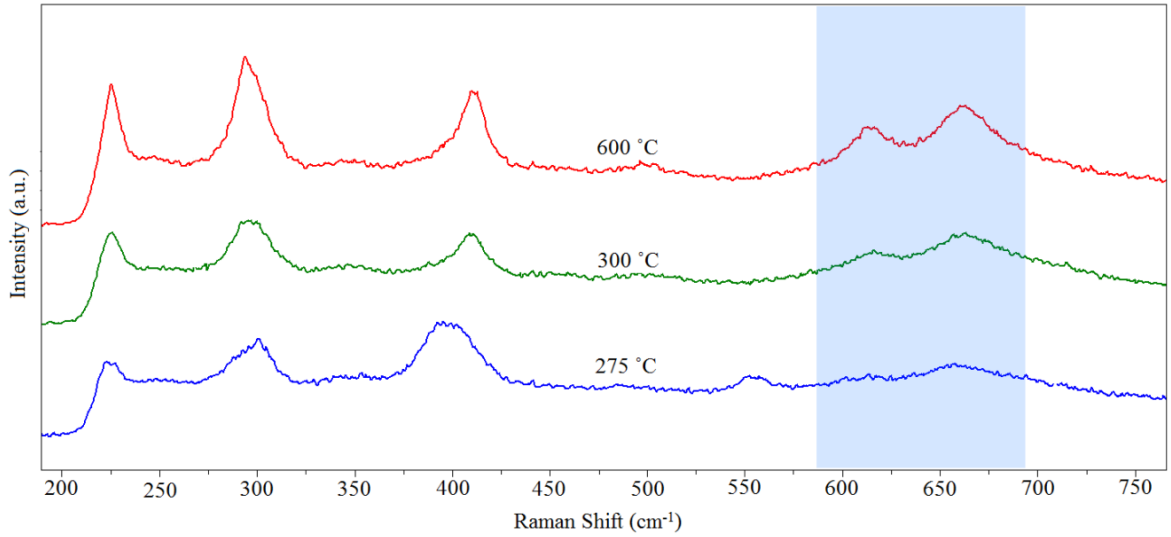

Figure 7.1.3 Raman spectra taken from in-situ heating experiment showing the changes described in text. The pale blue box highlights Feature B and spectra have been offset for clarity.

The peak positions for both peaks are relatively constant between 500 and 1100 ˚C, with a variation of ~5 wavenumbers for both peaks (Figure 7.1.4). There is a greater difference in peak positions in the temperature range 275 to 400 ˚C, of 5 wavenumbers for peak 1 and 8 wavenumbers for peak 2. This could be a result of the combination of the relatively low intensity of these peaks and noise, making it difficult for the curve fitting function to accurately identify them, or there is a genuine shift in peak position with temperature.

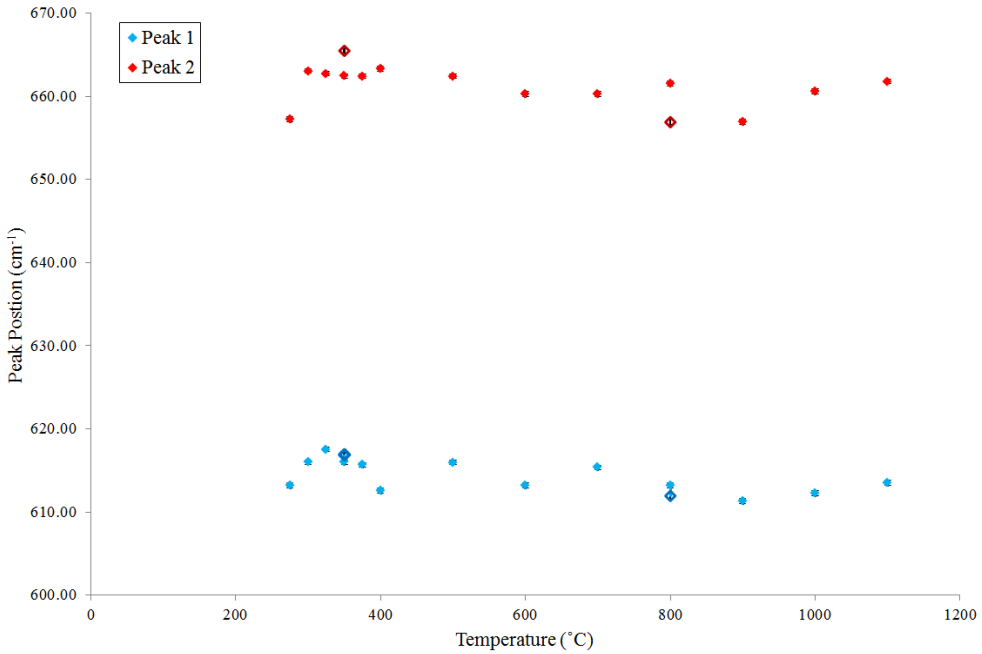

Figure 7.1.4 Peak position for peaks 1(blue) and 2 (red) of Feature B from goethite in-situ heating experiments. Error bars represent the spectral resolution for the configuration of the Raman spectrometer (0.3 cm^{-1}), which is smaller than the size of the data marker.

Figure 7.1.5 shows the ratio of the peak width and intensity for Feature B and shows a change with increasing temperature. Peak 2's intensity is greater than peak 1 between 275 and 600 ˚C and both peaks have the same intensity at 700 ˚C, after which peak 1 has the greater intensity. This trend for the increasing intensity of peak 1 with temperature begins at 500 ˚C. Absolute intensity values for peak 1 (Table 7.1.1) shows there is an increase with temperature, from 10 to 61 counts at 275 and 1100 ˚C, respectively. Peak width ratios between 325 and 375 ˚C between peak 1 and peak 2 do not show any clear relationship, but the two peaks do appear to have approximately the same widths. The absolute peak width values (Figure 7.1.6) do show there is an overall decrease in width with increasing temperature after 800 ˚C for peak 2, and after 500 ˚C for peak 1. After 500 ˚C peak 2 increases in peak width before becoming narrower after 800 ˚C. The increase in peak intensity, particularly for peak 1, and decrease in peak width shows the sample is becoming more crystalline with temperature.

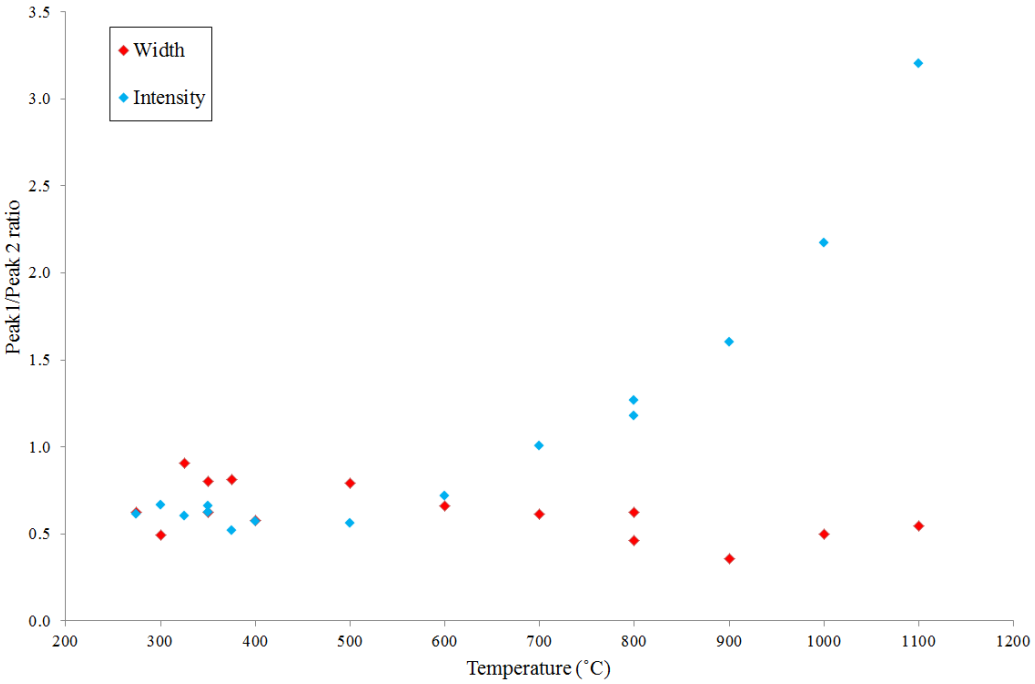

Figure 7.1.5 Peak width (red) and intensity (blue) ratios for Feature B peaks from the goethite in-situ experiment.

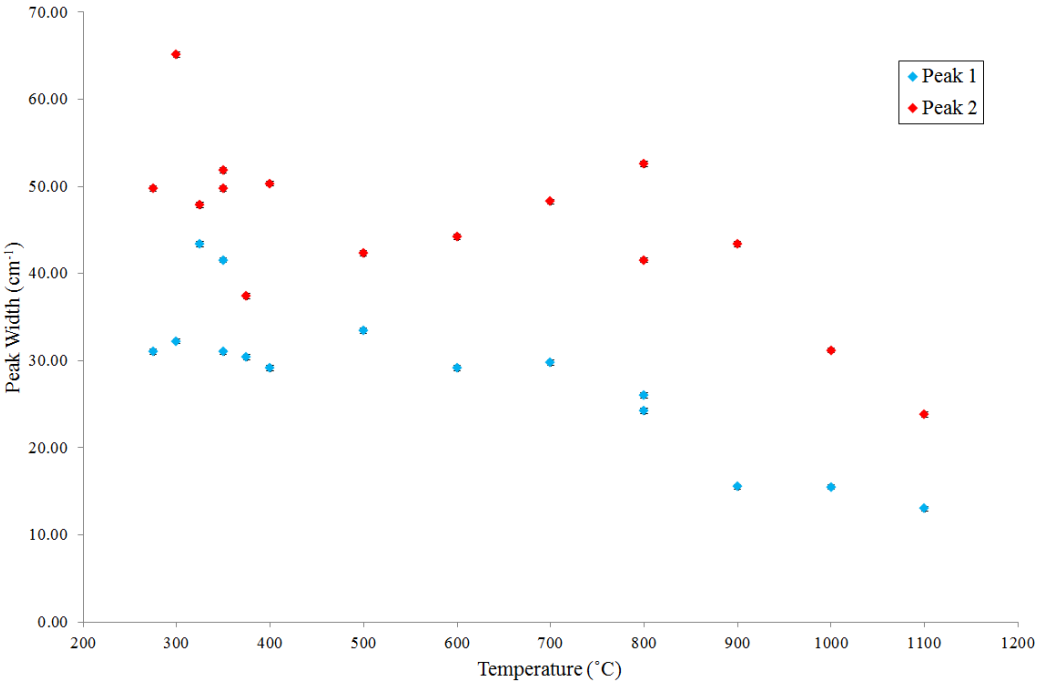

Figure 7.1.6 Peak widths for Feature B peak 1 (blue) and peak 2 (red) from the goethite in-situ experiment. Error bars represent the spectral resolution for the configuration of the Raman spectrometer (0.3 cm^{-1}), which is smaller than the size of the data marker.

As with Feature A, there is some variability in peak width for temperatures that crosses over two days. However, unlike Feature A there is not a consistent decrease in peak width

from the first day to the second day. This indicates that the variation between widths may not be due to the sample being warm when the spectrum taken. Instead the variation in peak widths might be a result of the sample moving slightly, most likely when calibration was conducted on the morning of the new day.

7.1.2 Ex-situ Raman/Mass Loss Experiment

A sample of goethite, 5.00 × 1.81 × 3.16 mm, was heated in an *Elite* furnace and weighed to determine mass loss as a result of heating. In addition to weighing the sample, Raman spectra was also taken after heating. The sample was heated to the target temperature at a rate of 5 ˚C per minute, held for 10 minutes, and then allowed to cool.

Mass Measurements

Table 7.1.2 shows the absolute weight, change in mass and percentage mass change taken at the temperature the sample was heated to. The cumulative mass change values show a considerable change in mass occurs between 330 and 340 ˚C, until that point there is only a slight change between -0.1847 and +0.0661 %. Considerable changes in mass stops after 700 ˚C and then from 800 ˚C values of <0.2500 % in mass loss occurs.

After taking a mass measurement at 400 ˚C a small piece of the sample broke off, and the main sample was weighed immediately. The new reading was used as the before measurement and used to determine the mass loss from the sample for temperatures at 500 ˚C and above. The total mass loss, in percent, for values for 500 ˚C and greater should not be considered as exact values. The difference in mass (0.0106 mg) between the measurements taken before and after the sample broke was added to the total mass loss values from 500 ˚C onwards. This was done to account for the fragment that had come away from the main sample and to relate it to the starting mass. The values for change in mass as a percentage were determined by subtracting the difference in mass, also in percent, between the reading taken at 400 ˚C and the new reading (taken after the sample broke), which produced a value of 0.0139 % of mass loss from the original mass. This value was then later subtracted from the values taken from 500 ˚C onwards. Therefore, the values from 500 to 1200 ˚C do not account for the mass lost from heating the piece of goethite that broke off, meaning the values should be slightly lower for the total change in mass in mg and higher for the total change in mass as a percentage.

Table 7.1.2 Goethite Ex-situ Raman/mass loss experiment

Temperature (˚C)	Weight (mg)	Total change in mass (mg)	Total change in mass (%)
22	76.3915	0.0000	0.0000
100	76.2504	-0.1411	-0.1847
110	76.2420	-0.1495	-0.1957
120	76.2925	-0.0990	-0.1296
130	76.2908	-0.1007	-0.1318
140	76.2463	-0.1452	-0.1901
150	76.2661	-0.1254	-0.1642
160	76.2153	-0.1762	-0.2307
170	76.1746	-0.2169	-0.2839
180	76.1567	-0.2348	-0.3074
190	76.2002	-0.1913	-0.2504
200	76.1444	-0.2471	-0.3235
210	76.1483	-0.2432	-0.3184
220	76.0984	-0.2931	-0.3837
230	76.1192	-0.2723	-0.3565
240	76.0731	-0.3184	-0.4168
250	76.0794	-0.3121	-0.4086
260	76.0244	-0.3671	-0.4806
270	76.0254	-0.3661	-0.4792
280	75.9697	-0.4218	-0.5522
290	75.9792	-0.4123	-0.5397
300	75.9068	-0.4847	-0.6345
310	75.9055	-0.4860	-0.6362
320	75.8282	-0.5633	-0.7374
330	75.8001	-0.5914	-0.7742
340	75.5452	-0.8463	-1.1078
350	75.2459	-1.1456	-1.4996
360	73.7376	-2.6539	-3.4741
370	73.5416	-2.8499	-3.7307
380	71.4686	-4.9229	-6.4443
390	69.7138	-6.6777	-8.7414
400	69.8297	-6.5618	-8.5897
500*	69.3027	-7.0676	-9.2657
600	68.4143	-7.9560	-10.4286
700	67.3332	-9.0371	-11.8438
800	67.1477	-9.2226	-12.0867
900	66.9730	-9.3973	-12.3154
1000	66.8065	-9.5638	-12.5333
1100	66.7835	-9.5868	-12.5634
1200	66.7610	-9.6093	-12.5929

*After taken the mass reading for 400 ˚C a piece broke off, a new mass reading of 69.8191 mg was taken and used.

N.B. Weight measurements in red indicate instances where the balance did not settle to provide a single reading. In these cases readings were taken after 3 minutes. Values in purple are the calculated values, which take into account the mass lost from the broken fragment.

Figure 7.1.7 shows the change in mass in-between each heating cycle. The errors on the values at temperatures at 340 ˚C and above are 2.7354 % and 2.7493 % (after the sample

broke) as the balance would not stabilise from 340 ˚C onwards, so measurements were taken after three minutes. The instability of the balance here could indicate that water adsorption (from the atmosphere) may have been occurring; it could also be possible that water was completely lost from only part of the sample, resulting in spectra being taken for a partially hydrated sample. The errors for these temperatures were determined by allowing the mass measurement to stabilise and determining the difference between this value and that taken after three minutes. The mass measurements show that there is an overall gradual loss in weight, ranging between 0.0013 to 0.1012 %, when heating the sample up to 330 ˚C. Between 340 and 700 ˚C greater mass loss between 0.3337 and 2.7137 % occurs, after 700 ˚C the mass loss ranges between 0.0295 and 0.2428 %. This pattern of mass loss resembles the trend shown in the TGA analysis (see Chapter VI, Section 6.1.4) where there was a small and gradual decrease in mass until dehydration ensued at 271.8 ˚C and smaller changes in mass occurred from 357.0 ˚C until 1000 ˚C. The mass loss after heating to 700 ˚C is still relatively high, at 0.8294 %, considering the sample should have lost all OH well below this temperature. Mass measurements suggest water loss occurs between 330 and 340 ˚C with a large change in mass of 0.3337%. Incipient mass loss occurs between 290 and 300 ˚C, which is evident through an increase in mass loss of 0.0948 %, until that point the greatest change in mass was 0.0730 %.

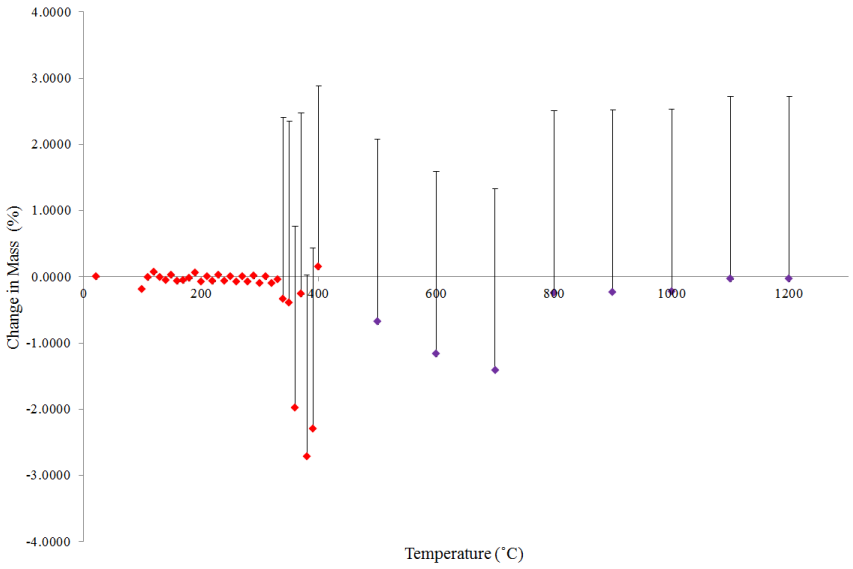

Figure 7.1.7 The graph shows the change in mass (in %) between each of the heating cycles, with the purple points indicating the values taken after a fragment broke off from the main sample. The value for 500 ˚C was determined using the new mass taken immediately after the fragment fell away. The positive values represent an increase in mass and negative values the loss of mass. The error for the balance is 0.0087% which falls within the size of the markers. The errors calculated for measurements from 340 ˚C onwards are described in the text.

Table 7.1.3 Mass loss and average peak position for Feature A and Feature B

Temperature (˚C)	Total change in weight (%)	Feature A Peak position (cm^{-1})	Feature B Peak positions (cm^{-1})	
			Peak 1	Peak 2
22	0.0000	390.9	-	686.1
100	-0.1847	388.3	-	685.4
110	-0.1957	386.5	-	682.3
120	-0.1296	389.8	-	686.4
130	-0.1318	388.7	-	685.3
140	-0.1901	389.0	-	686.1
150	-0.1642	388.8	-	684.6
160	-0.2307	390.1	-	686.8
170	-0.2839	389.1	-	686.6
180	-0.3074	388.7	-	685.6
190	-0.2504	388.8	-	684.2
200	-0.3235	388.6	-	684.2
210	-0.3184	388.8	-	686.5
220	-0.3837	390.0	-	686.7
230	-0.3565	388.6	-	684.9
240	-0.4168	389.0	-	686.2
250	-0.4086	389.8	-	688.9
260	-0.4806	389.2	-	685.9
270	-0.4792	388.6	-	685.4
280	-0.5522	388.8	-	684.7
290	-0.5397	388.9	-	687.4
300	-0.6345	389.1	-	681.0
310	-0.6362	389.1	-	682.1
320	-0.7374	392.5	610.8	667.3
330	-0.7742	391.9	618.4	667.4
340	-1.1078	403.7	615.9	662.2
350	-1.4996	407.8	614.9	660.9
360	-3.4741	407.2	615.2	661.1
370	-3.7307	408.6	614.9	661.9
380	-6.4443	408.0	615.5	661.6
390	-8.7414	407.7	615.9	661.6
400	-8.5897	407.9	615.7	661.8
500	-9.2657	409.3	614.9	661.8
600	-10.4286	409.37	614.1	661.3
700	-11.8438	409.5	611.4	658.7
800	-12.0867	410.3	611.8	659.0
900	-12.3154	411.2	611.9	659.2
1000	-12.5333	412.0	612.7	659.7
1100	-12.5634	411.9	612.7	659.4
1200	-12.5929	412.2	613.0	660.0

N.B. Values in purple are the calculated values, which take into account the mass lost from the broken fragment.

All Raman spectra were obtained using a 633 nm laser, 10% N.D. filter, × 50 microscope objective and a 2 second exposure time with 15 accumulations.

Feature A Analysis

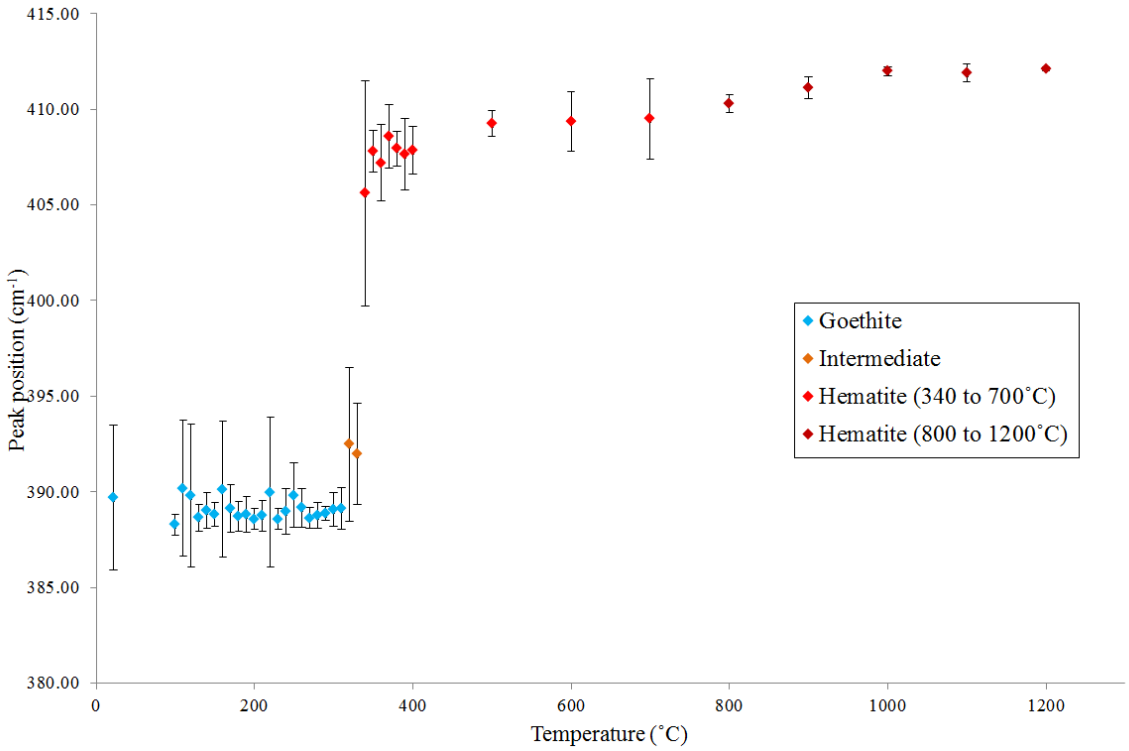

Figure 7.1.8 The averaged peak position for Feature A with increasing temperature. Blue data points show temperatures that had a higher number of goethite spectra, orange indicates a higher number of intermediate spectra and red shows temperatures with a greater number of spectra classified as hematite. The standard deviation for each temperature (from the absolute data) was calculated to generate the error bars.

Raman spectra show the complete change from goethite to hematite, for all spectra, occurred after heating the sample to 350 ˚C. It also suggests incipient mass loss occurs after heating to 310 ˚C, as there are multiple spectra classified as intermediate and they continuously appear with an increasing frequency at subsequent temperatures until 350 ˚C (Appendix F, Table F1).

Average peak positions for Feature A shows an average peak position between 388 and 390 cm^{-1} for a temperature range of 22 to 310 ˚C (Figure 7.1.8 and Table 7.1.3). At temperatures from 340 ˚C to 1200 ˚C average peak positions fall in a range of 405 and 412 cm^{-1}, with a gradual increase in peak position with temperature. When examining all spectra obtained for each temperature (Figure 7.1.9), a large range of peak positions are observed between 22 and 330 ˚C, with a maximum variation of 13 wavenumbers. The variation in peak positions for the temperature ranges 350 to 700 ˚C and 800 to 1200 ˚C are even smaller at 7 and 2 wavenumbers respectively. The variation in peak positions, particularly for spectra taken between 22 and 310 ˚C, suggest some previous, partial dehydration has already occurred. This could have been from the shaping process, or may

have occurred prior to collection, as SEM EDX analysis does not show any elements that may have substituted for Fe in the structure that could result in variations in peak positions.

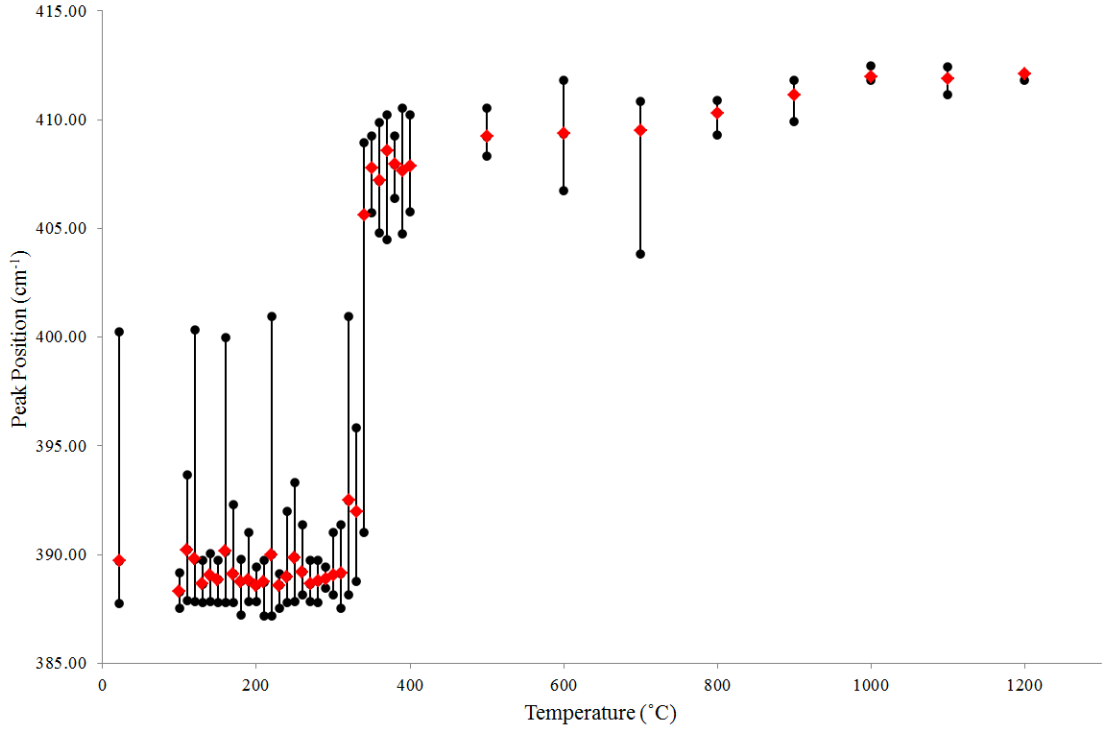

Figure 7.1.9 The graph shows the average peak position (red) and the minimum and maximum peak positions (black lines), for Feature A, taken after heating to the indicated temperature. The error in peak position is 0.3 cm^{-1}, which would be hidden by the points.

Figure 7.1.10 shows the mass loss and the peak position of Feature A, which indicates that the larger changes in mass occur after the sample begins to show a more dominate hematite spectrum. This might be due to the size of the sample and might show that the sample is not completely dehydrated, or that the majority of mass loss occurs after the sample transforms to hematite. The mass loss becomes more stable when the peak positions are at 412 cm^{-1}, which indicates that the sample is now completely dehydrated. These results would indicate that it might be possible to quantify the devolatilisation from the Raman spectra.

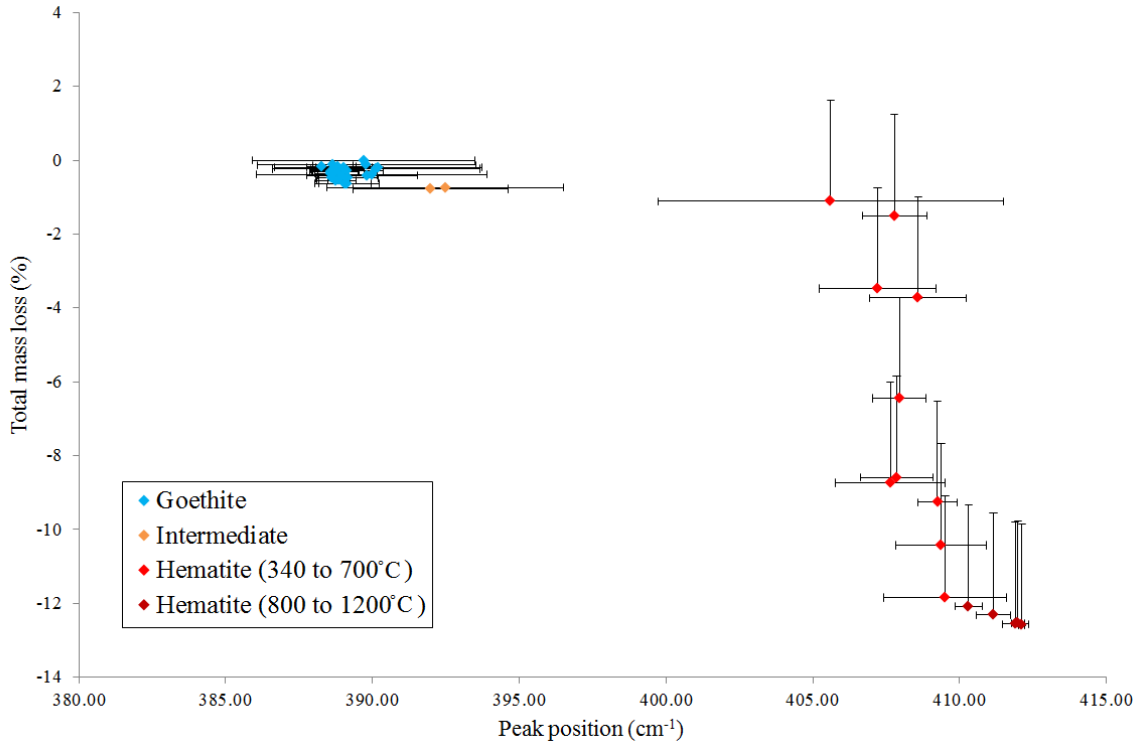

Figure 7.1.10 The total mass loss (in %) as a function of the Feature A peak position. The colour of the data points correspond to the dominate spectra classification (from the absolute data) for each temperature, i.e. goethite (blue), intermediate (orange) and hematite (red). The standard deviation for each temperature (from the absolute data) was calculated to generate the error bars for peak position and error bars for the mass measurements are described in the mass measurements sub-section of this section (7.1.2 Ex-situ/Mass Loss Experiment).

The average peak widths for Feature A (Figure 7.1.11) shows a similar trend to that seen with the in-situ results. Overall the average peak widths show widths between 20 and 25 cm^{-1} between 22 to 310 ˚C, an increase in width at 320 and 330 ˚C and finally an overall decrease from 340 to 1200 ˚C. The variability in average peak width from 22 to 310 ˚C is most likely due to the spectra showing some dehydration, as with the variability in peak positions. Between 340 and 400 ˚C there is a variation in peak width of 1.7 wavenumbers, but there are large variations in peak widths from the raw data. Mass measurements show that at these temperatures large amounts of water is lost, between 0.1159 to 1.5083 mg, which would result in variations in crystallinity and this is also apparent in the average peak widths at the these temperatures. Interestingly, the classification for all the peaks in this temperature range is hematite, indicating that a sample with a hematite Raman spectrum and broad peaks might still be hydrated. Peak positions from 500 to 1200 ˚C show a more linear decrease in peak width as a function of temperature, which results from the sample becoming more ordered.

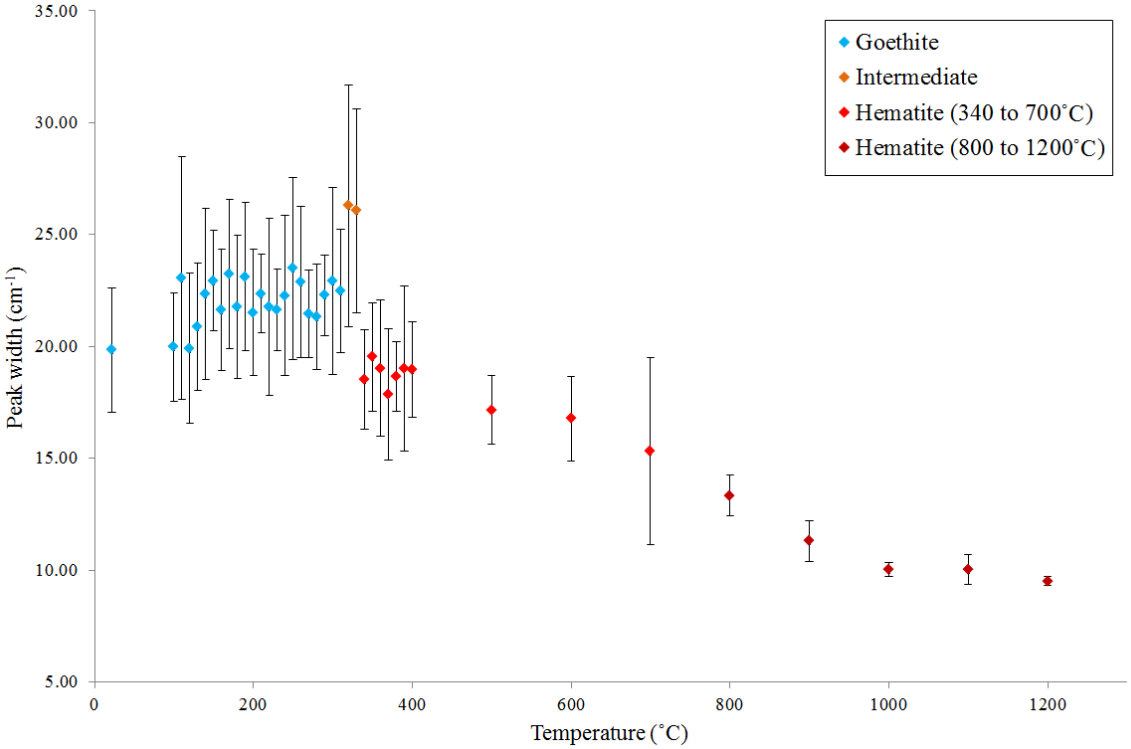

Figure 7.1.11 Average peak widths of Feature A for the goethite ex-situ heating experiment. The standard deviation for each temperature (from the absolute data) was calculated to generate the error bars.

Feature B Analysis

Feature B becomes more readily identifiable in the spectra at 330 ˚C, but is noticeable (qualitatively) in spectra from 320 ˚C. However, it is not until 350 ˚C that all spectra obtained this feature. The two separate peaks that make up Feature B became more recognisable as two individual peaks in some spectra at 500˚C and this is seen in all spectra at 600 ˚C. At 700 ˚C they begin to appear as two, almost completely separate, peaks of roughly equal intensity. In some spectra for 800 ˚C Peak 1 appears to have a greater intensity and is seen in all spectra for 900 ˚C. The change in width and amplitude occurs as the mineral becomes more crystalline, with increasing temperature, where it also becomes the more recognisable hematite spectra.

The average peak positions for both peaks in Feature B (Figure 7.1.12) are overall reasonably consistent, with little variation, with the exception of peak positions for 320 and 330 ˚C. However, these specific temperatures also posses the most spectra classified as intermediate.

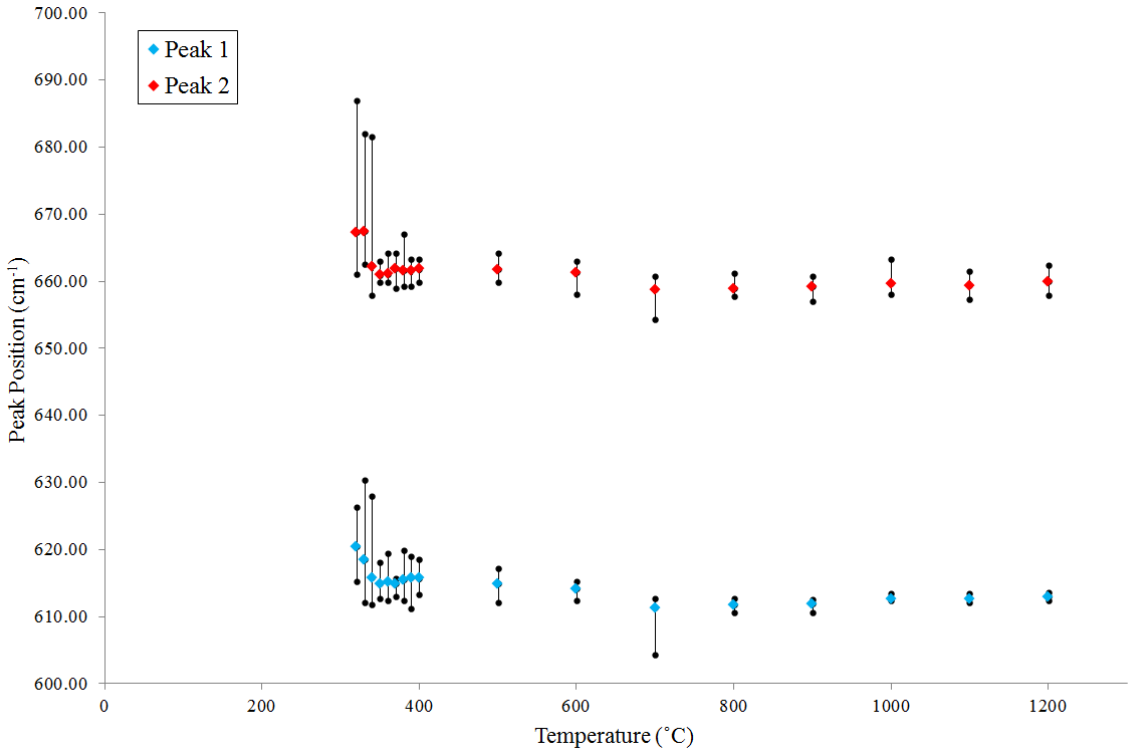

Figure 7.1.12 Average peak positions for Feature B from goethite ex-situ experiment. The coloured points represent the average peak positions and the capped black lines indicate the range of peak positions recorded for each temperature. The peak position error is 0.3 cm^{-1}. Note, there are no data below 300 degrees ˚C as these features only become observable above that temperature.

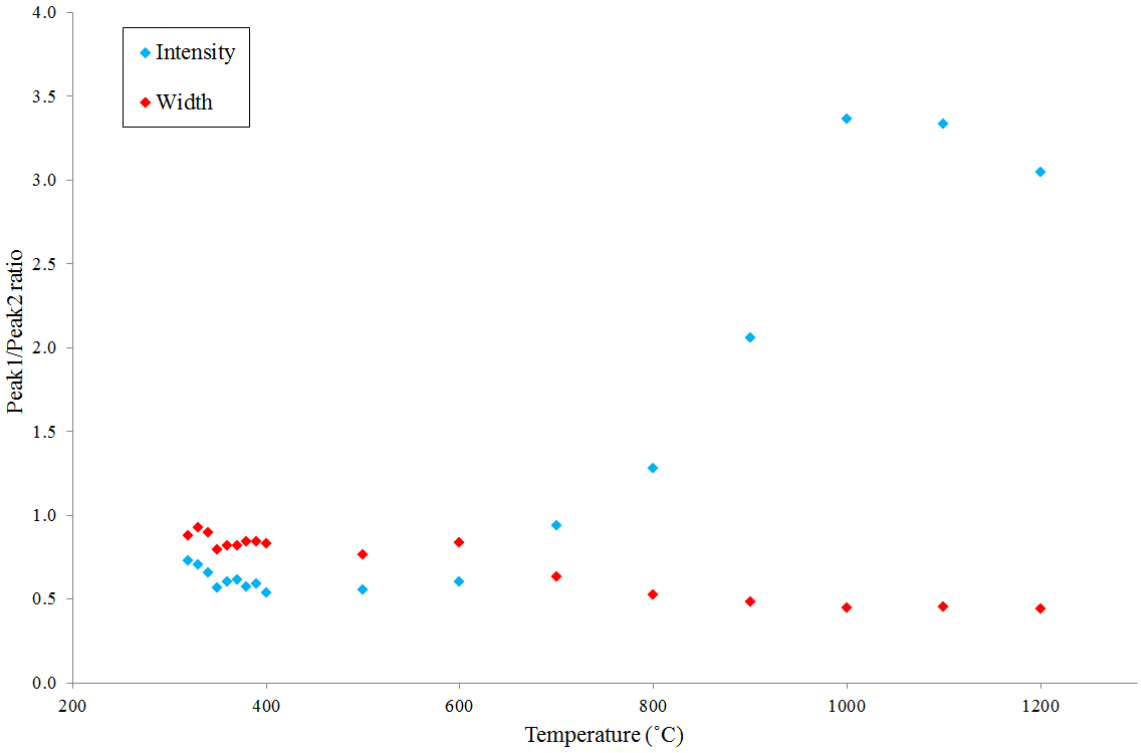

Figure 7.1.13 Ratio of the average peak intensities and widths for Feature B.

The ratio of peak widths (Figure 7.1.13) shows both peaks have roughly the same widths from 320 to 600 ˚C with ratios of 0.9 and 0.8. Above 700 ˚C there is a decrease with peak 1 becoming narrower. The average for peak widths show there is a decrease as a function of temperature for both peaks (Figure 7.1.14). Data points between 340 and 400 ˚C are scattered and do not show a direct trend, as with points from 500 ˚C onwards. The ratio of peak intensities (Figure 7.1.13) shows that from 500 to 1000˚C there is a clear increase in peak 1 intensities with increasing temperature. At 1000 to 1100 ˚C the ratio of peak intensities remain stable and then peak 1 decrease in intensity at 1200 ˚C. But overall the results show that at temperatures of 1000 ˚C and greater produce a ratio (of peak 1/ peak 2) of 3.0 or higher. The combined decrease in peak width and the increase in peak intensity, specifically peak 1, shows the sample is becoming increasingly crystalline from 500 to 1000˚C.

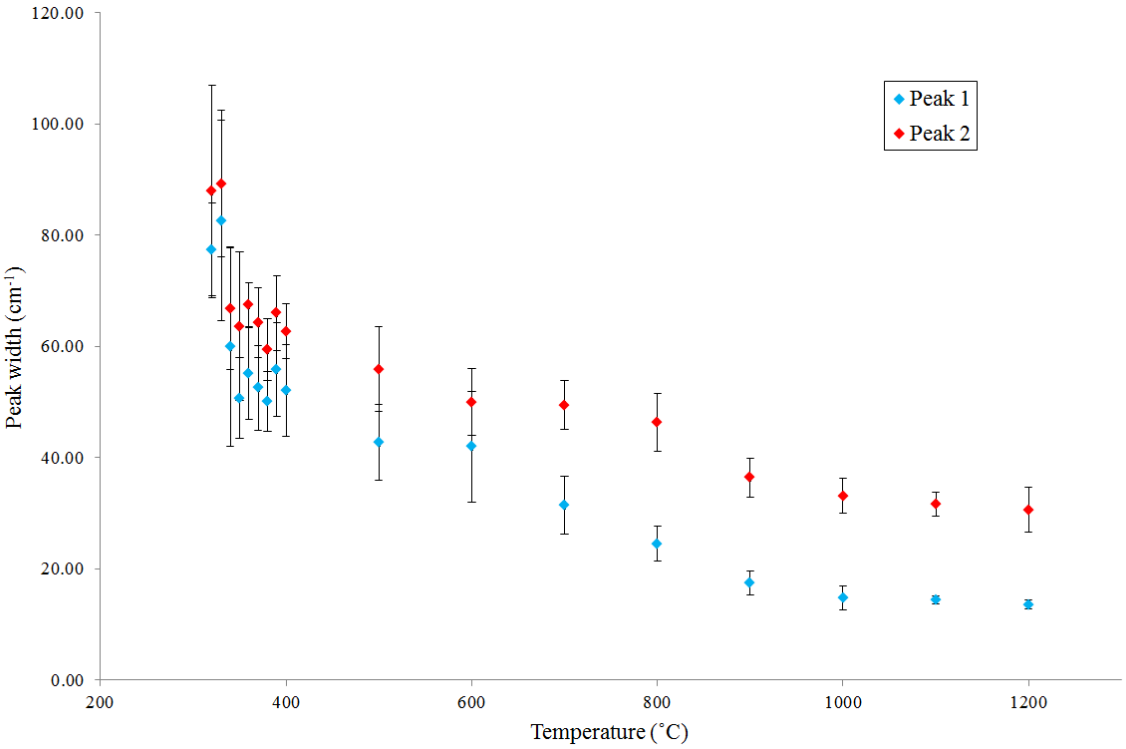

Figure 7.1.14 Average peak widths for Feature B from ex-situ goethite experiment. The standard deviation for each temperature (from the absolute data) was calculated to generate the error bars.

7.1.3 Discussion

The overall changes in Raman spectra as goethite transforms to hematite occurs at different temperatures for the two experiments. Incipient transformation occurs between 250 and

275 ˚C for in-situ, and between 310 and 340 ˚C for the ex-situ experiments. However, the variation in dehydration temperature may be a result of the furnace not achieving and holding at the correct temperature. A previous study conducted by de Faria & Lopes (2007) determined the onset of dehydration occurs at 250 ˚C, which is close to the result obtained from the in-situ results. The Raman spectra is classified as a hematite spectra at 300 ˚C for in-situ, and all spectra were classified hematite at 350 ˚C for the ex-situ experiment. An additional study conducted by Gialanella *et al.,* (2010), presented two different results from a natural goethite sample and a commercial sample of goethite. At 300 ˚C the natural sample shows a goethite spectrum, whereas a more hematite spectrum is observed for the commercial sample at the same temperature. Interestingly the result of Gialanella *et al.,* (2010) obtained for the commercial sample corresponds to the in-situ results and the natural goethite resembles the results from the ex-situ experiment. It is unclear as to why this is the case as the material used in the experiments conducted here came from the same sample.

The transition temperatures (where hematite spectra are produced) for both experiments conducted here fall within the temperature range obtained from the TGA analysis (discussed in Chapter VI), which show mass loss occurs between 271.8 and 357.0 ˚C, and both the temperature found by Gialanella *et al.,* (2010) of 300 ˚C and the range of 260 to 360 ˚C determined by Dekkers (1990). Peak temperatures from the DSC curve for transformation occur at 317.0 and 322.0 ˚C, which is greater than that observed in the Raman spectra for both in-situ and ex-situ experiments. However, these transition temperatures do not indicate incipient temperature. The Raman spectra show an intermediate-type spectrum at 275 ˚C for in-situ results and from 310 ˚C for the ex-situ experiment, which again fall within the range determined by the TGA analysis. A study conducted by Ruan *et al.,* (2001) examined the transition of synthetic goethite to hematite, using XRD and FTIR analysis, and found this transition occurs within a temperature range of 180 – 270 ˚C, which is lower than the temperatures observed here. However, Ruan *et al.,* (2007) used a synthetic goethite sample, which had a higher water content (at 16%) than the expected values for goethite (10%), which may have contributed to the early onset of water loss.

Changes in mass from the ex-situ experiment begin to occur at slightly higher temperatures, with incipient mass loss occurring between 290 and 300 ˚C, than the temperature shown in TGA analysis. There is a greater difference, of 347 ˚C, between the end temperature for the large drop (in mass) in the ex-situ experiment and TGA analysis,

as mentioned earlier. The temperature (700 ˚C) obtained here for the ending of dehydration (seen via mass loss) is comparable to Gialanella *et al.*, (2010) who show TGA temperatures of their natural sample continued to lose water up to 730 ˚C. However, a total mass of 2% is lost between the end of the main fall in mass ~350 ˚C and 730 ˚C in Gialanella *et al.*, (2010), whereas in the ex-situ experiment 700 ˚C is the end temperature of the main fall in mass.

Feature B best shows the changes that occur in crystallinity as a result of increasing temperature, once the sample has formed hematite. The appearance of this feature occurs at 275 ˚C for the in-situ experiment and in the ex-situ experiment at 320 ˚C in some spectra and all spectra from 330 ˚C, which reflects the incipient temperatures for water loss. Both sets of ratio data show the almost linear trend for the increasing intensity for peak 1 occurring at 500 ˚C. The trend for the peak width data from the in-situ experiment is not as clear, with linear trends beginning at 500 ˚C and 800 ˚C for peak 1 and 2, respectively. Peak width data for both peaks from the ex-situ experiment show this linear decrease starting at 500 ˚C, which does correlate with peak 1 from the in-situ results.

Figure 7.1.15 shows peak width and peak position data for Feature A from both experiments (data from the ex-situ heating experiment has been averaged). The results show three regions, which represent the three classifications used to classify the spectra: goethite, intermediate and hematite. Intermediate spectra have the greatest peak widths, which corresponds to the two peaks that make up Feature A (discussed in section 7.1.1 and in Appendix E) having the same intensity, causing the broad feature. The series of points that are representative of hematite spectra cover a much larger region of the plot, which is a result of the feature's decreasing peak widths which represents increasing crystallinity. The absolute data (complete dataset from the ex-situ heating experiment) for Feature A peak positions and peak widths (Figure 7.1.16) only identifies two distinct regions (as there is some overlap between spectra classified as goethite and intermediate). There is a gap, 401.0 to 403.8 cm^{-1}, between these two regions that can, in theory, be used to identify the two phases formed as a result of heating alone. There is an additional cluster of spurious points at about 400 cm^{-1} and with peak widths of 18.90 to 12.15 cm^{-1}, these are spurious points that have been generated as a result of the peak fitting program not fitting peaks correctly. This cluster is predominantly composed of peaks with a goethite spectrum and is representative of a region where peaks that are incorrectly fitted can be found. A comparison of Feature A peak positions and Feature B peak intensity ratios (Figure 7.1.17) also shows a clear distinction between spectra classified as intermediate and hematite. In

addition to this, it also shows two separate regions for hematite spectra, above and below 800˚C. Previous analysis shows that a high ratio value of 3.0 for the peak intensities for Feature B, specifically for ex-situ results, indicates a temperature of 1000˚C or higher, which is again shown in Figure 7.1.17. However, in-situ results would indicate a temperature of greater than 1000 ˚C, are required for a ratio of 3.0 or greater. The absolute data for this Feature A and Feature B plot (Appendix F, Figure F1) shows the same characteristics that are seen when averaged ex-situ data are used. However, the absolute data show a higher P1/P2 intensity ratio than what is seen in the averaged data. The regions shown in these plots can be used to identify hematite that has been formed from high temperatures (800 to 1200 ˚C).

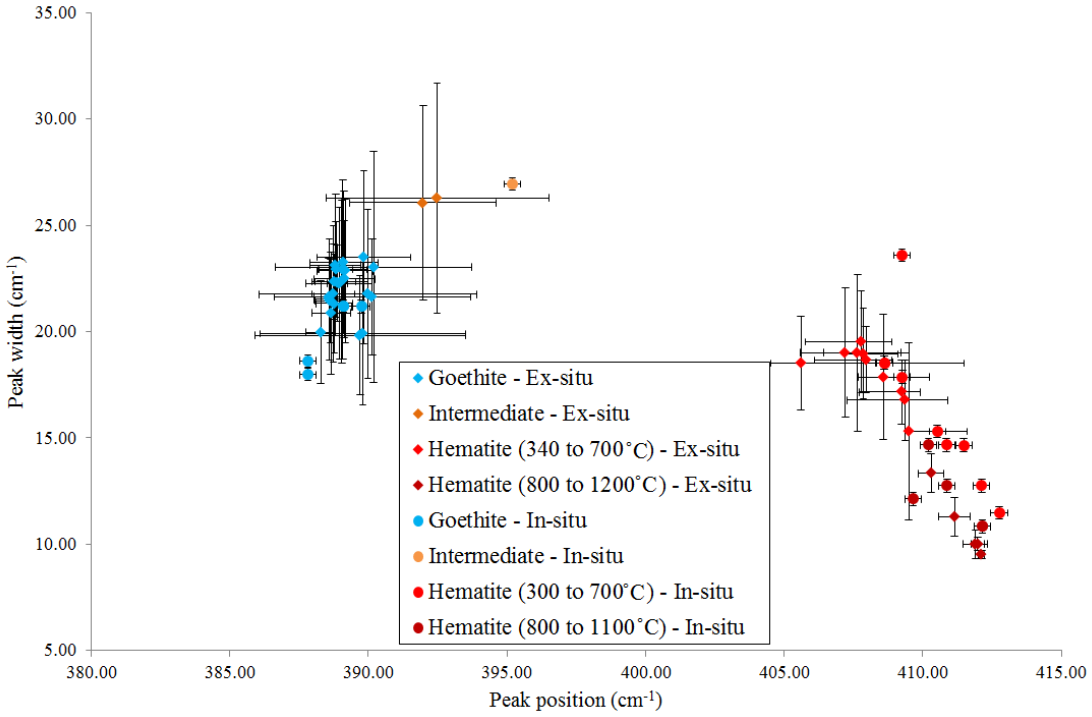

Figure 7.1.15 Peak width against peak position for both in-situ and averaged ex-situ results for Feature A. The colours of the various points represent a specific temperature range for that experiment. In general, goethite spectra are shown with light and dark blue, intermediate spectra are in orange and both shades of red represent hematite. The standard deviation for each temperature (from the absolute data) was calculated to generate the error bars for the averaged ex-situ results. Error bars for in-situ data represent the spectral resolution for the configuration of the Raman spectrometer (0.3 cm^{-1}).

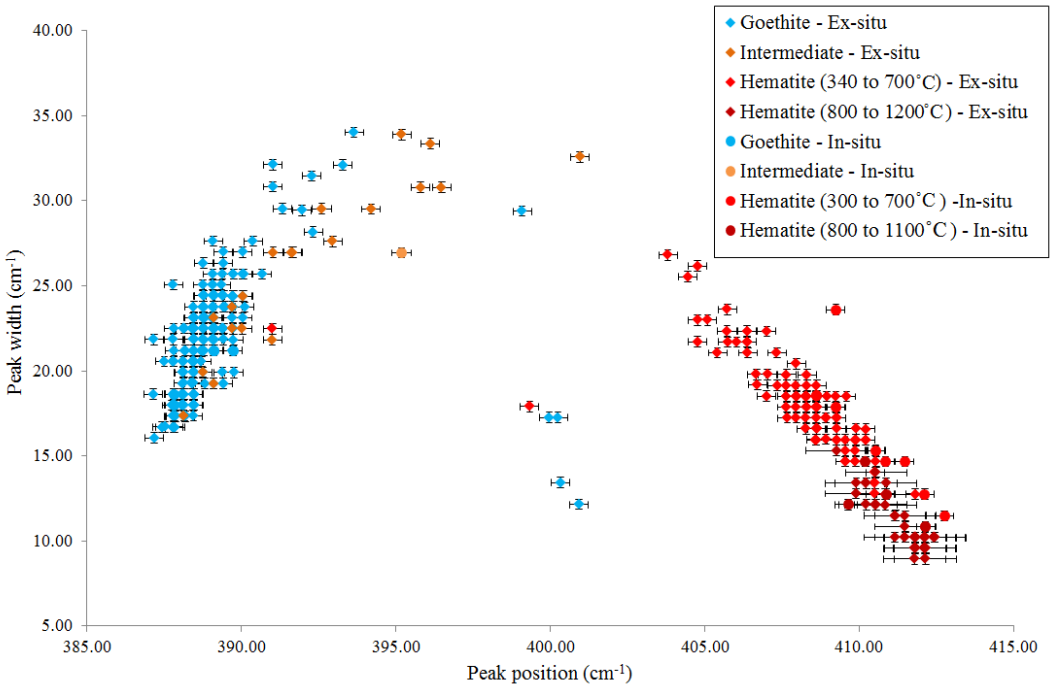

Figure 7.1.16 Peak width against peak position for both in-situ and absolute ex-situ results for Feature A. The colours of the various points represent a specific temperature range for that experiment. In general, goethite spectra are shown with light and dark blue, intermediate spectra are in orange and both shades of red represent hematite. Error bars for data represent the spectral resolution for the configuration of the Raman spectrometer (0.3 cm^{-1}).

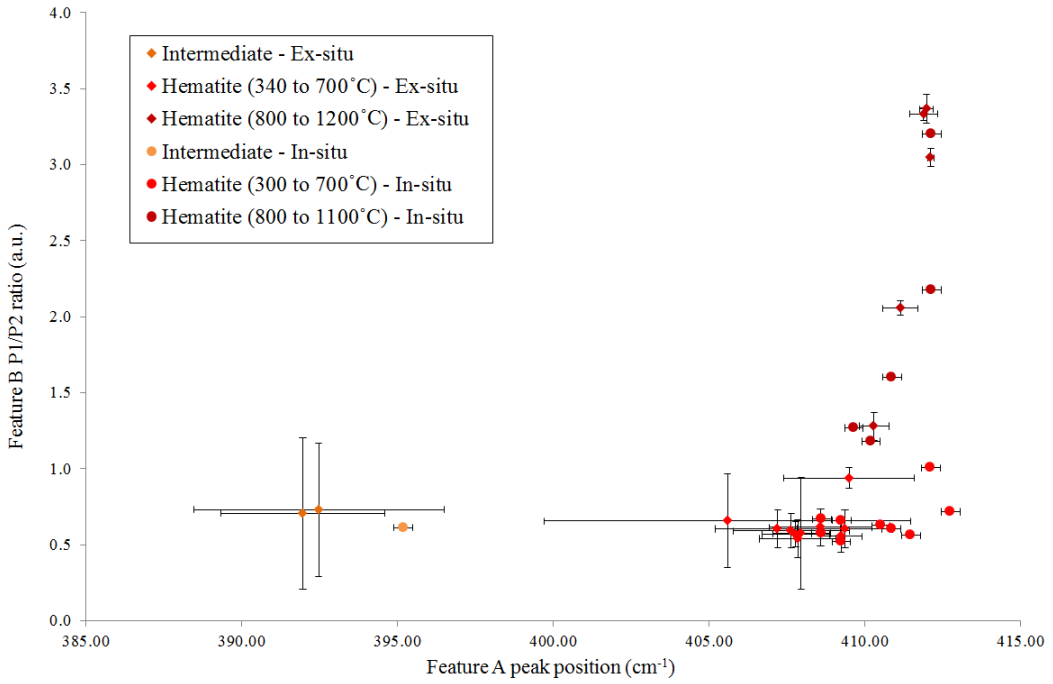

Figure 7.1.17 Feature A peak position and Feature B intensity ratios for both in-situ and averaged ex-situ experiments. Orange points represent temperatures where spectra were classified as intermediate and both shades of red show temperatures where spectra were classified as hematite. The standard deviation for each temperature (from the absolute data) was calculated to generate the error bars for the averaged ex-situ results. Error bars for in-situ data represent the spectral resolution for the configuration of the Raman spectrometer (0.3 cm^{-1}).

7.2 Gypsum

Analysis of Raman spectra from these experiments focused on the peaks from two specific SO_4 modes, U1 and U2. A 532 nm laser and a 10% N.D. filter, resulting in a power of 1.04 mW interacting with the sample, were used throughout. This laser was chosen as it provided the best spectrum for gypsum. As with the goethite analysis, a single spectrum was taken for each temperature step in the in-situ experiment and ten spectra were taken for the ex-situ experiment. Unlike the goethite experiments Raman spectra were not classified according to their dehydration state, as the specific peaks being analysed are present in all three phases. The peaks that show the water modes are presented here, but are not discussed in great detail as they are not present in the anhydrous phase.

7.2.1 In-situ Raman Heating Experiment

In-situ heating of a grain of natural gypsum, 90 × 300 µm, was conducted using the environmental stage of the Raman spectrometer. The sample was heated to the target temperature at a rate of 50 ˚C per minute, held for 10 minutes and cooled back down to room temperature before a Raman spectrum was taken. A single Raman spectrum was taken after each heating cycle in exactly the same position (or as close as possible) each time, to a maximum temperature of 1400 ˚C. However, at 1400 ˚C, Raman spectra were fluorescent and the sample had clearly melted, so a spectrum was not obtained at this temperature. Table 7.2.1 displays the peak positions and widths for SO_4 U1 and U2 bands and Table 7.2.2 details the peak positions and peak widths for the H_2O bands. As with the goethite in-situ experiment, this experiment was carried out over multiple days, with a Raman spectrum taken before the first new heating cycle on the new day.

Results from both H_2O and SO_4 data show there are two dominant changes in peak positions at 150 and 350 ˚C, which indicates the transformation to bassanite and anhydrite, respectively.

Table 7.2.1 Raman peak positions and widths of SO_4 U1 and U2 bands from the in-situ heating of gypsum.

Temperature (˚C)		U1		U2 (1)		U2 (2)	
		Position (cm^{-1})	Width (cm^{-1})	Position (cm^{-1})	Width (cm^{-1})	Position (cm^{-1})	Width (cm^{-1})
Day 1	26	1008.4	4.6	415.1	7.9	493.6	8.9
	50	1008.4	4.6	414.6	6.9	494.6	8.9
	100	1008.8	4.6	414.6	6.9	494.1	9.9
	150	1015.3	8.3	429.5	16.8	488.2	13.9
	200	1015.7	7.4	430.0	15.0	488.7	13.9
	250	1015.7	7.4	430.0	15.8	488.7	12.9
	300	1015.7	7.4	426.5	22.9	488.7	12.9
	350	1017.1	6.5	416.6	3.0	499.1	7.9
	400	1017.6	5.5	417.1	5.0	499.1	10.9
Day 2	400	1017.2	5.5	416.6	4.0	497.6	8.9
	450	1016.9	5.5	417.1	4.0	499.7	7.9
	500	1017.3	5.5	416.6	4.0	499.2	11.9
	550	1017.3	5.5	417.1	3.0	500.2	13.9
	600	1017.3	6.5	417.1	5.0	498.2	10.9
	650	1017.3	5.5	416.6	4.0	499.7	8.9
	700	1017.3	5.5	416.6	3.0	499.7	5.9
Day 3	700	1017.8	4.6	417.1	4.0	499.7	9.9
	800	1017.8	4.6	417.1	3.0	499.2	6.9
	900	1017.8	4.6	417.1	3.0	499.7	6.9
	1000	1017.8	4.6	417.1	3.0	499.7	7.9
	1100	1017.8	4.6	417.6	3.0	499.7	7.9
	1200	1017.8	4.0	417.1	3.0	499.7	7.9
Day 4	1200	1017.8	3.7	417.6	3.0	500.2	6.9
	1300	1017.3	6.5	417.1	4.0	496.2	8.9

N.B. Raman spectra were taken using a 532 nm laser, 10 % N.D. filter, ×10 objective and 1800 g/mm grating.

Table 7.2.2 Raman peak positions and widths of H_2O bands from the in-situ heating of gypsum.

Temperature (˚C)	H_2O (1)		H_2O (2)	
	Position (cm^{-1})	Width (cm^{-1})	Position (cm^{-1})	Width (cm^{-1})
26	3402.8	32.2	3493.4	23.9
50	3405.7	30.1	3491.8	23.9
100	3407.9	39.7	3493.4	23.3
150	3555.3	31.3	-	-
200	3555.9	25.5	-	-
250	3552.8	19.9	-	-
300	3559.9	32.8	-	-
350	-	-	-	-

N.B. Raman spectra were taken using a 532 nm laser, 10 % N.D. filter, ×10 objective and 1800 g/mm grating.

H_2O Peak Analysis

In gypsum form two H_2O peaks are present: at 3402.8 to 3407.9 and 3493.4 to 3491.8 cm^{-1}, and a single peak is present at 3552.8 to 3559.9 cm^{-1} when the sample turns into bassanite. Table 7.2.2 shows there is an increase in the peak position in H_2O (1) from 26 to 100 ˚C, which is greater than the instrumental positioning error of 0.4 cm^{-1}. In the semi-hydrous phase the H_2O (1) peak also shows some variation in peak position; there is a change in peak position from 3555.3 and 3555.9 cm^{-1} at 150 and 200 ˚C, respectively, to 3552.8 cm^{-1} at 250 ˚C and then an increase at 300 ˚C to 3559.9 cm^{-1}. The change between 150 and 200 ˚C falls within the range of positional error of the spectrometer, but the decrease in peak position at 250 ˚C is much greater than this error, as is the increase in peak position at 300 ˚C. There is an increase in peak width of 9.6 and 12.9 wavenumbers before transitioning to bassanite and anhydrite, respectively. Indications of an increase in peak width could be a sign the mineral is about to transition from one phase to another.

SO_4 U1 Peak Analysis

Changes in the peak positions of the SO_4 U1 mode (Figure 7.2.1) does not show the same changes seen in the H_2O (1) peak positions over specific temperature ranges. The changes in the U1 peak position for the temperatures ranges 26 to 100 ˚C and 150 to 300 ˚C are 0.4 cm^{-1}, which is similar to the spectrometer's positioning error. After the sample becomes anhydrite there is very little change in peak position, with the exception of a single point at 450 ˚C, which shows a decrease in peak position from 1017.2 cm^{-1} at 400 ˚C to 1016.9 cm^{-1}, but then increases again to 1017.03 cm^{-1}. This could either be a spurious point, or indicate a second or third order phase change that occurs between 300 and 400 ˚C, but smaller temperature steps would be needed to determine this. The dominant changes in peak position occur at 150 and 350 ˚C, which correspond to the changes seen in the H_2O peaks, where changes in hydrous phases occur at 150 and 350 ˚C.

At temperatures where spectra were taken over two days, the peak widths show a very small variation of -0.4 and +0.5 cm^{-1} for 400 and 700 ˚C respectively, from the day 1 to day 2. 1200 ˚C was the third temperature (where spectra were taken over two days), which showed no difference in peak positions. The changes in peak position for these two temperatures could be a result of the sample being warm, or it could be an

error with the position, as 0.4 cm^{-1} is also the spectral resolution when using the 532 nm laser.

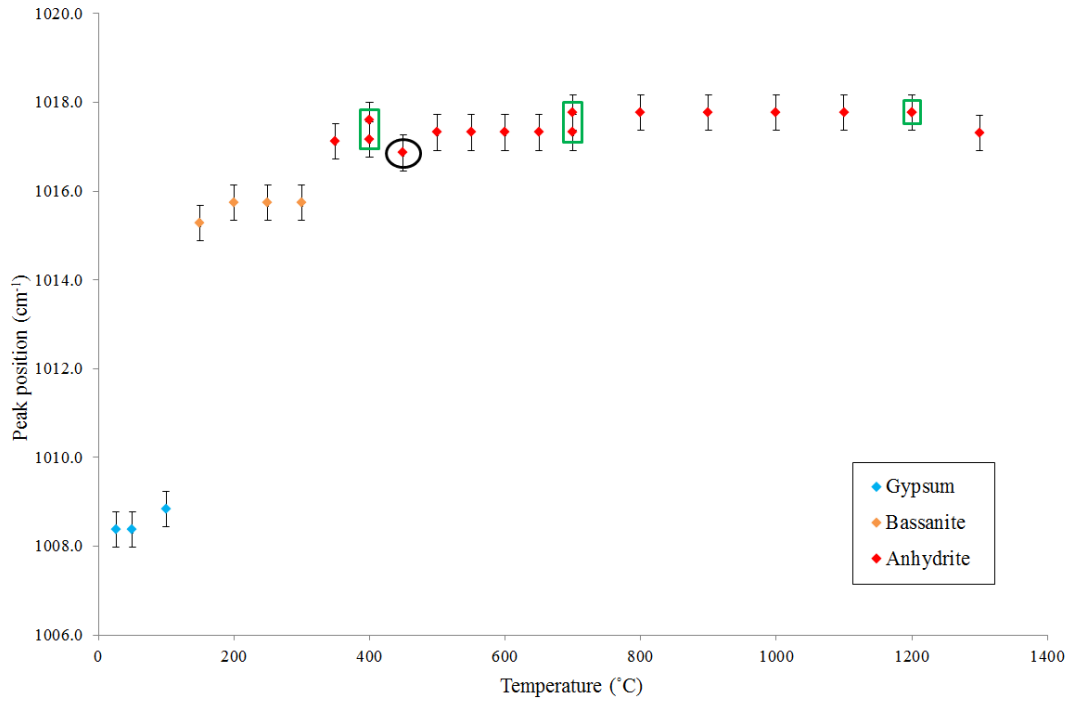

Figure 7.2.1 The peak position for the SO_4 U1 mode. A spurious value is highlighted by the black circle and the green boxes highlight temperatures where two spectra were taken over two days. Error bars represent the maximum difference in peak position for spectra taken at the same temperature.

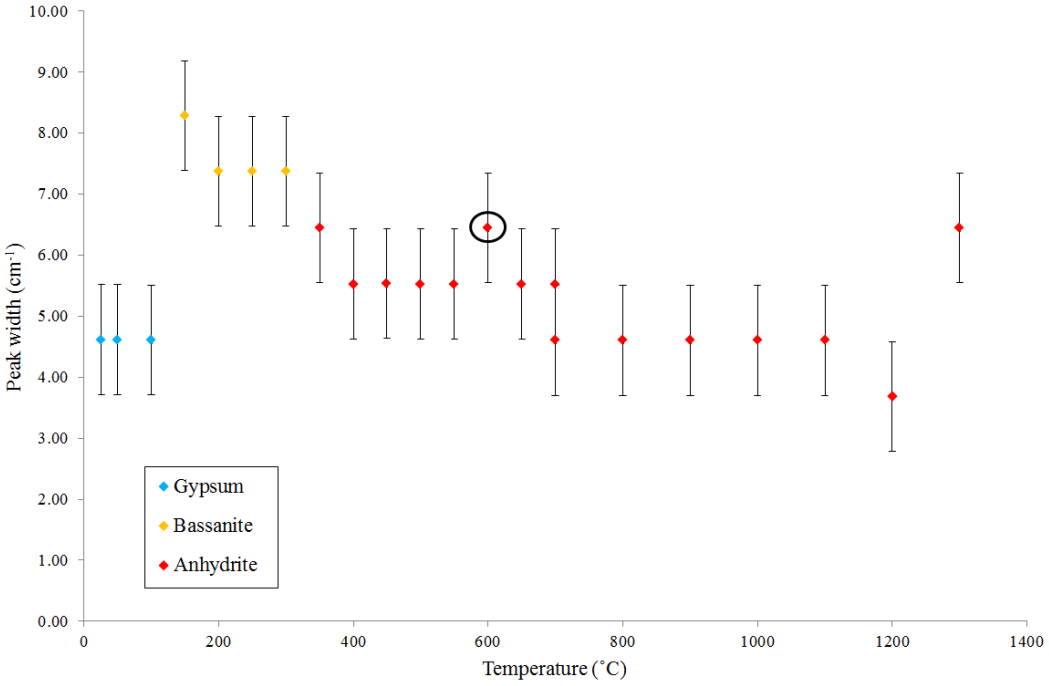

Figure 7.2.2 The peak widths for the SO_4 U1 mode. The black circle highlights an apparent spurious point. Error bars represent the maximum difference in peak width for spectra taken at the same temperature.

The peak widths of the U1 mode (Figure 7.2.2) increases after transitioning to bassanite, decreases to 1200 ˚C and then increases again from 1300 ˚C, which indicates changes in crystallinity. There is a spurious point at 600 ˚C that could indicate the sample was warm, but the there is no variation in peak position to confirm this. There is only one instance at 700 ˚C; where there is as discrepancy in peak widths taken on two separate days, where there is a variation of 0.9 cm^{-1}. The changes in peak width due to increasing crystallinity with temperature is gradual between 300 to 400 ˚C and a sharp step at 650 to 800 ˚C, which could be a result of the temperatures intervals being used or the gradual change in width corresponds to a gradual loss in water (specifically for 300 to 400 ˚C where there is a gradual change). Unlike the peak widths for H_2O (1), at 100 ˚C and 300 ˚C, there is no increase in width at the same temperature for the U1 peak before transitioning from one phase to another. The change in peak width, for the U1 peak, occurs after the transition, except at 1300 ˚C where the peak width increases just before desulfurisation occurs.

SO_4 U2 Peak Analysis

The SO_4 U2 peak positions (Figure 7.2.3) show a similar trend to that seen in the U1 and H_2O peak positions, with prominent changes in peak positions occurring at 150 ˚C and 350 ˚C. There is an overall slight fluctuation in peak position of 0.5 cm^{-1}, within each of the temperature ranges that represent each hydrous state (26 to 100 ˚C for gypsum, 150 to 300 ˚C for bassanite and 350 to 1300 ˚C for anhydrite) for peak 1. At 300 ˚C for U2 (1) there is a decrease in position of 3.5 cm^{-1}, which could be an indicator of the sample transitioning form semi-hydrous to anhydrous. Contrary to this, U2 (2) shows greater variations in peak position within two of the three temperature ranges: 1.0 cm^{-1} for 26 to 100 ˚C and 4.0 cm^{-1} for 350 to 1300 ˚C. Two larger changes in peak position occur at 600 and 1300 ˚C of 2.0 and 4.0 cm^{-1} respectively, the change at 1300 ˚C presumably indicates a transition is about to occur. However, it is unclear as to why there is a relatively large decrease in peak position at 600 ˚C, when it is not seen in the peak position for U1.

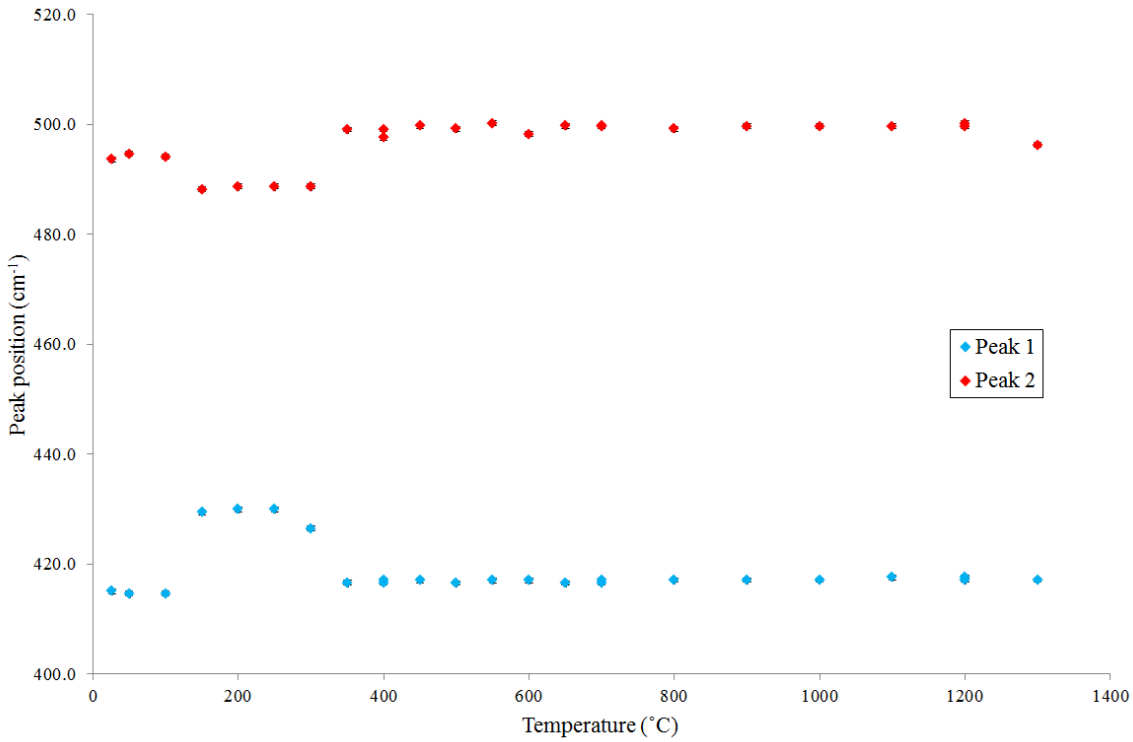

Figure 7.2.3 Peak positions of U2 peaks taken from in-situ measurements. Error bars represent the spectral resolution for the configuration of the Raman spectrometer (0.4 cm^{-1}), which is smaller than the size of the data marker.

Peak widths for U2 (2) (Figure 7.2.4) show a very scattered trend, there is an increase in peak width at 150 ˚C when the sample forms the bassanite state, and then a decrease at 350 ˚C when anhydrite is formed. However, there appears to be an increase in peak width at 550 ˚C, then it begins to fall at 600˚C and, finally, there is a slight increase of 1.0 ±1.0 cm^{-1} at 1300 ˚C. U2 (1) widths on the other hand, shows some variation within each of the three temperature ranges for each hydrous state. Between 26 and 100 ˚C there is a decrease in peak width from 7.9 to 6.9 cm^{-1} and then there is an increase in width, of 9.9 cm^{-1}, as the sample transitions from gypsum to bassanite. In the temperature range representing bassanite, the width deceases between 150 to 200 ˚C and then increases between 250 to 300 ˚C. As peak width describes the crystallinity of the sample, this indicates an increase in crystallinity, and then a decrease with temperature, suggesting that as the sample is about to transition to another phase the peak width increases, which is not seen in the peak widths of U1. The anhydrite phase shows varied widths between 350 and 800 ˚C, where there is an increase at 400 ˚C of 1.0 cm^{-1}, a decrease at 550 ˚C of 1.0 cm^{-1} and an increase at 600 ˚C of 1.9 cm^{-1}. After 600 ˚C the

peak width remains stable at 3.0 cm^{-1} before increasing at 1300 ˚C to 4.0 cm^{-1}, which is also seen for U1 peak widths.

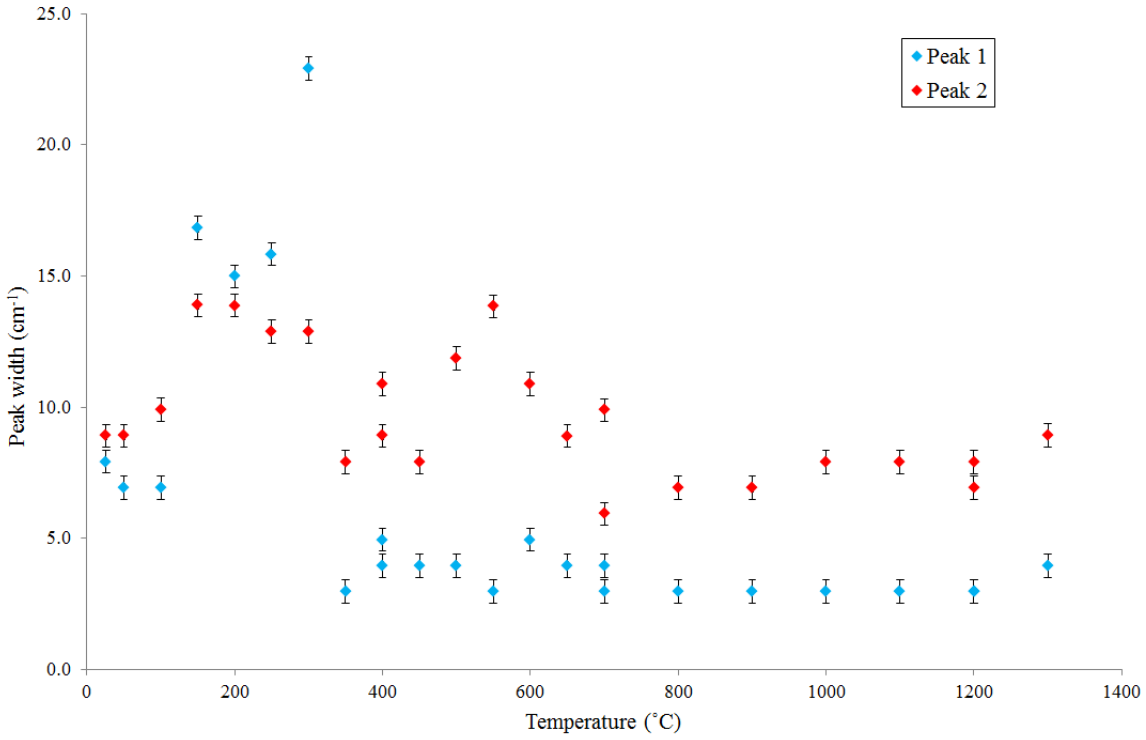

Figure 7.2.4 SO_4 U2 peak widths for the in-situ experiment. . Error bars represent the spectral resolution for the configuration of the Raman spectrometer (0.4 cm^{-1}).

7.2.2 Ex-situ Raman/Mass Loss Experiment

A sample of gypsum, 2.44 × 2.20 × 6.06 mm, was heated in an *Elite* furnace, and mass measurements and Raman spectra were taken after each heating cycle. The sample was heated to the target temperature at a rate of 5 ˚C per minute, held for 10 mins and then allowed to cool.

Mass Measurements

Mass measurements were taken within 10 minutes of removing the sample from the furnace, to minimise any interaction the sample may have with the atmosphere, such as the adsorption of water.

After heating the sample to 170 ˚C, the balance would not stabilise and provide a stable mass measurement. Therefore, mass measurements were taken three minutes from

placing the sample on the balance, for this temperature and onwards. This produced an error of 0.5671 %, which was calculated by allowing the balance to stabilise and then determining the difference between this mass measure and the measurement taken after three minutes. The instability of the balance may have resulted from the sample absorbing water from the atmosphere, or water was not fully lost from the sample, similar to what was seen with the goethite sample. Whilst heating the sample at 370 ˚C a piece of sample broke off, both pieces of the sample were weighed. So, values from 370 ˚C onwards have a greater error than at previous temperatures. An estimation of total mass loss values (in mg) from 370 ˚C were calculated by added the mass of the fragment, 0.2738 mg, to the mass readings of the main and larger sample. Total mass change values (in %) were calculated by first calculating the total mass loss of the main sample from the starting mass, and then subtracting the percentage mass of the fragment (again from the starting mass) of 0.4785 % from the main sample values. These values are only estimates, as they do not account for additional smaller pieces that may have come away when the larger piece broke away; nor do they account for any water lost as a result of heating the fragment. Therefore, the change in mass (in %) should be lower and the change in mass (in mg) should be higher. The sample breaking produced a larger error for the mass measurements of 1.0456 %, which also takes into account the error produced from the instability of the balance. The main sample broke again after heating to 800 ˚C with multiple small fragments being produced, so it was decided to stop taking mass measurements.

Mass measurements in Table 7.2.3 show that between 22 and 110 ˚C there is an increase in mass of 0.0007 % and then a decrease of 0.0178 % between 120 and 160 ˚C. An initial, and slightly lower, decrease in mass occurred between 130 and 160 ˚C, where masses of 0.0035 and 0.0084 % are lost for each temperature step (except at 150 ˚C where only 0.0014 % was lost). The start of this mass change at 130 ˚C may represent the onset of water loss from the gypsum, which corresponds to the onset temperature of 127.2 ˚C, previously determined by TGA analysis (Chapter VI, Section 6.1.4).

Table 7.2.3 Gypsum measurements from the ex-situ mass loss/Raman experiment.

Temperature (˚C)	Weight (mg)	Total change in mass (mg)	Total change in weight (%)
22	57.2218	0.0000	0.0000
100	57.2219	+0.0001	+0.0002
110	57.2222	+0.0004	+0.0007
120	57.2212	-0.0006	-0.0010
130	57.2192	-0.0026	-0.0045
140	57.2172	-0.0046	-0.0080
150	57.2164	-0.0054	-0.0094
160	57.2116	-0.0102	-0.0178
170	54.5538	-2.6680	-4.6626
180	50.9887	-6.233	-10.8929
190	49.6465	-7.5753	-13.2385
200	46.5964	-10.6254	-18.5688
210	46.3680	-10.8538	-18.9679
220	46.5893	-10.6325	-18.5812
230	46.2324	-10.9894	-19.2049
240	46.2381	-10.9837	-19.1950
250	46.2518	-10.9700	-19.1710
260	46.1815	-11.0403	-19.2939
270	46.2268	-10.9950	-19.2147
280	46.2949	-10.9269	-19.0957
290	46.1216	-11.1002	-19.3986
300	46.0751	-11.1467	-19.4798
310	46.2233	-10.9985	-19.2208
320	46.0464	-11.1754	-19.5300
330	46.1459	-11.0759	-19.3561
340	46.3403	-10.8815	-19.0164
350	45.9769	-11.2449	-19.6514
360	45.8860	-11.3358	-19.8103
370*	45.7387	11.4831	19.5892
380	45.5251	-11.9705	-19.9625
390	45.2873	-11.2083	-20.3781
400	45.2351	-11.2605	-20.4693
500	44.9821	-12.5135	-20.9114
600	44.7579	-12.7377	-21.3032
700	44.5953	-12.9003	-21.5874
800	-	-	-
900	-	-	-
1000	-	-	-
1100	-	-	-
1200	-	-	-
1300	-	-	-

*A piece of gypsum, with a mass of 0.2783 mg, broke off from the sample after heating the sample at 370 ˚C. The total mass change (in percent) accounts for this piece

N.B. values in red represent measurements where the balance was unstable, so measurements were taken after 3 minutes. Values in purple are estimated values that account for broken fragment.

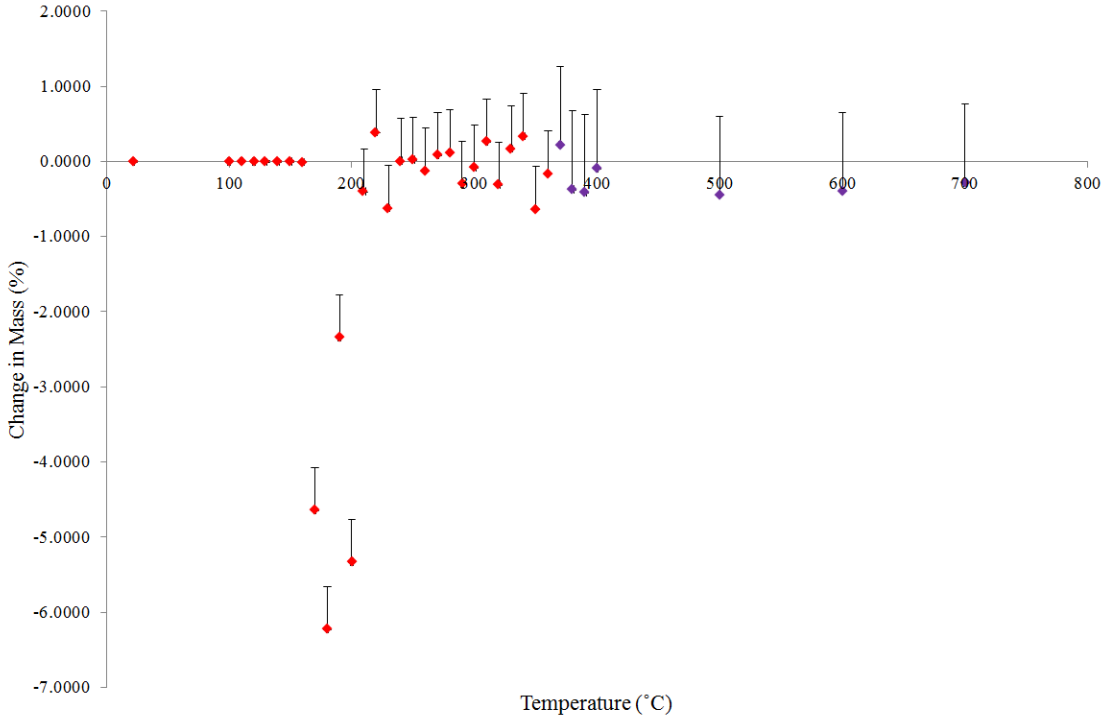

Figure 7.2.5 Relative change in mass, in %, between each heating cycle. Points in purple represent values taken after the sample broke at 370 ˚C. The error for the balance is 0.0087% which falls within the size of the markers. The errors calculated for measurements from 170 ˚C onwards are described in the text.

The main fall in mass occurs between 170 and 200 ˚C, with loss between 0.3991 and 6.2303 % for each temperature step. Figure 7.2.5 shows the change in mass after each temperature step. The onset of a large change in mass begins at 130 ˚C, which corresponds to the onset of dehydration shown by DSC analysis, which also shows the end at 207.1 ˚C, which is close to 200 ˚C that marks the end of the large decrease in mass in the ex-situ experiment. TGA analysis showed (see Chapter VI, Section 6.1.4) that after the episode of dehydration ends, the mass of the sample remained fairly constant, with changes in mass of ±0.1 %, until reaching a temperature of 1284.2 ˚C, where the sample became a liquid-crystal and mass changes of ±0.2% begin to occur. The results from this ex-situ heating experiment shows mass is continually lost up to 700 ˚C, with a total loss of 2.6195% between 210 and 700 ˚C. This could be a result of the entire sample not completely dehydrating, meaning at any particular temperature Raman spectra would represent a mix of two hydrous states. It could also be possible that very small crystals were coming away from the main sample as it was being heated.

Table 7.2.4 Peak positions (U1 and U2 bonds) total change in weight for the ex-situ heating of natural gypsum.

Temperature (˚C)	Total change in weight (%)	U1 Peak position (cm^{-1})	U2 (1) Peak position (cm^{-1})	U2 (2) Peak position (cm^{-1})
22	0.0000	1008.5	415.0	494.0
100	+0.0002	1008.5	415.0	493.9
110	+0.0007	1008.5	415.0	493.8
120	-0.0010	1008.4	414.9	493.8
130	-0.0045	1008.4	415.0	493.8
140	-0.0080	1008.5	414.9	493.9
150	-0.0094	1009.0	415.3	494.4
160	-0.0178	1008.5	415.0	494.0
170	-4.6626	1015.9	428.3	489.4
180	-10.8929	1015.9	428.8	489.2
190	-13.2385	1015.9	428.7	489.2
200	-18.5688	1015.9	428.4	489.2
210	-18.9679	1015.8	428.4	489.3
220	-18.5812	1015.8	428.5	489.3
230	-19.2049	1015.8	428.4	489.3
240	-19.1950	1015.7	428.0	489.3
250	-19.1710	1016.1	428.0	489.3
260	-19.2939	1015.8	428.0	489.2
270	-19.2147	1016.1	428.0	489.2
280	-19.0957	1016.2	427.8	489.4
290	-19.3986	1015.7	427.7	489.2
300	-19.4798	1016.1	427.3	489.2
310	-19.2208	1016.6	426.6	490.1
320	-19.5300	1016.3	427.3	489.6
330	-19.3561	1017.0	428.7	490.4
340	-19.0164	1016.5	428.0	490.0
350	-19.6514	1016.7	428.6	490.1
360	-19.8103	1016.6	427.5	491.4
370*	-19.5892	1017.1	426.6	496.2
380	-19.9625	1017.2	419.2	497.7
390	-20.3781	1017.4	417.2	498.6
400	-20.4693	1017.4	417.1	499.0
500	-20.9114	1017.0	417.1	499.0
600	-21.3032	1017.2	417.1	499.0
700	-21.5874	1017.6	417.1	499.2
800	-	1017.4	417.0	499.2
900	-	1017.8	417.0	499.3
1000	-	1017.5	417.1	499.3
1100	-	1017.4	417.0	499.4
1200	-	1017.5	417.1	499.7
1300	-	1017.2	416.7	498.8

*A piece of gypsum, with a mass of 0.2783 mg, broke off from the sample after heating the sample at 370 ˚C. The total mass change (in percent) accounts for this piece.

Table 7.2.5 Peak positions and widths (for H_2O bonds) total change in weight for the ex-situ heating of natural gypsum.

		H2O (1)		H2O (2)	
Temperature (˚C)	**Total change in weight (%)**	Peak position (cm^{-1})	Peak width (cm^{-1})	Peak position (cm^{-1})	Peak width (cm^{-1})
22	0.0000	3408.8	50.9	3492.8	28.1
100	+0.0002	3405.0	38.2	3492.3	31.3
110	+0.0007	3404.6	37.4	3492.6	29.2
120	-0.0010	3404.5	36.6	3492.4	29.6
130	-0.0045	3403.5	35.0	3492.5	31.8
140	-0.0080	3404.2	36.2	3492.0	34.7
150	-0.0094	3404.1	35.7	3493.4	32.2
160	-0.0178	3404.6	37.2	3492.9	31.7
170	-4.6626	3554.9	25.2	-	-
180	-10.8929	3554.8	25.2	-	-
190	-13.2385	3555.1	25.4	-	-
200	-18.5688	3554.7	24.6	-	-
210	-18.9679	3554.8	24.6	-	-
220	-18.5812	3554.4	24.4	-	-
230	-19.2049	3553.1	24.4	-	-
240	-19.1950	3555.0	25.6	-	-
250	-19.1710	3554.4	23.9	-	-
260	-19.2939	3554.9	24.9	-	-
270	-19.2147	3554.7	24.4	-	-
280	-19.0957	3554.5	24.7	-	-
290	-19.3986	3555.4	26.1	-	-
300	-19.4798	3555.0	26.2	-	-
310	-19.2208	3555.7	26.5	-	-
320	-19.5300	3555.4	25.6	-	-
330	-19.3561	3556.2	31.4	-	-
340	-19.0164	3555.1	24.6	-	-
350	-19.6514	3556.2	28.3	-	-
360	-19.8103	3556.5	35.4	-	-
370*	-19.5892	3557.7	25.7	-	-
380	-19.9625	3561.6	33.5	-	-
390	-20.3781	-	-	-	-
400	-20.4693	-	-	-	-
500	-20.9114	-	-	-	-
600	-21.3032	-	-	-	-
700	-21.5874	-	-	-	-

*A piece of gypsum, with a mass of 0.2783 mg, broke off from the sample after heating the sample at 370 ˚C. The total mass change (in percent) accounts for this piece.

N.B. Peak positions and widths are an average of ten spectra, except for 330 to 380 ˚C, where two spectra for each temperature had a spectral range of -90 to 4000 cm^{-1}. This was done due to time restrictions and the fluorescent nature of the spectra. Mass measurements were not recorded after 700 ˚C on account of the sample breaking.

Averaged Raman spectra shows there are two changes at 170 and 390 ˚C, before the sample melts at 1400 ˚C (Table 7.2.4 and Table 7.2.5; see Appendix F, Table F2 and F3 for absolute data). The first transition occurs when the sample goes from gypsum to bassanite, and the second transition represents the change from bassanite to anhydrite.

H_2O Peak Analysis

The average peak positions of the H_2O (1) (Figure 7.2.6) shows there is a subtle change in peak position between 100 and 130 ˚C, where there is a decrease of 1.5 cm^{-1} and then an increase of 1 cm^{-1} between 130 and 160 ˚C. H_2O (2) does not show the same pattern as H_2O (1), but there is an increase in peak position from 3492.0 cm^{-1} at 140 ˚C to 3492.9 cm^{-1} at 160 ˚C, which is greater than the 0.4 cm^{-1} error for peak position. An increase in peak position of 5.4 cm^{-1} occurs within the temperature range of 350 to 380 ˚C. Trends in the average peak widths for H_2O peaks (Figure 7.2.7) are not as clear as those displayed for the peak position.

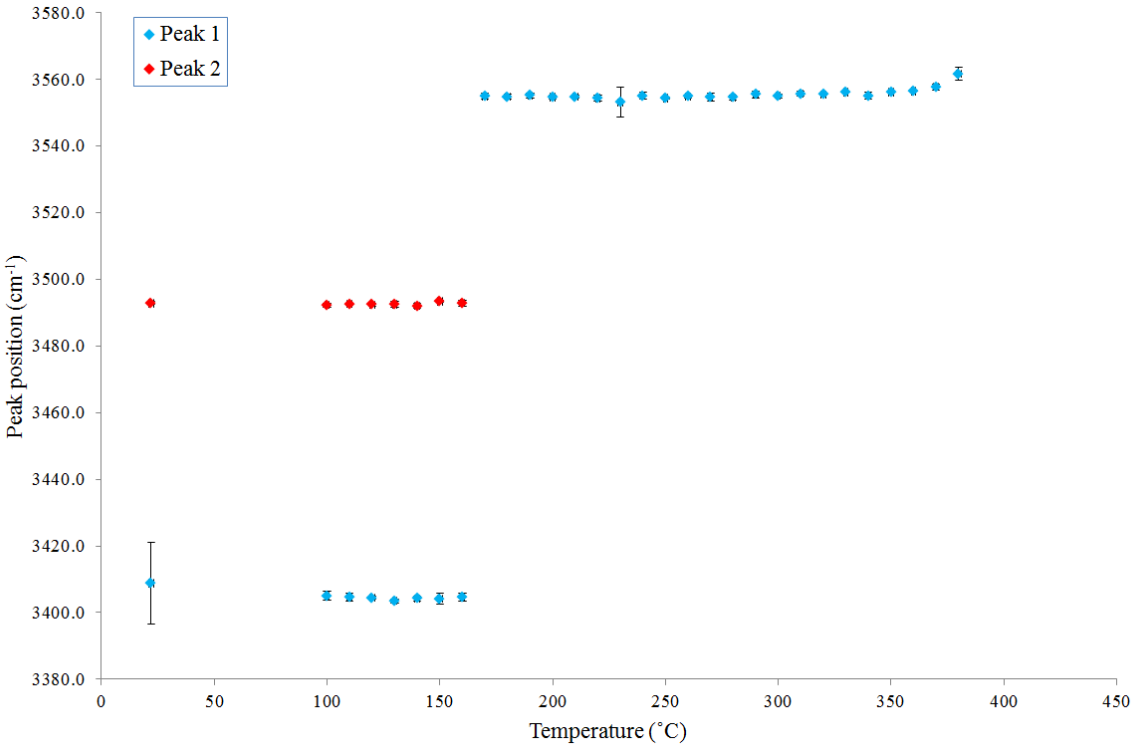

Figure 7.2.6 Average peak positions of gypsum H_2O peaks. The loss of the H_2O (2) peak and the large increase in peak position for H_2O (1) shows the transition from hydrous to semi-hydrous states. The complete loss of peak 1 indicates the loss of water from the sample. The standard deviation for each temperature (from the absolute data) was calculated to generate the error bars.

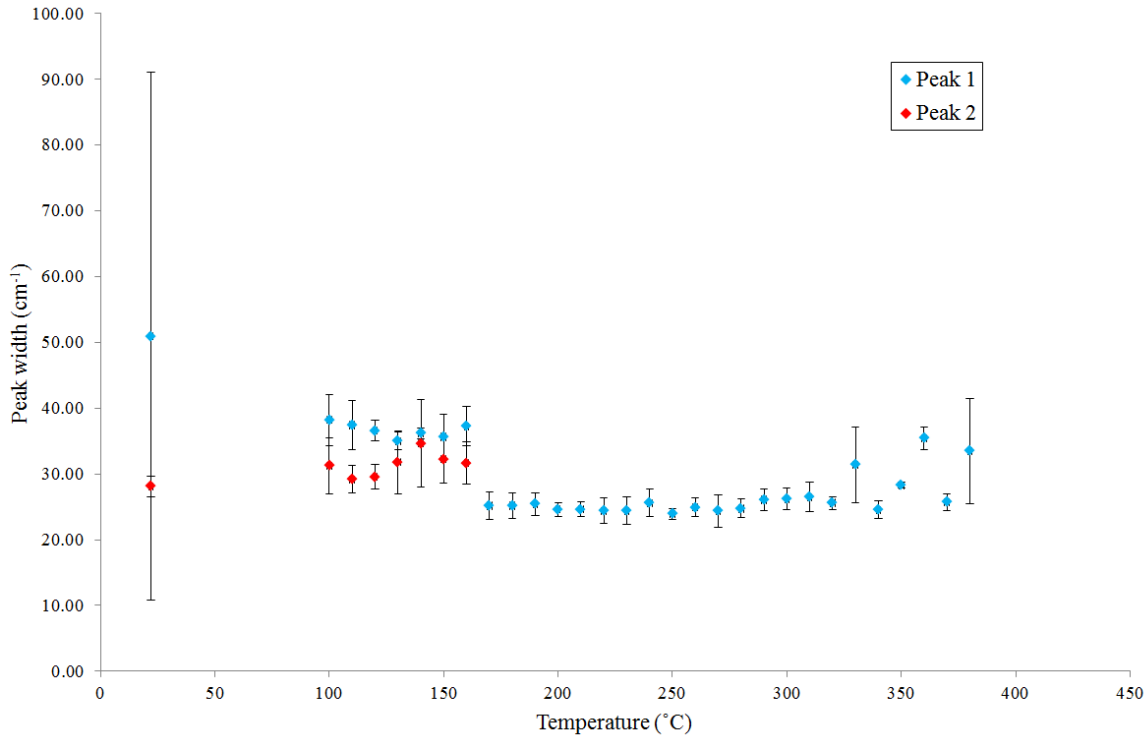

Figure 7.2.7 Average peak widths of gypsum H_2O peaks. The loss of peak 2, and the change in peak width between 160 and 170 ˚C, marks the transition between the sample's hydrous and semi-hydrous states. The standard deviation for each temperature (from the absolute data) was calculated to generate the error bars.

The average peak widths for H_2O (2) shows two episodes of decreasing peak width between 100 to 110 ˚C and 140 to 160 ˚C respectively, and two episodes of increasing peak widths between 22 to 100 ˚C and 110 to 140 ˚C. The increasing peak widths suggest the sample is becoming less crystalline, and the opposite is true for the episodes where there is a decrease in peak width. However, an increase in width would be expected before there is a transition to another phase, which is seen in H_2O (1) peak widths. In the gypsum phase of H_2O (1), peak width decreases before increasing from 35.0 cm^{-1} at 130 ˚C to 37.2 cm^{-1} at 160 ˚C. Once the sample becomes semi-hydrous there is an overall increase in widths from 170 to 380 ˚C, but there is also more variation in widths, particularly between 280 and 380 ˚C with a range of 24.6 to 35.4 cm^{-1}.

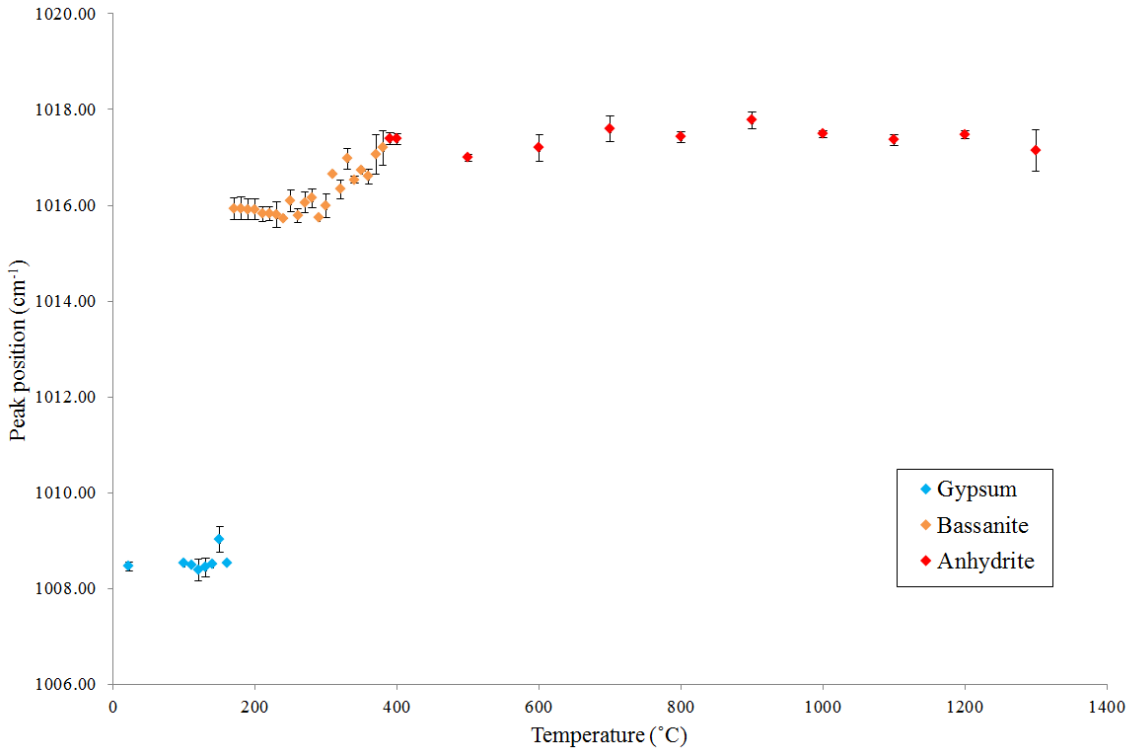

Figure 7.2.8 Average peak positions for SO_4 U1 from the ex-situ heating experiments. Data points in blue represent gypsum spectra, those in orange signify bassanite and anhydrite spectra are shown in red. The standard deviation for each temperature (from the absolute data) was calculated to generate the error bars.

The average peak positions for U1 (Figure 7.2.8) shows two clearly separate regions, with the range of 1008.5 to 1009.0 cm^{-1} and 1015.7 to 1017.8 cm^{-1} at temperatures of 22 to 160 ˚C and 170 to 1300 ˚C, respectively. However, between 240 and 400 ˚C there is a gradual increase in peak position, which most likely indicates the transition between bassanite and anhydrite that occurs at 390 ˚C, and is evident by the disappearance of the H_2O peaks at this temperature. Above 390 ˚C the average peak positions slightly fluctuate within the range of 1017.0 to 1017.8 cm^{-1}. The transition between gypsum and bassanite appears to be abrupt, but the transition from bassanite to anhydrite is more gradual. This gradual change in the average peak position could be due to not all the sample reaching the phase at the same time, similar to goethite, except with gypsum there is not a clear and identifiable intermediate stage in between the transitions. The main changes in mass and peak positions correspond to each other, which is to be expected. However, the gradual change in peak position from 240 to 400 ˚C is also apparent in the total change in mass for the same temperature range, which means it might be possible to correlate a specific peak

position to changes in mass (and hence degree of dehydration). Figure 7.2.9 presents the average peak positions and the minimum and maximum peak positions from the ten spectra taken after heating to each temperature. These results show there is more variation in peak positions taken between 170 and 400 ˚C. The four temperatures with the greatest variation in peak position are 150, 230, 380 and 1300 ˚C, with the following differences 0.92, 0.92, 1.32 and 1.39 cm^{-1} respectively, between the minimum and maximum position. Two of the four temperatures, at 150 and 380 ˚C, are 20 ˚C lower than the transition temperature and 1300 ˚C also marks the last temperature step before the sample melted. These large differences in peak positions of a sample may be an indicator of the Raman spectra beginning to record the transition from one phase to another.

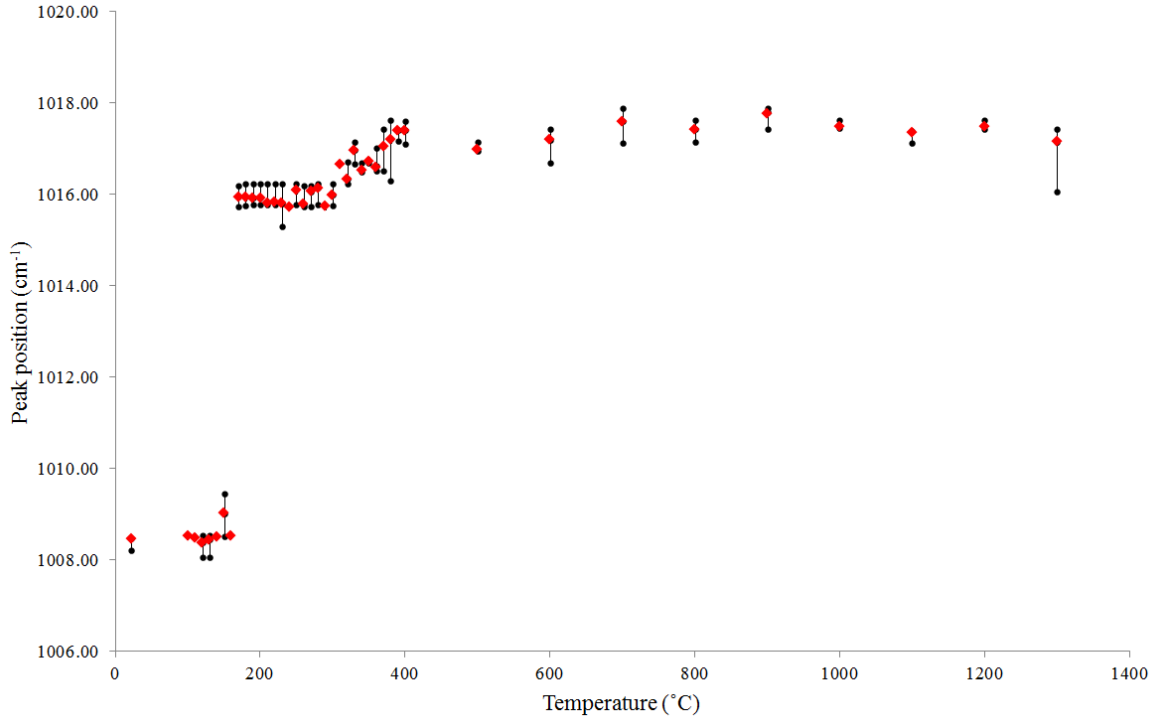

Figure 7.2.9 Averaged peak positions of the SO_4 U1 mode (red) and the minimum and maximum peak positions (black capped lines), taken from the ten spectra taken after heating the sample to each temperature.

The changes in phases (according to the peak positions for SO_4 U1 peaks) appear to generally correspond to loss in mass (Figure 7.2.10). Before the sample begins to show a bassanite spectrum there is very little mass lost from the sample, which may indicate the onset of a change in phase due to loss of water. The larger changes in mass occur when the sample appears to be bassanite, suggesting that sample has not fully formed bassnite. During these larger changes in mass the average peak position of the U1 peak remains at 1015.9 cm^{-1} and when the mass loss is ~19% there is a range of peak positions, between

1015 and 1017 cm^{-1}. The peak position increases as the remaining water is lost and the sample forms anhydrite. The increase in peak position when the sample has lost ~19% of its total mass, might signify the change from bassanite to anhydrite, however, there is fluctuation in the mass that might show some absorption from the atmosphere.

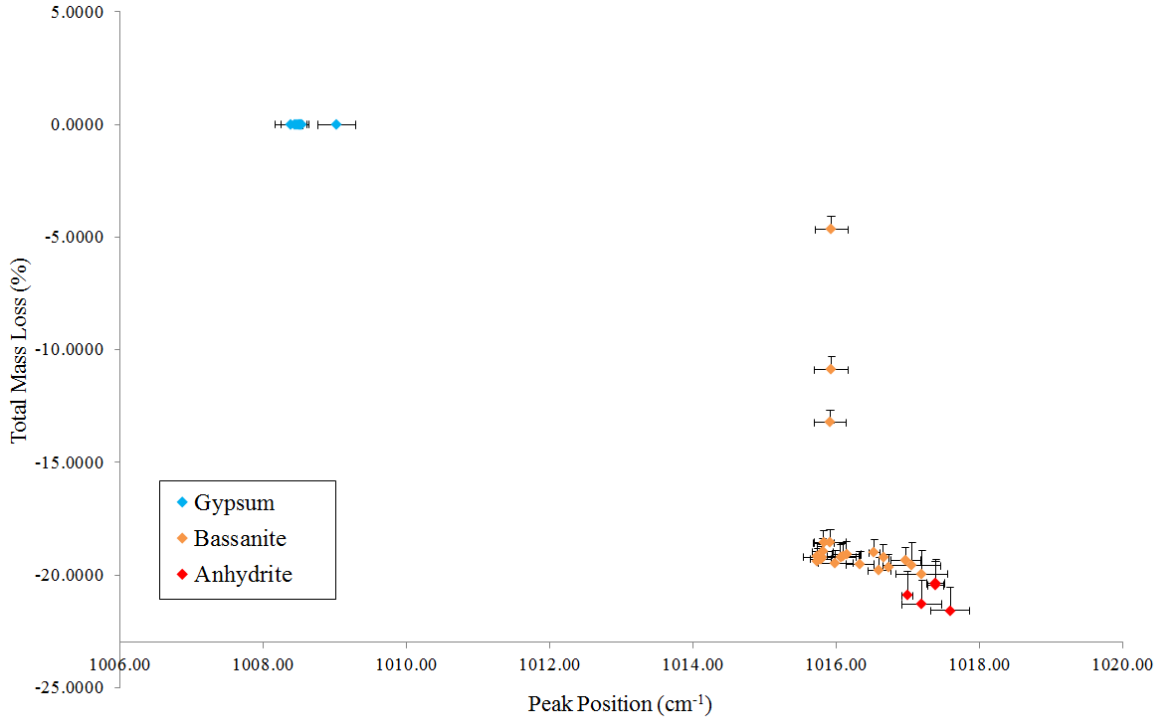

Figure 7.2.10 The total mass lost from gypsum as function of the averaged SO_4 U1 peak position. The colour of the data points represent the dominant mineral phase; gypsum (blue), bassanite (orange) and anhydrite (red). The standard deviation for each temperature (from the absolute data) was calculated to generate the error bars for peak position. Error bars for the mass measurements are described in the mass measurements sub-section of this section (7.2.2 Ex-situ/Mass Loss Experiment).

The U1 average peak widths (Figure 7.2.11) shows a clear distinction in widths from 160 and 170 ˚C, which corresponds to the sample's transition from gypsum to bassanite. There is an overall increase in width between 170 and 360 ˚C, with the maximum width of 6.9 cm^{-1} occurring at 360 ˚C, and a variation of widths ranging between 5.8 and 6.6 cm^{-1}. The increasing average peak widths probably indicate the more gradual loss in H_2O, which is similar to what is seen in the U1 peak positions, although there is more of a fluctuation in widths. The average width begins to increase again from 3.7 to 4.4 cm^{-1} at 900 and 1300 ˚C, respectively, which indicates changes in the crystallinity of the sample are occurring. This change in width corresponds to a decrease in average peak positions, which combined, are signs of changes occurring within the sample.

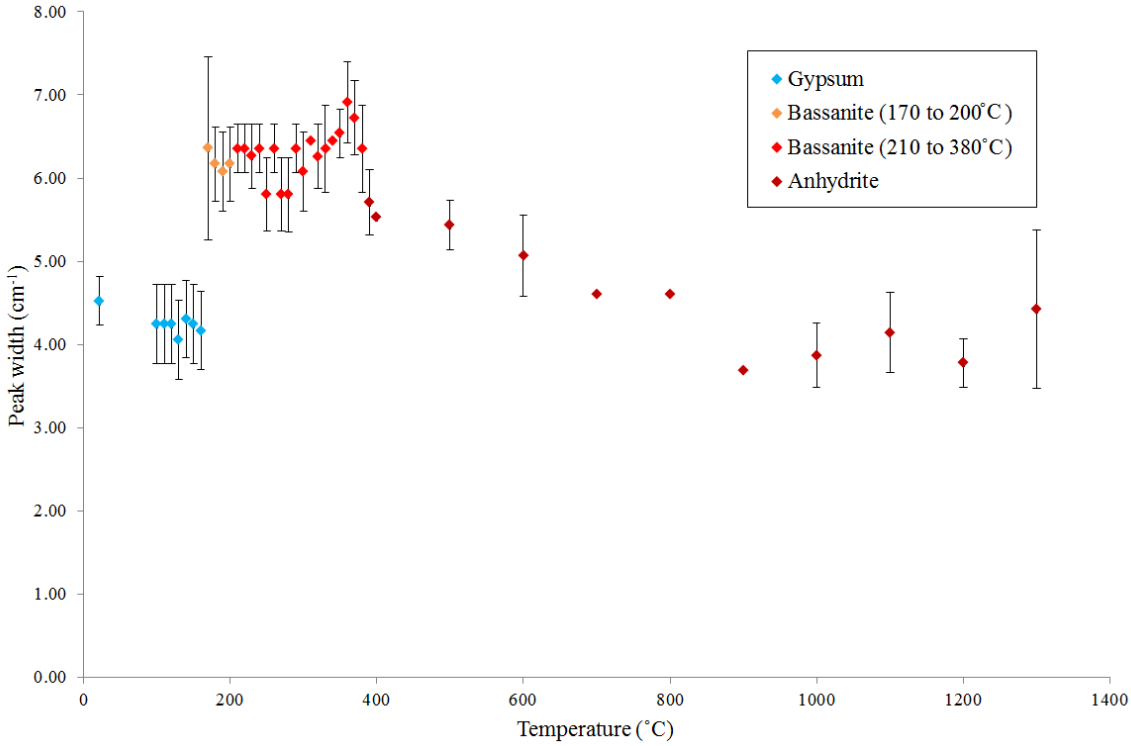

Figure 7.2.11 Average peak widths of U1 from ex-situ Raman/mass loss experiment. Blue points show the sample in a hydrous state, orange and red points represent semi-hydrous material and dark red indicates anhydrous material. The orange points also show the temperatures where the largest decrease in mass occurred. The standard deviation for each temperature (from the absolute data) was calculated to generate the error bars for peak position.

SO_4 U2 Peak Analysis

Average U2 (1) peak positions (Figure 7.2.12) show three dominant regions at 415.0 to 415.2 cm^{-1}, 426.6 to 428.7 cm^{-1} and 416.7 to 419.2 cm^{-1} within the temperature ranges of 22 to 160 ˚C, 170 to 370 ˚C and 380 to 1300 ˚C respectively. These temperature ranges agree with the transitions seen in the H_2O peaks as the sample moves through its various hydrous states. The U2 (2) peak does not show the same clear and abrupt changes in peak positions as seen with U2 (1). Instead there is one abrupt change in peak position between 160 and 170 ˚C and a gradual change in peak position from 290 to 400 ˚C, which marks the transition from bassanite to anhydrite. This gradual change in peak position is similar to that seen in U1, expect the gradual change begins earlier at 240 ˚C and there is more fluctuation in peak position for U1. Surprisingly, a third peak appears between 310 and 380 ˚C with a peak position of 417 cm^{-1}, although this peak is only present in two out of the ten spectra taken at 380 ˚C. This peak could be mistaken for a feature generated by a cosmic ray or an instrumental artefact, but it is present in all ten spectra and in roughly the same position. In addition, it has roughly the same peak position for U2 (1) anhydrite

peaks. The additional peak appears in Raman spectra at the same time as higher fluorescence and stepped spectra are being produced as a result of photo-bleaching (see Chapter IV, Section 4.2.3). This results in the actual peaks being almost hidden within the spectra, however the curve fitting function was able to fit a peak to this new/additional peak. The appearance of this additional peak coincides with relatively larger fluctuations, with peak positions in the range of 426.6 to 428.7 cm^{-1}, occurring in the peak position of U2 (1). Up until 310 ˚C the difference in the maximum and minimum average peak positions was 1.0 cm^{-1} for the temperature range for bassanite. It is believed that spectra taken between 310 and 380 ˚C represents a mixture of bassanite and anhydrite, as this additional peak has approximately the same position as the U2 (1) peak in anhydrite. A gradual decrease in average peak position for both U2 (1) and (2) occurs after 1100 ˚C, as temperatures lower than this, show a general fluctuation of ±0.1 cm^{-1} for U2 (1) and an increase in peak position from 498.6 cm^{-1} at 390 ˚C to 499.3 cm^{-1} at 1000 ˚C for U2 (2).

U2 (1) and (2) peak widths (Figure 7.2.13) show three clear regions representing gypsum, bassanite and anhydrite, at 22 to 160 ˚C, 170 to 370 ˚C and 380 to 1300 ˚C respectively, which again correspond to the transition temperature from the H_2O peaks. The variation in peak widths for the additional peak is much greater than that seen for either U2 (1) or (2), with a maximum width of 37.1 cm^{-1} at 320 ˚C and minimum of 4.3 cm^{-1} at 370 ˚C. U2 (1) and (2) peaks show a general trend of a decrease in the average peak width before an increase in widths for each phase. However, due to the fluctuations in U2 (1) peak widths for bassanite this increase in peak width near a phase transition is not very reliable. U2 (2) shows this trend much clearer, particularly for bassanite, where the increase in peak width gradually increases from 12.9 cm^{-1} at 250 ˚C to 16.1 cm^{-1} at 370 ˚C. Both U2 (1) and (2) show an increase in peak width between 1200 and 1300 ˚C. The decrease and then increase in peak widths show where the crystallinity changes within each of the three phases. After the sample transitions from one phase to the other, the sample becomes more crystalline, before a reduction in crystallinity signifying another transition is about to occur.

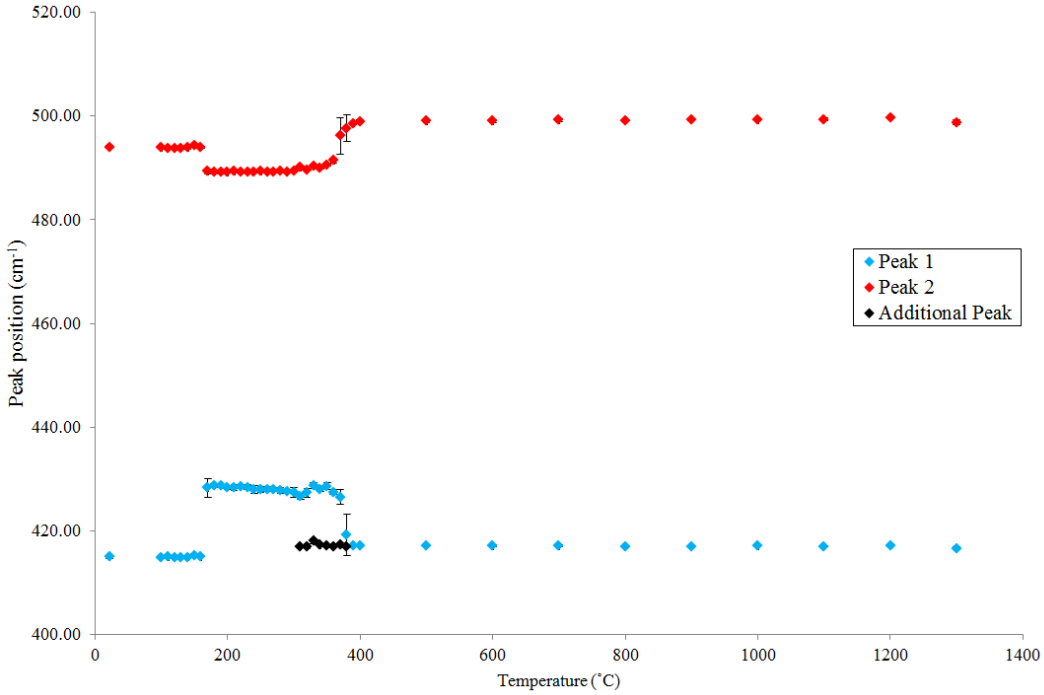

Figure 7.2.12 Average peak positions for U2 (1), (2) and an addition peak. The additional peak is found within the temperature range 310 to 380 ˚C**.** The standard deviation for each temperature (from the absolute data) was calculated to generate the error bars.

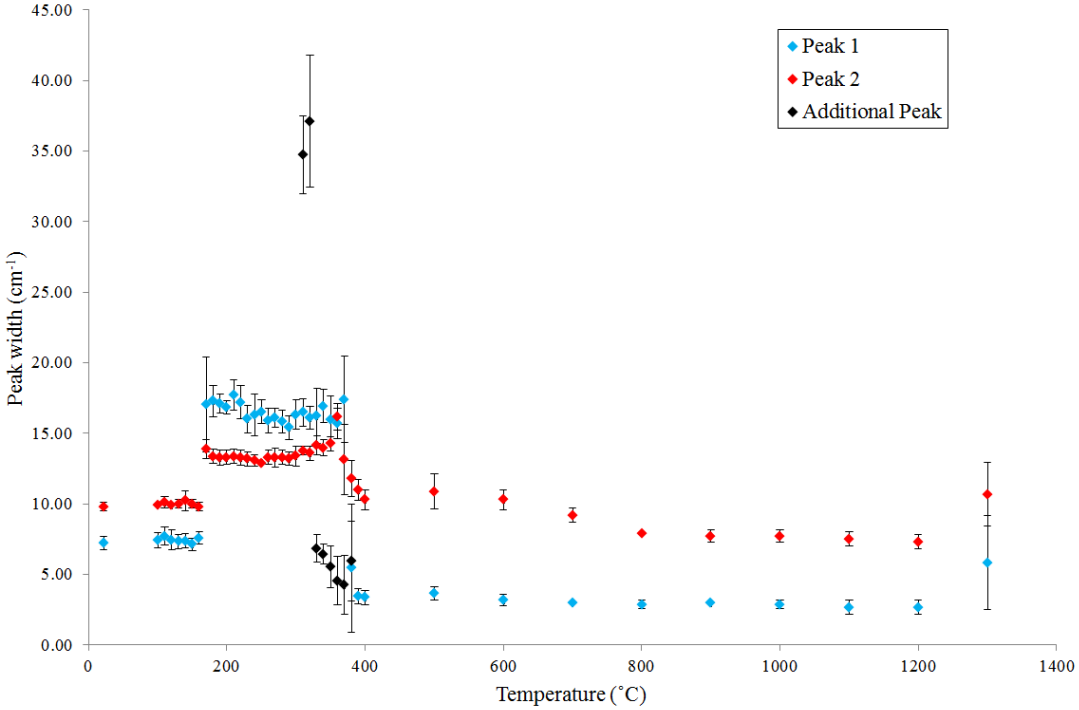

Figure 7.2.13 Average peak widths for U2 (1), (2) and the additional peak. The additional peak is only present between 310 and 380 ˚C. The standard deviation for each temperature (from the absolute data) was calculated to generate the error bars.

Figure 7.2.14 shows the total mass loss as a function of the peak position of SO_4 U2 (2) peak. These results are similar to those presented in Figure 7.2.10 with the larger mass

steps occurring in the bassanite phase. The peak position for these larger changes in mass remains relatively constant, at a peak position of 489 cm^{-1}. When the total mass loss is ~19% there are a range of peak positions, between 489 and 497 cm^{-1}, which corresponds to changes in mass of less than 1%. These slight changes in mass in the bassanite phase most likely correspond to the remaining water being lost as the sample forms anhydrite.

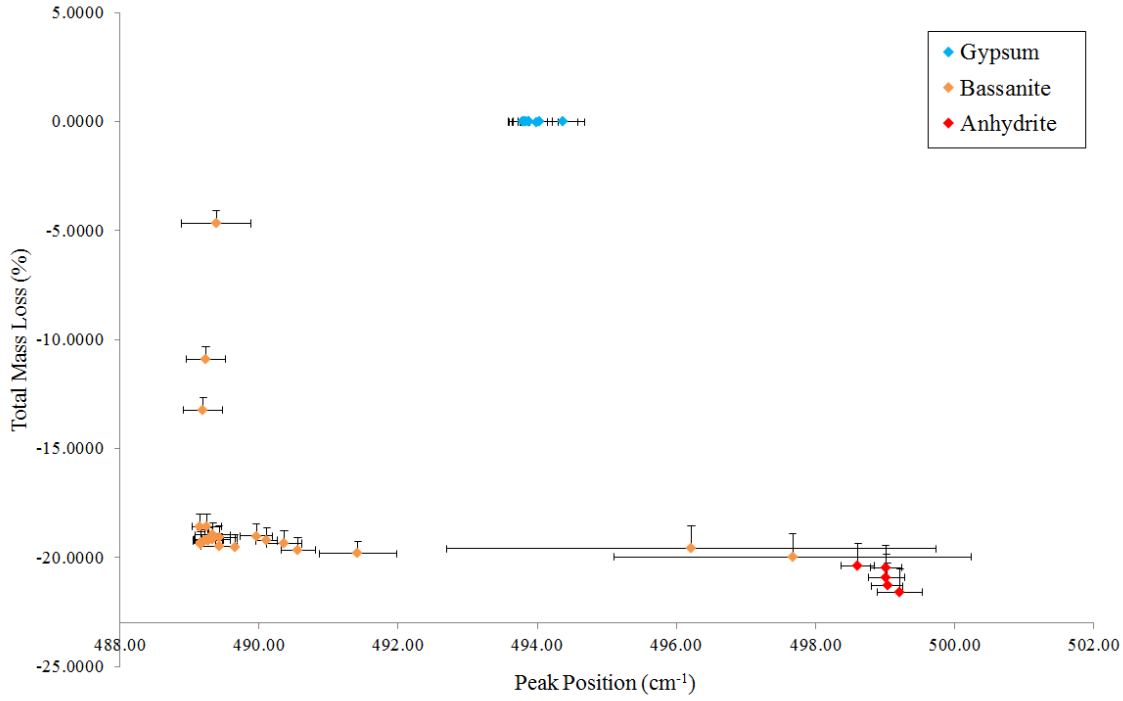

Figure 7.2.14 The total mass lost from gypsum as function of the SO_4 U2 (2) peak position. The colour of the data points represent the dominant mineral phase; gypsum (blue), bassanite (orange) and anhydrite (red). The standard deviation for each temperature (from the absolute data) was calculated to generate the error bars for peak position. Error bars for the mass measurements are described in the mass measurements sub-section of this section (7.2.2 Ex-situ/Mass Loss Experiment).

In five out of the ten spectra taken of gypsum after heating to 1300 ˚C a peak is present at 927.4 cm^{-1}. This peak could be the result of some contamination of the sample, or it could represent changes in the crystal structure from the decomposition of the sample. DSC analysis shows the material forms a liquid-crystal at 1219.1 ˚C.

7.2.1 Discussion

The transition (for changes in Raman spectra, specifically from changes to H_2O modes) temperatures for in-situ and ex-situ experiments do not correspond to each other, similar as the results from the goethite experiments. The gypsum-to-bassanite transition occurs at

150 ˚C for the in-situ experiment, and at 170 ˚C for ex-situ experiments. DSC analysis showed the peak temperature for the gypsum to bassanite transition occurs at 167.2 ˚C, which corresponds to the ex-situ results and is 17 ˚C greater than the temperature determined by in-situ results. Although the transition might have occurred earlier between 100 and 150 ˚C for the in-situ experiment, which would correspond to the onset of the dehydration determined by DSC analysis. The onset of dehydration determined by TGA analysis occurs at 127.2 ˚C, which is in close proximity to the onset temperature determined by DSC analysis. These temperatures correspond to the in-situ transition from gypsum to bassanite, but not with the transition temperature ranges determined by ex-situ results of 160 - 170 ˚C. However, ex-situ mass measurements indicate the onset of mass change occurs earlier, at 130 ˚C, than what is observed in the Raman spectra. Although, gypsum transition experiments using Raman spectroscopy were conducted by Prasad *et al.*, (2001), who determined that the gypsum to bassanite transition occurred around a temperature of 96 °C (or 370 K), which is much lower than the temperatures presented from the in-situ and ex-situ results and those from TGA/DSC analysis. However, this may be due to Prasad *et al.,* (2001) taking the Raman spectra at temperature, instead of the heating and cooling cycling used in these experiments. On the other hand Sirokman (2014) explains that the formation of semi-hydrous materials occurs at 120 ˚C, which would correspond to the temperature range determined by in-situ experiments, but is lower that the temperature found in the ex-situ experiments.

The transition from bassanite to anhydrite again occurs at different temperatures for both the in-situ and ex-situ experiments, at 350 and 390 ˚C, respectively. This maybe a result of differences in the samples; in-situ experiments used a grain 90 × 300 µm and the ex-situ experiment using a sample 2.44 × 2.20 × 6.06 mm. However, both temperatures are much greater that the peak temperature determined by DSC analysis, of 182.3 ˚C, which is believed to mark the transition from bassanite to anhydrite. Both samples appears to melt and decompose after heating to 1400 ˚C, which corresponds to the final change determined by DSC analysis, which shows the onset occurs at 1354.3 ˚C and the peak change at 1469.5 ˚C. Miao *et al.,* (2012) explains that the decomposition temperature of gypsum is over 1350 ˚C, which corresponds to the results presented here. The decomposition temperatures also correspond to the results obtained by van der Merwe *et al.,* (1999), who found decomposition occurs between 1080 and 1300 ˚C. Although, the onset of decomposition occurs at a lower temperature; if ex-situ mass measurements were taken we may have seen a loss in mass before heating to 1400 ˚C, which would be similar

to what was seen with the onset of water loss (described earlier). TGA analysis shows a final change in mass begins a 1299.2 ˚C, which cannot be compared to ex-situ results as the sample broke at 700 ˚C, and no more mass measurements were taken. The differences in the transition temperatures are most likely related to the fact that ex-situ Raman spectra may actually be showing a mixture of hydrous phases, as not all the water is able to escape the sample.

The change in U1 peak positions shows a similar trend for both experiments, whereby there is abrupt change in peak positions from gypsum to bassanite, but a more gradual change in peak position as the ex-situ sample changes from bassanite to anhydrite. However, due to the temperature steps used in the in-situ experiment, there does appear to be a somewhat abrupt change in peak position. Once the sample is anhydrite, the peak position increases to a maximum of 1017.8 cm^{-1} and then decrease in peak position at 1300 ˚C. U1 peak widths do not show similar trends between the in-situ and ex-situ experiments. In-situ results show U1 peak widths increase as the sample transitions from gypsum to bassanite and then decrease until a temperature of 1300 ˚C, where the width increases again. Ex-situ results shows the average peak width decreases, once the sample transitions to bassanite, and then increases again before changing to anhydrite. After turning to anhydrite, the peak width decreases and then increases again at 1300 ˚C, similar to that observed in the in-situ experiment. There is a decrease in peak position for U2 (1) as bassanite changes to anhydrite, for both in-situ and-ex-situ results. There is also a decrease in U2 (2) peak positions before gypsum changes to bassanite and at 1300 ˚C, which, again, occurs in both experiments. As with the U1 peak widths, U2 peak widths in ex-situ experiments show a decrease in width after a change from one phase to another, and then an increase in peak width as the sample is about to change to another phase, unfortunately this trend is not as clear in the in-situ results. The overall changes in peak widths show, close to phase transitions, the peak widths begin to increase, which indicates the sample is becoming less crystalline and less ordered. Once the sample is in a new phase it will begin to increase in crystallinity (the peaks become narrower) with temperature. These changes in peak widths, combined with the changes in peak positions, particularly for U1 and U2 (2) peaks, could be used to help determine the temperature of a sample. Figure 7.2.15 shows there are three separate regions that can be distinguished when peak width is plotted against peak position for U1. Although, there is some overlap with the in-situ results, where two anhydrite points can be found in the region consisting of bassanite, which represent temperatures of 350 and 600 ˚C. 350 ˚C is the transition

temperature for bassanite to anhydrite and 600 ˚C was identified earlier as a spurious peak (Figure 7.2.2). This same trend is seen in the absolute data (Appendix F, Figure F2). However, there is a greater range of gypsum SO_4 U1 peak positions that range between 1008.1 and 1009.4 cm^{-1}. Three distinct regions can be identified representing gypsum, bassanite and anhydrite for U2 (2) peak (Figure 7.2.16), which is similar to the U1 peaks. However, there is a spurious ex-situ bassanite point found in a region that is dominantly anhydrite. This particular point represents 380 ˚C, which is the last temperature where the H_2O peaks can be found. Again, the absolute data (Appendix F, Figure F3) shows the same trend as with the averaged data, with the exception of higher peak widths found for spectra classified as bassanite (up to 18 cm^{-1}) and anhydrite (up to 14.9 cm^{-1}). The overlapping points for both Figure 7.2.15 and 7.2.16 represents temperatures where the transformation of bassanite to anhydrite is occurring, indicating that there might be some difficulty in discriminating between the two phases if just using U1 and U2 (2) peaks.

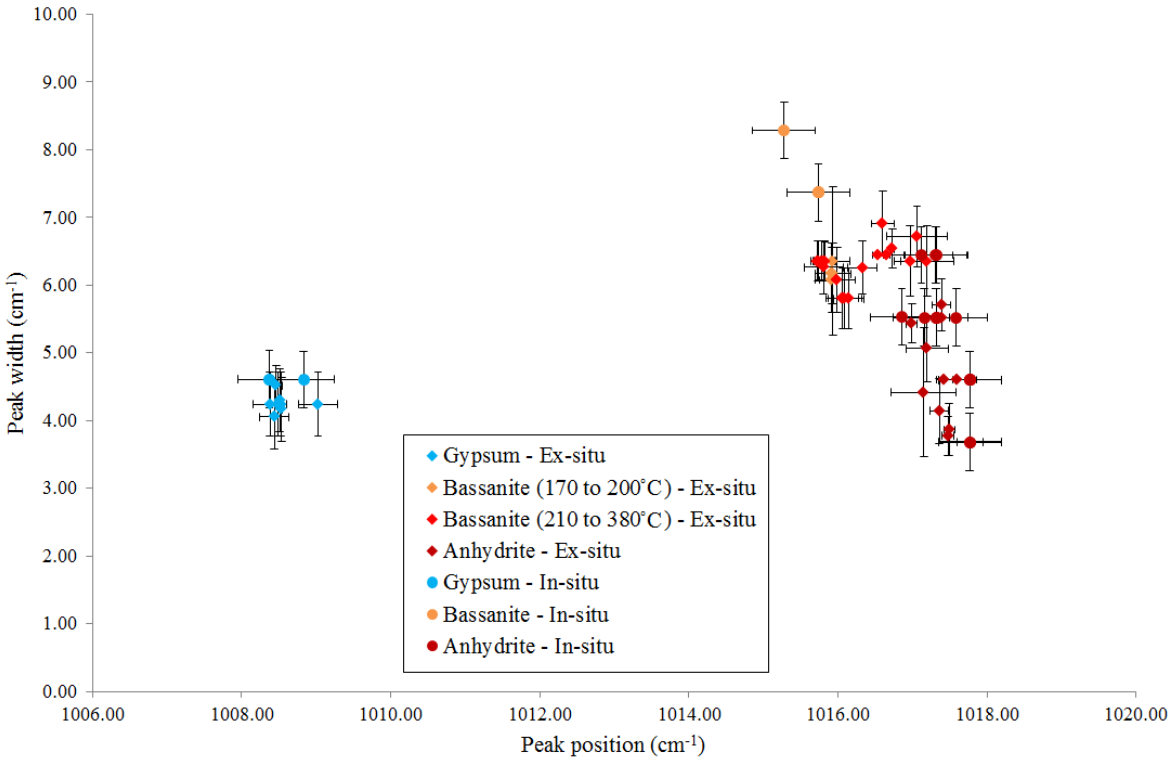

Figure 7.2.15 Peak widths against peak positions for the SO_4 U1 peak, from both in-situ and averaged ex-situ results. The blue points indicate gypsum, orange and light red indicate bassanite and dark red identifies anhydrite. The standard deviation for each temperature (from the absolute data) was calculated to generate the error bars for the averaged ex-situ results. Error bars for in-situ data represent the spectral resolution for the configuration of the Raman spectrometer (0.4 cm^{-1}).

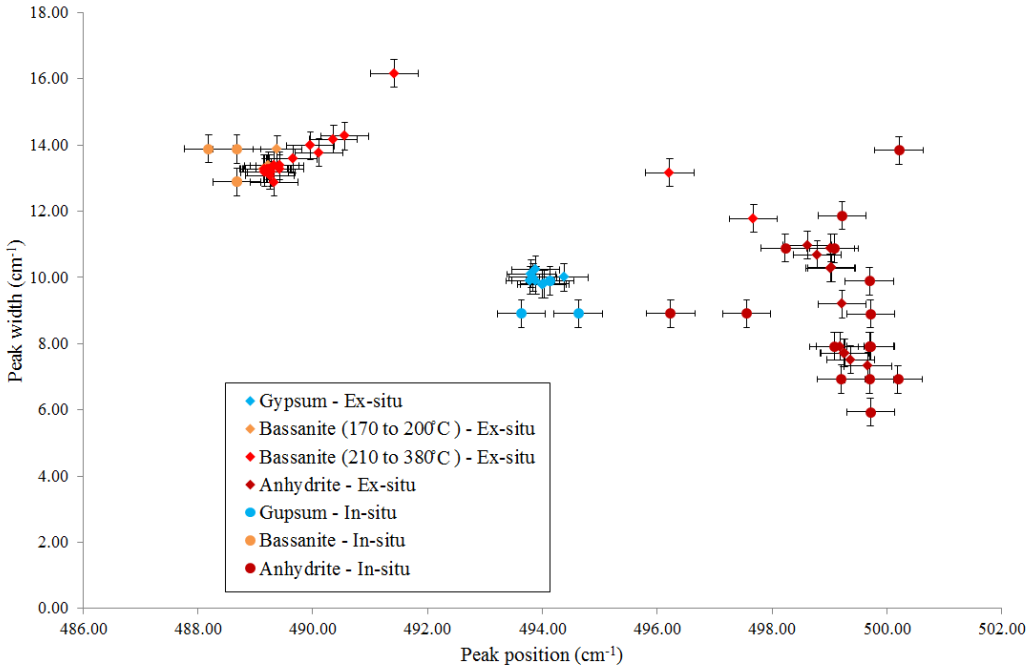

Figure 7.2.16 Peak widths against peak positions for the SO_4 U2 (2) peak, from both in-situ and averaged ex-situ results. The blue points indicate gypsum, orange and light red indicate bassanite and dark red identifies anhydrite. The standard deviation for each temperature (from the absolute data) was calculated to generate the error bars for the averaged ex-situ results. Error bars for in-situ data represent the spectral resolution for the configuration of the Raman spectrometer (0.4 cm^{-1}).

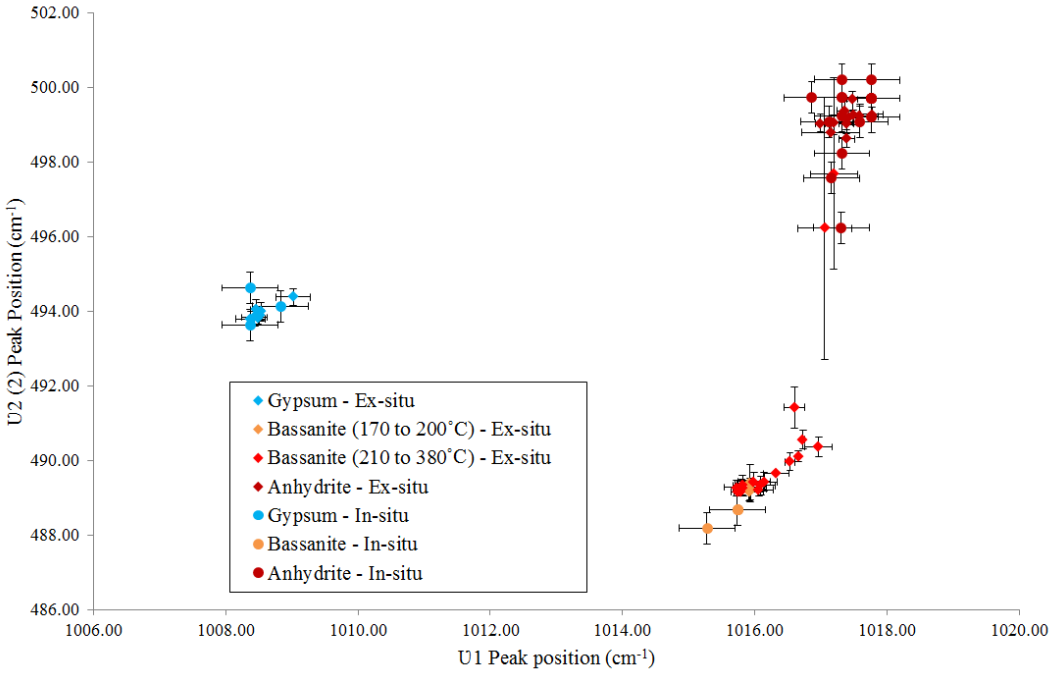

Figure 7.2.17 Graph showing U2 (2) peak positions against U1 peak positions for in-situ and averaged ex-situ heating experiments. Blue points show spectra representing gypsum, orange and light red highlight bassanite and dark red indicate anhydrite. The standard deviation for each temperature (from the absolute data) was calculated to generate the error bars for the averaged ex-situ results. Error bars for in-situ data represent the spectral resolution for the configuration of the Raman spectrometer (0.4 cm^{-1}).

Figure 7.2.17 shows three clear regions, again representing gypsum, bassanite and anhydrite, when U2 (2) peak positions are plotted against U1 peak positions. There is, again, a single bassanite point from the ex-situ results that falls within the anhydrite region, which represents 380 ˚C. The two spurious points found in-between the bassanite and anhydrite regions, representing 1300 ˚C for the anhydrite in-situ point and 370 ˚C for the ex-situ bassanite point, which all corresponds to transitions from bassanite to anhydrite (370 and 380 ˚C) and the desulfurisation of the sample (1300 ˚C). The absolute data for U2 (2) peak positions against U1 peak positions (Appendix F, Figure F4) show a similar trend to what is seen in Figure 7.2.17. There are three clearly distinct regions that correspond to gypsum, bassanite and anhydrite minerals phases. However, there are some bassanite data points found within the anhydrite region, which are again representative of temperatures of 370 to 380 ˚C. These temperatures mark the end of range of temperatures for bassanite, therefore, these points found within the anhydrite region may show the transitioning of the sample from bassanite to anhydrite. This, again, shows H_2O peaks would be required to confidently discern between bassanite and anhydrite phases.

7.3 Chapter Summary

Results from these heating experiments show that the vibration frequencies of specific bonds in the Raman spectra of minerals can be used to determine the maximum temperature experienced by a sample. They also show that peak positions could also be used to determine the amount of water (in %) lost from a sample as a result of heating. However, ex-situ experiments should be repeated to confirm this. The results here are used to assist in understanding the results from the devolatilisation impacts experiments presented in Chapter VIII.

Chapter VIII

Results and Analysis: Impacts

The results presented in this chapter were obtained from impacts experiments using the University of Kent's light gas gun (LGG; see Chapter IV, Section 4.1). Both sets of experiments have used Raman spectroscopy for analysis, as it has the ability to identify different minerals within a single sample and its incorporation on-board the *ExoMars* and *Mars 2020* rovers (Bost *et al.*, 2015; Berlanga *et al.*, 2015; Beegle *et al.*, 2014) have made it ideal for use in these experiments.

Serpentinisation experiments examined whether or not impacts can induce the serpentinisation of olivine - and thus produce methane - when in a mixture of H_2O and CO_2 ices. Previous works that have examined the role impacts can play in the formation of serpentine have focused on large impacts creating hydrothermal systems (Schwenzer *et al.*, 2012a; 2012b; Schwenzer & Kring, 2013). Here, we focus on if an instantaneous reaction can result in the serpentinisation of olivine, similar to work conducted by Furukawa *et al.*, (2011).

Devolatilisation experiments focused on two Mars relevant minerals: goethite and gypsum, to determine if it is possible to detect impact induced devolatilisation, and if Raman measurements of these minerals can be used as a shock barometer. Analysis of these results used the previously presented results obtained from heating experiments (Chapter VII). Impact experiments conducted on $CaSO_4 \cdot 2H_2O$ (Bell & Zolensky, 2011) has shown that shock events can cause noticeable changes in Raman spectra. Here, we also examine if the effects of shock on gypsum and goethite can be used as shock barometers, and see if it is possible to determine the degree of devolatilistion from the Raman spectra of shocked material.

8.1 Serpentinisation Experiments

8.1.1 Targets

These serpentinisation experiments used an olivine, H_2O ice and CO_2 ice mixture as targets, which were then impacted at velocities between 3.90 and 5.82 km s^{-1} with a 2 mm (diameter) stainless steel sphere (for more details see Chapter V, Section 5.3).

Impacted material was collected as soon as the target chamber had returned to atmospheric pressure. Olivine grains were separated from the mixture of ices by filtering, which allowed H_2O to drain away as it melted, and the sublimation of CO_2 ice to occur. Each segment of the Ejecta Capture System (ECS) and the control were prepared for analysis using separate filtering systems. Once the olivine grains were completely dry they were then analysed using the Horiba LabRam-HR Raman spectrometer at the University of Kent.

Determination of whether or not serpentinisation had occurred focused on the hydration of olivine and the presence (or absence) of a hydroxyl peak. The hydroxyl stretch in Raman spectra can be found between 3200 and 4000 cm^{-1} (Socrates, 2001) and the hydroxyl peak for serpentine is between 3600 and 3740 cm^{-1}. The presence of a peak in this region indicates that hydration of the olivine has occurred. The presence of talc in the sample may have also be an indication that serpentinisation had taken place. Serpentine can form talc in the presence of CO_2, through either regional or contact metamorphism or low grade metamorphism and hydrothermal alteration (Deer *et al.*, 1992). However, analysis of the grains prior to the experiment showed traces of actinolite and talc, in the form of small inclusions in the grains. The presence of talc prior to the impact meant it would be difficult to determine if any talc detected had been the result of the impact. A mixture of compounds, or in this case minerals, will result in a mixture of peaks from both minerals in the Raman spectrum. It was therefore important to identify peaks found between 150 and 1000 cm^{-1} to assist in verifying that any hydration detected was the result of serpentine formation, and not due to the presence of talc or actinolite.

Raman spectra of fifty grains (where possible) were taken from the samples collected from the ESC and control for each velocity. Spectra was taken using a 473 nm laser at 10% of the total laser power, a 600 g/mm grating, ×10 objective and acquisition

parameters of 15 accumulations for 2 seconds for shot G220313#1 and 10 accumulations of 2 seconds for the remaining shots.

Table 8.1.1 Results from serpentinisation impact shot program.

Shot I.D.	Velocity (kms^{-1})	Number of potential hydrated grains detected					Number of confirmed hydrated olivine grains detected*				
		Control	ECS 1	ESC 2	ESC 3	ESC 4	Control	ECS 1	ESC 2	ESC 3	ESC 4
G220313#1	3.90	0	1	3	1	3	0	0	0	0	0
G240413#1	4.97	2	6	9	0	2	0	0	0	0	0
G100513#2	5.52	5	6	6	6	4	0	0	2	0	0
G230513#1	5.82	4	8	4	5	0	0	0	0	0	0

*Grains here have a confirmed hydration peak between 3690 and 3710 cm^{-1}, the grain is olivine and the peak has not been attributed to the presence of talc or actinolite.
N.B. Only 25 random grains were selected for G220313#1 as the amount of control sample did not allow for 50 using the random sampling method used.

Table 8.1.1 presents the number of grains that showed the presence of hydration features between 3200 and 4000 cm^{-1}, and the number of those grains that were attributed to the hydration of olivine, which would indicate serpentinisation had occurred. Raman spectra with a peak within the OH region were first identified, before further scrutiny confirmed if this hydration was the result of the serpentinisation of olivine. To confidently verify this three criteria needed to be met: 1) The random grains analysed needed to be identified as olivine, which was through the presence of a distinctive doublet peak at 820 and 850 cm^{-1}, which Keubler *et al.*, (2006) identify as a result of the internal stretching of SiO_4 bonds in olivine. 2) The hydration peak needed to be within the range of 3600 to 3740 cm^{-1}. 3) the hydration could not be attributed to talc or actinolite (Chapter VI, Section 6.4). These results show that there is only one instance were hydrated olivine grains were detected, at a velocity of 5.52 km s^{-1}. However, only two grains were detected (1% of the total shocked grains for this shot), making it difficult to confidently say that impacts can induce serpentinisation. But this result does suggest it might be possible, as any previous hydration was removed prior to impact (by heating the grains to 600 ˚C), indicating that these two occurrences were a result of the impact.

Peak Shock Pressures and Temperatures

The approximate peak shock pressures were calculated using several methods (Chapter III explains this in more detail): 1) Rankine-Hugoniot plots (Figure 8.1.1), 2) the planar impact approximation (PIA), and 3) Autodyn simulations. Autodyn was also used to determine the peak temperatures experienced on impact. Laboratory impact experiments used stainless steel-420 ball bearings (from Spheric Trafalgar Ltd) as projectiles, but material data for this specific alloy was not available and so stainless steel 18C18N10T, with shock wave velocity and particle velocity data (used to find the material constants) obtained from the *Shockwave database* (http://www.ihed.ras.ru/rusbank/), was used as it had the closest composition to stainless steel-420. Unconsolidated and compacted targets, made up of H_2O ice, CO_2 ice and olivine, were used in laboratory experiments, which would have been particularly difficult to mimic in Autodyn simulations. As such, simulations used a simple Langrangian mesh to represent the target materials (olivine and H_2O ice) and SPH particles made up the projectile of steel-1006, which had the closest density, material constants ("c" and "S" values) to stainless steel-406. All three materials used a simple Shock Equation-of-State (EoS) and both target materials used a simple von Mises strength model, whereas stainless-steel uses a Johnson-Cook strength model (Johnson & Cook, 1983). Table 8.1.2 shows the peak pressures experienced upon impact for both olivine and H_2O ice targets using all three methods.

Table 8.1.2 Peak Pressure upon impact versus projectile velocity as calculated using three different methods (see text).

Shot I.D.	Projectile velocity (kms^{-1})	H_2O ice Peak pressure (GPa)			Olivine Peak pressure (GPa)		
		PIA	Hugoniot	Autodyn	PIA	Hugoniot	Autodyn
G220313#1	3.90	21.89	22.13	48.21	60.98	58.65	63.91
G240413#1	4.97	32.69	32.20	78.65	82.98	82.02	81.61
G100513#2	5.52	38.98	37.93	98.24	95.16	94.64	94.42
G230513#1	5.82	42.61	44.11	109.69	102.06	101.19	100.12

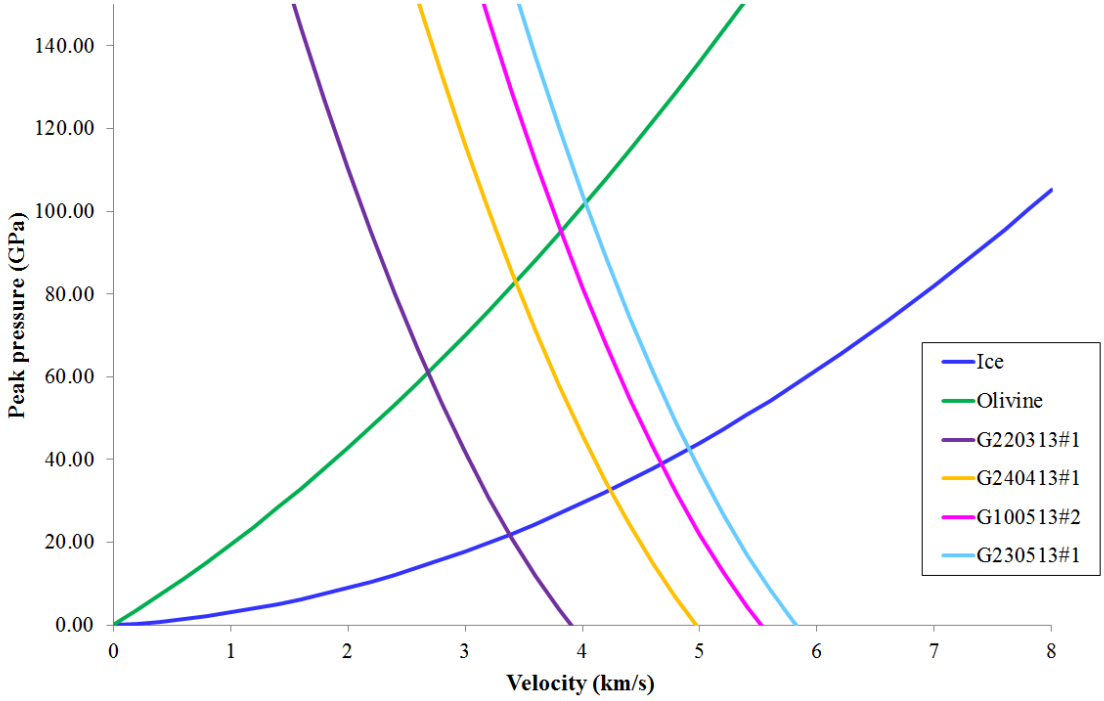

Figure 8.1.1 Hugoniot plots for H_2O ice (blue line) and olivine (green line), and the reverse Hugoniot plots for stainless steel at velocities of 3.90, 4.97, 5.52 and 5.82 km s^{-1} (purple, yellow, pink and light blue lines, respectively). The intersection between the Hugoniot plots and the reverse Hugoniot plots show the peak pressure upon impact (which are given in Table 8.1.2).

Previous studies (Vance *et al.*, 2007; Seyfried *et al.*, 2007; Alt & Shanks, 1998) have suggested that the serpentinisation occurs at temperatures of ~20 to 430 ˚C and at pressures in the range of 10 to 200 MPa. Furukawa *et al.*, (2011) detected serpentine on the surface of olivine grains in shock experiments, and believed it was the result of water becoming supercritical, which would have had incipient pressures and temperatures of 22.06 MPa and 373.95 ˚C (Pioro & Mokry, 2011), however, it is unclear as to what the maximum pressure and temperature would be. The critical pressure and temperature for supercritical water falls within the temperature and pressure ranges determined by Vance *et al.*, (2007), Seyfried *et al.*, (2007) and Alt & Shanks, (1998). However, Hyndman & Peacock have suggested that serpentinisation can occur at 400 ˚C and a pressure of 1 GPa for forsterite. Therefore, a range of 22.06 MPa to 1.0 GPa for pressure, and 373.95 to 430 ˚C for temperature will be used to identify the conditions for the serpentinisation of olivine to occur. The peak pressures calculated for both materials are much greater than the pressure range of 22.06 MPa to 1 GPa. The high peak pressures are due to the initial impact velocities ranging between 3.90 and 5.82 km s^{-1}. High velocities were chosen as the average impact velocity in the asteroid belt is 5 km s^{-1} (Bottke *et al.*, 1994) and is also the

approximate escape velocity of Mars, and therefore would be more representative of meteorite impact velocities for Mars. Using the PIA calculation it was determined that a velocity of 0.5 km s^{-1} would be required to obtain a peak shock pressure of 1.0 GPa, at the point of impact when using a stainless steel projectile and a H_2O ice target, which is the upper pressure for serpentinisation to occur as suggested by Hyndman & Peacock (2003). Although the peak pressures and temperatures at the initial impact point may be too great for impact induced serpentinisation to occur, it could be that at some distance from this point the conditions would be conducive for serpentinisation. Tables 8.1.3 and 8.1.4 shows the peak pressures and temperatures experienced by the H_2O target at varying distances from the centre of the target (the point of contact for the projectile and target upon impact). The pressures provided here are representative of the initial pressure experienced before the target crumbled. Pressure and temperature readings were taking at the front and rear of the target (Figure 8.1.2), from the centre of the target outwards. Autodyn simulations show that the pressure required for supercritical H_2O occurs between 3.03 and 4.63 mm away from the centre at the front of the target. At the rear of the target the critical pressure occurs at approximately 8.43 mm from the centre of the target. However, the temperature at the critical point is only achieved at 0.05 mm from the centre of the target at impact velocities of 3.90, 4.97 and 5.52 km s^{-1}, and up to a distance of 0.85 mm at 5.82 km s^{-1}, determined from the temperatures estimated from pressure. However, the temperatures generated by Autodyn suggest that temperatures greater than 373.95 ˚C occur up to 0.85 mm from the centre of the target for all velocities.

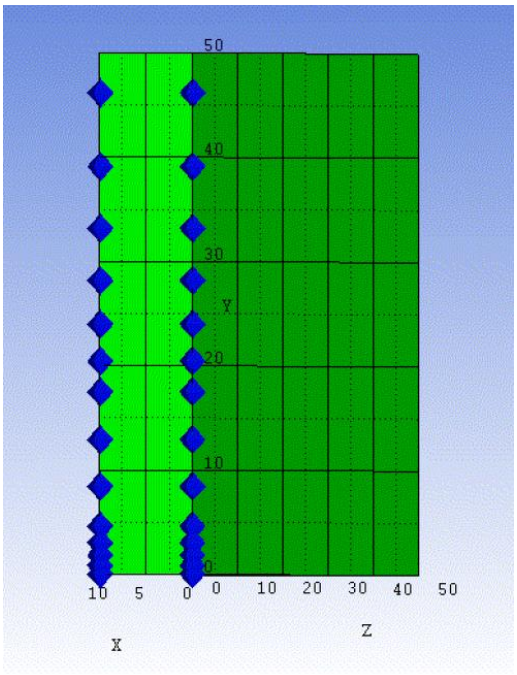

Figure 8.1.2 Gauge locations (blue) at the front and rear of the targets used in H_2O ice and olivine Autodyn simulations. The simulations are modelled in 3D and is shown here as ¼ of the actual size. The centre of the target is located at 0,0,0.

Autodyn simulations show that a crater approximately 10 mm in diameter would form for each of the four shots. This indicates that if supercritical water were to form here, it would have been formed within the crater and would most likely have been detected in sections 3 or 4 of the ECS, as sections 3 and 4 of the ECS collects material being ejected from a lower ejection angle (where 0˚ is along the projectile path). Raman results show that only two grains identified as potential grains that had possibly undergone serpentinisation. The low occurrence of hydrated grains does not necessarily indicate that instantaneous serpentinisation does not occur. It is possible that serpentinisation did occur, but was not detected as a very small amount of serpentine was formed. In these experiments if serpentinisation did occur, it would have formed within 10 mm of the point of impact, meaning a small number of grains would have undergone serpentinisation. Therefore, it is possible that this small number of grains were lost within a mixture of grains that had not experienced serpentinisation. Lafay *et al.,* (2012) and Furukawa *et al.,* (2011) have shown that serpentine crystals would form on the surface of grains. Therefore, it might be possible that any serpentine formed may have been destroyed/lost as grains were ejected or during the filtering process. The temperature of olivine after impact may also effect whether or not serpentine can be detected, as was shown in Chapter V, Section 5.3, heating serpentine to 600 ˚C will result in olivine and H_2O being formed. However, the temperatures experienced in these impacts may not be experienced for a sufficient length of time for any serpentine to convert back to olivine.

The horizontal nature of the LGG meant that the targets had to be mounted horizontally, which means that it is difficult to identify the original location of the grains after being impacted. If it was possible to collecte olivine grains from within an impact crater they might show some signs of serpentinisation. However, this would require the target to be impacted at either a very shallow angle, or the use of a vertical LGG. Doing this would prevent the target from crumbling upon impact and enable the collection from material within the crater itself.

Table 8.1.3 Autodyn calculated pressures experienced by H_2O ice target at varying distances from the centre of the target.

	Distance (mm)	Pressure (GPa)			
		3.90 (km s^{-1})	4.97 (km s^{-1})	5.52 (km s^{-1})	5.82 (km s^{-1})
Front of target	0.0	48.21	78.65	98.24	109.69
	0.85	6.83	25.11	35.45	37.70
	1.85	0.28	0.37	0.39	0.42
	3.03	0.06	0.08	0.09	0.11
	4.63	0.02	0.03	0.09	0.01
	8.43	<0.01	-	-	-
	12.9	<0.01	-	-	-
	50.0	<0.01	-	-	-
Rear of target	0.0	1.77	2.92	5.30	3.88
	0.85	1.78	2.87	4.91	4.08
	1.85	1.63	2.45	4.00	3.48
	3.03	1.17	1.77	2.28	2.22
	4.63	0.41	0.58	0.62	0.71
	8.43	0.05	0.06	0.06	0.07
	12.9	<0.01	-	-	-
	50.0	<0.01	-	-	-

Table 8.1.4 Estimated temperatures experience by H_2O ice, from Autodyn simulations.

	Distance (mm)	Temperature (˚C)							
		3.90 (km s^{-1})		4.97 (km s^{-1})		5.52 (km s^{-1})		5.82 (km s^{-1})	
		From pressure*	Autodyn	From pressure*	Autodyn	From pressure*	Autodyn	From pressure*	Autodyn
Front of target	0.0	900 - 1500	11780.9	>1500	20313.9	>2500	24797.9	>2500	27514.9
	0.85	100	509.8	170-275	1323.7	300	2038.4	300-900	2398.1
	1.85	<100	<50.0	<100	<50.0	<100	<50.0	<100	<50.0
	3.03	<100	<50.0	<100	<50.0	<100	<50.0	<100	<50.0
Rear of target	0.0	<100	65.3	<100	123.4	100	290.0	<100	195.8
	0.85	<100	63.5	<100	114.0	<100	220.0	<100	170.5
	1.85	<100	53.3	<100	85.2	<100	135.2	<100	129.3
	3.03	<100	<50.0	<100	50.8	<100	62.5	<100	56.5
	4.63	<100	<50.0	<100	<50.0	<100	<50.0	<100	<50.0
	8.43	<100	<50.0	<100	<50.0	<100	<50.0	<100	<50.0

*Temperatures are estimated from the pressures given in Table 8.1.3 using French (1998) and reference therein.

8.2.2 Projectiles

Targets impacted with olivine and H_2O ice projectiles were also analysed using the Raman spectrometer to detect for hydration of the olivine by the appearance of a hydroxyl peak found between 3629 and 3710 cm^{-1}.

The shot identified as G140813#3 used a mixture of three Al alloy plates; the first plate had a thickness of 3 mm and plates two and three had a thickness of 1.5 mm, with a

projectile made of H_2O ice and olivine grains contained within a hollow "sabot". The projectile punched through plate 1 (3 mm thick) and plate 2 (1.5 mm thick), but not plate 3 (1.5 mm thick). Craters appear on plates 2 and 3, but mineral residue only appears to be within craters on plate 3. Craters on plate 2 appear to have been generated mostly from the ejecta of plate 1. Raman spectra taken from crater residues on plate 3 (Figure 8.1.3a and Appendix G, Figure G1) did not show any evidence of olivine hydration, and thus serpentinisation, as a result of the impact.

Shot G220813#1 used a solid projectile made from H_2O ice and olivine grains and was impacted onto a stainless steel plate positioned at the end of the blast tank (Chapter IV, Section 4.1.). Craters on the target plate appear to be no larger than 1 mm in diameter (Figure 8.1.3b). There are four larger craters, between 2.5 and 3.5mm, which were made from pieces of the burst disc that broke off as a result of the burst disc rupturing. Raman spectra were taken from multiple craters and, again, showed no evidence of serpentinisation having occurred.

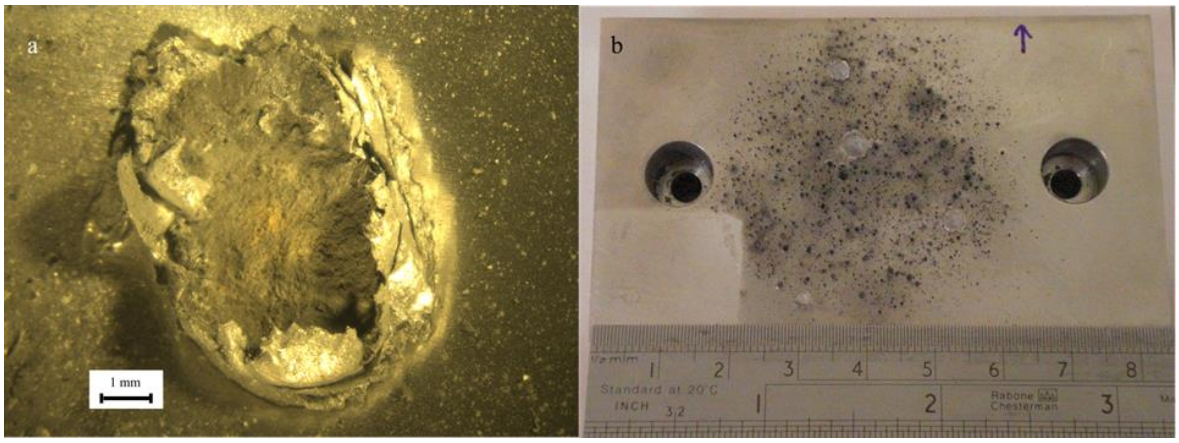

Figure 8.1.3 a) An example of a crater generated from G140813#3, where olivine and H_2O ice are inside a sabot. b) Craters generated from olivine and H_2O ice projectile (G220813#1). The four larger craters are fragments from the burst disc.

Tables 8.1.5 and 8.1.6 shows the peak pressures and estimated impact temperatures experienced when impacting the targets. Pressures determined from Autodyn simulations are much greater than those determined by PIA calculations and Hugoniot plots. This could be a result of the H_2O ice and olivine being contained within a sabot, which cannot be accounted for in PIA calculations or Hugoniot plots. However, it could also be a result of the SPH solver being used in Autodyn simulation. When using SPH particles the spatial relationship between individual nodes to their neighbouring nodes is ignored, as upon

impact material can become highly distorted and entangled. Instead the SPH particles act as a fluid and when calculating variables, in this case pressure, a kernel approximation is used that examines the distribution of nodes in a given area (Hayhurst & Clegg, 1997). So, the value for a given parameter is based on the density of nodes in a defined area, which means compression will play a large role when determining node characteristics, like pressure and temperatures.

The impact peak pressures for H_2O ice were greater than the pressure range, of 22.06 MPa to 1.0 GPa, determined for serpentinisation to occur. But we are uncertain of the upper limit for the formation of supercritical water. The temperatures determined from the pressures are too low and would indicate that supercritical water would not have formed, even if these higher pressures would allow the formation of supercritical to occur. Although, the temperatures from Autodyn are much higher, but these temperatures may have been affected by the manner in which the SPH solver calculates the temperature (as explained earlier). If serpentinisation did occur as the ice impacted the target, the subsequent impact of olivine may have destroyed any serpentine that may have formed.

Table 8.15 Peak pressures experienced by H_2O ice and olivine projectiles.

Shot I.D.	**Plate**	**Initial Projectile velocity (kms^{-1})**	**H_2O ice pressure (GPa)**			**Olivine Peak pressure (GPa)**		
			PIA	Hugoniot	Autodyn	PIA	Hugoniot	Autodyn
G140813#3	1	2.90	10.88	9.86	25.97	28.99	27.45	37.25
	2*	-	15.87	14.45	33.83	45.02	44.32	54.01
	3*	-	17.29	15.90	35.45	50.70	49.74	58.25
G220813#1	-	2.37	9.85	7.65	9.26	33.46	36.22	12.92

*Pressures shown are the total peak pressures experienced by H_2O ice and olivine when impacting each plate.

Table 8.1.6 Estimated temperatures experienced by H_2O ice and olivine projectiles.

Shot I.D.	**Plate**	**Initial Projectile velocity (kms^{-1})**	**H_2O ice Temperature (˚C)**		**Olivine Temperature (˚C)**	
			From pressure*	Autodyn	From pressure*	Autodyn
G140813#3	1	2.90	100	1630.45	170-275	697.71
	2	-	150	2216.15	900	862.15
	3	-	150	2323.45	900-1500	899.45
G220813#1	-	2.37	100	1552.85	300-900	354.93

* Estimated post shock temperatures determined from French (1998) and references therein, using the peak pressures calculated from PIA calculation.

8.2 Devolatilistion Experiments

Raman spectra taken from impact residues and mineral targets were analysed in the same fashion as Raman spectra from the heating experiments (detailed in Chapter VII). Using Horiba's *Labspec* 5 software, baseline correction was carried using an 8th degree polynomial, and a Gaussian-Lorentzian peak fitting function was used to determine peak position, peak width and peak intensity. The results from the heating experiments (Chapter VII) have been used here to assist with the analysis of shot data, and to help identify the effects shock pressure had on the mineral samples.

Autodyn simulations were carried out to determine the peak pressures and temperatures for all impact experiments. Gauges were placed on either the projectile, or the target, to record various variables throughout the simulation. The variables of interest were: velocity along the *x*-axis (specifically for goethite projectile simulations), pressure and temperature. Mineral projectiles had gauges placed at the front and rear of the projectiles, which would show any variation in pressure and temperature experienced by the different areas of the projectile (Figure 8.2.1). Similarly, gauges were placed from the centre of mineral target outwards to record the pressure and temperatures experienced throughout the target.

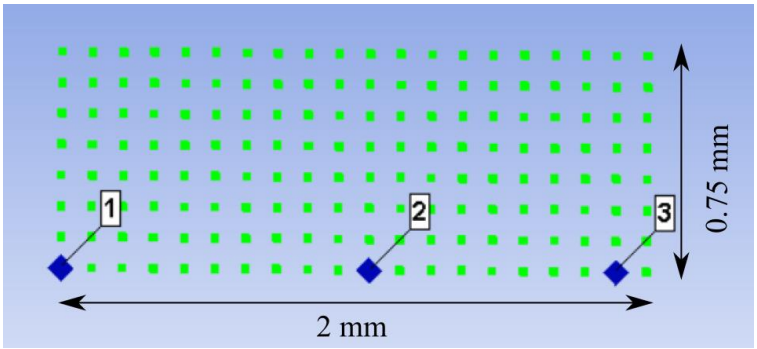

Figure 8.2.1 A 3D example of a projectile in Autodyn. The blue markers represent the gauges placed on the projectile to record pressure and temperature data.

8.2.1 Goethite Projectiles

Goethite projectiles were fired at targets composed of at least two plates, this set-up also meant material had experienced two shock events, and meant material would have experienced higher impact pressures. The first shock event would occur upon impacting the first plate, and the second shock taking place when the remaining material impacted the witness plate, with the exception of G241013#1 which used three plates.

Examination of the target plates (Appendix H, Figures H1 to H9) showed that in some cases craters were formed on both plates, which meant both sets of plates could be analysed and compared. Craters on the first plate (referred to as plate 1) were most likely formed from fragments that came off the main projectile as it travelled down the LGG, and it is assumed they were travelling at the same velocity. Craters from the plates showed a residue in the bottom of craters, which was dark red/brown in colour. Raman spectra were taken from craters on the plates using a 633 nm laser, 10% of laser power, a grating of 600 g/mm and ×50 microscope objective (the acquisition time and number of accumulations were varied to obtain a satisfactory spectrum). The number of spectra taken for each crater and plate varied depending on the size of the craters and number of craters available, with some impacts repeated to obtain more data.

Impact Pressures and Temperatures

Pressures were again determined using the PIA, Hugoniot plots and Autodyn simulations, and temperatures were estimated by Autodyn and from peak pressures. However, there is slightly more uncertainty in the parameters for goethite, particularly for the strength model used in Autodyn, as they were not found in the literature. It was decided that hematite values would be used for the missing parameters. The peak pressures for impacts on the witness plates (the last plate) were calculated using the velocities determined by Autodyn. Goethite projectile simulations were designed to replicate the exact setup of the laboratory experiments. To achieve this, plate 1 was made of both a lagrangian mesh and a central section made up of SPH particles, which are joined together. The inclusion of the SPH section meant the resulting debris cloud produced was more realistic (Hayhurst & Clegg, 1997; unpublished work by K. Styles, 2013). The simulation for shot I.D. G241013#1, with a velocity 5.13 km s^{-1}, had two of these plates, but the witness plates for all shots were made using a lagrangian mesh only. The material properties for target plates used aluminium 6061-T6, obtained from the Autodyn library, which used a Puff EoS and von Mises strength model. SPH solver was used to create the projectile, as it is believed this solver would be able to manage the compression of the projectile better than a lagrangian solver, which would have become highly distorted and entangled on impact.

Simulations showed some variation in the secondary velocities of the projectile as it travelled between the front plates and witness plates (Figure 8.2.2), particularly for shot G121213#2, which has an initial velocity of 1.363 km s^{-1}. A variation of 0.27 km s^{-1} was

found for G1212113#2 (1.363 km s^{-1}), but the remaining shots showed much smaller variations of -0.05 to +0.03 km s^{-1}. This relatively large change in velocity seen for G121213#2 (1.363 km^{-1}) is peculiar, as there were no additional forces added to the simulation that would have resulted in a change in velocity. Regardless, velocities used in the PIA and Hugoniot calculations were taken just prior to the impacting the witness plate in these simulations.

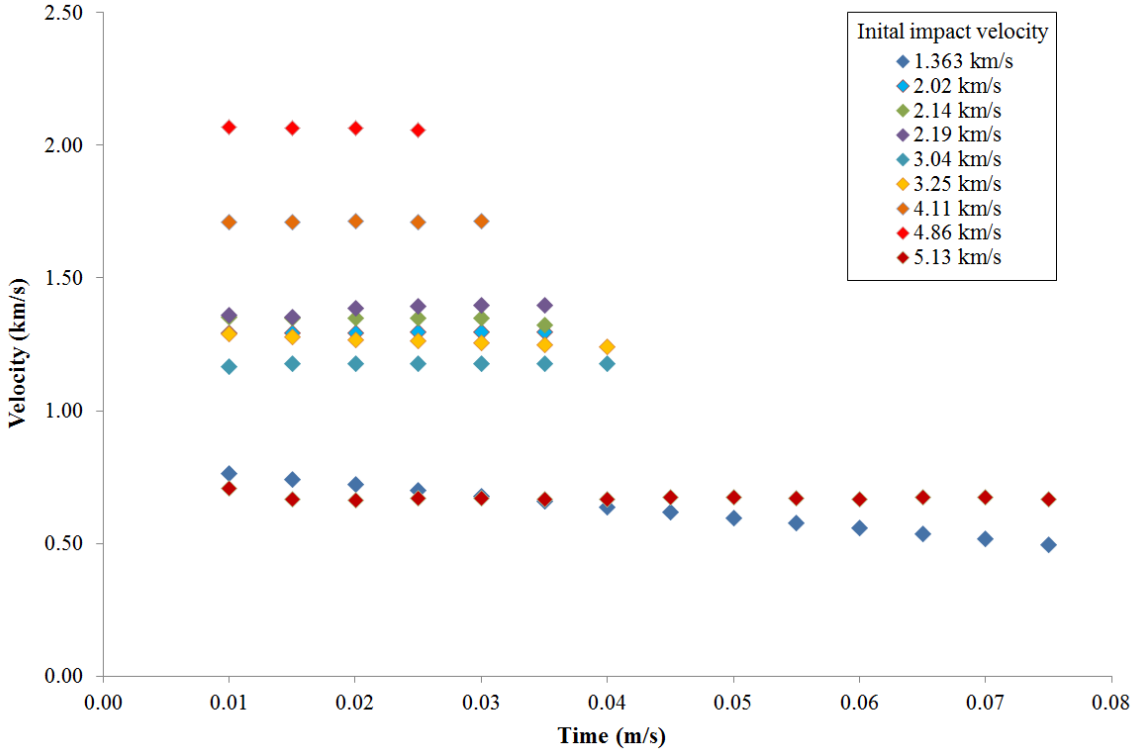

Figure 8.2.2 Autodyn modelled velocities of projectile material taken as it travelled between plate 1 and plate 2. In the case of 5.13 kms^{-1} values were taken between plate 2 and the witness plate.

Table 8.2.1 Goethite projectile peak impact pressures from Autodyn simulations.

Shot I.D.	**Velocity (km s^{-1})**	**Peak Pressure (GPa)**		
		Front of Projectile	Target plate	Average
G121213#2	1.363	18.31	10.06	14.18
G050215#1	2.02	28.71	17.59	23.15
G090114#1	2.14	30.77	19.08	24.93
G260215#2	2.19	31.65	19.71	25.68
G260215#1	3.04	48.26	30.55	39.41
G061113#2	3.25	53.41	33.73	43.57
G111013#2	4.11	74.34	47.41	60.87
G180215#1	4.86	95.43	60.81	78.12
G241013#1	5.13	103.32	67.25	85.29

Table 8.2.1 shows there is a large variation (40 GPa) between Autodyn calculations of peak pressure at the front of the projectile and the target plate for a velocity of 5.13 km s^{-1} (Shot G241013#1). This is unexpected as the peak pressures experienced for both target plate and projectile, at the point of contact, should be the same. The variation in peak pressure is most likely due to the method in which the program calculates pressure for the different numerical solvers. As mentioned earlier, the density of nodes in a given area, which is effected by compression of the projectile, plays a role in the in determining the node characteristics. Therefore, higher impact velocities would have a much greater impact peak pressure and temperatures. This is seen in the data, as the variation between the target plate and projectile increases with increasing impact velocity. However, it is believed that the peak impact pressure falls within the range described by the front of the projectile and the target plate, therefore an average of the two values will be used in subsequent analysis. This averaged value of peak pressure from Autodyn shows a better correlation with the peak pressure obtained using PIA and Hugoniot plots (Figure 8.2.3).

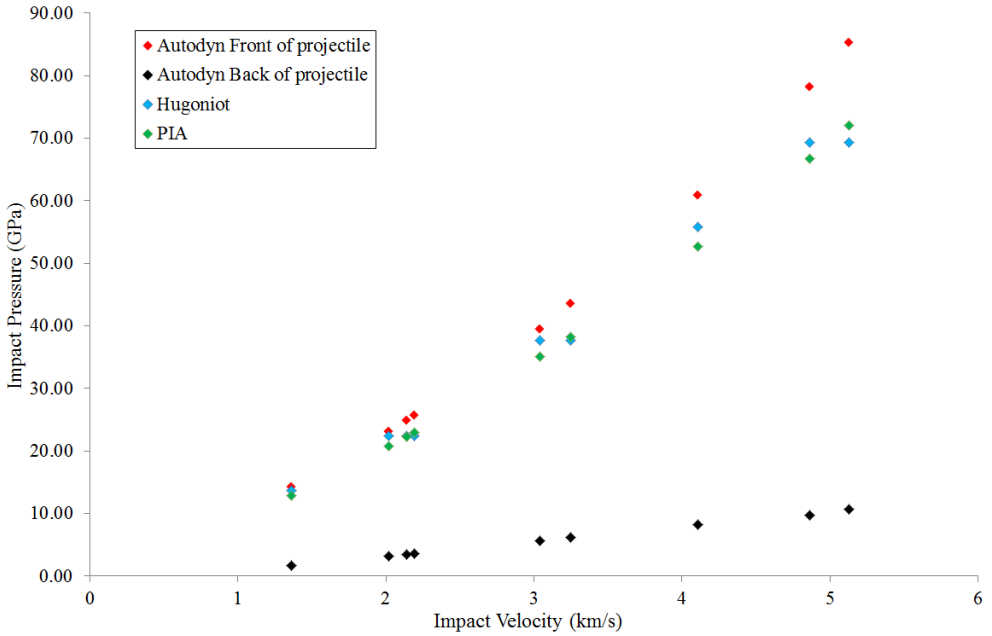

Figure 8.2.3 A comparisons of impact pressures, for Plate 1, using all three methods. The pressures determined for the front of the projectile are an average value calculated using data from a gauge placed at the front of the projectile and on the target plate in Autodyn simulations.

The peak pressures from Autodyn (Figure 8.2.3 and Tables 8.2.2 and 8.2.3) show there is a difference in peak pressure between the front and rear of the projectile, with a variation of 8.4 to 56.53 GPa at initial impact velocities of 1.363 and 5.13 kms^{-1}, respectively. The peak

temperatures determined from Autodyn (Table 8.2.2 and 8.2.3) also show a similar trend, whereby there is a temperature gradient between the front and rear of the projectile. A difference of 376 ˚C and 3090 ˚C occurs between the front and the rear of the projectile, at velocities of 1.363 and 5.13 km s^{-1}, respectively. The differences in peak pressures experienced between the regions of the projectile upon impact also increases with increasing velocity. These differences in pressures and temperatures, experienced across the projectile, indicate that different changes should occur upon impact. For example, in the case of G241013#1 (5.13 km s^{-1}) the rear of the projectile experienced similar pressures as that experienced at the front of G1121213#2 (1.363 km s^{-1}).

The initial Autodyn simulations used to determine the peak impact pressures and temperatures for plate 1 also collected impact data as the projectile material impacted the witness plate (as the gauges were attached to the projectile). The peak pressures are 2.59 to 13.13 GPa lower than the values calculated using the PIA. Therefore, a second series of Autodyn simulations were completed, where a projectile (1.5 × 1.5 × 2.0 mm) impacted an Al plate at velocities determined by the initial series of Autodyn simulations. Peak pressures for the witness plate, using PIA and Hugoniot plots, were determined by using the secondary velocities (after the projectile penetrated the initial plates in Autodyn simulations) to calculate the new peak pressures. These new pressures were then added to the pressures from plate 1. As expected, the pressure experienced on the witness plate for each velocity increases, which produces new pressures for comparison. PIA and Hugoniot peak pressures fall within ±3GPa of each other, whereas Autodyn peak pressure are much higher, up to 15 GPa, for the shots with high initial impact velocities, which is most likely a result of the solver used in Autodyn simulations. As mentioned earlier, two methods were used to estimate the temperatures experienced by projectiles as they impacted both plates, which were Autodyn and an estimation of temperature determined from peak pressure using data collated by French (1998).

Table 8.2.2 Peak pressures and temperatures for goethite projectiles impacting plate 1.

Shot I.D.	Impact Velocity (km s^{-1})	Peak Pressure (GPa)				Temperature (˚C)				
				Autodyn		Autodyn			Estimated from pressure*	
		Hugoniot	PIA	Front of projectile	Rear of projectile	Front of projectile	Middle of projectile	Rear of projectile	Front of projectile	Rear of projectile
G121213#2	1.363	13.75	12.95	14.18	1.66	432.13	275.46	55.97	150	<100
G050215#1	2.02	22.45	20.79	23.15	3.24	762.75	248.90	83.08	170-275	<100
G090114#1	2.14	22.45	22.34	24.93	3.50	862.95	273.29	89.62	170-275	<100
G260215#2	2.19	22.45	22.99	25.68	3.59	878.65	311.73	91.02	170-275	<100
G260215#1	3.04	37.76	35.04	39.41	5.66	1568.75	452.12	176.86	300-900	100
G061113#2	3.25	37.76	38.29	43.57	6.18	1665.55	464.01	184.59	300-900	100
G111013#2	4.11	55.79	52.69	60.87	8.20	2512.05	736.95	266.74	>1500	100
G180215#1	4.86	69.33	66.72	78.12	9.71	3191.05	1438.95	342.51	>1500	100
G241013#1	5.13	69.33	72.10	85.29	10.72	3411.45	1088.55	321.27	>2500	100

*Estimated post shock temperatures determined from French (1998) and references therein, using the peak pressure.

Table 8.2.3 Total peak pressures and temperatures for goethite projectiles impacting the witness plate.

Shot I.D.	Initial Velocity (km s^{-1})	Impact Velocity (km s^{-1})	Peak Pressure (GPa)				Peak temperature (˚C)			
			Hugoniot	PIA	Autodyn		Autodyn		Estimated from pressure*	
					Front of projectile	Rear of projectile	Front of projectile	Rear of projectile	Front of projectile	Rear of projectile
G121213#2	1.363	0.48	17.53	17.00	17.71	5.18	508.06	57.08	150-170	<100
G050215#1	2.02	1.30	34.22	33.04	34.30	14.38	904.65	307.69	275-300	150
G090114#1	2.14	1.32	35.20	34.81	36.27	14.84	1042.45	306.47	275-300	150
G260215#2	2.19	1.39	35.20	36.24	37.69	15.60	1151.75	479.76	300-900	150-170
G260215#1	3.04	1.18	48.57	45.99	49.76	16.02	2589.45	389.48	900-1500	150-170
G061113#2	3.25	1.24	49.53	49.88	54.15	16.76	2168.25	357.38	900-1500	150-170
G111013#2	4.11	1.71	72.66	69.65	76.33	23.65	3334.85	875.65	>1500	170 -275
G180215#1	4.86	2.06	90.62	88.02	97.47	29.06	3740.55	521.13	>2500	170 -275
G241013#1	5.13	0.67	75.60	78.00	90.75	16.18	4727.15	1094.70	1500-2500	150-170

*Estimated post shock temperatures determined from French (1998) and references therein, using the peak pressures.

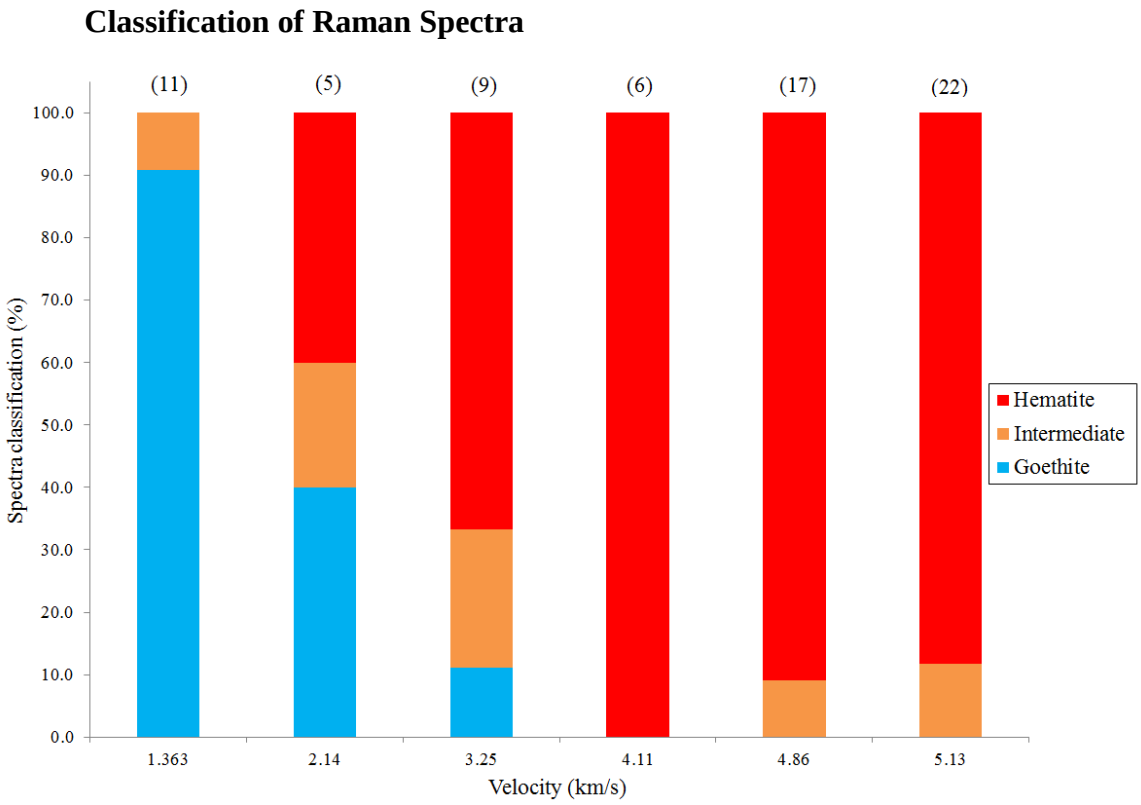

Figure 8.2.4 Classification of spectra (%) from goethite projectiles impacts on plate 1. The numbers in the brackets at the top of each bar represent the total number of spectra taken for each impact velocity.

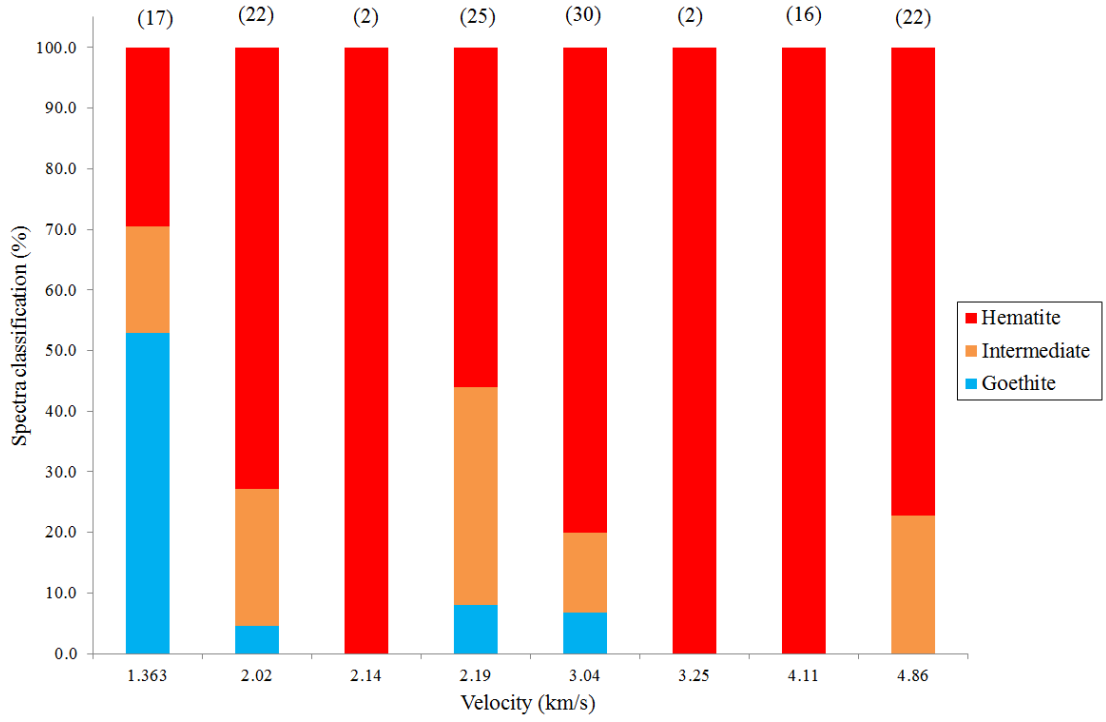

Figure 8.2.5 Classification of spectra (%) from goethite projectiles impacts on the witness plate. The numbers in the brackets represent the total number of spectra taken for each impact velocity.

The collected Raman spectra were first classified according to their resemblance to a goethite, hematite or intermediate spectrum (Appendix I Tables I1 and I2). Spectra classified as intermediate would have a mixture of features found in goethite and hematite, but could not be definitively classified as either one of them. Spectra taken from plate 1 (Figure 8.2.4) show there is a gradual change in Raman spectral classification from low velocity to high velocity. Raman spectra from higher velocities produce a larger percentage of Raman spectra classified as hematite, with 100% of spectra classified as hematite at a velocity of 4.11 km s^{-1}, whereas 91.9% of spectra were classified goethite for a lower impact velocity of 1.363 km s^{-1}. The total number of spectra classified as goethite decreases with increased impact velocity, with no spectra classified as goethite at impact velocities greater than 4.11 km s^{-1}. However, classification results for the witness plates (Figure 8.2.5) do not show the same trend as with plate 1. This is most likely a result of the range of temperatures seen across the projectile as it passes through plate 1. Results for 2.14 and 3.25 km s^{-1}, which shows 100 % of spectra were classified as hematite, could be misleading, as only two spectra were taken for these impact velocities from the witness plate. The classification spectra taken for both 4.86 (both plates) and 5.13 km s^{-1} are interesting, as they show some intermediate spectra, even though Autodyn temperature estimations suggest only hematite should be detected, particularly for the witness plate. However, temperature estimations determined from the pressure at the rear of the projectile are much lower and would imply goethite could also be detected.

The two estimations of temperature (presented in Tables 8.2.2 and 8.2.3) differ from each other, particularly for temperatures at the front of the projectile, which again makes it difficult to determine exactly how the temperatures are affecting the samples. But it is reasonable to assume that the actual temperature experienced by the projectile falls between the two estimated temperatures. Overall, temperatures estimated from the peak pressure are much lower. However, they do both show that a range of temperatures are experienced across the projectile. These temperature estimations also show temperatures >1500 ˚C can be achieved at the front of the projectile for impacts on both plate 1 and the witness plate. The boiling point of metallic Fe is 1538 ˚C, which means that impact temperatures greater than this could result in the vaporisation of the projectile material. This will most likely occur in the higher velocity impacts, with velocities of 4.11 km s^{-1} or greater for both plate 1 and the witness plate. Interestingly, impacts onto the witness plate have spectra that are classified as goethite and intermediate, at initial velocities of 2.19, 3.04 and 4.86 km s^{-1}. Temperatures at these initial velocities indicate, particularly at the

front of the projectile, that the material should be hematite. Temperatures at the rear of the projectiles suggest goethite spectra would be present and thus we might be able to distinguish between material originally located at the front and rear of the original projectile. However, the phase boundary between goethite and hematite + water shows an increase in temperature is required to form hematite as pressure rises (Majzlan *et al.*, 2003; Gleason *et al.*, 2008). However, the experiments conducted by Majzlan *et al.*, (2003) and Gleason *et al.*, (2008) have a maximum pressure of 10 GPa, and at higher pressures the opposite might be true, resulting in lower dehydration temperatures, which is what is seen with gypsum (Comodi *et al.*, 2008). This increase in dehydration temperature with pressure suggests that at lower impact pressures goethite dehydration occurs at higher temperatures, particularly for plate 1, which might explain why intermediate spectra are found at 4.86 and 5.13 km s^{-1}. It is believed that the craters on plate 1 are formed from projectile fragments that had broken away from the main projectile as it was accelerated in the LGG. Even though these fragments are smaller, they would have experienced the same peak impact pressures, which should produce similar peak temperatures in the fragments. However, the fragment size would most likely effect the duration the peak temperature is experienced for, similar to how projectile size effects the duration of peak pressure (Burchell, 2015). The duration the temperature is held for could also explain why intermediate spectra are found in residues for plate 1 impact velocities of 4.86 and 5.13 km s^{-1}.

Appendix I, Tables I1and I2 shows Raman data for Feature A (found between 380 and 415 cm^{-1}) and Feature B (a double peak feature found between 600 and 700 cm^{-1}) collected from both plate 1 and the witness plate. In some spectra only one peak for Feature B was detected, which did not occur whilst conducting the heating experiments. Dekkers (1990) suggests that magnetite can form as goethite transforms to hematite, which could be an explanation for the single Feature B peak. However, it is believed that this has not occurred here, as the Raman spectra exhibited fluorescence (most likely a result of contamination from the LGG) that may have hidden a lower intensity second peak for Feature B. In addition to this, the single peak that was detected for these spectra also appeared quite broad; as a result of this the peak fitting programme may have assumed there was only a single peak, which was actually a blended broad and narrow peak.

Feature A Analysis: Plate 1

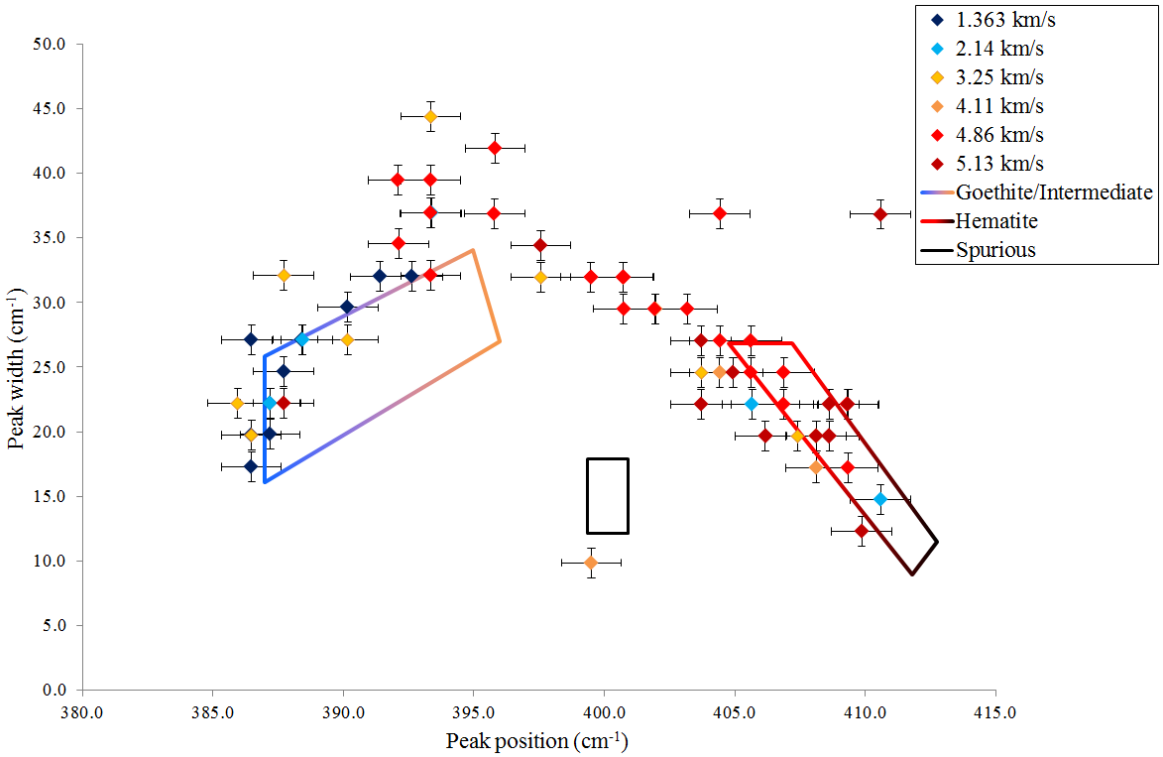

Figure 8.2.6 Raman spectra of impact residues from craters on plate 1. The two standard regions of goethite/intermediate and hematite spectra are highlight by the coloured boxes. The ends of each box represents "end-members" where clustering of specific spectra were located. Blue represents goethite and orange indicates intermediate spectra for the goethite/intermediate standard region. The hematite region is separated by temperature, 300 to 700 ˚C (red) and 800 to 1200 ˚C (black). The solid black box highlights a cluster of spurious points found in the heating experiments.

The absolute data (not averaged) from in-situ and ex-situ heating experiments (see Chapter VII, Section 7.3.1) showed two separate regions when Feature A's peak positions and peak widths were plotted together, which provide "standard" calibration regions (referred to as standard regions from the remainder of this thesis) that are formed as a result of heating from 22 to 1200 ˚C. These two standard regions can also be divided into two "end-members", the goethite/intermediate region has an end that represents more goethite-like spectra and the other has the majority of intermediate spectra. The hematite standard region also shows two "end-members", but this time they represent two temperature ranges, 275 to 700 ˚C and 800 to 1200 ˚C. Although there is a distinction between the ends of each of the standard regions, there is an overlap that makes it difficult to confidently discriminate them into separate areas. A small cluster of five spurious points was also found between 399 and 400 cm^{-1} and had peak widths between 12.15 and 18.9 cm^{-1}, which are made-up of points with a goethite spectrum. However, this specific cluster of points is believed to be a result of the peak fitting program not fitting the peak correctly. These

standard regions represent the changes that occur as a result of heating alone, therefore, points that are found outside of these regions are believed to show the effects of pressure.

Shot data for Feature A, plate 1 (Figure 8.2.6) shows that, overall, impacts at 1.363 km s^{-1} fall within or near (within two wavenumbers) of the standard goethite/intermediate region. The majority of these points are found towards the goethite end of the region, with two points closer to the intermediate end, this corresponds to the classification data, which shows 90 % of spectra are goethite. All but three data points for 5.13 km s^{-1} fall within (or within two wavenumbers) of the hematite standard region, and one point in the goethite region and one point near (three wavenumbers) the intermediate end of the goethite/intermediate region. An additional data point is located away from the main cluster of points, and has a peak position of 412.6 cm^{-1} and a large peak width of 36.8 cm^{-1}. The high number of points found in the hematite region, again, appears to correspond to the classification data, and also shows a 10% (the equivalent of two) of spectra are intermediate. The 4.11 km s^{-1} data points are found near, within a wavenumber, of the hematite standard region, and near the lower temperature range (275 to 700 ˚C), except for a single point which has a peak position of 399.5 cm^{-1} and a low peak width of 9.9 cm^{-1}. These data corresponds with the spectra classification data which shows 100% of spectra were hematite. The majority of data points for 4.86 km s^{-1} are located in the void between the two standard regions. Some data points are located within the hematite standard region and one point is found in the intermediate end of the goethite/intermediate standard region. Classification data shows 90% of spectra are hematite, but this is not evident in the data for this feature. Data points at velocities of 2.14 and 3.25 km s^{-1} are found within three wavenumbers of both regions determined by the heating experiments. There are a couple of data points for 3.25 km s^{-1} that have peak widths of 32.1 and 44.4 cm^{-1}, which is greater than expected for their peak positions at 387.7 and 393.3 cm^{-1}, respectively. However, spectral classification data for 3.25 km s^{-1} does not correspond to what is seen in the peak position and peak width data, as classification data shows 66.7% of the spectra are hematite. The wide range of peak positions and the large peak widths may show a pressure/velocity transition, where at greater velocities/pressures peaks will become narrower. Approximately half of the data points for 2.14 km s^{-1} are found within the standard goethite region and the other half are within/near the hematite standard region. This result is representative of the spectra classification results, which shows an equal number of spectra are classified as goethite or hematite, and the remaining points classified intermediate.

Feature A Analysis: Witness Plate

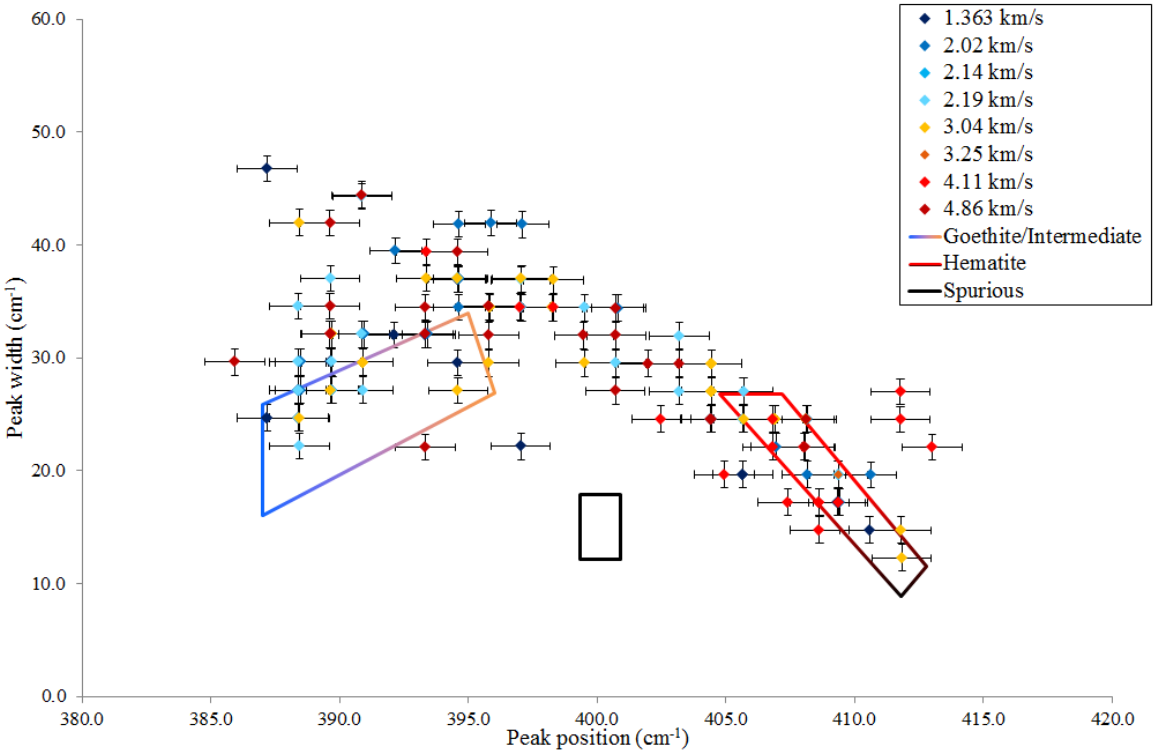

Figure 8.2.7 Raman spectra of impact residues from craters on the witness plate. Again, the two standard regions of goethite/intermediate and hematite spectra are highlighted by the coloured boxes. The ends of each box represents "end-members" where clustering of specific spectra were located. Blue represents goethite and orange indicates intermediate spectra for the goethite/intermediate standard region. The hematite region is separated by temperature, 300 to 700 ˚C (red) and 800 to 1200 ˚C (black). The solid black box highlights a cluster of spurious points.

The peak position and peak widths for Feature A were also plotted for the witness plate, along with the standard goethite/intermediate and hematite regions (Figure 8.2.7). These results have more data points within both standard regions than what is seen with plate 1. However, this is most likely a result of pressure, than being representative of temperatures, particularly for shots with peak pressures greater than 38.29 GPa (initial velocities of 3.04 km s^{-1} or greater). Initial impact velocities of 1.363, 2.02 and 2.19 km s^{-1} have data points that are clustered within the standard goethite/intermediate region, but they have much greater peak width, up to 46.8 cm^{-1}. These velocities also have data points found within the region of standard hematite, which is represented in the classification data. 1.363 km s^{-1} shows half the data points are classified as goethite, 17.6% as intermediate and 29.4% are hematite, which corresponds to what is seen in the Feature A witness plate shot data. Such an agreement between Feature A data and classification is not seen at velocities of 2.02 km s^{-1} on the witness plate impacts. Classification data shows 72.7% of the spectra were

classified as hematite, however, peak positions would suggest more than half of the spectra should be goethite or intermediate. Data for 3.04 km s^{-1} shows a wide range of peak positions and peak widths, resulting in some of the data being found within both standard regions, suggesting almost an equal number of goethite/intermediate and hematite spectra should be detected. This is not in agreement with classification results, which indicates 80% of the spectra were classified as hematite. Impact velocities of 4.11 and 4.86 km s^{-1} exhibit a range of peak positions and peak widths, which would, again, indicate a mixture of goethite, intermediate and hematite spectra should be detected at these initial impact velocities. However, spectra classification shows no goethite spectra were found at these velocities, indicating that impact pressures has caused shifts in the peak positions of this feature. A number of data points for velocities of 1.363, 3.04 and 4.11 km s^{-1} are found within the high temperature (800 to 1200 ˚C) end of the standard hematite region. However, these are the only evidence of spectra in this region, suggesting some of these points may not actually be as a result of high temperatures, but more of an indication of peak pressure.

The peak widths in Raman spectra also show the degree of crystallinity in the material: the narrower the peak, the more crystalline (or ordered) the material (Beyssac *et al.,* 2003). As was seen from the heating experiments, as goethite begins to lose water Feature A broadens, and then becomes narrower with increasing temperature as it transforms to hematite, it then becomes even narrower as it becomes more crystalline. The peak widths from Feature A for both plates are clearly greater than the maximum of 34.0 cm^{-1} previously seen in the heating experiments. The broadening of peaks is clearly a result of pressure, which has also been observed by Farrell-Turner *et al.*, (2005). However, the lower velocity shots, 1.363 and 2.14 km s^{-1} of plate 1 and 1.363 km s^{-1} for the witness plate, do not appear to have been as affected by pressure than those at higher velocities – as would be expected.

Feature A and Feature B Analysis

Figure 8.2.8 shows the peak position of Feature A and the peak intensity ratio of Feature B peaks. In heating experiments this plot showed a distinction between hematite spectra resulting from high (800 to 1200 ˚C) and low temperature (275 to 700 ˚C). Raman spectra data of crater residues for both plates indicates the highest temperature experienced was not greater than 700 ˚C. This corresponds to the expected temperatures near the rear of the

projectile, but does not correspond to the expected temperatures experienced at the front of the projectile. As with the results from only Feature A data, plate 1 data (Figure 8.2.8a) for 1.363 and 2.14 km s^{-1} corresponds to the classification data. Impacts at 5.13 km s^{-1} are clustered in the low temperature hematite region; at 3.25 km s^{-1} points are found within the low temperature hematite region and some spectra show indications of being goethite. Data for 4.11 km s^{-1} again indicate some intermediate spectra should be detected, which is not seen in the classification data.

The witness plate (Figure 8.2.8b) also shows that at velocities of 1.363 km s^{-1} the data corresponds to the classification results. However, unlike Feature A data, none of these data points indicate a temperature greater than 700 ˚C has been experienced. Points for 2.19 km s^{-1} do appear to correspond to the classification data, with a mixture of hematite, intermediate and goethite spectra being detected. However, the quantities of each classification do not exactly correspond to the results seen here, which indicates just over half of the spectra should be classified as goethite, or intermediate. This is not seen in the classification data, with 56.0% of spectra having a hematite classification. Heating experiments showed a peak intensity ratio of 1 occurs at a temperature of 700 ˚C for Feature B, which signified the increasing crystallinity of the sample with an increase in intensity of peak 1 over peak 2. Peak intensity ratios greater than 1.0 are not seen in the shot data, however peak intensities are known to decrease when shocked, as there is a reduction in crystallinity and increased disorder, which is shown in shock experiments conducted by Bell (2016) and Jaret *et al.*, (2014).

Interestingly, Raman spectra data for velocities of 1.363 and 2.14 km s^{-1} correspond to the classification data for plate 1, whereas above these velocities the classification does not completely correspond to data for this plate. This could indicate there is a threshold where, above 2.02 km s^{-1}, pressure has a greater effect on Raman spectra. In-situ and ex-situ heating experiments demonstrated the peak position for hematite has a lower limit of 405.0 cm^{-1}. This data also shows spectra classified as goethite, or intermediate, have peak positions within 387 to 401 cm^{-1}, which makes it difficult to distinguish between these two classifications from peak position alone, but they do provide an upper limit for peak positions classified as goethite or intermediate.

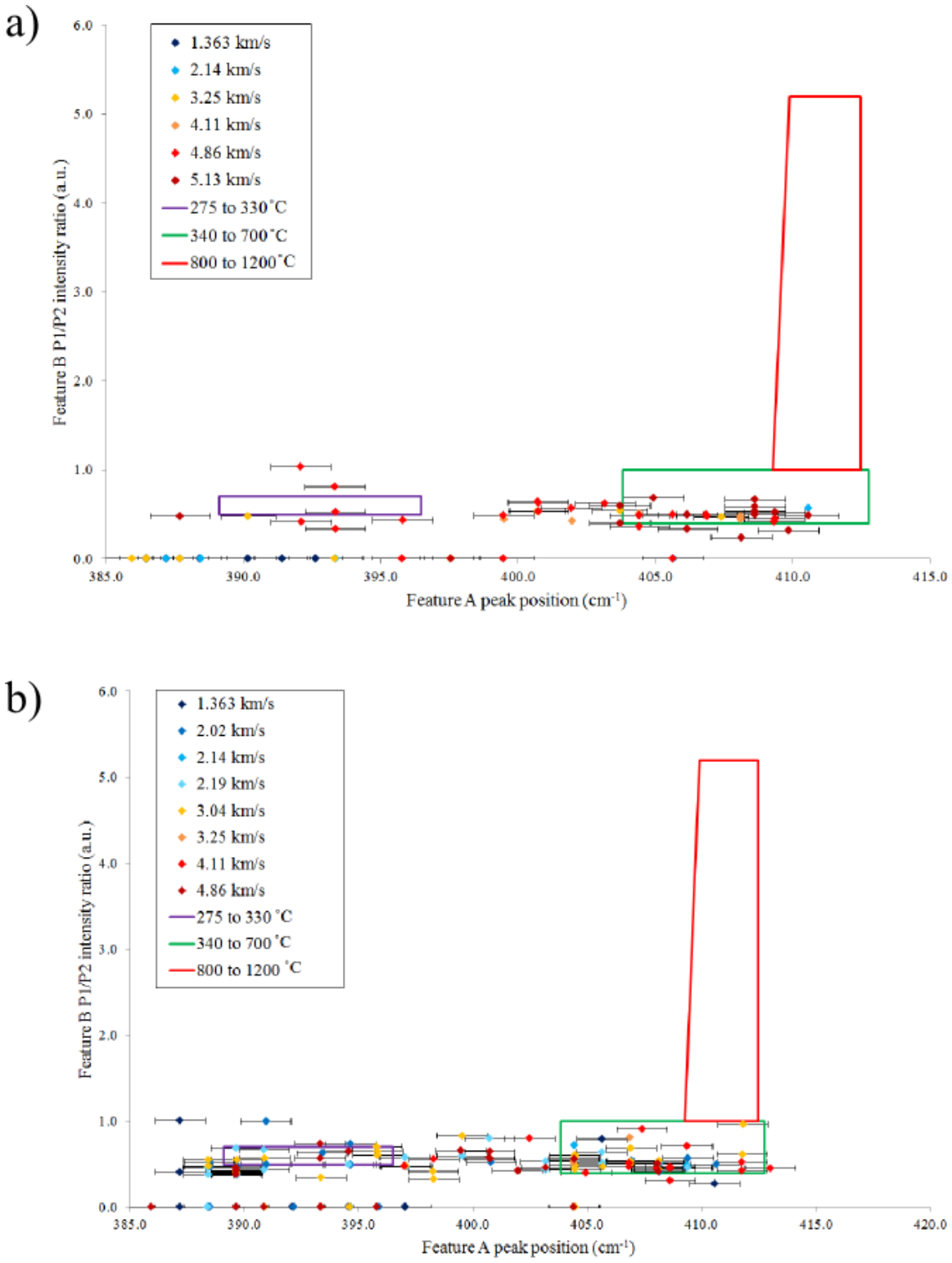

Figure 8.2.8 Feature A, peak position and Feature B, peak intensity ratios for impact craters on plate 1 (a) and the witness plate (b). The boxes represent different standard temperature ranges. Both red and green boxes indicate the regions for hematite and intermediate spectra are highlighted by the purple box. Points with a Feature B, P1/P2 ratio of 0 are a result of either Feature B not being detected or only a single peak being identified.

Feature A Peak Positions

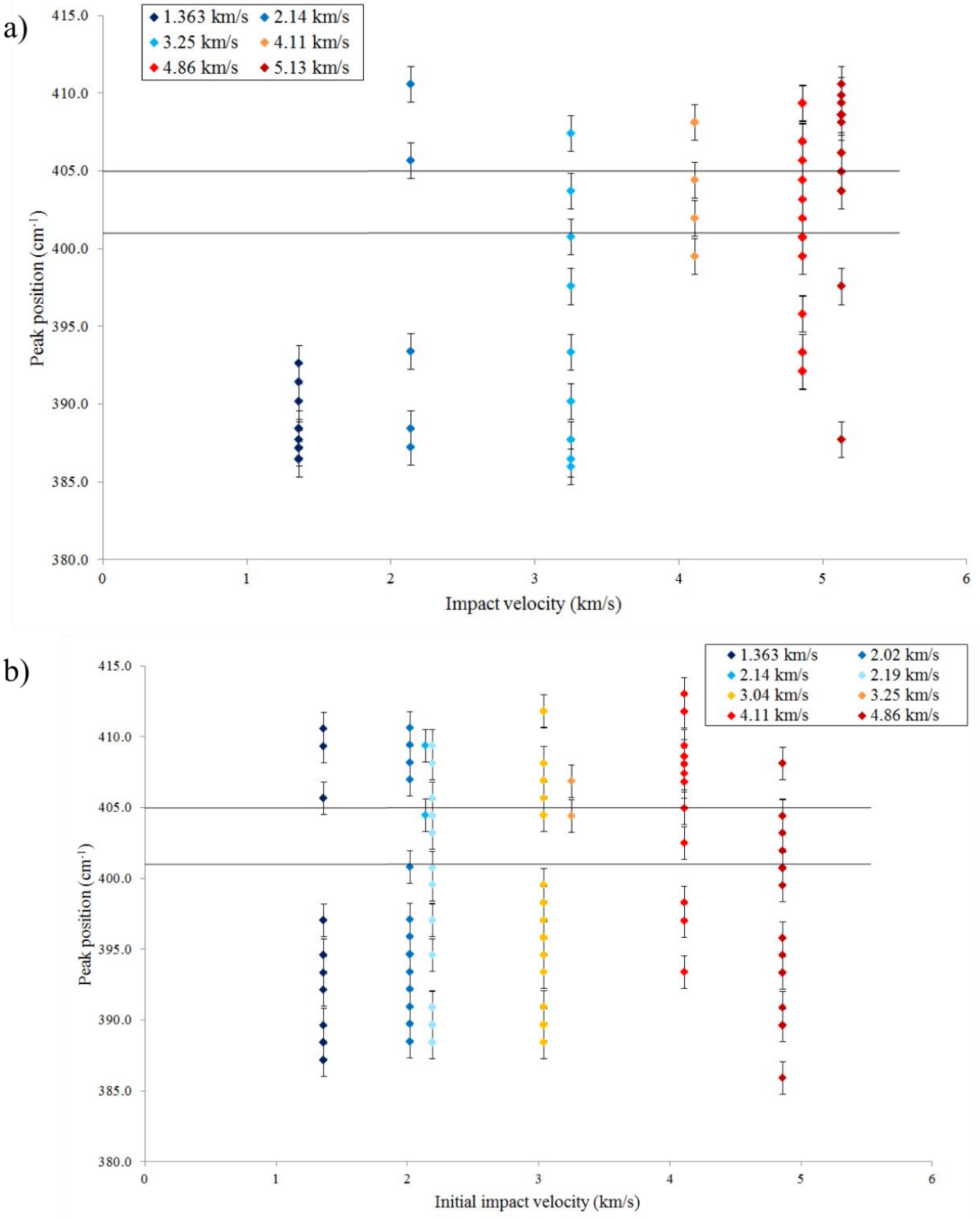

Figure 8.2.9 Peak positions for Feature A on plate 1(a) and the witness plate (b). The two black lines indicate the hematite lower limit and upper goethite peak position. Grey lines represent the upper limit for spectra classified as goethite or intermediate (401 cm^{-1}) and the lower limit for hematite (405 cm^{-1}).

Feature A peak positions for plate 1 (Figure 8.2.9a) shows similar results to that observed in the spectra classification data, with 1.363 km s^{-1} having goethite/intermediate spectra and no hematite, and at 2.14 km s^{-1} showing a mixture of goethite/intermediate and hematite spectra. At 3.25 km s^{-1} the number of spectra assumed to be hematite, from Feature A peak position data, is less than what is observed in the classification data. The same is true at the higher velocities (above 3.25 km s^{-1}); where between 90 to 100% of spectra are classified as hematite and therefore would have peak positions above 405 cm^{-1}. A similar trend is seen the Feature A peak positions for the witness plate (Figure 8.2.9b), where, at an initial impact velocity of 1.363 km s^{-1}, there is a correlation with the classification data. However, a correlation between the peak positions and the classification does not occur for initial impact velocities of 2.02 km s^{-1} and greater, for the witness plate data. Here we see a greater proportion of spectra (at these initial impact velocities) have a peak position lower than 401 cm^{-1}, which would indicate a goethite or intermediate spectra. This is indicative that the impact pressure has resulted in large changes in peaks positions (potentially 19 wavenumbers in the case of 4.86 km s^{-1}) for the witness plate, which can produce misleading results. Figure 8.2.10 shows the peak positions for all spectra classified as hematite, which confirms this assumption, as it clearly shows the peak positions for some hematite falls below the lower limit at 401 cm^{-1}. As mentioned previously, there is a correlation between the classification data of 1.363 and 2.14 km s^{-1} for Feature A peak positions of plate 1, which suggests there is boundary at the pressures generated at 2.14 km s^{-1} (22.34 GPa). At pressures below those generated at velocities less than 2.14 km s^{-1}, the Raman peak data for Feature A and B could be representative of the temperatures experienced by the sample.

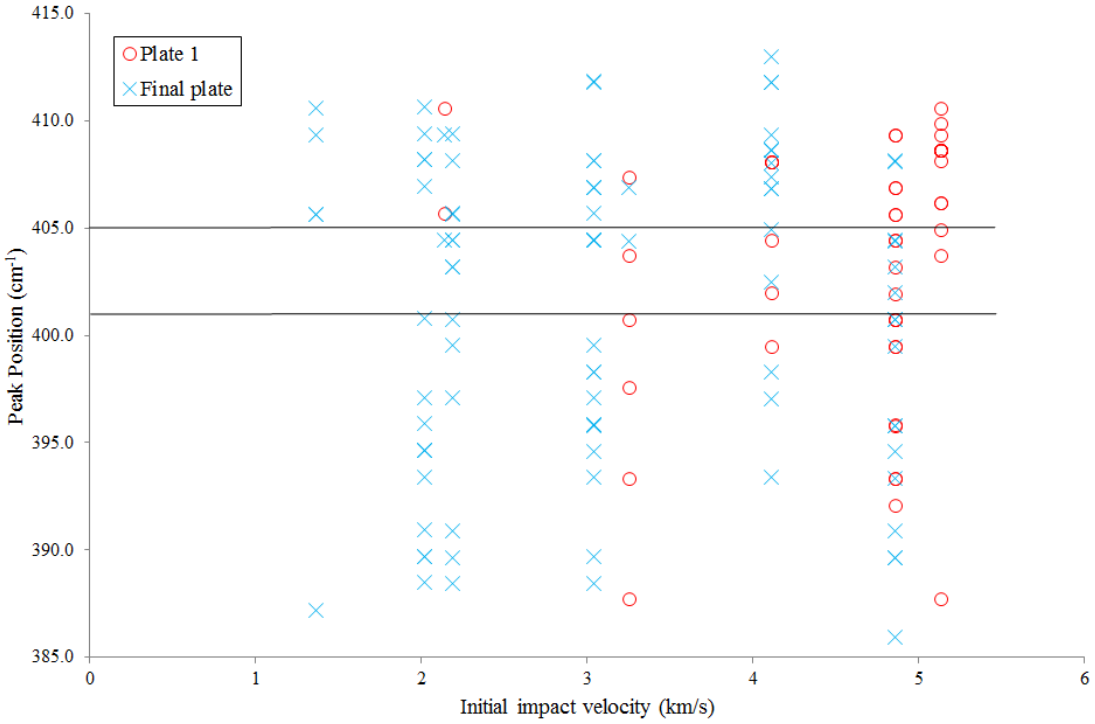

Figure 8.2.10 Absolute peak positions for spectra classified as hematite form both plate 1 and the witness plate Grey lines represent the upper limit for spectra classified as goethite or intermediate (401 cm^{-1}) and the lower limit for hematite (405 cm^{-1}).

Figure 8.2.11 appears to show a limit at a peak pressure of 22.34 GPa (peak pressure for shots are found in Tables 8.2.2 and 8.2.3), where the peak position for specific spectra are located in the correct region, i.e. hematite spectra are found above 405 cm^{-1}; goethite and intermediate spectra are located below 401 cm^{-1}. At peak pressures above 33.04 GPa there is more variation in the peak positions for hematite spectra, where they start to have peak positions lower than 401 cm^{-1}. This is further evidence that suggests there is limit where the impact shock begins to play a larger role in altering peak positions. The occurrences of goethite and intermediate spectra are lower in number at pressures greater than 52.69 GPa, which would suggest higher temperatures are experienced. However, their presence does indicate there might be some lower pressure/temperature regions existing within the projectile material producing these occurrences of goethite and intermediate material, assuming it is travelling at the same initial velocity.

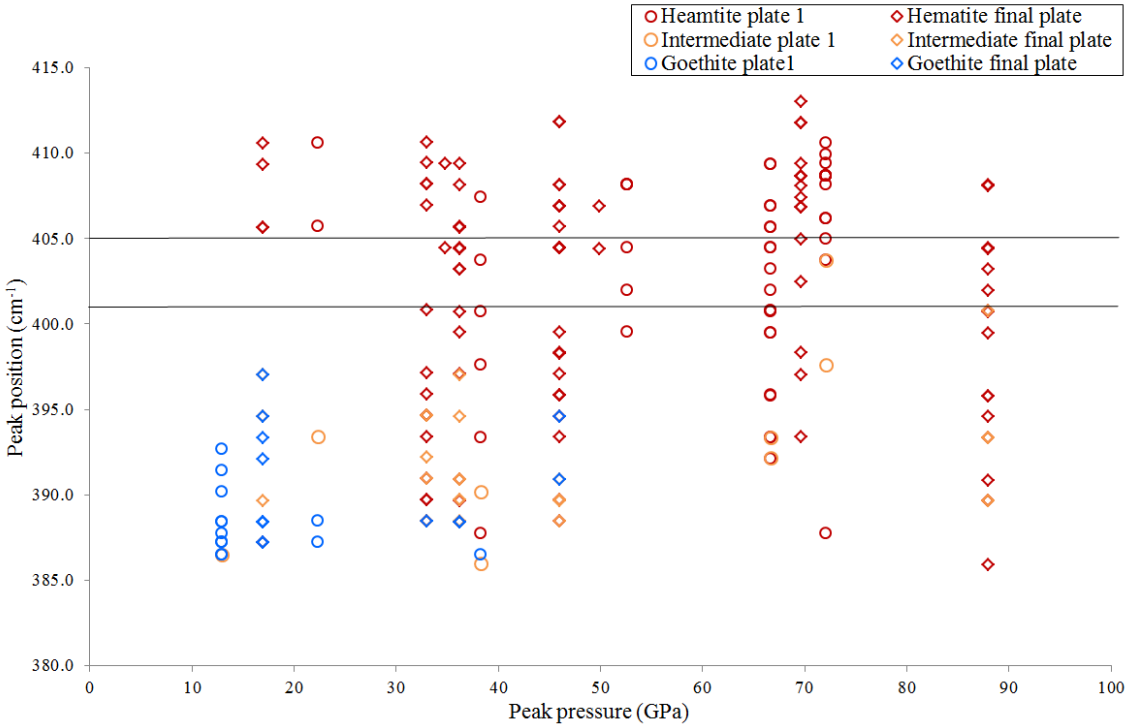

Figure 8.2.11 Feature A peak positions for both plate 1 and the witness plate. The grey lines indicate the maximum peak position for goethite/intermediate spectra (401 cm^{-1}) and the hematite lower limit (405 cm^{-1}).

The presence of hematite shows temperatures greater than 300 to 340 ˚C (at least) were achieved in some regions upon impact, which means all hematite spectra should have had peak positions between 405 and 413 cm^{-1}. Figure 8.2.11 shows that some spectra classified as hematite have peak positions located between 385.6 to 413.0 cm^{-1} for peak pressures of 33.04 GPa and greater; below this pressure hematite spectra are located within the expected region. Overall, the results show no real trend in peak position as a result of increasing pressure. Although a peak position of 413.0 cm^{-1}, found at 69.65 GPa, would normally indicate a highly crystalline hematite sample, and in the heating experiments was only produced at a temperature of 1200 ˚C. The spectral classification data clearly shows that a range of temperatures were experienced upon impact for both plates, with the presence of goethite and intermediate spectra identified on both plates, which makes it difficult to distinguish between the hematite spectra, that would have formed at high temperatures, to those that would have formed at low temperatures. However, Feature A peak positions and widths for hematite spectra (Figure 8.2.12) do appear to show two different areas separated at 397 cm^{-1}. At peak positions greater than 397 cm^{-1} peak widths appear to be generally located within a narrow corridor of ~8 wavenumbers wide and, overall, there is a general decrease in peak width with increasing peak position. Below a

peak position of 397 cm^{-1} data points appear to be more spread out with a large variation in peak widths for each peak position. For example, at 393.4 cm^{-1}, peak widths range from 44.4 to 32.1 cm^{-1}, at 389.7 cm^{-1} peak widths fall into a region between 42.0 and 27.1 cm^{-1} and at 395.8 cm^{-1} peak widths between 29.5 and 41.9 cm^{-1} can be found. This difference in the spread of data points might be an indication of the crystallinity and, expected peak positions if the residues were affected by temperature alone under quasi-static conditions. The more defined and narrow region (peak positions greater than 397 cm^{-1}) may show residues that would have had peak positions between 409 to 413 cm^{-1} and the more spread out data (peak positions below 397 cm^{-1}) may have had peak positions in the range of 405 to 409 cm^{-1}, if only thermal alteration had occurred. If this is correct, then this would indicate that poorly crystalline hematite would produce large shifts of up to 20±4 wavenumbers and highly crystalline hematite could produce peak shifts of up to 16±4 wavenumbers as a result of impacts. There also appears to be a greater proportion of points generated by peak pressures greater than 60 GPa located at peak positions greater than 397.0 cm^{-1}, which would suggest more crystalline hematite was generated at these greater pressures.

Feature A Analysis: Hematite Data

Hematite data points (Figure 8.2.12) at pressures of 17.00 and 22.34 GPa are clustered at peak positions between 405 and 410 cm^{-1}, and have peak widths within the range of 14.7 and 22.1 cm^{-1}. This again suggests there might be a pressure limit, above which pressure begins to have a greater effect on peak positions and width. At pressures of 33.04 to 49.88 GPa, data points appear to be spread across both regions (separated at 397 cm^{-1}) almost evenly, whereas at pressures of 52.69 GPa and greater there is a larger proportion of points in the region above 397 cm^{-1}. However, it is still quite difficult to drawn a confident relationship with pressure, as it is believed a range of pressures were experienced throughout the projectile. A study conducted by Shim & Duffy (2002) examines the effect of pressure (up to 62 GPa) on the Raman spectra of hematite which showed that there is an increase in peak positions with pressure, and the double peak found at 293 cm^{-1} clearly separates into two peaks at a pressure of 17.9 GPa. These results also show that the peak positions approximately return to their original peak positions after the pressure has been released, with a maximum increase in peak position of ~5 wavenumbers. However, as part of a study conducted by Ovsyannikov *et al.,* (2012) Raman spectra were taken before, and

after, cycling crystalline hematite to pressures of 17 to 22 GPa, which showed both a decrease in peak position of 17 wavenumbers and broadening of peaks by ~20 wavenumbers. The results seen by Ovsyannikov *et al.*, (2012) show what is believed to have occurred in these experiments, albeit as a result of much lower pressures. If we assume points below 397 cm^{-1} (Figure 8.2.12) would have produced a poorly crystalline hematite (if only heating occurred), then decreases of 22 to 16 wavenumbers would occur. However, these results were generated at much higher pressures, whereas Ovsyannikov *et al.*, (2012) results were produced from the cycling of pressure to its target pressure of 22 GPa. These differences make it difficult to truly compare the results from these impact experiments to pressure experiments conducted under quasi-static conditions. Ovsyannikov *et al.*, (2012) believes the changes in peak position and broadening of peaks to be a result of phonon softening, which indicates the weakening of the bonds from the cycling of pressure, which is similar to what is believed to cause these changes in Raman spectra of the shocked material.

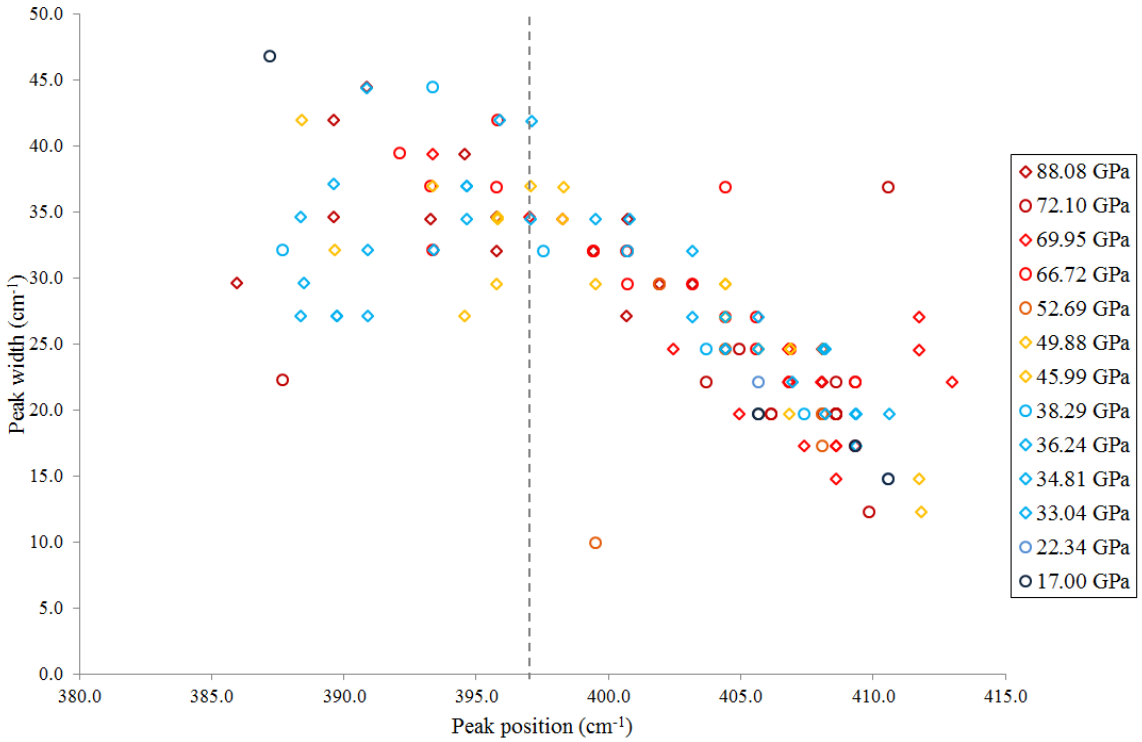

Figure 8.2.12 Feature A peak positions and peak widths for all spectra classified as hematite and the grey dotted line highlights the peak position boundary of 397 cm^{-1}. The points shown as open circles indicate values from plate 1 and the open diamonds are from the witness plate. The peak pressures used have been generated from PIA calculations.

Heating experiments showed that at temperatures above 500 ˚C the two peaks that make up Feature B start to become more identifiable as two individual peaks, and the peak width ratio begins to decrease from 0.8 to 0.4, as a result of the peaks becoming narrower. Plate 1 peak width ratios (Figure 8.2.13) shows only a single point falls below 0.4 at a peak pressure of 72.10 GPa, but the vast majority of the remaining data points lie within the range of 1.1 and 0.5. This indicates that peaks are either similar in width (ratio of 1.0) or peak 1 is narrower than peak 2 (ratio less than 1.0). Although, for the witness plate, (Figure 8.2.13) the peak width ratios do not fall as low as 0.4, approximately 80% of data points fall within the range of 1.0 and 0.5, indicating narrow peaks. There are instances where the peak width ratio is greater than 1.0, which shows peak 1 is wider than peak 2. This broadening of peak 1 is clearly an indication of shock, as the maximum ratio found from the heating experiments was a peak width ratio of 1.1. The witness plate shows a maximum width ratio of 2.0, whereas the maximum for plate 1 is 1.2. The much larger peak width ratio values seen in the witness plate indicates a greater degree of disorder occurred as a result of these impacts.

Feature B Analysis: Hematite Data

Feature B peak intensities ratios for both plates (Figure 8.2.14) do not exceed 1.0, which indicates that peak 2 has a greater intensity that peak 1 for all impacts. Witness plate values are generally clustered between ratios of 0.7 and 0.3, with some points found up to 0.9. Whereas for plate 1 there is more of a spread of data points up to a ratio of 1.0, especially at peak pressures of 17.00 and 66.72 GPa. This might be suggestive of the peak pressures for plate 1 not being held as long, due to the size of the fragments impacting the plate. de Faria & Lopes (2007) point out that the greater intensity of peak 2 in hematite spectra is representative of the low crystallinity of the material, which is what is represented here. Overall the peak intensity ratios suggest spectra obtained came from a poorly crystalline hematite. However, the degree of disorder does not increase with increasing pressure; instead it appears to occur to a greater degree in the witness plate data.

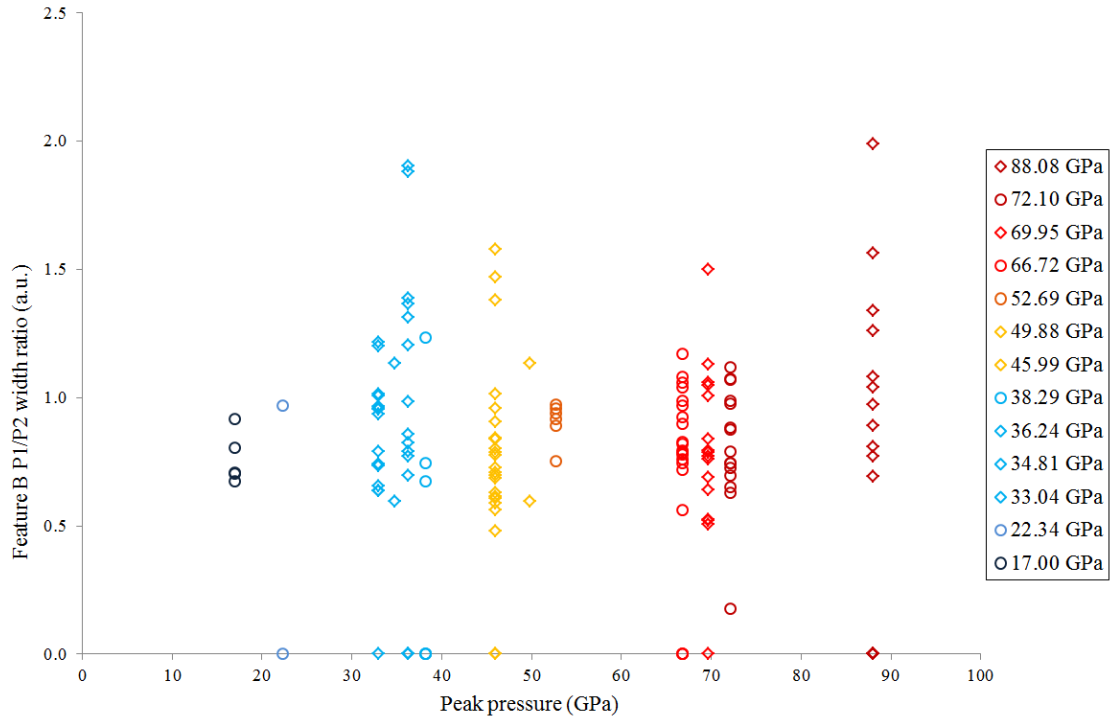

Figure 8.2.13 Feature B peak width ratios for P1/P2 from hematite data. Open circles represent data from plate 1 and open diamonds show data from the witness plate. Data points with a ratio of 0 indicate spectra where only one peak was detected for Feature B, or no peaks were detected due to fluorescence.

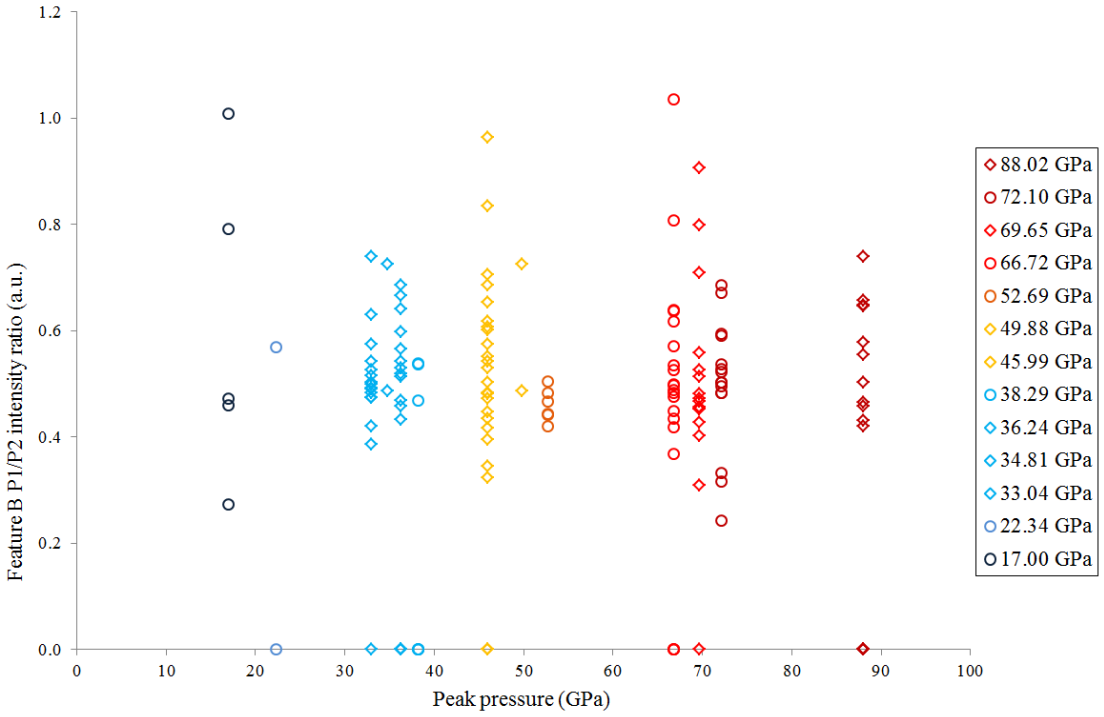

Figure 8.2.14 Feature B peak intensity ratios (P1/P2) for hematite spectra. Peak pressures presented here are values taken from PIA calculations. Open circles show data from plate 1 and open diamonds represent data from the witness plate. Intensity ratio values of 0 indicate spectra where only a single peak or no peaks were found for Feature B.

Summary of Goethite Projectile Results

The mixture of goethite, intermediate and hematite spectra found on both plates indicates the entire sample did not experience complete devolatilisation, whereas the peak temperatures determined by Autodyn suggest they should have, especially for impacts onto the witness plate. This is mostly likely caused as a result of the pressure and temperature gradients found along the length of the projectile, and the size of the fragments reducing the time duration of peak temperatures and pressure experienced. However, results do show there is a potential boundary at 22.34 GPa which marks a limit where peak pressures begin to have a larger effect on the peak positions and widths of Raman spectra. The results also show that the hematite spectra produced from impacting goethite resembles a poorly crystalline material, regardless of peak temperatures. Although it is difficult to determine the temperatures experienced by the sample after dehydration has occurred in the same way as determined by the heating experiments, Feature A might provide a clue. These data shows two distinct areas that may have resulted from pressure affecting poorly crystalline and highly crystalline hematite differently. However, additional work would be required to examine how poorly crystalline and highly crystalline hematite are effected by impacts. Unfortunately, the changes in peak positions and increased peak widths caused by impacts make it difficult to determine the amount of volatiles lost from the Raman spectra. As the heating experiments showed that determining the amount of volatiles lost was dependent on specific peak positions and peak widths. However, if there is a pressure boundary at 22.34 GPa it might be possible to determine the degree of volatiles lost and the temperatures experienced from materials surrounding a larger impact crater, where the peak pressure is below this pressure limit. A series of low velocity (< 2.00 km s^{-1}) impact experiments would be able to determine this.

8.2.2 Goethite target

In order examine the changes that occur away from the crater, and not at the point of contact with the projectile, a shot using a goethite target was carried out. The remainder of the goethite nodule was embedded in epoxy resin and impacted at 3.07 km s^{-1} with a 0.8 mm (in diameter) stainless steel projectile (Figure 8.2.15). Raman maps were taken from inside the crater and around the exterior of the crater. 30 spectra were taken from these maps and used for analysis.

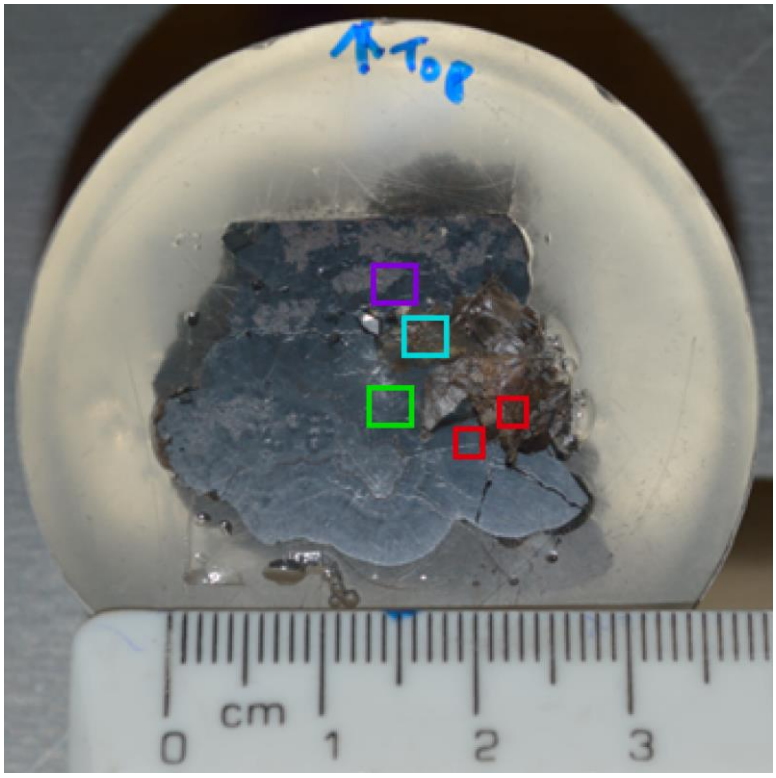

Figure 8.2.15 Goethite target after impact. Boxes highlight the areas where Raman maps, and single Raman spectra were taken from. Map 1 (blue), map 2 (purple), map 3 (green) and the two areas where individual spectra were taken (red).

Peak Pressure and Temperature

Table 8.2.4 show the impact peak pressures and temperatures determined by the PIA, Hugoniot plots and Autodyn simulations. The peak pressure determined by the PIA and Hugoniot calculations are 57.22 and 60.80 GPa, respectively. The estimated temperatures determined from these impact pressures shows that the centre of the crater should have experienced temperatures of 900 to 1500 ˚C. Heating experiments showed that at these temperatures highly crystalline hematite should be formed, and results from goethite projectiles showed hematite was formed at similar impact pressures. Autodyn simulations show much lower impact pressures (Table 8.2.4), where the pressures generated present temperatures do not exceed the transition temperatures determined for hematite to form (275 to 330 ˚C). However, Autodyn temperatures (not determined form the pressure) suggest that hematite may have formed within 1.05 mm from the initial contact point, which would be found within the crater (which is ~8 mm in diameter).

Table 8.2.4 Peak pressures and temperatures experienced by the goethite target.

	Distance from point of contact (mm)		Peak Pressure (GPa)	Temperature (˚C)	
				From pressure	Autodyn
PIA	-		57.22	900 – 1500	-
Hugoniot	-		60.80	1500	-
Autodyn	*x*-axis (depth)	0.05	28.14	275	1380.05
		0.25	35.72	300	401.33
		0.45	20.96	170	308.42
		0.65	23.69	170	299.42
		0.85	18.50	150	257.01
		1.05	19.07	150-170	225.90
		2.05	9.93	100	117.43
		3.05	7.33	100	70.91
		4.05	5.50	<100	44.53
		5.85	3.32	<100	29.05
		10.9	1.68	<100	21.85
		19.9	0.10	<100	20.00
	y-axis (front surface of target)	0.05	32.74	275	1165.55
		0.25	27.70	170	850.45
		0.45	10.16	100	
		0.65	1.9	<100	308.53
		0.85	7.11	100	308.53
		1.05	2.41	<100	274.58
		2.05	0.38	<100	36.79
		3.05	0.37	<100	52.38
		4.05	0.25	<100	44.80
		5.85	0.21	<100	22.34
		11.9	0.03	<100	20.00
	y-axis (rear of target)	0.05	0.10	<100	20.35
		0.25	0.10	<100	20.34
		0.45	<0.10	<100	20.31
		0.65	<0.10	<100	20.27
		11.9	<0.10	<100	20.00

Raman Data

Results showed a goethite-like spectrum for all spectra analysed, and there were no instances where Feature B was detected. This would indicate that the temperatures experienced by the target did not exceed 275 - 330 ˚C, which differs to the results seen with mineral projectiles, which showed impacts residues at the similar pressures were mostly hematite. This is probably a result of the difference in size between the mineral target and mineral projectiles. When using goethite as the projectile, it is easier to locate material that has experienced high pressures and temperatures, as it is the only material found on the Al target plates. However, when using goethite at the target (at this scale) any potential devolatilised material could be hidden by the Raman signature for goethite. It is also possible that the absence of hematite being detected in the goethite target may

simply be a result of it not being the in the area within the crater where spectra were collected.

Raman data gathered for Feature A (Figure 8.2.16 and Appendix I, Tables I3 and I4) corresponds to the classification data, indicating that Raman spectra from the sample has not undergone dehydration and formed hematite. In fact none of the spectra analysed could be classed as intermediate, again showing no evidence that dehydration had occurred. Raman spectra of the sample taken before impact show peak positions of 381 to 384 cm^{-1} and four spectra have peak positions of 395 or 396 cm^{-1}. These before peak positions are lower than those previously seen from the heating experiments, which had initial peak positions of 387 to 388 cm^{-1}. This would indicate that some alteration may have occurred when shaping the samples for the heating experiments, which would also explain why the before spectra of the target falls outside of the standard goethite region determined form the heating experiments. Raman spectra taken after impact shows there is a general increase in peak position, which indicates some alteration may have taken place. Goethite projectile data showed a clear increase in peak width as a result of impact pressure, which is also observed by Farrell-Turner *et al.,* (2005) in shocked olivine, indicating an increase in peak width is a feature of highly shocked material. This increase in peak width is not seen in the Raman spectra taken from outside the crater, which would suggest low impact pressures were experienced. However, there does seem to be a difference between maps taken outside the crater and those taken within the impact crater. As maps 2 and 3 were taken just outside of the crater and show an increase in peak position, but no real increase in peak width. Whereas, map 1 was taken from inside the crater and there is more of an increase in the peak width and there is very little change in peak positions. Two of the individual spectra were taken from inside the crater and a two were also taken outside the crater. Individual spectra taken from inside the crater have large peak widths of 29.6 cm^{-1} and peak positions of 384.7 cm^{-1} and spectra taken outside the crater do not show a large increase in peak width, but do show an increase in peak positions, which corresponds to what is seen in the data obtained from the Raman maps. There does not appear to be a change in peak position for spectra taken from inside the crater. However, it might be that the effects of impact pressure caused a decrease in peak position, similar to what may have resulted in the changes of peak positions for the mineral projectile. It could be that the increases of peak positions are a result of thermal alteration, although this is unlikely. The differences in the initial peak positions between the target and the before peak positions from heating experiments make it difficult to determine the

temperatures experienced. However, the absence of intermediate spectra indicates temperatures did not exceed 250 to 310 ˚C.

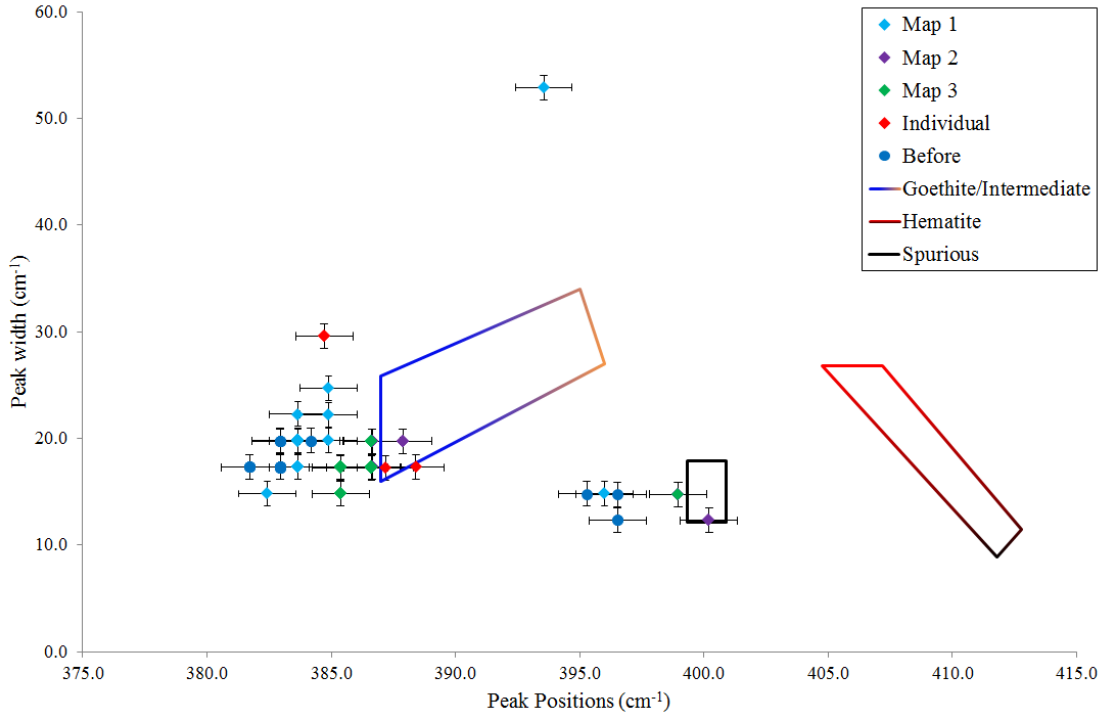

Figure 8.2.16 Raman data for Feature A for the goethite target (shot I.D. G310114#2). The goethite/intermediate (blue/orange), hematite (red/black) and spurious (black) standard regions, determined from the heating experiments (Chapter VII), are highlighted by the boxes. Raman spectra were taken using a 633 nm laser, 600 g/mm grating and a ×50 microscope objective.

8.2.3 Gypsum projectiles

PoP Projectiles

Initial impact experiments examining gypsum projectiles used gypsum in Plaster-of-Paris (PoP) form. Semi-hydrous PoP powder (particle sizes ranged from 90 to 125 µm) was also fired onto aluminium plates at 4.26 km s^{-1}, shot I.D. G141113#2. Raman analysis of impact residue (Figure 8.2.17b) from this shot showed a spectrum that did not resemble any of the three hydration states of gypsum, or that of gypsum when heated to 1450 ˚C. However, the Raman spectrum did show some similarity with the spectrum of $CaCO_3$, which is believed to form after desulfurisation occurs. As Bell (2010) explained, that one of the materials formed from the decomposition of gypsum, bassanite and anhydrite is CaO, which will then react with CO_2 to form $CaCO_3$. Subsequent SEM EDX analysis

confirmed there was a decrease in sulphur (Figure 8.2.18), when compared to the spectrum of PoP.

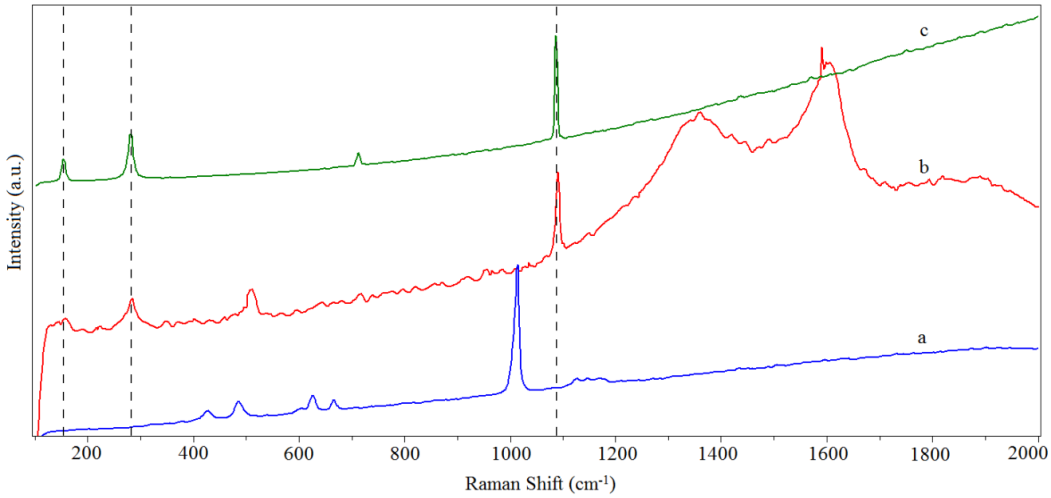

Figure 8.2.17 a) Bassanite (semi-hydrous PoP), b) impact residue from G141113#2, and c) sample of calcite ($CaCO_3$). The two broad peaks seen in b at 1350.7 and 1596.2 cm^{-1} represent the D and G bands of amorphous carbon, which is contamination from the LGG. Raman spectra was taken using the 473 nm laser for a) and b), and a 532 nm laser was used for sample c).

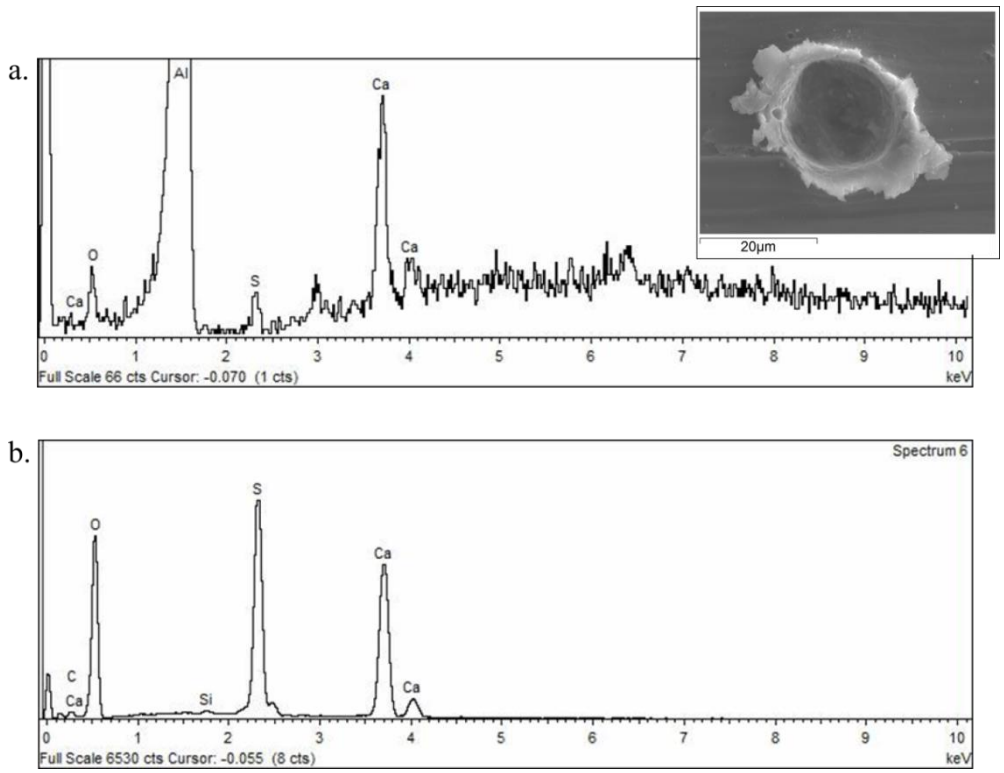

Figure 8.2.18 EDX results from crater residue of G141113#2 (a) and sample of PoP (b). The inserted image is a SEM BSE image of the crater the EDX measurement was taken from.

Two shots using hydrous PoP powder (between 90 to 125 µm in diameter) were fired onto Al plates at velocities of up 4.57 and 4.38 km s^{-1}, to determine if decomposition would

also occur. Results from these impacts showed the gypsum lost all its water and formed anhydrite, but did not show the complete decomposition of the mineral. Table 8.2.5 shows the peak pressures and temperatures experienced by PoP (both hydrous and semi-hydrous) powder projectiles. Shots G141113#2 (semi-hydrous PoP) and G020414#2 (hydrous PoP) both experienced similar pressures and temperatures, but only semi-hydrous PoP underwent decomposition. This indicates that the initial make-up of the projectile will effect whether or not complete decomposition occurs. Shock recovery experiments conducted by Zhang & Sekine (2007), which used bassanite as the starting material, did not show the decomposition of the material at pressures up to 24.40 GPa. This may suggest that the decomposition of bassanite occurs at pressures between 24.40 and 43.46 GPa, however, this may be affected by the size of the particles.

Table 8.2.5 Calculated impact pressures and temperatures for PoP powder projectiles.

Shot I.D.	Velocity (km s^{-1})	Hydrous state	Peak Pressure (GPa)			Temperature (˚C)	
			Hugoniot	PIA	Autodyn	Autodyn	From Pressure*
G141113#2	4.26	Semi-hydrous	43.46	43.77	40.83	2375.55	300-900
G020414#2	4.57	Hydrous	43.46	42.09	42.66	3866.35	300-900
G160414#2	4.38	Hydrous	37.86	39.59	34.26	3766.15	300-900

*Estimated impact temperatures determined from French (1998) and references therein, using the peak pressures.

A PoP cuboid was shaped (as detailed in Chapter VI) and fired onto an aluminium plate (G281113#1) at 3.72 km s^{-1}, but fragmented before impacting the plate. Therefore, it was decided to use natural gypsum to reduce the chances of the projectile fragmenting upon acceleration, and to obtained more residue for analyses.

Natural Gypsum Projectiles: Peak Pressures and Temperatures

Projectiles made from natural gypsum (Chapter VI) were fired onto 6.0 mm thick Al plates, at velocities between 0.97 and 6.00 km s^{-1}. Similar to the PoP cuboid projectile, these projectiles also broke up in flight, except S060814#1 at 0.97 kms^{-1}, before impacting the target plate (Appendix J, Figure J4). However, it is believed that the cuboid broke into needle like fragments (resulting from the crystal structure), which produced multiple craters on the target plates (Appendix J, Figures J5 to J12). At velocities greater than 0.97 km s^{-1} in the majority of spectra obtained, only the U1 peak was detected due to the low intensity of the peaks. Spectra also showed fluorescence, which was a result of

contamination from the LGG. Raman data for all shots are presented in Appendix K, in addition to the classification data for spectra with all SO_4 modes detected. SEM EDX analysis was conducted on a selection of craters formed at a range of velocities (Appendix L, Figures L1 to L6) to ensure that calcium and sulphur were present in crater residues, which serves to confirm that the complete decomposition of the projectile did not occur, which in turn indicates the peaks detected by Raman spectroscopy were a result of SO_4 bonds. Table 8.2.6 and 8.2.7 shows the peak pressures and temperatures determined for natural gypsum projectiles onto aluminium plates. Temperatures predicted by Autodyn show there is a variation between the front and rear of the projectile, similar to that seen with goethite projectiles. They also show at velocities greater than 2.09 km s^{-1} temperatures are greater than the temperatures required for the complete transformation of gypsum to anhydrite, which occurs at 350 to 380 ˚C. However, temperatures estimated from the pressures at the front of the projectile show the complete dehydration of projectiles would only occur at velocities of 3.97 km s^{-1} or greater. At the rear of the projectile temperatures determined by Autodyn exceed 350 ˚C at velocities of 3.97 km s^{-1}, and do not exceed the 350 ˚C at any velocity for the temperatures estimated from the pressures. These temperatures are interesting as they show there should be traces of either bassanite or gypsum at velocities of 2.21 km s^{-1} or lower, yet at all velocities the Raman spectra for residues show an anhydrite spectrum (where all SO_4 peaks were detectable). However, TGA/DSC analysis determined that the peak transition temperature for the complete dehydration of gypsum occurs at a temperature of 182.3 ˚C. This suggests that it might be possible for the complete dehydration of gypsum to occur for all impact velocities, particularly for material at the front of the projectile. (although the complete dehydration of material at the rear of the projectile will still only occur at velocities greater than 2.21 km s^{-1}). All spectra obtained from the crater produced at 0.97 km s^{-1} were shown to be anhydrite, which showed the complete dehydration of gypsum at low impact velocities and pressures. Results from impacts experiments conducted by Bell & Zolensky (2011), using a mixture of gypsum and quartz, also showed anhydrite material being formed at impact pressures as low as 6.4 GPa, similar to what is observed here. Although, Bell & Zolensky (2011) state that recovered samples were impregnated with epoxy, which may have effected their analysis, as substantial heat can be released when curing epoxy, but it is unclear if this issue was addressed. Shock experiments performed by Bucio *et al.*, (2015), similar to those conducted by Bell & Zolensky (2011), showed that a mixture of bassanite and anhydrous material was detected after being impacted and experiencing a

peak pressure of 14 GPa, in planar shockwave experiments. These results are contradictory to what is observed in the results presented here, but this may be due to the differences in their shock experiments. The anhydrite spectra at all impact velocities seen in this series of impact experiments might signify that increasing the pressure will reduce the temperature dehydration occurs at, which is seen in dehydration experiments conducted by Comodi *et al.*, (2012), where at 2.5 GPa bassanite become anhydrite at a temperature of 215.9 ˚C. In addition to this, Comodi *et al.*, (2008) found that hydrogen bonds within gypsum becomes stronger and so concluded that dehydration from pressure alone would not occur.

Table 8.2.6 Calculated peak pressures experienced by natural gypsum projectiles.

Shot I.D	**Impact Velocity (km/s)**	**Peak pressure (GPa)**			
		Hugoniot	PIA	Autodyn	
				Front of projectile	Rear of projectile
S060814#1	0.97	6.27	5.71	5.96	1.27
G060614#1	2.09	13.75	14.66	14.41	2.47
G131114#1	2.21	13.75	15.76	15.44	2.63
G161014#1	3.97	37.76	34.97	39.77	5.67
G270614#1	4.09	37.47	36.49	42.31	6.00
G100714#2	4.90	49.47	47.42	56.52	8.70
G060814#1	5.83	62.41	61.45	75.17	12.32
G071114#1	5.86	62.41	61.92	75.85	12.44
G201114#1 (Anhydrite)	3.88	49.48	40.32	34.18	6.31

Table 8.2.7 Calculated peak temperatures determined for natural gypsum projectiles

Shot I.D	**Impact Velocity (km/s)**	**Temperature (˚C)**			
		Autodyn		From pressure*	
		Front of projectile	Rear of projectile	Front of projectile	Rear of projectile
S060814#1	0.97	217.53	65.58	100	<100
G060614#1	2.09	782.15	140.20	150	<100
G131114#1	2.21	936.55	153.94	150	<100
G161014#1	3.97	3316.05	363.45	300 -900	100
G270614#1	4.09	3556.55	388.75	300 -900	100
G100714#2	4.90	4742.15	496.41	> 1500	100
G060814#1	5.83	6605.25	899.85	> 1500	150
G071114#1	5.86	6748.95	829.15	> 1500	150
G201114#1 (Anhydrite)	3.88	5008.95	608.09	275-900	100

*Estimated impact temperatures determined from French (1998) and references therein, using the peak pressures determined from all three methods for the front of the projectile, and using Autodyn pressures for the rear of the projectile.

A single shot of an anhydrite cuboid (2 × 1.5 × 1.5 mm) was also fired onto a 6.0 mm thick aluminium plate at 3.88 km s^{-1}, to assist with determining the effects shock would have on a sample that is already anhydrite. This sample was heated to 400 ˚C prior to the impact experiment and Raman spectra were also obtained. The U1 modes peak position for the projectile prior to impact was 1019.6 cm^{-1}, which is greater than the peak positions previously obtained for anhydrite. Previous heating experiments that showed a maximum peak position of 1017 cm^{-1} was achieved when a sample of gypsum was heated to form anhydrite. There were also differences in the pre-shock spectra of the natural gypsum projectiles, which is surprising as natural gypsum for both heating and impact experiments came from the same parent sample of gypsum and SEM EDX analysis showed that the sample was homogenous (these results are found in Chapter VI). In addition to this, the peak width of G100714#2 is also wider by ~17 wavenumbers than the peak widths for the remaining gypsum projectiles. However, this quite large peak width is due to the peak fitting for these Raman spectra, and the actual peak widths for the projectile prior to impact is 13 cm^{-1}. The lowest peak position obtained for these peaks was 1006 cm^{-1}, it is unclear as to why this has occurred, but it might be a result of the method used to shape the projectile, or it might have been a result of an unknown effect that occurred prior to acquiring the samples.

Natural Gypsum Projectiles: SO_4 U1 Peak Analysis

Similar to goethite, the heating experiments for gypsum showed gypsum, bassanite and anhydrite can be distinguished using the peak width and peak positions of specific peaks; in this case the SO_4 U1 and U2 (2) peaks. There is some overlap of bassanite and anhydrite when examining SO_4 U1 peaks, but this does not occur for the U2 (2) peak. Natural gypsum shot data shows U1 peaks (Figure 8.2.19) fall outside the standard regions determined by heating experiments, which clearly shows impact pressures have a large effect on gypsum. Overall the peak widths are greater than their original peak widths which ranged between 6 and 9 cm^{-1}, except for the shot at 4.90 km s^{-1} (G100714#1) which had a peak width of 13 cm^{-1}. Peak widths for this shot either remains at 13 cm^{-1} or decreased to 11.5 cm^{-1}, however, due to the greater peak width it had to start with it these results are somewhat anomalous. There is also an increase in peak position from the lower peak position values for gypsum, which normally results from a loss of water from the crystal structure.

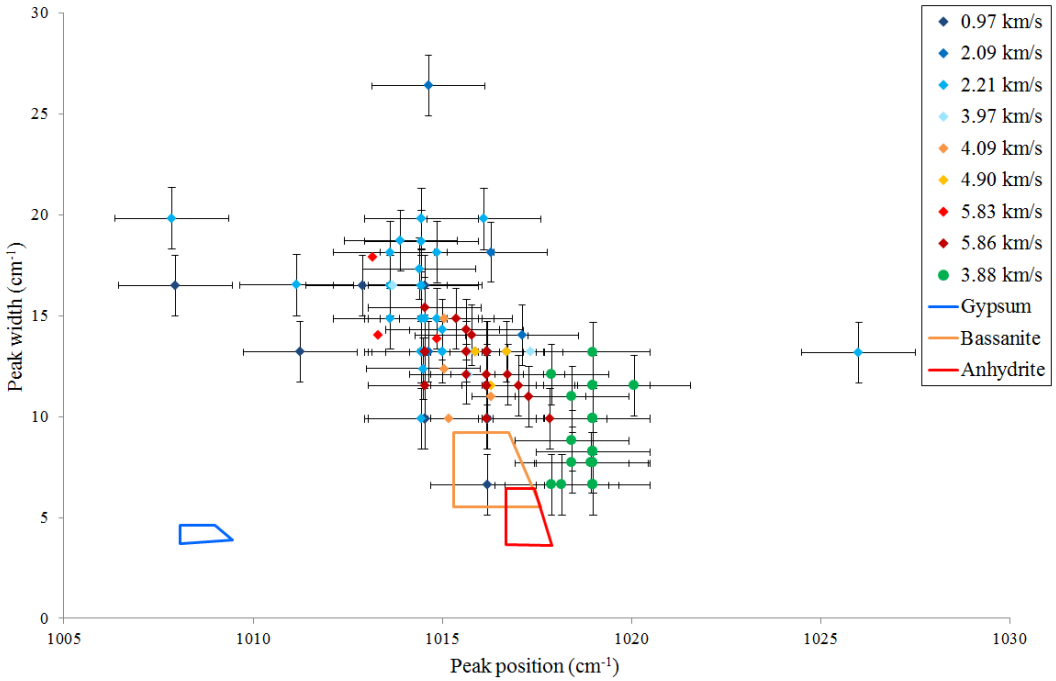

Figure 8.2.19 Peak positions and widths for gypsum (coloured diamonds) and anhydrite (green circles) projectiles after impact. The coloured boxes represent the standard regions determined form the gypsum heating experiments. Raman spectra were taken using the 532 nm laser at 10%, 600 groves per mm grating, 50× microscope objective.

The majority of peak positions are found between 1013.0 and 1017.3 cm^{-1}, which overlaps with the peak positions for bassanite and anhydrite at 1015.3 to 1017.9 cm^{-1}. However, for crater 12, spectrum 1, at an impact velocity of 2.21 km s^{-1} a single peak was detected at 509.7 cm^{-1}, it is unclear as to the cause of the peak and it is the only occurrence seen in all data, as such it was not included in the analysis. There does appear to be a separation of data points at an impact velocity of 3.97 km s^{-1}, above this velocity peak positions are generally higher (1015.2 to 1017.8 cm^{-1}) and peak widths are relatively narrower (14.8 to 9.9 cm^{-1}). At velocities less than 3.97 km s^{-1}, peak positions are generally lower (1014.5 to 1011.2 cm^{-1}) and peaks are much broader (14.8 to 19.8 cm^{-1}). This would indicate that above a certain pressure, peak widths start to become narrower again, although not as narrow as their original width prior to impact. The anhydrite shot (G201114#1 at 3.88km s^{-1}) also shows some change in peak position from its before-shot peak position at 1019.6 cm^{-1}, however, 83% of spectra collected have a peak position of 1019.0 cm^{-1} which is within the margin of error for the Raman spectrometer. 16.1% of the spectra for this shot shows a decrease in peak position to 1017.3 cm^{-1} and 1.8% (the equivalent of a single spectrum) displays an increase in peak position to 1020.6 cm^{-1}, (however this falls within

the margin of error). This would suggest that impact pressures would normally result in a decrease in peak positions as the bonds within anhydrite become strained. Changes in the peak position as a result of shock have also been observed in olivine (Foster *et al.*, 2013; Hibbert *et al*., 2014; Harriss & Burchell, 2016) and quartz (Hibbert *et al*., 2015b).

Initially the 473 nm laser was going to be used to analyse natural gypsum impacts, and so before spectra of projectiles used in shots at velocities of 2.09, 4.09 and 4.90 km s^{-1} were taken using this laser. There is calibration error of 0.5 cm^{-1} between the 473 nm and the 532 nm laser, which is less than one wavenumber and so does not affect the results. However, the data presented showing the change in peak positions (Figures 8.2.20 and 8.2.23) has been corrected for the change in laser. The change in peak position (Figure 8.2.20) between pre- and post-impacted gypsum shows and increase in peak positions occur as a result of impact, with the exception of two instances at velocities of 2.21 and 5.83 km s^{-1} where there was a decrease in peak position. The anhydrite projectile shows the opposite, where there is generally a decrease in peak position to a maximum change of 2.3 wavenumbers. As mentioned earlier, the increase in peak position for gypsum projectiles is most likely due to the loss of water from the structure and the pressure of the impact. The changes in peak position from the anhydrite projectile is almost certainly due to the strain induced by the impact pressures on the SO_4 crystal structure. Similar changes in peak positions, as a result of impact, are also found in olivine, where the effect of impact pressures also produced a decrease in peak position (Foster *et al.*, 2013). Overall, the increase in peak positions for all shots is confined to a relatively narrow range of 3 to 5 wavenumbers, when outliers are excluded. However, the changes in peak positions fall within values of 5.0 to 10.9 cm^{-1} at velocities of 3.87 km s^{-1}, and at lower velocities have changes in peak positions between 3.3 and 10.0 cm^{-1}, which shows there is a difference in the minimum changes in peak positions at velocities above and below 3.87 km s^{-1}. This may be an indication of the effects peak pressures have on gypsum, whereby larger changes in peak position are produced at higher impact pressures.

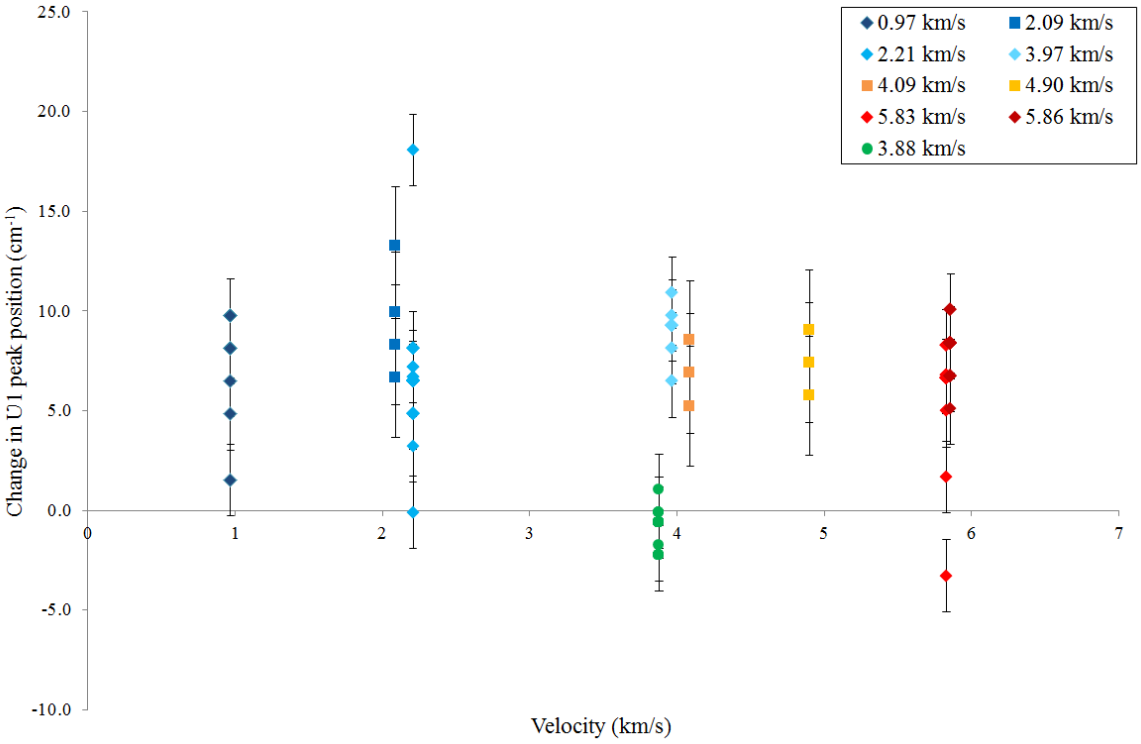

Figure 8.2.20 Changes in SO_4 U1 peak position, calculated using the average peak positions taken of the projectile before impact. Square data points represent three velocities where Raman spectra of the projectiles were taken using the 473 nm laser, which has been corrected to account for changing lasers. Circles represent the single anhydrite projectile.

The change in peak widths for the SO_4 U1 peak (Figure 8.2.21) shows that, overall, there is an increase in peak width for gypsum projectiles, with the exception of 4.90 km s^{-1}. It has been observed previously that Raman spectra of this projectile prior to impact had very broad peaks, almost double the width of the remaining gypsum projectiles. The changes in peak widths show a variation of ~10 wavenumbers for all shots, except at velocities of 2.09 and 2.21 km s^{-1}, which show slightly larger variations of 16.5 and 13.2 wavenumbers, respectively. This larger variation of peak widths might indicate changes in crystallinity with increasing velocity/pressure. So, there could be a velocity/pressure range, around 2 to 2.5 km s^{-1} or 13.85 to 18.53 GPa, where material is relatively poorly crystalline and is disordered, and at velocities/pressures above and below this pressure range would indicate more crystalline material. Unlike the change in peak positions there is no trend in the minimum peak widths. At 0.97 km s^{-1} the minimum value for the change in peak width occurs at 0, however, this is the only instance where there is zero change in peak width at this velocity. The minimum change in widths for the remaining velocities have values between 1.4 and 3.3 cm^{-1}, and do not show any trend with increasing velocity. The single anhydrite impact at 3.88 km s^{-1} also shows there is an overall increase in peak width upon

impact. However, 48.2% of the spectra obtained for this shot showed a decrease in peak width of 0.4 wavenumbers, which is smaller than the positioning error for the 532 nm laser (which is 1.8 cm^{-1}). In addition to this, no other spectra for this shot showed a decrease of peak width greater than 0.4 cm^{-1}, so this apparent decrease in peak width might just be a result of the fitting function.

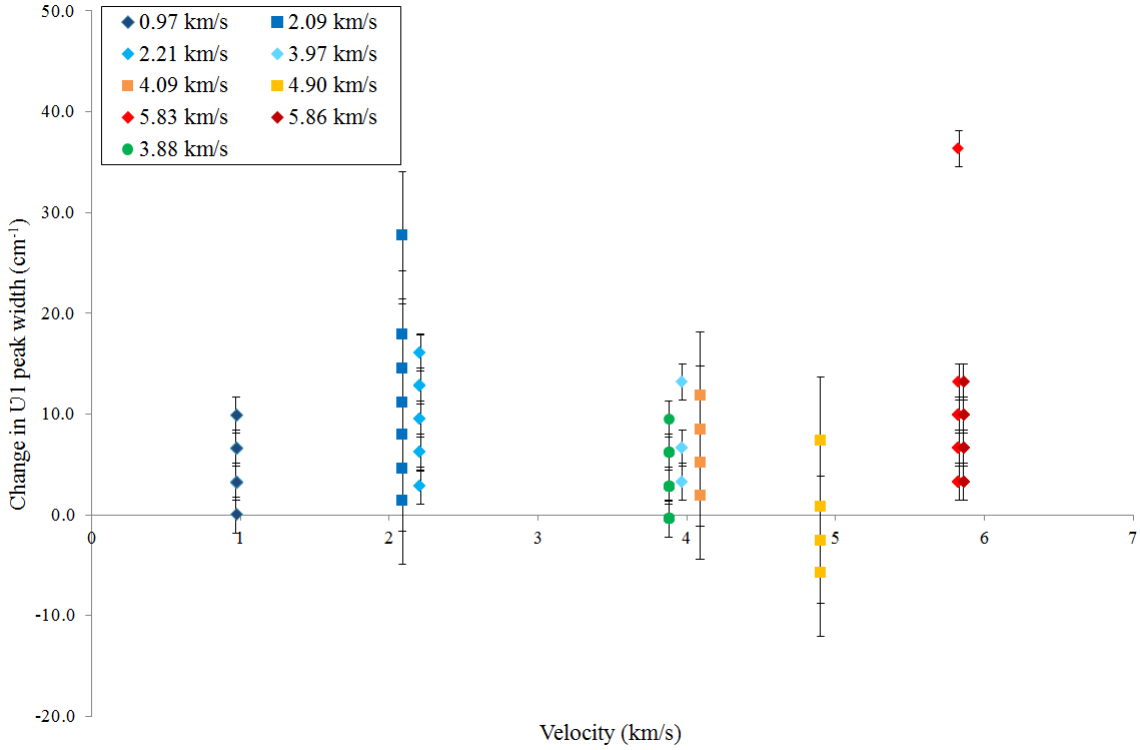

Figure 8.2.21 Changes in SO_4 U1 peak width, calculated using the average peak positions taken of the projectile before impact. Square data points represent three velocities were Raman spectra of the projectiles were taken using the 473 nm laser and circle data points represent the single anhydrite projectile.

As mentioned previously not all SO_4 peaks were detected for all spectra obtained at each velocity, therefore, the analysis of U2 (2) peaks does not provide a complete view of what is occurring. At some velocities, only five spectra showed the U2 mode and at 2.09 km s^{-1} this mode was not detected in any of the spectra. Similar to the U1 peak, the U2 (2) peaks do not fall within the standard regions for gypsum, bassanite or anhydrite (Figure 8.2.22) determined from the heating experiments (Chapter VII, Section 7.2.3). There are two instances where data points from the gypsum projectiles fall within the bassanite and anhydrite standard regions at velocities of 3.97 and 4.09 km s^{-1}, respectively. However, it is seen from the spectra classification that no spectra were classified as bassanite, meaning that this point is not representative of the actual impact residue. The data point within the

anhydrite standard region is representative of the correct hydrous state. However, it is difficult to determine why this single point falls within the correct standard. It could be a result of this particular spectra representing material from the rear of the projectile and, as such, it experienced lower impact pressures, but this is an assumption as it would be impossible to confidently determine from the data presented here. All but two data points have peak positions found within a range of 492.2 to 499.4 cm $^{-1}$ and peak widths between 14.0 and 28.0 cm^{-1}, which covers the area in-between the bassanite and anhydrite standard regions. Peak widths are also greater than those normally seen for anhydrite, with the exception of four data points at velocities of 2.09, 4.09, 5.83 and 5.86 km s^{-1} that have peak widths of 0.9 wavenumbers lower than the maximum peak width found from the heating experiments. Data points for the anhydrite projectile are clustered around the standard anhydrite region, with four data points inside the region and 22 data points within 1 wavenumber of the region. However, due to the variation seen in the peak position of Raman spectra taken before projectiles were fired onto the Al plates, it is difficult to determine the true effect pressures have had on the materials.

Natural Gypsum Projectiles: SO_4 U2 Peak Analysis

The changes in U2 (2) peak positions (Figure 8.2.23) for each velocity are not as large as those seen for the U1 mode. These U2 (2) peaks show large decreases in peak position for half of the gypsum projectile impacts, at velocities of 0.97, 2.21, 5.83 and 5.86 km s^{-1}, and there is an increase in peak position at all velocities for gypsum projectiles. The greatest decrease in peak position occurs at an impact velocity of 5.86 km s^{-1}, which could be indicative of higher impact pressures. Although the decrease in peak position seen at all velocities only accounts for 1 to 3 of the total number of spectra for this mode, indicating that it is more likely there is an overall increase in peak positions, similar to U1. However, it is difficult to determine as U2 (2) peaks were not detected for all spectra, and those that have been collected may not be a true representation of the effects impact pressures have on the samples. Anhydrite U2 (2) peaks show an overall decrease in peak positions, similar to the decrease seen in U1 modes. These, again, show that generally impacts of gypsum projectiles produce increases of peak positions and impacts of anhydrite projectiles result in decreases in peak positions.

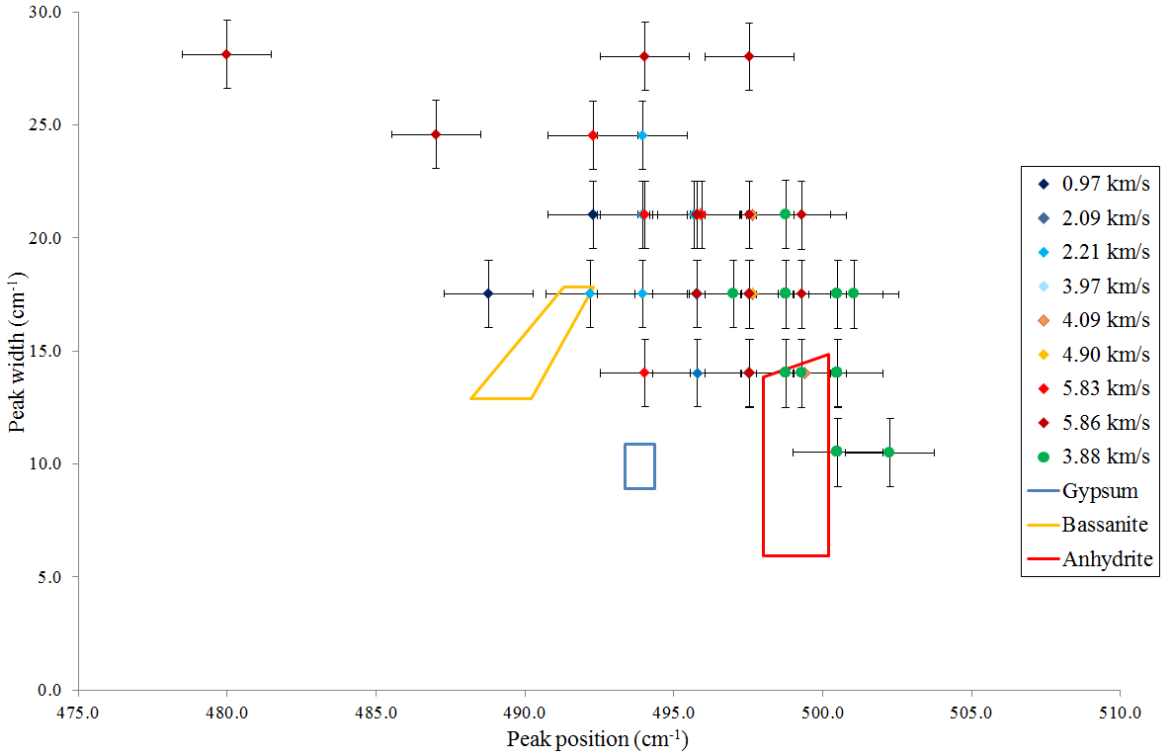

Figure 8.2.22 Peak positions and peak widths of U2 (2) peaks for both gypsum (diamonds) and anhydrite projectiles (circles). Raman spectra were take using the 532 nm laser at 10%, 600 groves per mm grating, 50 microscope objective and the exposure time and accumulations varied. The coloured boxes denote the standard regions for gypsum, bassanite and anhydrite determined from heating experiments.

Changes in U2 (2) peak widths (Figure 8.2.24) show that peaks broaden as a result of impact. There does appear to be a variation in the amount of change in peak widths with increasing impact velocity. At lower velocities, 0.97 and 2.21 km s^{-1}, the change in peak widths fall within 7 wavenumbers of each other and at higher velocities, 5.83 and 5.86 km s^{-1}, data points fall within 10.5 and 14.2 wavenumbers, respectively, of each other. The smallest increase in peak width is found at higher velocities than those at low impact velocities. This would suggest that a larger variation in crystallinity occurs at high impact velocities, potentially due to the higher peak pressures experienced by the projectile. Results from the anhydrite projectile also show an increase in peak widths upon impact.

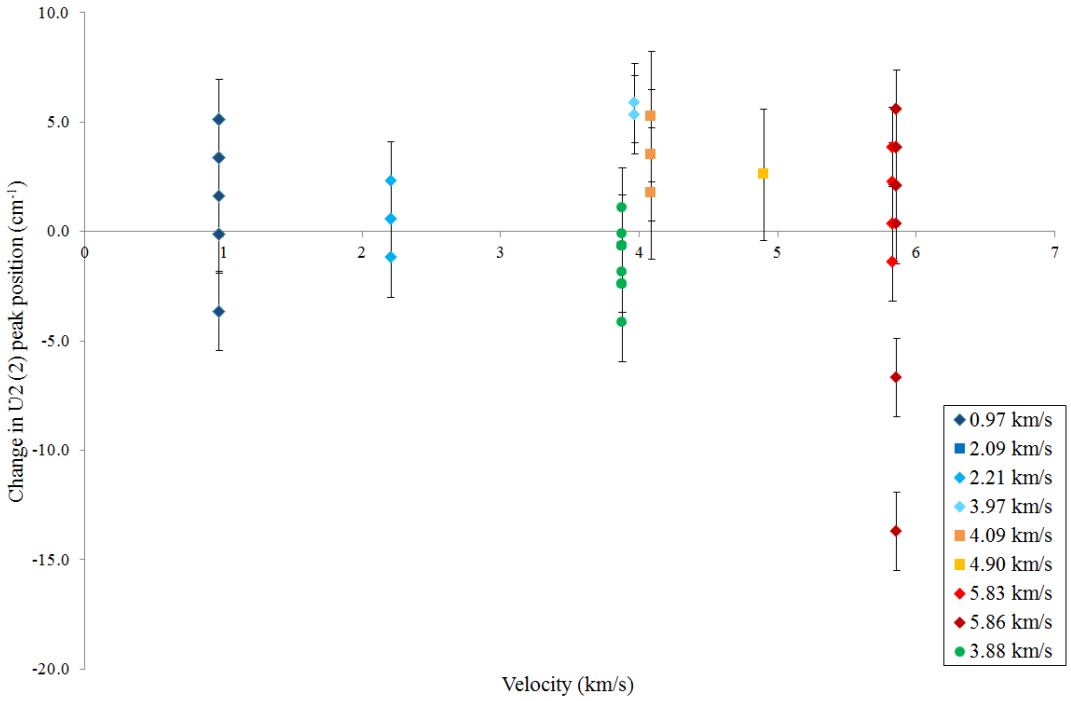

Figure 8.2.23 Changes in SO_4 U2 (2) peak positions, calculated using the average peak positions taken of the projectile before impact. Square data points represent three velocities where Raman spectra of the projectiles were taken using the 473 nm laser (which has been corrected for the change in laser) and circle data points represent the single anhydrite projectile.

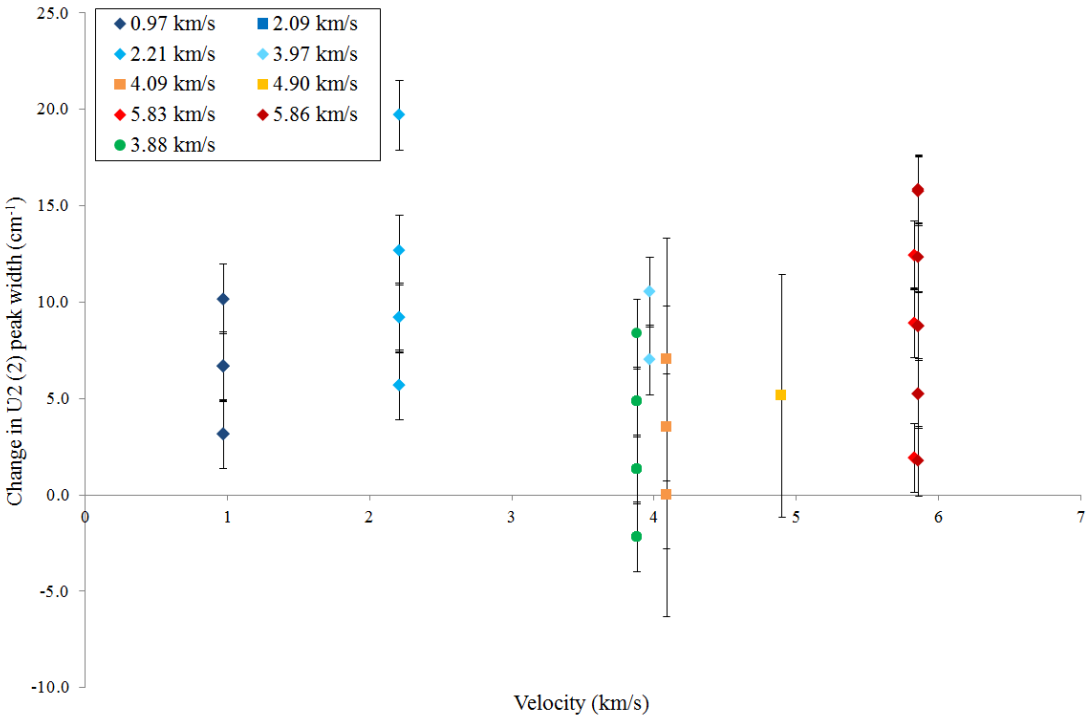

Figure 8.2.24 Changes in SO_4 U2 (2) peak width, calculated using the average peak positions taken of the projectile before impact. Square data points represent three velocities were Raman spectra of the projectiles were taken using the 473 nm laser and circle data points represent the single anhydrite projectile.

Analysis of gypsum projectiles shows an increase in peak position occurs as a result of impacts. However, there is no discernible trend that shows a specific increase in peak position with increasing impact velocity (and thus pressure). This may be a result of the varying pressure acting along the length of the projectile, causing the peak positions to shift varying amounts. The anhydrite projectile, on the other hand, shows an overall decrease in peak positions. Pressure experiments conducted on gypsum by Huang *et al.*, (2000) showed that as pressure is increased (up to 23.47 GPa) so did the Raman peak position, but upon releasing the pressure the peak positions returned to their original positions. These results are contradictory to the results obtained by Knittle *et al.,* (2001), who, upon releasing gypsum from a pressure of 19.7 GPa, noted a slight increase in peak positions of up to ~10 wavenumbers for U1 mode and a decrease of ~ 10 wavenumber U2 (2). These results (loosely) agree with the results seen here, as the U1 mode shows an increase in peak position upon impact, but there is an overall increase in the U2 (2) peak data, and there are a number of occurrences of decreases in peak positions for both peaks.

Summary of Results for Gypsum Projectiles

The results presented here for natural gypsum projectiles, indicate that the dehydration temperature of gypsum decreases with increasing pressure. As all impact residues are classified as anhydrite. There is a clear increase in peak widths for both gypsum projectiles and the single anhydrite projectile, which is a clear indication of disorder within the crystal structure. The changes in peaks widths for the U1 mode may show that at impact velocities between 2.09 and 2.21 km s^{-1} a greater degree of disorder occurs as, at velocities above and below this range, the variation in peak widths are not as large. Much larger changes in peak widths for the U2 (2) peak are also seen at 2.21 km s^{-1}, which may also be representative of a velocity range that generates highly disorder material. However, due to the low number of occurrences for this mode it is difficult to draw any confident conclusions. Peak positions of both U1 and U2 (2) peaks show an increase in peak position for gypsum projectiles, whereas the anhydrite projectile shows a decrease in peak position. This indicates that the strain on SO_4 bonds, induced by pressure, causes a decrease in peak position, which could explain why peak positions of the U1 peaks, especially, are found at peak positions lower than that of anhydrite.

Semi-hydrous PoP powder (>90 - <120 μm) appeared to experience loss of sulphur, resulting in the decomposition of the material, when experiencing pressures of ~40 GPa.

However, an anhydrite projectile (1.5 × 1.5 × 2.0 mm) and hydrous PoP powder did not undergo decomposition when experiencing similar pressures. This indicates that both projectile size and initial hydrous state plays a role in whether or not decomposition occurs, which may suggest that the decomposition of gypsum, bassanite and anhydrite will occur at different impact pressures.

8.2.4 Gypsum Targets

Plaster of Paris (PoP) was used for the gypsum target impact experiments. Three shots were conducted to examine devolatilisation of mineral targets, at velocities of 7.12, 6.15 and 5.24 km s^{-1}, with a 1 mm (7.12 and 6.15 km s^{-1}) or 2 mm (5.24 km s^{-1}) diameter stainless steel sphere projectile. All three PoP targets were made six days prior to the day of the impact experiment being conducted, as initial experiments showed the PoP lost all of its excess water through evaporation and stopped losing mass after five days (see Chapter VI, Section 6.1.2).

The first target, shot I.D. G130913#1, was made up of nine separate blocks, which form a larger block when placed together. This was originally done to assists with analysis later, as cutting the blocks may have resulted in some devolatilisation, specifically of H_2O. However, when impacted at 7.12 km s^{-1} with a 1 mm stainless steel sphere, the central block was completely destroyed and some fragmentation of the surrounding blocks occurred, which made it difficult to piece together for any analysis to be carried out. As a result of this initial shot, the two subsequent targets were completely solid blocks. G111013#1 (11.2 × 11.3 × 2.2 cm) was impacted at a velocity of 6.15 kms^{-1} with a 1 mm diameter stainless steel sphere projectile, which produced a single crater (Figure 8.2.25a) with a depth of 10.5 mm. A second solid PoP target (shot I.D. G070314#1 measuring 7.6 × 7.6 × 2.6 cm) was impacted at 5.24 km s^{-1} with a 2 mm diameter stainless steel sphere projectile. Upon impact this target fragmented into a number of pieces of varying sizes (Figure 8.2.25b). Although measures were taken to try and collect all the ejected material, not all the material could be collected, which made piecing the block together difficult.

a) b)

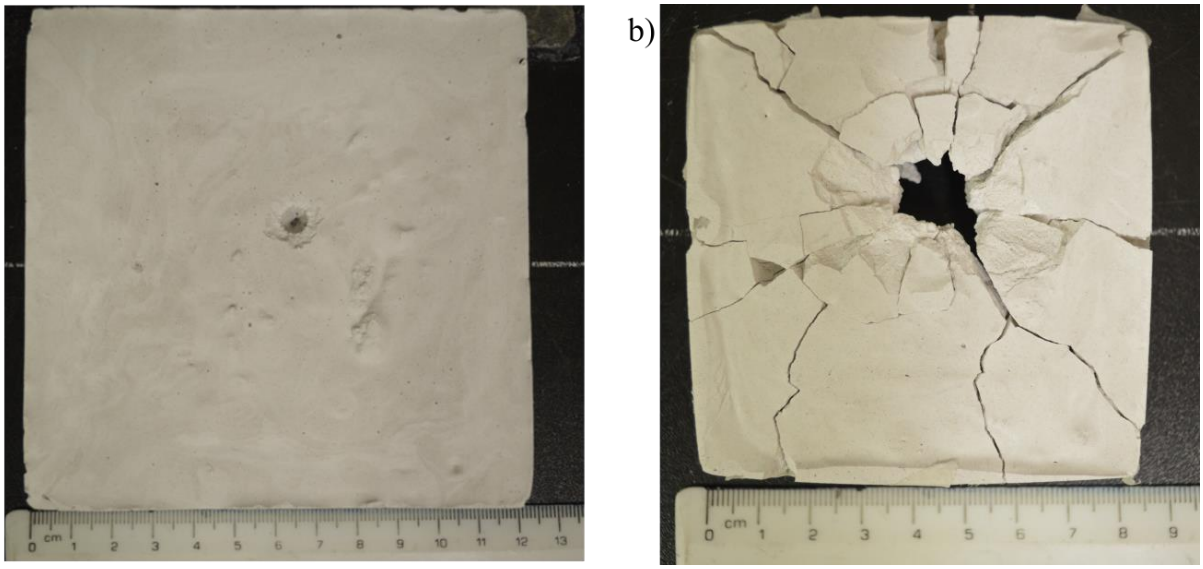

Figure 8.2.25 PoP targets, G111013#1 (image a) and G070314#1 (image b) after being impacted with stainless steel spheres at 6.15 and 5.24 km s^{-1} respectively.

Peak Pressures and Temperatures

Tables 8.2.8 and 8.2.9 shows the peak pressures and the estimated temperatures experienced by each of the targets. These results show that the impact pressures decrease considerably at the rear of the target, from the centre outwards, with impact pressures between 0.08 and 0.01 GPa for both targets. The temperatures experienced at the rear of the target (again from the centre outwards) are less than 50 ˚C, for both targets, and so it is unlikely that any loss of H_2O would occur at the back of the target. These simulations also show temperatures greater than 100 ˚C are generated within 1.35 mm of the centre of the target, which falls within the diameter of the crater for both targets. Temperatures of 100 ˚C or greater occurs up to a distance between 3.65 and 4.55 mm for G111013#1 and up to 7.65 mm for G071314#1 along the *x*-axis (the depth). This suggests that if any devolatilisation were to occur in these impacts it would occur within the crater and would presumably be detected along the crater walls, or the crater floor.

Table 8.2.8 Peak pressure and temperatures experienced by G111013#1 (6.15 km s^{-1}).

Pressure calculation	Distance from centre of target (mm)		Pressure (GPa)	Temperature from Autodyn (˚C)	Temperature from pressure (˚C)
Hugoniot		0.00	101.83	N/A	>2500
PIA		0.00	100.91	N/A	>2500
Autodyn	*x*-axis (depth)	0.05	142.58	16996.9	>2500
		0.95	45.97	3631.4	900
		1.85	22.54	1035.0	170-275
		2.75	13.75	422.9	150
		3.65	7.49	171.0	100
		4.55	4.55	79.6	<100
		5.45	3.30	58.9	<100
		6.35	2.55	50.5	<100
		7.25	2.00	<50.0	<100
		8.15	1.58	<50.0	<100
		9.05	1.27	<50.0	<100
		9.95	1.04	<50.0	<100
		22.0	0.01	<50.0	<100
	Front surface of target	0.05	142.58	16995.9	>2500
		0.35	100.97	7409.2	>2500
		1.35	1.21	50.1	<100
		3.04	0.30	<50.0	<100
		2.35	0.18	<50.0	<100
		4.71	0.05	<50.0	<100
		8.84	<0.05	<50.0	<100
		52.5	0.01	<50.0	<100
	Rear surface of target	0.05	0.01	<50.0	<100
		0.35	0.01	<50.0	<100
		1.35	0.01	<50.0	<100
		2.35	0.01	<50.0	<100
		3.04	0.01	<50.0	<100
		4.71	0.01	<50.0	<100
		8.84	0.01	<50.0	<100
		11.9	0.01	<50.0	<100
		19	0.01	<50.0	<100
		26.5	0.01	<50.0	<100
		52.5	0.01	<50.0	<100

Table 8.2.9 Peak pressure and temperatures experienced by G070314#1 (5.24 km s^{-1}).

Pressure calculation	Distance from centre of target (mm)		Pressure (GPa)	Temperature from Autodyn (˚C)	Temperature from Pressure (˚C)
Hugoniot		0.00	73.95	N/A	>1500
PIA		0.00	78.56	N/A	>1500
Autodyn	*x*-axis (depth)	0.05	137.28	10113.9	>2500
		1.95	34.66	1977.1	275-300
		3.85	15.29	551.9	150
		5.75	8.21	154.0	100
		7.65	5.37	100.3	100
		9.55	3.46	54.7	<100
		11.50	2.61	<50.0	<100
		13.40	1.98	<50.0	<100
		15.30	1.54	<50.0	<100
		17.20	1.24	<50.0	<100
		19.10	1.01	<50.0	<100
		21.00	<1.00	<50.0	<100
		26.00	0.08	<50.0	<100
	Front surface of target	0.05	137.28	10113.9	>2500
		0.35	80.03	2812.6	>2500
		0.85	47.47	2861.4	900-1500
		1.35	5.93	121.3	100
		1.85	1.78	55.4	<100
		2.35	0.84	<50.0	<100
		3.01	0.44	<50.0	<100
		3.74	0.24	<50.0	<100
		4.46	0.17	<50.0	<100
		6.07	<0.10	<50.0	<100
		35.30	0.01	<50.0	<100
	Front surface of target	0.05	0.08	<50.0	<100
		0.35	0.08	<50.0	<100
		0.85	0.08	<50.0	<100
		1.35	0.08	<50.0	<100
		2.35	0.08	<50.0	<100
		3.01	0.08	<50.0	<100
		3.74	0.09	<50.0	<100
		4.46	0.00	<50.0	<100
		6.07	0.07	<50.0	<100
		7.65	<0.05	<50.0	<100
		35.30	0.01	<50.0	<100

Raman Data

Raman spectra of G111013#1 and G070314#1 were taken using a 473 nm laser, 600 g/mm grating and a ×50 microscope objective. The depth and diameter of the crater for

G111013#1 made it difficult to use a higher magnification microscope object and as a result only a few Raman spectra were taken of the crater floor. The overall Raman spectra from G111013#1 showed the sample was still hydrated, as both SO_4 and H_2O modes were present (Table 8.2.10). There are only two instances where there was a change in peak position greater than the margin of error (~2.2 cm^{-1}), both of which were from spectra taken from the floor of the crater. Spectrum 1 of the crater spectra shows a decrease in peak position of the H_2O (2) peak, which could indicate some dehydration has occurred. Heating experiments of natural gypsum did show that a slight decrease in this peak position occurs with increasing temperature, and there is also a very slight decrease in mass of 0.0010%. Spectrum 3 of the crater spectra showed an increase of 4.4 wavenumbers in the peak position of SO_4 U4 (1) peak. Although this peak was not analysed as part of the heating experiments, it is believed that this is an indication of the devolatilisation of the PoP, as this peak is bonded with hydrogen (Berenblut *et al.*, 1973; Giacomazzi & Scandolo, 2010), which means it will be affected by the loss of water. In addition, this spectrum shows the presence of a third H_2O peak at 3553.1 cm^{-1}, which is within the error (2.2 cm^{-1}) of the OH peak found in the semi-hydrous phase of gypsum at 3554.7 cm^{-1}. Changes in peak position are also found for G070314#1 (Table 8.2.11), with the largest changes of peak positions occurring from spectra taken from the spall of the crater than on the fragments. The peak positions of hydrous, and semi-hydrous, PoP shows that there is an increase in the peak positions for SO_4 U1, U2 (2) and U4 (1) peaks as PoP becomes semi-hydrous, which is also seen in the heating experiments for natural gypsum for the U1 and U2 (2) peaks. As mentioned earlier, the heating experiments also show that there is a decrease in the peak position of the H_2O (2) peak as the sample loses water. There is only one instance (spall, spectrum 10) where a decrease in peak position of H_2O (2) peak occurs. However, the decrease in peak positions of all SO_4 peaks would suggest that the shifts in peak positions may not be a result of loss of water, and was probably caused by pressure. Unfortunately, as this target fragmented upon impact no spectra could be taken from the floor of the crater, which may have shown the presence of an OH peak similar to what was seen in G111013#1. Both PoP targets show there is an increase in the peak width, which indicates a disruption of the crystal structure, and a relatively lower crystallinity. The broadening of peaks occurs as a result impact pressure which makes it difficult to determine if a loss of water has occurred from Raman spectroscopy alone, especially where that is no obvious change in hydrous state. A previous experiment conducted by Miljokvić *et al.,* (2013), used both Raman and infrared (IR) spectroscopy to

analyse an impacted PoP targets. IR analysis of these targets showed a loss of H_2O to form bassanite, in spectra taken from the crater floor and at some distance away from the crater, when a PoP target was impacted at 2 km s^{-1} with a 1 mm diameter stainless sphere projectile. Miljković *et al.*, also fired a 2 mm diameter stainless steel sphere onto another PoP target at 5.15 km s^{-1}, which showed similar IR results, except there is no clear semi-hydrous feature, just a reduction in intensity for the H_2O feature. However, no results using Raman spectroscopy are provided from the Miljković *et al.*, (2013) impacts experiments. Although the detection of semi- hydrous PoP within the impact crater corresponds to the findings from G111013#1 of this investigation, assuming the feature at 3553.1 cm^{-1} is, indeed, representative of bassanite. To confirm this theory a mixture of 50% hydrated PoP and 50% semi-hydrous PoP were mixed together and Raman spectra of this sample were taken. Hydrous and semi-hydrous samples were crushed together using a pestle and mortar to create a fine grained powder. Results from this test (Figure 8.2.26) showed that all spectra represented hydrous PoP. However, a number of spectra did show a low intensity OH peak at 3558.8 cm^{-1}, indicating the detection of semi-hydrous material in the sample. This confirms that the third H_2O peak found at 3553.1 cm^{-1} in the Raman spectra of G111013#1 (crater floor, spectrum 3) does indeed show the presence of semi-hydrous material within the crater.

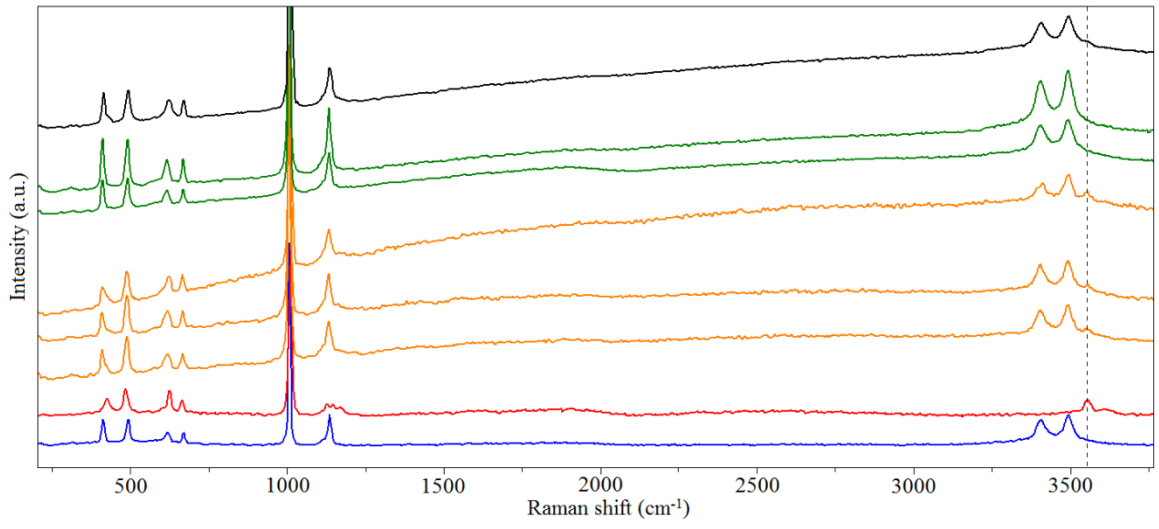

Figure 8.2.26 Results from the PoP mixture test are divided into two groups, those which show the presence of an OH peak (orange) and those that do not (green). Raman spectra of hydrous and semi-hydrous PoP are shown in blue and red, respectively, and the spectrum of interest from G111013#1 is shown in black for reference. Raman spectra have been offset for clarity and the dashed line highlights the position of the OH peak at 3553.1 cm^{-1}.

Table 8.2.10 Raman data for G111013#1.

Location	Spectrum	U1		U2 (1)		U2 (2)		U3 (1)		U4 (1)		U4 (2)		H2O (1)		H2O (2)		H2O (3)	
		Position (cm^{-1})	Width (cm^{-1})	Position (cm^{-1})	Width (cm^{-1})	Position (cm^{-1})	Width (cm^{-1})	Position (cm^{-1})	Width (cm^{-1})	Position (cm^{-1})	Width (cm^{-1})	Position (cm^{-1})	Width (cm^{-1})	Position (cm^{-1})	Width (cm^{-1})	Position (cm^{-1})	Width (cm^{-1})	Position (cm^{-1})	Width (cm^{-1})
		1007.4	8.5	414.6	9.0	493.5	13.5	1135.8	14.0	618.4	20.7	670.0	13.2	3405.7	41.6	3493.9	38.9	-	-
Crater Floor	1	1007.4	8.5	414.6	13.6	493.5	18.0	1136.5	16.8	620.6	22.1	671.5	13.2	3405.1	49.3	3491.6	58.4	-	-
	2	1007.4	8.5	414.6	13.6	493.5	18.0	1134.4	16.8	620.6	26.6	669.3	13.2	3406.7	55.9	3493.2	55.1	-	-
	3	1009.5	12.8	414.6	13.6	493.5	18.0	1136.5	21.0	622.8	26.6	669.3	13.2	3406.7	55.9	3494.8	51.9	3553.1	74.0
Spall	1	1007.4	8.5	414.6	9.0	493.5	13.5	1134.4	12.6	618.4	22.2	669.3	13.2	3406.7	46.0	3494.8	38.9	-	-
	2	1009.5	8.5	414.6	13.6	493.5	13.5	1136.5	12.6	618.4	22.2	671.5	8.8	3405.1	39.4	3494.8	35.7	-	-
Outside Spall	1	1009.5	8.5	414.6	13.6	493.5	13.5	1136.5	21.0	620.6	17.7	671.5	8.8	3405.1	46.0	3493.2	45.4	-	-
Edge of block	1	1007.4	8.5	414.6	13.6	493.5	13.5	1136.5	16.8	620.6	17.7	671.5	13.2	3405.1	46.0	3493.2	45.4	-	-
	2	1007.4	8.5	414.6	13.6	493.5	13.5	1136.5	16.8	618.4	22.2	669.3	13.2	3405.1	42.7	3493.2	35.7	-	-

N.B. Values in red show the averaged peak positions and peak widths of the target before being impacted.

Table 8.2.11 Raman data for G070314#1.

Location	Spectrum	U1		U2 (1)		U2 (2)		U3 (1)		U4 (1)		U4 (2)		H2O (1)		H2O (2)	
		Position (cm^{-1})	Width (cm^{-1})	Position (cm^{-1})	Width (cm^{-1})	Position (cm^{-1})	Width (cm^{-1})	Position (cm^{-1})	Width (cm^{-1})	Position (cm^{-1})	Width (cm^{-1})	Position (cm^{-1})	Width (cm^{-1})	Position (cm^{-1})	Width (cm^{-1})	Position (cm^{-1})	Width (cm^{-1})
		1008.0	8.5	414.2	11.3	493.8	13.5	1135.6	14.7	618.8	21.5	670.5	11.7	3405.8	42.1	3494.4	38.0
Fragment	1	1005.5	8.5	412.6	13.6	491.5	18.0	1134.6	16.8	618.6	22.2	669.5	17.6	3406.7	39.4	3496.5	35.7
	2	1005.5	8.5	412.6	13.6	493.7	17.9	1134.6	21.0	618.6	26.6	669.5	17.6	3408.4	36.1	3496.5	29.2
	3	1005.5	8.5	414.8	9.0	493.7	17.9	1134.6	16.8	618.6	22.2	669.5	13.2	3406.7	36.1	3498.1	32.4
	4	1007.6	12.8	414.8	13.6	493.7	13.5	1134.6	16.8	618.6	22.2	669.5	13.2	3408.4	42.7	3496.5	38.9
	5	1007.6	12.8	412.6	13.6	493.7	17.9	1134.6	16.8	618.6	26.6	669.5	26.4	3408.4	46.0	3496.5	39.0
	6	1007.6	12.8	414.8	13.6	493.7	17.9	1136.7	16.8	618.6	22.2	669.5	17.6	3405.1	39.4	3496.5	35.7
Spall	1	1005.4	8.5	410.3	13.6	491.4	18.0	1132.4	16.8	616.4	22.2	669.4	17.6	3405.2	49.3	3493.3	35.7
	3	1005.4	8.5	412.5	18.1	491.4	18.0	1134.5	16.8	616.4	31.0	667.2	26.5	3403.5	49.3	3495.0	48.6
	4	1005.4	8.5	410.3	18.1	491.4	18.0	1132.4	21.0	616.4	26.6	667.2	17.6	3403.5	45.9	3493.3	42.2
	5	1005.4	12.8	412.5	13.6	489.2	22.4	1132.4	21.0	611.9	22.2	665.0	26.5	3410.1	49.1	3495.0	58.4
	6	1005.4	8.5	410.3	13.6	489.2	18.0	1132.4	21.0	614.2	26.6	665.0	17.7	3406.8	36.1	3493.3	38.9
	7	1005.4	8.5	412.5	9.0	489.2	13.5	1134.5	16.8	616.4	22.2	667.2	13.2	3406.8	36.1	3493.3	29.2
	8	1005.4	8.5	410.3	13.6	491.4	13.5	1132.4	16.8	616.4	22.2	667.2	17.6	3405.2	46.0	3493.3	32.5
	9	1005.4	8.5	412.5	13.6	489.2	13.5	1132.4	12.6	616.4	17.7	667.2	13.2	3403.5	42.7	3488.5	29.3
	10	1005.4	8.5	410.3	13.6	491.4	18.0	1132.4	16.8	616.4	17.7	667.2	13.2	3403.5	46.0	3493.3	35.7
	11	1005.4	8.5	412.5	9.0	489.2	13.5	1132.4	12.6	616.4	22.2	667.2	13.2	3405.2	39.4	3493.3	35.7
Edge of block	1	1005.4	8.5	410.3	13.6	491.4	13.5	1132.4	16.8	616.4	17.7	667.2	13.2	3405.2	46.0	3493.3	38.9

N.B. Values in red show the averaged peak positions and peak widths of the target before being impacted.

The programme of impact experiments using PoP targets does show evidence, albeit very subtle, that devolatilistion has occurred. However, it has been restricted to a single occurrence in shot G111013#1. These results also show that the effects of impact pressure can potentially mask any indication of devolatilistion, which may have been suggested by changes in peak positions. However, the ability to detect mixtures with different hydrous phases does mean it is still possible to use Raman spectroscopy even when there are not any obvious changes in phases resulting from the loss of volatiles.

8.3 Chapter Summary

In this chapter the Raman spectra taken from impacted targets are presented. In the case of the devolatilistion impact experiments they are analysed using the results from the heating experiments provided in the previous chapter (Chapter VII). Both sets of experiments are used to determine the effects impacts can have on Martian relevant minerals. Chapter IX summarises these findings in the context of the three aims proposed at the start of this thesis.

Chapter IX

Conclusions and Future Work

9.1 Conclusions

The overarching objective of this investigation was to examine the effects of impacts on minerals and determine if it is possible to indirectly detect these affects post-impact using Raman spectroscopy. This was completed by accomplishing the following goals:

1) Determining if impacts could trigger chemical changes in a mineral that would result in serpentinisation and thus the production of methane.
2) Determining if we can identify the loss of volatiles found within mineral structures as a result of impact, and if the degree of loss could be used as a shock barometer.
3) Determining if either of these changes (goals 1 and 2) can be detected using Raman spectroscopy to support future missions to Mars equipped with such instrumentation.

9.1.1 Goal 1: Serpentinisation Experiments

The serpentinisation experiment (described in Chapter V) was conducted to answer goal 1, which was achieved by impacting a target of olivine grains, H_2O ice and CO_2 ice with a stainless steel projectile at velocities between 3.90 and 5.82 km s^{-1}. Results from these experiments did not show a strong indication that impact induced serpentinisation had occurred. There were only two instances (from shot G100513#2) where grains indicated olivine hydration had occurred (suggesting serpentinisation). However, this is not conclusive evidence for impact induced serpentinisation, but it does suggest it is a possibility. Previous work conducted by Furkawa *et al.,* (2011) showed the formation of serpentine after a target of olivine and water had been impacted: they believed this was a result of the formation of supercritical water. The peak pressures determined from Hugoniot plots, PIA calculations and Autodyn simulations, and estimated peak temperatures were greater than the critical pressure and temperature required for the

formation of critical water to form (which is 22 MPa and 373.95 ˚C). Figure 9.1.1 shows the peak temperatures and peak pressures calculated for each impact and the temperatures and pressures range identified for serpentinisation to occur. The diagram clearly shows that for these impacts the peak pressures and temperatures are greater than the range suggested for serpentinisation to occur. However, Hydmann & Peakcock (2003) stated that serpentinisation normally arises at a pressure of 1 GPa, which is much lower than the pressures seen in these impacts. Autodyn simulations showed that pressures between 22 MPa and 1 GPa occurred within the impact crater. This indicated that the most likely region to find grains that have undergone serpentinisation would be within the crater. However, in these experiments the target was mounted horizontally to the door of the target chamber, which resulted in the target crumbling after impact. This made it difficult to confidently retrieve and sample grains that would have been located within the crater. The ability to sample olivine grains from within the crater would potentially increase the chances of detecting grains that have undergone serpentinisation.

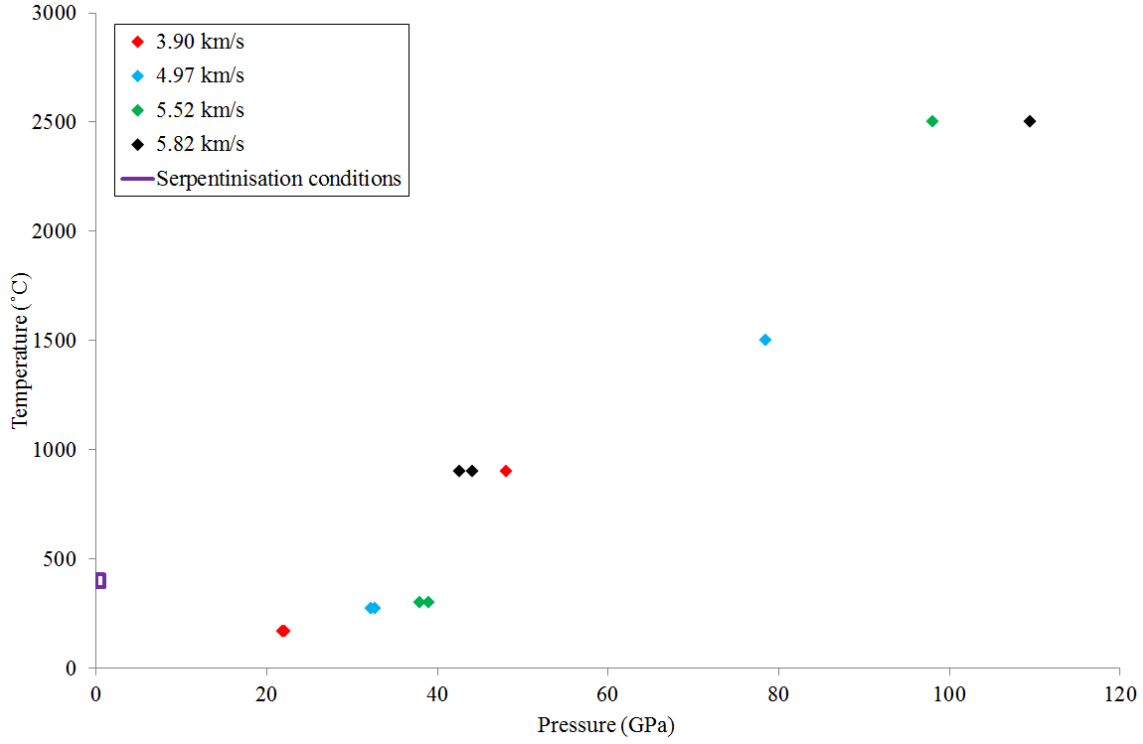

Figure 9.1.1 Peak pressures (determined by Autodyn simulations, Hugoniot plots and PIA calculations) and peak temperatures (estimated from the pressure using French, 1998 and references therein) for each of the four shots. The pressure and temperature range determined for critical water to from is highlight by the purple box.

Two additional shots were conducted with a water ice and olivine grain projectile impacting a metal target. Results from these impacts did not show any indication that

serpentinisation had occurred. The pressures generated from these impacts were again greater than the 22.06 MPa to1 GPa pressure range. However, it is possible that any serpentinisation that may have formed form these impacts may have been destroyed by the subsequent impact of the olivine onto the target.

9.1.2 Goal 2: Devolatilisation Experiments

To accomplish goal 2, goethite and gypsum were impacted at a range of velocities using the light gas gun (described in Chapter VI). In addition to this, these minerals were heated to temperatures up to 1000 and 1400 ˚C to examine the loss of volatiles without shock. These controlled heating experiments also helped to determine if the Raman spectra of these minerals could be used as geo-thermometers and quantify the loss of volatiles. These heating experiments showed that specific peaks/features that represent bonds with volatiles can be used to identify temperatures experienced by the sample. Results showed that the peak positions and peak widths of specific spectral features from goethite provided a much better correspondence to temperatures than gypsum (Figures 9.1.2 and 9.1.3). In particular, peak widths became narrower with increasing temperature from 500 to 1000 ˚C. This is most likely due to a difference in Raman spectra between goethite and hematite (which forms after the dehydration of goethite) and as only water could be lost. Gypsum has two volatile components (water and sulphur) that can both be lost when heated to high enough temperatures. The dominant Raman peaks in the spectra of gypsum and its dehydrated phases (bassanite and anhydrite) are a result of the SO_4 bonds. Therefore, the overall spectrum does not completely change as water is lost, which is what happens with goethite. Complete changes to the Raman spectra of gypsum only occur when sulphur is lost. However, the results did show that the peaks are relatively broader just before, and after, a phase transition occurs, which could be used to help determine the temperature history of the sample. These results indicate that the best volatile bearing minerals to use as geo-thermometers would be those that present a different mineral, with a different mineral structure, once the volatile component has been lost. It also indicates that mineral such as gypsum, could be used as a crude geo-thermometer indicating the minimum temperatures experienced before a phase transition or decomposition occurred.

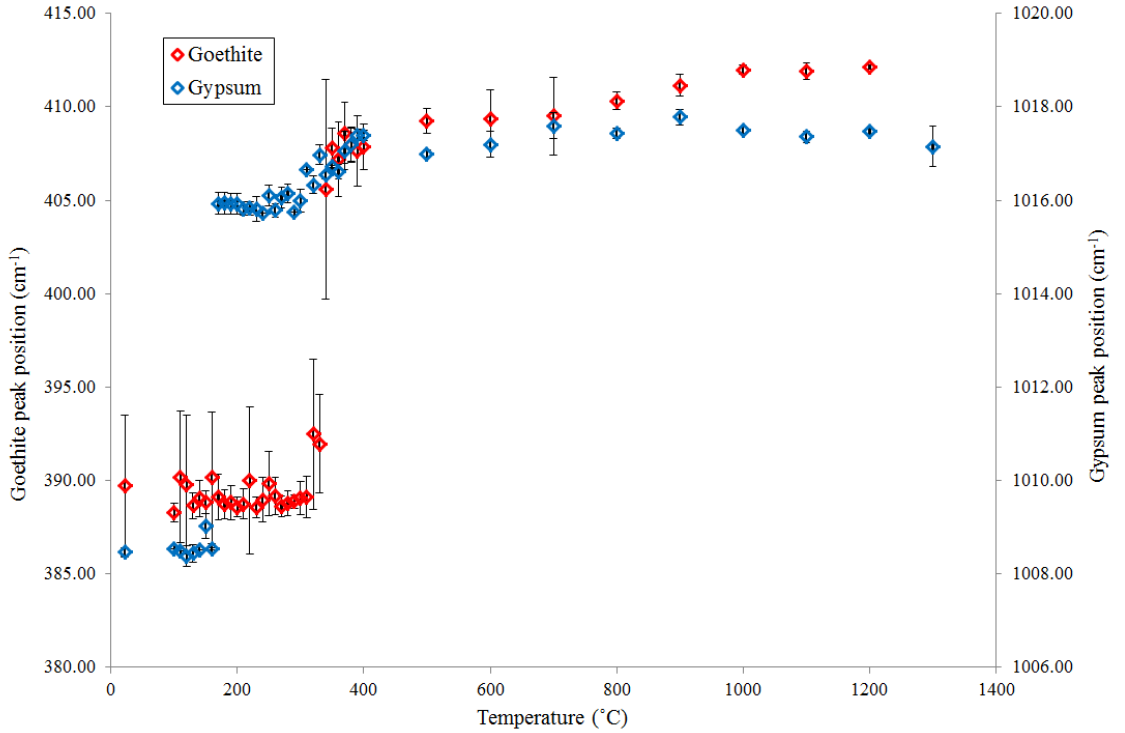

Figure 9.1.2 Averaged peak positions for goethite Feature A and gypsum SO_4 U1 taken from ex-situ heating experiments. It shows there is a stronger correspondence with change in peak positon and temperature for goethite data. The standard deviation for each temperature (from the absolute data) was calculated to generate the error bars.

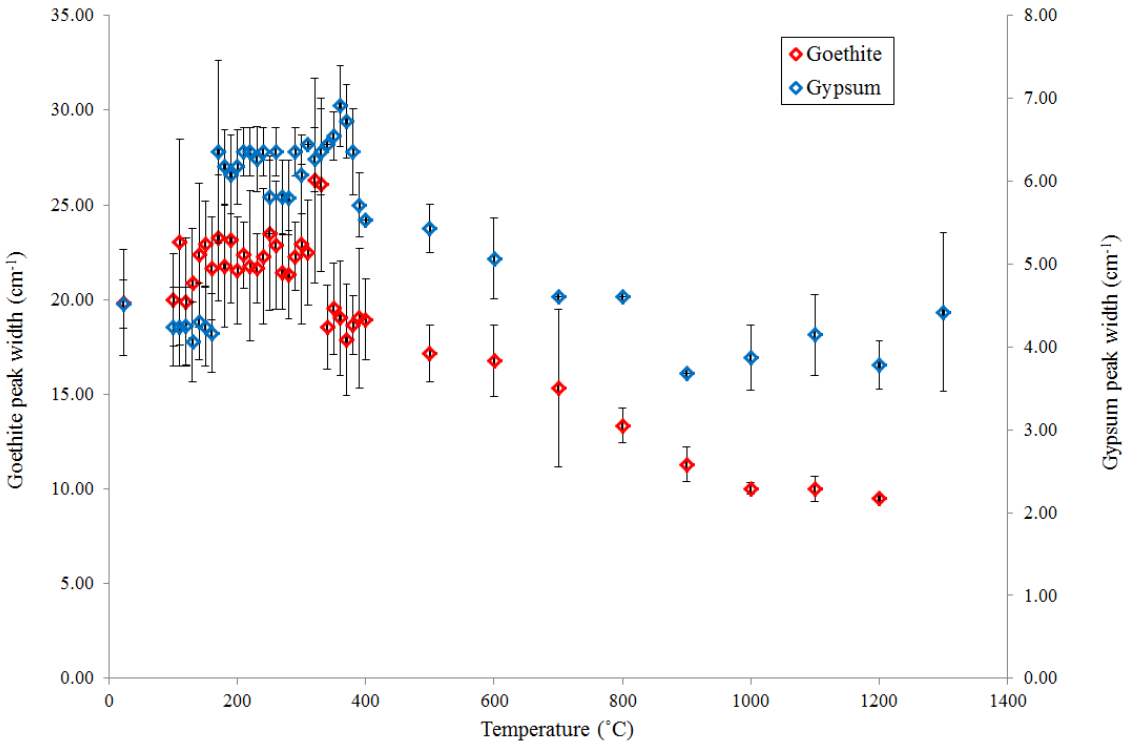

Figure 9.1.3 Averaged peak widths (from ex-situ heating experiments) for goethite Feature A and gypsum SO_4 U1 peaks. It shows there goethite peaks widths become much narrower with increasing temperature. The standard deviation for each temperature (from the absolute data) was calculated to generate the error bars.

The averaged peak position for Feature A of goethite did show some correlation with mass loss from the sample, whereby the averaged peak position appeared to increase with increasing mass loss (Figure 9.1.4). Ex-situ heating experiments for gypsum showed similar changes in peak position with a decrease in mass. These results indicate it is possible to quantify the mass lost from these volatile bearing minerals. However, this mass loss experiment was conducted on a single piece of mineral, and the grain size of the minerals may affect these results. Therefore, additional tests should be conducted to determine if the mass loss and changes in peak positions are the same for different sized samples.

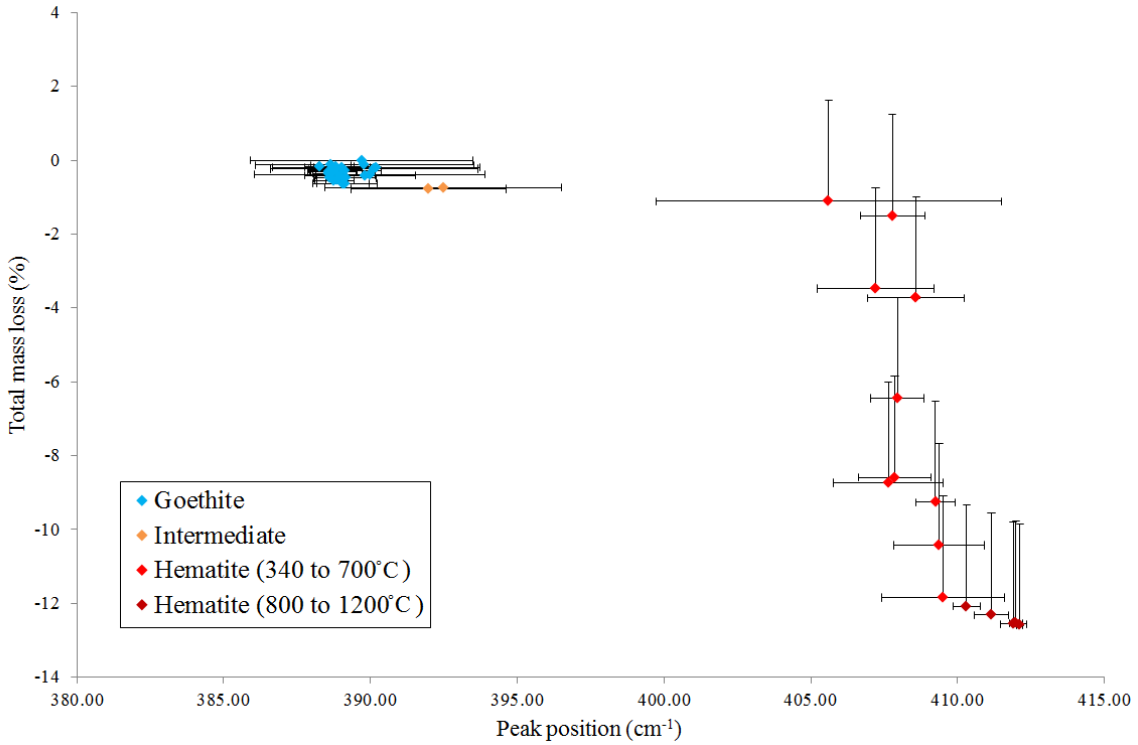

Figure 9.1.4 The total mass loss (in %) as a function of the Feature A peak position. The colour of the data points correspond to the dominate spectra classification (from the absolute data) for each temperature, i.e. goethite (blue), intermediate (orange) and hematite (red). The standard deviation for each temperature (from the absolute data) was calculated to generate the error bars for peak position and error bars for the mass measurements are described in the mass measurements sub-section of Section 7.1.2.

Raman spectra analysis of shocked goethite and gypsum illustrated that changes in both peak position and peak width occurred, which made it difficult to determine the temperature experienced on impact (Figures 9.1.5 and 9.1.6).

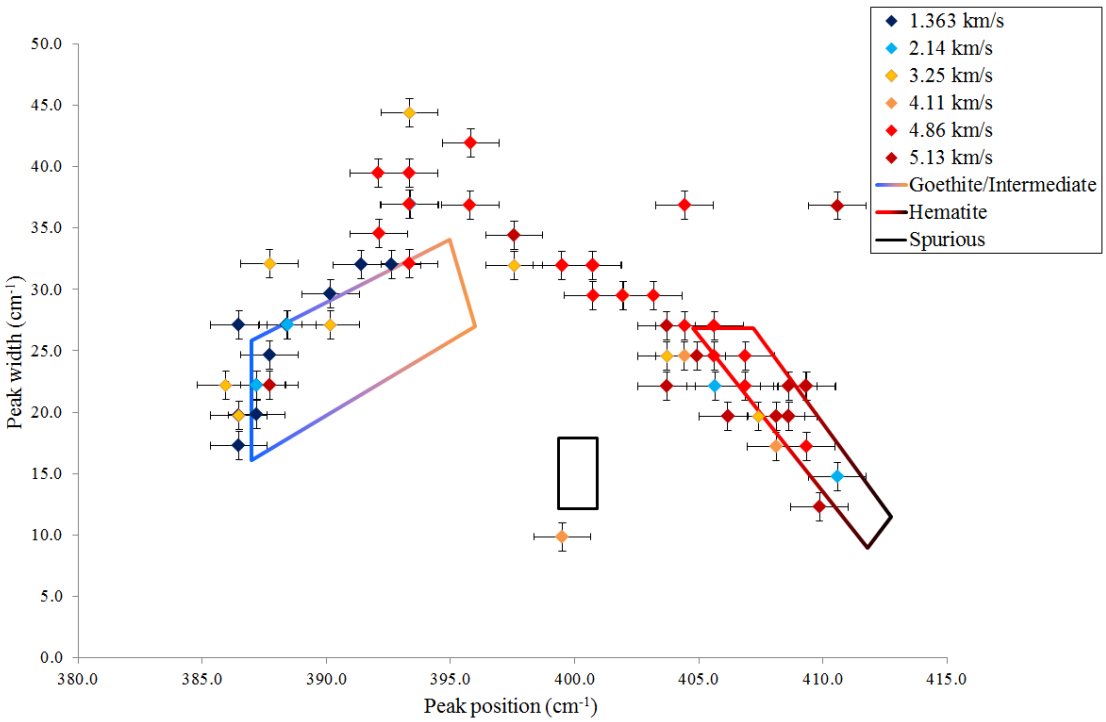

Figure 9.1.5 Raman spectra of impact residues from craters on plate 1. The two standard regions (determined form the heating experiments) of goethite/intermediate and hematite spectra are highlight by the coloured boxes. The solid black box highlights a cluster of spurious points. Error bars show the spectral resolution of the Raman configuration, which is 1.1 cm^{-1}.

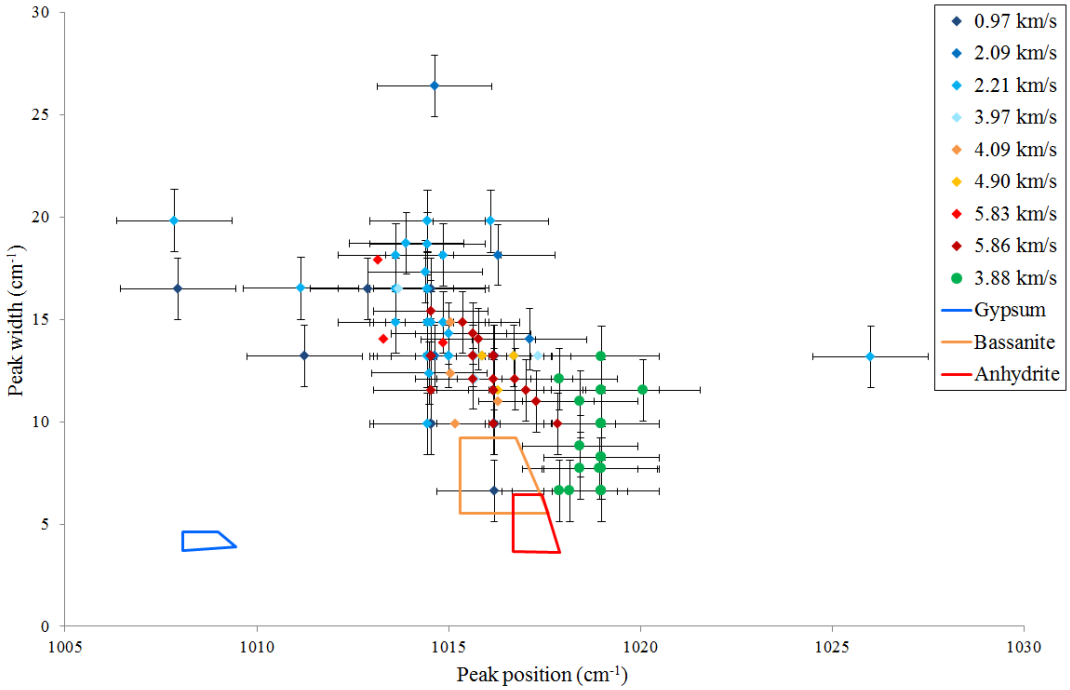

Figure 9.1.6 Peak positions and widths for gypsum (coloured diamonds) and anhydrite (green circles) projectiles after impact. The coloured boxes represent the standard regions determined form the gypsum heating experiments. Error bars show the spectral resolution of the Raman configuration, which is 1.5 cm^{-1}.

Even the simplest temperature gauge of volatile loss (in this case water) can be affected by an impact. For example, the use of natural gypsum projectiles showed that water loss can occur at impact velocities between 0.97 and 5.86 km s^{-1}. At 0.97 km s^{-1} the temperatures (determined from pressure) are expected to be lower than 100 ˚C or lower, and those determined by Autodyn at the rear of the projectile would be ~65 ˚C. These temperatures would normally not result in the dehydration of the sample. Therefore, some gypsum should be detected within the crater, which was not the case and spectra showed an anhydrite signature. These results showed that the increased pressures from the impact caused the dehydration temperature to change to a lower temperature. Comodi *et al.*, (2008) conducted experiments examining the behaviour of gypsum at high pressures and concluded that pressure alone would not result in dehydration, as the hydrogen bonds actually became stronger with increased pressure. However, these experiments conducted by Comodi *et al*., (2008) only reached a pressure of 3.9 GPa and the pressures experienced in these impact experiments are greater than 5 GPa. Therefore, additional quasi-static pressure experiments could be conducted to confirm this. Goethite also showed differences between the expected temperatures causing dehydration and the calculated impact temperatures, which may also indicate changes to the transition temperature of the goethite as a result of pressure.

Unlike gypsum, goethite impact residues showed a mixture of goethite, intermediate and hematite spectra. The mixture of materials detected on the witness plates are most likely due to the size of the projectile, as a range of pressure and temperatures acted along the length of the projectile. Impacts onto the first (target) plate appear to generally fall within the expected standard goethite and hematite regions for their spectra classification (goethite, intermediate or hematite), determined from heating experiments, although the peak widths are greater than those found in the heating experiments. However, impacts onto the witness plate do not show the same strong correlation, particularly for impact velocities greater than 3.04 km s^{-1}. At higher velocities some spectra classified as hematite have peak positions that are normally associated with goethite spectra, which is a result of the impact pressure straining the bonds within the sample. The correlation between the classification and peak characteristics for lower impact velocities suggest that at lower peak pressures (<22 GPa) it might be possible to determine the temperature history experienced by the material in an impact environment, but not necessarily at the centre of an impact crater. Figure 9.1.7 shows this potential

pressure boundary, where at pressures <22 GPa the classification of the Raman spectra corresponds to expected peak positions.

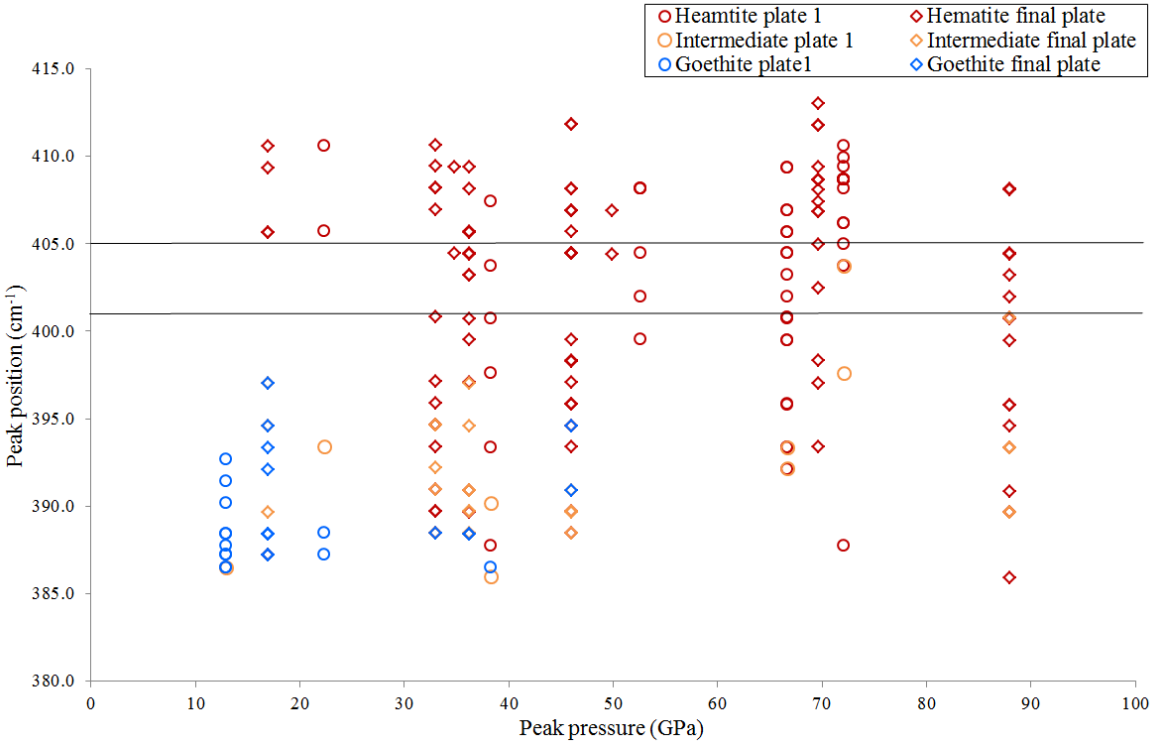

Figure 9.1.7 Feature A peak positions for both plate 1 and the witness plate. The grey lines indicate the maximum peak position for goethite/intermediate spectra (401 cm^{-1}) and the hematite lower limit (405 cm^{-1}).

The peak characteristics from spectra classified as hematite did show two distinct regions, which may indicate material that would have formed highly crystalline or poorly crystalline hematite had they only experienced the temperatures from the impact (Figure 9.1.8). However, an additional shot programme would be required to determine the changes that occur when poorly crystalline and highly crystalline hematite experiences shock.

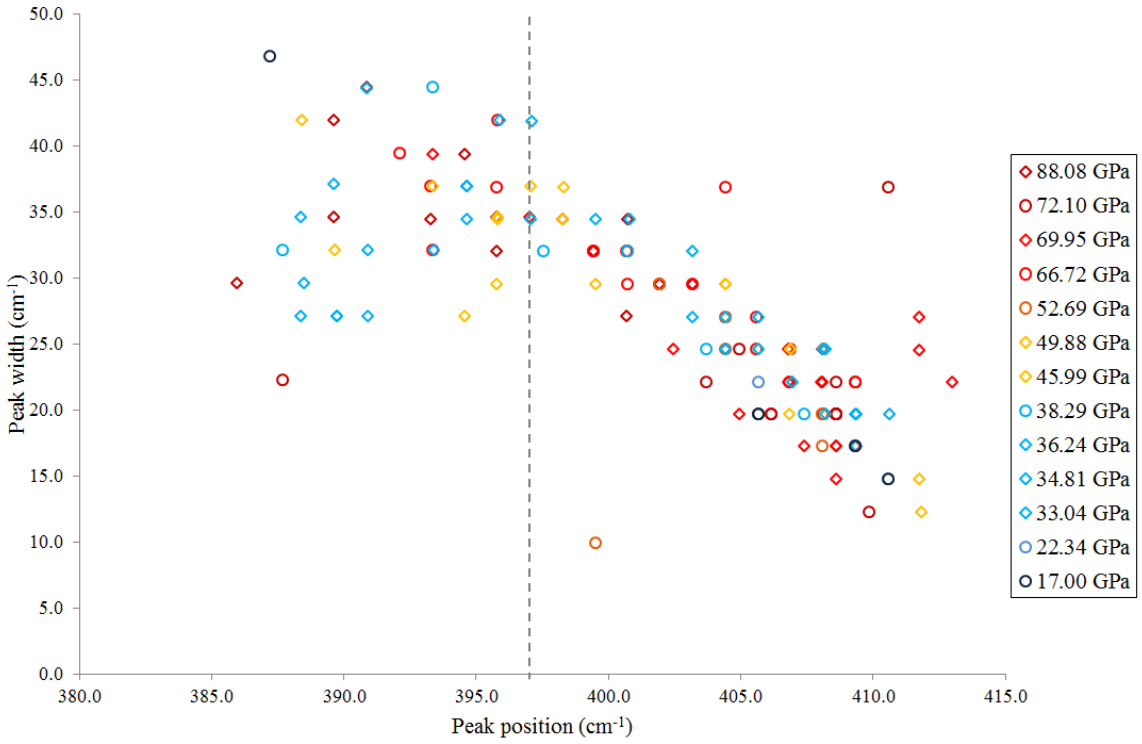

Figure 9.1.8 Feature A peak positions and peak widths for all spectra classified as hematite and the grey dotted line highlights the peak position boundary of 397 cm^{-1}. The points shown as open circles indicate values from plate 1 and the open diamonds are from the witness plate.

There was not much evidence from the mineral targets to determine if devolatilisation had occurred after experiencing an impact. Shot G111013#1 (a PoP target) did show some indication that devolatilisation had occurred from the appearance of a bassanite peak mixed in with a dominant gypsum spectrum taken from the crater floor (Figure 9.1.9). This indicates, at this scale, any devolatilisation would be restricted to the impact crater and would most likely show up as part of a mixture of both volatile and non-volatile bearing phases. Goethite spectra showed changes in the peak width of spectra taken from within the crater, indicating the material had been shocked (Figure 9.1.10). Spectra taken from outside the crater showed a greater difference in peak position than what is seen in spectra taken from within the crater. The spectra taken from within the crater would have experienced a greater impact pressure and the resulting strain on the bonds possibly causing a decrease in peak position. Changes in the peak positions of minerals that have been impacted are also observed by Foster *et al.*, (2013), Hibbert *et al.*, (2014), Hibbert *et al.*, (2015) and Harriss & Burchell, (2016).

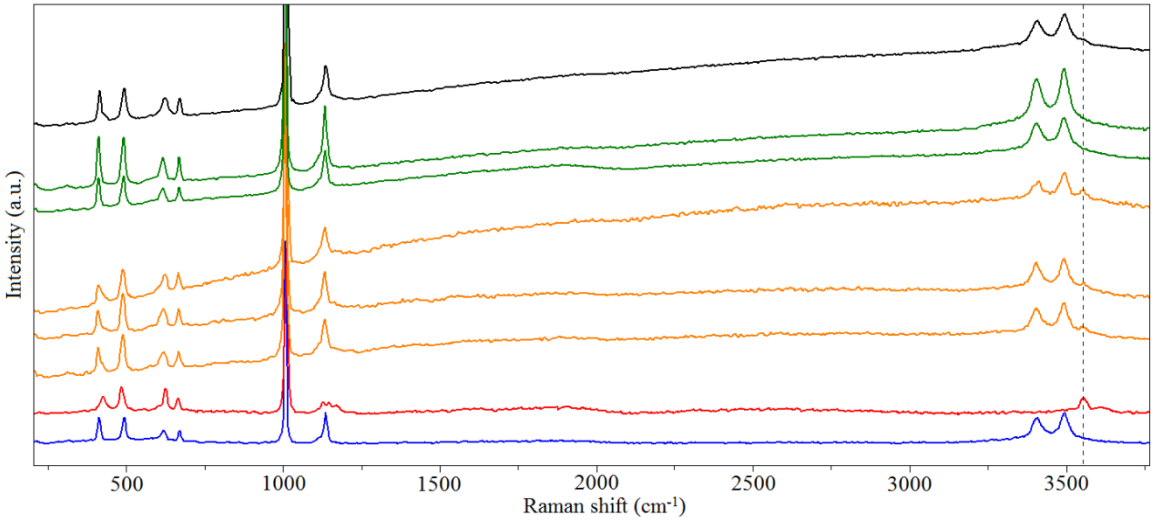

Figure 9.1.9 Raman spectra of hydrous and semi-hydrous PoP are shown in blue and red, respectively, and the spectrum of interest from G111013#1 is shown in black. Results from the PoP mixture test are divided into two groups, those which show the presence of an OH peak (orange) and those that do not (green). Raman spectra have been offset for clarity and the dashed line highlights the position of the OH peak at 3553.1 cm^{-1}.

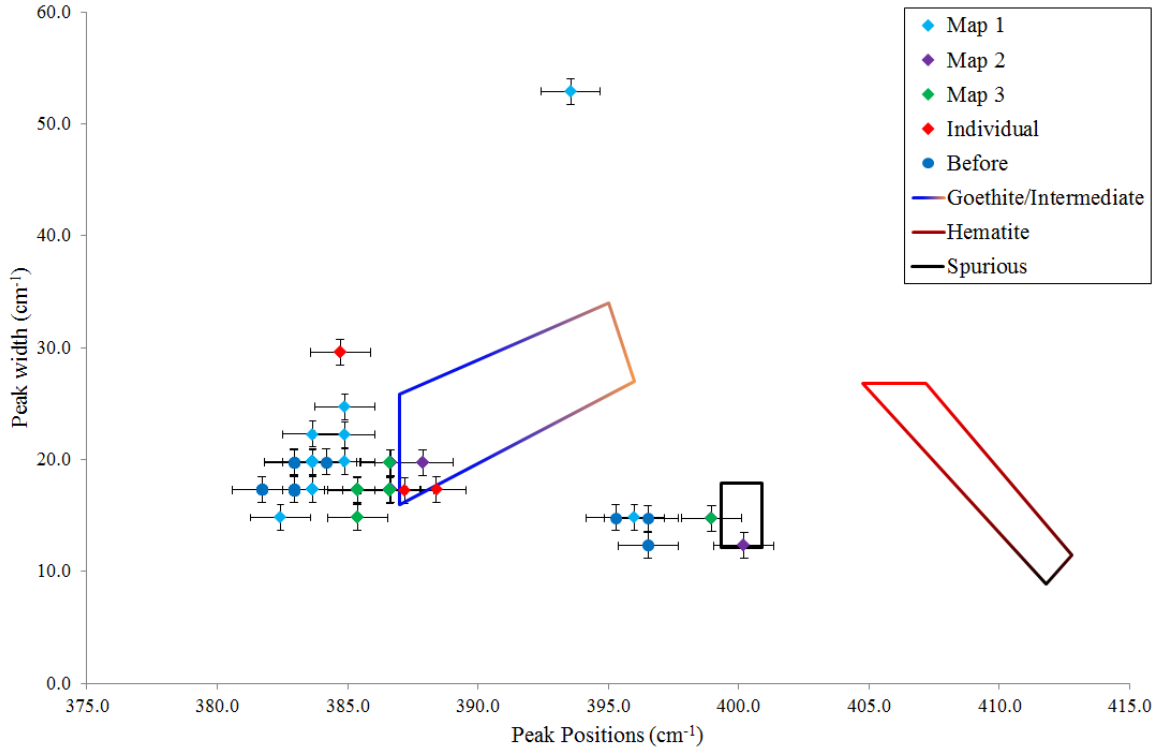

Figure 9.1.10 Raman data for Feature A for the goethite target (shot I.D. G310114#2). The goethite/intermediate (blue/orange), hematite (red/black) and spurious (black) standard regions, determined from the heating experiments are highlighted by the boxes. Raman spectra taken from Map1 were taken from inside the crater and Raman data from Maps 2 and 3 were taken from outside the crater.

Overall the results from the devolatilisation experiments showed that it is possible to identify the loss of volatiles from these minerals, and goethite could potentially be used as a shock barometer. The Raman spectra for these minerals have the overall appearance (i.e. peaks) as non-shocked material. However, peak characteristics (peak width and peak position) are altered to a greater degree than what is seen under quasi-static temperature changes (established from the heating experiments). The heating experiments produced standard regions (using peak width and peak position) that are observed when heating alone. The impacted sample spectral data presented in this thesis predominantly falls outside of these regions for both goethite and natural gypsum projectiles. Therefore, the impact data clearly shows these spectral changes have been caused as a result of the shock experienced upon impact. Both goethite and natural gypsum show a clear increase in peak width, which indicates the sample has become disordered, and to a degree greater than what is observed when the minerals change from one phase/classification to another (i.e. goethite → intermediate → hematite or gypsum → bassanite → anhydrite). In addition to this, goethite shock data shows data points within an area in-between the two standard regions (between 401 and 405 cm^{-1}), which are not present in the results from the heating experiments (Figure 9.1.7). Therefore, the presence of data points in the area between the two standard regions can be used as an indicator for shock. Such a clear indicator for shock in the gypsum data is not present, but there are changes in peak position as a result of the impacts straining the bonds, and peak widths increase as the impact causes increased disorder. Therefore, changes in peak characteristic could potentially be used as a shock barometer indicating a shock has occurred. Unfortunately, there was not much literature available to determine how the Raman spectra of these minerals and their anhydrous products change after experiencing high pressures under quasi-static conditions. Results from high pressure experiments (Shim & Duffy, 2002; Ovsyannikov *et al.*, 2012; Huang *et al.*, 2000; Knittle *et al.*, 2001) that did measure Raman spectra after releasing a sample from pressure were contradictory. In some cases peak characteristics returned to their initial state and in others there were changes in peak position and increases in peak width. In one of these instances the changes in peak characteristics of Raman spectra may have been due to the sample being cycled up to a pressure of 22 GPa (Ovsyannikov *et al.*, 2012). If it is determined that the changes in peak characteristics only occur as a result of cycling a sample to a specific pressure under quasi-static conditions, then the changes in peak characteristic we have seen in these impact experiments could be used as a shock barometer, as cycling of pressure would not normally occur in nature. If specific peak

characteristics are generated at specific peak pressures, then it would be possible to use minerals to determine the degree of shock.

It was believed that the minerals would show the same spectral changes that were seen in the heating experiments, meaning it would be possible to use the peak characteristics to determine the temperatures experienced upon impact. However, the effect of pressure seems to change the peak characteristics to such a degree that it makes it difficult to achieve this. Although the literature for examining minerals that have experienced high pressures under quasi-static conditions are contradictory, they are also interesting. If cycling the pressure is the only reason changes in peak characteristic occurs, then it could mean that this process of cycling pressure causes the bonds to strain. In an impact onto volatile bearing minerals two things occur: 1) the straining of the bonds caused by pressure and 2) changes to the bonds from the high temperature, through (for example) loss of volatiles. It could be this combination of pressure and temperature is what causes the shock spectral data to fall outside the standard regions (determined by the heating experiments). The very short timescale (~microseconds) that the pressure and temperature are experienced within the mineral makes it difficult for the mineral to equilibrate to the new pressure/temperature environment, particularly for impacts of this scale. This could explain why we see different peak characteristics for minerals that have experienced shock to those that have experience high pressures and high temperatures under quasi-static conditions.

9.1.3 Goal 3: Raman Spectroscopy

Raman spectroscopy has been used as the primary analysis technique for both serpentinisation and devolatilisation experiments. It has shown that it can be used to determine if these processes occurred. In addition to this, the devolatilisation experiments indicate that Raman spectroscopy is a useful tool in determining material that has undergone an impact, and could be used to identify the degree of shock in mineral. These results have shown that Raman spectroscopy can be used to provide more information than just the identification of minerals. The results presented here could help understand the Raman spectra of volatile bearing minerals (particularly hydrated minerals) received from the *ExoMars* and *Mars 2020* rovers. This work has shown that peak characteristics of goethite and gypsum change when impacted at a range of velocities, with peak widths increasing to values that are greater those seen under quasi-static temperatures. It might

help to determine whether volatiles were lost as a result of an impact or from a thermal process, such as a dyke emplacement. The Raman spectrometer on board the *Exomars* rover will have a spectral resolution of ~7 cm^{-1} (Rull *et al.*, 2013), which is worse than the spectral resolution for the spectrometer used for analysis in this thesis (~1-2 cm^{-1}, depending on the laser being used). This relatively poor resolution is greater than the changes that would be seen as a result of gypsum being impacted, but it could be sufficient to show if goethite had been impacted, as the shifts seen for this mineral can be greater than 7 cm^{-1}. These results show that a spectral resolution of at least 2 cm^{-1} would be needed to provide any meaningful quantitative data to determine the thermal and shock histories for volatile bearing minerals on Mars.

9.2 Future Work

In hindsight the impact experiments undertaken in this thesis could have been performed differently. However, at the outset we did not know the best way to carry out such experiments, but we are starting to learn "best practise". Sub-sections 9.2.1 and 9.2.2 describe additional experiments that could be undertaken to further this work.

9.2.1 Serpentinisation Experiment

The detection of two hydrated grains from G100513#2 does indicate serpentinisation could be induced by impact and warrants further investigation. Autodyn simulations suggest the most likely region for this process to occur is within the craters of olivine, H_2O ice and CO_2 ice targets. The best ways to achieve this would be to use a vertical light gas gun and/or have a larger target impacted at a shallower angle. These two methods would ensure the crater is preserved, allowing material to be sampled from this region. It would also be beneficial to use high purity olivine that have been ground into a coarse grained powder, which would insure no inclusion of hydrated minerals were present in the olivine. This would mean that any talc detected after impact would have been formed from serpentine and CO_2, which would also demonstrate serpentinisation had occurred, and methane had been produced. Finally, the use of a gas spectrometer would also be beneficial, as it would mean the direct detection of methane could be achieved.

9.2.2 Devolatilisation Experiment

There are a number of experiments that can be conducted to further the work for the devolatilisation experiments:

1) The use of a TGA would assist in examining the relationship between mass loss (as a result of heating) and Raman spectra of volatile bearing minerals for a range of grain sizes. This technique would allow mass measurements to be collected as the sample is heated, and immediately after the heating and cooling cycle. Doing this would minimise any effects that interaction with the atmosphere could have on the mass of the sample, providing more accurate mass measurements.
2) Determining the effects pressure, under quasi-static conditions, have on the Raman spectra of volatile bearing minerals and their non-volatile mineral products. These experiments could be conducted at a range of pressure up to 80 GPa to simulate the pressure experienced by impacts, which could be achieved using a diamond anvil cell. It would be beneficial to both cycle the pressure up gradually to the target pressure (i.e. increasing the pressure and then releasing it to ambient pressure in steps until the target pressure is achieved) and just increase the pressure in one step. This would help to determine what type of pressure changes are required to show alteration in the Raman peak characteristics under quasi-static conditions.
3) The pressure experiments outlined in (2) could also be conducted at ambient temperature and at high temperatures (that would induce the devolatilisation of the minerals). This would show the effects of both high pressure and high temperature on these minerals. Results from these pressure experiments could then be compared to the results determined from impact experiments, in a similar way to what was done here with the heating experiments.
4) A series of impact experiments using coarse and fine grained minerals could be conducted to assist in refining the degree of shock. The minerals used would need to be representative of the volatile bearing mineral and its non-volatile mineral product, in addition to poorly crystalline and highly crystalline material. This would determine if impacts will effects the Raman spectra of different minerals and different crystallinities in different ways.
5) In order to determine the effects of post-impact temperatures on the Raman spectra of impacted minerals, samples could be placed inside a furnace. This would help to determine if post-impact temperatures could erase the effects pressure has on the

Raman spectra of minerals. In addition to this, it would mean that these results could be compared to the much larger impacts that occur on Earth and other planetary bodies.

These experiments will, hopefully, help us better understand and quantify the changes that occur in Raman spectra from the loss of volatiles as a result of impacts. It will assist in our understanding and interpretation of Raman spectra obtained from Mars (or other terrestrial surfaces that have experienced impacts), which in turn could help to determine palaeosurface and palaeoenvironments.

References

Adar, F. (2001) Evolution and Revolution of Raman Instrumentation – Application of Available Technologies to Spectroscopy and Microscopy, In: Lewis, I. R. Edwards, H. G. M., *Handbook of Raman Spectroscopy from the research laboratory to the process line*, CRC Press, New York.

Adar, F., Delhaye, M., SaDilva, E. (2007) Evolution of instrumentation for detection of the Raman effect as driven by available technologies and by developing applications, *Journal of Chemical Education*, 84, 50-60.

Adar, F. (2013) Considerations of Grating Selection in Optimizing a Raman Spectrograph, *Spectroscopy*, 18.

Allen, C. C., Griffin, C., Steele, A., Wainwright, N., and Stansbury, E. (2000) Microbial life in Martian regolith stimulant JSC Mars-1, *Lunar and Planetary Science Conference XXXI*, *Abstract# 1287*.

Allen, C. C., Morris, R. V., Jager, K. M., Lindstrom, D. J., Lindstrom, M. M., Lockwood, J. P. (1998) Martian regolith stimulant JSC MARS-1, *Lunar and Planetary science XXIX*, *Abstract# 1960*.

Allen, C. C., Morris, R. V., Lindstrom, D. J., Lindstrom, M. M., Lockwood, J. P. (1997) JSC MARS-1: Martian regolith simulant, *Lunar and Planetary science XXVII*, *Abstract# 1797*.

Alt, J. C., Shanks III, W. C. (1998) Sulfur in serpentinized oceanic peridotites: Serpentinization processes and microbial sulfate reduction, *Journal of Geophysical Research*, 103, 9917 – 9929.

Andreani, M., Muñoz, Marcaillou, C., Delacour, A. (2013) µXANES study of iron redox state in serpentine during oceanic serpentinisation, *Lithos*, 178, 70-83.

Angrilli. F., Pavarin, D., De Cecco, M., Francesconi, A. (2003) Impact facility based upon high frequency two-stage light-gas gun, *Acta Astronautica*,5., 185-189.

Atreya, S. K., Mahaffy, P.R., Wong, A-S. (2007) Methane and related trace species on Mars: Origin, loss, implications for life, and habitability, *Planetary and Space Science*, 55,358-369.

Atreya, S. K., Witasse, O., Chevier, V. F., Forget, F., Mahaffy, P. R., Price, P. B., Webster, C. H., Zurek, R. W. (2011) Methane on Mars: Current observations, interpretation, and future plans, *Planetary and Space Science, special issue on methane on Mars*, 59, 133-136.

Banfield, J. L. (2002) Global mineral distribution on Mars, *Journal of Geophysical Research*, 107, 5042.

Barlow, N. G. (2008) *Mars an introduction to its interior, surface and atmosphere*, Cambridge University Press, Cambridge.

Barlow, N. G., Bradley, T. L. (1990) Martian Impact Craters: Correlations of ejecta and interior morphologies with diameter, latitude and terrain, *Icarus*, 87, 156-179.

Bar-Nun, A., Chang, S. (1983) Photochemical reactions of water and carbon monoxide in the Earth's primitive atmosphere, *Journal of geophysical research*, 88, 6662-6672.

Bar-Nun, A., Dimitrov, V. (2006) Methane on Mars: a product of H_2O photolysis in the presence of CO, *Icarus*, 181, 320 – 322.

Beegle, L. W., Bhartia, R., DeFlores, L., Darrach, M., Kidd, R. D., Abbey, W., Asher, S., Burton, A., Clegg, S., Conrad, P. G., Edgett, K., Ehlmann, B., Langenhorst, F., Fries, M., Hug, W., Nealson, K., Popp, J., Sorbon, P., Steele, A., Wiens, R., Williford, K. (2014) SHERLOC: Scanning Habitable Environments With Raman and Luminescence for Organics and Chemicals, an Investigation for 2020, *45th Lunar and Planetary Science Conference Abstract# 2835*.

Bell, M. S. (2010) Relative shock effects in mixed powders of calcite, gypsum, and quartz: A calibration scheme from shock experiments, *Geological Society of America Special papers*, 465, 593-608.

Bell, M. S. (2014) Relative shock effects in mixed powders of calcite, gypsum, and quartz: A calibration scheme from shock experiments, *Geological Society of America Special Papers*, 465, 593-608.

Bell, M. S. (2016) Characterization of shock effects in calcite by Raman spectroscopy: results of experiments, *47th Lunar and Planetary Science Conference, Abstract # 1196.*

Bell, M. S., Zolensky, M. E. (2011) Experimental shock transformation of gypsum to anhydrite: a new low pressure Regime shock indicator, *42nd Lunar and Planetary Science Conference, Abstract#2008.*

Benlow, A., Meadows, A. J. (1977) The formation of the atmospheres of the terrestrial planets by impact, *Astrophysics and Space Science*, 46, 293 – 300.

Berenblut, B. J., Dawson P., Wilinson, G.R. (1973) A comparison of the Raman spectra of anhydrite ($CaSO_4$) and gypsum ($CaSO_4.2H_2O$), *Spectrochimica Acta*, 29, 29-36.

Berlanga, A. G., Acosta-Maeda, T. E., Misra, A. K., Sharma, S. K., Flynn, L. P. (2015) Standoff Time-Resolved Fast Fluorescence of Organics and Amino Acids, *46th Lunar and Planetary Science Conference, Abstract# 2613*.

Beyssac, O., Goffé, B., Petitet, J.-P, Froigneux, E., Moreau, M., R, J-N. (2003) On the characterization of disordered and heterogeneous carbonaceous materials by Raman spectroscopy, *Spectrochimica Acta Part A*, 59, 2267-2276.

Bishop, A. C., Woolley, A. R., Hamilton, W. R. (2003) *Minerals, Rocks and Fossils*, Philip's, London.

Blamey, N. J. F., Parnell, J., McMahon, S., Mark, D. F, Tomkinson, T., Lee, M., Shivak, J., Izawa, M. R. M., Banerjee, N. R., Flemming, R. L. (2015) Evidence for methane in Martian meteorites, *Nature Communications*, 6, 7339, 0.1038.

Bogner, A., Jouneau., P.-H., Tholet, G., Basset, D., Gauthier, C. (2007) A history of scanning electron microscopy developments: Towards "wet – STEM" imaging, *Micron*, 38, 390 – 401.

Boslough, M. B., (1991), Shock modification and chemistry and planetary geological, *Annual review of Earth and Planetary Sciences*, 19, 101-130.

Boslough, M. B., Cygan, R. T., (1988), Shock-Enhanced Dissolution of Silicate Minerals and Chemical Weathering on Planetary Surfaces, *Proceedings of the 18th Lunar and Planetary Science Conference*, 443 – 453.

Boslough, M. B., Weldon, R. J., Ahrens, T. J. (1980) Impact-induced water loss from serpentine, nontronite and kernite, *Proceedings from the 11th Lunar and planetary science conference*, 2145-2158.

Bost, N., Ramboz, C., LeBreton, N., Foucher, F., Lopez-Reyes, G., De Angelis, S., Josset, M., Venegas, G., Sanz-Arranz, A., Rill, F., Medina, J., Josset, J-L, Souchon, A., Ammannito, E., De Sanctis, M. C., Di Iorio, T., Carli, C., Vago, J.-L., Westall, F. (2015) Testing the ability of the ExoMars 2018 payload to document geological context and potential habitability on Mars, *Planetary and Space Science*, 108, 87-97.

Bottke, W. F., Nolan, M. C., Greenberg, R., Kolvoord, R. A. (1994) Velocity distribution among colliding asteroids, *Icarus*, 107, 255 – 268.

Brand, J. C. D. (1989) The discovery of the Raman effect, *The Royal Society*, 43, 1-23.

Bridges, J. C., Catling, D. C., Saxton, J. M., Swindle, T. D., Lyon, I. C., Grady, M.M. (2001) Alteration assemblages in Martian meteorites: implications for near-surface processes, *Space Science Reviews*, 96, 365 -392.

Brosseau, C. L., Rayner, K. S., Casadlo. F., Grzywacz, C. M., Van Duyne, R. P. (2009) Surface-Enhanced Raman Spectroscopy: A direct Method to Identify Colorants in Various Artist Media, *Analytical Chemistry*, 81, 7443-7447.

Bucio, L., Rosales, I., Thions, C., Soullard, J., Orozco, E. (2015) Phase transition induced by shock compression on a gypsum mineral: X-ray and micro-Raman analysis, *High Pressure Research*, 35, 355-362.

Burchell, M. J. (2015), Shocked rocks: impacts from the laboratory to the solar system, In: Lee, M. R., Leroux, H., *EMU Notes in mineralogy 15, Planetary mineralogy*, London, European Mineralogical Union and the Mineralogical Society of Great Britain and Ireland.

Burchell, M. J., Cole, M. J., McDonnell, J. A. M., Zarnecki, J. C. (1999) Hypervelocity impact studies using the 2 MV Van de Graaff accelerator and two-stage light gas gun of the University of Kent at Canterbury, *Measurement Science and Technology*, 10, 41 -50.

Burchell, M. J., Mann, J., Creighton, J. A., Kearsley, A. T., Graham, G., Franchi, I. A. (2006) Identification of minerals and meteoritic materials via Raman techniques after capture in hypervelocity impacts on aerogel, *Meteoritics and Planetary Science*, 41, 218 – 232.

Carr, M. H. (2012) The fluvial history of Mars, *Philosophical Transactions of The Royal Society*, 30, 2193 – 2215.

Carr, M.H., Head III, J. W. (2010) Geological history of Mars, *Earth and Planetary Science Letters*, 294, 185-203.

Carter, J., Poulet, F., Bibring, J. -P., Mangold, N., Murchie, S. (2013) Hydrous minerals on Marls as seen by CRISM and OMEGA imaging spectrometer: Updated global view, *Journal of Physical Research: Planets*, 118, 831 – 858.

Chambers, J. E. (2001) Making More Terrestrial Planet, *Icarus*, 152, 205 – 224.

Chambers, J. E. (2004) Planetary accretion in the inner Solar System, *Earth and Planetary Science Letters*, 223, 241 – 252.

Chen, G., Tyburczy, J. A., Ahrens, T. J. (1994) Shock-induced devolatilization of calcium sulfate and implication for K-T extinctions, *Earth and Planetary Science Letters*, 128, 615 – 628.

Charters, A. C. (1995) The early years of aerodynamics ranges, light-gas guns, and high-velocity impacts, *International Journal of Impact engineering*, 17, 151 -182.

Chassefière, E., Leblanc, F. (2011) Constraining methane release due to serpentinization by the observed D/H ratio on Mars, *Earth and Planetary Science Letters*, 310, 262 – 271.

Chastain, B. K., Chevrier, V. (2007) Methane clathrate hydrates as a potential source for Martian atmospheric methane, *Planetary and Space Sciences*, 55, 1246 – 1256.

Christensen, P. R., Wyatt, M. B., Glotch, T. D., Rogers, A. D., Anwar, S., Arvidson, R. E., Bandfield, J. L., Blaney, D. L., Budney, C., Calvin, W. M., Fallacaro, A., Fergason, R. L., Gorelick, N., Graff, T. G., Hamilton, V. E., Hayes, A. G., Johnson, J. R., Knudson, A. T., McSween, H. Y., Mehall, G. L., Moersch, J. E., Morris, R. V., Smith, M. D., Squres, S. W. Ruff, S. W., Wolff, M. J. (2004) Mineralogy at Meridiani Planum from the Mini-TES experiment on the Opportunity rover, *Science*, 306, 1733 – 1739.

Clark, R. J. H., Dines, T. J. (1986) Resonance Raman spectroscopy, and its applications o inorganic chemistry, *Angewandte Chemie International Edition*,25, 131-158.

Clark, B. C., Morris, R. V., McLennan, S. M., Gellert, R., Jolliff, B., Knoll, A. H., Squyres, S. W., Lowenstei, T. K., Ming, D.W., Tosca, N. J., Yen, A., Christensen, P. R., Gorevan, S., Brückner, J., Calvin, W., Dreibus, G., Farrand, W., Klingelhoefer, G., Waenke,H., Zipfel, J., Bell III, J. F., Grotzinger, J., McSween, H. Y., Rieder, R. (2005) Chemistry and mineralogy of outcrops at Meridiani Planum, *Earth and Planetary Science Letters*, 240, 73 – 94.

Collins, S. A. (1971) *The Mariner 6 and 7 pictures of Mars*, NASA, Washington.

Collin, G. S., Melosh, H. J., Morgan, J. V., Warner, M. R. (2002) Hydrocode Simulations of Chicxulub Crater Collapse and Peak-Ring Formation, *Icarus*, 157, 24-33.

Collins, G. S., Wünnemann, K., Artemieva, N., Pierazzo, E., (2013), Numerical modelling of impact processes, In: Osinski, G. R., Pierazzo, E., *Impact cratering processes and products*, Wiley-Blackwell, Malaysia.

Comodi, P., Nazzareni, S., Zanazzi, P. F., Speziale, S. (2008) High-pressure behaviour of gypsum: a single-crystal X-ray study, *American Mineralogist*, 93, 1530-1537.

Comodi, P., Kurnosov, A., Nazzareni, S., Dubrovinsky, L. (2012) The dehydration prcess of gypsum under high pressure, *Physics and Chemistry of Minerals*, 39, 65-71.

Cortés, J., Trigo-Rodríguez, J. M., Mestres, N., Madiedo, J M. (2012) Raman Characterisation of mineral in two lunar achondrites: NWA 2700 and Dhofar 1085, *European Planetary Science Congress, Abstract# 26-3.*

Craddock, R. A., Howard, A. D. (2002) The case for rainfall on a warm, wet early Mars, *Journal of Geophysical Research*, 107, E11, 5111.

Crozier, W. D., Hume, W. (1957) High-velocity, Light-Gas Gun, *Journal of Applied Physics*, 28, 892.

Das, R. S., Agrawal, Y. K. (2011) Raman spectroscopy: Recent advancements, techniques and applications, *Vibrational Spectroscopy*, 57, 163-176.

Daubar, I. J., McEwen, A. S., Byrne, S., Kennedy, M. R., Ivanov, B. (2013) The current Martian cratering rate, *Icarus*, 225,506-156.

Deer, W. A., Howie, R.A., Zussman, J. (1992) *An Introduction to the Rock Forming Minerals, 2nd edition*, Pearson, Edinburgh.

Deer, W. A., Howie, R. A., Zussman, J. (2013) *An introduction to the rock forming minerals 3rd edition*, The Mineralogical Society, Hertfordshire, UK.

de Faria, D. L. A., Lopes, F. N. (2007) Heated goethite and natural hematite: can Raman spectroscopy be used to differentiate them? *Vibrational spectroscopy*, 45, 117 – 121.

Dekkers, M. J. (1990) Magnetic properties of natural goethite – III. Magnetic behaviour and properties of mineral originating from goethite dehydration during thermal demagnetization, *Geophysical Journal International*, 103, 233-250.

de Niem, D., Kühurt, Morbidelli, A., Motschmann, U. (2012) Atmospheric erosion and replenishment induced by impacts upon Earth and Mars during a heavy bombardment, *Icarus*, 221, 495-507.

Deutsch, A., Poelchau, M. H., Kenkmann, T., (2015), Impact metamorphism in terrestrial and experimental cratering events, In: Lee, M. R., Leroux, H., *EMU Notes in mineralogy 15, Planetary mineralogy*, European Mineralogical Union and the Mineralogical Society of Great Britain and Ireland, London.

Diaspro, A., Chirico, G., Usai, C., Ramoino, P., Dobrucki, J. (2006) Photobleaching In: Pawley, J. B., *Handbook of Biological Confocal Microscopy third edition,* Springer Science and Business media, New York.

Downs, R. T., Wallace, M. (2003) The American mineralogist crystal structure database, *American Mineralogist*, 88, 247-250.

Doolan, C. J. (2001) *A two-stage light gas gun for the study of high speed impact in propellants*, Department of Defence, Salisbury, Technical Report, 1092.

Ehlmann, B. L., Mustard, J. F., Murchie, S. L. (2010) Geological setting for serpentine deposits on Mars, *Geophysical Research Letters*, 37, L06201.

Encrenaz, Th., Lellouch, E., Atreya, S. K., Wong, A. S. (2004) Detectability if minor constituents in the Martian atmosphere by infrared and submillimeter spectroscopy, *Planetary and Space Science*, 52, 1023 – 1037.

Etiope, G. Klusman, R. W. (2002) Geological emissions of methane to the atmosphere, *Chemosphere*, 49, 777 – 789.

Farrell, W. M., Delroy, G. T., Atreya, S. K. (2006) Martian dust storms as a possible sink for atmospheric methane, *Geophysical Research letters*, 33.

Farrell-Turner, S., Reimold, W. U., Nieuwoudt, M., Erasmus, R M. (2005) Raman spectroscopy of olivine in dunite experimentally shocked to pressure between 5 go 59 GPa, *Meteoritics and Planetary Science*, 40, 1311-1327.

Ferraro, J. R., Nakamoto, K., Brown, C. W. (2003) *Introductiory Raman Spectroscopy, second edition*, Elsevier Science, USA.

Flahaut, J., Quantin, C., Clenet, H., Allemand, P., Mustard, J. F., Thomas, P. (2012) Pristine Noachian crust and key geological transitions in the lower walls of Valles Marineris: Insight into early igneous processes on Mars, *Icarus*, 221, 420 – 435.

Fleischmann, M., Hendra, P. J., McQuillan, A. J. (1974) Raman Spectra of pyridine adsorbed at a silver electrode, *Chemical Physics Letters*, 26, 163-166.

Flynn, G. J. (1996) The delivery of organic matter from asteroids and comets to the early surface of Mars, *Earth, Moon, and Planets*, 72, 469 – 474.

Fonti, S., Marzo, G. A. (2010) Mapping methane on Mars, *Astronomy and Astrophysics*, 512.

Formisano, V., Atreya, S., Encrenaz, T., Ignatiev, N., Giuranna, M. (2004) Detection of Methane in the Atmosphere of Mars, *Science*, 306, 1758-1761.

Foster, N. J., Wozniakiewicz, P. J., Price, M. C., Kearsley, A. T., Burchell, M. J. (2013) Identification by Raman spectroscopy of Mg-Fe content of olivine samples after impact at 6 k s^{-1}, onto aluminium foil and aerogel: In the laboratory and in Wild-2 cometary samples, *Geochimica et Cosmochimica Acta*, 121, 1-14.

Freedman, R. A., Kaufmann III, W. J. (2005) *Universe, seventh edition,* W.H. Freeman and Company, New York.

French, B. M., (1998), *Traces of Catastrophe: A Handbook of Shock-Metamorphic Effects on Terrestrial Meteorite Impact Structures,* LPI Contribution No. 954, Lunar and Planetary Institute, Houston, 120.

French, B. M., Koebrel, C., (2010), The convincing identification of terrestrial meteorite impact structures: What works, what doesn't, and why, *Earth Science Reviews*, 98, 123-170.

Frey, H. Schultz, R. (1989) Overlapping large impacts and the origin of the northern lowlands of Mars, *12th LPSC, Abstract # 698*.

Furukawa, Y., Nakazawa, H., Sekine, T., Kakegawa, T. (2007) Formation of ultrafine particles from impact generated supercritical water, *Earth and Planetary Science Letters*, 258, 543 – 549.

Furukawa, Y., Sekine, T., Kakegawa, T., Nakazawa, H. (2011) Impact-induce phyllosilicate formation from olivine and water, *Geochimica et Cosmoschimica Acta*, 75, 6461 – 6472.

Geminale, A., Formisano, V., Giurana, M. (2008) Methane in the Martian atmosphere: average spatial, diurnal and seasonal behaviour, *Planetary and Space Science*, 56, 1194 – 1203.

Gialanella, S., Girardi, F., Iscia, G., Lonardelli, I., Mattarelli, M., Montagna, M. (2010) On goethite to hematite phase transformation, *Journal of Thermal Analysis and Calorimetry*, 102, 867 – 873.

Giacomazi, L., Scandolo, S. (2010) Gypsum under pressure: A first principal study, *Physical Review B*, 82, 064103 1- 064103 10.

Gillet, P., Barrat, J. A., Deloule, E., Wadhwa, M., Jambon, A., Sautter, V., Devouard, B., Neuville, D., Benzerara, K., Lesourd, M. (2002) Aqueous alteration in the Northwest Africa 817 (NWA 817) Martian meteorite, *Earth and Planetary Science Letters*, 203, 431-444.

Gleason, A. E., Jeanloz, R., Kunz, M. (2008) Pressure temperature stability studies of FeOOH using X-ray diffraction, *American Mineralogists*, 93, 1882-1885.

Gloesener, E., Karatekin, Ö., Dehant, V. (2013) Martian methane and stability of clathrates in the crust of Mars, *European Planetary Science Congress 2013, Abstract #896.*

Glotch, T. D., Bandfield, J. L., Christensen, P. R., Calvin, W. M., McLennan, S. M., Clark, B. C., Rogers, A. D., Squyres, S. W. (2006) Mineralogy of the light toned outcrop at Meridiani Planum as seen by the Miniature Thermal Emission Spectrometer and implications for its formation, *Journal of Geophysical Research*, 111, E12S06.

Glushak, B. L. Mochalov, M. A. (2006) Studies of Phase Transformations, In: Zhernokletov, M. V. Glushak, B. L., *Material Properties under Intensive Dynamic Loading*, Springer, Berlin.

Godard, M., Luquot, L., Andreani, M., Gouze, P. (2013) Incipient hydration of mantle lithosphere at ridges: A reactive-percolation experiment, *Earth and Planetary Science Letters*, 371 – 372, 92 – 102.

Goldspiel, J., Squyres, S. W. (2000) Groundwater sapping formation Mars, *Icarus*, 148, 176 – 192.

Goldstein, J. I., Newbury, D. E., Echlin, P., Joy, D. C., Lifshin, E. (1981) *Scanning electron microscopy and X-ray microanalysis*, New York, Plenum Press.

Grady, M., Pratesi, G., Cecchi, V. M. (2014) *Atlas of Meteorites*, Cambridge University Press, Cambridge.

Greeley, R. (2013) *Introduction to planetary geomorphology*, Cambridge University Press, Cambridge.

Grieve, R. A. F., (1987), Terrestrial impact structures, *Annual Review of Earth and Planetary Sciences*, 15, 245 – 270.

Grüneisen, E. (1912) Theorie des festen Zustandes einatomiger Elemente, *Annalen der Physik*, 344, 257–306.

Gupta, S. C., Love, S. G., Ahrens, T. J. (2002) Shock temperature in calcite ($CaCO_3$) at 95-160 GPA, *Earth and Planetary Science Letters* 201, 1-12.

Guzmán-Marmolgo, A., Segura, A., Escobar-Briones, E. (2013) Abiotic Production of Methane in Terrestrial Planets, *Astrobiology*, 13, 550 – 559.

Hanesch, M. (2009) Raman spectroscopy of iron oxides and (oxy)hydroxides at low laser power and possible applications in environmental magnetic studies, *Geophysical Journal International*, 177, 941 -948.

Harrison, K. P., Grimm, R. E. (2005) Groundwater-controlled valley networks and the decline of surface runoff on early Mars, *Journal of Geophysical Research*., 110, E12S16.

Harriss, K. H., Burchell, M. J. (2016) A study of the observed shift in the peak position of olivine Raman spectra as a result of shock induced by hypervelocity impacts, *Meteoritics and Planetary Science*, doi:10.1111/maps.12660.

Hawkes, P. (2004) Recent advances in electron optics and electron microscopy, *Annales de la Foundation Louis de Broglie*, 29, 1, 837 – 855.

Haynes, C. L., McFarland, A. D., Duyne, R. P. V. (2005) Surface-enhanced Raman spectroscopy. *Analytical Chemistry*, *77*, 338-A.

Hayhurst, C. J., Clegg, R. A. (1997) Cylindrically symmetric SPH simulations of hypervelocity impacts on thin plates, *International Journal of Impact Engineering*, 20 (1 – 5), 337-348.

He, S., Zhang, W., Liu, L., Huang, Y., He, J., Xie, W., Wu, P., Du, C. (2014) Baseline correction for Raman spectra using an improved asymmetric least square method, *Analytical Methods*, 6, 4402 – 4407.

Head, J. W., Wilson, L., Mitchell, K. L. (2003) Generation of recent massive water floods at Cerberus Fossae, Mars by dike emplacement, cryospheric cracking, and confined aquifer ground water release, *Geophysical Research Letters*, 30, 1577.

Hibbert, R., Price, M. C. (2014) Characterisation of Raman spectra of high purity olivine as a function of temperature and shock history: preparation for Exomars, *45th Lunar and Planetary Science Conference, Abstract # 1350.*

Hibbert, R., Price. M. C., Kinner, T. M., Cole, M. J., Burchell, M. J. (2015a) The effects of temperature on the Raman spectrum of high purity quartz crystals, *46th Lunar and Planetary Science Conference, Abstract#1826.*

Hibbert, R., Price. M. C., Kinnear, T. M., Cole, M. J., Burchell, M. J. (2015b) The effects of shock pressure on the Raman spectrum of high purity quartz crystals, *46th Lunar and Planetary Science Conference, Abstract#1826.*

Hildebrand, A. R., Penfield, G. T., Kring, D. A., Pilkington, M., Camargo, A Z., Jacobson, S. B., Boynton, W. V. (1991) A possible Creataceous-Tertiary boundary impact crater on the Yucatan peninsula, Mexico, *Geology*, 19, 867-871.

Hoefen, T. M., Clark, R. N., Bandfield, J. L., Smith, M. D., Pearl, J. C., Christensen, P. R. (2003) Discovery of Olivine in the Nili Fossae Region of Mars, *Science*, 302, 627 – 630.

Hollas, J. M. (2004) *Modern Spectroscopy, Fourth edition*, John Wiley & Sons Ltd, Chichester.

Hollricher, O. (2010) Chapter 3 Raman Instrumentation for Confocal Raman Microscopy, In: Dieing, T., Hollricher, O., Toporski, J., *Confocal Raman Microscopy,* Springer, Germany.

Holmquist, T.J., Johnson, G.R., Cook, W.H. (1993) A Computational Constitutive Model For Concrete Subjected To Large Strains, High Strain Rates, and High Pressures, *Proceedings from the 14th International Symposium on Ballistics*, Quebec, Canada, pp. 591-600.

Holsapple, K., Giblin, I., Housen, K., Nakamura, A., Ryan, E. (2002) Asteroid Impacts: Laboratory Experiments and Scaling Laws, In: Bottke, W., Cellino, A., Paolicchi, P., Binzel, R. P., *Asteroids III*, The University of Arizona Press, USA.

Huang, E., Xu, J-A., Lin, J-F., Hu, J-Z. (2000) Pressure induced phase transitions in gypsum, *High Pressure Research*, 17, 57-75.

Hudson-Lamb, D. L., Strydom, C. A., Potgieter, J. H. (1996) The thermal dehydration of natural gypsum and pure calcium sulphate dehydrate (gypsum), *Thermochimica Acta*, 282/283, 483-492.

Hyndman, R., D., Peacock, S., M. (2003) Serpentinization of the forearc mantle, *Earth and Planetary Science Letters*, 212, 417-432

Hynek, B. M., Beach, M., Hoke, M. R. T. (2010) Updated global map of Martian valley networks and implications for climate and hydrological processes, *Journal of Geophysical Research,* 115, E09008.

Isobell, W. M., (2005), *Shock waves: Measuring the dynamic response of material*, Imperial College Press, London.

Ivanov, B. A., Melosh, H. J., McEwen, A. S. (2010) New small impact craters in high resolution HiRes images, *41st Lunar and Planetary Science Conference, Abstract # 2020.*

Jakosky, B. M. (1999) Atmospheres of the terrestrial planes, In: Beatty, J K., Petersen, C. C., Chaikin, A. *The New Solar System, fourth edition*, Cambridge University Press, Cambridge.

Jaret, S. J., Glotch, T. D., Johnson, J. R. (2014) Characterizing shock metamorphism in feldspar using micro-Raman spectroscopy, *11th International GeoRaman Conference, Abstract#5095.*

Jensen, S. J. K., Skibsted, J., Jakobsen, H. J., ten Kate, I. L., Gunnlaugsson, H. P., Merrison, J. P., Finster, K., Bak, E., Iversen, J. J., Kondrup, J. C., Nørnberg, P. (2014) A sink for methane on Mars? The answer is blowing in the wind, *Icarus*, 236, 24 -27.

Johansson, J., Pettersson, S., Taylor, L. S. (2002) Infrared imaging of laser-induced heating during Raman spectroscopy of pharmaceutical solids, *Journal of Pharmaceutical and Biomedical analysis*, 30, 1223 – 1231.

Johnson, R. E. (1994) Plasma-induced sputtering of an atmosphere, *Space Science Reviews*, 69, 215 - 253

Johnson, R. E., Combi, M R.m Fox, J. L., Ip, W. H., Leblanc, F., McGrath, M. A., Shematovich, V. I., Strobel, D. F., Waite Jr, J. H. (2008) Exosphere and Atmospheric Escape, *Space Science Reviews*, 139, 355 – 397.

Johnson, G.R., Cook, W.H. (1983) A constitutive model and data for metals subjected to large strains, high strain rates and high temperatures, *Proceedings of the 7th International Symposium on Ballistics*, 541–547.

Joy, D. C. (1991) Contrast in high-resolution scanning electron microscope images *k*, *Journal of Microscopy*, 161: 343–355.

Kawaragi, K., Sekine, T., Kadono, T., Sugita, S., Ohno, S., Ishibashi, K., Kurosawa, K., Matsui, T., Ikeda, S. (2009) Direct measurements of chemical composition of shock-induced gasses from calcite: an intense global warming after the Chicxulub impact due to the indirect greenhouse effect of carbon monoxide, *Earth and Planetary Science Letters*, 282, 56-64.

Keller, T. Tackley, P.J. (2008) Towards a self-consistent modelling of the Martian dichotomy: The influence of one-ridge on the crustal thickness distribution, *Icarus*, 202, 429 – 443.

Kenkmann, T., Poelchau, M. H. Wulf, G., (2014), Structural geology of impact craters, *Journal of Structural Geology*, 62, 156 – 182.

Klingelhöfer, G., DeGrave, E., Morris, R. V., Van Alboon, A., de Resendw, V. G., De Souza, P. A., Rodionov, D., Schröder, C., Ming, D. W., Yen, A. (2005) Mössbauer spectroscopy on Mas: goethite in the Columbia Hills at Gusev crater, In: Lippens, P. E., Jumas, J. C., Génin, J. M., *ICAME 2005, Proceedings of the 28th International Conference on the Applications of the Mössbauer Effect (ICAME 2005)*, Springer, France.

Knittle, E., Phillips, W., Williams, Q. (2001) An infrared and Raman spectroscopic study of gypsum at high pressures, *Physics and Chemistry of Minerals*, 28, 630 -640.

Koeberl, C. (1993) Chicxulub Crater, Yucatan: Tektites, impact glasses and the geochemistry of target rocks and breccias, *Geology*,21, 211 – 214.

Kounaves, S. P., Hecht, M. H., Kapit, J., Gospodinova, K., DeFlores, L., Quinn, R. C., Boynton, W.V., Clark, B. C., Catling, D. C., Hredzak, P., Ming, D. W., Moore, Q., Shustermann, J., Stroble, S., West, S. J., Young, S. M. M. (2010) Wet chemistry experiments on the 2007 Phoenix Mars Scout Lander mission: Data analysis and results, *Journal of Geophysical Research*, 115, E00E10.

Krasnopolsky, V. A., Maillard, J. P., Owen, T. C. (2004) Detection of methane in the Martian atmosphere: evidence for life? *Icarus*, 172, 537-547.

Krasnopolsky V. A. (2012) Search for methane and upper limits to ethane and SO_2 on Mars, *Icarus*, 217, 144-152.

Kring, D. (2007) The Chicxulub impact event and its environmental consequences at the Cretaceous-Tertiary boundary, *Palaeogeography, Palaeoclimatology, Palaeoecology*, 255, 4 – 21.

Krinsley, D. H., Pye, K., Boggs Jr, S., Tovey, N.K. (1998) *Backscattered scanning electron microscopy and image analysis of sediment and sedimentary rocks*, Cambridge University Press, Cambridge.

Kuebler, K. E., Jolliff, B. L., Wang, A., and Haskin, L. A. (2006) Extracting olivine (Fo – Fa) compositions from Raman spectral peak positions, *Geochemica et Cosmochemia Acta*, 70, 6201 – 6222.

Lafay, R., Montes-Hernandez, G., Janots, E., Chiriac, R., Findling, N., Toche, F. (2012) Mineral replacement rate of olivine by chrysotile and brucite under high alkaline conditions, *Journal of Crystal Growth*, 347, 62 – 72.

Lambert, P., Lange, M. A. (1982) Processes of shock dehydration on accreting planets, *Conference on Planetary Volatiles*, 104-105.

Landsberg, Gr., Mandelstam, L. (1928) Über die Lichtzerstreuung in Kristallen, *Zeitschrift für Physik*, 50, 769 – 780.

Lange, M. A., Ahrens, T. J. (1982) The Evolution of an Impact Generated Atmosphere, *Icarus*, 51, 96 – 120.

Lange, M.A., Lambert, P., Ahrens, T. J. (1985) Shock effects on hydrous minerals and implications for carbonaceous meteorites, *Geochimica et Cosmochimica Acta*, 49, 171-1726.

Langenhorst, F. (2002) Shock metamorphism of some minerals: Basic introduction and microstructural observations, *Bulletin if the Czech Geological Survey*, 77, 265 – 282.

Langevin, Y., Poulet, F., Bibring, J. P., Gondet, B. (2005) Sulfates in the north polar region of Mars detected by OMEGA/Mars Express, *Science*, 307, 1584 – 1586.

LaPlant, F. (2010) Lasers, Spectrographs and Detectors, In: Matousek, P., Morris, M. D., *Emerging Raman Applications and Techniques in Biomedical and Pharmaceutical Fields*, Berlin, Springer Berlin Heidelberg.

Larkin, P. J. (2011) *IR and Raman Spectroscopy Principals and Spectral Interpretation*, USA, Elsevier.

Legodi, M. A., de Waal. D. (2007) The preparation of magnetite goethite, hematite and maghemite of pigment quality from mill scale iron waste, *Dyes and pigments*, 74, 161-168.

Levèvre, F., Forget, F. (2009) Observed variations of methane on Mars unexplained by known atmospheric chemistry and physics, *Nature letters*, 460, 720-723.

Lexow, B., Wickert, M., Thoma, K, Schafer, F., Poelchau, M. H., Kenkmann, T. (2013) The extra-large light-gas gun of the Fraunhofer EMI: Applications for impact cratering research, *Meteoritics & Planetary Science*, 48, 3-7.

Ling, Z. C., Wang, A. (2014) Secondary minerals in Martian meteorite MIL 03346 as detected by Raman imaging spectroscopy, *11th International GeoRaman Conference, Abstract~5089.*

Liu. W., Wang, A., Freeman, J. J. (2009) Raman, MIR and NIR spectroscopic study of calcium sulfates: gypsum, bassanite and anhydrite, *40th LPSC, Abstract #2128.*

Lodders, K., Fegley Jr, B. (1998) *The planetary Scientist's Companion,* Oxford University Press, Oxford.

Long, D. A. (2002) *The Raman Effect, A unified treatment of the theory of Raman scattering by molecules*, John Wiley & Sons, LTD, Chichester.

Long, D. A. (2008) 80th Anniversary of the discovery of the Raman Effect: a celebration, *Journal of Raman Spectroscopy*, 39, 316 – 321.

Lyons, J. R., Manning, C., Nimmo, F. (2005) Formation of methane on Mars by fluid-rock interaction in the crust, *Geophysical Research Letters*, 32, L13201.

Mahaffy, P.R., Benna, M., Elrod, M., Bougher, S. W., Yelle, R., Jakosky, B. (2015) Early composition, structure, ad isotope measurements in the upper atmosphere of Mars from MAVEN's neutral gas and ion mass spectrometer (NGIMS), *46th Lunar and Planetary Science Conference, Abstract# 1981*.

Mahaffy, P. R., Webster, C. R., Cabane, M., Conrad, P. G., Coll, P., Atreya, S. K., Arvey, R., Barciniak, M., Benna, M., Bleacher. L., Brinckerhoff, W. B., Eigenbrode, J. L., Carignan, D., Cascia, M., Chalmers, R. A., Dworkin, J. P., Errigo, T., Everson, P., Franz, H., Farley, R., Feng, S., Frazier, G., Freissient, C., Glavin, D. P., Harpold, D. N., Hawk, D., Holmes, V., Johnson, C. S., Jones, A., Jordan, P., Kellogg, J., Lewis, J., Lyness, E., Malespin, C. A., Martin, D. K., Maurer, J., McAdam, A. C., McLennan, D., Nolan, T. J., Noriega, M., Pavlov, A. A., Prats, B., Raaen, E., Sheinman, O., Sheppard, D., Smith, J., Stern, J. C., Tan, F., Trainer, M., Ming, D. W., Morris, R. V., Jones, J., Gundersen, C., Steele, A., Wray, J., Botta, O., Leshin, L. A., Owen, T., Battel, S., Jakosky, B. M., Manning, H., Squyres, S., Navarro-González, R., McKay, C. P., Raulin, F., Sternberg, R., Buch, A., Sorensen, P., Kline-Schoder, R., Coscia, D., Szopa, C., Teinturier, S., Baffes, D., Woodward, S., Block, B. P., Arnett, K., Miller, R., Edmonson, C., Gorevan, S., Mumm, E. (2012) The Sample Analysis as Mars Investigation and Instrument Suite, *Space Science Reviews*, 170, 401 – 478.

Majzlan, J., Lang, B. E., Stevens, R., Navrostsky, A., Woodfield, B., Boerio-Goates, J. (2003) Thermodynaics of Fe oxides: Part 1. Entropy at standard temperatures and pressure and heat capacity of goethite (α-FeOOH), Lepidocrocite (γ-FeOOH) and maghemite (γ-Fe_2O_3), *American Mineralogist*, 88, 846-854.

Malin, M. C., Edgett, K. S., Posiolova, L. V., McColley, S. M., Noe Deobrea, E. Z. (2006) Present-day impact cratering rate and contemporary gully activity on Mars, *Science*, 314, 1573-1577.

Mangold, N., Quantin, C., Ansan, V., Delacourt, C., Allemand, P. (2004) Evidence for precipitation on Mars from dendritic valleys in the Valles Marineris area, *Science*, 305, 78 – 81.

Marsh, S. P., (1980), *LASL shock Hugoniot data (Los Alamos series on dynamic material properties)*, University of California Press, Berkeley.

Martín-Torres, F., Zorzzano, M-P., Valentín-Serrano, Harri, A-M., Genzer, M., Kemppinen, O., Rivera-Valentin, E. G., Jun, I., Wray, J., Madsen, M. B., Goetz, W., McEwan, A. S., Hardgrove, C., Renno, N., Chavrier, V. F., Michna, M., Navarro-González, R., Martínez-Frías, J., Conrad, P., McConnochie, T., Cockell, C., Berger, G., Vasavada, A. R., Sumner, D., Vaniman, D. (2015) Transient liquid water and water activity at Gale crater on Mars, *Nature Geoscience*, 8, 357 – 361.

Martins Ferreira, E. H., Moutinho, M. V. O., Stavale, F., Lucchese, M. M., Capaz, R. B., Achete, C. A, Jorio, A. (2010) Evolution of the Raman spectra from single-, few-, and may-layer graphene with increasing disorder, *Physical Review B,* 82.

Masson, P., Carr, M. H., Costard, F., Greenley, R., Hauber, E., Jaumann, R. (2001) Geomorphological evidence for liquid water, *Space Science Reviews,* 96, 333 – 364.

Max, M. D., Clifford, S. (2004) The origin and distribution of methane hydrate in the Martian crust, *Second conference on Early Mars, Abstract #8083*.

Max, M. D., Clifford, S. M. (2000) The state, potential distribution, and biological implications of methane in the Martian crust, *Journal of Geophysical Research,* 105, 4165-4171.

McCauley, J. F., Carr, M. H., Cutts, J. A., Hartmann, W. K., Masursky, H., Milton, D. J., Sharp, R. P., Wilhelms, D. E. (1972) Preliminary mariner 9 report on the geology of Mars, *Icarus,* 17, 289-327.

McEwen, A., Daubar, I., Ivanov, B., Oberst, J., Malhotra, R., JeongAhn, Y., Byrne, S. (2015) Current impact rate on Earth, Moon and Mars, *46th Lunar and Planetary Science Conference, Abstract# 1854.*

Mckay, D. S., Gibson Jr, E. K., Thomas-Keprta, K. L., Vali, H., Romanek, C. S., Clemett, S. J., Chillier, X. D. F., Maechling, C. R., Zare, R. N. (1996) Search for past life on Mars: Possible relic biogenic activity in Martian meteorite ALH84001, *Science,* 273, 924-930.

McMahon, S., Parnell, J., Blamey, N. J. F. (2012a) Sampling methane in basalts on Earth and Mars, *International Journal of Astrobiology,* 12, 2, 113-122.

McMahon, S., Parnell, J., Burcell, M. J., Blamey, N. J. F. (2012b) Methane retention by rocks following simulated meteorite impacts: implications for Mars, *43rd LPSC Abstract # 1040.*

McMillan, P. F. (1989) Raman spectroscopy in mineralogy and geochemistry, *Annual Reviews of Earth and Planetary Science*, 17, 255-283.

McMullan, D. (1995) Scanning Electron Microscopy 1928 – 1965, *Scanning*, 17, 175 – 185.

Meier, R. J. (2005) On art and science in curve-fitting vibrational spectra, *Vibrational Spectroscopy* short communication, 39, 266 – 269.

Melosh, H. J. (1989) *Impact Cratering: A Geologic Process*, Oxford University Press (Oxford Monographs on Geology and Geophysics, No. 11), New York.

Melosh, H. J. (2011) *Planetary Surface Processes*, Cambridge University Press, Cambridge.

Melosh, H. J. (2013) The contact and compression stage of impact cratering, In: Osinski, G. R., Pierazzo, E., *Impact cratering processes and products*, Wiley-Blackwell, Malaysia.

Melosh, H. J., Ivanov, B. A. (1999) Impact Crater Collapse, *Annual Review of Earth and Planetary Science*, 27, pp 385-415.

Melosh, H. J., Vickery, A. M. (1989) Impact erosion of the primordial atmosphere of Mars, *Nature,* 338, 487-489.

Miao, Z., Yang, H., Wu, Y., Zhag, H., Zhang, X. (2012) Experimental studies on decomposing properties of desulfurization gypsum in thermogravimetric analyser and multi-atmosphere fluidized beds, *Industrial & Engineering Chemistry Research,* 51, 5419-5423.

Mie, G. (1903) Zur kinetischen Theorie der einatomigen Körper**,** *Annalen der Physik,* 316, 657–697.

Milazzo, M. P., McEwen, A. S. (2005) Endogenic thermal activity at Cerberus Fossae, Mars? *LPSC XXXVI Abstract #1998.*

Miljković, K., Price, M. C., Wozniakiewicz, P. J., Mason, N. J., Zarnecki, J. C. (2013) Impacted-induced devolatilisation of natural gypsum and plaster of Paris: an infrared and Raman spectroscopic study, *44th Lunar and Planetary Science Conference, Abstract # 1940*.

Mises, R. V. (1913) Mechanik der festen Körper im plastisch-deformablen Zustand. *Nachrichten von der Gesellschaft der Wissenschaften zu Göttingen, Mathematisch-Physikalische Klasse*, 1, 582-592.

Miyahara, M., El Goresy, A., Ohtani, E., Nagase, T., Nishijima, M., Vashaei, Z., Ferroir, T., Gillet, P., Dubrovinsky, L., Simionovici, A. (2008) Evidence for fractional crystallization of wadsleyite and ringwoodite from olivine melts in chondrules entrained in shock –melt veins, *Proceedings of the National Academy of Sciences of the United States of America,*105, 8542 – 8547.

Montmerle, T., Augereau, J-C., Chaussidon, M., Gounelle, M., Marty, B., Morbidelli, A. (2006) Solar System formation and Early Evolution: the first 100 million years, *Earth, Moon and Planets*, 98, 39 – 95.

Moritoh, T., Kawai, N., Matsuoka, S., Nakamura, K. G., Kondo, K., and Katayama, M. (2003) Hypervelocity Impacts Experiments up to 9 km/s by a Compact Multi-Stage Light-Gas Gun, *International Journal of Impact Engineering*, 29, 459 – 467.

Mosier-Boss, P. A., Lieberan, S. H., Newberry, R. (1995) Fluorescence rejection in Raman spectroscopy by shifted-spectra, edge, detection and FFT filtering techniques, *Appled Spectroscopy*, 49, 630-638.

Mumma, J. M., Villanueva, G. L., Novak, R. E., Hewagama, T., Bonev, B. P., DiSanti, M. A., Mandell, A. V., Smith, M. D. (2009) Strong Release of Methane on Mars in Northern Summer 2003, *Science*, 323, 1041 – 104.

Murchie, S., Mustard, J., Bishop, J., Head, J., Pieters, C. (1993) Spatial variations in the spectral properties of bright regions on Mars, *Icarus*, 105, 454 – 468.

Mustard, J. F., Pulet, F., Gendrin, A., Bibring, J. –P., Langevin, Y., Gondet, B., Mangold, N., Bellucci, G., Altieri, F. (2005) Olivine and Pyroxene Diversity in the Crust of Mars, *Science*, 307, 1594 – 1597.

NASA (2014) *Mars 2020 Rover*. <http://mars.nasa.gov/mars2020/mission/instruments/sherloc/for-scientists/> Accessed 5 September 2016

Norton, O. R. (2002) *The Cambridge Encyclopaedia of Meteorites*, Cambridge University Press, Cambridge.

Neubeck, A., Duc, N. T., Bastviken, D., Crill, P., Holm, N. G. (2011) Formation of H_2 and CH_4 by weathering of olivine at temperatures between 30 and 70 ˚C, *Geochemical Transactions*, 12:6.

Newman, W. I., Symbalisty, E. M. D., Ahrens, T. J., Jones, E. M., (1999), Impact Erosion of Planetary Atmospheres: Some Surprising Results, *Icarus*, 138, 224 - 240

Ojha, L., Wilhelm, M. B., Murchie, S. L., McEwen, A. S., Wray, J. J., Hanley, J., Massé, M., Chojnacki, M. (2015) Spectral evidence for hydrated salts in recurring slope lineae on Mars, *Nature Geoscience*, 8, 829-832.

Osinski, R. O., Pierazzo, E. (2013) Impact cratering: processes and products, In: Osinski, G. R., Pierazzo, E., *Impact cratering processes and products*, Wiley-Blackwell, Malaysia.

Osinski, G. R., Tornabene, L. L., Banerjee, N. R., Cockell, C. S., Flemming, R., Izawa, M. R. M., McCutcheon, J., Parnell, J., Preston, L. J., Pickersgill, A. E., Pontefract, A., Sapers, H. M., Southam, G. (2013) Impact – generated hydrothermal systems n Earth and Mars, *Icarus*, 224, 247 – 363.

Ostroovmov, M., Hernández-Bernal, M. d. S. (2011) Mineralogical composition of the meteorite El Pozo (Mexico): A Raman, infrared and XRD study, *Specrohimica Acta Part A: Molecuar and Biomolecular Spectrosscpoy*, 83, 437 – 443.

Ovsyannikov, S. V., Morozova, N. V., Karkin, A, E., Shchennikov, V. V. (2012) High pressure cycling of α-Fe_2O_3: Nanostructing, in-situ electronic transport, and possible charge disproportionation, *Physical Review B*, 86, 205131.

Owen, T., Bar-Nun, A., Klienfeld, I. (1992) Possible cometary origin of heavy noble gases in the atmospheres of Venus, Earth and Mars, *Nature*, 358, 43-45.

Oze, C., Sharma, M. (2005) Have olivine, will gas: Serpentinization and the abiogenic production of methane on Mars, *Geophysical Research Letters*, 32, L10203.

Oze, C., Sharma, M. (2007) Serpentinisation and the inorganic synthesis of H_2 in planetary surfaces, *Icarus*, 186, 557 – 561.

Papike, J. J., Karner, J. M., Shearer, C. K., Burger, P.V. (2009) Silicate mineralogy of Martian meteorites, *Geochimica et Cosmochimica Acta*, 73, 7443-7485.

Pask, H. M. (2001) The design and operation of solid-stat Raman lasers, *Progress in Quantum Electronics*, 27, 3 – 56.

Pepin, R. O. (2006) Atmospheres on the terrestrial planets: Clues to origin and evolution, *Earth and Planetary Science Letters*, 252, 1 – 14.

Perminov, V. G. (1999) *The difficult road to Mars - A brief history of Mars exploration in the Soviet Union*, NASA History Division.

Pierazzo, E., (2006), Numerical modelling of impact cratering, *Proceedings 1st international conference on impact cratering in the solar system ESA special publication*, 612, 115 – 122.

Pierazzo, E., Collins, G., (2004), A brief introduction to hydrocode modelling of impact cratering, In: Dypvik, H., Burchell, M. J., Claeys, P., *Cratering in marine environments and on ice*, Springer, Berlin.

Pierazzo, E., Melosh, H. J. (1999) Hydrocode modelling of Chicxulub as an oblique impact event, *Earth and Planetary Science Letters*, 165, 163-176.

Pierrehumbert, R. T. (2010) *Principals of planetary climate*, Cambridge University Press, Cambridge.

Pioro, I., Mokry, S. (2011) Thermophysical Properties at Critical and Supercritical Pressures, Heat Transfer - Theoretical Analysis, Experimental Investigations and Industrial Systems, Prof. Aziz Belmiloudi (Ed.), ISBN: 978-953-307-226-5, InTech, Available from: http://www.intechopen.com/books/heat-transfer-theoreticalanalysis-experimental-investigations-and-industrial-systems/thermophysical-properties-at-critical-andsupercritical-pressures.

Plescia, J. B. (1992) An assessment of the volatile release from recent volcanism in Elysium, Mars, *Icarus*, 104, 20-32.

Pope, K. O., Baines, K. H., Ocampo, A. C., Ivanov, B. A. (1994) Impact winter and the Cretaceous/Tertiary extinctions: Results of a Chicxulub asteroid impact model, *Earth and Planetary Science Letters*, 128, 719-725.

Pope, K. O., Baines, K. H., Ocampo, A. C. (1997) Energy, volatile production, and climatic effects of the Chicxulub Cretaceous/Tertiary impact, *Journal of Geophysical Research*, 102, 645-664.

Popp, J., Tarccea, N. Kiefer, W., Hilchenbach, M., Thomas, N., Stuffler, T., Hofer, S., Stöffler, D., Greshake, A. (2002) The effect of surface texture on the mineralogical analysis of chondritic meteorites using Raman spectroscopy, *Planetary and Space Science*, 50, 865-870.

Prasad, P.S. R., Pradhan. A., Gowd, T. N. (2001) In situ micro-Raman investigation of dehydration mechanism in natural gypsum, *Current Science*, 80, 1203-1207.

Price, M. C., Ramkissoon, N. K., McMahon, S., Miljkovic, K., Parnell, J., Wozniakiewicz, P. J., Kearsley, A. T., Blamey, N. J. F., Cole, M. J., Burchell, M. J. (2013) Limits on methane release and generation via hypervelocity impacts of Martian analogue materials, *International Journal of Astrobiology*, 13(2), 132-140.

Price, M. C., Wozniakiewicz, P. J., Bridges, J.C., Hicks, L.J., Burchell, M. J. (2012) Raman analyses of Stardust terminal grain in Track 170, *European Planetary Science Congress Abstract# 333*.

Price, M. C., Wozniakiewicz, P. J., Bridges, J.C., Hicks, L.J. (2014) Results from Raman analyses of thirty-six Stardust cometary grains from tracks 170, 176, 177, 178, *45th Lunar and Planetary Science Conference Abstract# 1252*.

Quesnel, Y., Sotin, C., Langlais, B., Costin, S., Mandea, M., Gottschalk, M., Dyment, J. (2009) Serpentinization of the martian crust during Noachian, *Earth and Planetary Science Letters*, 277, 184 -193.

Raman, C. V. (1928) A new radiation, *Indian Journal of Physics*, 2, 387 – 398.

Raymond, L. A. (2002) *Petrology: The study of Igneous, Sedimentary and Metamorphic Rocks, Second edition*, McGraw-Hill Higher education, New York.

Reed, S. J. B. (2005) *Electron Microprobe Analysis and Scanning Electron Microscopy in Geology*, Cambridge Universuty Press, Cambridge.

Ru, E. C. L., Schroeter, L. C., Etchegoin, P. G. (2012) Direct Measurement of Resonance Raman Spectra and Cross Sections by a Polarization Difference Technique, *Analytical chemistry*, 84, 5074 – 5079.

Ruan, H. D., Frost, R. L., Kloprogge, J. T. (2001) The behaviour of hydroxyl unit of synthetic goethite and is dehydroxylated product hematite, *Spectrochimica Acta PeatA*. 57, 2575 – 2586.

Rull, F., Maurice, S., Diaz, E., Tato, C., Pacro, A., and the RLS Team. (2011) The Raman Laser Spectrometer (RLS) on the ExoMars 2018 Rover Mission, *42nd Lunar and Planetary Science Conference, Abstract# 2400.*

Rull, F., Maurice, S., Diaz, E., Lopez, G., Catala, A., and the RLS team. (2013) Raman Laser Spectrometer (RLS) for ExoMars 2018 Rover mission: Current Status and Science Operation Mode on Powdered Samples, *44th Lunar and Planetary Science Conference, Abstract# 3110*.

Ryan, E., Dlugokencky, E. J., Tans, P. P., Trudeau, M. E. (2006) Mauna Loa volcano is not a methane source: Implications for Mars, *Geophysical Research Letters*, 33, L12301.

Sagan, C., Toon, O.B., Gierasch, P. J. (1973) Climatic change in Mars, Science, 181, 1045-1049.

Sarma, L. P., Prasad, P. S. R., Ravikumar, N. (1998) Raman Spectroscopic study of phase transitions in natural gypsum, *Journal of Raman Spectroscopy*, 29, 851 – 856.

Sauer, M., Hofkens, J., Enderlein, J. (2011) *Handbook of Fluorescence Spectroscopy and Imagining: From Ensemble to Single Molecules*, Wiley-VCH, Germany.

Schuerger, A. C., Moores, J. E., Clausen, C. A., Barlow, N. G., Britt, D. T. (2012) Methane from UV-irradiated carbonaceous chondrites under simulated Martian conditions, *Journal of Geophysical Research*, 117 E08007.

Schrenk, M. O., Brazelton, W. J., Lang, S. Q. (2013) Serpentinization, Carbon, and Deep Life, *Reviews in Mineralogy & Geochemistry*, 75, 575 – 606.

Schaefer, L., Fegley Jr, B. (2010) Chemistry of atmosphere formed during accretion of the Earth and other terrestrial planets, *Icarus*, 208, 438-488.

Schwenzer, S. P., Abramov, O., Bridges, J. C., Clifford, S. M., Filiberto, J., Kring, D. A., Lasue, J., McGovern, P. J., Newsome, H. E., Treiman, A. H., Vaniman, D. T., Wiens, R. C. (2012a), Gale Crater: Formation and post-impact hydrous environments, *Planetary and Space Science*, 70, 84 – 95.

Schwenzer, S. P., Abramov, O., Allen, C. C., Clifford, S. M., Cockell, C. S., Filiberto, J., Kring, D. A., Lasue, J., McGovern, P. J., Newsom, H. E., Treiman, A. H., Vaniman, D. T., Wines, R. C. (2012b) Puncturing Mars: How impact crater interact with the Martian cryosphere, *Earth and Planetary Science Letters*, 335-336, 9-17.

Schwenzer, S. P., Kring, D. A. (2013) Alteration minerals in impact –generated hydrothermal systems – Exploring host rock variability, *Icarus*, 226, 487-496.

Scott, D. H., Carr., M. H. (1978) *Geologic map of Mars: U.S. Geological Survey Miscellaneous Investigations Series Map I–1083*, scale 1:25,000,000.

Seyfried, W. E., Foustoukos, D. I., Fu, Q. (2007) Redox evolution and mass transfer during serpentinization: An experimental and theoretical study at 200 ˚C, 500bar with implications for ultramafic-hosted hydrothermal systems at Mid-Ocean Ridges, *Geochimica et Cosmochimica Acta*, 71, 3872 – 3886.

Segura, T. L., Toon, O.B., Colaprete, A., Zahnle, K. (2002) Environmental effects of large impacts on Mars, *Science*, 298, 1977-1980.

Segura, T. L., Toon, O.B., Colaprete, A. (2008) Modeling the environmental effects of moderate-sized impacts on Mars, *Journal of Geophysical Research*, 133, E11007, 1-15.

Seiferlin, K., Ehrenfreund, P., Garry, J., Gunderson, K., Hutter, H., Kargl, G., Maturilli, A., Merrison, J. P. (2008) Simulating Martian regolith in the laboratory, *Planetary and Space science*, 56, 2009 – 2025.

Sharp, R. P., Malin, M. C. (1975) Channels on Mars, *Geological Society of America Bulletin*, 86, 593-609.

Shim, S-H., Duffy, T. S. (2002) Raman spectroscopy of Fe_2O_3 to 62 GPa, *American Mineralogist*, 87, 318-326.

Showstack, R. (2011) Mars Opportunity rover finds gypsum veins, *Eos*, 92, 479.

Singer, R. B. (1982) Spectral evidence for the mineralogy of high-albedo soils and dust on Mars, *Journal of Geophysical Research*, 87, 159-10.168.

Sirokman, G. (2014) Synthesis, dehydration and rehydration of calcium sulfate (gypsum, Plaster of Paris), *Journal of chemical Education*, 91, 557-559.

Slater, J. B., Tedesco, J. M., Fairchild, R. C., Lewis, I. R. (2001) Raman Spectrometry and Its Adaptation to the Industrial Environment, In: Lewis, I. R. Edwards, H. G. M., *Handbook of Raman Spectroscopy from the research laboratory to the process line*, CRC Press, New York.

Smith, E., Dent, G. (2005) *Modern Raman Spectroscopy – A Practical Approach*, John Wiley & Sons, England.

Socrates, G. (2001) *Infrared and Raman characteristic group frequencies, Tables and charts Third edition*, Wiley, Chichester, UK.

Soderblom, L. A., Bell III, J.F. (2008) Expolation of the Martian surface: 1992 – 2007, In: Bell III, J. F., *The Martian surface: Composition, Mineralogy and Physical properties*, Cambridge University Press, Cambridge.

Squyres, S. W., Kasting, J. F. (1994) Early Mars: How warm and how wet?, *Science*, 265, 744-748.

Steinberg, D. J., Cochran, S. G., Guinan, M. W. (1980) A constitutive model for metal applicable at high-strain rate, *Journal of Applied Physics*, 51, 1498-1504.

Stöffler, D., Hornemann, U. (1972) Quartz and feldspar glasses produced by natural and experimental shock, *Meteoritics and Planetary Science*, 7, 371-394.

Stooke, P. J. (2012) *The international atlas of Mars exploration the first five decades*, Cambridge University Press, Cambridge.

Stopar, J. D., Taylor, G. J., Hamilton, V. E., Browning, L., Pickett, D. (2003) Maximum rates of olivine dissolution of Mars. *Sixth International Conference on Mars, Abstract# 3151*.

Tanaka, K. (1986) The Stratigraphy of Mars, *Proceedings of the 17th Lunar and Planetary Science Conference, Journal of the Geophysical Research*¸ 9, 139-158.

Tarduno, J. A., Blackman, E. G., Mamajek, E. E. (2014) Detecting the oldest geodynamo and attendant shielding from the solar wind: Implications for habitability, *Physics of the Earth and Planetary Interiors*, 233, 68 – 87.

ten Kate, I. L. (2010) Organics on Mars?, *Astrobiology*, 10, 589 – 603.

Thoma, K., Hornemann, U., Sauer, M., Schneider, E. (2005) Shock waves – Phenomenology, experimental , and numerical simulation, *Meteoritics and Planetary science*, 40, 1283 – 1298.

Tillotson., J. H. (1962) *Metallic Equations of State for Hypervelocity Impact*, GA-3216, General Atomic, San Diego, California.

Trunin, R. F. (1998) *Shock compression of condensed materials*, Cambridge University Press, Cambridge.

Vance, S., Harnmeijer, J., Kimura, J., Hussmann, H., Demartin, B., Brown, J. M. (2007) Hydrothermal systems I Small Ocean Planets, *Astrobiology*, 7, 987 – 1005.

Vandenabeele, P., Edwards, H. G. M., Moens, L. (2007) A decade of Raman Spectroscopy in Art and Archaeology, *Chemical Reviews*, 107, 675 - 686.

Van der Merwe, E. M., Strydom, C. A., Potgieter, J. H. (1999) Thermogravimetric analysis of the reaction between carbon and $CaSO_4.2H_2O$, gypsum and phophogypsum in an inert atmosphere, *Thermochimica Acta*,340-341, 431-437.

Vernon – Parry, K. D. (2000) Scanning Electron Microscopy: and introduction, *III-Vs Review*, 13, 4, 40 – 44.

Vernooij, M. G. C., Lnagenhorst, F. (2005) Experimental reproduction of tectonic deformation lamellae in quartz and comparison to shock-induced planar deformation features, *Metoeritics and Planetary Science*,40, 1353-1361.

Vignjevic, R., Hughes, K., Walker, A., Taylor, E. A., (2001), Overcoming element erosion limitations within lagrangian finite element codes, *Proceedings of the third European Conference on Space Debris*, Germany, 595 – 601.

Wang, A., Jolliff, B. L., Haskin, L. A. (1995) Raman spectroscopy as a method for mineral identification on lunar robotic exploration missions, *Journal of Geophysical Research*, 100, 21,189-21,199.

Wang, A., Korotev, R. L., Jolliff, B. L., Ling, Z. (2015) Raman imaging of extra-terrestrial materials, *Planetary and Space Science*, 112, 23 -34.

Wartewig, S. (2003) *IR and Raman Spectroscopy Fundamental Processing*, Germany, Wiley-VCH.

Webster, C. R., Mahaffy, P. M., Atreya, S. K., Flesch, G. J., Mischna, M. A., Meslin, P., Farley, K. A., Conrad., P. G., Christensen, L. E., Pavlov., A. A., Martin-Torres, J., Zorzano, M., McConnochie, T. H., Owen, T., Eigenbrode, J. L., Glavin, D. P., Steele, A., Malespin, C. A., Douglas Archer Jr, P., Sutter, B., Coll, P., Freissinet, C., ckay, C. P., Moores, J. E., Schwenzer, S. P., Bridges, J. C., Navarro-Gonzalez, R., Gellert, R., Lemmon, M. T., the MSL science team. (2014) Mars Methane detection and variability at Gale crater, *Science*, 347, 415-417.

Wenk, H. R., Bulakh, A. (2013) Minerals, Their constitution and origin, Cambridge University Press, Cambridge.

Wilhelms, D. E. Squyres, S. W. (1984) The Martian hemispheric dichotomy may be due to a giant impact, *Nature*, 309, 138 - 140

Wittmann, A., Kenkmann, T., Schmitt, R. T., Stöffler, D. (2006) Shock-metamorphosed zircon in terrestrial impact craters, *Meteoritics and Planetary Science*, 41, 433 – 454.

Wray, J. J., Squyres, S. W., Roach, L. H., Bishop, J. L., Mustard, J. F. Noe Dobrea, E. Z. (2010) Identification of the Ca-Sulfate bassanite in Mawrth Vallis, Mars, *Icarus*¸ 209, 416 – 421.

Wümmemann, K., Nowka, D., Collins, G. S., ELbeshausen, D., Bierhaus, M. (2011) Scaling of impact crater formation on planetary surfaces – insight from numerical modelling, *Proceedings of the 11th Hypervelocity Impact Symposium*, 1 -16.

Xie, Z., Li, X., Sharp T. G., De Carli, P. S. (2012) Shock-induced ringwoodite rims around olivine fragments in melt veils of Antarctic chondrite GRV022321: Transformation mechanism, *43rd Lunar and Planetary Science Conference, Abstract# 2776.*

Yokoo, M., Kawai, N., Nakamura, K. G., and Kando, K. (2008) Hugoniot measurement by hyper-velocity impact at velocities up to 9 km/s using a two-stage light-gas gun under optimized shot conditions, *International Journal of Impact Engineering*, 35, 1878-1883.

Zahnle, K., Freedman, R., S., Catling, D., C. (2011) Is there methane on Mars?, *Icarus*, 212, 493-503.

Zhang, W.R., Lowe, C., Smith, R. (2009a) Depth profiling of clear coil coating by confocal Raman microscopy, *Progress in organic coatings*, 66, 141-148.

Zhang, Z-M., Chen, S., Liang, Y-Z., Liu, Z-X., Zhang, Q-M., Ding, L-X., Ye, F., Zhou, H. (2009b) An intelligent background-correction algorithm for highly fluorescent samples in Raman spectroscopy, *Journal of Raman Spectroscopy*, 41, 659 – 669.

Zhang, F., Sekine, T. (2007) Impact-shock behaviour of Mg- and Ca-sulfates and their hydrates, *Geochimica et Cosmochimica Acta*, 71, 4125-4133.

Zhou, W., Apkarian, R., Wang, Z. L., & Joy, D. (2007) Fundamentals of Scanning Electron Microscopy (SEM). In Zhou, W. & Wang, Z., L., *Scanning Microscopy for Nanotechnology*, Springer, New York.

Zhu, Q., Guivey Jr, R. G., Berger, A. J. (2007) Raman Spectroscopic Measurements of Relative Concentrations in mixtures of Oral Bacteria, *Applied Spectroscop*,61, 11, 1233 – 1237.

Zubrin, R., Lovelock, J., Allaby, M., Williams, D. R. Atkinson, N. (2009) C*olonization of Mars*, Iphascript publishing, U. S. A.

Zukas, J. A., (2004), Introduction to Hydrodynamics, *Elsevier*, Oxford, UK.

Appendices

Appendix A – Characterisation of Grains

Using an optical microscope, 5-10 grains of each colour (as determined by eye) were collected for characterisation tests. In total, nine sets of grains were identified (Figure A1). One to two grains from each set were embedded in epoxy resin before being polished flat for analysis.

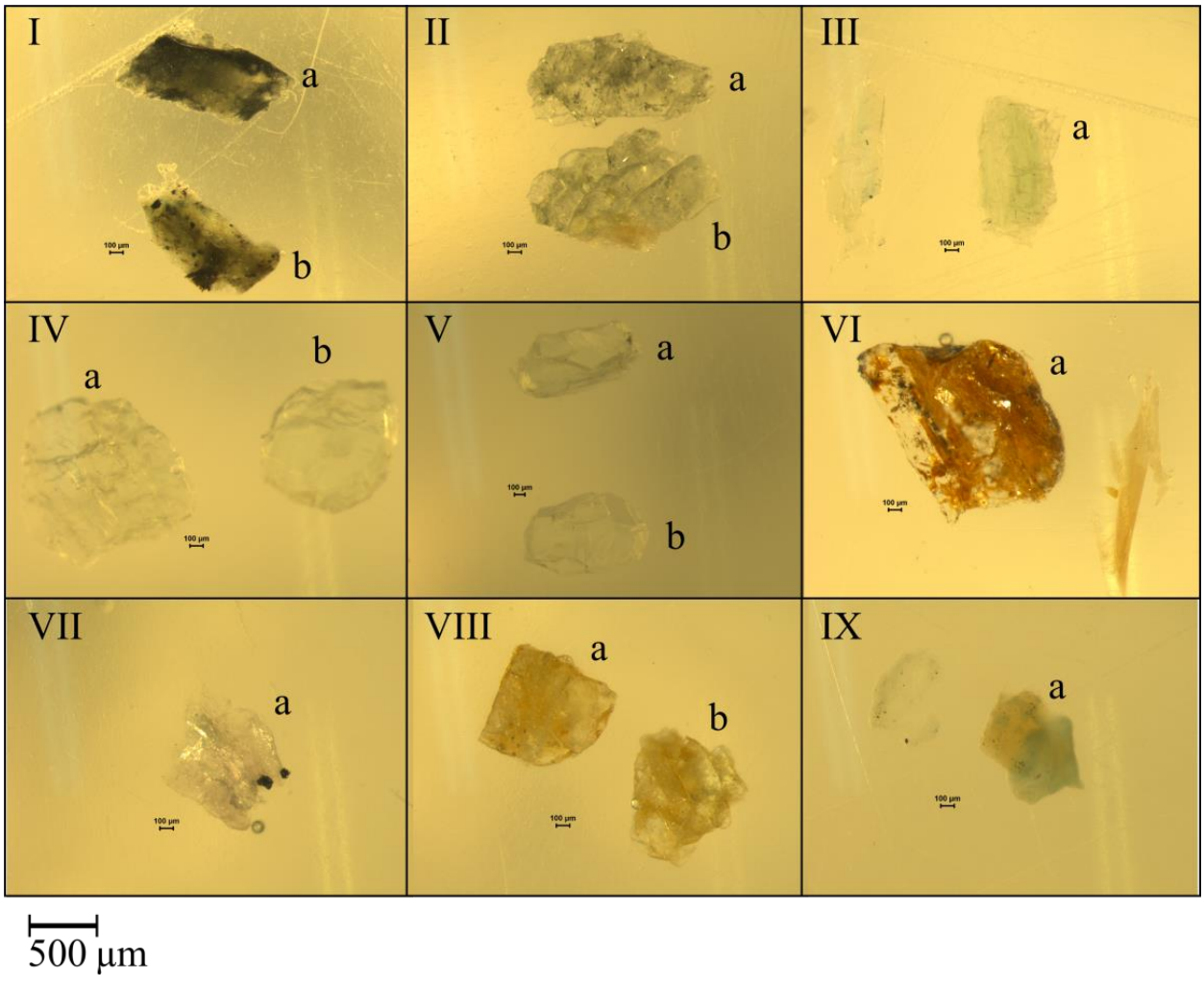

Figure A1 Optical images of olivine grains available for use in these laboratory impact experiments. Two from each group, separated according to their colour, were prepared in resin for characterisation All images were taken using a Leica MZ16 microscope.

The grains were characterised using three instruments: 1) an optical microscope (using reflected light), 2) a Hitachi S-3400N Scanning Electron Microscope (SEM) and, 3) a Horiba LabRam-HR Raman spectrometer. SEM EDX analysis was used to determine the composition of each grain, and thus its mineralogy. BSE images and quantitative data obtained from SEM EDX analysis (Table A1) were taken using a 20 kV electron beam and with the SEM in variable pressure mode (at a pressure of 20 Pa) to avoid charging of the sample, as the samples were uncoated. Quantitative data obtained needed to be normalised due to element weight percentages greater than the acceptable value (between 99 – 102%). Doing this meant any possible hydration, that had occurred prior to collection, would not be detected via this analysis. Some of the Al detected in the EDX may have come from SEM, as this analysis was conducted in variable pressure mode. However, Al was detected in the EDX data for only some grains and so it might be real. Raman spectroscopy was used to verify the mineralogy determined from the EDX results.

Table A1 SEM EDX data showing a representative spectrum of each phase for all 9 grain types.

		Atomic %													
	Element	Grain type I a	Grain type I b	Grain type II a	Grain type II b	Grain type III a	Grain type IV a	Grain type IV b	Grain type V a	Grain type V b	Grain type VI a	Grain type VII a	Grain type VIII a	Grain type VIII b	Grain type IX a
Phase 1 (bulk phase)	Mg	21.23	20.30	26.55	26.41	26.87	26.35	26.37	26.46	26.89	-	19.62	26.58	26.19	22.80
	Al	-	5.23	-	-	-	-	-	-	-	-	6.25	-	-	0.46
	Si	18.28	14.57	14.79	14.93	14.57	14.75	14.91	14.85	14.49	33.33	13.58	14.69	14.80	16.78
	Cl	0.15	-	-	-	-	-	-	-	-	-	-	-	-	-
	Cr	-	0.28	-	-	-	-	-	-	-	-	1.22	-	-	-
	Fe	1.28	0.95	1.26	1.19	1.27	1.53	1.26	1.27	1.38	-	0.66	1.39	1.62	1.45
	O	59.06	58.66	57.4	57.47	57.29	57.37	57.46	57.42	57.24	66.67	58.66	57.34	57.40	58.51
	Total	**100.00**	**99.99**	**100.00**	**100.00**	**100.00**	**100.00**	**100.00**	**100.00**	**100.00**	**100.00**	**99.99**	**100.00**	**100.01**	**100.00**
Phase 2	Mg	13.87	26.36	24.08	22.65	23.11	-	-	-	-	-	-	26.16	-	20.86
	Al	-	-	-	-	-	-	-	-	-	-	-	-	-	2.01
	Si	21.11	15.01	16.06	17.18	16.8	-	-	-	-	32.85	-	14.61	-	15.97
	Ca	3.94	-	-	-	-	-	-	-	-	-	-	-	-	-
	K	-	-	-	-	-	-	-	-	-	-	-	-	-	0.40
	Cr	-	-	-	-	-	-	-	-	-	-	-	-	-	0.07
	Fe	0.52	1.13	1.82	1.58	1.69	-	-	-	-	0.72	-	1.92	-	2.29
	O	60.56	57.5	58.03	58.59	58.4	-	-	-	-	66.43	-	57.31	-	58.40
	Total	**100.00**	**100.00**	**99.99**	**100.00**	**100.00**	**0.00**	**0.00**	**0.00**	**0.00**	**100.00**	**0.00**	**100.00**	**0.00**	**100.00**
Phase 3 (high density)	Mg	-	5.49	7.64	-	-	-	-	-	-	-	4.87	-	-	-
	Al	-	2.13	-	-	-	-	-	-	-	-	2.18	-	-	-
	Si	-	1.13	2.87	-	-	-	-	-	-	24.42	0.85	-	-	-
	Ca	-	-	-	-	-	-	-	-	-	0.27	-	-	-	-
	Cr	-	23.03	-	-	-	-	-	-	-	-	22.98	-	-	-
	Fe	-	11.38	37.5	-	-	-	-	-	-	13.1	12.39	-	-	-
	Ni	-	-	0.56	-	-	-	-	-	-	-	-	-	-	-
	O	-	56.85	51.43	-	-	-	-	-	-	62.21	56.72	-	-	-
	Total	**0.00**	**100.01**	**100.00**	**0.00**	**0.00**	**0.00**	**0.00**	**0.00**	**0.00**	**100.00**	**99.99**	**0.00**	**0.00**	**0.00**

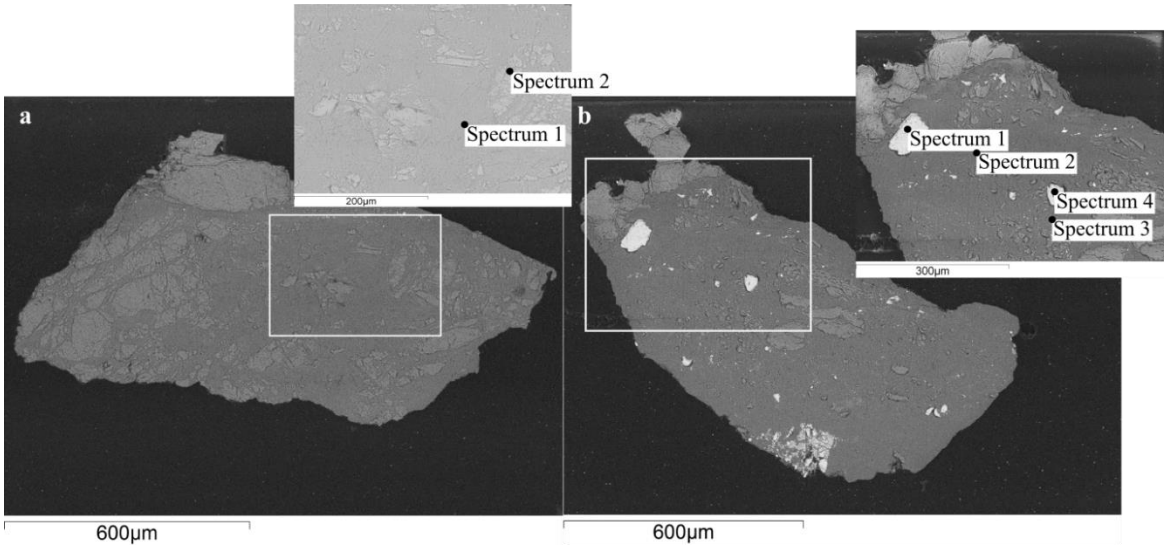

Figure A2 SEM BSE images the embedded grains of grain type I, with inserts showing the locations where the point spectra were taken (see Table 5.1.1 for general SEM EDX data).

Grain type I (Figure A2 Ia and Ib) exhibits the darkest colour, appearing smoky black with small opaque inclusion. Backscatter electron (BSE) images of the grains (Figure A2) shows there are three dominant phases within the grains: a fine-grained darker (low density) phase, a large grained, moderately dense phase and a bright (high density) phase. The high density phase is most likely the opaque phases seen in the optical images. Grain "b" has more visible areas of the high density composition relative to the surrounding matrix compared to grain "a", which have a few, small instances of this phase. SEM EDX data shows these high density objects are Cr- rich. In addition, the results show this grain has a pyroxene, composition (see Appendix A, Tables A2 and A3 for the complete dataset). However, the second phase in grain Ib appears to be olivine, but Raman spectroscopy confirms the grains are pyroxene (Figure A3).

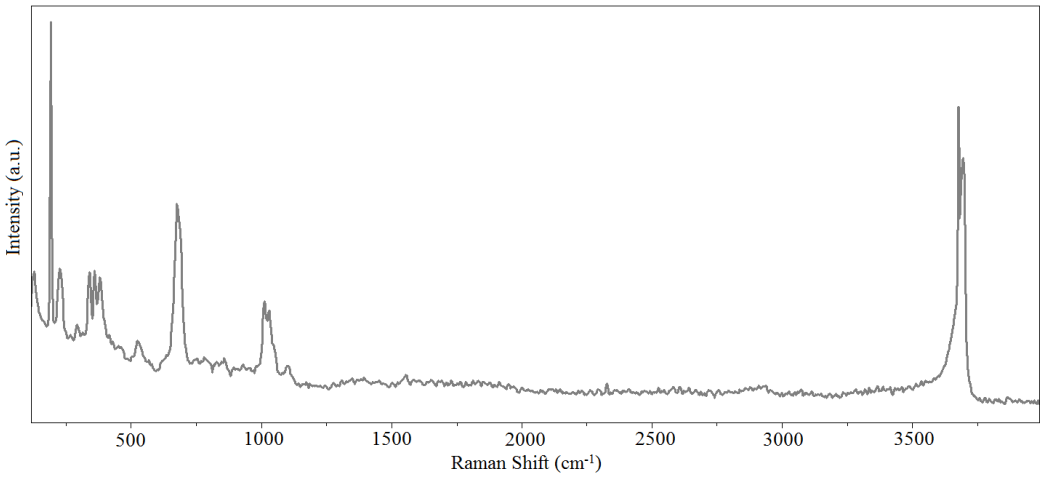

Figure A3 A standard Raman spectrum for grain type I. The spectrum was taken with a 473 nm laser, 10 % N.D. filter, × 10 objective and 600 g/mm grating.

Table A2 SEM EDX data for grain colour I a.

	Element	Weight%	Atomic%	Compd%	Formula	Number of ions	
Spectrum 1	Mg K	25.17	21.23	41.73	MgO	2.87	2.15
	Si K	25.03	18.28	53.55	SiO2	2.47	1.85
	Cl K	0.26	0.15	0.00		0.02	0.02
	Fe K	3.47	1.28	4.47	FeO	0.17	0.13
	O	46.07	59.06			7.98	6.00
	Totals	**100.00**	**100.00**	**99.75**			
					Cation sum	5.51	
Spectrum 2	Mg K	16.16	13.87	26.80	MgO	1.83	1.3725
	Si K	28.43	21.11	60.81	SiO2	2.79	2.0925
	Ca K	7.57	3.94	10.59	CaO	0.52	0.39
	Fe K	1.40	0.52	1.80	FeO	0.07	0.0525
	O	46.44	60.56			8	6
	Totals	**100.00**	**100.00**	**100.00**			
					Cation sum	5.21	

Table A3 SEM EDX data for grain colour I b

	Element	**Weight%**	**Atomic%**	**Compd%**	**Formula**	**Number of ions**	
Spectrum 1	Mg K	4.50	5.49	7.46	MgO	0.77	0.58
	Al K	1.94	2.13	3.66	Al2O3	0.30	0.23
	Si K	1.07	1.13	2.28	SiO2	0.16	0.12
	Cr K	40.39	23.03	59.03	Cr2O3	3.24	2.43
	Fe K	21.43	11.38	27.57	FeO	1.60	1.20
	O	30.68	56.85			8.00	6.00
	Totals	**100.00**	**100.01**	**100.00**			
					Cation sum	6.07	
Spectrum 2	Mg K	24.07	20.30	39.91	MgO	2.77	2.08
	Al K	6.88	5.23	13.01	Al2O3	0.71	0.53
	Si K	19.96	14.57	42.70	SiO2	1.99	1.49
	Cr K	0.72	0.28	1.05	Cr2O3	0.04	0.03
	Fe K	2.59	0.95	3.33	FeO	0.13	0.10
	O	45.78	58.66			8.00	6.00
	Totals	**100.00**	**99.99**	**100.00**			
					Cation sum	5.64	
Spectrum 3	Mg K	31.33	26.36	51.95	MgO	3.67	2.75
	Si K	20.61	15.01	44.09	SiO2	2.09	1.57
	Fe K	3.08	1.13	3.96	FeO	0.16	0.12
	O	44.98	57.50			8.00	6.00
	Totals	**100.00**	**100.00**	**100.00**			
					Cation sum	5.91	
ect ru m	Mg K	5.78	6.90	9.58	MgO	0.97	0.73

	Al K	3.05	3.28	5.77	Al2O3	0.46	0.35
	Si K	1.21	1.25	2.58	SiO2	0.18	0.14
	Cr K	37.06	20.69	54.17	Cr2O3	2.92	2.19
	Fe K	21.69	11.27	27.90	FeO	1.59	1.19
	O	31.21	56.62			8.00	6.00
	Totals	**100.00**	**100.01**	**100.00**			
					Cation sum	6.13	

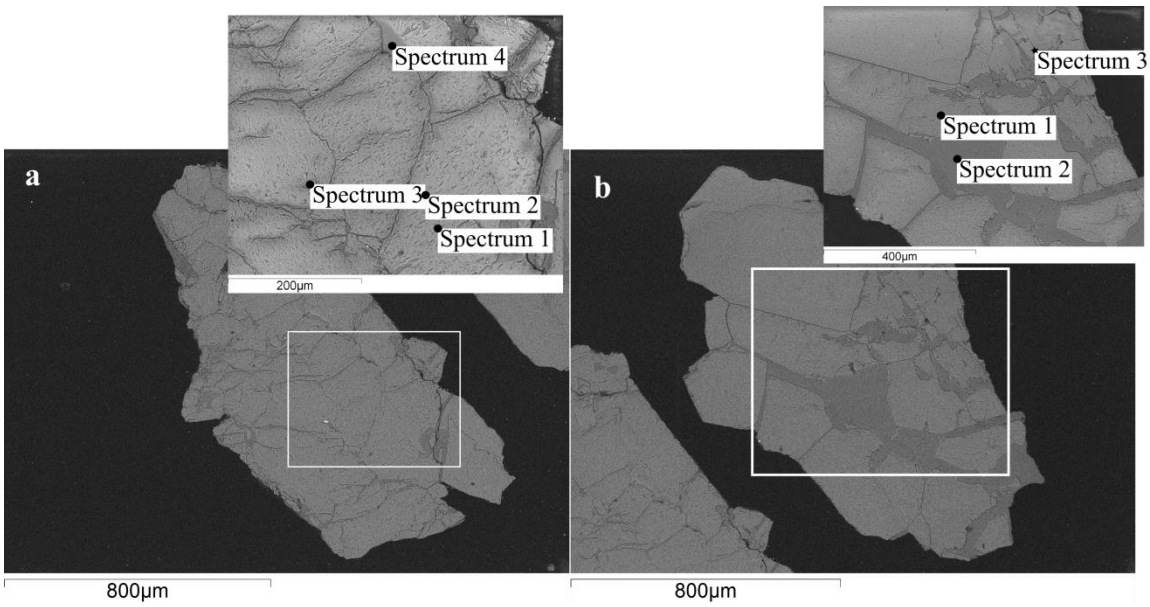

Figure A4 SEM BSE images of the embedded grains of grain type II with inserts showing the locations where the point spectra were taken.

Grain type II has a cloudy grey colour, again with translucent areas (Figure A4 IIa and IIb). The grains show a number of fractures, particularly in grain a, but with no dominant direction visible. SEM BSE images of grain a show that these fractures are surrounded by darker phase than the bulk grain, indicating there is a difference in composition around the fractures. SEM EDX data show both grains are olivine in composition (Table A4 and A5), confirmed by Raman spectroscopy (Figure A5). SEM EDX data does not show a difference in composition between the darker phase around the fractures and bulk phase of the grain seen in the BSE images. This difference in composition is likely the result of aqueous alteration, as the compositional difference is restricted to the location of fractures within the grains. Spectrum 3 of grain IIa was taken of a high density feature of the grain, which is a metallic feature with a high Fe content. Raman spectroscopy of the same grain sample shows slight hydration, as demonstrated by the presence of a spectral feature at 3665 - 3715 cm^{-1} Raman shift, indicative of H_2O.

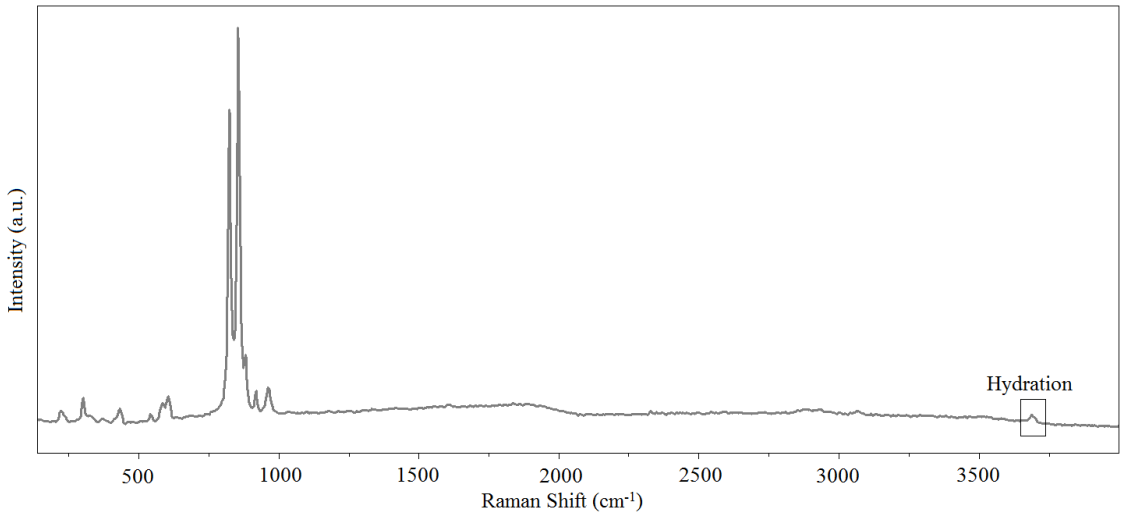

Figure A5 A standard Raman spectrum for grain type II. The black box highlights the OH (hydration peak). The spectrum was taken with a 473 nm laser, 10 % N.D. filter, × 50 objective and 600 g/mm grating.

Table A4 SEM EDX data for grain IIa

	Element	Weight%	Atomic%	Compd%	Formula	Number of ions	
Spectrum 1	Mg K	28.33	24.08	46.97	MgO	3.32	1.66
	Si K	21.83	16.06	46.70	SiO2	2.21	1.105
	Fe K	4.92	1.82	6.33	FeO	0.25	0.125
	O	44.92	58.03			8	4
	Totals	**100.00**	**99.99**	**100.00**			
					Cation sum	5.79	
Spectrum 2	Mg K	31.5	26.55	52.22	MgO	3.7	1.85
	Si K	20.27	14.79	43.37	SiO2	2.06	1.03
	Fe K	3.43	1.26	4.41	FeO	0.18	0.09
	O	44.80	57.40			8	4
	Totals	**100.00**	**100.00**	**100.00**			
					Cation sum	5.94	
Spectrum 3	Mg K	5.77	7.64	9.57	MgO	1.19	0.595
	Si K	2.51	2.87	5.36	SiO2	0.45	0.225
	Fe K	65.12	37.5	83.78	FeO	5.83	2.915
	Ni K	1.02	0.56	1.29	NiO	0.09	0.045
	O	25.59	51.43			8	4
	Totals	**100.00**	**100.00**	**100.00**			
					Cation sum	7.55	
Spectrum 4	Mg K	31.5	26.63	52.23	MgO	3.72	1.86
	Si K	19.98	14.62	42.74	SiO2	2.04	1.02
	Fe K	3.90	1.44	5.02	FeO	0.2	0.1
	O	44.61	57.31			8	4
	Totals	**100.00**	**100.00**	**99.99**			
					Cation sum	5.96	

Table A5 SEM EDX data for grain IIb

	Element	Weight%	Atomic%	Compd%	Formula	Number of ions	
Spectrum 1	Mg K	31.36	26.41	52.00	MgO	3.68	1.84
	Si K	20.48	14.93	43.82	SiO2	2.08	1.04
	Fe K	3.25	1.19	4.18	FeO	0.17	0.085
	O	44.9	57.47			8	4
	Totals	**100.00**	**100.00**	**100.00**			
					Cation sum	5.92	
Spectrum 2	Mg K	26.74	22.65	44.34	MgO	3.09	1.545
	Si K	23.43	17.18	50.13	SiO2	2.35	1.175
	Fe K	4.29	1.58	5.52	FeO	0.22	0.11
	O	45.53	58.59			8	4
	Totals	**100.00**	**100.00**	**99.99**			
					Cation sum	5.65	
Spectrum 3	Mg K	22.05	18.71	36.56	MgO	2.52	1.26
	Al K	3.12	2.39	5.90	Al2O3	0.32	0.16
	Si K	23.6	17.33	50.48	SiO2	2.34	1.17
	Ca K	1.73	0.89	2.42	CaO	0.12	0.06
	Cr K	1.1	0.44	1.61	Cr2O3	0.06	0.03
	Fe K	2.36	0.87	3.03	FeO	0.12	0.06
	O	46.04	59.37			8	4
	Totals	**100**	**100.0**	**100.00**			
					Cation sum	5.47	

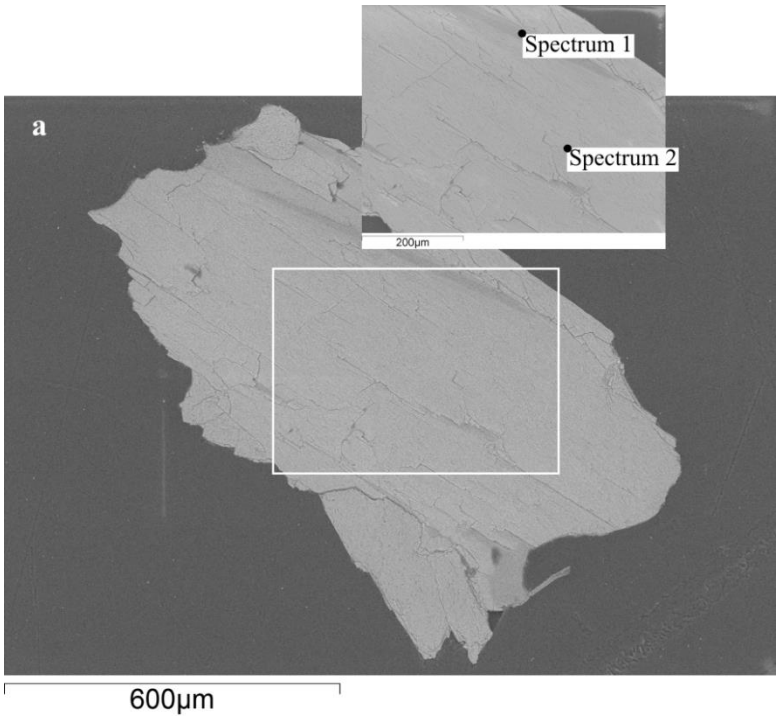

Figure A6 SEM BSE images of the embedded grains of grain type III with inset image showing the locations where the point spectra were taken.

Grain type III is very light green in colour with small fractures along the long axis of the grain (Figure A1 IIIa). Some of the fractures may have resulted from polishing. There are also some small opaque crystals along one of the fractures. The BSE image (Figure A6) shows very little variation in composition of the grain and does not identify a phase that for the opaque crystal seen in the optical image (possibly due to their size). SEM EDX data indicates the grain is olivine in composition (Table A6), which is confirmed by Raman spectroscopy (Figure A7).

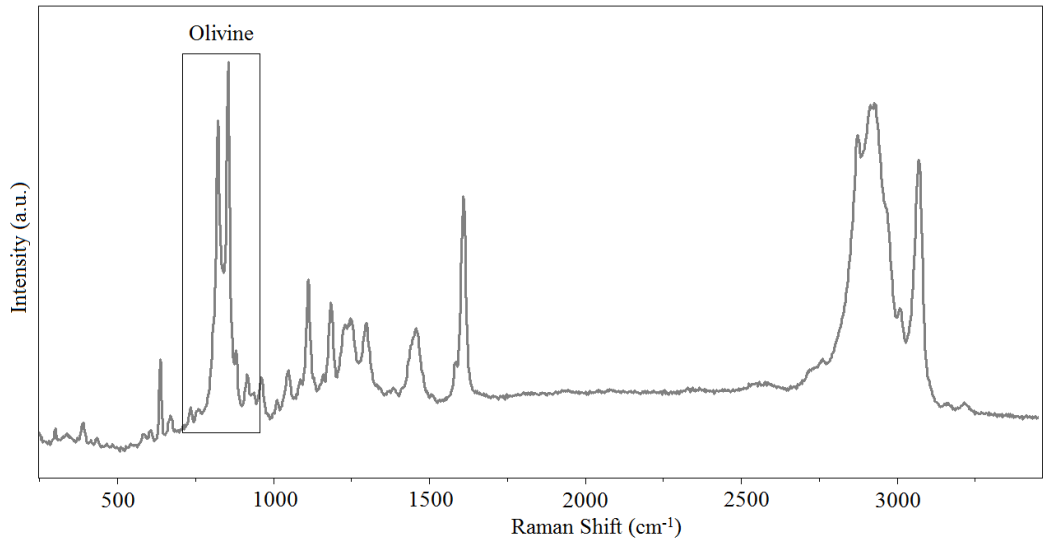

Figure A7 A standard Raman spectrum for grain type III. The black box highlights the doublet peak used to identify olivine and the remainder of the spectrum represents epoxy. The spectrum was taken with a 473 nm laser, 10 % N.D. filter, × 10 objective and 600 g/mm grating.

Table A6 SEM EDX data for grain IIIa

	Element	**Weight%**	**Atomic%**	**Compd%**	**Formula**	**Number of ions**	
Spectrum 1	Mg K	31.87	26.87	52.84	MgO	3.75	1.90
	Si K	19.96	14.57	42.71	SiO2	2.03	1.02
	Fe K	3.46	1.27	4.45	FeO	0.18	0.09
	O	44.71	57.29			8	4
	Totals	**100.00**	**100.00**	**100.00**			
					Cation sum	5.64	
Spectrum 2	Mg K	27.42	23.11	45.16	MgO	3.17	1.59
	Si K	22.88	16.80	48.95	SiO2	2.3	1.15
	Fe K	4.58	1.69	5.89	FeO	0.23	0.12
	O	45.3	58.40			8	4
	Totals	**100.00**	**100.00**	**100.00**			
					Cation sum	5.7	

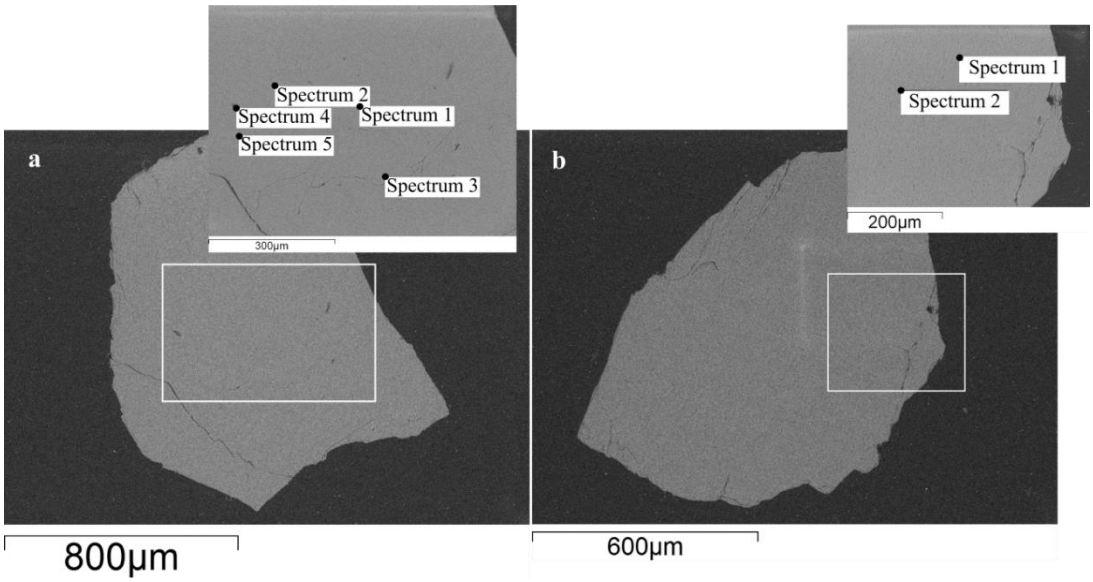

Figure A8 SEM BSE images of the embedded grains of grain colour IV with inserts showing the locations where the point spectra were taken.

Grain type IV grains are more rounded than the previous grains types I – III, and have a very slight green tint (appearing almost completely transparent in the optical images). The optical image showed that the grains appear to have lines going through the grains, which might be the edges of faces, and not actual fractures or groves in the grains. BSE images (Figure A8) reveal a homogenous composition, with almost no fracturing within the grain. SEM EDX data reveals an olivine composition with a high Mg content (~Fo_{90}; Tables A7 and A8). Raman spectroscopy (Figure A9) confirms these grains are olivine.

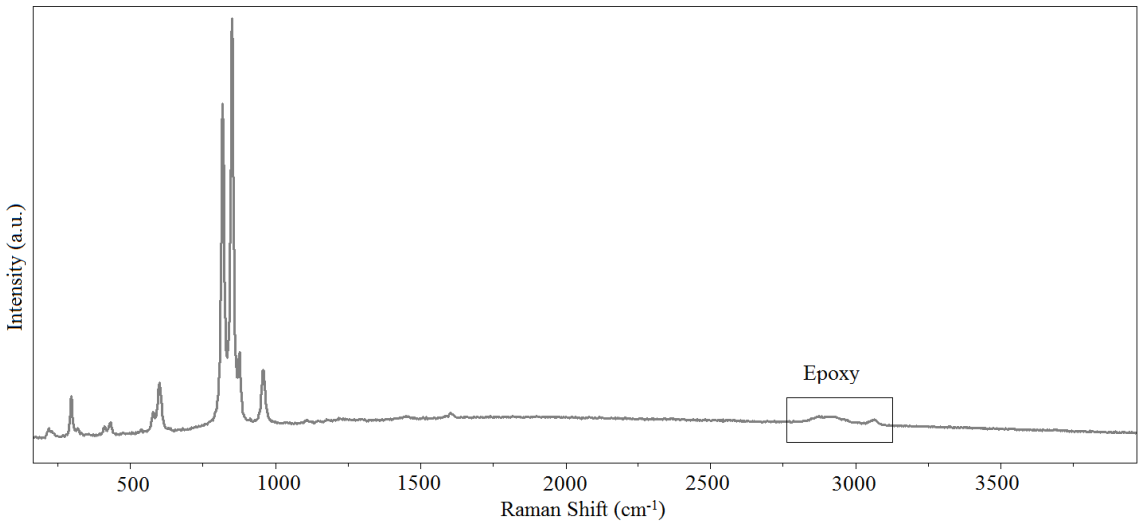

Figure A9 A standard Raman spectrum for grain type IV. The black box shows a Raman feature that is attributed to epoxy. The spectrum was taken with a 473 nm laser, 10 % N.D. filter, × 10 objective and 600 g/mm grating.

Table A7 SEM EDX data for grain IVa

	Element	Weight%	Atomic%	Compd%	Formula	Number of ions	
Spectrum 1	Mg K	31.51	26.58	52.24	MgO	3.71	1.855
	Si K	20.19	14.74	43.19	SiO2	2.06	1.03
	Fe K	3.55	1.30	4.57	FeO	0.18	0.09
	O	44.75	57.37			8	4
	Totals	**100.00**	**99.99**	**100.00**			
					Cation sum	5.94	
Spectrum 2	Mg K	31.51	26.55	52.24	MgO	3.7	1.85
	Si K	20.32	14.82	43.46	SiO2	2.06	1.03
	Fe K	3.34	1.22	4.29	FeO	0.17	0.085
	O	44.84	57.41			8	4
	Totals	**100.00**	**100.00**	**99.9**			
					Cation sum	5.94	
Spectrum 3	Mg K	31.12	26.35	51.61	MgO	3.67	1.835
	Si K	20.12	14.75	43.04	SiO2	2.06	1.03
	Fe K	4.16	1.53	5.35	FeO	0.21	0.105
	O	44.6	57.37			8	4
	Totals	**100.00**	**100.00**	**100.00**			
					Cation sum	5.94	
Spectrum 4	Mg K	27.2	23.32	45.11	MgO	3.19	1.595
	Si K	21.11	15.66	45.16	SiO2	2.15	1.075
	S K	0.55	0.36	1.36	SO3	0.05	0.025
	Cl K	1.15	0.68	0.00		0.09	0.045
	K K	1.05	0.56	1.27	K2O	0.08	0.04
	Fe K	4.62	1.73	5.95	FeO	0.24	0.12
	O	44.31	57.71			7.91	3.955
	Totals	**100.00**	**100.02**	**98.85**			
					Cation sum	5.7	
Spectrum 5	Mg K	31.63	26.66	52.44	MgO	3.72	1.86
	Si K	20.2	14.74	43.22	SiO2	2.06	1.03
	Fe K	3.37	1.24	4.34	FeO	0.17	0.085
	O	44.8	57.37			8	4
	Totals	**100.00**	**100.01**	**100.00**			
					Cation sum	5.94	

Table A8 SEM EDX data for grain IVb

	Element	Weight%	Atomic%	Compd%	Formula	Number of ions	
Spectrum 1	Mg K	31.27	26.37	51.85	MgO	3.67	1.835
	Si K	20.44	14.91	43.72	SiO2	2.08	1.04
	Fe K	3.44	1.26	4.43	FeO	0.18	0.09
	O	44.85	57.46			8	4
	Totals	**100.00**	**100.00**	**100.00**			
					Cation sum	5.92	
Spectrum 2	Mg K	31.06	26.18	51.49	MgO	3.64	1.82
	Si K	20.34	14.84	43.52	SiO2	2.06	1.03
	S K	0.23	0.15	0.57	SO3	0.02	0.01
	Fe K	3.43	1.26	4.41	FeO	0.17	0.085
	O	44.94	57.57			8	4
	Totals	**100.00**	**100.00**	**99.99**			
					Cation sum	5.9	

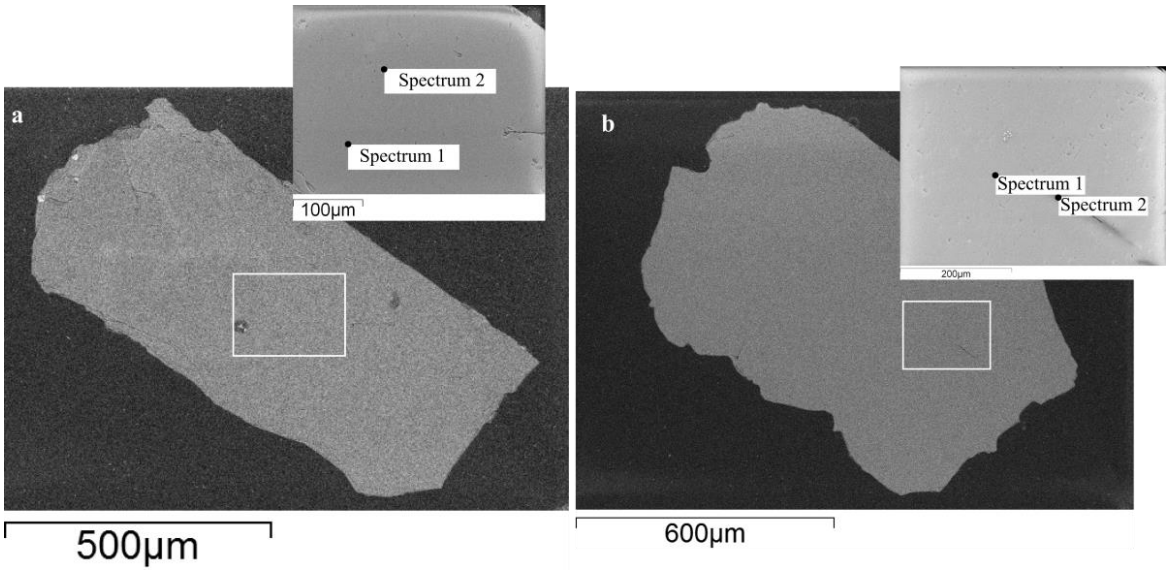

Figure A10 SEM BSE images of the embedded grains of grain type V with inserts showing the locations where the point spectra were taken.

Grains of type V are very similar to those of grain type IV, however, they are slightly darker in colour. It also has fewer, almost no, fractures (which are potentially the edges of faces). BSE images obtained for these grains also shows very little fracturing and the grains themselves are homogenous (Figure A10). SEM EDX analyses shows these grains are olivine in composition (Fo_{90}; Tables A9 and A10), which was confirmed with Raman spectroscopy (Appendix A, Figure A11).

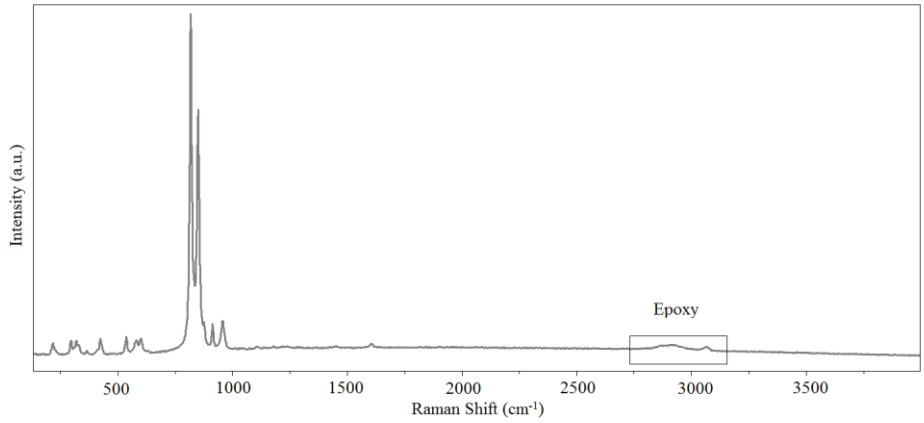

Figure A11 A standard Raman spectrum for grain type V. The spectrum was taken with a 473 nm laser, 10 % N.D. filter, × 10 objective and 600 g/mm grating.

Table A9 SEM EDX data for grain Va

	Element	Weight%	Atomic%	Compd%	Formula	Number of ions	
Spectrum 1	Mg K	31.38	26.46	52.03	MgO	3.69	1.845
	Si K	20.34	14.85	43.52	SiO2	2.07	1.035
	Fe K	3.46	1.27	4.45	FeO	0.18	0.09
	O	44.82	57.42			8	4
	Totals	**100.00**	**100.00**	**100.00**			
					Cation sum	5.93	
Spectrum 2	Mg K	31.41	26.57	52.08	MgO	3.71	1.855
	Si K	19.99	14.64	42.76	SiO2	2.04	1.02
	Fe K	3.59	1.32	4.62	FeO	0.18	0.09
	Ni K	0.42	0.15	0.54	NiO	0.02	0.01
	O	44.59	57.32			8	4
	Totals	**100.00**	**100.00**	**100.00**			
					Cation sum	5.96	

Table A10 SEM EDX data for grain Vb

	Element	Weight%	Atomic%	Compd%	Formula	Number of ions	
Spectrum 1	Mg K	31.84	26.89	52.79	MgO	3.76	1.88
	Si K	19.82	14.49	42.39	SiO2	2.02	1.01
	Fe K	3.74	1.38	4.81	FeO	0.19	0.095
	O	44.60	57.24			8	4
	Totals	**100.00**	**100.00**	**99.99**			
					Cation sum	5.98	
Spectrum 2	Mg K	31.6	26.68	52.40	MgO	3.72	1.86
	Si K	20.06	14.66	42.91	SiO2	2.05	1.025
	Fe K	3.64	1.34	4.68	FeO	0.19	0.095
	O	44.69	57.33			8	4
	Totals	**100.00**	**100.01**	**99.99**			
					Cation sum	5.95	

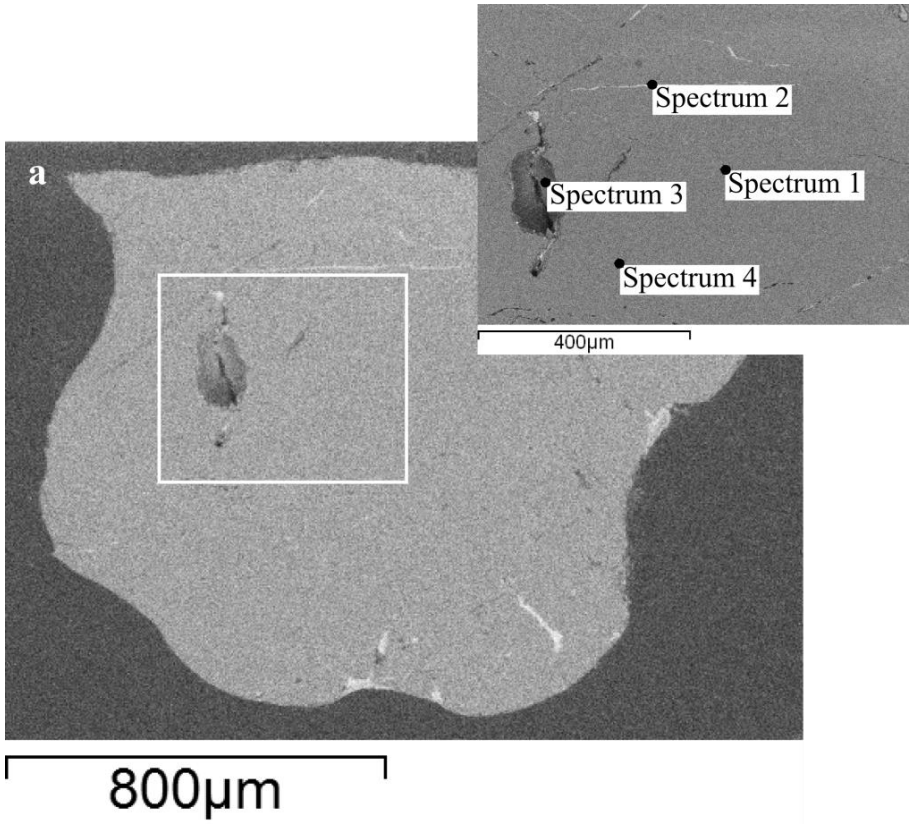

Figure A12 SEM BSE images of the embedded grains of grain colour VI with inserts showing the locations where the point spectra were taken.

Grain type VI is red/brown in colour with a few small opaque inclusions. It is again translucent in regions where the grain is thin. A BSE image (Figure A12) shows the grain is slightly variable with no fractures running through it. SEM EDX data for the grain shows the mineral is quartz, with some Fe present within small vein like features (Table A11). Raman spectroscopy confirms this grain is quartz (Figure A13).

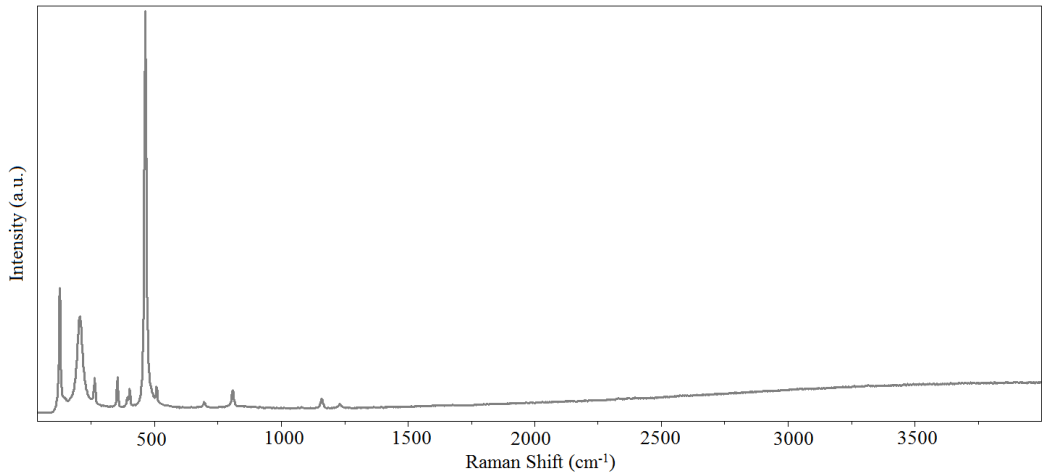

Figure A13 A standard Raman spectrum for grain type VI. The spectrum was taken with a 473 nm laser, 10 % N.D. filter, × 10 objective and 600 g/mm grating.

Table A11 SEM EDX data for grain VIa

	Element	Weight%	Atomic%	Compd%	Formula	Number of ions	
Spectrum 1	Si K	46.74	33.33	100.00	SiO2	4	1
	O	53.26	66.67			8	2
	Totals	**100.00**	**100.00**	**100.00**			
					Cation sum	4	
Spectrum 2	Si K	28.3	24.42	60.55	SiO2	3.14	0.785
	Ca K	0.45	0.27	0.62	CaO	0.03	0.0075
	Fe K	30.18	13.1	38.83	FeO	1.68	0.42
	O	41.07	62.21			8	2
	Totals	**100.00**	**100.00**	**100.0**			
					Cation sum	4.86	
Spectrum 3	Si K	45.55	32.85	97.44	SiO2	3.96	0.99
	Fe K	1.99	0.72	2.56	FeO	0.09	0.0225
	O	52.46	66.43			8	2
	Totals	**100.00**	**100.00**	**100.00**			
					Cation sum	4.04	
Spectrum 4	Si K	46.74	33.33	100.00	SiO2	4	1
	O	53.26	66.67			8	2
	Totals	**100.00**	**100.00**	**100.00**			
					Cation sum	4	

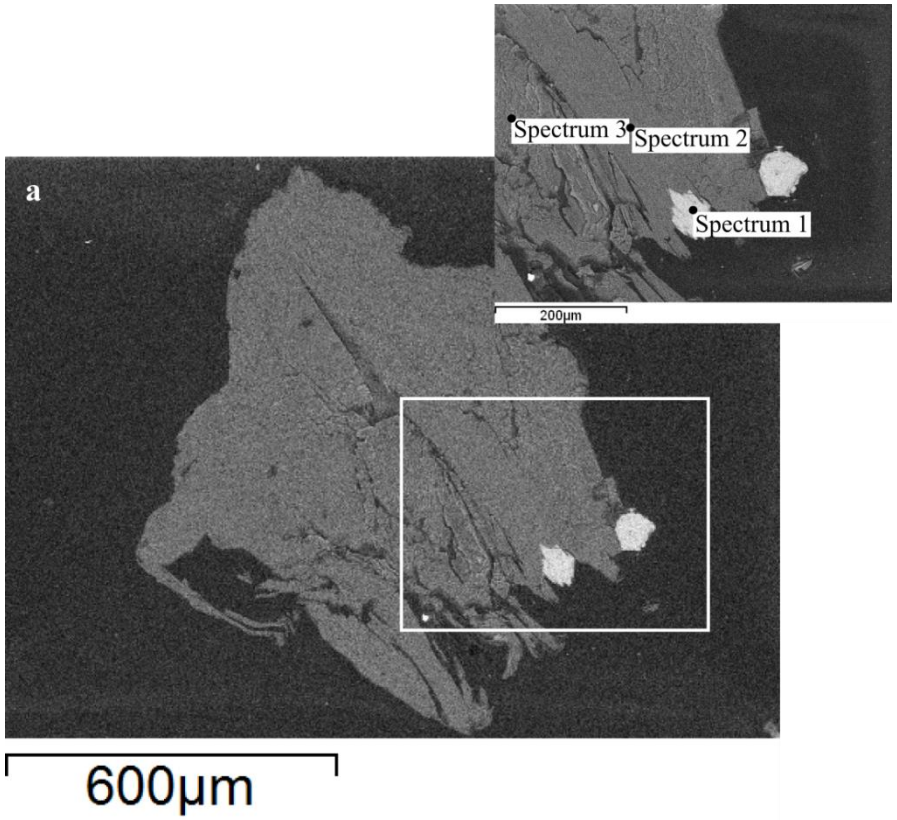

Figure A14 SEM BSE images of the embedded grains of grain colour VII with inserts showing the locations where the point spectra were taken.

Grain type VII has a very light pink-to-lilac colour with two opaque spots. The grain itself seems to be composed of very thin layers (similar to mica). SEM BSE images show that the bulk of this grain appears uniform in composition, although along one edge are two bright features which correspond to opaque spots in the optical images (Figure A14). SEM EDX analyses of this grain show the bulk to be pyroxene in composition, while the bright phases are Cr-rich with Fe-oxide (Table A12). However, Raman spectroscopy of this grain type indicates it could be a pyroxene or amphibole, but it was difficult to obtain a good spectrum (Figure A15).

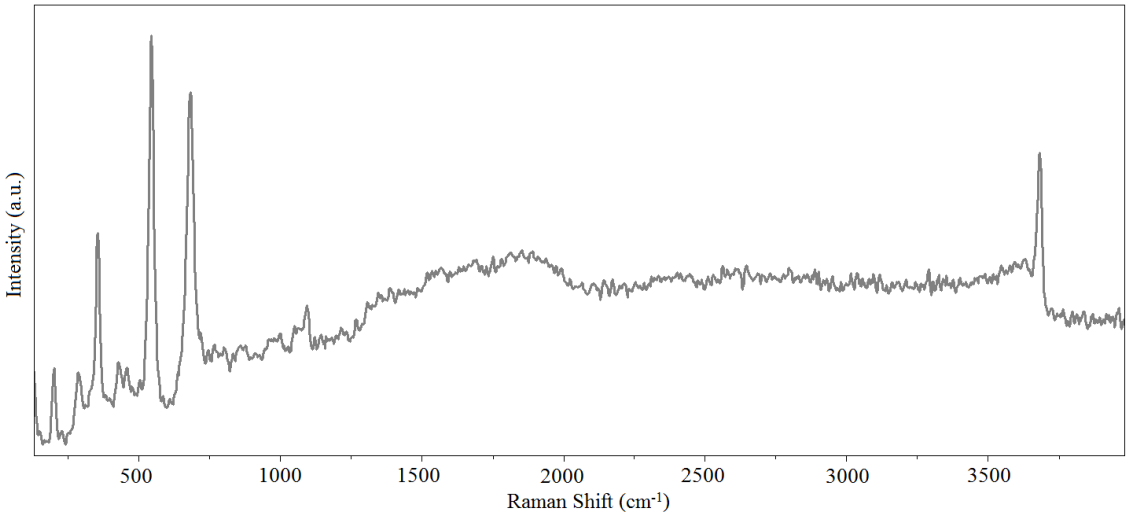

Figure A15 A standard Raman spectrum for grain type VII. The spectrum was taken with a 473 nm laser, 10 % N.D. filter, × 10 objective and 600 g/mm grating.

Table A12 SEM EDX data for grain VIIa

	Element	Weight%	Atomic%	Compd%	Formula	Number of ions	
Spectrum 1	Mg K	3.96	4.87	6.56	MgO	0.69	0.345
	Al K	1.97	2.18	3.71	Al2O3	0.31	0.155
	Si K	0.8	0.85	1.71	SiO2	0.12	0.06
	Cr K	39.89	22.98	58.3	Cr2O3	3.24	1.62
	Fe K	23.1	12.39	29.71	FeO	1.75	0.875
	O	30.29	56.72			8	4
	Totals	**100.00**	**99.99**	**99.99**			
					Cation sum	6.1	
Spectrum 2	Mg K	23.09	19.62	38.28	MgO	2.68	2.01
	Al K	8.17	6.25	15.43	Al2O3	0.85	0.6375
	Si K	18.46	13.58	39.5	SiO2	1.85	1.3875
	Cr K	3.08	1.22	4.5	Cr2O3	0.17	0.1275
	Fe K	1.78	0.66	2.29	FeO	0.09	0.0675

	O	45.42	58.66			8	6
	Totals	**100.00**	**99.99**	**100.00**			
					Cation sum	5.64	
Spectrum 3	Mg K	21.93	18.89	36.37	MgO	2.57	1.9275
	Al K	7.66	5.94	14.46	Al2O3	0.81	0.6075
	Si K	18.18	13.55	38.88	SiO2	1.85	1.3875
	Cr K	4.76	1.92	6.95	Cr2O3	0.26	0.195
	Fe K	2.59	0.97	3.34	FeO	0.13	0.0975
	O	44.89	58.74			8	6
	Totals	**100.00**	**100.01**	**100.00**			
					Cation sum	5.62	

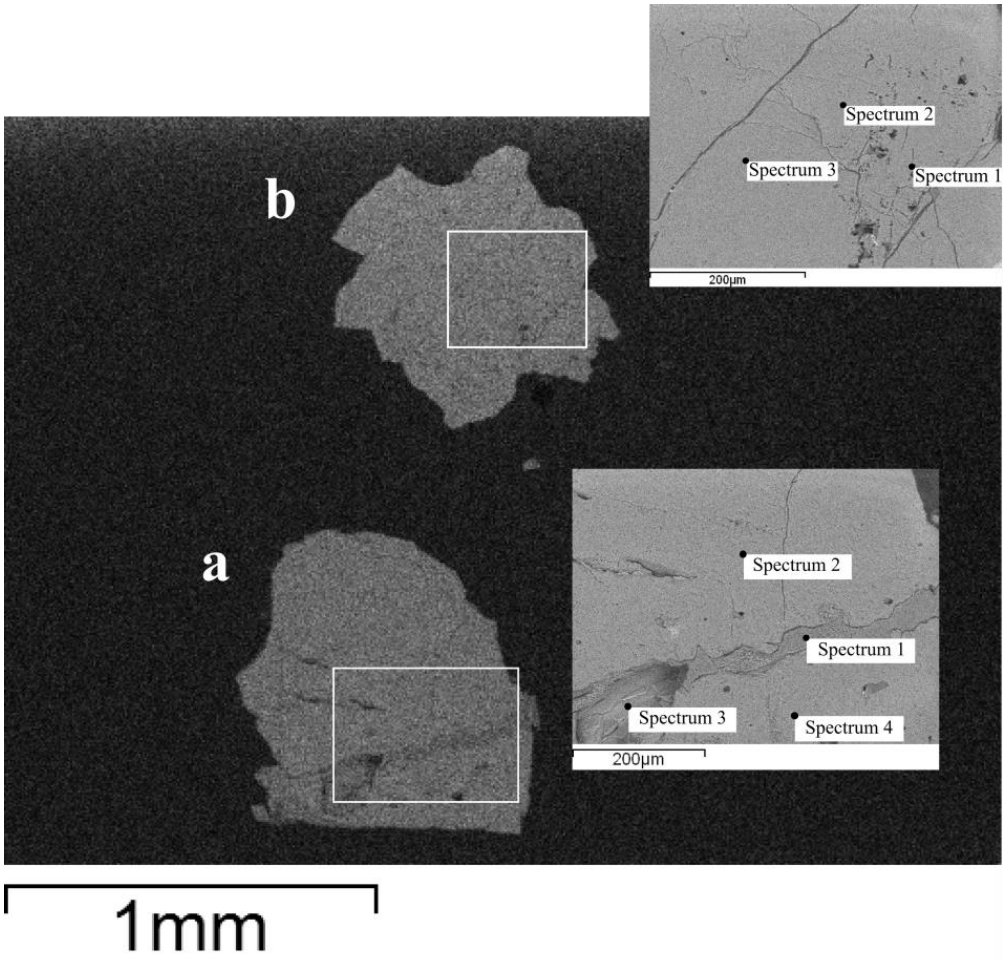

Figure A16 SEM BSE images of the embedded grains of grain type VIII with inserts showing the locations where the point spectra were taken.

Grain type VIII is yellow in colour with small opaque inclusions. BSE images show the grains have some small fractures/cracks and are overall homogenous in composition, with the exception of a vein like structure running through grain a (Figure A16). SEM EDX data shows the grains are Mg rich olivines (Fo_{90}), which Raman spectroscopy confirms

(Figure A17). The vein (found in grain VIIIa) has a similar composition to the main phase, however, spectrum 1 shows a slightly lower Mg content than the remainder of the grain (Tables A13 and A14).

Table A13 SEM EDX data for grain VIIIa

	Element	Weight%	Atomic%	Compd%	Formula	Number of ions	
Spectrum 1	Mg K	20.07	16.66	33.28	MgO	2.18	1.09
	Si K	30.65	22.02	65.58	SiO2	2.89	1.445
	Fe K	0.89	0.32	1.14	FeO	0.04	0.02
	O	48.39	61.01			8	4
	Totals	**100.00**	**100.01**	**100.00**			
					Cation sum	5.11	
Spectrum 2	Mg K	31.43	26.56	52.11	MgO	3.71	1.855
	Si K	20.05	14.67	42.9	SiO2	2.05	1.025
	Fe K	3.88	1.43	4.99	FeO	0.2	0.1
	O	44.64	57.34			8	4
	Totals	**100.00**	**100.00**	**100.00**			
					Cation sum	5.95	
Spectrum 3	Mg K	30.72	26.16	50.93	MgO	3.65	1.825
	Si K	19.82	14.61	42.4	SiO2	2.04	1.02
	Fe K	5.18	1.92	6.67	FeO	0.27	0.135
	O	44.28	57.31			8	4
	Totals	**100.0**	**100.00**	**100.0**			
					Cation sum	5.96	
Spectrum 4	Mg K	31.47	26.58	52.17	MgO	3.71	1.855
	Si K	20.09	14.69	42.97	SiO2	2.05	1.025
	Fe K	3.77	1.39	4.85	FeO	0.19	0.095
	O	44.67	57.34			8	4
	Totals	**100.00**	**100.00**	**99.99**			
					Cation sum	5.95	

Table A14 SEM EDX data for grain VIIIb

	Element	Weight%	Atomic%	Compd%	Formula	Number of ions	
Spectrum 1	Mg K	24.75	24.08	41.04	MgO	3.51	1.755
	Si K	11.63	9.80	24.88	SiO2	1.43	0.715
	Fe K	26.49	11.22	34.08	FeO	1.64	0.82
	O	37.13	54.9			8	4
	Totals	**100.00**	**100.00**	**100.00**			
					Cation sum	6.57	
Spectrum 2	Mg K	30.89	26.19	51.22	MgO	3.65	1.825
	Si K	20.16	14.8	43.13	SiO2	2.06	1.03
	Fe K	4.39	1.62	5.65	FeO	0.23	0.115
	O	44.56	57.40			8	4

	Totals	**100.00**	**100.01**	**100.00**			
					Cation sum	5.94	
Spectrum 3	Mg K	31.17	26.37	51.68	MgO	3.68	1.84
	Si K	20.14	14.75	43.08	SiO2	2.06	1.03
	Fe K	4.08	1.5	5.25	FeO	0.21	0.105
	O	44.62	57.37			8	4
	Totals	**100.00**	**99.99**	**100.01**			
					Cation sum	5.94	

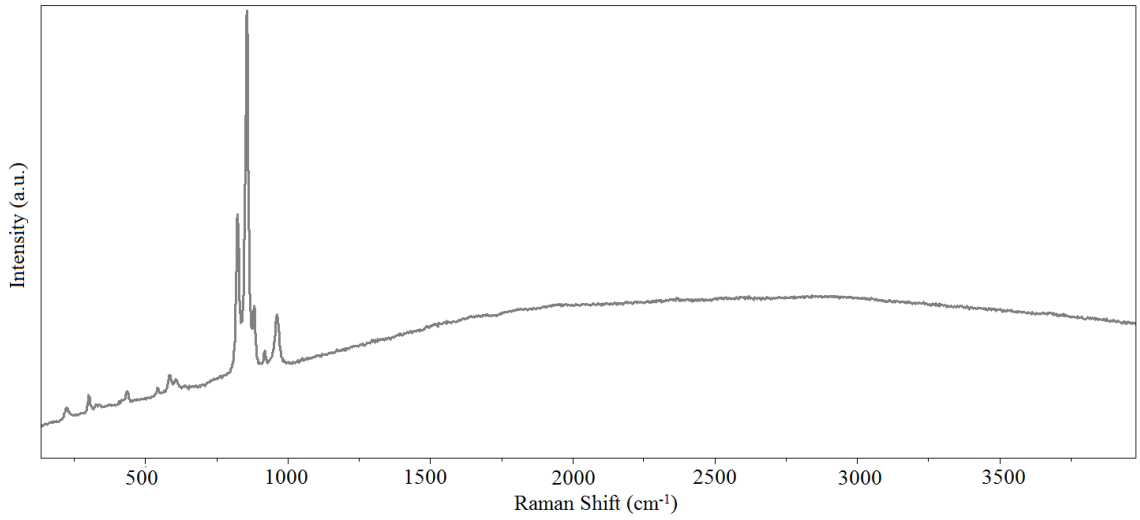

Figure A17 A standard Raman spectrum for grain type VIII. The spectrum was taken with a 473 nm laser, 10 % N.D. filter, × 10 objective and 600 g/mm grating.

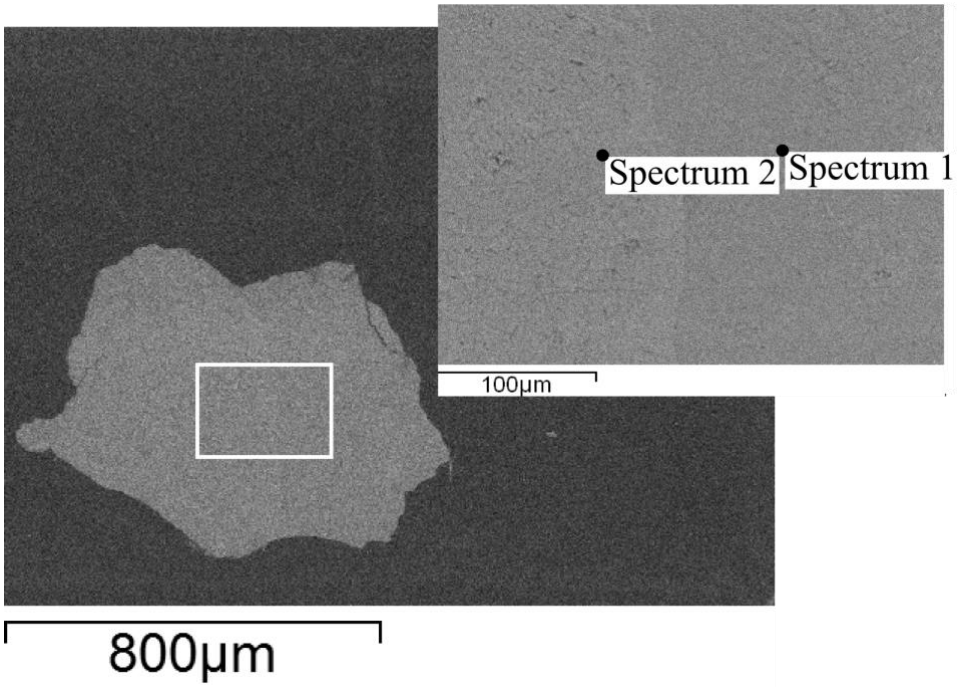

Figure A18 SEM BSE images of the embedded grains of grain type IX with inserts showing the locations where the point spectra were taken (see Table 5.1.1 for general SEM EDX data).

Grain type IX exhibit two distinct colours: one half is green and the other half is yellow (similar to grain type VIII). The SEM BSE images also show the presence of two different phases, with one side slightly lighter in colour than the other (Figure A18), SEM EDX results (Table A15) indicate these two phases may be pyroxene with one phase having traces of Cr and K. Raman spectra for this grain is similar to grain type VII, indicating that it could be a pyroxene or amphibole (Figure A19). However, spectra were very fluorescent which made it difficult to obtain good spectrum.

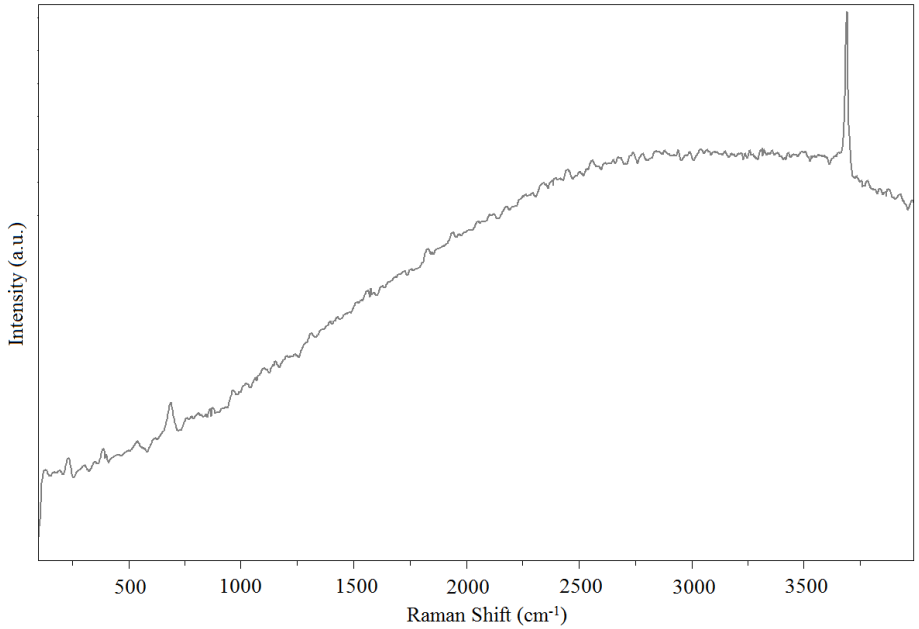

Figure A19 A standard Raman spectrum for grain type IX. The spectrum was taken with a 473 nm laser, 10 % N.D. filter, × 10 objective and 600 g/mm grating.

Table A15 SEM EDX data for grain IX.

	Element	**Weight%**	**Atomic%**	**Compd%**	**Formula**	**Number of ions**	
Spectrum 1	Mg K	26.97	22.80	44.72	MgO	3.12	2.34
	Al K	0.61	0.46	1.15	Al2O3	0.06	0.045
	Si K	22.94	16.78	49.07	SiO2	2.29	1.7175
	Fe K	3.93	1.45	5.06	FeO	0.2	0.15
	O	45.55	58.51			8	6
	Totals	**100.00**	**100.00**	**100.00**			
					Cation sum	**5.67**	
Spectrum 2	Mg K	24.25	20.86	40.21	MgO	2.86	2.145
	Al K	2.59	2.01	4.89	Al2O3	0.28	0.21
	Si K	21.45	15.97	45.88	SiO2	2.19	1.6425
	K K	0.74	0.40	0.90	K2O	0.05	0.0375
	Cr K	0.17	0.07	0.25	Cr2O3	0.01	0.0075
	Fe K	6.12	2.29	7.87	FeO	0.31	0.2325
	O	44.68	58.40			8	6
	Totals	**100.00**	**100.00**	**100.00**			
					Cation sum	**5.7**	

Appendix B - EDX Data for Devolatilisation Minerals

Table B1 SEM EDX data for goethite sample.

Area 1							
	Element	Weight%	Atomic%	Compd%	Formula	Number of ions	
Spectrum 1	Si K	1.07	1.75	2.29	SiO2	0.23	0.06
	Fe K	46.04	37.89	65.83	Fe2O3	5.02	1.26
	O	21.01	60.35			8.00	2.00
	Totals	**68.12**	**99.99**	**68.12**			
					Cation sum	**5.26**	
Spectrum 2	Si K	2.13	3.36	4.55	SiO2	0.44	0.11
	Fe K	45.28	35.96	64.73	Fe2O3	4.74	1.19
	O	21.88	60.67			8.00	2.00
	Totals	**69.29**	**99.99**	**69.28**			
					Cation sum	**5.19**	
Spectrum 3	Si K	1.55	2.49	3.32	SiO2	0.33	0.08
	Fe K	45.92	37.02	65.65	Fe2O3	4.90	1.23
	O	21.5	60.50			8.00	2.00
	Totals	**68.97**	**100.01**	**68.97**			
					Cation sum	**5.22**	
Spectrum 4	Si K	0.78	1.32	1.67	SiO2	0.18	0.05
	Fe K	45.01	38.41	64.35	Fe2O3	5.10	1.28
	O	20.23	60.26			8.00	2.00
	Totals	**66.02**	**99.99**	**66.02**			
					Cation sum	**5.27**	
Area 2							
	Element	Weight%	Atomic%	Compd%	Formula	Number of ions	
Spectrum 1	Si K	0.79	1.36	1.70	SiO2	0.18	0.05
	Fe K	44.60	38.37	63.77	Fe2O3	5.09	1.27
	O	20.07	60.27			8.00	2.00
	Totals	**65.47**	**100.00**	**65.47**			
					Cation sum	**5.27**	
Spectrum 2	Si K	0.64	1.12	1.38	SiO2	0.15	0.04
	Fe K	44.32	38.66	63.36	Fe2O3	5.14	1.28
	O	19.78	60.22			8.00	2.00
	Totals	**64.74**	**100.00**	**64.03**			
Spectrum 3	Si K	0.59	1.03	1.26	SiO2	0.14	0.04
	Fe K	43.91	38.76	62.77	Fe2O3	5.15	1.29
	O	19.54	60.21			8.00	2.00
	Totals	**64.03**	**100.00**	**64.03**			
					Cation sum	**5.29**	

Spectrum 4	Si K	0.76	1.3	1.63	SiO2	0.17	0.04
	Fe K	45.05	38.45	64.41	Fe2O3	5.10	1.28
	O	20.23	60.26			8.00	2.00
	Totals	**66.04**	**100.01**	**66.04**			
					Cation sum	**5.28**	

Table B2 SEM/EDX data for natural gypsum**.**

Area 1							
	Element	Weight%	Atomic%	Compd%	Formula	Number of ions	
Spectrum 1	S K	12.82	16.43	32.00	SO3	1.98	1.49
	Ca K	16.71	17.14	23.38	CaO	2.06	1.55
	O	25.85	66.43			8.00	6.00
	Totals	**55.38**	**100.00**	**55.38**			
					Cation sum	**4.04**	
Spectrum 2	S K	13.09	16.7	32.68	SO3	2.00	1.50
	Ca K	16.27	16.61	22.77	CaO	1.99	1.49
	O	26.09	66.7			8.00	6.00
	Totals	**55.45**	**100.01**	**55.45**			
					Cation sum	**3.99**	
Spectrum 3	S K	12.69	16.65	31.68	SO3	2.00	1.50
	Ca K	15.90	16.69	22.25	CaO	2.00	1.50
	O	25.34	66.65			8.00	6.00
	Totals	**53.93**	**99.99**	**53.93**			
					Cation sum	**4**	
Spectrum 4	S K	12.85	16.57	32.09	SO3	1.99	1.49
	Ca K	16.36	16.87	22.88	CaO	2.03	1.52
	O	25.77	66.57			8.00	6.00
	Totals	**54.98**	**100.01**	**54.97**			
					Cation sum	**4.02**	
Area 2							
	Element	Weight%	Atomic%	Compd%	Formula	Number of ions	
Spectrum 1	S K	13.07	16.55	32.65	SO3	1.99	1.49
	Ca K	16.70	16.91	23.36	CaO	2.03	1.52
	O	26.24	66.55			8.00	6.00
	Totals	**56.01**	**100.01**	**56.01**			
					Cation sum	**4.02**	
Spectrum 2	S K	12.78	16.62	31.92	SO3	2.00	1.50
	Ca K	16.12	16.77	22.56	CaO	2.01	1.5075
	O	25.57	66.62			8.00	6.00
	Totals	**54.48**	**100.01**	**54.48**			
					Cation sum	**4.01**	
Spectrum 3	S K	12.51	16.56	31.23	SO3	1.99	1.4925
	Ca K	15.94	16.88	22.30	CaO	2.03	1.5225

	O	25.09	66.56			8.00	6.00
	Totals	**53.53**	**100.00**	**53.53**			
					Cation sum	**4.02**	
Spectrum 4	S K	12.70	16.36	31.71	SO3	1.97	1.4775
	Ca K	16.76	17.28	23.45	CaO	2.08	1.56
	O	25.70	66.36			8.00	6.00
	Totals	**55.16**	**100.00**	**55.16**			
					Cation sum	**4.06**	

Appendix C - Raman Tests on Devolatilisation Materials

PoP Drying Test

Table C1 Peak position from Raman spectra of PoP drying test samples

	Material	Spectrum	Peak position (cm^{-1})					
			U1 (1)	U2 (1)	U2 (2)	U3 (1)	U4 (1)	U4 (2)
Before	Table	1	1009.72	414.83	493.71	1136.67	620.83	671.67
	Foil	1	1009.72	414.83	493.71	1136.67	620.83	671.67
	Paper	1	1009.72	414.83	495.95	1136.67	620.83	671.67
	Glass	1	1009.72	414.83	495.95	1136.67	620.83	671.67
	Plastic	1	1009.72	414.83	495.95	1138.77	620.83	671.67
After*	Table	1	1011.67	416.91	495.76	1138.59	620.64	673.69
		2	1011.67	416.91	495.76	1138.59	620.64	673.69
		3	1011.67	416.91	495.76	1138.59	620.64	673.69
	Foil	1	1011.67	416.91	495.76	1138.59	620.64	673.69
		2	1011.67	416.91	495.76	1138.59	622.86	673.69
		3	1011.67	416.91	495.76	1138.59	622.86	673.69
	Paper	1	1011.67	416.91	495.76	1138.59	622.86	673.69
		2	1011.67	416.91	495.76	1138.59	622.86	673.69
		3	1011.67	416.91	495.76	1138.59	622.86	673.69
	Glass	1	1011.67	416.91	495.76	1138.59	622.86	673.69
		2	1011.67	416.91	495.76	1138.59	622.86	673.69
		3	1011.67	416.91	495.76	1138.59	622.86	673.69
	Plastic	1	1011.67	416.91	495.76	1138.59	622.86	673.69
		2	1011.67	416.91	495.76	1138.59	622.86	673.69
		3	1011.67	416.91	495.76	1138.59	622.86	673.69

*After spectra taken one week after making of the samples.

Raman damage tables

Table C2 Time exposure Raman damage test on goethite grains.

Sample	Objective	N.D. filter (%)	Total exposure time (mins)	Grating	Peak position (cm^{-1})
1	50	10	0	600	388.0
1	50	10	3	600	388.0
1	50	10	6	600	388.0
1	50	10	9	600	388.0
1	50	10	12	600	388.0
1	50	10	15	600	388.0
2	50	25	0	600	389.2
2	50	25	3	600	389.2
2	50	25	6	600	389.2
2	50	25	9	600	389.2
2	50	25	12	600	389.2
2	50	25	15	600	389.2
3	50	10	0	1800	388.84
3	50	10	3	1800	388.8
3	50	10	6	1800	388.8
3	50	10	9	1800	388.8
3	50	10	12	1800	388.5
3	50	10	15	1800	388.5
4	50	25	0	1800	387.6
4	50	25	3	1800	387.9
4	50	25	6	1800	387.9
4	50	25	9	1800	387.9
4	50	25	12	1800	387.9
4	50	25	15	1800	387.9

N.B. All spectra were taken using the 633 mn laser.

Table C3 Time exposure Raman damage test on natural gypsum grains.

Sample	Objective	N.D. filter (%)	Total exposure time (mins)	Peak position (cm^{-1})		
				Ʊ1	Ʊ2 (1)	Ʊ2 (2)
1	10	10	0	1008.2	414.7	493.7
1	10	10	3	1008.2	414.2	493.7
1	10	10	6	1008.2	414.7	493.7
1	10	10	9	1008.2	414.2	493.2
1	10	10	12	1007.7	414.2	493.2
1	10	10	15	1007.7	414.2	493.2
2	10	10	0	1088.2	414.7	493.7
2	10	25	3	1008.2	414.7	493.7
2	10	25	6	1008.2	414.7	493.7
2	10	25	9	1008.2	414.7	493.7
2	10	25	12	1008.2	414.7	493.7
2	10	25	15	1008.2	414.7	493.7
3	10	10	0	1007.7	414.7	493.8
3	10	50	3	1008.2	414.7	493.8
3	10	50	6	1008.2	141.7	493.8
3	10	50	9	1008.2	414.7	493.8
3	10	50	12	1008.2	414.7	493.8
3	10	50	15	1008.2	414.7	493.8
4	50	10	0	1008.2	414.7	494.2
4	50	10	3	1008.2	414.7	494.2
4	50	10	6	1008.2	414.7	494.2
4	50	10	9	1008.2	414.7	494.2
4	50	10	12	1008.2	414.7	494.2
4	50	10	15	1008.2	414.7	494.2
5	50	10	0	1008.7	414.7	493.7
5	50	25	3	1008.7	414.7	493.7
5	50	25	6	1008.7	414.7	493.7
5	50	25	9	1008.7	414.7	493.7
5	50	25	12	1008.7	414.7	493.7
5	50	25	15	1008.7	414.7	493.7

N.B. All spectra were taken using the following parameters: 532nm lasers, 10% N.D. filter, 1800 g/mm, a 2 sec exposure and 10 accumulations.

Table C4 Time exposure Raman damage test on PoP gypsum grains

Sample	Objective	N.D. filter (%)	Total exposure time (mins)	Peak position (cm^{-1})		
				υ1	υ2 (1)	υ2 (2)
1	10	10	0	1008.6	415.2	494.7
1	10	10	3	1008.6	415.2	494.7
1	10	10	6	1008.6	415.2	494.7
1	10	10	9	1008.6	415.2	494.7
1	10	10	12	1008.6	415.2	494.7
1	10	10	15	1009.1	415.2	494.7
2	50	10	0	1009.1	415.7	494.7
2	50	10	3	1009.1	415.7	494.7
2	50	10	6	1009.1	415.7	494.7
2	50	10	9	1009.1	415.7	494.7
2	50	10	12	1009.1	415.2	494.7
2	50	10	15	1009.1	415.2	494.7
3	50	25	0	1009.1	415.7	494.6
3	50	25	3	1009.1	415.7	495.1
3	50	25	6	1009.6	415.7	495.1
3	50	25	9	1009.6	415.7	495.1
3	50	25	12	1009.6	415.7	495.1
3	50	25	15	1009.6	415.7	495.1
4	50	50	0	1009.6	415.7	495.6
4	50	50	3	1009.6	415.7	495.6
4	50	50	6	1009.6	415.7	495.6
4	50	50	9	1009.6	415.7	495.1
4	50	50	12	1009.6	416.2	495.1
4	50	50	15	1009.6	416.2	495.1

N.B. All spectra were taken using the following parameters: 532nm lasers, 10% N.D. filter, 1800 g/mm, a 2 sec exposure and 10 accumulations.

Appendix D - Baseline Correction Test

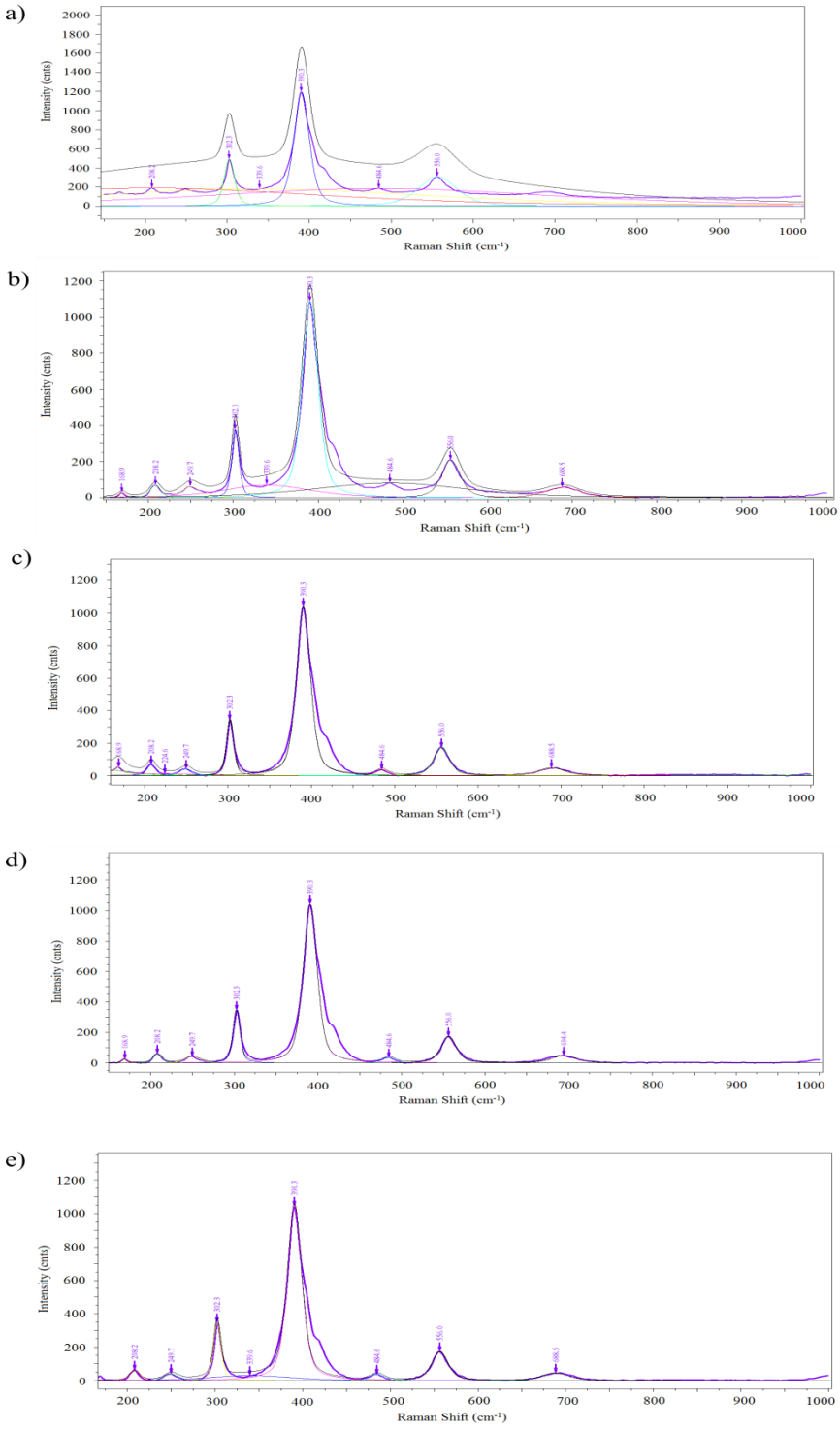

Figure D1 Raman spectra of goethite showing the peak fits to different baseline corrections: a) no baseline correction, b) 2nd degree polynomial baseline correction, c) 4th degree polynomial baseline correction, d) 6th degree polynomial baseline correction and e) 8th degree polynomial baseline correction. These spectra show that broad peaks are fitted to relatively lower intensity peaks when no baseline correction is used and when using a 2nd degree polynomial. 6th and 8th degree polynomials provide a much better peak fit to the Raman spectrum (purple).

Appendix E - Goethite Feature A Formation

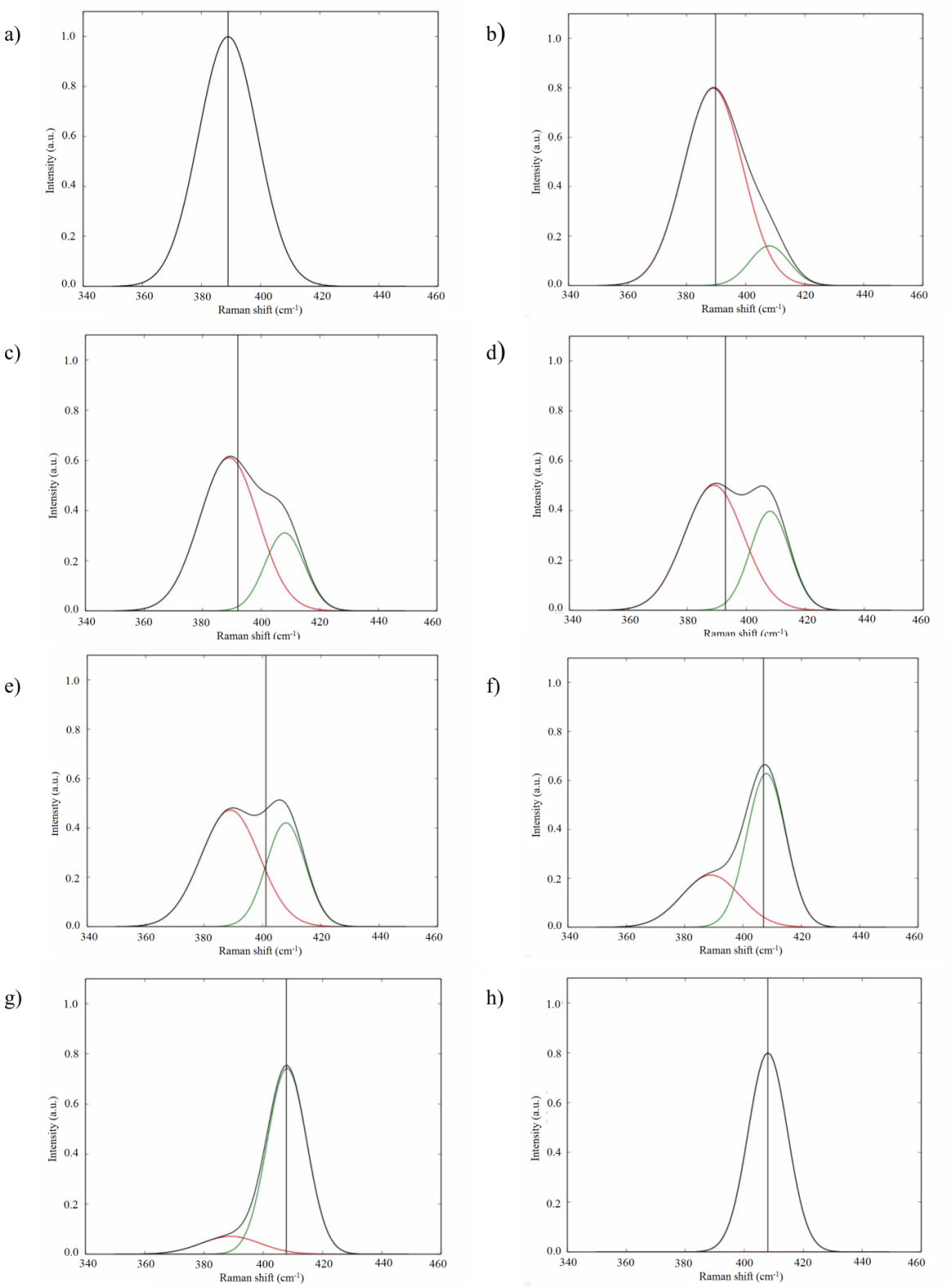

Figure E1 Plots (a-h) demonstrating the overall change in Raman spectrum (black line) as the Fe-OH peak (red) becomes less intense, as water is lost, and the increasing intensity of the Fe-O peak (green). The black vertical line indicates the apparent peak position of the feature.

Feature is believed to be made up of two peaks Fe-OH and Fe-O, but in some Raman spectra it appears as a single peak with a shoulder. As the sample dehydrates the Fe-OH peak becomes less intense, causing the overall feature to change and makes the overall peak position appear to change. Figure D1 shows how the Raman spectrum of this feature alters as the peak intensities of the Fe-OH and Fe-O peak change. A goethite spectrum normally has a dominant Fe-OH peak (Figure D1a), but as water is lost the intensity if this peak decreases and it is believed that the Fe-O peak begins to increase (Figure D1b and D1c). Eventually the two peaks have a similar intensity and at some point the dominant the peak changes from the Fe-OH peak to the Fe-O peak (Figure D1d to D1e). The intensity of the Fe-O peak continues to increase until the sample is dehydrated, leaving only the Fe-O peak in hematite Raman spectrum (Figure Df to Dh). The black line in Figure D1 shows the peak position of the overall Raman spectrum for this feature. As you can see, the peak position of the overall spectrum appears to increase as the sample changes from goethite to hematite. Figure D2 shows the change peak position and peak width (taken at the FWHM) for the overall Raman spectrum as it transitions from goethite to hematite. It shows that there is a region between ~395 and ~ 401 cm^{-1} (in this instance) where no data points are present. This "empty" region represents the change in dominant peak from Fe-OH to Fe-O, and peak positions after this jump would be associated more hematite Raman spectrum. The plots in Figures D1 and D2 represent an ideal model and so, the peak positions in reality may be slightly different.

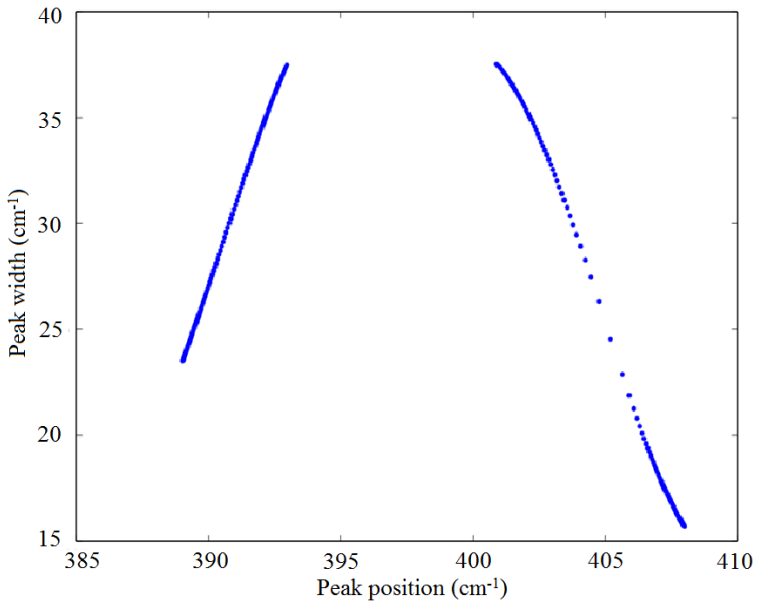

Figure E2 Peak position and peak width of the Raman spectrum as then the spectrum changes from goethite to hematite (from Figure D1).

Appendix F - Heating Experiments

Table F1 Raman data for Feature A and Feature B from goethite ex-situ heating experiment.

Temperature (˚C)	Spectrum	Classification*	Feature A		Feature B					
			Peak 1		Peak 1			Peak 2		
			Peak Position (cm^{-1})	Peak Width (cm^{-1})	Peak Position (cm^{-1})	Peak Intensity (cnts)	Peak Width (cm^{-1})	Peak Position (cm^{-1})	Peak Intensity (cnts)	Peak Width (cm^{-1})
22	1	G	389.4	25.0	-	-	-	-	-	-
	2	G	388.1	18.0	-	-	-	-	-	-
	3	G	388.7	21.2	-	-	-	-	-	-
	4	G	387.8	18.0	-	-	-	-	-	-
	5	G	388.1	18.6	-	-	-	-	-	-
	6	G	388.7	20.5	-	-	-	-	-	-
	7	G	400.3	17.3	-	-	-	-	-	-
	8	G	387.4	16.7	-	-	-	-	-	-
	9	G	388.4	19.3	-	-	-	-	-	-
	10	G	390.1	23.8	-	-	-	-	-	-
100	1	G	387.5	16.7	-	-	-	-	-	-
	2	G	388.8	23.1	-	-	-	-	-	-
	3	G	388.2	21.2	-	-	-	-	-	-
	4	G	387.9	16.7	-	-	-	-	-	-
	5	G	387.9	18.0	-	-	-	-	-	-
	6	G	388.5	21.2	-	-	-	-	-	-
	7	G	388.2	22.5	-	-	-	-	-	-
	8	G	389.1	22.5	-	-	-	-	-	-
	9	G	387.9	18.6	-	-	-	-	-	-
	10	G	388.8	19.3	-	-	-	-	-	-
110	1	G	388.2	17.3	-	-	-	-	-	-
	2	G	388.2	17.3	-	-	-	-	-	-
	3	G	388.2	21.2	-	-	-	-	-	-
	4	G	389.2	22.5	-	-	-	-	-	-
	5	G	388.8	23.1	-	-	-	-	-	-
	6	G	387.9	17.3	-	-	-	-	-	-
	7	G	389.2	24.4	-	-	-	-	-	-
	8	I	393.7	34.0	-	-	-	-	-	-
	9	G	389.5	23.8	-	-	-	-	-	-
	10	G	399.1	29.4	-	-	-	-	-	-
120	1	G	388.5	22.5	-	-	-	-	-	-
	2	G	400.3	13.4	-	-	-	-	-	-
	3	G	388.8	21.2	-	-	-	-	-	-
	4	G	387.8	17.3	-	-	-	-	-	-
	5	G	388.5	18.6	-	-	-	-	-	-
	6	G	388.5	18.0	-	-	-	-	-	-
	7	G	388.8	23.8	-	-	-	-	-	-
	8	G	389.1	23.1	-	-	-	-	-	-

	9	G	389.1	23.1	-	-	-	-	-	-
	10	G	388.5	18.0	-	-	-	-	-	-
130	1	G	388.5	23.1	-	-	-	-	-	-
	2	G	388.8	21.2	-	-	-	-	-	-
	3	G	389.7	24.4	-	-	-	-	-	-
	4	G	389.7	23.8	-	-	-	-	-	-
	5	G	389.1	24.4	-	-	-	-	-	-
	6	G	388.1	18.0	-	-	-	-	-	-
	7	G	387.8	18.0	-	-	-	-	-	-
	8	G	387.8	17.3	-	-	-	-	-	-
	9	G	388.5	18.6	-	-	-	-	-	-
	10	G	388.5	19.9	-	-	-	-	-	-
140	1	G	390.1	24.4	-	-	-	-	-	-
	2	G	387.8	18.6	-	-	-	-	-	-
	3	G	390.1	27.0	-	-	-	-	-	-
	4	G	388.8	22.5	-	-	-	-	-	-
	5	G	390.1	23.1	-	-	-	-	-	-
	6	G	388.1	18.0	-	-	-	-	-	-
	7	G	388.1	18.0	-	-	-	-	-	-
	8	G	388.1	18.6	-	-	-	-	-	-
	9	G	390.1	25.7	-	-	-	-	-	-
	10	G	389.1	27.6	-	-	-	-	-	-
150	1	G	389.1	23.8	-	-	-	-	-	-
	2	G	388.4	19.3	-	-	-	-	-	-
	3	G	389.4	25.7	-	-	-	-	-	-
	4	G	388.1	20.5	-	-	-	-	-	-
	5	G	387.8	21.8	-	-	-	-	-	-
	6	G	388.8	23.8	-	-	-	-	-	-
	7	G	389.7	23.8	-	-	-	-	-	-
	8	G	389.1	25.7	-	-	-	-	-	-
	9	G	389.4	24.4	-	-	-	-	-	-
	10	G	388.4	20.5	-	-	-	-	-	-
160	1	G	389.1	23.1	-	-	-	-	-	-
	2	G	388.8	21.2	-	-	-	-	-	-
	3	G	390.7	25.7	-	-	-	-	-	-
	4	G	400.0	17.3	-	-	-	-	-	-
	5	G	387.8	18.0	-	-	-	-	-	-
	6	G	388.8	21.8	-	-	-	-	-	-
	7	G	389.4	19.9	-	-	-	-	-	-
	8	G	388.8	21.8	-	-	-	-	-	-
	9	G	388.8	25.0	-	-	-	-	-	-
	10	G	389.4	22.5	-	-	-	-	-	-
170	1	G	388.8	22.5	-	-	-	-	-	-
	2	G	387.8	20.5	-	-	-	-	-	-
	3	G	388.1	19.3	-	-	-	-	-	-
	4	G	389.7	24.4	-	-	-	-	-	-
	5	G	388.8	23.1	-	-	-	-	-	-
	6	G	389.1	25.0	-	-	-	-	-	-

	7	G	389.1	21.8	-	-	-	-	-	-
	8	G	389.1	21.8	-	-	-	-	-	-
	9	G	392.3	31.5	-	-	-	-	-	-
	10	G	388.4	22.5	-	-	-	-	-	-
180	1	G	388.8	23.8	-	-	-	-	-	-
	2	G	389.8	25.7	-	-	-	-	-	-
	3	G	388.5	18.6	-	-	-	-	-	-
	4	G	388.5	23.1	-	-	-	-	-	-
	5	G	388.5	19.9	-	-	-	-	-	-
	6	G	388.8	23.1	-	-	-	-	-	-
	7	G	389.8	24.4	-	-	-	-	-	-
	8	G	388.2	18.6	-	-	-	-	-	-
	9	G	389.4	24.4	-	-	-	-	-	-
	10	I	387.2	16.1	-	-	-	-	-	-
190	1	G	387.8	22.5	-	-	-	-	-	-
	2	G	389.1	23.8	-	-	-	-	-	-
	3	G	388.5	23.8	-	-	-	-	-	-
	4	G	389.1	24.4	-	-	-	-	-	-
	5	G	388.5	22.5	-	-	-	-	-	-
	6	G	387.8	18.6	-	-	-	-	-	-
	7	G	391.0	30.8	-	-	-	-	-	-
	8	G	388.5	21.8	-	-	-	-	-	-
	9	G	389.1	19.3	-	-	-	-	-	-
	10	G	388.8	23.8	-	-	-	-	-	-
200	1	G	388.5	21.8	-	-	-	-	-	-
	2	G	388.5	17.3	-	-	-	-	-	-
	3	G	388.8	21.2	-	-	-	-	-	-
	4	G	388.8	23.8	-	-	-	-	-	-
	5	G	387.8	18.0	-	-	-	-	-	-
	6	G	388.5	20.5	-	-	-	-	-	-
	7	G	389.4	27.0	-	-	-	-	-	-
	8	G	387.8	20.5	-	-	-	-	-	-
	9	G	389.4	23.8	-	-	-	-	-	-
	10	G	388.5	21.2	-	-	-	-	-	-
210	1	G	388.8	21.8	-	-	-	-	-	-
	2	G	389.7	22.5	-	-	-	-	-	-
	3	G	389.4	26.3	-	-	-	-	-	-
	4	G	389.1	22.5	-	-	-	-	-	-
	5	G	389.7	21.2	-	-	-	-	-	-
	6	G	388.8	23.1	-	-	-	-	-	-
	7	G	387.2	21.8	-	-	-	-	-	-
	8	G	388.5	22.5	-	-	-	-	-	-
	9	G	388.1	19.3	-	-	-	-	-	-
	10	G	388.1	22.5	-	-	-	-	-	-
220	1	G	389.1	23.1	-	-	-	-	-	-
	2	G	387.8	20.5	-	-	-	-	-	-
	3	G	387.2	18.6	-	-	-	-	-	-
	4	G	390.1	25.7	-	-	-	-	-	-

	5	G	400.9	12.1	-	-	-	-	-	-
	6	G	389.1	23.8	-	-	-	-	-	-
	7	G	388.8	23.1	-	-	-	-	-	-
	8	G	389.1	23.8	-	-	-	-	-	-
	9	G	388.8	21.8	-	-	-	-	-	-
	10	G	389.1	25.0	-	-	-	-	-	-
230	1	G	389.1	21.8	-	-	-	-	-	-
	2	G	388.2	22.5	-	-	-	-	-	-
	3	G	387.5	20.6	-	-	-	-	-	-
	4	G	388.5	20.5	-	-	-	-	-	-
	5	G	389.1	22.5	-	-	-	-	-	-
	6	G	389.1	23.8	-	-	-	-	-	-
	7	G	388.5	23.1	-	-	-	-	-	-
	8	G	389.1	22.5	-	-	-	-	-	-
	9	G	388.5	21.8	-	-	-	-	-	-
	10	G	388.2	17.3	-	-	-	-	-	-
240	1	G	388.1	18.0	-	-	-	-	-	-
	2	G	388.8	24.4	-	-	-	-	-	-
	3	G	389.4	24.4	-	-	-	-	-	-
	4	G	392.0	29.4	-	-	-	-	-	-
	5	G	389.1	22.5	-	-	-	-	-	-
	6	G	388.4	22.5	-	-	-	-	-	-
	7	G	389.4	22.5	-	-	-	-	-	-
	8	I	387.8	16.7	-	-	-	-	-	-
	9	G	388.1	19.9	-	-	-	-	-	-
	10	G	388.4	22.5	-	-	-	-	-	-
250	1	G	392.3	28.2	-	-	-	-	-	-
	2	G	389.4	22.5	-	-	-	-	-	-
	3	G	388.8	23.1	-	-	-	-	-	-
	4	G	393.3	32.1	-	-	-	-	-	-
	5	G	390.1	25.7	-	-	-	-	-	-
	6	G	389.1	21.8	-	-	-	-	-	-
	7	G	387.8	18.6	-	-	-	-	-	-
	8	G	388.8	21.8	-	-	-	-	-	-
	9	G	389.8	19.9	-	-	-	-	-	-
	10	G	388.8	21.2	-	-	-	-	-	-
260	1	I	388.1	18.6	-	-	-	-	-	-
	2	I	389.4	19.3	-	-	-	-	-	-
	3	G	388.1	22.5	-	-	-	-	-	-
	4	G	390.4	27.6	-	-	-	-	-	-
	5	G	388.5	23.1	-	-	-	-	-	-
	6	G	389.1	22.5	-	-	-	-	-	-
	7	G	391.4	29.5	-	-	-	-	-	-
	8	G	389.1	21.8	-	-	-	-	-	-
	9	I	388.8	22.5	-	-	-	-	-	-
	10	G	388.8	21.2	-	-	-	-	-	-
270	1	G	388.8	24.4	-	-	-	-	-	-
	2	G	388.8	24.4	-	-	-	-	-	-

	3	G	388.8	22.5	-	-	-	-	-	-
	4	G	389.8	21.8	-	-	-	-	-	-
	5	G	388.5	19.3	-	-	-	-	-	-
	6	G	387.8	21.2	-	-	-	-	-	-
	7	G	389.1	21.8	-	-	-	-	-	-
	8	G	388.2	19.9	-	-	-	-	-	-
	9	G	388.5	20.5	-	-	-	-	-	-
	10	G	388.2	18.6	-	-	-	-	-	-
280	1	G	388.1	19.9	-	-	-	-	-	-
	2	G	389.4	22.5	-	-	-	-	-	-
	3	G	388.8	23.1	-	-	-	-	-	-
	4	G	387.8	25.1	-	-	-	-	-	-
	5	G	389.7	23.1	-	-	-	-	-	-
	6	G	388.8	19.9	-	-	-	-	-	-
	7	G	388.5	22.5	-	-	-	-	-	-
	8	I	389.7	21.2	-	-	-	-	-	-
	9	G	388.5	18.0	-	-	-	-	-	-
	10	G	388.5	18.0	-	-	-	-	-	-
290	1	G	389.1	25.0	-	-	-	-	-	-
	2	G	388.8	21.8	-	-	-	-	-	-
	3	G	388.8	23.8	-	-	-	-	-	-
	4	G	388.8	23.1	-	-	-	-	-	-
	5	G	389.4	24.4	-	-	-	-	-	-
	6	G	389.4	22.5	-	-	-	-	-	-
	7	G	388.5	21.2	-	-	-	-	-	-
	8	G	389.1	21.2	-	-	-	-	-	-
	9	G	388.5	19.9	-	-	-	-	-	-
	10	G	388.5	19.9	-	-	-	-	-	-
300	1	G	389.1	22.5	-	-	-	-	-	-
	2	G	388.8	26.3	-	-	-	-	-	-
	3	G	388.5	22.5	-	-	-	-	-	-
	4	G	389.4	19.3	-	-	-	-	-	-
	5	I	391.0	32.1	-	-	-	-	-	-
	6	G	388.5	21.2	-	-	-	-	-	-
	7	G	389.7	25.7	-	-	-	-	-	-
	8	G	389.4	21.8	-	-	-	-	-	-
	9	G	388.1	20.5	-	-	-	-	-	-
	10	G	388.1	17.3	-	-	-	-	-	-
310	1	I	389.1	22.5	-	-	-	-	-	-
	2	G	388.2	20.6	-	-	-	-	-	-
	3	I	391.4	25.7	-	-	-	-	-	-
	4	I	388.5	23.1	-	-	-	-	-	-
	5	G	388.8	23.8	-	-	-	-	-	-
	6	G	389.4	25.7	-	-	-	-	-	-
	7	G	387.5	16.7	-	-	-	-	-	-
	8	G	389.8	23.1	-	-	-	-	-	-
	9	G	388.5	19.9	-	-	-	-	-	-
	10	G	390.1	23.8	-	-	-	-	-	-

320	1	I	396.5	30.8	616.5	15.9	71.4	661.1	27.6	93.2
	2	G	388.2	17.3	-	-	-	662.3	4.4	66.3
	3	I	391.0	27.0	-	-	-	669.9	14.1	106.3
	4	I	389.1	19.3	615.2	8.8	66.4	659.8	13.8	65.8
	5	I	395.2	33.9	621.1	14.3	80.7	658.3	24.5	107.1
	6	I	393.0	27.6	619.9	10.5	82.6	669.0	16.8	106.9
	7	G	389.1	23.1	-	-	-	687.0	9.6	59.4
	8	G	390.1	24.4	626.3	7.6	74.4	665.4	13.9	84.2
	9	I	391.7	27.0	623.9	11.2	89.3	666.3	18.4	107.6
	10	I	401.0	32.6	-	-	-	673.9	12.4	82.2
330	1	I	392.6	29.5	612.1	10.6	55.9	662.6	19.9	99.8
	2	G	390.0	22.5	-	-	-	681.8	13.9	65.6
	3	I	391.0	21.8	619.2	11.6	95.1	666.9	20.1	101.5
	4	I	395.8	30.8	617.1	11.1	79.5	662.9	19.8	70.1
	5	I	396.1	33.4	630.3	18.0	102.9	667.5	25.7	106.3
	6	I	389.7	23.8	-	-	-	663.2	15.1	96.0
	7	I	394.2	29.5	613.3	12.3	79.6	664.1	20.4	85.2
	8	I	391.7	27.0	-	-	-	663.2	18.2	91.9
	9	G	388.8	19.9	-	-	-	676.0	10.0	85.8
	10	I	389.7	22.5	-	-	-	666.2	16.5	90.6
340	1	H	408.6	17.2	616.1	22.7	48.4	659.5	39.3	63.5
	2	H	408.3	18.5	613.0	12.3	43.4	658.3	22.6	56.5
	3	H	406.4	22.3	615.5	19.3	73.3	660.4	31.3	78.6
	4	H	408.0	18.5	614.6	23.1	67.7	659.2	35.7	72.6
	5	I	391.0	22.5	627.9	19.4	99.2	662.6	29.8	90.1
	6	H	408.3	16.6	615.5	23.9	58.3	660.1	43.2	62.2
	7	G	399.3	17.9	-	-	-	681.5	4.6	58.9
	8	H	408.9	17.2	612.1	18.5	44.7	658.0	33.6	68.9
	9	H	408.6	18.5	616.1	21.4	55.8	662.6	37.3	54.9
	10	H	408.6	15.9	611.8	25.1	48.4	659.8	37.7	62.2
350	1	H	408.6	16.0	613.4	22.0	47.8	662.0	37.7	59.2
	2	H	408.0	19.1	612.7	21.6	50.9	660.4	37.5	62.2
	3	H	407.0	22.3	614.9	7.5	32.2	658.0	18.4	35.6
	4	H	406.4	21.7	618.0	18.6	55.2	661.1	36.7	69.5
	5	H	408.0	17.9	614.9	19.1	54.0	662.9	35.1	78.6
	6	H	409.3	18.5	616.1	20.7	51.5	662.0	35.6	54.3
	7	H	405.7	23.6	614.9	32.4	55.8	659.8	53.8	73.2
	8	H	408.3	17.9	614.9	21.0	55.2	659.8	35.7	78.0
	9	H	408.6	17.9	614.9	22.5	47.8	662.6	37.8	54.3
	10	H	408.0	20.4	614.3	24.3	56.5	660.7	39.6	71.3
360	1	H	409.6	15.3	618.9	28.1	66.4	659.8	45.8	64.7
	2	H	408.0	17.2	613.3	23.1	50.3	660.1	35.8	67.1
	3	H	407.7	19.8	614.0	19.7	49.0	664.1	34.7	63.4
	4	H	408.6	16.6	612.4	24.3	45.9	658.9	43.4	65.9
	5	H	405.1	23.0	619.2	15.8	69.5	660.4	25.3	65.9
	6	H	404.8	23.0	615.5	31.4	59.0	660.7	46.4	70.7
	7	H	409.9	15.3	616.4	18.3	52.7	662.6	35.2	65.8
	8	H	405.4	21.1	610.3	25.7	46.6	661.4	40.5	63.4

	9	H	404.8	21.7	615.8	25.7	62.1	661.7	42.9	75.6
	10	H	408.3	17.2	615.8	30.4	50.9	661.1	50.4	71.9
370	1	H	410.2	15.9	616.1	20.5	56.5	663.5	35.3	66.4
	2	H	409.9	14.7	615.2	21.6	49.0	662.0	38.9	68.3
	3	H	408.6	17.9	614.6	30.2	56.5	664.1	45.2	74.3
	4	H	404.5	25.5	614.3	17.2	68.3	662.0	25.7	66.5
	5	H	409.9	15.9	613.0	33.1	40.3	662.9	46.1	54.9
	6	H	408.6	17.9	615.2	26.7	49.6	661.1	42.6	70.1
	7	H	408.9	17.2	615.5	22.6	51.5	663.5	37.6	63.4
	8	H	408.9	17.2	616.8	20.4	57.7	658.9	38.0	55.6
	9	H	407.7	17.9	613.7	22.6	49.0	659.2	36.6	64.1
	10	H	408.6	18.5	614.6	21.9	47.1	662.0	39.5	59.2
380	1	H	408.3	18.5	616.2	24.1	49.0	661.1	42.2	63.4
	2	H	408.6	19.1	619.9	31.3	58.9	666.9	54.8	68.2
	3	H	408.3	19.1	618.6	21.0	56.4	662.3	40.3	56.1
	4	H	406.4	21.1	611.8	21.0	43.4	662.9	35.6	55.5
	5	H	408.0	18.5	613.4	27.3	47.2	659.2	46.4	65.9
	6	H	407.0	19.8	615.5	15.6	45.9	659.9	34.1	56.5
	7	-	-	-	-	-	-	-	-	-
	8	H	407.7	17.2	612.4	14.5	47.8	659.9	21.8	53.1
	9	-	-	-	-	-	-	-	-	-
	10	H	409.3	15.9	616.2	36.9	52.7	660.5	58.9	56.8
390	1	H	409.2	17.9	614.0	21.6	38.4	662.9	40.1	53.7
	2	H	409.6	15.9	613.7	33.6	45.3	662.3	53.7	61.6
	3	H	408.3	18.5	613.7	26.3	54.0	662.0	43.1	76.2
	4	H	408.6	16.0	617.7	18.8	55.2	658.6	34.7	69.5
	5	H	407.0	18.5	617.1	23.0	62.0	662.9	40.6	65.8
	6	H	406.1	21.7	617.7	18.0	67.0	659.2	30.8	67.1
	7	H	404.8	26.2	614.9	24.8	59.6	663.2	38.6	73.1
	8	H	405.7	22.3	618.9	22.6	60.8	662.0	37.2	69.5
	9	H	406.7	19.8	611.2	24.1	55.3	659.8	36.7	65.3
	10	H	410.5	13.4	619.8	19.9	60.1	662.9	37.4	58.5
400	1	H	410.2	14.7	616.1	28.1	52.7	663.2	52.3	53.7
	2	H	408.3	17.9	618.6	23.6	62.0	662.6	44.2	62.2
	3	H	407.3	21.1	614.3	25.1	47.1	663.5	45.0	66.4
	4	H	406.4	21.7	616.1	18.6	62.1	660.8	32.8	65.3
	5	H	408.3	18.5	614.6	19.8	42.2	659.8	38.1	56.2
	6	H	407.7	18.5	618.6	24.2	58.3	662.9	44.2	67.7
	7	H	408.3	18.5	614.6	21.1	40.9	662.6	38.7	65.2
	8	H	408.6	17.9	613.4	20.4	47.8	661.1	39.7	60.4
	9	H	405.7	21.7	614.6	22.2	60.8	662.0	39.5	68.9
	10	H	407.7	19.1	616.1	21.6	47.1	659.8	42.0	61.6
500	1	H	409.6	18.5	615.8	32.3	57.1	662.3	53.1	62.8
	2	H	409.9	15.9	615.2	31.6	38.4	663.5	57.0	53.7
	3	H	409.3	17.2	616.7	25.6	39.0	660.1	48.8	45.4
	4	H	409.0	18.5	616.7	14.2	38.4	660.7	32.5	43.6
	5	H	408.6	16.6	614.0	27.1	45.3	660.4	48.6	59.2
	6	H	409.3	16.6	612.1	21.9	40.9	662.0	41.4	57.3

	7	H	409.3	15.9	617.0	24.7	51.5	662.6	49.0	58.5
	8	H	408.3	19.8	613.6	27.7	41.6	659.8	49.3	68.9
	9	H	408.6	17.9	613.3	33.7	40.9	664.1	57.4	57.9
	10	H	410.6	14.7	614.0	43.3	34.1	662.6	70.5	51.6
600	1	H	409.3	17.2	612.4	31.0	39.1	661.1	47.6	51.9
	2	H	406.7	19.2	613.4	24.6	39.1	662.9	45.9	48.2
	3	H	410.2	16.6	615.2	22.3	37.8	662.6	40.5	43.9
	4	H	408.3	17.9	614.9	30.9	65.8	658.0	49.0	64.1
	5	H	407.4	19.1	614.9	23.1	51.5	660.5	35.3	47.6
	6	H	410.5	15.3	614.3	26.3	32.2	662.0	42.0	42.7
	7	H	409.3	17.2	614.0	28.4	39.1	661.7	48.0	51.3
	8	H	409.9	16.6	614.0	28.9	36.6	661.7	46.8	47.6
	9	H	411.8	12.8	612.4	19.6	34.1	661.1	34.4	49.7
	10	H	410.2	15.9	615.2	29.4	44.7	661.4	47.0	53.1
700	1	H	410.5	12.8	612.7	31.9	26.7	660.7	36.6	42.8
	2	H	409.6	14.7	612.7	29.0	31.0	660.1	35.9	47.0
	3	H	409.6	14.7	611.2	30.3	28.5	659.8	30.6	49.5
	4	H	410.5	13.4	612.7	41.0	36.6	656.5	47.7	56.8
	5	H	410.5	14.0	612.7	28.8	29.8	660.7	28.2	52.5
	6	H	410.5	13.4	612.7	29.1	28.5	660.1	30.5	46.4
	7	H	410.8	12.8	611.5	23.9	24.8	660.4	24.2	45.8
	8	H	410.2	14.7	612.7	39.5	37.8	656.1	41.3	53.8
	9	H	403.8	26.8	604.4	19.2	41.0	654.3	18.4	53.2
	10	H	408.9	16.0	610.3	46.8	29.8	658.0	46.7	47.0
800	1	H	410.6	12.1	611.8	34.8	18.6	658.9	23.7	44.0
	2	H	410.2	12.1	611.2	36.8	21.7	657.7	28.4	54.4
	3	H	410.2	13.4	612.1	33.6	22.9	661.1	26.5	44.0
	4	H	410.9	12.8	612.1	28.0	25.4	659.9	26.8	39.7
	5	H	410.9	13.4	610.6	38.4	22.9	657.7	37.8	43.4
	6	H	409.3	15.3	611.8	58.5	29.0	657.7	48.9	41.0
	7	H	410.2	13.4	612.1	62.5	26.0	658.0	41.7	53.1
	8	H	409.9	13.4	611.8	53.7	27.9	659.9	43.5	52.5
	9	H	410.6	14.0	612.8	42.5	26.0	660.2	32.3	45.2
	10	H	410.2	13.4	611.2	61.0	24.8	658.6	41.8	47.0
900	1	H	410.5	12.1	611.2	77.4	19.2	658.9	36.8	40.9
	2	H	411.8	10.2	612.4	89.5	13.6	660.8	25.0	34.2
	3	H	411.2	11.5	612.4	43.1	17.3	658.6	25.6	34.8
	4	H	410.9	12.1	611.8	60.3	20.5	659.2	31.7	42.8
	5	H	411.5	11.5	612.1	64.0	18.5	660.1	31.7	34.8
	6	H	411.5	10.2	612.1	35.7	15.5	660.5	17.3	34.2
	7	H	411.5	10.2	612.1	47.3	16.1	658.6	19.6	35.5
	8	H	409.9	12.8	610.6	132.1	19.8	657.1	74.6	40.3
	9	H	411.2	11.5	612.1	51.7	18.6	658.9	29.3	32.4
	10	H	411.5	10.8	612.4	34.4	16.1	659.5	17.4	34.2
1000	1	H	412.5	10.2	613.4	71.6	13.6	663.2	14.9	31.1
	2	H	411.8	10.2	612.4	131.5	14.2	659.9	29.8	30.0
	3	H	412.1	10.2	612.8	129.9	13.6	661.1	24.9	33.6
	4	H	411.8	9.6	612.4	33.6	14.2	659.2	12.4	39.1

	5	H	411.8	9.6	612.4	74.6	14.9	658.3	25.3	31.8
	6	H	411.8	10.2	612.4	148.9	14.2	658.0	35.0	35.5
	7	H	412.1	9.6	612.4	105.0	13.0	658.3	24.6	36.7
	8	H	411.8	10.2	612.8	62.4	14.8	660.2	38.0	31.3
	9	H	411.8	10.2	612.8	123.0	14.8	659.2	36.3	33.0
	10	H	412.1	10.2	612.8	29.2	20.4	659.2	29.0	29.3
1100	1	H	412.4	10.2	613.4	100.7	13.6	661.4	25.2	31.8
	2	H	411.8	8.9	612.4	75.2	14.2	659.2	31.2	32.4
	3	H	411.2	10.2	612.1	101.7	15.5	661.1	33.3	28.7
	4	H	412.1	9.6	612.7	124.4	13.6	659.2	29.6	33.0
	5	H	411.8	9.6	612.7	133.0	14.2	659.8	42.5	28.7
	6	H	411.8	10.2	612.4	158.5	14.2	659.2	46.8	29.3
	7	H	412.1	10.2	612.7	130.4	14.9	658.6	44.4	31.2
	8	H	411.2	11.5	612.1	112.6	15.5	657.4	38.1	34.2
	9	H	412.4	10.2	613.4	159.9	14.2	658.9	35.8	34.8
	10	H	412.1	9.6	612.7	67.1	14.2	658.9	22.2	32.4
1200	1	H	412.2	9.6	613.3	75.6	13.0	658.6	26.2	30.6
	2	H	412.2	9.6	612.7	100.7	13.6	660.7	36.6	26.9
	3	H	412.2	9.6	613.0	94.9	13.0	660.7	30.8	25.7
	4	H	412.2	9.6	613.0	40.1	14.8	661.0	17.7	37.3
	5	H	412.2	8.9	613.0	84.3	13.6	660.4	24.2	26.9
	6	H	412.2	9.6	612.7	76.9	13.6	659.8	22.3	28.1
	7	H	411.8	9.6	612.7	77.6	14.8	659.8	30.3	28.7
	8	H	412.2	9.6	613.6	29.1	12.4	662.3	9.9	34.3
	9	H	412.2	9.6	612.4	111.6	13.6	658.0	36.2	32.4
	10	H	412.2	9.6	613.0	102.0	13.6	658.3	25.9	35.5

*Spectra classification: G = goethite, I= Intermediate and H= Hematite.

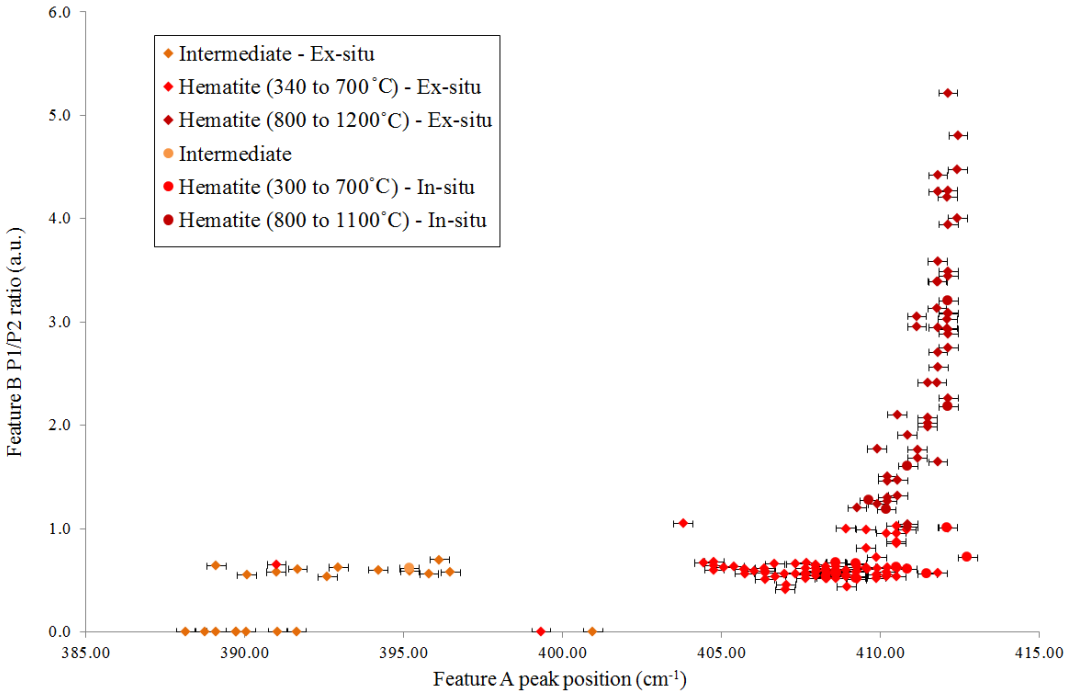

Figure F1 Feature A peak position and Feature B intensity ratios for both in-situ and absolute ex-situ experiments. Orange points represent temperatures where spectra were classified as intermediate and both shades of red show temperatures where spectra were classified as hematite.

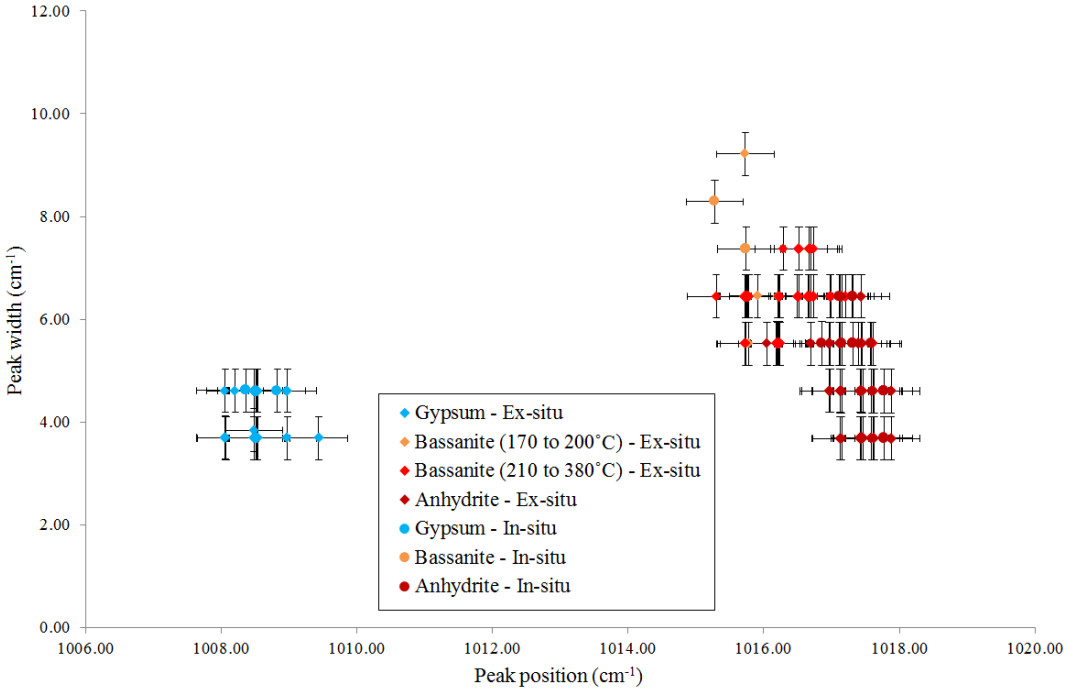

Figure F2 Peak widths against peak positons for the SO_4 U1 peak, from both in-situ and absolute ex-situ results. The blue points indicate gypsum, orange and light red indicate bassanite and dark red identifies anhydrite. The orange points also show the points where increased mass loss occurs in the ex-situ experiment.

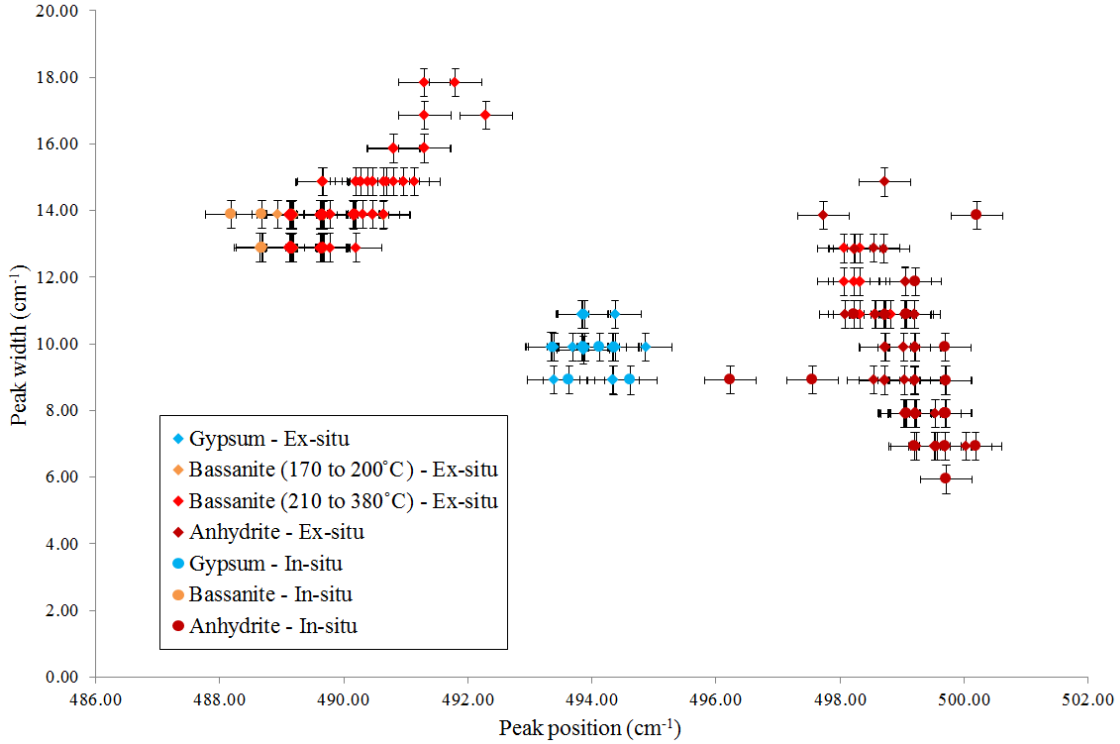

Figure F3 Peak widths against peak positons for the SO_4 U2 (2) peak, from both in-situ and absolute ex-situ results. The blue points indicate gypsum, orange and light red indicate bassanite and dark red identifies anhydrite. The orange points also show the points where increased mass loss occurs in the ex-situ experiment

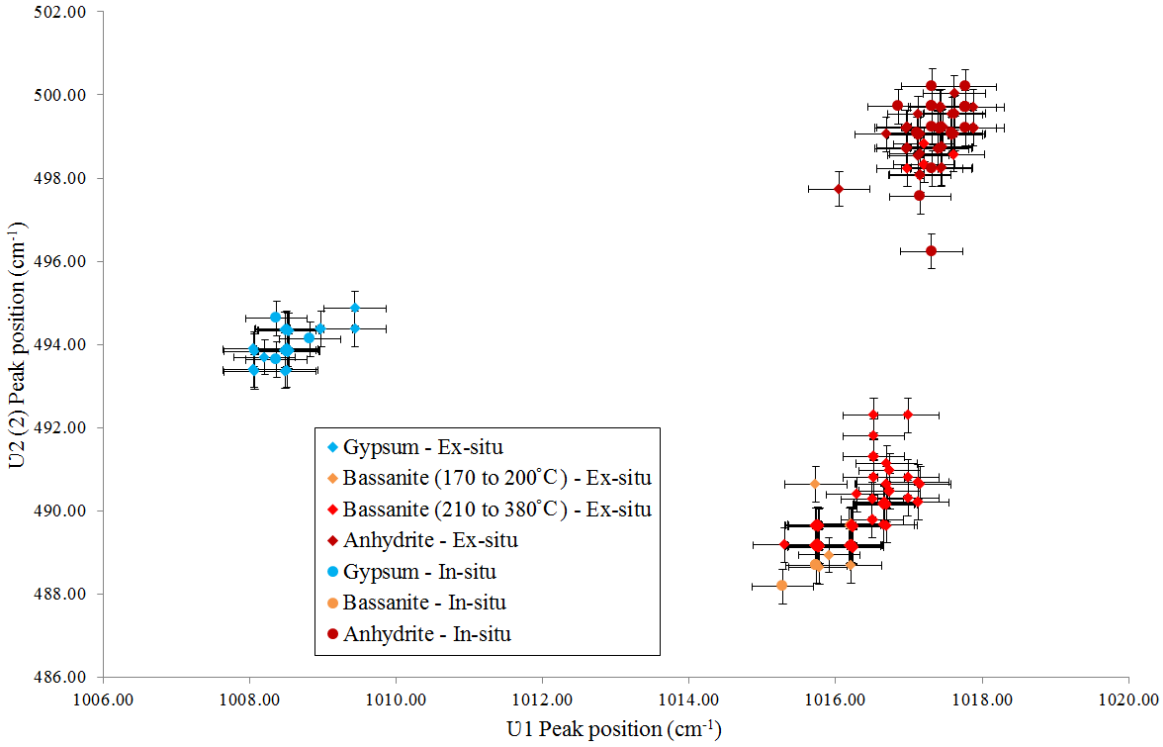

Figure F4 Graph showing U2 (2) peak positions against U1 peak positions for both in-situ and absolute ex-situ data. Blue points show spectra representing gypsum, orange and light red highlight bassanite and dark red indicate anhydrite. Orange points also indicates were high mass loss occurred from ex-situ experiment.

Table F2 Raman data for SO_4 U1 and SO_4 U2 from Natural gypsum ex-situ heating experiment.

Temperature (˚C)	Spectrum	U1		U2 (1)		U2 (2)		U2 (extra peak)	
		Peak Position (cm^{-1})	Peak Width (cm^{-1})	Peak Position (cm^{-1})	Peak Width (cm^{-1})	Peak Position (cm^{-1})	Peak Width (cm^{-1})	Peak Position (cm^{-1})	Peak Width (cm^{-1})
22	1	1008.2	4.6	414.5	6.9	493.7	9.9	-	-
	2	1008.5	4.6	415.0	6.9	493.9	9.9	-	-
	3	1008.5	3.7	415.0	6.9	494.4	8.9	-	-
	4	1008.5	4.6	415.5	6.9	494.4	9.9	-	-
	5	1008.5	4.6	415.0	7.9	493.9	9.9	-	-
	6	1008.5	4.6	415.0	7.9	494.4	9.9	-	-
	7	1008.5	4.6	415.0	7.9	493.9	9.9	-	-
	8	1008.5	4.6	415.0	6.9	493.9	9.9	-	-
	9	1008.5	4.6	415.0	6.9	493.9	9.9	-	-
	10	1008.5	4.6	415.0	6.9	494.4	9.9	-	-
100	1	1008.5	3.7	414.9	7.9	493.8	9.9	-	-
	2	1008.5	3.7	414.9	7.9	493.8	9.9	-	-
	3	1008.5	3.7	414.9	6.9	493.8	9.9	-	-
	4	1008.5	4.6	414.9	6.9	493.8	9.9	-	-
	5	1008.5	4.6	414.9	7.9	493.8	9.9	-	-
	6	1008.5	4.6	414.9	7.9	493.8	9.9	-	-
	7	1008.5	4.6	414.9	6.9	493.8	9.9	-	-
	8	1008.5	4.6	414.9	7.9	494.3	9.9	-	-
	9	1008.5	3.7	414.9	6.9	493.8	9.9	-	-
	10	1008.5	4.6	414.9	6.9	493.8	9.9	-	-
110	1	1008.5	4.6	415.0	6.9	493.9	10.9	-	-
	2	1008.5	4.6	415.0	7.9	493.4	9.9	-	-
	3	1008.5	3.7	415.0	6.9	493.9	9.9	-	-
	4	1008.5	4.6	415.0	7.9	493.9	9.9	-	-
	5	1008.5	3.7	415.0	7.9	493.9	9.9	-	-
	6	1008.5	4.6	415.0	7.9	493.9	10.9	-	-
	7	1008.5	3.7	415.0	7.9	493.9	9.9	-	-
	8	1008.5	4.6	415.0	6.9	493.9	9.9	-	-
	9	1008.5	3.7	415.0	8.9	493.9	9.9	-	-
	10	1008.5	4.6	415.0	7.9	493.9	9.9	-	-
120	1	1008.1	4.6	414.5	6.9	493.4	9.9	-	-
	2	1008.1	3.7	415.0	6.9	493.9	9.9	-	-
	3	1008.5	3.7	415.0	7.9	493.9	9.9	-	-
	4	1008.5	4.6	415.0	6.9	493.9	9.9	-	-
	5	1008.1	3.7	414.5	6.9	493.4	9.9	-	-
	6	1008.5	4.6	415.0	8.9	493.9	9.9	-	-
	7	1008.5	3.7	415.0	6.9	493.9	9.9	-	-
	8	1008.5	4.6	415.0	7.9	493.9	9.9	-	-
	9	1008.5	4.6	415.0	6.9	493.9	9.9	-	-
	10	1008.5	4.6	415.0	7.9	493.9	9.9	-	-
130	1	1008.5	4.6	414.9	6.9	493.8	10.9	-	-
	2	1008.5	4.6	414.9	6.9	494.3	9.9	-	-

	3	1008.5	3.7	414.9	7.9	493.8	9.9	-	-
	4	1008.5	4.6	414.9	6.9	493.8	9.9	-	-
	5	1008.1	3.7	414.9	7.9	493.8	9.9	-	-
	6	1008.5	4.6	414.9	7.9	493.8	9.9	-	-
	7	1008.5	3.7	414.9	7.9	493.8	9.9	-	-
	8	1008.5	3.7	414.9	6.9	493.8	9.9	-	-
	9	1008.1	3.7	414.9	6.9	493.3	9.9	-	-
	10	1008.5	3.7	414.9	6.9	493.8	9.9	-	-
140	1	1008.5	3.7	414.9	6.9	493.9	9.9	-	-
	2	1008.5	4.6	414.9	6.9	494.4	9.9	-	-
	3	1008.5	4.6	414.9	6.9	493.9	9.9	-	-
	4	1008.5	4.6	414.9	6.9	493.9	9.9	-	-
	5	1008.5	3.7	414.9	7.9	493.9	10.9	-	-
	6	1008.5	4.6	414.9	7.9	493.4	8.9	-	-
	7	1008.5	4.6	414.9	7.9	493.9	10.9	-	-
	8	1008.5	4.6	414.9	7.9	493.9	10.9	-	-
	9	1008.5	3.7	414.9	6.9	493.9	10.9	-	-
	10	-	-	-	-	-	-	-	-
150	1	1008.5	4.6	415.0	7.9	493.9	9.9	-	-
	2	1009.0	4.6	415.5	7.9	494.4	9.9	-	-
	3	1009.0	4.6	415.0	6.9	494.4	10.9	-	-
	4	1009.0	4.6	415.0	6.9	494.4	9.9	-	-
	5	1009.0	3.7	415.5	6.9	494.4	9.9	-	-
	6	1009.4	3.7	415.5	6.9	494.4	9.9	-	-
	7	1009.4	3.7	415.5	6.9	494.9	9.9	-	-
	8	1009.0	4.6	415.5	6.9	494.4	9.9	-	-
	9	1009.0	4.6	415.5	6.9	494.4	9.9	-	-
	10	1009.0	3.7	415.0	6.9	494.4	9.9	-	-
160	1	1008.5	4.6	415.0	6.9	493.8	9.9	-	-
	2	1008.5	3.7	415.0	6.9	494.3	8.9	-	-
	3	1008.5	4.6	415.0	7.9	493.8	9.9	-	-
	4	1008.5	3.8	415.0	7.5	493.9	9.8	-	-
	5	1008.5	3.7	415.0	6.9	493.8	9.9	-	-
	6	1008.5	4.6	415.0	7.9	494.3	9.9	-	-
	7	1008.5	3.7	415.0	7.9	494.3	9.9	-	-
	8	1008.5	4.6	415.0	7.9	493.8	9.9	-	-
	9	1008.5	3.7	415.0	7.9	493.8	9.9	-	-
	10	1008.5	4.6	415.0	7.9	493.8	9.9	-	-
170	1	1015.9	6.5	428.8	19.8	488.9	13.9	-	-
	2	1016.2	5.5	428.5	16.8	489.2	13.9	-	-
	3	1015.7	6.4	429.0	17.8	489.2	13.9	-	-
	4	1015.7	6.4	428.5	17.8	489.2	13.9	-	-
	5	1016.2	5.5	429.0	17.8	489.2	13.9	-	-
	6	1015.7	6.4	428.5	17.8	489.2	12.9	-	-
	7	1016.2	5.5	429.5	17.8	489.7	14.9	-	-
	8	1016.2	5.5	429.0	16.8	489.2	12.9	-	-

	9	1015.7	9.2	423.1	7.9	490.6	13.9	-	-
	10	1015.7	6.4	429.0	19.8	489.7	14.9	-	-
180	1	1016.2	5.5	428.5	18.8	489.2	13.9	-	-
	2	1015.8	6.4	428.5	15.9	489.2	12.9	-	-
	3	1015.8	6.4	428.5	17.8	489.2	12.9	-	-
	4	1015.8	6.4	429.0	17.0	489.2	13.9	-	-
	5	1015.8	6.4	428.5	17.8	489.2	13.9	-	-
	6	1016.2	5.5	429.0	18.8	489.7	13.9	-	-
	7	1016.2	6.4	428.5	15.9	489.7	12.9	-	-
	8	1015.8	6.4	428.5	15.9	489.2	12.9	-	-
	9	1016.2	5.5	429.5	17.0	488.7	12.9	-	-
	10	1015.8	6.4	429.0	18.0	489.2	13.9	-	-
190	1	1015.8	5.5	428.5	16.8	489.1	12.9	-	-
	2	1015.8	6.4	428.5	16.8	488.7	12.9	-	-
	3	1015.8	6.4	428.5	16.8	489.1	13.9	-	-
	4	1016.2	5.5	428.5	17.8	489.6	12.9	-	-
	5	1015.8	6.4	429.0	17.8	489.1	13.9	-	-
	6	1015.8	6.4	429.0	15.8	489.1	12.9	-	-
	7	1015.8	6.4	428.5	16.8	489.1	12.9	-	-
	8	1015.8	6.4	428.5	17.8	489.1	13.9	-	-
	9	1016.2	5.5	429.0	16.8	489.1	12.9	-	-
	10	1016.2	5.5	429.0	17.8	489.6	13.9	-	-
200	1	1015.8	6.4	428.5	16.8	489.1	12.9	-	-
	2	1016.2	5.5	428.5	16.8	489.1	13.9	-	-
	3	1016.2	5.5	428.5	16.8	489.1	13.9	-	-
	4	1015.8	6.4	428.0	16.8	489.1	12.9	-	-
	5	1015.8	6.4	428.0	16.8	489.1	12.9	-	-
	6	1015.8	6.4	428.0	17.8	489.1	12.9	-	-
	7	1016.2	5.5	428.5	16.8	489.1	12.9	-	-
	8	1015.8	6.4	428.0	16.8	489.1	13.9	-	-
	9	1015.8	6.4	428.5	16.8	489.1	12.9	-	-
	10	1015.8	6.4	429.0	15.8	489.1	13.9	-	-
210	1	1015.8	6.4	428.5	17.8	489.6	12.9	-	-
	2	1015.8	6.4	429.0	16.8	489.1	12.9	-	-
	3	1015.8	6.4	428.5	17.8	489.6	12.9	-	-
	4	1016.2	5.5	428.5	18.8	489.1	13.9	-	-
	5	1015.8	6.4	428.0	16.8	489.6	12.9	-	-
	6	1015.8	6.4	429.0	16.8	489.1	13.9	-	-
	7	1015.8	6.4	427.5	19.8	489.1	13.9	-	-
	8	1015.8	6.4	428.5	16.8	489.6	12.9	-	-
	9	1015.8	6.4	428.5	18.8	489.1	13.9	-	-
	10	1015.8	6.4	427.5	16.8	489.1	13.9	-	-
220	1	1015.8	6.4	428.5	18.8	489.1	13.9	-	-
	2	1015.8	6.4	429.0	18.8	489.1	13.9	-	-
	3	1015.8	6.4	428.5	17.8	489.1	12.9	-	-
	4	1015.8	6.4	428.0	16.8	489.1	12.9	-	-

	5	1015.8	6.4	428.5	15.8	489.6	12.9	-	-
	6	1016.2	5.5	428.5	16.8	489.1	13.9	-	-
	7	1015.8	6.4	428.5	17.8	489.1	13.9	-	-
	8	1015.8	6.4	428.5	17.8	489.6	12.9	-	-
	9	1015.8	6.4	428.5	15.8	489.1	12.9	-	-
	10	1015.8	6.4	428.0	15.8	489.1	12.9	-	-
230	1	1015.3	6.4	427.5	16.0	489.2	13.9	-	-
	2	1015.8	6.4	428.5	16.0	489.2	12.9	-	-
	3	1015.8	6.4	428.5	17.0	489.2	12.9	-	-
	4	1015.8	6.4	428.5	15.8	489.2	12.9	-	-
	5	1016.2	5.5	429.0	16.8	489.7	12.9	-	-
	6	1016.2	5.5	428.5	15.8	489.2	12.9	-	-
	7	1015.8	6.4	428.5	16.8	489.7	12.9	-	-
	8	1015.8	6.4	428.0	14.0	489.2	13.9	-	-
	9	1015.8	6.4	428.5	17.0	489.2	12.9	-	-
	10	1015.8	6.4	429.0	15.0	489.2	13.9	-	-
240	1	1015.7	6.4	427.5	17.8	489.2	13.9	-	-
	2	1015.7	6.4	428.0	15.8	489.2	12.9	-	-
	3	1015.7	5.5	429.0	14.8	489.2	12.9	-	-
	4	1015.7	6.4	427.5	16.8	489.7	12.9	-	-
	5	1015.7	6.4	428.5	14.8	489.7	12.9	-	-
	6	1015.7	6.4	428.0	16.8	489.2	12.9	-	-
	7	1015.7	6.4	428.5	14.8	489.2	12.9	-	-
	8	1015.7	6.4	426.5	18.8	489.2	13.9	-	-
	9	1015.7	6.4	427.5	17.8	489.2	12.9	-	-
	10	1015.7	6.4	428.5	14.8	489.2	12.9	-	-
250	1	1015.8	6.4	428.5	16.8	489.1	12.9	-	-
	2	1016.2	5.5	427.5	16.8	489.1	12.9	-	-
	3	1015.8	6.4	427.5	17.8	489.6	12.9	-	-
	4	1016.2	5.5	428.5	17.8	489.1	12.9	-	-
	5	1016.2	5.5	428.0	16.8	489.6	12.9	-	-
	6	1015.8	6.4	427.0	15.8	489.6	12.9	-	-
	7	1016.2	5.5	428.0	15.8	489.6	12.9	-	-
	8	1016.2	5.5	428.5	15.8	489.1	12.9	-	-
	9	1016.2	5.5	428.5	15.8	489.1	12.9	-	-
	10	1016.2	5.5	428.5	15.8	489.1	12.9	-	-
260	1	1015.7	6.4	427.5	14.8	489.2	13.9	-	-
	2	1015.7	6.4	428.0	16.8	489.2	12.9	-	-
	3	1015.7	6.4	428.5	14.8	489.2	13.9	-	-
	4	1016.2	5.5	428.0	16.8	489.2	13.9	-	-
	5	1015.7	6.4	428.5	14.8	489.2	12.9	-	-
	6	1015.7	6.4	428.5	15.8	489.2	12.9	-	-
	7	1015.7	6.4	428.0	15.8	489.2	13.9	-	-
	8	1015.7	6.4	427.0	16.8	489.2	12.9	-	-
	9	1015.7	6.4	427.5	16.8	489.2	12.9	-	-
	10	1015.7	6.4	428.5	15.8	489.2	12.9	-	-

270	1	1015.7	6.4	428.5	16.8	489.7	14.9	-	-
	2	1016.2	5.5	427.5	15.8	489.2	12.9	-	-
	3	1015.7	6.4	428.0	15.8	489.2	12.9	-	-
	4	1016.2	5.5	428.0	16.8	489.2	12.9	-	-
	5	1016.2	5.5	428.0	16.8	489.2	12.9	-	-
	6	1015.7	6.4	427.5	15.8	489.2	13.9	-	-
	7	1016.2	5.5	428.0	15.8	489.2	12.9	-	-
	8	1016.2	5.5	428.5	14.8	489.2	13.9	-	-
	9	1016.2	5.5	428.0	16.8	489.2	12.9	-	-
	10	1016.2	5.5	428.0	15.8	489.2	12.9	-	-
280	1	1016.2	5.5	428.5	14.8	489.1	12.9	-	-
	2	1015.8	6.4	428.0	14.8	489.6	13.9	-	-
	3	1016.2	5.5	428.0	15.8	489.1	12.9	-	-
	4	1016.2	5.5	427.5	15.8	489.6	13.9	-	-
	5	1016.2	6.4	427.5	16.8	489.6	13.9	-	-
	6	1016.2	5.5	427.5	15.8	489.6	13.9	-	-
	7	1016.2	5.5	427.5	16.8	489.6	12.9	-	-
	8	1016.2	5.5	427.5	16.8	489.6	12.9	-	-
	9	1015.8	6.4	429.0	14.9	489.1	12.9	-	-
	10	1016.2	5.5	427.0	15.8	489.1	12.9	-	-
290	1	1015.7	5.5	428.0	15.8	489.2	12.9	-	-
	2	1015.7	6.4	428.0	14.8	489.2	13.9	-	-
	3	1015.7	6.4	427.5	14.8	489.2	12.9	-	-
	4	1015.7	6.4	427.5	16.8	489.2	12.9	-	-
	5	1015.7	6.4	427.5	16.8	489.2	12.9	-	-
	6	1015.7	6.4	427.5	14.8	489.2	13.9	-	-
	7	1015.7	6.4	427.5	14.8	489.2	12.9	-	-
	8	1015.7	6.4	427.5	15.8	489.2	13.9	-	-
	9	1015.7	6.4	428.0	14.8	489.2	12.9	-	-
	10	1015.7	6.4	427.5	14.8	489.2	12.9	-	-
300	1	1016.2	5.5	428.0	18.0	489.2	12.9	-	-
	2	1015.8	6.4	429.0	16.0	489.7	13.9	-	-
	3	1015.8	6.4	428.0	17.8	489.7	13.9	-	-
	4	1015.8	6.4	427.0	16.9	489.2	12.9	-	-
	5	1015.8	6.4	426.5	14.9	489.2	12.9	-	-
	6	1016.2	5.5	427.0	15.9	489.7	13.9	-	-
	7	1016.2	6.4	427.5	16.0	489.7	12.9	-	-
	8	1016.2	5.5	428.0	16.0	489.2	12.9	-	-
	9	1015.8	6.4	427.0	14.9	489.2	12.9	-	-
	10	1016.2	5.5	425.5	16.9	489.7	14.9	-	-
310	1	1016.7	6.4	426.0	17.9	490.2	13.9	-	-
	2	1016.7	6.4			490.2	13.9	-	-
	3	1016.7	6.4			489.7	12.9	-	-
	4	1016.7	6.4	426.0	15.9	490.2	13.9	-	-
	5	1016.7	6.4	426.0	15.9	490.2	13.9	417.1	30.7
	6	1016.7	6.4	427.0	15.9	490.2	13.9	416.6	34.7
	7	1016.7	6.4	427.0	17.9	490.2	13.9	417.1	36.7

	8	1016.7	6.4			490.2	13.9		
	9	1016.7	6.4	427.0	15.9	490.2	13.9	417.1	33.7
	10	1016.7	6.4	427.5	15.9	490.2	13.9	417.1	37.7
320	1	1016.2	6.4	428.0	16.9	489.7	12.9		
	2	1016.2	6.4	428.0	16.9	489.7	13.9		
	3	1016.7	5.5	426.0	15.9	489.7	12.9	416.1	34.7
	4	1016.2	6.4	427.0	16.9	489.7	13.9	417.1	37.7
	5	1016.2	6.4	427.5	15.9	489.7	13.9	417.1	38.7
	6	1016.7	5.5	428.0	15.9	489.7	12.9		
	7	1016.2	6.4	426.0	14.8	489.7	13.9	417.1	30.7
	8	1016.2	6.4	427.0	14.9	489.7	13.9	417.1	32.7
	9	1016.2	6.4	428.0	16.9	489.7	13.9	417.6	42.7
	10	1016.2	6.4	428.0	15.9	489.7	13.9	417.1	42.7
330	1	1016.7	6.4	428.5	15.9	490.1	13.9	417.6	5.9
	2	1016.7	6.4	428.6	15.8	490.2	12.9	419.2	8.9
	3	1017.1	6.4	428.6	14.8	490.7	14.9	418.2	6.9
	4	1017.1	6.4	428.1	14.8	490.2	14.9	417.7	7.9
	5	1017.1	5.5	429.1	15.8	490.2	13.9	418.2	6.9
	6	1016.7	7.4	429.1	20.8	490.2	14.9	417.7	5.9
	7	1017.1	5.5	429.6	13.8	490.2	13.9	418.2	6.9
	8	1017.0	6.4	429.4	15.8	490.8	14.9	418.0	5.9
	9	1017.0	6.4	427.9	16.8	490.3	13.9	417.5	6.9
	10	1017.2	6.4	428.5	17.9	490.6	13.9	418.1	5.9
340	1	1016.7	6.4	428.0	16.9	490.2	13.9	417.1	5.9
	2	1016.5	6.4	427.4	18.8	489.8	13.9	417.5	6.9
	3	1016.5	6.4	427.4	18.8	489.8	13.9	417.0	5.9
	4	1016.5	6.4	428.4	15.8	489.8	13.9	417.0	6.9
	5	1016.5	6.4	427.9	15.8	490.3	14.9	417.0	5.9
	6	1016.5	6.4	428.4	16.8	490.3	14.9	417.5	6.9
	7	1016.5	6.4	428.4	15.8	489.8	12.9	417.5	6.9
	8	1016.5	6.4	427.4	16.8	489.8	13.9	417.5	6.9
	9	1016.5	6.4	428.4	15.8	489.8	13.9	417.5	6.9
	10	1016.7	6.4	428.5	17.9	490.2	13.9	417.1	5.0
350	1	1016.7	6.4	428.0	19.9	490.2	13.9	417.1	8.9
	2	1016.7	6.4	429.0	15.5	490.5	13.9	417.1	5.0
	3	1016.7	6.4	428.0	16.8	490.5	13.9	417.1	5.9
	4	1016.7	6.4	429.0	15.5	490.5	13.9	417.1	5.0
	5	1016.7	6.4	428.0	15.8	491.0	14.9	417.1	5.9
	6	1016.7	6.4	429.5	13.8	490.5	13.9	417.1	5.0
	7	1016.7	7.4	428.0	15.8	491.0	14.9	417.1	5.0
	8	1016.7	6.4	429.5	14.5	490.5	14.9	417.1	5.9
	9	1016.7	6.4	429.0	14.8	490.5	14.9	417.1	5.9
	10	1016.7	6.5	428.0	16.9	490.7	13.9	417.6	3.0
360	1	1016.7	7.4	427.5	13.9	491.1	14.9	417.1	3.0
	2	1016.5	7.4	426.9	16.8	491.3	15.9	417.0	5.0
	3	1016.5	7.4	427.9	15.8	491.3	15.9	417.0	4.0
	4	1016.5	6.5	427.4	16.8	491.8	17.8	417.0	4.0
	5	1017.0	6.4	427.4	16.8	492.3	16.9	417.0	3.0

	6	1016.5	6.5	427.9	15.8	491.3	15.9	417.0	4.0
	7	1016.5	7.4	427.4	15.8	491.3	16.9	417.0	5.0
	8	1016.5	7.4	427.9	15.8	492.3	16.9	417.0	4.0
	9	1016.5	6.4	427.4	15.8	490.8	15.9	417.0	5.0
	10	1016.7	6.4	426.5	13.8	490.6	14.9	416.6	8.9
370	1	1017.2	6.4	426.0	11.9	498.1	12.9	417.1	3.0
	2	1017.4	6.4	424.5	21.8	498.2	11.9	417.5	3.0
	3	1017.4	6.4	424.5	21.8	498.7	10.9	417.5	3.0
	4	1017.4	6.4	426.4	19.8	498.7	10.9	417.5	3.0
	5	1016.5	7.4	428.9	14.8	491.3	15.9	417.0	5.0
	6	1016.5	7.4	426.9	15.8	490.8	15.9	417.0	8.9
	7	1017.4	6.4	426.4	16.8	498.7	10.9	417.5	3.0
	8	1017.0	6.4	426.4	17.8	498.2	12.9	417.0	4.0
	9	1016.5	7.4	426.9	17.8	491.3	17.8	417.0	6.9
	10	1017.2	6.4	428.5	15.9	498.1	11.9	417.1	3.0
380	1	1017.6	5.5	427.0	11.9	498.6	10.9	417.1	4.0
	2	1016.3	7.4	426.3	15.8	490.4	14.9	416.9	7.9
	3	1017.2	6.4	417.4	3.0	498.3	11.9	-	-
	4	1017.2	6.4	417.4	3.0	498.3	11.9	-	-
	5	1017.2	6.4	417.4	3.0	498.8	10.9	-	-
	6	1017.2	6.4	417.4	3.0	498.3	10.9	-	-
	7	1017.2	6.4	417.4	4.0	498.8	10.9	-	-
	8	1017.2	6.4	417.4	4.0	498.3	12.9	-	-
	9	1017.2	6.4	417.4	3.0	498.3	11.9	-	-
	10	1017.6	5.5	417.1	4.0	498.6	10.9	-	-
390	1	1017.2	6.4	417.1	3.0	498.1	10.9	-	-
	2	1017.5	5.5	417.0	4.0	498.7	10.9	-	-
	3	1017.5	5.5	417.0	4.0	498.7	10.9	-	-
	4	1017.5	5.5	417.0	4.0	498.7	9.9	-	-
	5	1017.5	5.5	417.5	3.0	498.7	10.9	-	-
	6	1017.5	5.5	417.5	4.0	498.3	12.9	-	-
	7	1017.5	5.5	417.5	3.0	498.7	10.9	-	-
	8	1017.5	5.5	417.0	3.0	498.7	10.9	-	-
	9	1017.5	5.5	417.0	3.0	498.7	10.9	-	-
	10	1017.2	6.4	417.1	4.0	498.6	10.9	-	-
400	1	1017.6	5.5	417.1	3.0	499.0	9.9	-	-
	2	1017.4	5.5	417.0	4.0	498.7	10.9	-	-
	3	1017.4	5.5	417.0	3.0	499.2	9.9	-	-
	4	1017.4	5.5	417.0	3.0	499.2	10.9	-	-
	5	1017.4	5.5	417.0	3.0	499.2	10.9	-	-
	6	1017.4	5.5	417.0	4.0	498.7	10.9	-	-
	7	1017.4	5.5	417.0	4.0	499.2	9.9	-	-
	8	1017.4	5.5	417.0	4.0	498.7	10.9	-	-
	9	1017.4	5.5	417.0	3.0	499.2	8.9	-	-
	10	1017.1	5.5	417.1	3.0	499.0	9.9	-	-
500	1	1017.1	5.5	417.1	4.0	498.5	12.9	-	-
	2	1017.0	5.5	417.0	4.0	498.7	10.9	-	-

	3	1017.0	5.5	417.5	3.0	499.2	9.9	-	-
	4	1017.0	5.5	417.0	4.0	499.2	10.9	-	-
	5	1017.0	5.5	417.0	4.0	499.2	10.9	-	-
	6	1017.0	4.6	417.5	3.0	499.2	10.9	-	-
	7	1017.0	5.5	417.0	4.0	498.7	12.9	-	-
	8	1017.0	5.5	417.0	4.0	499.2	9.9	-	-
	9	1017.0	5.5	417.0	4.0	499.2	8.9	-	-
	10	1017.1	5.5	417.1	3.0	499.0	10.9	-	-
600	1	1016.7	5.5	417.1	3.0	499.1	10.9	-	-
	2	1017.4	4.6	417.0	3.0	499.2	9.9	-	-
	3	1017.0	5.5	417.0	3.0	499.2	9.9	-	-
	4	1017.4	4.6	417.0	3.0	498.7	9.9	-	-
	5	1017.4	5.5	417.5	3.0	499.2	9.9	-	-
	6	1017.4	4.6	417.0	4.0	498.7	9.9	-	-
	7	1017.0	5.5	417.0	4.0	498.7	10.9	-	-
	8	1017.4	4.6	417.0	3.0	499.2	9.9	-	-
	9	1017.0	4.6	417.0	3.0	499.2	9.9	-	-
	10	1017.2	5.5	417.1	3.0	499.1	11.9	-	-
700	1	1017.1	4.6	417.1	3.0	498.5	8.9	-	-
	2	1017.4	4.6	417.0	3.0	499.2	8.9	-	-
	3	1017.9	4.6	417.0	3.0	499.7	8.9	-	-
	4	1017.4	4.6	417.0	3.0	499.7	8.9	-	-
	5	1017.4	4.6	417.0	3.0	499.2	9.9	-	-
	6	1017.4	4.6	417.0	3.0	499.2	8.9	-	-
	7	1017.9	4.6	417.0	3.0	499.2	9.9	-	-
	8	1017.9	4.6	417.5	3.0	499.2	8.9	-	-
	9	1017.9	4.6	417.0	3.0	499.2	9.9	-	-
	10	1017.6	4.6	417.1	3.0	499.0	8.9	-	-
800	1	1017.2	4.6	416.6	3.0	499.1	7.9	-	-
	2	1017.4	4.6	417.0	2.0	499.2	7.9	-	-
	3	1017.4	4.6	417.0	3.0	499.2	7.9	-	-
	4	1017.4	4.6	417.0	3.0	499.2	7.9	-	-
	5	1017.4	4.6	417.0	3.0	499.2	7.9	-	-
	6	1017.4	4.6	417.0	3.0	499.2	7.9	-	-
	7	1017.4	4.6	417.0	3.0	499.2	7.9	-	-
	8	1017.4	4.6	417.0	3.0	499.2	7.9	-	-
	9	1017.4	4.6	417.0	3.0	499.2	7.9	-	-
	10	1017.6	4.6	417.1	3.0	499.1	7.9	-	-
900	1	1017.6	3.7	416.6	3.0	499.0	7.9	-	-
	2	1017.9	3.7	417.0	3.0	499.2	7.9	-	-
	3	1017.9	3.7	417.0	3.0	499.2	7.9	-	-
	4	1017.9	3.7	417.0	3.0	499.2	7.9	-	-
	5	1017.4	3.7	417.0	3.0	499.7	6.9	-	-
	6	1017.9	3.7	417.0	3.0	499.2	7.9	-	-
	7	1017.9	3.7	417.0	3.0	499.2	7.9	-	-
	8	1017.9	3.7	417.0	3.0	499.2	7.9	-	-

	9	1017.9	3.7	417.0	3.0	499.2	7.9	-	-
	10	1017.6	3.7	417.1	3.0	499.5	6.9	-	-
1000	1	1017.6	3.7	417.1	3.0	499.1	7.9	-	-
	2	1017.5	3.7	417.0	3.0	499.2	7.9	-	-
	3	1017.5	3.7	417.0	3.0	499.2	7.9	-	-
	4	1017.5	4.6	417.0	3.0	499.2	7.9	-	-
	5	1017.5	3.7	417.0	3.0	499.2	7.9	-	-
	6	1017.5	3.7	417.0	3.0	499.2	7.9	-	-
	7	1017.5	3.7	417.0	3.0	499.2	6.9	-	-
	8	1017.5	3.7	417.0	3.0	499.2	7.9	-	-
	9	1017.5	3.7	417.0	3.0	499.2	7.9	-	-
	10	1017.6	4.6	417.1	2.0	499.6	6.9	-	-
1100	1	1017.1	4.6	416.6	3.0	499.0	7.9	-	-
	2	1017.4	4.6	417.0	3.0	499.2	7.9	-	-
	3	1017.4	3.7	417.0	2.0	499.2	7.9	-	-
	4	1017.4	4.6	417.0	3.0	499.2	7.9	-	-
	5	1017.4	3.7	417.0	2.0	499.7	6.9	-	-
	6	1017.4	4.6	417.0	3.0	499.7	6.9	-	-
	7	1017.4	4.6	417.0	3.0	499.2	7.9	-	-
	8	1017.4	3.7	417.0	3.0	499.7	6.9	-	-
	9	1017.4	3.7	417.0	3.0	499.2	7.9	-	-
	10	1017.1	3.7	417.1	2.0	499.5	6.9	-	-
1200	1	1017.6	3.7	417.1	3.0	499.5	7.9	-	-
	2	1017.4	3.7	417.0	3.0	499.7	6.9	-	-
	3	1017.4	3.7	417.0	3.0	499.7	6.9	-	-
	4	1017.4	3.7	417.0	3.0	499.7	6.9	-	-
	5	1017.4	3.7	417.0	3.0	499.7	6.9	-	-
	6	1017.4	3.7	417.5	2.0	499.7	6.9	-	-
	7	1017.4	3.7	417.0	2.0	499.2	7.9	-	-
	8	1017.4	3.7	417.5	2.0	499.7	7.9	-	-
	9	1017.4	4.6	417.0	3.0	499.7	7.9	-	-
	10	1017.6	3.7	417.1	3.0	500.0	6.9	-	-
1300	1	1017.2	3.7	416.6	5.0	499.1	11.9	-	-
	2	1017.4	3.7	416.5	6.9	498.7	8.9	-	-
	3	1017.0	4.6	416.5	4.0	498.7	10.9	-	-
	4	1017.0	4.6	416.5	5.0	498.7	10.9	-	-
	5	1017.4	6.4	416.5	14.9	498.7	14.9	-	-
	6	1016.1	5.5	416.5	4.0	497.7	13.8	-	-
	7	1017.4	3.7	416.5	5.0	499.2	8.9	-	-
	8	1017.4	3.7	417.0	3.0	499.2	9.9	-	-
	9	1017.4	3.7	417.0	5.0	498.7	8.9	-	-
	10	1017.2	4.6	416.6	5.9	499.1	7.9	-	-

Table F3 Raman data for H_2O peaks from Natural gypsum ex-situ heating experiment.

Temperature (°C)	Spectrum	H2O (1)		H2O (2)	
		Peak Position (cm^{-1})	Peak Width (cm^{-1})	Peak Position (cm^{-1})	Peak Width (cm^{-1})
22	1	3405.6	39.9	3493.0	26.4
	2	3407.3	44.2	3493.1	27.0
	3	3403.8	35.2	3492.8	28.3
	4	3404.4	37.7	3492.5	27.7
	5	3403.8	35.2	3493.8	32.1
	6	3443.7	164.8	3492.8	27.0
	7	3405.4	39.0	3492.5	28.9
	8	3405.4	39.7	3493.1	27.0
	9	3405.4	38.4	3492.5	28.3
	10	3403.4	35.2	3492.2	28.3
100	1	3404.4	35.8	3491.9	32.7
	2	3403.8	34.5	3492.5	33.9
	3	3406.0	42.9	3492.5	27.7
	4	3404.7	37.1	3492.2	30.2
	5	3404.4	37.1	3492.5	29.6
	6	3404.7	36.5	3491.9	35.2
	7	3408.6	46.7	3492.8	26.4
	8	3404.4	35.8	3493.1	29.5
	9	3404.1	35.2	3490.9	40.2
	10	3404.7	40.3	3492.8	27.0
110	1	3406.0	41.6	3492.8	27.0
	2	3404.4	36.5	3492.5	28.9
	3	3403.5	35.8	3492.5	27.7
	4	3404.1	35.2	3492.2	32.1
	5	3403.8	33.9	3492.5	31.4
	6	3403.8	36.5	3493.1	27.0
	7	3403.1	33.3	3492.5	31.4
	8	3407.0	45.4	3493.1	26.4
	9	3405.1	37.1	3492.2	30.2
	10	3405.4	39.0	3492.5	29.6
120	1	3404.1	35.8	3492.2	28.9
	2	3404.4	37.1	3493.7	27.7
	3	3404.4	35.8	3492.5	29.6
	4	3404.1	33.3	3492.5	27.7
	5	3404.4	39.0	3492.2	27.7
	6	3405.0	36.5	3492.5	30.9
	7	3405.0	37.1	3491.8	32.7
	8	3404.4	38.4	3492.5	29.6
	9	3404.4	35.8	3492.5	32.1
	10	3404.4	37.1	3492.2	28.9
130	1	3402.8	36.4	3492.8	28.3
	2	3403.1	34.5	3493.1	27.7

	3	3404.4	37.1	3492.2	28.9
	4	3403.4	33.9	3492.5	36.5
	5	3404.1	35.8	3492.8	29.5
	6	3403.4	35.2	3492.8	29.5
	7	3403.7	34.6	3492.2	28.9
	8	3402.8	32.6	3491.8	34.6
	9	3404.1	35.8	3494.0	31.4
	10	3403.4	33.9	3491.2	42.7
140	1	3404.4	36.5	3490.6	49.6
	2	3405.1	36.5	3492.2	35.8
	3	3405.1	36.5	3492.2	38.3
	4	3403.8	35.2	3492.8	30.2
	5	3403.5	35.2	3492.2	32.7
	6	3404.4	36.5	3491.9	34.6
	7	3404.4	37.1	3491.9	33.9
	8	3403.1	35.2	3491.2	29.7
	9	3404.4	37.1	3493.1	27.0
	10	-	-	-	-
150	1	3403.8	35.2	3493.4	31.4
	2	3403.1	33.3	3493.1	30.8
	3	3406.0	39.7	3493.4	27.7
	4	3405.0	39.7	3493.4	28.3
	5	3405.0	36.5	3493.7	35.8
	6	3401.2	30.1	3493.1	35.2
	7	3406.0	40.3	3493.7	27.7
	8	3404.4	34.6	3493.1	37.7
	9	3404.4	35.2	3493.4	33.9
	10	3402.5	32.0	3493.4	33.9
160	1	3404.1	35.8	3493.1	28.3
	2	3407.3	43.5	3493.4	27.0
	3	3405.0	38.4	3493.1	28.9
	4	3404.7	39.1	3491.6	29.9
	5	3404.1	34.6	3492.8	33.3
	6	3402.5	33.3	3491.5	37.1
	7	3404.1	35.8	3494.1	32.7
	8	3404.1	35.2	3492.5	35.8
	9	3404.7	37.8	3494.1	32.1
	10	3405.0	39.0	3493.1	31.4
170	1	3553.5	23.0	-	-
	2	3556.5	28.5	-	-
	3	3555.0	24.9	-	-
	4	3554.6	24.9	-	-
	5	3556.2	28.0	-	-
	6	3554.6	24.2	-	-
	7	3555.6	26.1	-	-
	8	3554.3	21.1	-	-

	9	3554.3	25.5	-	-
	10	3554.6	25.5	-	-
180	1	3554.3	24.2	-	-
	2	3555.9	27.3	-	-
	3	3555.3	26.7	-	-
	4	3554.3	24.9	-	-
	5	3554.9	25.5	-	-
	6	3553.4	21.8	-	-
	7	3555.3	28.0	-	-
	8	3555.3	25.5	-	-
	9	3553.7	22.4	-	-
	10	3555.3	25.5	-	-
190	1	3554.6	24.9	-	-
	2	3556.2	28.0	-	-
	3	3555.2	24.9	-	-
	4	3555.6	26.7	-	-
	5	3554.6	24.2	-	-
	6	3556.5	27.3	-	-
	7	3555.6	26.7	-	-
	8	3554.6	24.2	-	-
	9	3553.7	22.4	-	-
	10	3554.9	24.9	-	-
200	1	3555.0	24.9	-	-
	2	3554.0	23.6	-	-
	3	3554.0	23.6	-	-
	4	3554.3	24.9	-	-
	5	3554.6	24.2	-	-
	6	3555.6	26.7	-	-
	7	3554.6	23.6	-	-
	8	3554.6	24.2	-	-
	9	3555.6	26.1	-	-
	10	3554.6	24.2	-	-
210	1	3554.9	25.5	-	-
	2	3554.0	23.0	-	-
	3	3554.6	23.6	-	-
	4	3554.6	24.2	-	-
	5	3554.6	24.9	-	-
	6	3555.6	26.1	-	-
	7	3554.6	23.6	-	-
	8	3554.9	26.1	-	-
	9	3554.9	25.5	-	-
	10	3554.6	23.6	-	-
220	1	3554.3	24.2	-	-
	2	3554.3	22.4	-	-
	3	3552.8	25.5	-	-
	4	3554.0	22.4	-	-

	5	3555.3	25.5	-	-
	6	3554.6	25.5	-	-
	7	3556.2	28.6	-	-
	8	3554.3	23.0	-	-
	9	3554.0	23.6	-	-
	10	3553.7	23.0	-	-
230	1	3554.6	25.5	-	-
	2	3540.7	22.4	-	-
	3	3555.3	25.5	-	-
	4	3553.7	23.0	-	-
	5	3554.6	24.2	-	-
	6	3555.9	26.7	-	-
	7	3555.3	26.7	-	-
	8	3552.8	19.9	-	-
	9	3553.7	24.9	-	-
	10	3554.3	24.9	-	-
240	1	3555.6	28.6	-	-
	2	3553.7	23.0	-	-
	3	3557.1	27.3	-	-
	4	3555.6	27.3	-	-
	5	3554.6	24.9	-	-
	6	3554.3	23.0	-	-
	7	3555.6	26.1	-	-
	8	3555.6	27.3	-	-
	9	3553.7	23.0	-	-
	10	3554.6	25.5	-	-
250	1	3555.3	24.2	-	-
	2	3554.0	23.0	-	-
	3	3554.3	25.5	-	-
	4	3554.3	23.6	-	-
	5	3555.0	24.9	-	-
	6	3554.0	23.6	-	-
	7	3554.0	23.0	-	-
	8	3554.3	24.2	-	-
	9	3554.0	23.6	-	-
	10	3554.6	23.6	-	-
260	1	3554.6	24.2	-	-
	2	3554.6	23.6	-	-
	3	3554.6	24.2	-	-
	4	3555.9	26.1	-	-
	5	3554.6	24.2	-	-
	6	3554.9	26.1	-	-
	7	3555.2	26.1	-	-
	8	3554.3	22.4	-	-
	9	3554.6	25.5	-	-
	10	3555.5	26.7	-	-

270	1	3554.6	24.2	-	-
	2	3555.3	24.9	-	-
	3	3555.3	25.5	-	-
	4	3555.3	25.5	-	-
	5	3553.4	21.8	-	-
	6	3552.2	19.3	-	-
	7	3555.3	26.1	-	-
	8	3554.6	23.6	-	-
	9	3556.5	28.0	-	-
	10	3554.6	24.9	-	-
280	1	3555.5	26.7	-	-
	2	3553.7	23.6	-	-
	3	3554.9	24.9	-	-
	4	3553.7	23.6	-	-
	5	3554.0	23.0	-	-
	6	3554.6	24.9	-	-
	7	3554.6	25.5	-	-
	8	3554.9	27.3	-	-
	9	3554.3	23.6	-	-
	10	3555.2	24.2	-	-
290	1	3555.2	24.9	-	-
	2	3555.5	27.3	-	-
	3	3555.5	27.3	-	-
	4	3554.3	24.9	-	-
	5	3557.4	27.2	-	-
	6	3555.2	24.9	-	-
	7	3554.3	23.6	-	-
	8	3556.5	29.1	-	-
	9	3554.9	25.5	-	-
	10	3555.5	26.1	-	-
300	1	3554.0	25.5	-	-
	2	3554.3	24.2	-	-
	3	3554.9	24.2	-	-
	4	3556.2	28.0	-	-
	5	3554.9	26.1	-	-
	6	3555.3	25.5	-	-
	7	3554.3	25.5	-	-
	8	3555.3	25.5	-	-
	9	3555.3	28.6	-	-
	10	3555.9	28.6	-	-
310	1	3555.2	26.7	-	-
	2	3556.5	26.1	-	-
	3	3557.4	32.3	-	-
	4	3555.9	26.7	-	-
	5	3554.6	23.6	-	-
	6	3555.9	26.1	-	-
	7	3555.2	24.9	-	-

	8	3555.2	26.1	-	-
	9	3554.9	25.5	-	-
	10	3556.2	26.7	-	-
320	1	3555.3	24.2	-	-
	2	3556.2	27.3	-	-
	3	3555.6	26.7	-	-
	4	3555.3	24.9	-	-
	5	3555.6	26.1	-	-
	6	3555.3	24.9	-	-
	7	3555.6	26.1	-	-
	8	3555.3	25.5	-	-
	9	3555.3	25.5	-	-
	10	3555.3	24.9	-	-
330*	1	3556.2	35.4	-	-
	2	-	-	-	-
	3	-	-	-	-
	4	-	-	-	-
	5	-	-	-	-
	6	-	-	-	-
	7	-	-	-	-
	8	-	-	-	-
	9	-	-	-	-
	10	3556.2	27.3	-	-
340*	1	3554.3	25.5	-	-
	2	-	-	-	-
	3	-	-	-	-
	4	-	-	-	-
	5	-	-	-	-
	6	-	-	-	-
	7	-	-	-	-
	8	-	-	-	-
	9	-	-	-	-
	10	3555.9	23.6	-	-
350*	1	3556.2	28.0	-	-
	2	-	-	-	-
	3	-	-	-	-
	4	-	-	-	-
	5	-	-	-	-
	6	-	-	-	-
	7	-	-	-	-
	8	-	-	-	-
	9	-	-	-	-
	10	3556.2	28.6	-	-
360*	1	3556.5	36.7	-	-
	2	-	-	-	-
	3	-	-	-	-
	4	-	-	-	-
	5	-	-	-	-

	6	-	-	-	-
	7	-	-	-	-
	8	-	-	-	-
	9	-	-	-	-
	10	3556.5	34.2	-	-
370*	1	3558.3	26.6	-	-
	2	-	-	-	-
	3	-	-	-	-
	4	-	-	-	-
	5	-	-	-	-
	6	-	-	-	-
	7	-	-	-	-
	8	-	-	-	-
	9	-	-	-	-
	10	3557.1	24.8	-	-
380	1	3563.0	27.8	-	-
	2	-	-	-	-
	3	-	-	-	-
	4	-	-	-	-
	5	-	-	-	-
	6	-	-	-	-
	7	-	-	-	-
	8	-	-	-	-
	9	-	-	-	-
	10	3560.2	39.1	-	-

*At these temperatures only site 1 and site 10 covered the spectral range between -90 and 4000 cm^{-1}).

Appendix G - Serpentine Target Plates

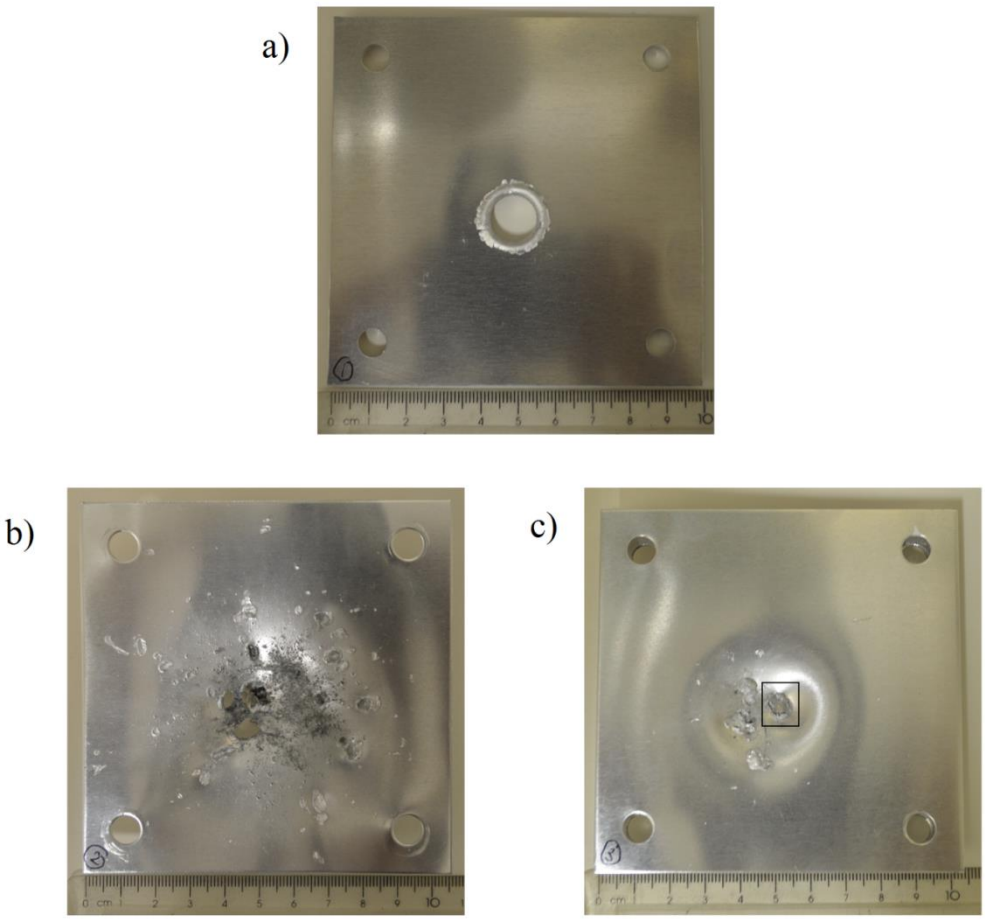

Figure G1 Al target plates (from G140813#3) impacted with an initial velocity of 2.90 km s^{-1} with olivine, water ice and nylon "container" projectile. a) The first target plated impacted by projectile. b) Plate 2 shows craters produced by Al from plate 1. c) The witness plate (or plate 3) shows craters produced by Al from the front plates and crater with olivine residue (black box).

Appendix H - Goethite Target Plates

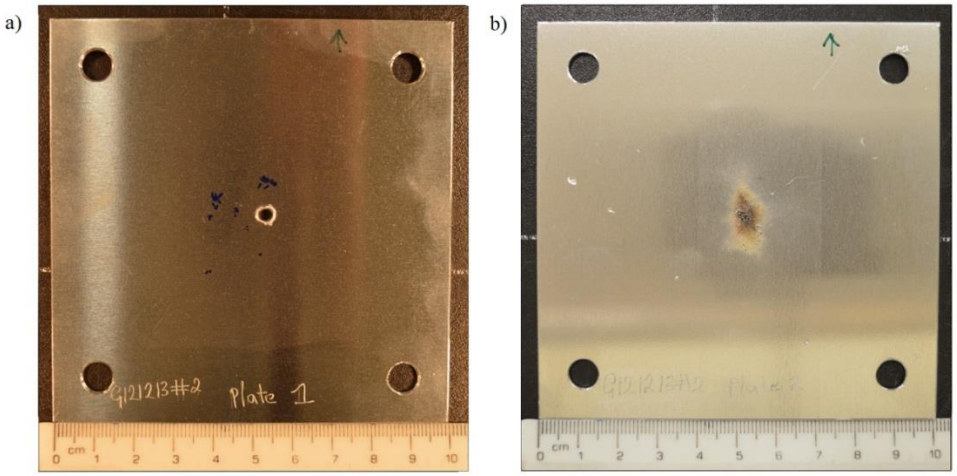

Figure H1 Target plates, a) plate 1 and b) witness plate, for shot I.D. G121213#2 (1.363 km s^{-1}).

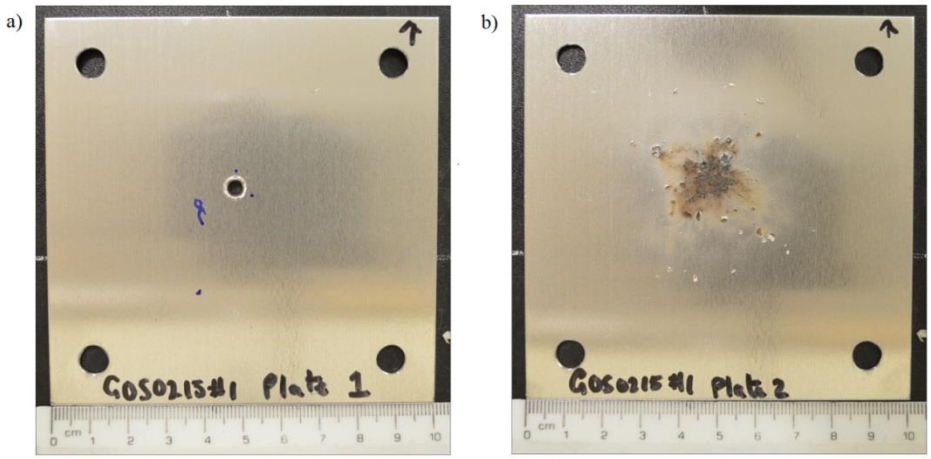

Figure H2 Target plates, a) plate 1 and b) witness plate, for shot I.D. G050215#1 (2.02 km s^{-1}).

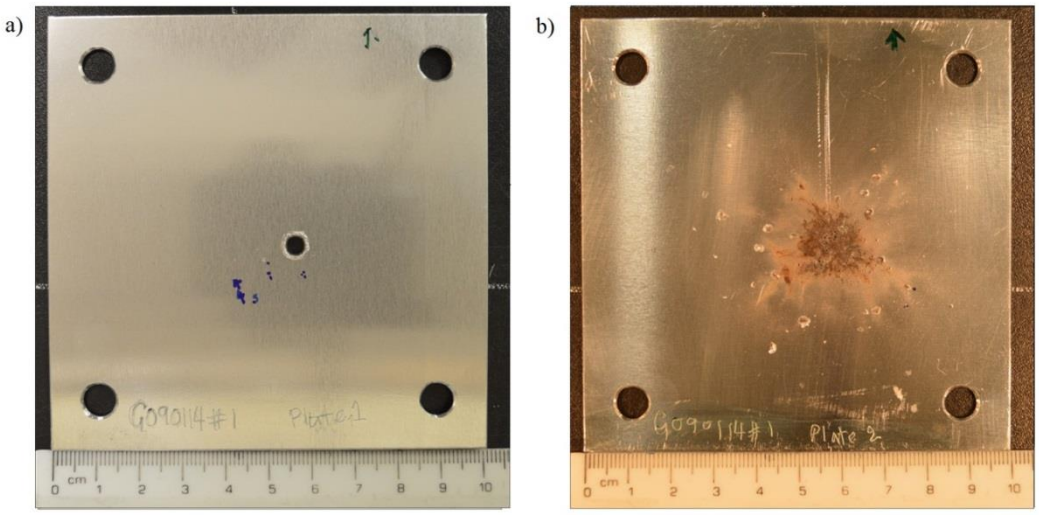

Figure H3 Target plates, a) plate 1 and b) witness plate, for shot I.D. G090114#1 (2.14 km s^{-1}).

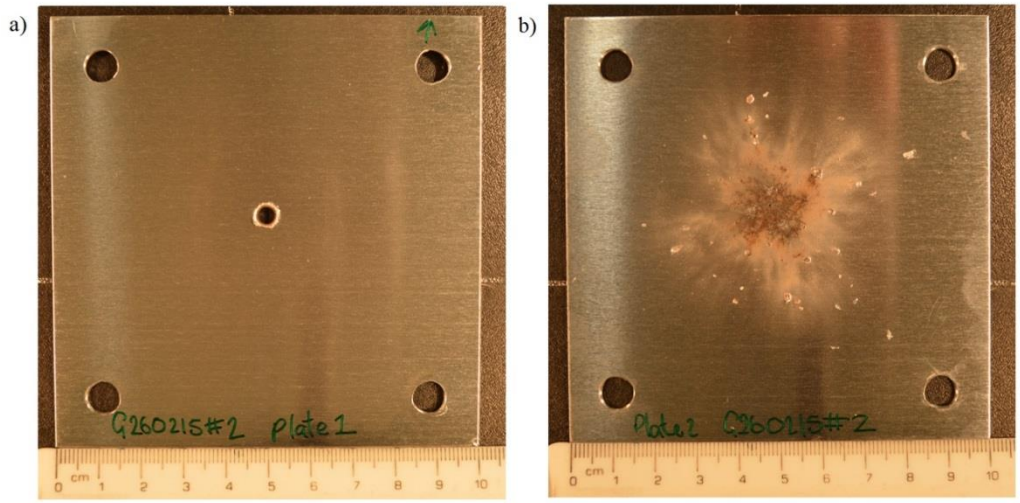

Figure H4 Target plates, a) plate 1 and b) witness plate, for shot I.D. G260215#2 (2.19 km s^{-1}).

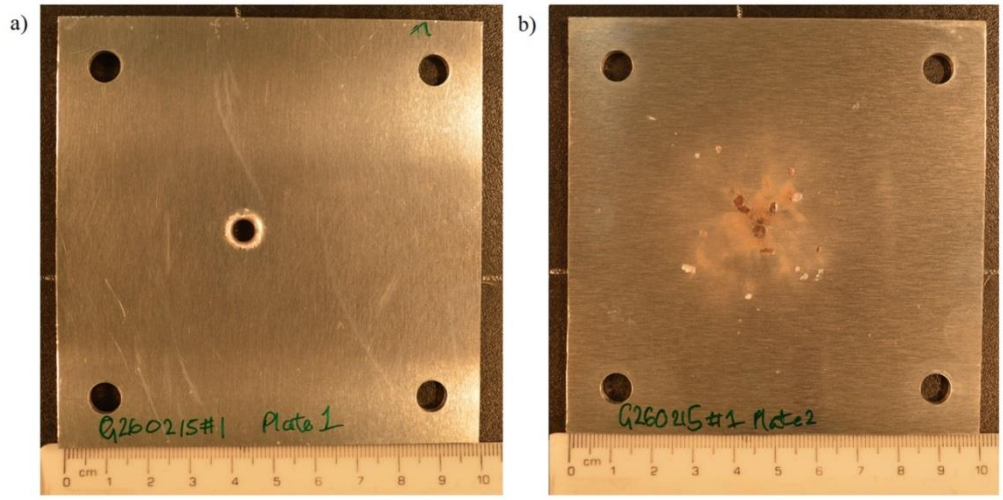

Figure H5 Target plates, a) plate 1 and b) witness plate, for shot I.D. G260215#1 (3.04 km s^{-1}).

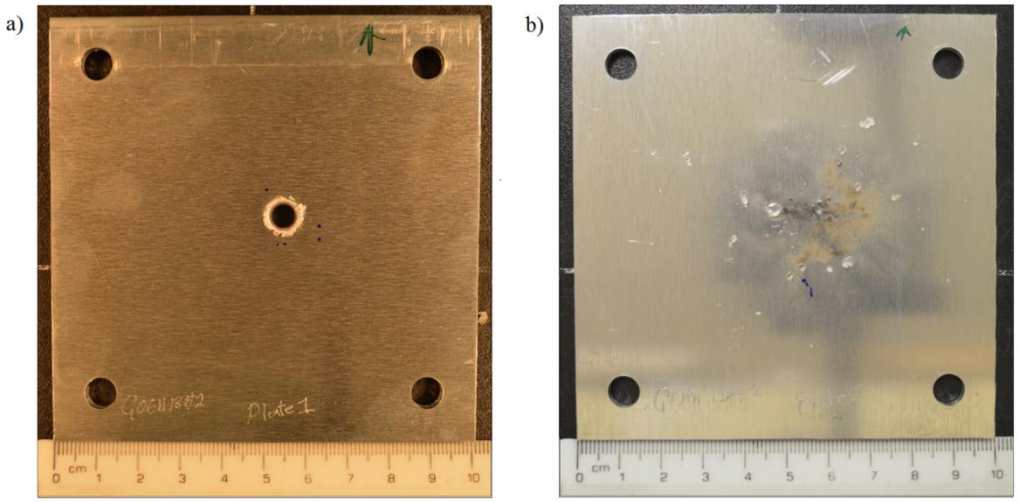

Figure H6 Target plates, a) plate 1 and b) witness plate, for shot I.D. G061113#2 (3.25 km s^{-1}).

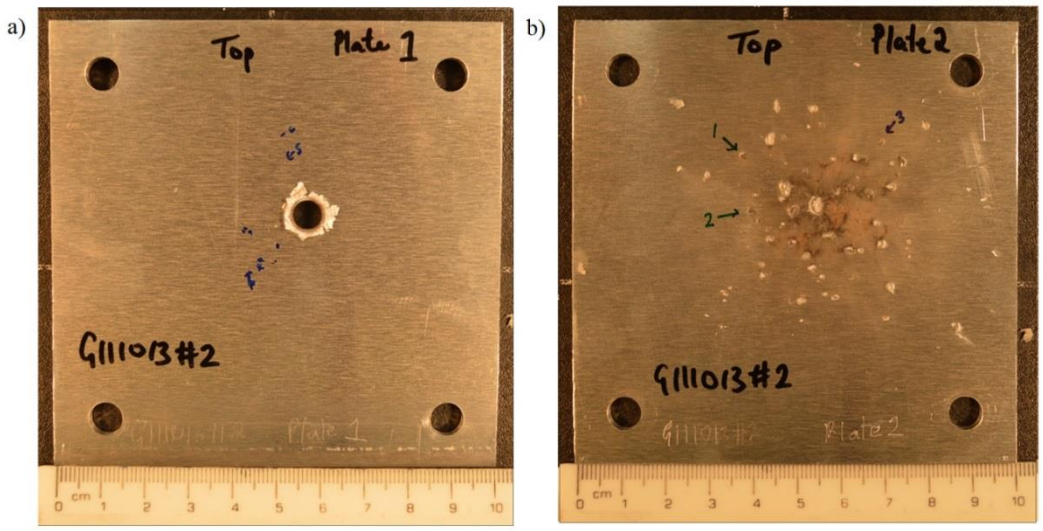

Figure H7 Target plates, a) plate 1 and b) witness plate, for shot I.D. G111013#2 (4.11 km s^{-1}).

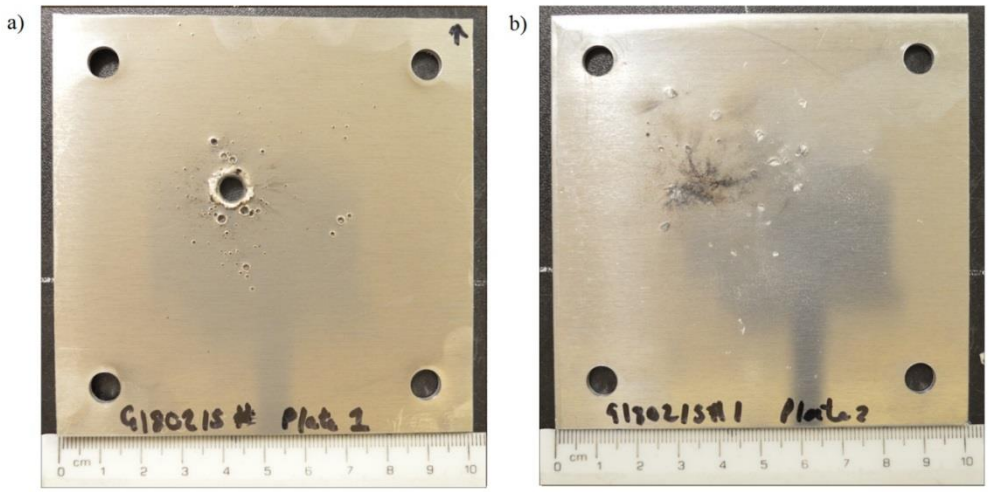

Figure H8 Target plates, a) plate 1 and b) witness plate, for shot I.D. G180215#1 (4.86 km s^{-1}).

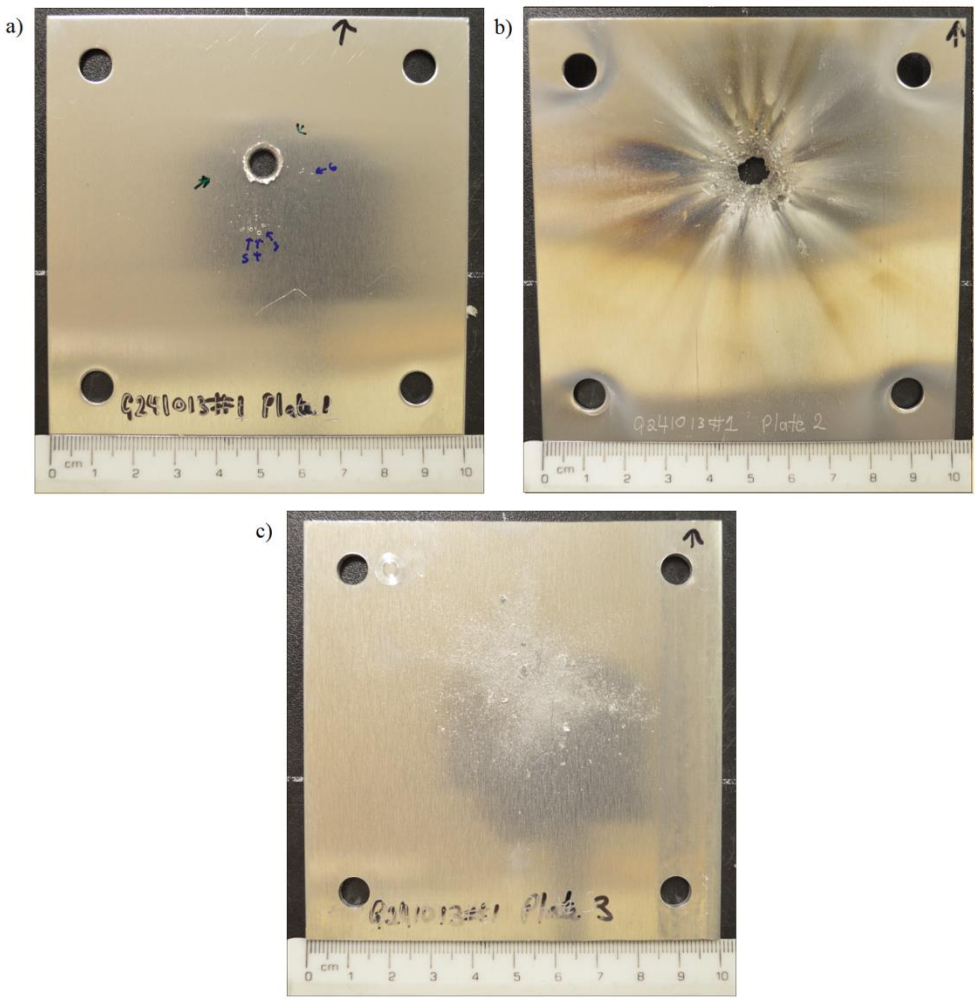

Figure H9 Target plates, a) plate 1, b) plate 2 and c) witness plate, for shot I.D. G241013#1 (5.13 km s^{-1}).

Appendix I - Goethite Raman Data (Impacts)

Table I1 Goethite projectile shot data for Feature A and B from plate 1

Impact velocity (km s^{-1})	Crater	Site*	Feature A Peak 1 Position (cm^{-1})	Feature A Peak 1 Width (cm^{-1})	Feature B Peak 1 Position (cm^{-1})	Feature B Peak 1 Intensity (counts)	Feature B Peak 1 Width (cm^{-1})	Feature B Peak 2 Position (cm^{-1})	Feature B Peak 2 Intensity (counts)	Feature B Peak 2 Width (cm^{-1})
1.363	1	1	387.2	19.8	-	-	-	-	-	-
		2	387.2	22.2	-	-	-	-	-	-
	2	1	388.4	27.1	-	-	-	-	-	-
		2	388.4	27.1	-	-	-	-	-	-
	3	1	392.6	32.0	-	-	-	-	-	-
		2	391.4	32.0	-	-	-	-	-	-
	4	1	386.5	19.7	-	-	-	-	-	-
		2	390.2	29.6	-	-	-	-	-	-
		3	386.5	17.3	-	-	-	-	-	-
		4	386.5	27.1	-	-	-	670.5	49.5	59.1
		5	387.7	24.7	-	-	-	-	-	-
2.14	2	1	388.4	27.1	-	-	-	683.1	31.2	52.1
		3	387.2	22.2	-	-	-	661.8	10.0	9.5
		5	393.4	36.9	-	-	-	655.8	25.8	76.2
	3	1	405.7	22.1	-	-	-	665.3	20.2	68.6
		2	410.6	14.7	616.5	26.2	57.4	662.9	46.2	59.2
3.25	1	1	393.3	44.4	-	-	-	668.9	161.4	56.8
		2	386.0	22.2	-	-	-	672.4	56.2	47.5
		3	400.7	32.0	612.9	107.3	59.9	659.4	200.4	80.5
		4	387.7	32.1	-	-	-	664.6	117.1	59.4
		5	407.4	19.7	602.6	145.2	64.59.42	658.7	308.8	54.7
		6	403.7	24.6	614.6	146.2	67.0	661.1	271.8	99.3
		8	390.2	27.1	612.3	79.5	81.5	664.6	166.6	90.4
		9	397.6	32.0	600.3	51.0	108.1	661.1	85.17.67	87.5
		10	386.5	19.7	-	-	-	-	-	-
4.11	2	1	408.1	19.7	617.7	232.1	64.6	660.6	480.3	68.7
		2	408.1	17.2	617.7	100.0	52.6	666.5	214.5	59.2
		3	408.1	19.7	611.7	85.5	47.9	662.9	193.3	63.9
		4	402.0	29.5	610.5	30.6	43.1	664.1	72.6	45.0
	3	1	404.4	24.6	615.3	156.1	69.4	660.6	310.0	75.8
		2	399.5	9.9	615.3	105.8	69.4	659.4	238.3	71.4
4.86	1	1	405.6	24.6	-	-	-	662.9	130.5	66.3
		3	393.3	36.9	600.9	32.1	86.4	658.2	39.7	115.9
		4	406.9	22.1	612.9	68.0	57.5	661.7	136.5	73.4
	2	1	392.1	39.5	658.2	46.7	100.1	672.4	45.2	101.5
		2	401.9	29.5	615.3	46.7	71.8	658.2	81.9	87.9
		3	403.2	29.5	614.1	50.2	71.9	658.2	81.1	92.3
	3	1	399.5	32.0	-	-	-	657.0	135.9	87.6
		2	405.6	27.0	612.9	33.7	57.5	660.5	67.7	75.8

		3	399.5	32.0	612.9	28.6	67.1	658.2	58.7	81.0
	4	2	409.3	22.1	616.5	30.1	52.6	662.3	71.8	49.7
		3	395.8	36.9	-	-	-	659.3	72.5	153.5
		4	400.7	32.0	604.5	51.4	72.0	658.2	80.6	80.5
	5	1	393.4	32.1	608.1	16.1	86.3	659.4	30.6	73.8
		2	404.4	36.8	609.3	10.3	33.5	6664.1	28.2	59.4
	7	1	393.4	39.5	612.3	15.8	50.2	673.6	46.5	71.3
		2	404.4	27.0	615.3	26.2	52.6	662.9	54.0	73.4
		3	392.1	34.5	614.1	11.6	45.5	661.7	28.2	64.2
	8	1	409.3	17.2	615.3	43.9	50.3	661.7	97.8	54.5
		3	406.9	24.6	614.1	26.0	55.1	662.9	54.5	56.8
	9	1	400.7	32.0	611.7	50.3	88.7	664.1	79.1	85.1
		2	395.8	41.9	609.3	19.1	62.3	662.9	43.9	78.5
		3	400.7	29.5	611.7	26.1	86.9	654.6	48.7	80.5
5.13	1	1	409.4	22.1	620.1	224.6	59.8	662.9	430.1	75.7
		2	408.1	19.7	605.8	37.8	47.9	671.2	156.9	54.4
		3	410.6	36.8	624.9	121.8	122.2	667.7	251.6	701.0
	3	1	406.2	19.7	619.4	43.0	38.2	663.4	129.6	54.7
		2	406.2	19.7	623.0	116.1	74.2	662.2	234.4	66.3
		3	403.7	22.1	624.2	66.2	88.5	662.2	111.4	82.8
		4	408.6	19.7	611.0	151.1	43.1	662.2	286.2	59.2
	4	1	408.6	19.7	613.4	162.9	43.1	664.6	243.0	66.3
		2	397.6	34.4	-	-	-	659.9	108.4	92.3
		3	409.9	12.3	620.6	20.2	38.2	661.1	63.7	35.6
		4	403.7	27.0	615.8	72.3	71.8	665.8	179.9	64.2
	5	1	408.6	19.7	613.4	101.6	35.9	662.2	189.6	57.1
		2	408.6	19.7	614.6	67.0	40.7	663.4	133.7	54.5
		3	408.6	19.7	614.6	67.0	40.7	663.4	133.7	54.5
		4	408.6	22.1	615.8	59.2	69.4	663.4	100.3	71.0
	6	2	404.9	24.6	609.8	214.7	83.9	661.1	313.2	85.2
		3	387.7	22.2	611.0	115.0	76.7	662.2	238.1	87.5

*The colour of the cell represents classification of the spectra; goethite (blue), intermediate (orange) and hematite (red).

Table I2 Goethite projectile witness plate shot data for Feature A and B

Impact velocity (km s^{-1})	Crater	Spectrum*	Feature A Peak 1 Position (cm^{-1})	Feature A Peak 1 Width (cm^{-1})	Feature B Peak 1 Position (cm^{-1})	Feature B Peak 1 Intensity (counts)	Feature B Peak 1 Width (cm^{-1})	Feature B Peak 2 Position (cm^{-1})	Feature B Peak 2 Intensity (counts)	Feature B Peak 2 Width (cm^{-1})
1.363	1	1	388.4	24.7	-	-	-	-	-	-
		2	392.1	32.0	-	-	-	-	-	-
		3	410.6	14.7	616.5	58.4	47.8	673.6	214.0	59.4
		4	397.0	22.1	-	-	-			
	2	1	387.2	46.8	666.5	87.9	92.8	696.1	87.3	101.2
		2	405.7	19.7	610.5	40.8	43.1	664.1	86.5	64.2
		4	405.7	19.7	608.1	183.5	33.5	658.2	231.7	47.4
	3	1	394.6	36.9	-	-	-	660.6	30.9	104.1
		2	389.7	29.6	-	-	-	653.4	29.5	118.3
	4	1	397.0	34.4	-	-	-	-	-	-
		2	388.4	27.1	-	-	-	681.9	43.4	63.8
		3	409.3	17.2	612.9	111.0	38.3	664.1	241.8	54.5
		4	388.4	27.1	-	-	-	-	-	-
	5	1	387.2	24.7	-	-	-	-	-	-
		2	394.6	29.5	-	-	-	-	-	-
		3	387.2	24.7	616.5	21.5	9.5	684.2	52.6	51.9
		4	393.3	32.0	-	-	-	-	-	-
2.02	1	1	389.7	27.1	613.0	12.0	55.1	666.5	31.1	57.0
		2	393.4	32.1	615.4	25.2	62.2	659.4	40.0	85.2
		3	397.1	41.8	616.6	16.1	43.1	661.8	33.9	45.2
		4	394.6	37.0	623.7	7.8	35.8	663.0	15.8	54.7
		5	395.9	41.9	-	-	-	664.2	20.4	71.3
	2	1	410.6	19.6	615.4	17.6	57.4	666.5	35.2	47.4
		2	408.2	24.6	614.2	14.0	56.9	666.5	33.3	59.4
		4	408.2	19.7	616.6	10.6	57.7	664.2	20.6	61.8
	3	1	409.4	17.2	613.0	142.6	38.3	661.8	248.9	52.1
		2	391.0	32.1	613.0	100.9	40.7	663.0	201.5	63.9
		3	391.0	32.1	551.8	50.4	31.4	663.0	50.4	31.7
		4	400.8	34.4	613.0	66.5	64.7	661.8	126.8	87.5
		5	389.7	27.1	616.6	38.4	52.6	665.4	79.5	66.6
	4	1	388.5	27.1	609.4	49.4	127.3	659.4	93.8	61.9
	5	1	407.0	22.1	615.4	78.5	52.6	660.6	145.3	52.2
		2	388.5	29.6	607.0	37.2	76.7	664.2	78.4	63.9
		3	388.5	29.6	-	-	-	-	-	-
		4	394.6	34.4	598.6	25.6	76.8	659.4	34.7	75.8
	6	1	394.6	37.0	610.6	27.8	64.7	661.8	55.6	75.7
		2	394.6	41.8	-	-	-	670.1	74.3	63.9
		3	392.2	39.5	-	-	-	663.0	81.4	88.1
		4	394.6	36.9	613.0	25.0	46.7	667.7	51.0	73.3
2.14	1	1	404.4	24.6	608.2	34.8	55.1	657.0	48.0	92.3
		2	409.4	19.7	617.7	27.1	64.6	664.1	55.9	57.1
2.19	1	1	388.4	22.2	622.5	47.5	57.4	667.7	125.0	54.6
		2	399.5	34.4	610.6	63.4	62.3	661.8	106.2	75.7

		3	390.9	27.1	-	-	-	667.7	44.0	66.5
		4	389.7	29.6	610.6	33.9	50.3	667.7	92.1	63.9
		5	397.1	34.4	616.5	24.8	153.7	668.9	52.7	80.8
	2	1	408.1	24.6	616.5	18.8	45.4	668.9	36.5	59.1
		3	405.7	27.0	615.3	67.9	52.6	664.1	131.0	75.7
		4	404.5	27.0	609.4	68.5	43.1	664.1	126.4	54.5
		5	389.7	27.1	628.5	35.7	69.3	667.7	88.6	59.4
	3	1	388.4	24.7	-	-	-	-	-	-
		2	388.4	27.1	-	-	-	-	-	-
		3	388.4	34.6	-	-	-	659.4	43.3	73.4
		4	390.9	32.1	620.1	40.0	71.8	666.5	91.4	64.2
		5	388.4	29.6	618.9	38.7	59.8	662.9	84.7	54.7
	4	1	390.9	44.3	610.5	33.3	91.1	659.4	49.9	75.8
		2	397.0	36.9	624.9	78.4	78.9	662.9	135.5	78.1
		3	403.2	31.9	621.3	28.7	88.6	670.0	66.4	63.9
	5	1	394.6	37.0	620.1	36.5	62.2	664.1	73.9	66.6
		3	388.4	27.1	-	-	-	550.5	71.4	24.1
		4	400.7	29.5	604.6	35.1	52.7	659.4	44.0	59.2
	6	1	409.4	19.7	614.1	51.2	52.7	665.3	112.0	61.5
		2	403.2	27.0	624.9	42.1	78.9	666.5	79.4	80.4
		3	404.4	24.6	608.1	36.8	74.3	658.2	65.2	54.5
		4	389.6	37.0	614.1	54.3	124.8	667.7	79.3	66.2
		5	405.7	24.6	618.9	62.1	83.8	661.7	97.0	63.9
3.04	1	1	389.7	32.1	617.7	46.2	71.8	661.8	83.9	56.8
		3	395.8	34.5	604.6	24.5	45.5	658.2	40.4	57.1
		4	411.8	12.3	612.9	83.6	26.3	661.8	86.8	42.7
		5	388.4	24.7	614.1	53.2	35.9	663.0	111.9	52.3
		6	404.5	29.5	610.6	38.2	55.1	663.0	79.0	71.0
		7	404.5	27.0	614.1	12.5	35.9	665.3	28.1	63.9
	2	1	393.4	37.0	615.3	36.4	38.3	663.0	105.5	54.7
		2	408.1	24.6	616.5	47.5	47.8	664.1	109.0	57.1
		3	408.1	24.6	612.9	49.6	67.1	661.8	91.7	66.3
		4	390.9	29.6	614.1	60.4	38.3	661.8	105.5	59.5
		5	404.5	27.0	607.0	38.3	59.9	658.2	63.7	71.1
		6	404.5	29.5	-	-	-	661.8	293.6	54.5
	3	1	399.5	29.5	602.2	40.7	43.1	660.6	48.8	89.9
		2	397.1	37.0	618.9	22.8	64.6	659.4	47.3	71.4
		3	398.3	36.9	601.0	25.2	43.1	668.9	77.7	73.7
		5	394.6	27.1	-	-	-	653.5	26.7	130.1
		6	394.6	37.0	-	-	-	-	-	-
		7	395.8	34.4	605.8	25.5	141.8	667.7	39.0	89.8
	4	1	404.5	27.0	608.2	74.9	50.3	660.6	130.5	71.0
		2	406.9	24.6	610.6	34.5	71.9	661.8	50.4	52.1
		3	388.4	42.0	616.5	27.0	81.4	664.1	49.0	111.9
		4	406.9	24.6	612.9	45.4	50.3	661.8	90.3	63.9
		5	389.7	32.1	612.9	23.0	35.9	665.3	58.2	59.4
		6	406.9	24.6	611.8	59.4	40.7	663.0	112.3	59.4
		7	390.9	29.6	-	-	-	-	-	-

		8	405.7	24.6	617.7	30.8	50.2	660.6	65.3	52.3
	5	1	411.8	14.7	614.1	110.8	35.9	662.9	179.6	56.8
		2	398.3	34.4	610.5	14.2	47.9	661.7	34.0	57.1
		3	389.6	27.1	628.4	26.1	66.9	666.5	63.1	59.91.56
		4	395.8	29.5	605.7	35.3	132.2	660.5	50.0	89.9
3.25	1	1	404.4	27.0	622.5	112.8	79.0	662.9	216.1	56.8
		2	406.9	19.7	609.3	241.4	38.3	657.0	297.6	54.5
4.11	1	1	411.8	24.5	616.5	50.7	52.6	665.3	96.4	66.3
		2	413.0	22.1	620.1	41.9	50.2	670.0	92.1	66.2
		3	411.8	27.0	623.6	53.5	52.6	665.3	124.8	52.3
		5	397.0	34.5	615.3	38.7	40.7	667.6	80.2	78.5
	2	1	406.8	22.1	612.9	320.0	45.5	660.5	623.6	59.2
		2	408.0	22.1	618.8	148.2	67.0	662.9	327.6	59.4
		3	406.8	24.6	618.8	83.4	95.8	662.9	178.4	63.9
		4	408.6	17.2	621.8	155.2	74.2	664.6	328.5	71.0
		5	402.5	24.6	606.3	216.7	45.5	657.5	271.5	71.1
		6	407.4	17.2	611.0	117.9	33.5	658.7	130.2	64.0
		7	408.6	14.7	618.2	29.3	45.4	663.4	95.0	42.8
	3	1	393.4	39.4	-	-	-	653.5	99.4	68.7
		2	398.3	34.4	603.4	116.7	33.5	661.8	209.7	66.6
		3	409.4	17.2	610.6	134.5	31.1	661.8	189.6	45.2
		4	408.6	17.2	614.6	74.5	47.9	662.2	164.7	57.1
		5	404.9	19.7	607.5	29.5	50.3	659.9	73.2	64.2
4.86	1	1	385.9	29.6	-	-	-	662.9	29.7	122.9
		2	404.4	24.6	-	-	-	665.3	112.7	61.8
		3	389.6	34.5	616.5	27.6	64.6	666.5	60.1	66.6
		4	395.8	34.5	-	-	-	668.8	67.7	78.5
	2	1	393.3	34.4	612.9	15.1	148.9	664.1	20.4	111.1
		2	389.6	32.1	-	-	-	667.7	63.1	76.1
		3	389.6	32.1	623.7	19.2	64.6	666.5	49.9	66.6
		4	390.9	44.4	-	-	-	671.2	35.6	52.2
		5	389.6	42.0	617.7	17.2	127.1	666.5	40.1	63.9
	3	1	395.8	32.0	-	-	-	661.7	53.8	85.2
		2	400.7	27.0	615.3	45.3	67.0	655.8	78.2	82.9
	4	1	399.5	32.0	611.7	33.5	136.9	665.8	51.0	87.6
		2	393.3	32.1	627.2	29.3	74.1	665.3	51.4	75.7
		3	408.1	22.1	617.7	57.8	55.0	664.1	115.1	71.4
	5	1	393.3	22.1	-	-	-	666.5	74.3	83.2
	6	1	394.6	39.4	609.3	29.8	79.1	660.6	46.1	73.4
		2	403.2	29.5	622.5	33.0	69.4	662.9	71.1	66.6
		3	404.4	24.6	612.9	44.6	69.5	659.4	80.1	78.1
	7	1	408.1	24.6	623.7	29.0	71.8	664.1	69.0	57.1
		2	400.7	32.0	612.9	63.5	64.7	660.6	112.9	78.1
		3	400.7	34.4	605.8	62.0	57.5	659.4	95.8	82.8
		4	402.0	29.5	609.3	50.2	47.9	660.6	117.4	71.4

*The colour of the cell represents classification of the spectra; goethite (blue), intermediate (orange) and hematite (red).

Table I3 Goethite target Raman data before impact.

Spectrum	Spectrum Classification	Feature A	
		Peak Position (cm^{-1})	Peak Width (cm^{-1})
1	Goethite	383.0	17.3
2	Goethite	383.0	17.3
3	Goethite	383.0	19.7
4	Goethite	383.0	19.7
5	Goethite	381.7	17.3
6	Goethite	381.7	17.3
7	Goethite	381.7	17.3
8	Goethite	381.7	17.3
9	Goethite	381.7	17.3
10	Goethite	381.7	17.3
11	Goethite	383.0	17.3
12	Goethite	395.3	14.8
13	Goethite	383.0	17.3
14	Goethite	383.0	17.3
15	Goethite	383.0	17.3
16	Goethite	383.0	17.3
17	Goethite	383.0	17.3
18	Goethite	383.0	19.7
19	Goethite	383.0	19.8
20	Goethite	383.0	19.8
21	Goethite	383.0	17.3
22	Goethite	396.5	12.3
23	Goethite	384.2	19.8
24	Goethite	383.0	17.3
25	Goethite	384.2	19.8
26	Goethite	383.0	17.3
27	Goethite	396.5	14.8
28	Goethite	383.0	17.3
29	Goethite	396.5	12.3
30	Goethite	383.0	17.3

Table I4 Goethite target Raman data after impact.

	Spectrum	Spectrum Classification	Feature A	
			Peak Position (cm^{-1})	Peak Width (cm^{-1})
Map1	1	Goethite	383.7	17.3
	2	Goethite	384.9	24.7
	3	Goethite	393.6	52.9
	4	Goethite	383.7	19.8
	5	Goethite	383.7	19.8
	6	Goethite	383.7	22.3
	7	Goethite	383.7	19.8
	8	Goethite	383.7	19.8
	9	Goethite	384.9	22.2
	10	Goethite	382.4	14.8
	11	Goethite	383.7	17.3
	12	Goethite	383.7	19.8
	13	Goethite	384.9	19.8
	14	Goethite	383.7	17.3
	15	Goethite	383.7	17.3
	16	Goethite	383.7	17.3
	17	Goethite	383.7	17.3
	18	Goethite	383.7	19.8
	19	Goethite	383.7	17.3
	20	Goethite	383.7	19.8
	21	Goethite	383.7	17.3
	22	Goethite	383.7	19.8
	23	Goethite	396.0	14.8
	24	Goethite	383.7	17.3
	25	Goethite	383.7	19.8
	26	Goethite	383.7	17.3
	27	Goethite	383.7	19.8
	28	Goethite	383.7	17.3
	29	Goethite	383.7	19.8
	30	Goethite	383.7	17.3
Map 2	1	Goethite	387.9	19.8
	2	Goethite	387.9	19.8
	3	Goethite	387.9	19.8
	4	Goethite	386.7	17.3
	5	Goethite	400.2	12.3
	6	Goethite	386.7	17.3
	7	Goethite	386.7	17.3
	8	Goethite	386.7	17.3

	9	Goethite	386.7	17.3
	10	Goethite	386.7	17.3
	11	Goethite	386.7	19.8
	12	Goethite	386.7	19.8
	13	Goethite	386.7	17.3
	14	Goethite	400.2	12.3
	15	Goethite	386.7	17.3
	16	Goethite	386.7	17.3
	17	Goethite	386.7	17.3
	18	Goethite	399.0	14.8
	19	Goethite	386.7	19.8
	20	Goethite	386.7	17.3
	21	Goethite	386.7	19.8
	22	Goethite	399.0	14.8
	23	Goethite	386.7	19.7
	24	Goethite	386.7	19.8
	25	Goethite	386.7	19.8
	26	Goethite	386.7	19.8
	27	Goethite	386.7	19.8
	28	Goethite	386.7	19.7
	29	Goethite	386.7	17.3
	30	Goethite	386.7	17.3
Map 3	1	Goethite	386.6	17.3
	2	Goethite	386.6	17.3
	3	Goethite	386.6	17.3
	4	Goethite	386.6	17.3
	5	Goethite	386.6	19.7
	6	Goethite	386.6	17.3
	7	Goethite	386.6	17.3
	8	Goethite	386.6	17.3
	9	Goethite	386.6	17.3
	10	Goethite	386.6	17.3
	11	Goethite	385.4	17.3
	12	Goethite	386.6	19.8
	13	Goethite	385.4	14.8
	14	Goethite	385.4	14.8
	15	Goethite	385.4	17.3
	16	Goethite	385.4	14.8
	17	Goethite	385.4	14.8
	18	Goethite	386.6	19.8
	19	Goethite	386.6	19.8
	20	Goethite	385.4	17.3

	21	Goethite	385.4	17.3
	22	Goethite	385.4	17.3
	23	Goethite	385.4	17.3
	24	Goethite	398.9	14.8
	25	Goethite	385.4	17.3
	26	Goethite	385.4	17.3
	27	Goethite	385.4	17.3
	28	Goethite	385.4	17.3
	29	Goethite	385.4	17.3
	30	Goethite	386.6	17.3
Individual spectra	1	Goethite	387.2	29.6
	2	Goethite	384.7	17.3
	3	Goethite	388.4	29.6
	4	Goethite	384.7	17.3

Appendix J - Gypsum Projectile Target Plates

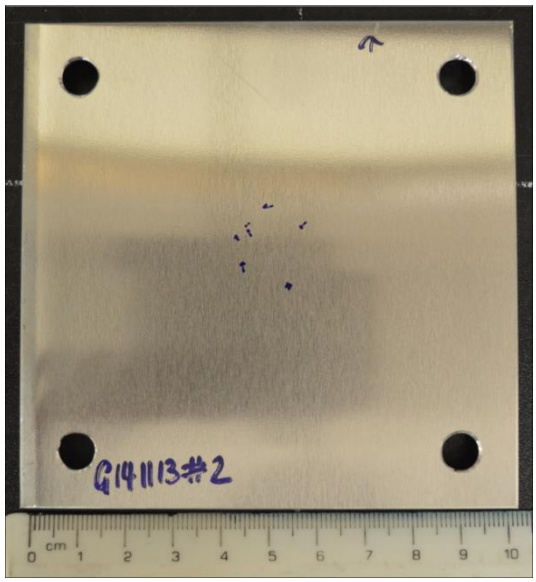

Figure J1 Target plate for semi-hydrous PoP powder projectile, shot I.D. G141113#2 (4.26 km s^{-1}).

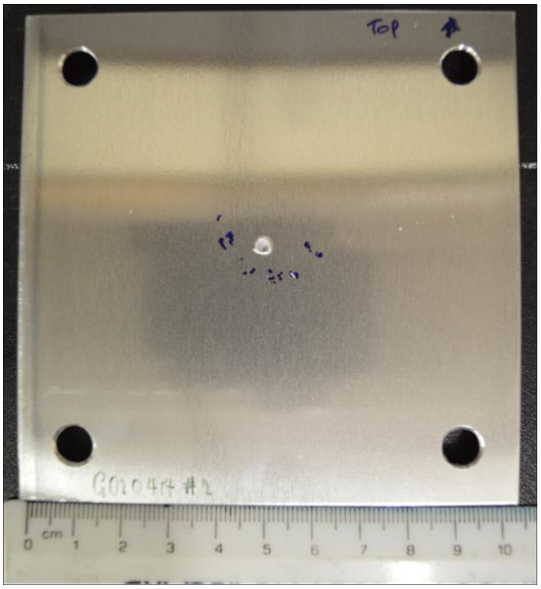

Figure J2 Target plate for hydrous PoP powder projectile, shot I.D. G020414#2 (4.57 km s^{-1}).

Figure J3 Target plate for hydrous PoP powder projectile, shot I.D. G160414#2 (4.38 km s^{-1}).

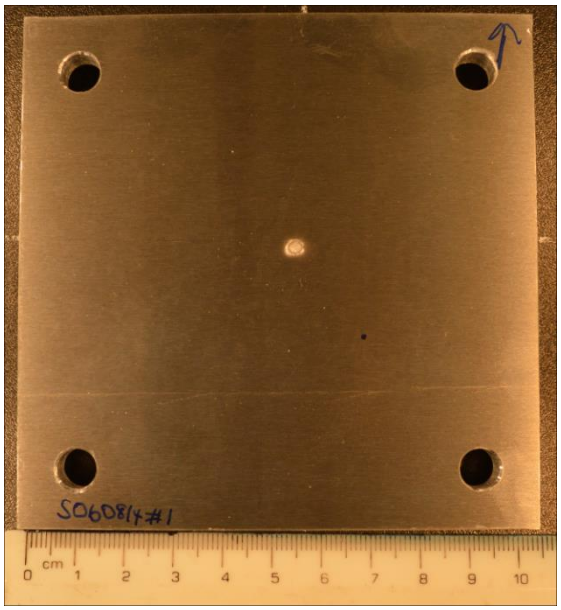

Figure J4 Target plate for natural gypsum projectile, shot I.D. S060814#1 (0.97 km s^{-1}).

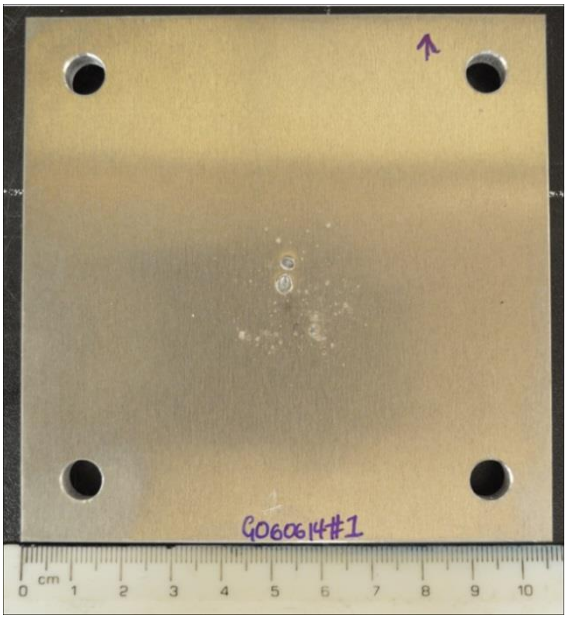

Figure J5 Target plate for natural gypsum projectile, shot I.D. G060614#1 (2.09 km s^{-1}).

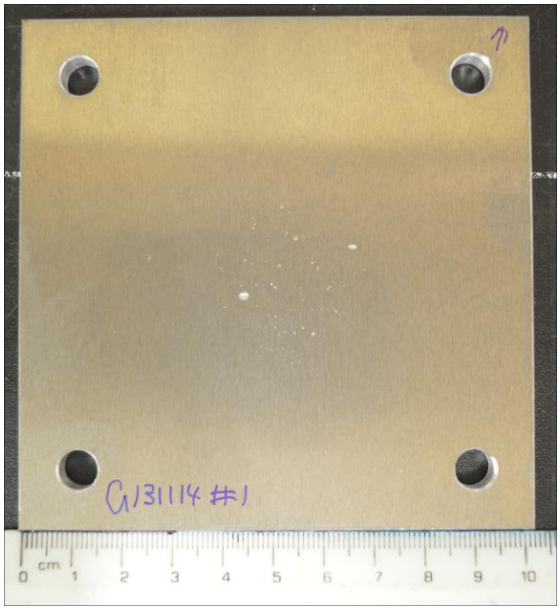

Figure J6 Target plate for natural gypsum projectile, shot I.D. G131114#1 (2.21 km s^{-1}).

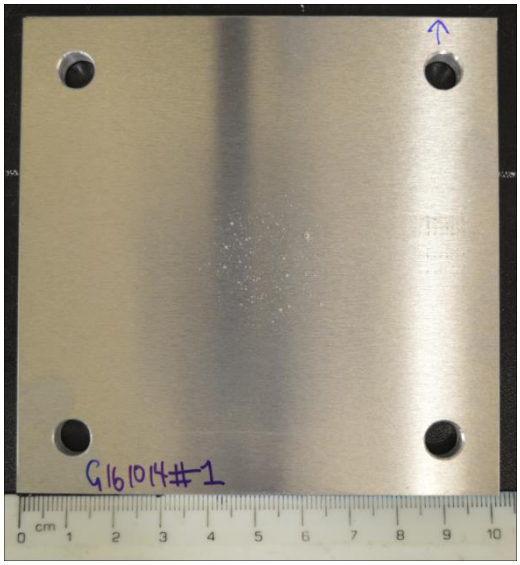

Figure J7 Target plate for natural gypsum projectile, shot I.D. G161014#1 (3.97 km s^{-1}).

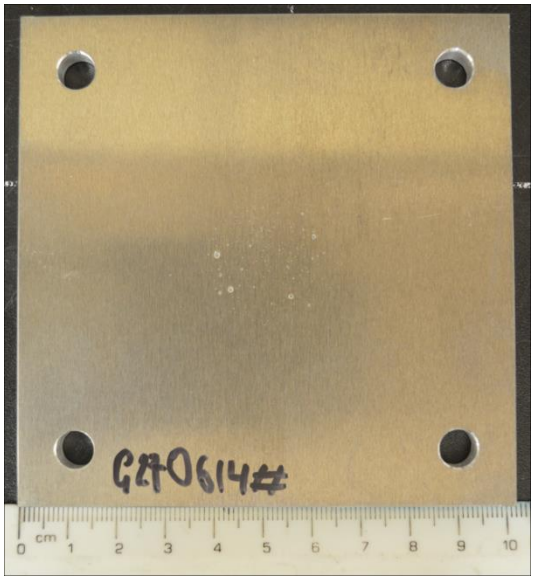

Figure J8 Target plate for natural gypsum projectile, shot I.D. G270614#1 (4.09 km s^{-1}).

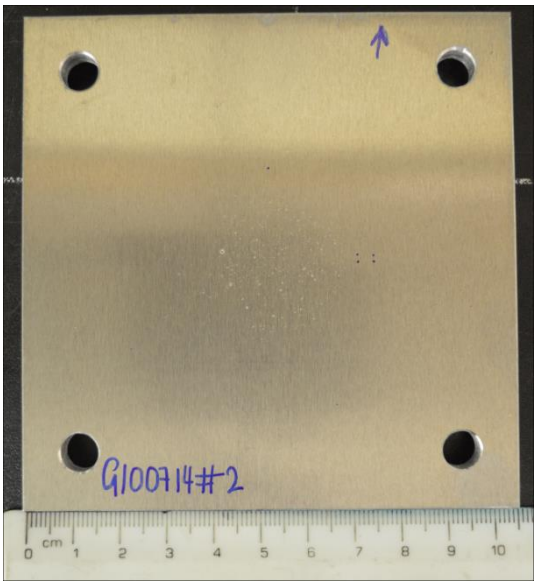

Figure J9 Target plate for natural gypsum projectile, shot I.D. G100714#2 (4.90 km s^{-1}).

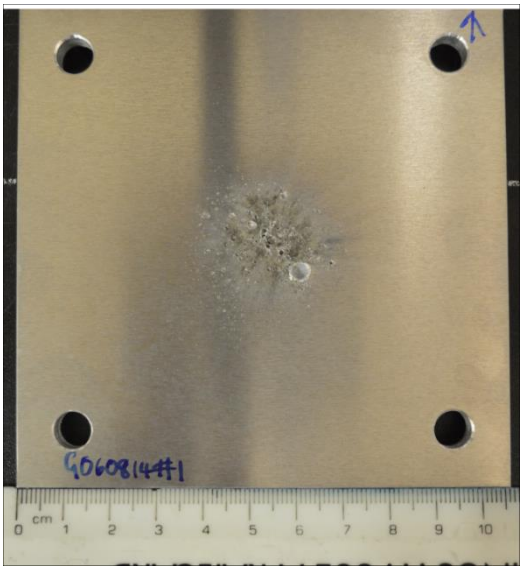

Figure J10 Target plate for natural gypsum projectile, shot I.D. G060814#1 (5.83 km s^{-1}).

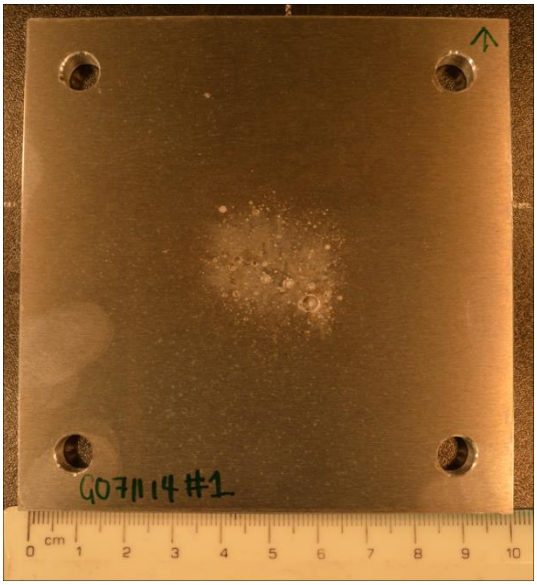

Figure J11 Target plate for natural gypsum projectile, shot I.D. G071114#1 (5.86 km s^{-1}).

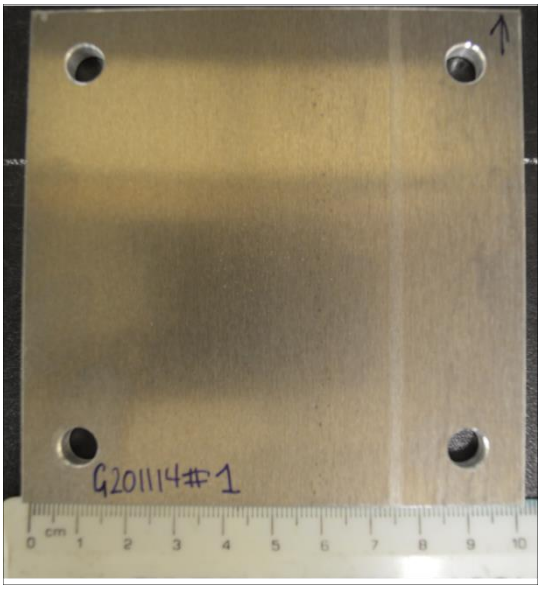

Figure J12 Target plate for anhydrite projectile, shot I.D. G201114#1 (3.88 km s^{-1}).

Appendix K Gypsum Projectile Raman Data

Table K1 Gypsum and anhydrite prjectiles Raman shot data for U1 and U2 (2) SO_4 modes.

Velocity (km s^{-1})	Crater	Spectrum	After impact				Change in peak positions/widths			
			U1		U2 (2)		U1		U2 (2)	
			Position (cm^{-1})	Width (cm^{-1})	Position (cm^{-1})	Width (cm^{-1})	Position (cm^{-1})	Width (cm^{-1})	Position (cm^{-1})	Width (cm^{-1})
0.97	1	1*	1014.5	13.2	492.3	21.0	8.1	6.6	-0.1	10.2
		2*	1016.2	9.9	497.5	14.0	9.8	3.3	5.1	3.2
		3*	1016.2	9.9	497.5	14.0	9.8	3.3	5.1	3.1
		4*	1016.2	13.2	495.8	17.5	9.8	6.6	3.4	6.7
		5*	1016.2	13.2	497.5	14.0	9.8	6.6	5.1	3.1
		6*	1014.5	13.2	497.5	17.5	8.1	6.6	5.1	6.6
		7*	1016.2	9.9	497.5	14.0	9.8	3.3	5.1	3.1
		8*	1016.2	9.9	497.5	14.0	9.8	3.3	5.1	3.1
		9*	1016.2	9.9	497.5	17.5	9.8	3.3	5.1	6.6
		10*	1016.2	9.9	497.5	17.5	9.8	3.3	5.1	6.6
		11*	1016.2	6.6	497.5	14.0	9.8	0.0	5.1	3.1
		12*	1014.5	9.9	494.0	21.0	8.1	3.3	1.6	10.2
		13*	1014.5	13.2	495.8	17.5	8.1	6.6	3.4	6.7
		14*	1012.9	16.5	492.3	21.0	6.5	9.9	-0.1	10.2
		15*	1014.5	9.9	495.8	17.5	8.1	3.3	3.4	6.7
		16*	1014.5	9.9	495.8	17.5	8.1	3.3	3.4	6.7
		17*	1014.5	16.5	488.8	17.5	8.1	9.9	-3.6	6.7
		18*	1014.5	9.9	495.8	14.0	8.1	3.3	3.4	3.2
		19*	1014.5	13.2	495.8	17.5	8.1	6.6	3.4	6.7
		20*	1011.2	13.2	495.8	21.0	4.8	6.6	3.4	10.2
		21*	1014.5	9.9	497.5	17.5	8.1	3.3	5.1	6.6
		22*	1007.9	16.5	495.8	17.5	1.5	9.9	3.4	6.7
2.09	1	1	1017.9	16.5	-	-	10.4	8.0	-	-
		2	1017.9	16.5	-	-	10.4	8.0	-	-
		3	1016.3	9.9	-	-	8.8	1.4	-	-
		4	1016.3	13.2	-	-	8.8	4.7	-	-
	3	1	1014.6	23.1	-	-	7.1	14.6	-	-
		2	1021.2	19.8	-	-	13.7	11.3	-	-
		3	1014.6	13.2	-	-	7.1	4.7	-	-
		4	1014.6	16.5	-	-	7.1	8.0	-	-
	4	1	1014.6	16.5	-	-	7.1	8.0	-	-
		2	1014.6	26.4	-	-	7.1	17.9	-	-
		3	1014.6	36.3	-	-	7.1	27.7	-	-
	5	1	1014.6	13.2	-	-	7.1	4.7	-	-
		2	1014.6	13.2	-	-	7.1	4.7	-	-
		3	1014.6	13.2	-	-	7.1	4.7	-	-
		4	1014.6	13.2	-	-	7.1	4.7	-	-
	6	1	1016.3	13.2	-	-	8.8	4.7	-	-

		2	1017.9	13.2	-	-	10.4	4.7	-	-
		3	1016.3	13.2	-	-	8.8	4.7	-	-
		4	1016.3	13.2	-	-	8.8	4.7	-	-
2.21	1	1	1015.2	16.5	-	-	7.2	9.5	-	-
		2	1015.2	16.5	-	-	7.2	9.5	-	-
		3	1014.5	16.5	-	-	6.5	9.5	-	-
		4	1012.8	19.8	-	-	4.9	12.8	-	-
	2	1	1014.5	13.2	-	-	6.5	6.2	-	-
		2	1014.6	16.5	-	-	6.7	9.5	-	-
	3	1	1012.8	19.8	-	-	4.9	12.8	-	-
		2	1014.5	23.1	-	-	6.5	16.1	-	-
		3	1014.5	13.2	-	-	6.5	6.2	-	-
	4	1	1014.5	16.5	-	-	6.5	9.5	-	-
		2	1014.5	16.5	-	-	6.5	9.5	-	-
		3	1014.5	23.1	-	-	6.5	16.1	-	-
	5	1	1014.5	16.5	-	-	6.5	9.5	-	-
		2	1016.1	13.2	-	-	8.2	6.2	-	-
		3	1014.5	13.2	-	-	6.5	6.2	-	-
	6	1	1014.5	13.2	-	-	6.5	6.2	-	-
		2	1014.5	13.2	-	-	6.5	6.2	-	-
		3	1014.6	13.2	-	-	6.7	6.2	-	-
		4	1014.5	9.9	-	-	6.5	2.9	-	-
	7	1	1014.5	13.2	-	-	6.5	6.2	-	-
		2	1014.5	13.2	-	-	6.5	6.2	-	-
		3	1014.5	13.2	-	-	6.5	6.2	-	-
	8	1	1012.8	16.5	-	-	4.9	9.5	-	-
		2	1014.5	16.5	-	-	6.5	9.5	-	-
	9	1	1014.5	13.2	-	-	6.5	6.2	-	-
		2	1016.1	16.5	-	-	8.2	9.5	-	-
		3	1016.1	19.8	-	-	8.2	12.8	-	-
		4	1012.8	23.1	-	-	4.9	16.1	-	-
	10	1	1016.1	13.2	-	-	8.2	6.2	-	-
		2	1016.1	13.2	-	-	8.2	6.2	-	-
		3	1014.5	16.5	-	-	6.5	9.5	-	-
		4	1012.8	16.5	-	-	4.9	9.5	-	-
	11	1	1014.5	13.2	-	-	6.5	6.2	-	-
	12	3	1014.5	16.5	-	-	6.5	9.5	0.6	9.2
		4	1012.8	23.1	493.9	21.0	4.9	16.1	-1.2	19.7
		5	1016.1	19.8	492.2	31.5	8.2	12.8		
	14	1	1014.5	13.2	-	-	6.5	6.2	0.6	5.7
		2	1014.5	16.5	493.9	17.5	6.5	9.5	-	-
		3	1016.1	9.9	-	-	8.2	2.9	-	-
	15	1	1014.5	19.8	-	-	6.5	12.8	-1.2	5.7
		2*	1014.5	13.2	492.2	17.5	6.5	6.2	-	-
	16	1	1014.5	16.5	-	-	6.5	9.5	-	-

		2	1014.5	13.2	-	-	6.5	6.2	-	-
	17	2	1014.5	16.5	-	-	6.5	9.5	-	-
	18	1	1007.9	19.8	-	-	-0.1	12.8	-	-
	19	1	1014.5	13.2	-	-	6.5	6.2	-	-
		2	1012.8	16.5	-	-	4.9	9.5	2.3	9.2
	20	1*	1014.5	13.2	495.7	21.0	6.5	6.2	-	-
		2	1014.5	16.5	-	-	6.5	9.5	0.6	12.7
		3*	1016.1	9.9	493.9	24.5	8.2	2.9	-	-
	21	1	1016.1	19.8	-	-	8.2	12.8	-	-
	22	1	1014.5	16.5	-	-	6.5	9.5	-	-
		2	1012.8	19.8	-	-	4.9	12.8	-	-
	23	1	1011.2	16.5	-	-	3.2	9.5	-	-
	24	1	1014.5	9.9	-	-	6.5	2.9	-	-
	25	1	1014.5	19.8	-	-	6.5	12.8	-	-
	26	1	1014.5	19.8	-	-	6.5	12.8	-	-
	27	1	1026.0	13.2	-	-	18.1	6.2	-	-
	28	1	1014.5	13.2	-	-	6.5	6.2	-	-
	29	1	1014.5	16.5	-	-	6.5	9.5	-	-
	30	1	1014.5	13.2	-	-	6.5	6.2	-	-
4.09	1	1*	1016.3	13.2	499.4	14.0	9.0	5.2	5.7	0.0
		2*	1014.6	16.5	497.6	21.0	7.4	8.5	4.0	7.0
		3*	1013.0	16.5	497.6	17.5	5.7	8.5	4.0	3.5
		4*	1016.3	13.2	495.9	21.0	9.0	5.2	2.2	7.0
	2	1	1016.3	9.9	-	-	9.0	1.9	-	-
		2	1016.3	19.8	-	-	9.0	11.8	-	-
		3	1014.6	13.2	-	-	7.4	5.2	-	-
		4	1016.3	9.9	-	-	9.0	1.9	-	-
	3	1	1014.6	16.5	-	-	7.4	8.5	-	-
		2	1014.6	9.9	-	-	7.4	1.9	-	-
		3	1014.6	13.2	-	-	7.4	5.2	-	-
		4	1016.3	9.9	-	-	9.0	1.9	-	-
	4	1	1014.6	9.9	-	-	7.4	1.9	-	-
		2	1016.3	9.9	-	-	9.0	1.9	-	-
		4	1014.6	9.9	-	-	7.4	1.9	-	-
	5	1	1016.3	9.9	-	-	9.0	1.9	-	-
		2	1016.3	13.2	-	-	9.0	5.2	-	-
		3	1016.3	9.9	-	-	9.0	1.9	-	-
4.90	1	1	1017.9	6.6	-	-	9.5	-5.8	-	-
		2	1014.6	19.8	-	-	6.2	7.4	-	-
		3	1016.3	13.2	-	-	7.9	0.8	-	-
		4	1017.9	13.2	-	-	9.5	0.8	-	-
	3	1	1016.3	13.2	-	-	7.9	0.8	-	-
		2	1016.3	13.2	-	-	7.9	0.8	-	-
		3*	1016.3	9.9	497.6	17.5	7.9	-2.5	3.1	5.1
		4	1016.3	9.9	-	-	7.9	-2.5	-	-

	4	1	1014.6	13.2	-	-	6.2	0.8	-	-
		2	1016.3	13.2	-	-	7.9	0.8	-	-
		3	1016.3	13.2	-	-	7.9	0.8	-	-
		4	1016.3	13.2	-	-	7.9	0.8	-	-
3.97	1	1	1012.9	19.8	-	-	6.5	13.2	-	-
		2	1014.5	13.2	-	-	8.1	6.6	-	-
		3	1014.5	13.2	-	-	8.1	6.6	-	-
		4	1012.9	19.8	-	-	6.5	13.2	-	-
	2	1*	1016.2	9.9	497.5	21.0	9.8	3.3	5.9	10.5
		2	1016.2	13.2	-	-	9.8	6.6	-	-
	3	1	1014.5	13.2	-	-	8.1	6.6	-	-
		2	1017.3	13.2	-	-	10.9	6.6	-	-
		3	1015.7	13.2	-	-	9.3	6.6	-	-
	4	1	1015.7	9.9	-	-	9.3	3.3	-	-
		2	1015.7	13.2	-	-	9.3	6.6	-	-
		3	1015.7	13.2	-	-	9.3	6.6	-	-
	5	1	1015.7	13.2	-	-	9.3	6.6	-	-
	7	1	1015.7	13.2	-	-	9.3	6.6	-	-
		2	1015.7	13.2	-	-	9.3	6.6	-	-
		3*	1015.7	9.9	497.0	17.5	9.3	3.3	5.3	7.0
	8	1	1015.7	13.2	-	-	9.3	6.6	-	-
		2	1015.7	13.2	-	-	9.3	6.6	-	-
		3	1015.7	13.2	-	-	9.3	6.6	-	-
	9	2	1017.3	13.2	-	-	10.9	6.6	-	-
5.83	1	1*	1014.7	13.2	495.9	21.0	6.8	6.6	2.3	8.9
		2	1014.7	16.5	-	-	6.8	9.9	-	-
		3	1012.9	16.5	-	-	5.0	9.9	-	-
		4	1004.6	42.9	-	-	-3.3	36.3	-	-
		5	1016.2	9.9	-	-	8.3	3.3	-	-
		6	1014.5	13.2	497.5	14.0	6.6	6.6	3.9	1.9
		7	1014.5	13.2	-	-	6.6	6.6	-	-
	2	2*	1016.2	13.2	-	-	8.3	6.6	-	-
		3	1016.2	9.9	497.5	14.0	8.3	3.3	3.9	1.9
		4	1014.5	16.5			6.6	9.9		
	3	1*	1014.5	13.2	492.3	24.5	6.6	6.6	-1.4	12.4
		2	1014.5	16.5	-	-	6.6	9.9	-	-
		3	1014.5	16.5	-	-	6.6	9.9	-	-
		4	1014.5	13.2	-	-	6.6	6.6	-	-
		5	1016.2	9.9	494.0	14.0	8.3	3.3	0.3	1.9
	4	1*	1014.5	9.9	492.3	24.5	6.6	3.3	-1.4	12.4
		2	1014.5	19.8	-	-	6.6	13.2	-	-
		3	1009.6	16.5	494.0	21.0	1.7	9.9	0.3	8.9
		4	1014.5	9.9	-	-	6.6	3.3	-	-
	5	1	1014.5	13.2	-	-	6.6	6.6	-	-
5.86	1	1*	1017.8	9.9	499.3	17.5	10.1	3.3	5.6	5.2

2	1	1014.5	9.9	480.0	28.1	6.8	3.3	-13.7	15.9
	3*	1014.5	13.2			6.8	6.6		
3	1	1016.2	9.9	495.8	17.5	8.4	3.3	2.1	5.3
	2	1016.2	13.2			8.4	6.6		
4	1	1016.2	13.2			8.4	6.6		
	2	1016.2	9.9	497.5	17.5	8.4	3.3	3.8	5.2
	3	1014.5	13.2			6.8	6.6		
5	1*	1016.2	9.9	497.5	28.0	8.4	3.3	3.8	15.8
	2*	1016.2	9.9	497.5	17.5	8.4	3.3	3.8	5.2
6	1	1016.2	13.2	-	-	8.4	6.6	-	-
7	1*	1016.2	13.2	495.8	21.0	8.4	6.6	2.1	8.8
	2	1012.9	16.5	-	-	5.1	9.9	-	-
	3	1014.5	16.5	499.3	21.0	6.8	9.9	5.6	8.7
9	1	1016.2	13.2	-	-	8.4	6.6	-	-
	2	1016.2	13.2	-	-	8.4	6.6	-	-
	3	1016.2	13.2	-	-	8.4	6.6	-	-
10	1	1017.8	9.9	-	-	10.1	3.3	-	-
	2	1016.2	13.2	-	-	8.4	6.6	-	-
	3	1017.8	9.9	-	-	10.1	3.3	-	-
11	1	1016.2	13.2	-	-	8.4	6.6	-	-
	2	1016.2	13.2	-	-	8.4	6.6	-	-
	3	1014.5	13.2	-	-	6.8	6.6	-	-
12	1	1016.2	16.5	-	-	8.4	9.9	-	-
	2*	1016.2	9.9	487.0	24.6	8.4	3.3	-6.7	12.3
13	1	1016.2	16.5	-	-	8.4	9.9	-	-
	2	1016.2	13.2	-	-	8.4	6.6	-	-
	3	1016.2	9.9	-	-	8.4	3.3	-	-
14	1	1014.5	13.2	-	-	6.8	6.6	-	-
15	1	1016.2	9.9	-	-	8.4	3.3	-	-
	2	1016.2	13.2	-	-	8.4	6.6	-	-
	3	1017.8	13.2	-	-	10.1	6.6	-	-
16	1	1014.5	16.5	-	-	6.8	9.9	-	-
	2	1016.2	13.2	-	-	8.4	6.6	-	-
	3	1016.2	13.2	-	-	8.4	6.6	-	-
17	1	1014.5	13.2	-	-	6.8	6.6	-	-
18	1	1016.2	13.2	-	-	8.4	6.6	-	-
	2*	1016.2	9.9	497.5	17.5	8.4	3.3	3.8	5.2
19	1	1016.2	13.2			8.4	6.6		
	2*	1016.2	13.2	494.0	28.0	8.4	6.6	0.3	15.8
	3	1016.2	13.2	-	-	8.4	6.6	-	-
21	1	1016.2	9.9	495.8	21.0	8.4	3.3	2.1	8.8
	2*	1016.2	13.2	495.8	21.0	8.4	6.6	2.1	8.8
	3*	1016.2	9.9	-	-	8.4	3.3	-	-
	4	1016.2	13.2	-	-	8.4	6.6	-	-
22	1	1016.2	13.2	-	-	8.4	6.6	-	-

		2	1017.8	9.9	-	-	10.1	3.3	-	-
	23	1	1014.5	19.8	-	-	6.8	13.2	-	-
		2	1016.2	9.9	-	-	8.4	3.3	-	-
	24	1	1016.2	13.2	-	-	8.4	6.6	-	-
		2	1014.5	19.8	-	-	6.8	13.2	-	-
		3	1016.2	9.9	497.5	21.0	8.4	3.3	3.8	8.7
		4	1016.2	13.2	497.5	14.0	8.4	6.6	3.8	1.7
3.88 (Anhydrite)	1	1	1017.8	6.6	499.3	14.0	-1.8	-0.4	-1.9	1.3
		2	1019.5	6.6	501.0	17.5	-0.1	-0.4	-0.1	4.8
		3	1019.5	9.9	-	-	-0.1	2.9	-	-
	2	1	1019.5	13.2	-	-	-0.1	6.2	-	-
		2	1020.6	9.9	-	-	1.0	2.9	-	-
	3	1	1019.0	9.9	-	-	-0.6	2.9	-	-
		2	1019.0	9.9	500.5	14.0	-0.6	2.9	-0.7	1.3
		3	1019.0	9.9	-	-	-0.6	2.9	-	-
	4	1	1017.3	6.6	498.8	14.0	-2.3	-0.4	-2.4	1.3
		2	1019.0	6.6	500.5	10.5	-0.6	-0.4	-0.7	-2.2
	5	1	1019.0	13.2	-	-	-0.6	6.2	-	-
		2	1019.0	9.9	500.5	17.5	-0.6	2.9	-0.7	4.8
	6	1	1019.0	6.6	500.5	17.5	-0.6	-0.4	-0.7	4.8
		2	1017.3	9.9	500.5	14.0	-2.3	2.9	-0.7	1.3
		3	1019.0	6.6	-	-	-0.6	-0.4	-	-
	7	1	1019.0	13.2	-	-	-0.6	6.2	-	-
	8	1	1019.0	6.6	500.5	10.5	-0.6	-0.4	-0.7	-2.2
	9	1	1019.0	9.9	-	-	-0.6	2.9	-	-
	10	1	1019.0	6.6	502.3	10.5	-0.6	-0.4	1.1	-2.2
		2	1019.0	9.9	-	-	-0.6	2.9	-	-
	11	1	1019.0	9.9	500.5	14.0	-0.6	2.9	-0.7	1.3
		2	1019.0	13.2	-	-	-0.6	6.2	-	-
	12	1	1019.0	9.9	500.5	10.5	-0.6	2.9	-0.7	-2.2
		2	1019.0	6.6	-	-	-0.6	-0.4	-	-
	13	2	1019.0	6.6	500.5	14.0	-0.6	-0.4	-0.7	1.3
		3	1019.0	6.6	500.5	10.5	-0.6	-0.4	-0.7	-2.2
	14	1	1019.0	9.9	-	-	-0.6	2.9	-	-
		3	1017.3	6.6	498.8	17.5	-2.3	-0.4	-2.4	4.8
		4	1019.0	9.9	-	-	-0.6	2.9	-	-
	15	1	1019.0	9.9	500.5	14.0	-0.6	2.9	-0.7	1.3
		2	1017.3	13.2	-	-	-2.3	6.2	-	-
		3	1017.3	13.2	-	-	-2.3	6.2	-	-
	16	1	1019.0	9.9	500.5	14.0	-0.6	2.9	-0.7	1.3
		2	1019.0	6.6	500.5	10.5	-0.6	-0.4	-0.7	-2.2
		3	1017.3	16.5	-	-	-2.3	9.5	-	-
	17	1	1019.0	6.6	498.8	17.5	-0.6	-0.4	-2.4	4.8
		2	1017.3	6.6	497.0	17.5	-2.3	-0.4	-4.2	4.8
		3	1017.3	6.6	498.8	14.0	-2.3	-0.4	-2.4	1.3

18	1	1019.0	9.9	500.5	14.0	-0.6	2.9	-0.7	1.3
	3	1019.0	6.6	498.8	14.0	-0.6	-0.4	-2.4	1.3
19	1	1019.0	6.6	500.5	14.0	-0.6	-0.4	-0.7	1.3
	2	1019.0	6.6	500.5	14.0	-0.6	-0.4	-0.7	1.3
20	1	1019.0	6.6	498.8	17.5	-0.6	-0.4	-2.4	4.8
	2	1019.0	6.6	498.8	17.5	-0.6	-0.4	-2.4	4.8
	3	1019.0	9.9	500.5	14.0	-0.6	2.9	-0.7	1.3
21	1	1019.0	6.6	500.5	10.5	-0.6	-0.4	-0.7	-2.2
	2	1019.0	9.9	500.5	14.0	-0.6	2.9	-0.7	1.3
22	1	1019.0	9.9	500.5	14.0	-0.6	2.9	-0.7	1.3
23	1	1019.0	6.6	500.5	14.0	-0.6	-0.4	-0.7	1.3
24	1	1019.0	6.6	498.8	21.0	-0.6	-0.4	-2.4	8.3
	2	1019.0	9.9	-	-	-0.6	2.9	-	-
	3	1019.0	6.6	500.5	10.5	-0.6	-0.4	-0.7	-2.2
25	1	1019.0	6.6	500.5	10.5	-0.6	-0.4	-0.7	-2.2
	2	1019.0	13.2	-	-	-0.6	6.2	-	-
26	1	1019.0	6.6	500.5	14.0	-0.6	-0.4	-0.7	1.3
	2	1019.0	9.9	-	-	-0.6	2.9	-	-

*****Raman spectrum where all SO_4 peaks were detected for gypsum projectiles. All of these spectra showed an anhydrite spectrum.

N.B. All spectra from the anhydrite projectile (3.88 km s^{-1}) had an anhydrite spectrum after impact.

Appendix L –EDX of Gypsum Projectile Craters

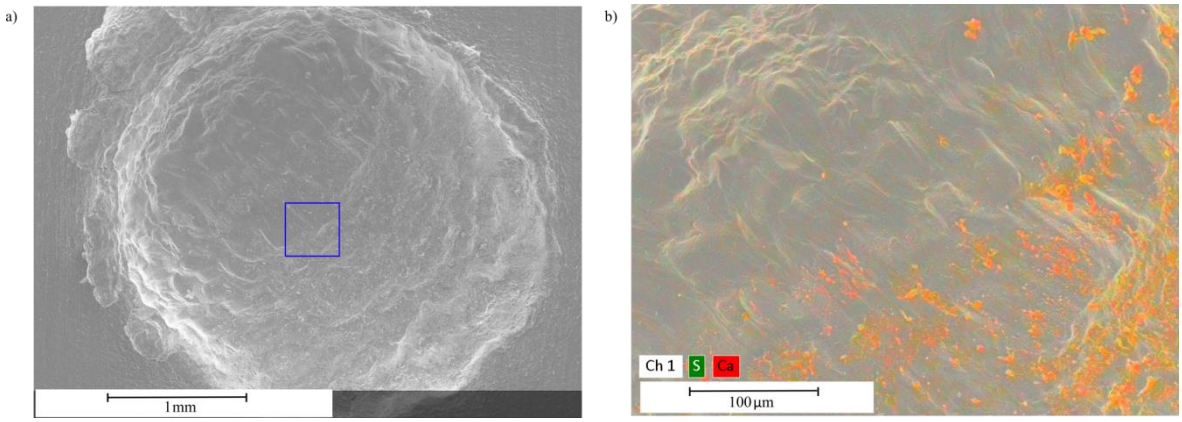

Figure L1 Secondary electron images of main crater from S060814#1(a); the blue box highlights area that is seen in image b. Image b is a secondary electron image from inside the crater and has been overlain with EDX data from sulphur (green) and calcium (red). The areas that appear orange represent the location of both sulphur and calcium, thus indicating anhydrite.

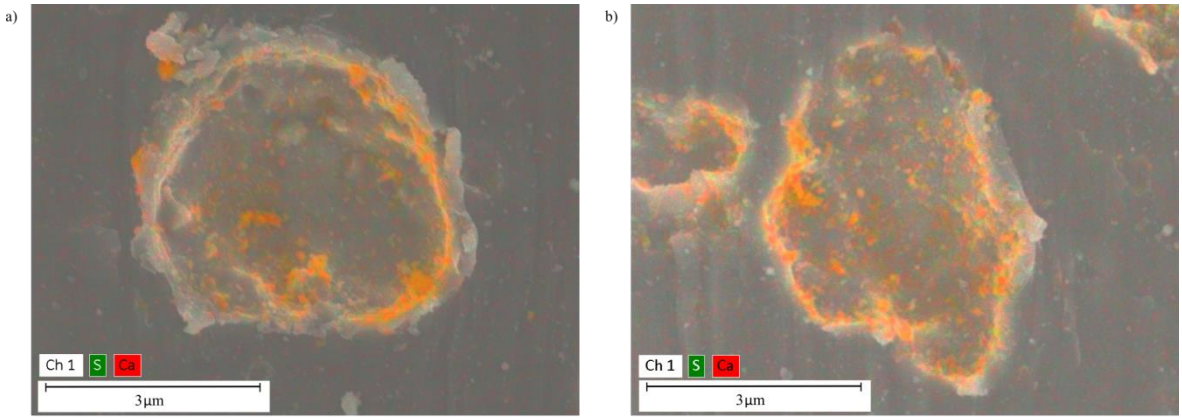

Figure L2 Secondary electron images of two craters from G060614#1 (2.09 km s^{-1}). The image has been overlain with EDX data from sulphur (green) and calcium (red). The areas that appear orange represent the location of both sulphur and calcium, thus indicating anhydrite.

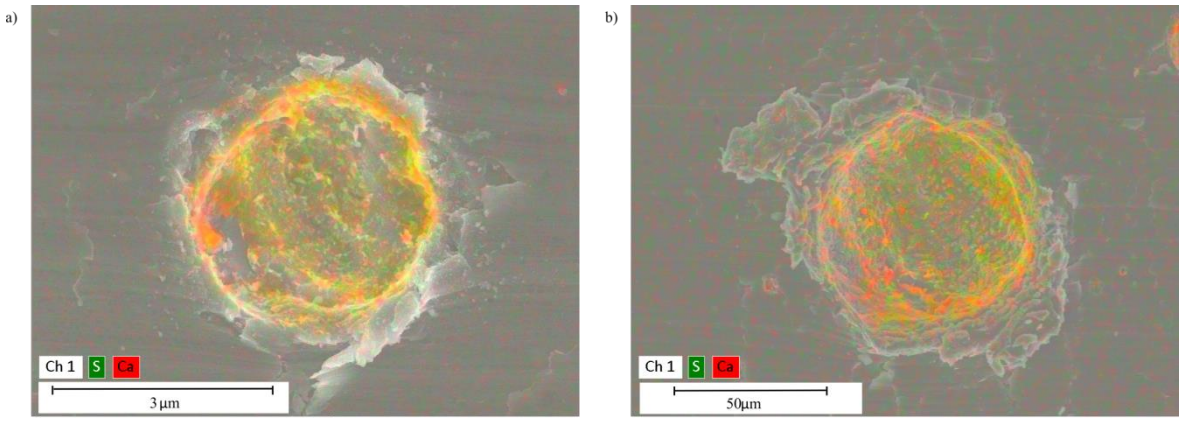

Figure L3 Secondary electron images of two craters from G161014#1 (3.97 km s^{-1}). The image has been overlain with EDX data from sulphur (green) and calcium (red). The areas that appear orange represent the location of both sulphur and calcium, thus indicating anhydrite.

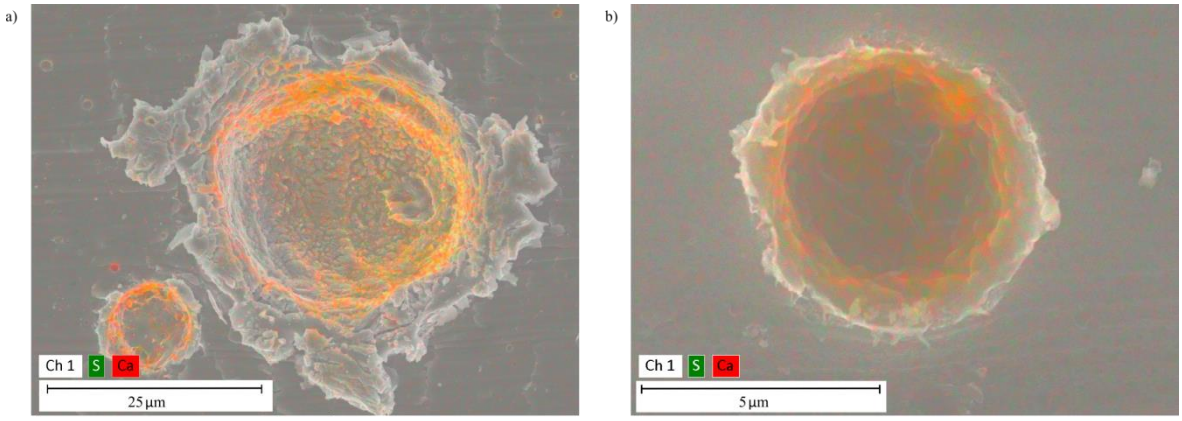

Figure L4 Secondary electron images of two craters from G100714#2 (4.90 km s^{-1}). The image has been overlain with EDX data from sulphur (green) and calcium (red). The areas that appear orange represent the location of both sulphur and calcium, thus indicating anhydrite.

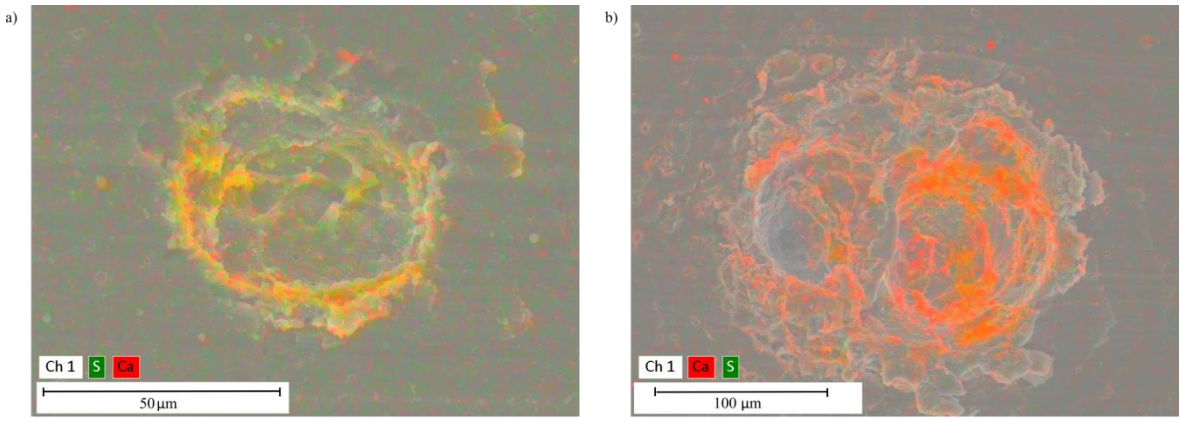

Figure L5 Secondary electron images of two craters from G071114#1 (5.86 km s^{-1}). The image has been overlain with EDX data from sulphur (green) and calcium (red). The areas that appear orange represent the location of both sulphur and calcium, thus indicating anhydrite.

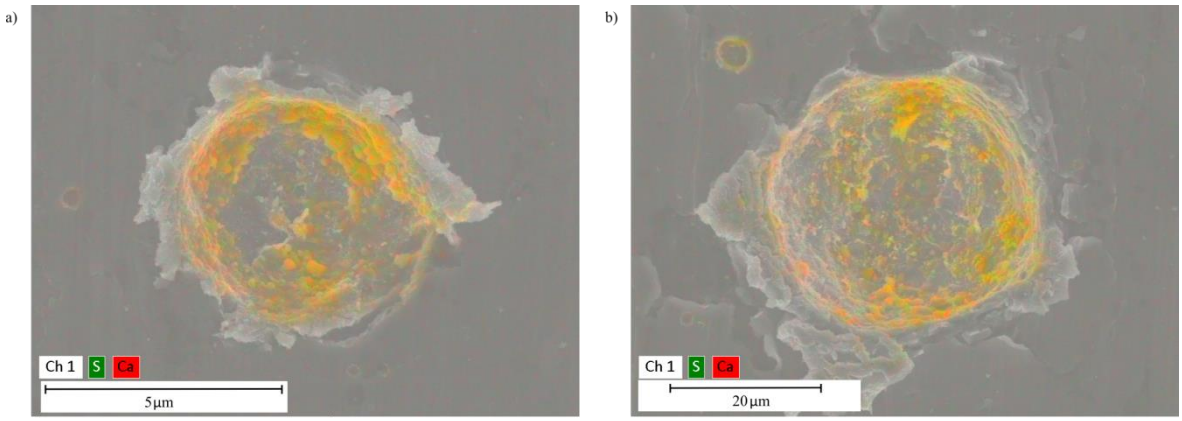

Figure L6 Secondary electron images of two craters from G201114#1 (anhydrite). The image has been overlain with EDX data from sulphur (green) and calcium (red). The areas that appear orange represent the location of both sulphur and calcium, thus indicating anhydrite.